Списак објављених радова и других публикација разврстаних по важећим категоријама прописаним Правилником **након избора у претходно звање**

1. МОНОГРСФИЈЕ, МОНОГРАФСКЕ СТУДИЈЕ, ТЕМАТСКИ ЗБОРНИЦИ, ЛЕСКИКОГРАФСКЕ И КАРТОГРАФСКЕ ПУБЛИКАЦИЈЕ МЕЂУНАРОДНОГ ЗНАЧАЈА (М 10)

М 14 монографска студија/поглавље у књизи М12 или рад у тематском зборнику међународног значаја

1. Dalibor L. Sekulić, **Zorica Ž. Lazarević**, Nebojša Ž. Romčević,
   Electrical characterization of nanostructured ferrite ceramics by using AC impedance spectroscopy
   W. E. Lee et al. (eds.), Proceedings of the III Advanced Ceramics and Applications Conference, Springer Atlantis Press, pp. 115-127, 2016, doi 10.2991/978-94-6239-157-4_9.

2. S. Kostić, **Z.Ž. Lazarević**, M. Gilić, M. Petrović, M. Romčević, N.Ž. Romčević, D.L. Sekulić,
   Structural and optical studies of oxide single crystals grown by the Czochralski method
   W. E. Lee et al. (eds.), Proceedings of the III Advanced Ceramics and Applications Conference, Springer Atlantis Press, pp. 193-203, 2016, doi 10.2991/978-94-6239-157-4_14.

2. РАДОВИ ОБЈАВЉЕНИ У НАУЧНИМ ЧАСОПИСИМА МЕЂУНАРОДНОГ ЗНАЧАЈА (М 20)

М 21 Рад у врхунском међународном часопису

1. **Z.Ž. Lazarević**, Č. Jovalekić, A. Recnik, V.N. Ivanovski, A. Milutinović, M. Romčević, M.B. Pavlović, B. Cekić, N.Ž. Romčević,
   Preparation and characterization of spinel nickel ferrite obtained by the soft mechanochemically assisted synthesis,
   Materials Research Bulletin, **48**(2), (2013) 404-415, **(IP-2.105, 55/232, Materials Science, Multidisciplinary).**

2. **Z.Ž. Lazarević**, Č. Jovalekić, A. Milutinović, D. Sekulić, V.N. Ivanovski, A. Rečnik, B. Cekić, N.Ž. Romčević,
   Nanodimensional spinel $NiFe_2O_4$ and $ZnFe_2O_4$ ferrites prepared by soft mechanochemical synthesis,
   Journal of Applied Physics, **113**, (2013) 187221-187221-11, (**IP-2.185, 39/136, Physics, Applied**).

3. **Z.Ž. Lazarević**, Č. Jovalekić, D.L. Sekulić, A. Milutinović, S. Baloš, M. Slankamenac, N.Ž. Romčević,
   Structural, electrical and dielectric properties of spinel nickel ferrite prepared by soft mechanochemical synthesis,

Materials Research Bulletin, **48**(10), (2013) 4368-4378, **(IP-2.105, 55/232, Materials Science, Multidisciplinary).**

4. A. Milutinović, **Z. Lazarević**, Č. Jovalekić, I. Kuryliszyn-Kudelska, M. Romčević, S. Kostić, N. Romčević,
   The cation inversion and magnetization in nanopowder zinc ferrite obtained by soft mechanochemical processing,
   Materials Research Bulletin, 48(11), (2013) 4759-4768, **(IP-2.105, 55/232, Materials Science, Multidisciplinary).**

5. Dalibor L. Sekulić, **Zorica Ž. Lazarević**, Miljko V. Satarić, Čedomir D. Jovalekić, Nebojša Ž. Romčević,
   Temperature-dependent complex impedance, electrical conductivity and dielectric studies of MFe_2O_4 (M=Mn, Ni, Zn) ferrites prepared by sintering of mechanochemical synthesized nanopowders,
   Journal of Materials Science: Materials in Electronics, **26**, (2015) 1291-1303, (**IP-1.966, 62/248, Engineering, Electrical & Electronic**).

6. S. Kostić, **Z.Ž. Lazarević**, V. Radojević, A. Milutinović, M. Romčević, N.Ž. Romčević, A. Valčić,
   Study of structural and optical properties of YAG and Nd:YAG single crystals,
   Materials Research Bulletin, **63**, (2015) 80-87, **(IP-2.435, 74/271, Materials Science, Multidisciplinary).**

7. **Zorica Ž. Lazarević**, Aleksandra N. Milutinović, Čedomir D. Jovalekić, Valentin N. Ivanovski, Nina Daneu, Ivan Mađarević, Nebojša Ž. Romčević,
   Spectroscopy investigation of nanostructured nickel-zinc ferrite obtained by mechanochemical synthesis,
   Materials Research Bulletin, **63**, (2015) 239-247, **(IP-2.435, 74/271, Materials Science, Multidisciplinary).**

8. N. Romcevic, M. Romcevic, W.D. Dobrowolski, L. Kilanski, M. Petrovic, J. Trajic, B. Hadzic, **Z. Lazarevic**, M. Gilic, J.L. Ristic-Djurovic, N. Paunovic, A. Reszka, B.J. Kowalski, I.V. Fedorchenko, S.F. Marenkin,
   Far-infrared spectroscopy of $Zn_{1-x}Mn_xGeAs_2$ single crystals: plasma damping influence on plasmon e phonon interaction,
   Journal of Alloys and Compound, **649**, (2015) 375-379, **(IP-3.014, 58/271, Materials Science, Multidisciplinary).**

<u>M 22 Рад у истакнутом међународном часопису</u>

1. **Z. Lazarević**, S. Kostić, V. Radojević, M. Romčević, M. Gilić, M. Petrović-Damjanović, N. Romčević,
   Raman spectroscopy of bismuth silicon oxide single crystals grown by the Czochralski technique,
   Physica Scripta, **T157**, (2013) 014046, (**IP-1.296, 40/78, Physics, Multidisciplinary**).

2. **Z.Ž. Lazarević**, Č. Jovalekić, V.N. Ivanovski, A. Rečnik, A. Milutinović, B.

Cekić, N.Ž. Romčević,
Characterization of partially inverse spinel $ZnFe_2O_4$ with high saturation magnetization synthesized via soft mechanochemically assisted route,
Journal of Physics and Chemistry of Solids, **75**(7), (2014) 869-877, (**IP-1.853, 33/67, Physics, Condensed Matter**).

3. J. Trajić, M. Gilić, M. Romčević, N. Romčević, G. Stanišić, **Z. Lazarević**, D. Joksimović, I.S. Yahia,
Far-infrared investigations of the surface modes in CdS thin films,
Physica Scripta, **T162**, (2014) 014031, (**IP-1.126, 43/78, Physics, Multidisciplinary**).

4. S. Kostić, **Z. Lazarević**, M. Romčević, V. Radojević, A. Milutinović, G. Stanišić, M. Gilić,
Spectroscopic characterization of YAG and Nd:YAG single crystals,
Physica Scripta, **T162**, (2014) 014026, (**IP-1.126, 43/78, Physics, Multidisciplinary**).

5. D. Sekulić, **Z.Ž. Lazarević**, Č. Jovalekić, A. Rečnik, M. Romčević, B. Hadžić, N.Ž. Romčević,
The comparative study of the structural and the electrical properties of the nano spinel ferrites prepared by the soft mechanochemical synthesis,
Science of Sintering, **46**(1), (2014) 235-245, **(IP-0.575, 14/26, Materials Science, Ceramics).**

6. Aleksandra Milutinović, **Zorica Ž. Lazarević**, Milka Jakovljević, Branka Hadzić, Milica Petrović, Martina Gilić, Witold Daniel Dobrowolski, Nebojša Ž. Romčević,
Optical properties of layered III-VI semiconductor γ-InSe:M (M:Mn, Fe,Co,Ni),
Journal of Physics and Chemistry of Solids, **89,** (2016) 120-127, **(IP-2.059, 34/67, Physics, Condensed Matter).**

7. Dalibor L. Sekulić, **Zorica Z. Lazarević**, Čedomir D. Jovalekić, Aleksandra N. Milutinović, Nebojša Z. Romčević,
Impedance spectroscopy of nanocrystalline $MgFe_2O_4$ and $MnFe_2O_4$ ferrite ceramics: effect of grain boundaries on the electrical properties,
Science of Sintering, **48**(1), (2016) 17-28, (**IP-0.736, 15/26, Materials Science, Ceramics**).

8. Hana Ibrahim Elswie, **Zorica Ž. Lazarević**, Vesna Radojević, Martina Gilić, Maja Rabasović, Dragutin Šević, Nebojša Ž. Romčević,
The Bridgman method growth and spectroscopic characterization of calcium fluoride single crystals,
Science of Sintering, **48**(3), (2016) 333-341, (**IP-0.736, 15/26, Materials Science, Ceramics**).

9. **Zorica Ž. Lazarević**, Čedomir Jovalekić, Martina Gilić, Valentin Ivanovski, Ana Umićević, Dalibor Sekulić, Nebojša Ž. Romčević,
Yttrium orthoferrite powder obtained by the mechanochemical synthesis,
Science of Sintering, **49**(3), (2017) 277-284, (**IP-0.736, 15/26, Materials Science, Ceramics**).

M23 Рад у међународном часопису

1. **Z.Ž. Lazarević**, S. Kostić, V. Radojević, M. Romčević, B. Hadžić, J. Trajić, N.Ž. Romčević,
   Spectroscopy study of $Bi_{12}GeO_{20}$ single crystals,
   Optoelectronics and Advanced Materials - Rapid Communications, **7**(1-2), (2013) 58-61, (**IP-0.449, 223/251, Materials Science, Multidisciplinary**).

2. J. Trajić, N. Romčević, M. Romčević, **Z. Lazarević**, T.A. Kuznetsova, D.R. Khokhlov,
   Plasmon - ionized impurity - phonon interaction in PbTe doped with Ni,
   Optoelectronics and Advanced Materials - Rapid Communications, **7**(7-8), (2013) 536-540, (**IP-0.449, 223/251, Materials Science, Multidisciplinary**).

3. **Z.Ž. Lazarević**, Č. Jovalekić, A. Milutinović, D. Sekulić, M. Slankamenac, M. Romčević, N.Ž. Romčević,
   Study of $NiFe_2O_4$ and $ZnFe_2O_4$ spinel ferrites prepared by soft mechanochemical synthesis,
   Ferroelectrics, **448**(1), (2013) 1-11, (**IP-0.433, 62/67, Physics, Condensed Matter).**

4. **Z.Ž. Lazarević**, Č. Jovalekić, A. Milutinović, D. Sekulić, M. Romčević, M. Slankamenac, N.Ž. Romčević,
   Spectroscopy investigation of nanostructured zinc ferrite obtained by mechanochemical synthesis,
   Optoelectronics and Advanced Materials - Rapid Communications, **7**(9-10), (2013) 720-725, (**IP-0.449, 223/251, Materials Science, Multidisciplinary**).

5. **Z.Ž. Lazarević**, Č. Jovalekić, A. Milutinović, N. Daneu, M. Romčević, Đ. Jovanović, N. Romčević,
   Spectroscopy investigation of nanostructured nickel-zinc ferrite obtained by mechanochemical synthesis,
   Optoelectronics and Advanced Materials - Rapid Communications, **9**(1-2), (2015) 102-106, (**IP-0.412, 252/271, Materials Science, Multidisciplinary**).

6. M. Petrović, M. Romčević**,** R. Kostić, N. Romčević, W.D. Dobrowolski, M. Gilić, B. Hadžić, J. Trajić, D. Stojanović, **Z.Ž. Lazarević**,
   Optical properties of Cd1-xMnxS nanoparticles: off-resonance Raman spectroscopy,
   Optoelectronics and Advanced Materials - Rapid Communications, **10**(3-4), (2016) 77-179, (**IP-0.470, 253/275, Materials Science, Multidisciplinary**).

7. H.I. Elswie, S. Kostić, V. Radojević, N.Ž. Romčević, B. Hadžić, J. Trajić, **Z.Ž. Lazarević**,
   Growth, characterization and optical quality of calcium fluoride single crystals grown by the Bridgman method,
   Optoelectronics and Advanced Materials - Rapid Communications, **10**(7-8), (2016) 522-525, (**IP-0.470, 253/275, Materials Science, Multidisciplinary**).

8. S.P. Dimitrijević, **Z.Ž. Lazarević**, M. Rajčić-Vujasinović, S.B. Dimitrijević,

M. Petrović, M. Gilić, B.M. Jokić,
Raman spectroscopy study of anodic film on $Ag_{43}Cu_{37}Zn_{20}$ alloy,
Optoelectronics and Advanced Materials - Rapid Communications, **10**(9-10), (2016) 777-780, (**IP-0.470, 253/275, Materials Science, Multidisciplinary**).

3. ЗБОРНИЦИ СА МЕЂУНАРОДНИХ НАУЧНИХ СКУПОВА (М 30)

М 32 Преавање по позиву са међународног скупа штампано у целини

1. **Z.Ž. Lazarević**, D. Sekulić, Č. Jovalekić, M. Romčević, A. Milutinović, N.Ž. Romčević,
New approach and comparative studies of structural and electrical properties of nano spinel ferites prepared by soft mechanochemical synthesis,
The Serbian Ceramic Society Conference - Advanced Ceramics and Application II, Sept 30-Oct 01, 2013, Belgrade, Serbia, Program and The Book of Abstracts, INV2, 12.

2. **Zorica Ž. Lazarević**,
Study of nanodimensional spinel $Ni_{0.5}Zn_{0.5}Fe_2O_4$ ferrite prepared by mechanochemical synthesis,
The Fourth Serbian Ceramic Society Conference - Advanced Ceramics and Application IV, September 21-23, 2015, Belgrade, Serbia, Program and The Book of Abstracts, INV2, 40-41.

3. **Zorica Ž. Lazarević,** Janez Križan, Gregor Križan, Valentin N. Ivanovski, Miodrag Mitrić, Martina Gilić, Nebojša Ž. Romčević,
Spectroscopy study of LiFePO4 cathode materials for Li-ion battery prepared in the thermo-acoustic,
The Sixth Serbian Ceramic Society Conference - Advanced Ceramics and Application, September 18-20, 2017, Belgrade, Serbia, Program and The Book of Abstracts, INV-REHA3, 56.

М 33 Саопштење са међународног скупа штампано у целини

1. Zorica Lazarević**, Stevan Dimitrijević, Silvana Dimitrijević, Milica Petrović,** Martina Gilić, Nebojša Romčević,

Raman spectroscopy study of $Ag_{43}Cu_{37}Zn_{20}$ alloy,

Ther 47th International October Conference on Mining and Metallurgy, October 4-6, 2015, Bor Lake, Bor, Serbia, Proceedings, 155-158.

2. M. Gilić, M. Petrović, B. Hadžić, **Z.Ž. Lazarević**, M. Romčević, J. Trajić, N.Ž. Romčević,
Optical properties of plastically deformed copper: ellipsometry and Raman study,
W.E. Lee et al. (eds.), Proceedings of the III Advanced Ceramics and Applications Conference, Springer Atlantis Press, pp. 173-182, 2016, doi 10.2991/978-94-6239-157-4_12.

3. M. Petrović, J. Trajić, M. Gilić, M. Romčević, B. Hadžić, **Z.Ž. Lazarević**, D. Stojanović,
Optical properties and electron-phonon interactions of CdTe1-XSex(In) single crystal,
W.E. Lee et al. (eds.), Proceedings of the III Advanced Ceramics and Applications Conference, Springer Atlantis Press, pp. 183-191, 2016, doi 10.2991/978-94-6239-157-4_13.

4. Dalibor L. Sekulić, **Zorica Ž. Lazarević** and Nebojša Ž. Romčević,
Structural, electrical conduction and dielectric studies of mechano-synthesized manganese nanoferrite,
Lee Bill et al. (eds.), Proceedings of the IV Advanced Ceramics and Applications Conference, Springer Atlantis Press, pp. 155-172, 2017, doi 10.2991/978-94-6239-213-7_13.

5. **Zorica Ž. Lazarević**, Martina Gilić, Milica Petrović, Nebojša Romčević, Čedomir Jovalekić, Dalibor L. Sekulić and Valentin N. Ivanovski,
Study of nanodimensional spinel $Ni_{0.5}Zn_{0.5}Fe_2O_4$ ferrite prepared by mechanochemical synthesis,
Lee Bill et al. (eds.), Proceedings of the IV Advanced Ceramics and Applications Conference, Springer Atlantis Press, pp. 187-202, 2017, doi 10.2991/978-94-6239-213-7_15.

6. M. Gilić, M. Petrović, B. Hadžić, M. Romčević, J. Trajić, N. Romčević and **Z. Lazarević**,
Structural properties of Cu-Se-$CuSe_2$ thin films,
Lee Bill et al. (eds.), Proceedings of the IV Advanced Ceramics and Applications Conference, Springer Atlantis Press, pp. 235-256, 2017, doi 10.2991/978-94-6239-213-7_18.

7. D. L. Sekulic, **Z. Lazarevic**, C. Jovalekic and N. Romcevic,
Characterization of yttrium orthoferrite ($YFeO_3$) nanoparticles as humidity sensor materials at room temperature,
2017 IEEE 30th International Conference on Microelectronics (MIEL 2017), Niš, Serbia, October, 9th-11th, 2017.

M 34 Саопштење са међународног скупа штампано у изводу

1. **Zorica Lazarević**, Dalibor Sekulić, Aleksandra Milutinović, Izabela Kuryliszyn-Kudelska, Nebojša Romčević,
Preparation, characterizatiion and investigations of structural, magnetic and electrical properties of nano size zinc ferrite,
2nd Conference of the Serbian Ceramic Society, Jun 5-7, 2013, Belgrade, Serbia, Program and Book of Abstracts, P-47, 91.

2. **Z.Ž. Lazarević**, S. Kostić, N.Ž. Romčević,
Growth and spectroscopic characterization of $Y_3Al_5O_{12}$ -YAG single crystals,
Fifteenth annual conference YUCOMAT 2013, Herceg Novi, Montenegro, September 2-6, 2013, Programme & the Book of Abstracts, P.S.B. 24, 107.

3. D.L. Sekulić, **Z.Ž. Lazarević**, N.Ž. Romčević,
Electrical and dielectric characterization of nanostructural ceramic materials by complex impedance spectroscopy,
The Third Serbian Ceramic Society Conference - Advanced Ceramics and Application, September 29-October 1, 2014, Belgrade, Serbia, Program and The Book of Abstracts, 53.

4. Dalibor L. Sekulić, **Zorica Ž. Lazarević**, Čedomir D. Jovalekić, Miloš Živanov, Nebojša Ž. Romčević,
Characterization of nanostructued Ni-ferrites as humidity sensor materials at room temperature,
10th European Conference on Magnetic Sensors and Actuators -EMSA 2014, July 6-9, 2014, Vienna, Austria, Book of Abstracts, TP26, 136.

5. Dalibor L. Sekulić, **Zorica Ž. Lazarević**, Čedomir D. Jovalekić, Miloš B. Živanov, Nebojša Ž. Romčević,
Study on electrical and dielectric properties of Ni–Zn ferrite nanoparticles synthesized by soft mechanochemical technique,
5th International Advances in Applied Physics and Materials Science Congress & Exhibition–APMAS 2015, 16–19 April 2015, Lykia, Oludeniz, Turkey, 79 (ID–72).

6. Dalibor L. Sekulić, **Z.Ž. Lazarević**, Č. Jovalekić N.Ž. Romčević,
Electrical and dielectric characterization of $Zn_xNi_{1-x}Fe_2O_4$ *ferrite ceramics prepared by sintering of nanopowders*,
The Fourth Serbian Ceramic Society Conference - Advanced Ceramics and Application IV, September 21-23, 2015, Belgrade, Serbia, Program and The Book of Abstracts, INV1, 40.

7. M. Petrovic, M. Gilic, B. Hadzic, M. Romcevic, N. Romcevic, J. Trajic, **Z. Lazarevic**,
The Fourth Serbian Ceramic Society Conference - Advanced Ceramics and Application IV, September 21-23, 2015, Belgrade, Serbia, Program and The Book of Abstracts, P15, 68.

8. Dalibor L. Sekulić, **Zorica Ž. Lazarević**, Čedomir D. Jovalekić, Nebojša Ž. Romčević,
Electrical characterization of $YFeO_3$ *nanoferrite and its potential application for humidity sensing*,
The Fifth Serbian Ceramic Society Conference - Advanced Ceramics and Application V, September 21-23, 2016, Belgrade, Serbia, Program and The Book of Abstracts, INV4, 37.

9. **Zorica Ž. Lazarević,** Čedomir Jovalekić, Dalibor Sekulić, Valentin N. Ivanovski, Ana Umićević, Martina Gilić, Nebojša Ž. Romčević,
Spectroscopy characterization of $YFeO_3$ *obtained by the mechanochemical synthesis*,
The Fifth Serbian Ceramic Society Conference - Advanced Ceramics and Application V, September 21-23, 2016, Belgrade, Serbia, Program and The Book

of Abstracts, OR4, 45-46.

10. **Zorica Ž. Lazarević,** Hana Ibrahim Elswie, Vesna Radojević, Dalibor Sekulić, Slobodanka Kostić, Maja Rabasović, Dragutin Šević, Nebojša Ž. Romčević, *The Bridgman method growth, spectroscopic characterization and photoluminescence of calcium fluoride single crystals,* The Fifth Serbian Ceramic Society Conference - Advanced Ceramics and Application V, September 21-23, 2016, Belgrade, Serbia, Program and The Book of Abstracts, P38, 73-74.

11. Hana Ibrahim Elswie, **Zorica Ž. Lazarević,** Vesna Radojević, C*haracterization of optical polymer composites based on single crystals,* The Sixth Serbian Ceramic Society Conference - Advanced Ceramics and Application, September 18-20, 2017, Belgrade, Serbia, Program and The Book of Abstracts, P4, 65-66.

12. Silvana B. Dimitrijević, **Zorica Ž. Lazarević,** Stevan P. Dimitrijević, C*haracterization of Au-mercaptotriazole crystals using the spectroscopy methods,,* The Sixth Serbian Ceramic Society Conference - Advanced Ceramics and Application, September 18-20, 2017, Belgrade, Serbia, Program and The Book of Abstracts, INV-BMS1, 47.

Electrical Characterization of Nanostructured Ferrite Ceramics by Using AC Impedance Spectroscopy

Dalibor L. Sekulić, Zorica Ž. Lazarević and Nebojša Z. Romčević

Abstract In this paper, we report the electrical properties of nanostructured ferrite ceramics by using AC impedance spectroscopy as a function of frequency (100 Hz–10 MHz) in the temperature range from 25 to 100 °C. The nanocrystalline $NiFe_2O_4$ and $ZnFe_2O_4$ ferrites were successfully prepared by a conventional sintering of nanosized powders, synthesized by a soft mechanochemical route. X-ray diffraction measurements and scanning electron microscope study confirmed the formation of single cubic spinel structure and nano-dimensional nature of the prepared samples. The temperature-dependent plots between real and imaginary parts of complex impedance reveal the presence of two relaxation regimes which are attributed to grain and grain boundary responses. Complex impedance analysis by means of an equivalent circuit model has been used to separate the grain and grain boundary resistance of these ferrite materials. The temperature dependence of both grain boundary and grain conductivity well follow the Arrhenius law with estimated activation energy of 0.481 and 0.401 eV for $NiFe_2O_4$, and 0.412 and 0.387 eV for $ZnFe_2O_4$, respectively. Moreover, the analysis of experimental impedance data indicates the negative temperature coefficient of resistance (NTCR) behavior of both samples usually shown by semiconductors. The conduction mechanism may be due to the hopping of charge carriers present in these ferrite materials.

Keywords Impedance spectroscopy · Nanostructured ceramics · Ferrites · Electrical properties

D.L. Sekulić (✉)
Faculty of Technical Sciences, University of Novi Sad, Novi Sad, Serbia
e-mail: dalsek@uns.ac.rs

Z.Ž. Lazarević · N.Z. Romčević
Institute of Physics, University of Belgrade, Belgrade, Serbia

W.E. Lee et al. (eds.), *Proceedings of the III Advanced Ceramics and Applications Conference*, DOI 10.2991/978-94-6239-157-4_8

1 Introduction

In the past two decades, there is a growing interest in nanostructured ceramic materials because of their properties which are different and very often superior to conventional material. Ceramic materials which belong to the ferrospinel family with general formula MFe_2O_4 (M is a divalent metal cation) are widely used in many electronic and magnetic devices because of their high electrical resistivity and consequently low eddy current losses, as well as high dielectric constant, high initial permeability and moderate saturation magnetization [1]. Spinel ferrites have attracted considerable attention due to technological importance in wide range of potential applications such as high frequency devices, sensors, computer memories, magnetic drug delivery, microwave absorbers etc.

In general, the cation distribution in the spinel lattice can be described with formula $(M_{1-\delta}Fe_{\delta})[M_{\delta}Fe_{2-\delta}]O_4$, where δ denotes the degree of inversion defined as the fraction of the tetrahedral sites occupied by Fe^{3+} cations and its value depends on the method of synthesis [2]. Typically two extreme type of spinel structure can be found: normal (δ = 0) and inverse (δ = 1) spinel. It is well known that Ni^{2+} and Zn^{2+} ions have very strong preferences for the octahedral and tetrahedral sites as depicted by square and curled brackets, respectively, making $NiFe_2O_4$ a model inverse ferrite and $ZnFe_2O_4$ a model normal ferrite. The schematic representations of the unit cells of the nickel and zinc ferrite spinel structure are given in Fig. 1.

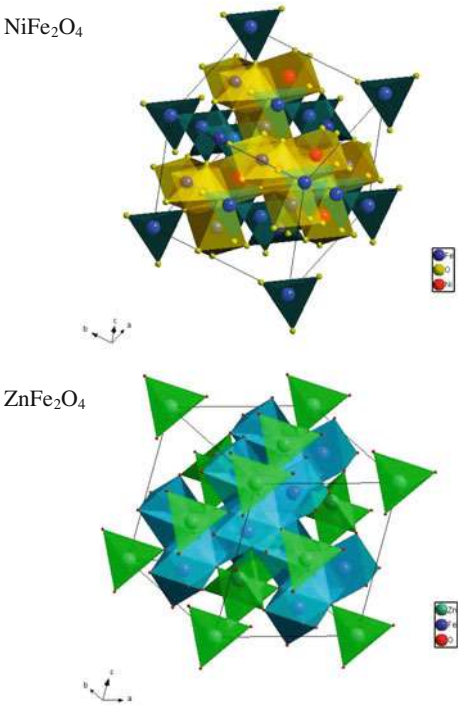

Fig. 1 Schematic representations of the unit cells of $NiFe_2O_4$ and $ZnFe_2O_4$ ferrite spinel structures

However, the mixed spinel structure is more often present in the case of nano–sized ferrites, where cations are distributed in a mixed mode (M^{2+} occupying both octahedral and tetrahedral sites).

It is well known that the physical properties of the ferrite nanomaterials are strongly dependent on the method of preparation. To date a broad variety of techniques were successfully developed for synthesis of nanocrystalline ferrites such as sol–gel [3], co-precipitation [4], solid-state reaction [5] and others.

Electrical resistivity is one of the important properties of the ferrites, especially in view of their potential applications. A common approach to investigate electrical properties of polycrystalline ferrite materials is based on application of AC impedance spectroscopy [6]. Impedance spectroscopy is a non-destructive and widely used technique for the characterization of electrically responses arising from different electrical active regions in a material, both qualitatively by demonstrating their existence and quantitatively by utilizing appropriate impedance data analysis. The complex impedance analysis enables us to resolve the effect of grains and grain boundaries, two main components which comprise the microstructure of ceramics, and the correspondence between them is important in understanding the overall properties of ceramic materials [7]. To extract the information about the resistive and capacitive values of grain and grain boundary regions, it is necessary to adopt electrical model that most precisely represents electrical characteristics of the considered material at different frequencies and temperatures. In general, each region can be modeled using an electroactive element ideally consisting of a resistance R and a capacitance C connected in parallel and the simplest appropriate equivalent circuit is a series array of parallel R–C elements [8]. These quantities can be treated as fitting parameters whose values can be evaluated from the best fit to the impedance spectrum. The fitting is relatively unambiguous since the elements of equivalent circuits dominate in different frequency regions.

In this paper, we have carried out the AC impedance studies of nanostructured $NiFe_2O_4$ and $ZnFe_2O_4$ ceramics with the main objective to investigate the electrical properties and its correlation with their microstructure. Electrical properties associated with grains and grain boundaries were studied in a wide range of frequencies and temperatures. The novel approach to mechanochemical processing, so–called soft mechanochemical route [9] was used for the synthesis of the ferrite materials. This method does not require expensive starting materials or extremely high temperature and is environmentally friendly.

2 Experimental Details

The $NiFe_2O_4$ and $ZnFe_2O_4$ ferrites were synthesized by means of soft mechanochemical route using high-purity hydroxide precursors of Merck $Ni(OH)_2$ and $Zn(OH)_2$ with 95 % purity, respectively, and $Fe(OH)_3$ made in the laboratory with 99.5 % purity. The $Fe(OH)_3$ powder was prepared by adding equimolar amounts of NaOH solution (25 % mass), made from 99 % purity NaOH (Merck), to

the $FeCl_3$ solution (25 % mass), made from 99 % purity $FeCl_3 \times 6H_2O$ (Merck). Obtained hydrated ferric hydroxide ($Fe(OH)_3 \times nH_2O$) in the form of dark brown was filtrated, washed with large amounts of water and dried in a vacuum desiccator. Before milling, the $Fe(OH)_3 \times nH_2O$ powder was heated at 105 °C for 24 h. Mechanochemical synthesis was carried out by planetary ball mill (Fritsch Pulverisette 5) in air atmosphere for 18 and 25 h for $ZnFe_2O_4$ and $NiFe_2O_4$, respectively. Required milling time for obtaining single-phase ferrites was experimentally determined by X-ray diffraction technique. Using a cold isostatic press, obtained ferrite powders were pressed into circular disc shaped pellets with a diameter of 8 mm and a thickness of 2 mm. The so prepared pallets were sintered at 1100 °C for 2 h (Lenton–UK oven) without pre-calcinations step. Heating rate was 10 °C/min with nature cooling in air atmosphere.

The phase purity and crystal structure of sintered samples were analysed by using X-ray diffraction (XRD, Model Philips PW 1050 diffractometer) with Ni filtered CoKα radiation of 1.78897 Å at room temperature. XRD data were collected in a wide range of Bragg's angles ($10° \leq 2\theta \leq 80°$) with the scanning step size of 0.05° in a 10 s per step of counting time. The lattice parameter and crystallite (grain) size were calculated from XRD data. The microstructures of sintered ferrites were recorded at room temperature using scanning electron microscope (SEM, Model JEOL JSM–6460 LV) applied on a gold coated surface of samples. The sintered (bulk) density of the samples was measured by applying Archimedes' principle [2] at room temperature.

In order to study the electrical properties of ferrite ceramics by means of complex impedance spectroscopy, the surfaces of as–prepared pellets were polished properly and electrodes were formed by with high purity silver paste deposited on opposite sides of the pellets, which were cured for 24 h. The AC electrical parameters of $NiFe_2O_4$ and $ZnFe_2O_4$ were measured in a wide frequency range of 100 Hz to 10 MHz at different temperatures between 25 and 100 °C using a computer-controlled Impedance Analyzer HP–4194A with a laboratory set of temperature control equipment. The experimentally measured parallel values of the resistance R_p and the capacitance C_p were converted and displayed in the form of complex impedance as follows [7]:

$$Z^*(\omega) = Z'(\omega) - jZ''(\omega) = \left(\frac{1}{R_p} + j\omega C_p\right)^{-1}. \quad (1)$$

The details of this measurement procedure are same as presented in [2]. For fitting and analysis of the impedance data, commercially available EIS Spectrum Analyzer software [10] is used with about 1.5 % of fitting errors.

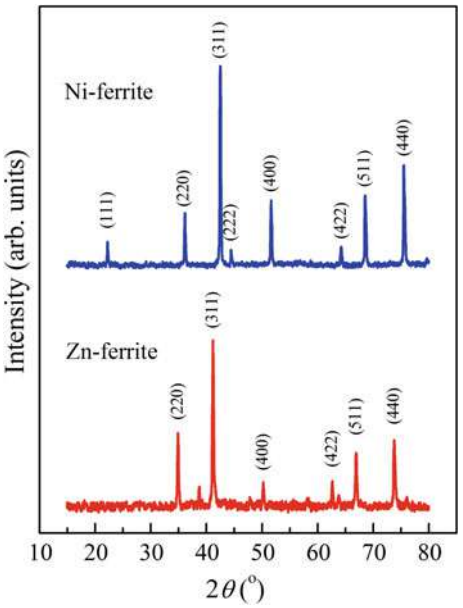

Fig. 2 X-ray diffraction patterns of $NiFe_2O_4$ and $ZnFe_2O_4$ ferrites sintered at 1100 °C/2 h

3 Results and Data Analysis

3.1 Structural Analysis

The room temperature X-ray diffraction patterns of as-prepared ferrite ceramic samples are presented in Fig. 2. All of the Bragg reflections appearing in the diffraction spectra were indexed with the standard patterns reported in PCPDF cards No. 89–4927 and No. 89–7412 for $NiFe_2O_4$ and $ZnFe_2O_4$, respectively. The presence of diffraction planes (111), (220), (311), (222), (400), (422), (511) and (440) confirms the formation of cubic spinel ferrite structure with the *Fd3 m* space group. No additional secondary phases, amorphous forms or impurities were detected, indicating the high quality and single phase of the prepared ferrite ceramics in both cases. Further, the sharp XRD peaks point to the polycrystalline nature of sintered samples.

From the full width at half maximum of the most intense line (311) in the XRD spectrum, the average crystallite size of spinel ferrite samples was calculated by using the Debye-Scherrer equation [11]. It was found that the average grain sizes are about 92 and 48 nm for $NiFe_2O_4$ and $ZnFe_2O_4$ ferrites, respectively. From the Rietveld refinement procedure, the related lattice constants were found to be 8.276 and 8.418 for sintered $NiFe_2O_4$ and $ZnFe_2O_4$ ferrite samples, respectively, which agrees well with the previously reported values [12]. The visible shift of Bragg reflections towards higher 2θ angles in the case of $NiFe_2O_4$ corresponds to the

Table 1 Structural characteristics of ferrite samples

Ferrite sample	Lattice constant (Å)	Crystallite size (nm)	Sintered density (g/cm^3)
$NiFe_2O_4$	8.276	92	4.43
$ZnFe_2O_4$	8.418	48	4.96

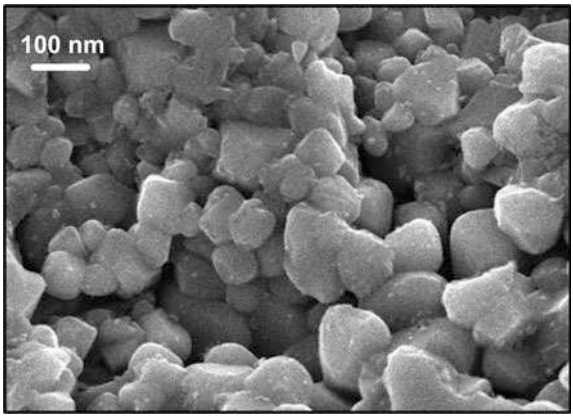

Fig. 3 SEM micrographs of $NiFe_2O_4$ ferrite sintered at 1100 °C/2 h

smallest lattice constant [2]. The bulk density values and other crystallographic data are summarized in Table 1.

The microstructures of ferrite sample sintered at 1100 °C for 2 h are given in Fig. 3. The SEM image of $NiFe_2O_4$ clearly show the presence of conducting grains separated from each other by the well-defined grain boundaries. These two main components comprise the microstructure of both ferrites under study and the correspondence between them is important in understanding the overall properties of these materials. The grain boundaries control the electrical properties of the ferrites, especially in the case of nanocrystalline ferrites [7].

3.2 Complex Impedance Analysis

In order to determine the correlation of the electrical properties of nanocrystalline ferrite samples with its microstructures, the AC impedance spectroscopy was used in a wide range of frequency and temperature. The experimental data for the complex impedance provide information on the resistive (real part, Z') and reactive (imaginary part, Z'') components.

Figure 4 shows the variation of Z' with frequency at different temperatures. It can be noticed that the magnitude of Z' decreases with an increase in both applied frequency and temperature, indicating an increase in AC electrical conductivity of the samples with increasing frequency and temperature. This trend provides an

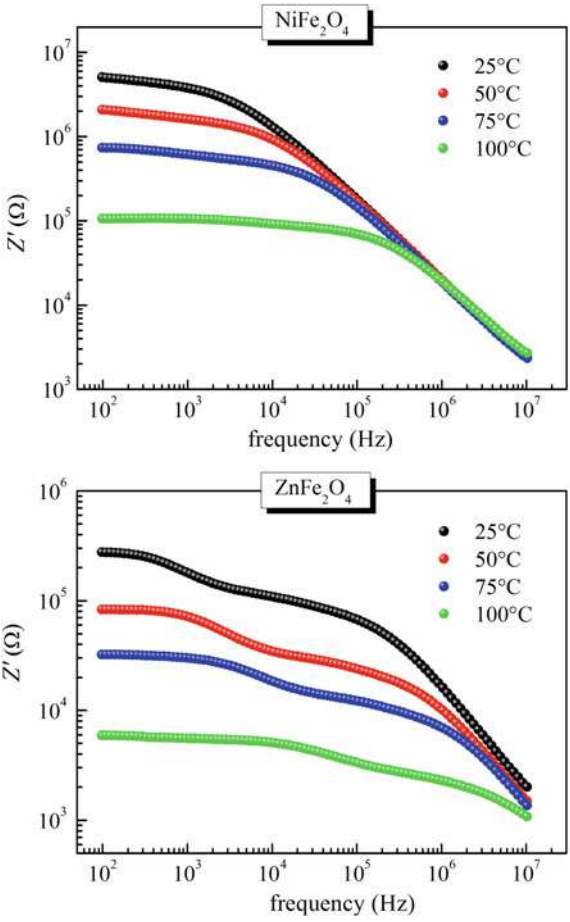

Fig. 4 Variation of the real part of complex impedance with frequency for $NiFe_2O_4$ and $ZnFe_2O_4$ ferrites at different temperatures

indication that the present ferrites behave like the semiconducting materials [2, 9]. Further, $ZnFe_2O_4$ shows lower values of real part of the impedance compared to the $NiFe_2O_4$ which means that $ZnFe_2O_4$ has a higher conductivity value at each frequency and temperature. In the case of $NiFe_2O_4$, the Z' shows only one dispersion, probably due to a limited frequency range used in this study (100 Hz–l0 MHz), unlike $ZnFe_2O_4$ where apparently exist two dispersions, that of the grains and that of the grain boundaries [2]. With increasing temperature, these individual dispersion regions are shifted to a higher frequency. In addition, temperature-dependent Z', especially in the case of $NiFe_2O_4$, shows a plateau from low frequency side which is followed by a nearly negative slope at high frequency side, indicating a crossover from low frequency relaxation behavior to high frequency dispersion phenomenon. This segment of nearly constant real impedance becomes predominated with increasing temperature, suggesting strengthened relaxation behavior [13].

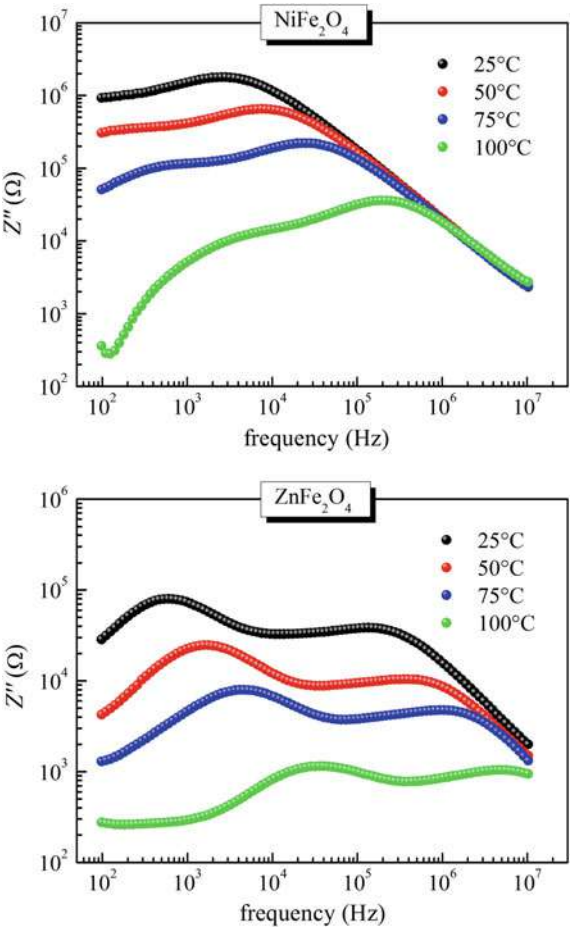

Fig. 5 Variation of imaginary part of complex impedance with frequency for $NiFe_2O_4$ and $ZnFe_2O_4$ ferrites at different temperatures

The variation of imaginary part of the impedance with frequency at different temperature is shown in the Fig. 5. In the case of $NiFe_2O_4$, room temperature curve shows that the Z'' value increases initially, reaches the maximum value at particular frequency and then it decreases continuously with increasing frequency. With increase in temperature another peak enters through low frequency window. Similar behavior of Z'' is observed in present $ZnFe_2O_4$, but two peaks appear at all temperatures. This suggests the coexistence of two relaxation effects which can be attributed to grain and grain boundary responses [2]. The maximum values of Z″ shift to high frequency side with increasing temperature, which corresponds to plateau relaxations observed earlier in real impedance spectra [13].

Nyquist or Cole-Cole plots of $NiFe_2O_4$ and $ZnFe_2O_4$ ferrites at different temperatures are given in Figs. 6 and 7, respectively. It is evident that the complex impedance spectra are characterized by the appearance of two semicircle arcs of different radii, which corresponds to grain boundary effect at the low-frequency

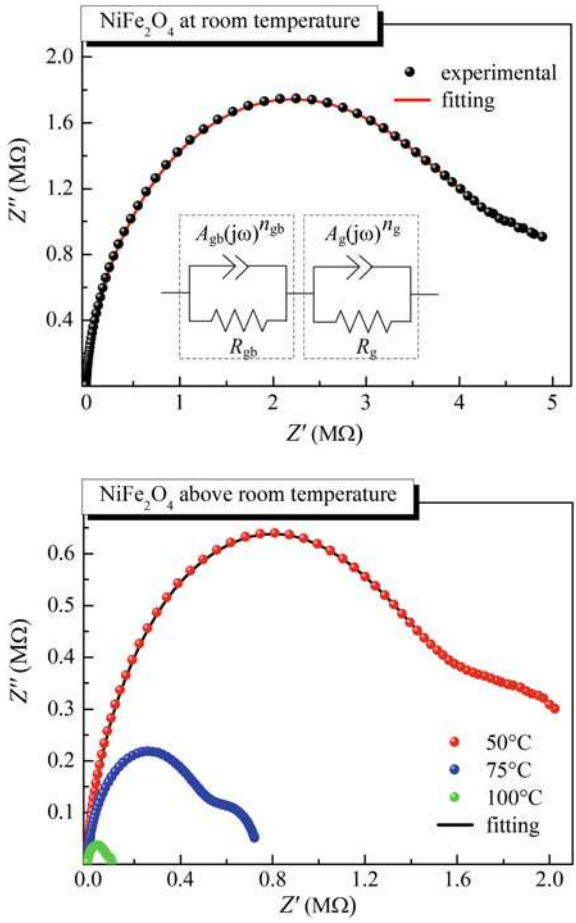

Fig. 6 Impedance spectra of $NiFe_2O_4$ ferrite at different temperatures. Inset shows the appropriate equivalent circuit model for analysis of the impedance data

region and grain effect at the high-frequency region for both samples. This appearance of two arcs in Cole-Cole plots at each temperature indicates the presences of two types of relaxation phenomena with sufficiently different relaxation times [12]. The results show that Nyquist plots are temperature dependent, since the diameters of both semicircles exhibit decreasing trends with increasing temperature. This means that the decrease in impedance supports the increase in conductivity and decrease in relaxation time [4]. Such behavior suggests that the samples possess a negative temperature coefficient of resistance (NTCR) [14], which implies a thermal activated conductivity of these ferrite materials.

It is usual to interpret the behavior of characteristic impedance spectra in terms of equivalent circuit model. The presence of two Nyquist semicircles in the impedance spectra of $NiFe_2O_4$ and $ZnFe_2O_4$ is consistent with the brick–layer model [7, 8] that is used to assign two semicircular arcs to the electrical response of polycrystalline materials. In order to correlate the electrical properties of samples with their microstructure, an equivalent circuit model consisting of two *R–CPE*

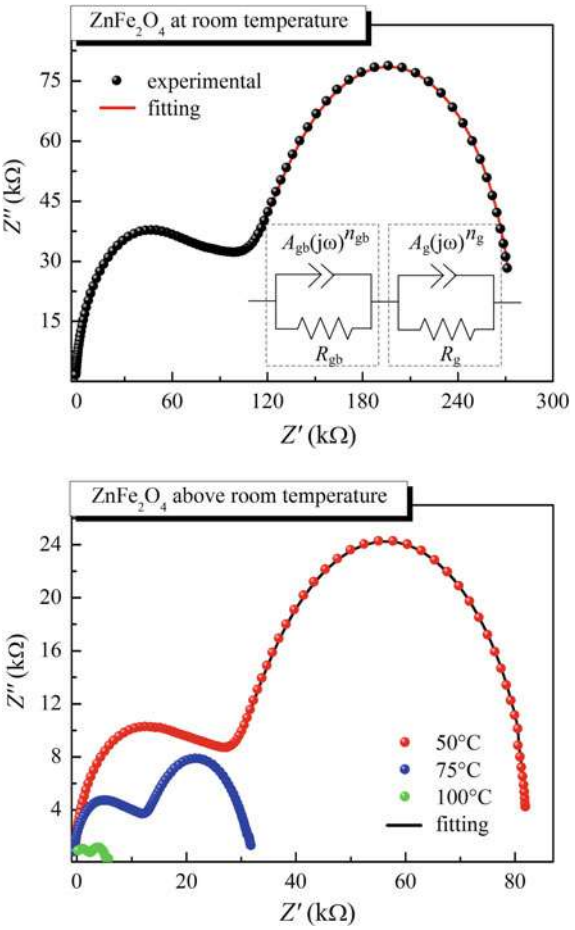

Fig. 7 Impedance spectra of $ZnFe_2O_4$ ferrite at different temperatures. Inset shows the appropriate equivalent circuit model for analysis of the impedance data

elements connected in series has been employed, see inset of Figs. 6 and 7. Here, R and CPE are the respective resistance and constant phase element for the grain boundaries (R_{gb}, CPE_{gb}) and the grain interiors (R_g, CPE_g). The CPE has been introduced to replace the capacitor in the equivalent circuit in order to accommodate the non-ideal Debye-like behavior of the capacitance [9]. The constant phase element has impedance defined by the following expression [8]:

$$Z^*_{\mathrm{CPE}}(\omega) = [A(j\omega)^n]^{-1}, \tag{2}$$

where parameter A is independent of frequency and n is the measure of non-ideal behavior having value between 1 and 0 ($0 \le n \le 1$). The CPE describes an ideal capacitor with $C = A$ for $n = 1$ and an ideal resistor with $R = 1/A$ for $n = 0$. As can be seen from Figs. 6 and 7, there is a close agreement between the experimental and theoretically fitted data which justifies the correctness of proposed equivalent electrical model.

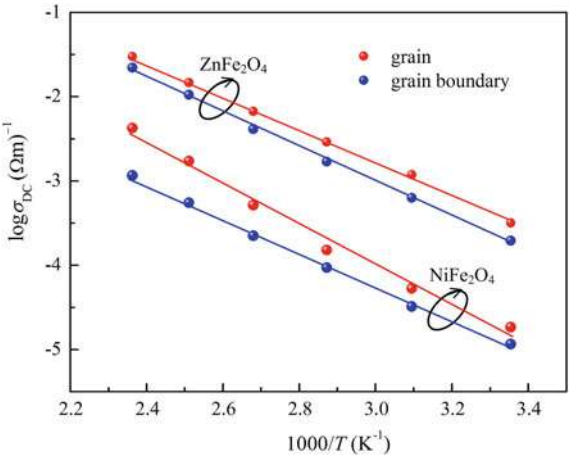

Fig. 8 Arrhenius plots of grain and grain boundary conductivity for $NiFe_2O_4$ and $ZnFe_2O_4$ ferrite samples

Based on the fitted values of grain boundary and grain resistance, the DC conductivity of grain boundaries and grain interiors for $NiFe_2O_4$ and $ZnFe_2O_4$ ferrites was estimated using the relation [12, 15]:

$$\sigma_{DC} = \frac{d}{RA}. \tag{3}$$

Here, R is the resistance values of the grain boundaries or grain which are evaluated from impedance spectra data, parameters d and A represent the thickness of sample and area of the electrode deposited on the sample, respectively. Figure 8 shows the temperature dependence of DC conductivity which well obeys the Arrhenius equation [7, 15]

$$\sigma_{DC}(T) = \sigma_0 \exp\left(-\frac{\Delta E}{k_B T}\right), \tag{4}$$

where σ_0 is the pre-exponential factor with the dimensions of $(\Omega m)^{-1}$, ΔE is the activation energy in (eV), k_B is the Boltzmann's constant and T is the absolute temperature. Using this Arrhenius plots, the corresponding activation energies for grain boundary and grain conductivity were determined from the slope of the $\log\sigma_{DC}$ versus $1000/T$. The estimated grain boundary and grain conductivity activation energies are 0.481 and 0.401 eV for $NiFe_2O_4$, and 0.412 and 0.387 eV for $ZnFe_2O_4$, respectively. In the case of both samples, the activation energy from grain boundaries is larger than that of grains. Such behavior is normal in view of the fact that the grain boundaries could play a blocking effect in many ionic oxides due to their high barrier [13]. Also, the resistance of grain boundaries exceeds that of the grains in many electroceramic materials [7]. This can be ascribed to the fact that the atomic arrangement near grain boundary region is disordered, resulting in a serious increase in electron scattering.

Table 2 The relaxation times of grain and grain boundary calculated from impedance response of ferrite samples

	$NiFe_2O_4$		$ZnFe_2O_4$	
Temperature (°C)	$\tau_{gb} = R_{gb}C_{gb}$ (ms)	$\tau_g = R_gC_g$ (μs)	$\tau_{gb} = R_{gb}C_{gb}$ (ms)	$\tau_g = R_gC_g$ (μs)
25	18.61	107.52	0.568	38.87
50	13.08	48.24	0.223	14.34
75	3.82	13.19	0.185	3.54
100	0.43	1.02	0.122	0.70

The relaxation times for both grain boundary and grain responses, $\tau_{gb} = R_{gb}C_{gb}$ and $\tau_g = R_gC_g$, were calculated using respective R and C values evaluated by fitting impedance data. The values are listed in Table 2. It is clear that the relaxation times decrease as temperature increases. This corroborates the observations made from Fig. 5; the maxima are shifted toward higher frequencies with increasing temperature. Further, the decrease in relaxation time with temperature results in an increase in hopping probability of charge carriers with temperature, since $\tau = (2P)^{-1}$, where P is the hopping probability, [16]. In addition, grain boundary relaxation times are about three orders of magnitude larger than those of the grain interior.

This means that in the grain boundary structure the time spent in the relaxation process is longer.

4 Conclusions

In this paper, detailed temperature and frequency dependent AC impedance studies were conducted on the $NiFe_2O_4$ and $ZnFe_2O_4$ ferrite ceramics, which were successfully fabricated by a conventional sintering of nanosized powders (1100 °C/2 h) synthesized by soft mechanochemical route. XRD analysis confirmed the cubic spinel structure of both ferrite samples with the lattice constants of 8.276 and 8.418 Å for sintered $NiFe_2O_4$ and $ZnFe_2O_4$, respectively, and the average crystallite sizes in the nm–range, which were determined on the basis of XRD data.

The complex impedance spectra studies clearly show the presence of both grain and grain boundary effects, and existence of negative temperature coefficient of resistance (NTCR) in the ferrite materials. The equivalent circuit consisting of two resistance-constant phase (*R–CPE*) elements connected in series is used to demonstrate electrical phenomenon occurring inside the samples. The temperature dependence of the grain boundary and grain conductivity well obey the Arrhenius law with activation energy of 0.481 and 0.401 eV for $NiFe_2O_4$, and 0.412 and 0.387 eV for $ZnFe_2O_4$, respectively. The present ferrites also exhibit the temperature dependent relaxation phenomena. The conduction mechanism may be due to the hopping of charge carriers present in these materials.

Acknowledgment This research was financially supported by the Ministry of Education, Science and Technological Development of the Republic of Serbia through Projects No. III43008 and III45003.

References

1. A. Goldman, *Modern Ferrite Technology*, 2nd edn. (Springer, New York, 2006)
2. D.L. Sekulic, Z.Z. Lazarevic, M.V. Sataric, C.D. Jovalekic, N.Z. Romcevic, Temperature-dependent complex impedance, electrical conductivity and dielectric studies of MFe$_2$O$_4$ (M = Mn, Ni, Zn) ferrites prepared by sintering of mechanochemical synthesized nanopowders. J. Mater. Sci.: Mater. Electron. **26**, 1291–1303 (2015)
3. M. Younas, M. Nadeem, M. Atif, R. Grossinger, Metal-semiconductor transition in NiFe$_2$O$_4$ nanoparticles due to reverse cationic distribution by impedance spectroscopy. J. Appl. Phys. **106**, 093704 (2011)
4. N. Kumari, V. Kumar, S.K. Singh, Structural, dielectric and magnetic investigations on Al^{3+} substituted Zn-ferrospinels. RSC Adv. **5**, 37925–37934 (2015)
5. D.K. Pradhan, P. Misra, V.S. Puli, S. Sahoo, D.K. Pradhan, Ram S. Katiyar, Studies on structural, dielectric, and transport properties of $Ni_{0.65}Zn_{0.35}Fe_2O_4$. J. Appl. Phys. **115**, 243904 (2014)
6. E. Barsoukov, J.R. Macdonald, *Impedance Spectroscopy—Theory, Experiment and Applications*, 2nd edn. (Wiley, New Jersey, 2005)
7. D.L. Sekulic, Z.Z. Lazarevic, C.D. Jovalekic, A.N. Milutinovic, N.Z. Romcevic, Impedance spectroscopy of nanocrystalline MgFe$_2$O$_4$ and MnFe$_2$O$_4$ ferrite ceramics: effect of grain boundaries on the electrical properties. Sci. Sinter. (in press)
8. R. Martínez, A. Kumar, R. Palai, J.F. Scott, R.S. Katiyar, Impedance spectroscopy analysis of $Ba_{0.7}Sr_{0.3}TiO_3/La_{0.7}Sr_{0.3}MnO_3$ heterostructure. J. Phys. D: Appl. Phys. **44**, 105302 (2011)
9. Z.Ž. Lazarević, Č. Jovalekić, D.L. Sekulić, A. Milutinović, S. Baloš, M. Slankamenac, N.Ž. Romčević, Structural, electrical and dielectric properties of spinel nickel ferrite prepared by soft mechanochemical synthesis. Mater. Res. Bull. **48**, 4368–4378 (2013)
10. A.S Bondarenko, G.A. Ragoisha, EIS Spectrum Analyser (a freeware program for analysis and simulation of impedance spectra). http://www.abc.chemistry.bsu.by/vi/analyser
11. D.L. Sekulić, Z.Ž. Lazarević, Č. Jovalekić, A. Rečnik, M. Romčević, B. Hadžić, N.Ž. Romčević, The comparative study of the structural and the electrical properties of the nano spinel ferrites prepared by the soft mehanochemical synthesis. Sci. Sinter. **45**, 235–245 (2014)
12. M. Younas, M. Atif, M. Nadeem, M. Siddique, M. Idrees, R. Grossinger, Colossal resistivity with diminished tangentlossin Zn-Ni ferrite nanoparticles. J. Phys. D: Appl. Phys. **44**, 345402 (2011)
13. W. Chen, W. Zhu, O.K. Tan, X.F. Chen, Frequency and temperature dependent impedance spectroscopy of cobalt ferrite composite thick films. J. Appl. Phys. **108**, 034101 (2010)
14. P. Kour, P. Kumar, S.K. Sinha, M. Kar, Study of dielectric and impedance spectroscopy of La substituted nanocrystalline $Pb(Zr_{0.52}Ti_{0.48})O_3$ ceramics. J. Mater. Sci.: Mater. Electron. **26**, 1304–1310 (2015)
15. P. Dhak, D. Dhak, M. Das, P. Pramanik, Dielectric and impedance spectroscopy study of $Ba_{0.8}Bi_{2.133}Nb_{1.6}Ta_{0.4}O_9$ ferroelectric ceramics, prepared by chemical route. J. Mater. Sci.: Mater. Electron. **22**, 1750–1760 (2011)
16. Z.Ž. Lazarević, Č. Jovalekić, A. Milutinović, D. Sekulić, M. Romčević, M. Slankamenac, N. Romčević, Spectroscopy investigation of nanostructured zinc ferrite obtained by mechanochemical synthesis. Optoelectron. Adv. Mater. Rapid Commun. **7**, 720–725 (2013)

Structural and Optical Studies of Oxide Single Crystals Grown by the Czochralski Method

S. Kostić, Z.Ž. Lazarević, M. Gilić, M. Petrović, M. Romčević, N.Ž. Romčević and D.L. Sekulić

Abstract In this paper, we used the Czochralski method to obtain good-quality yttrium aluminium garnet ($Y_3Al_5O_{12}$)—YAG and yttrium aluminium garnet doped with neodymium—Nd:YAG crystals. The investigations were based on the growth mechanisms and the shape of the liquid/solid interface on the crystal properties and incorporation of Nd^{3+} ions. The obtained single YAG and Nd:YAG crystals were studied by use of Raman and IR spectroscopy. There are strong metal oxygen vibrations in region 650–800 cm^{-1} which are characteristics of Al–O bond: peaks at 784/854, 719/763 and 691/707 cm^{-1} correspond to asymmetric stretching vibrations in tetrahedral arrangement. Peaks at 566/582, 510/547 and 477/505 cm^{-1} are asymmetric stretching vibrations, and 453/483 cm^{-1} is symmetric vibration of Al–O bond in octahedral arrangement of garnet structure. Lower energy peaks correspond to translation and liberation of cations in different coordinations—tetrahedral, octahedral and dodecahedral in the case of the lowest modes.

Keywords Single crystal · $Y_3Al_5O_{12}$ · Nd:YAG · Optical materials · Crystal growth

1 Introduction

Oxide crystals are of great importance for modern electrical and electro-optical applications in several devices. Diode-pumped Q-switched solid-state lasers have been demonstrated to have high efficiency, high average power and high energy per

S. Kostić · Z.Ž. Lazarević (✉) · M. Gilić · M. Petrović · M. Romčević · N.Ž. Romčević
Institute of Physics, University of Belgrade, Belgrade, Serbia
e-mail: lzorica@yahoo.com

D.L. Sekulić
Faculty of Technical Sciences, University of Novi Sad, Novi Sad, Serbia
e-mail: dalsek@yahoo.com

W.E. Lee et al. (eds.), *Proceedings of the III Advanced Ceramics and Applications Conference*, DOI 10.2991/978-94-6239-157-4_14

pulse. The applications of Q-switched lasers are well known: lidars, remote sensing, pollution detection, nonlinear optical processes and material processing [1–3].

There has been a continuing interest in the development of the technology of $Y_3Al_5O_{12}$ (YAG) garnet crystal growth because Nd:doped YAG is one of the most important laser hosts for the generation of 1.06 m infrared radiation. Its good optical, chemical and mechanical characteristics have made it the standard material in industrial applications where reliability is particularly important. Nd:YAG crystals are usually grown by the conventional Czochralski (CZ) technique [4–7]. Besides that, for miniature laser sources, Nd:YAG can grow by the micropulling-down (μ-PD) technique [8–10] and by the crucible laser heating pedestal method [11–13].

YAG crystallizes in a highly symmetric cubic structure [13]. The conventional unit cell of YAG contains 160 atoms comprising of 24 yttrium, 40 aluminium and 96 oxygen atoms, with a lattice parameter of 12.01 °A [14]. The relative arrangement of Y, O and Al can be described with polyhedra, and the symmetry is shown in Fig. 1.

The Czochralski technique has great advantages for the growth of the high-quality and large size YAG and Nd:YAG single crystals for usage as medium in high-power efficient lasers. A stable and equilibrant process of crystal growth with CZ technique is necessarily controlled by many different growth parameters. Each fluctuation in growth parameters could make the system unstable and directly affect on the crystal quality [3]. The temperature gradient adjusted by thermal shields, growth atmosphere and cooling system is the most important growth parameter in the furnace. This parameter influences the crystal perfection by effect on the fluid dynamic and kinetics of a growing crystal [15]. On the other hand, an improper thermal gradient during the growth causes the change of the convexity of solid–liquid interface, reduce/enlarge the size of central core and create large

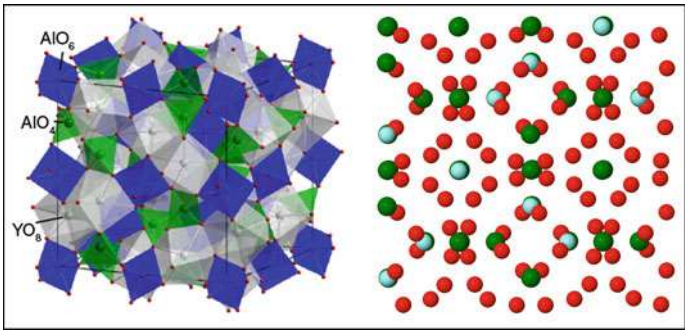

Fig. 1 The garnet structure consists of linked AO_8, BO_4 and MO_6 polyhedra. A and B are usually di- and tri-positive cations. In this model, the BO_4 is the *green* Al and the MO_6 the *blue* Al. The 8 coordinate site accommodates Y. Conventional unit cell YAG symmetry on [1 0 0] face. *Red* O, *Green* Al, *Blue* Y [14]

thermal stress and cracks in the crystal [16, 17]. The temperature gradient has to be stable during the growth of the crystal.

The aim of our work was to produce YAG single crystals with and without dopant Nd^{3+} and without a core; the growth parameters and annealing condition were investigated, by applying both theoretical and experimental treatment. The structural and optical properties obtained single YAG and Nd:YAG crystals were characterized using Raman and IR spectroscopy.

2 Experimental

The Czochralski process is a method of crystal growth used to obtain YAG and Nd:YAG single crystals. Both crystals (Fig. 2) were grown using a MSR 2 crystal puller controlled by a Eurotherm. The atmosphere of argon was used. The starting materials were powdered such as Y_2O_3, Al_2O_3 and Nd_2O_3 (all Koch and Light), all of 4 N purity. Powdered ZrO_2 (Koch and Light) of 4 N purity was used for isolation. The purity of argon (Tehnogas) was 4 N. The iridium crucible (40 mm diameter, 40 mm high) was placed into an alumina vessel surrounded by ZrO_2 wool isolation. Double walls were used to protect the high radiation. To decrease the radial temperature gradient in the melt, alumina was mounted around all the system. The best results were obtained with a pull rate of 2–3 mm h^{-1} for YAG and 1 mm h^{-1} for Nd:YAG crystals. The crystal rotation rates were between 6 and 100 rpm (YAG). The best results were obtained with a crystal rotation of 100 rpm

Fig. 2 A view of an obtained YAG ($Y_3Al_5O_{12}$) and Nd:YAG ($Nd:Y_3Al_5O_{12}$) single crystal plate

(YAG) and 20 rpm (Nd:YAG). The diameters of crystals were between 10 and 20 mm. The crucible was not rotated during the growth. After the growth run, the crystal boule was cooled at a rate of about 50 K h^{-1} down to room temperature.

Such obtained YAG and Nd:YAG crystals were cut either transversal to the growth axis, or along or parallel to the plane (110). Then, they were polished, smoothed and observed in polarized light.

Crystal slices with < 1 1 1 > orientation were cut from the as-grown crystal boule, and the slices were subsequently polished on both sides with diamond paste. The mechanically polished slices were chemically polished in liquid H_3PO_4 [18]. Various solutions of H_3PO_4 at different temperatures and for various exposure times were tried for chemical polishing and etching. For chemical polishing, exposure to a concentrated (85 %) solution of H_3PO_4 at 603 K (330 °C) for 20 min was confirmed to be suitable. Exposure for 1 h to an 85 % solution of H_3PO_4 at 493 K (220 °C) after was found to be a suitable for etching [8, 18].

The obtained crystal plates were observed in polarized light to visualize the presence of a core and/or striations. The absence of a core was confirmed by viewing both polished crystal slices in normal light (Fig. 2). The observations relating to the dislocation were recorded by observing an etched surface of YAG and Nd:YAG crystals, using a Metaval of Carl Zeiss Java metallographic microscope with magnification of 270x and 200x, respectively.

The Raman spectra in spectral range from 100 to 900 cm^{-1}, in backscattering geometry, were obtained by the micro-Raman Jobin Yvon T64000 spectrometer, equipped with nitrogen-cooled charge-coupled device detector. As excitation source, we used the 514-nm line of an Ar-ion laser. The measurements were performed at 20 mW.

The infrared (IR) measurements were carried out with a BOMMEM DA-8 FIR spectrometer. A DTGS pyroelectric detector was used to cover the wave number range from 50 to 900 cm^{-1}.

3 Results and Discussion

On the basis of our experimental results, it may be concluded that the crystals growing at higher rotation rates, when the inversion of the crystallization front from convex to planar has occurred, do not contain a core and the strains in them are considerable (Figs. 3 and 4).

Investigations that were carried out with YAG not containing Nd^{3+} ions helped us a lot in our studies of YAG containing Nd^{3+} ions. When investigating YAG containing no Nd^{3+} ions, we noticed that after the performed inversion of the liquid/solid interface, the crystals obtained did not have cores. On the contrary, when we analysed YAG containing Nd^{3+} ions, we immediately saw that the whole system was far more sensitive, due to the presence of Nd^{3+} ions, to any charge in growth conditions and all our attempts to obtain crystals without a core caused the blurring of the crystals.

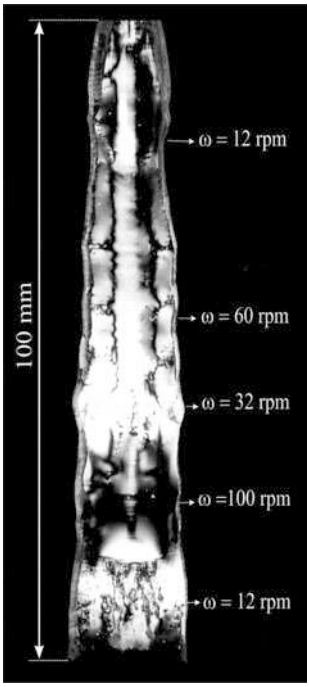

Fig. 3 YAG crystal grown with different rotation rates

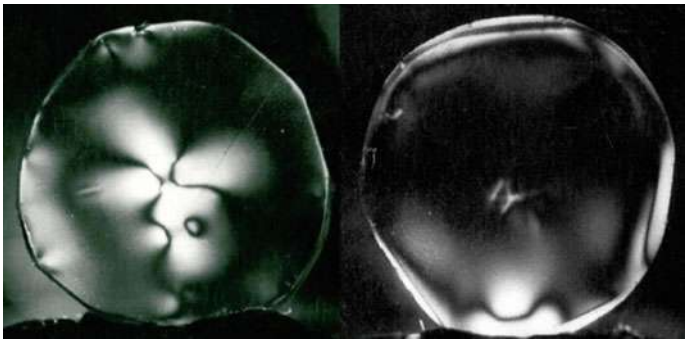

Fig. 4 Cross section of single YAG crystals grown

In recent years, studies on laser crystals show that YAG crystal has nearly optimal properties that are required of materials for lasers. However, a factor that partially restricts all potential possibilities of this crystal is the difficulty in obtaining single crystals containing a higher concentration of activator (neodymium), while at the same crystal contains all the necessary optical quality. This difficulty is caused by the significant difference of the ionic radii of Nd^{3+} compared to Y^{3+} which in

turn makes it difficult to isomorphic substitution of more than 1 % (atomic) Nd^{3+} in YAG crystal. Therefore, many studies in order to obtain Nd:YAG crystals oriented in the direction of getting other elements (e.g. lutenium—Lu), whose ionic radius much smaller than Y^{3+}, so their embedding in the crystal lattice of YAG achieves the effect of compensation between such ions and ions Nd^{3+} and crystal lattice parameter remains approximately 12.01 Å. The main defects of the crystal structure, not counting dislocations, which are the proper conduct of the process of crystal growth, may keep a level of 100 dislocations per cm^2, are also inhomogeneous incorporation of Nd^{3+} due to the appearance of (211) flat in the centre of the crystal orientation (111) zone of the stress in the direction (110) on the plane (111) and furrows caused by impurity character of the interface crystal-melt during the process of crystal growth.

From Fig. 5, it can observe dislocations on YAG and Nd^{3+}:YAG single crystals, respectively. Etch pits have the shape of a three-sided pyramid. Number of dislocations is of the order of 10^4 per cm^2. In most crystals are not observed dislocation.

YAG is one of the garnet family compounds. The garnets usually have a general formula of $[A]_3\{B\}_2(C)_3O_{12}$, where [], {} and () denote dodecahedral, octahedral and tetrahedral coordination, respectively. YAG and Nd:YAG have a cubic structure with O_h^{10} - *Ia3d* space group symmetry with eight units in the unit cell. Three different sites are available in the lattice. The dodecahedral site *c* with local symmetry, D_2, is normally occupied by the large Y^{3+} ions surrounded by eight O^{2-} ions, the octahedral site (local symmetry C_{3i}) is normally occupied by Al^{3+} surrounded by six O^{2-} ions, and the tetrahedral site *d* (local symmetry S_4) is occupied by Al^{3+}. The Al^{3+} cations occupy eight octahedral sites of C_{3i} symmetry and twelve tetrahedral sites of S_4 symmetry. Nd^{3+} ions usually replace Y^{3+} cations placed in twelve dodecahedral sites of D_2 symmetry [19]. The crystal structure of YAG, where Y^{3+} is coordinated with eight oxygen ions, some Al^{3+} are six-fold coordinated and others are four-fold coordinated. Each AlO_6 octahedron is connected to six AlO_4 tetrahedrons, and each AlO4 tetrahedron is connected to four AlO_6

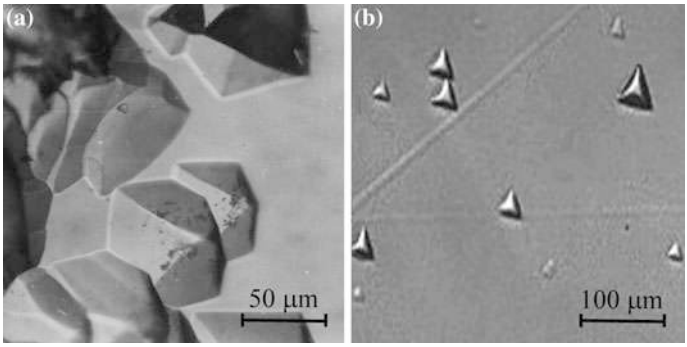

Fig. 5 The microscopic image of the surface of YAG Nd:YAG single crystal plate etched with H_3PO_4 in the direction (111). Magnification of 270x and 200x, respectively

octahedrons by sharing the corners. Y^{3+} locates at the space inside the AlO_x framework. The Nd^{3+} replaces the Y^{3+} of the Y-O dodecahedron in Nd^{3+}-doped YAG crystal.

The large number of atoms in the primitive cell leads to 240 (3 × 80) possible normal modes which can be classified according to the irreducible representation of the Oh group as follows: $3A_{1g} + 5A_{2g} + 8E_g + 14T_{1g} + 14T_{2g} + 5A_{1u} + 5A_{2u} + 10E_u + 18T1_u + 16T_{2u}$. The 25 modes having symmetries $A1$ g, E_g and T_{2g} are Raman active, while the 18 having T_{1u} symmetry are IR active [20–22]. Sixteen of the 25 Raman active vibrational modes can be observed in the Raman spectrum from 100 to 900 cm^{-1}. The Raman spectrum of rare earth-doped YAG compounds can be divided into two different parts: the high-frequency region (500–900 cm^{-1}) and the low-frequency region (<500 cm^{-1}). The high-frequency region accounts to the v_1 (breathing mode), v_2 (quadrupolar) and v_4 molecular internal modes associated with the (AlO_4) group, while the low-frequency region is due to: (i) translational motion of the rare earth ions, (ii) rotational and translational motion of the AlO_4 units and (iii) the v_3 molecular mode of the AlO_4 [21, 22].

The Raman spectra of YAG and Nd:YAG single crystals have been recorded in 100–900 cm^{-1} spectral range at room temperature (Fig. 6). The difference in the Raman spectral shape is indeed observed from the pure YAG crystal to Nd^{3+}-doped YAG.

This clearly indicates that Nd doping does replace ions in the crystal, thus changing the original YAG vibrational modes towards the Nd:YAG Raman spectrum. We believe that the replaced ions are centred instead of aluminium ions in the tetrahedrons and octahedrons. According to work by Su et al. on Nd:YAG [23], the peaks at 161, 219, 263, 340, 373, 402 and 407 cm^{-1} in Fig. 6 and Table 1 have been attributed to the translatory motion of the Y or Nd ions within the distorted cube

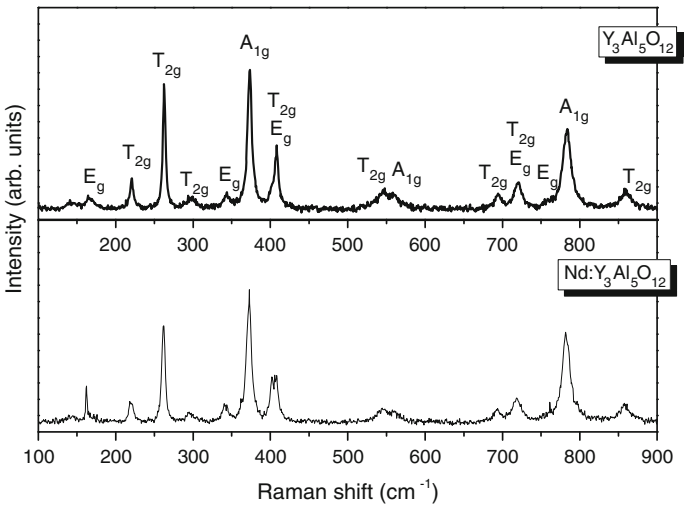

Fig. 6 Raman spectra of YAG ($Y_3Al_5O_{12}$) and Nd:YAG ($Nd:Y_3Al_5O_{12}$) single crystal

Table 1 Position (cm^{-1}) of the modes in the Raman spectra and symmetries of lines of YAG and Nd:YAG single crystals

Symmetry type	Experimental Frequency (cm^{-1})		
	YAG	Nd:YAG	Vibrations
E_g	164	162	Y or Nd Translation
T_{2g}	219	221	Y or Nd Translation
T_{2g}	263	263	Y or Nd Translation
T_{2g}	294	295	Translation + Rotation + v_3 (AlO_4)
E_g	340	343	Translation + Rotation + v_3 (AlO_4)
A_{1g}	373	373	Translation + Rotation + v_3 (AlO_4)
T_{2g}	403	409	Translation + Rotation + v_3 (AlO_4)
E_g	–	407	Translation + Rotation + v_3 (AlO_4)
T_{2g}	544	548	Translation + Rotation + v_3 (AlO_4)
A_{1g}	556	557	v_2 (AlO_4)
T_{2g}	690	693	v_2 (AlO_4)
E_g	720	720	v_2 (AlO_4)
T_{2g}	720	720	$v_1 + v_4$ (AlO_4)
A_{1g}	784	783	$v_1 + v_4$ (AlO_4)
T_{2g}	857	858	$v_1 + v_4$ (AlO_4)

with eight oxygen ions at the corners and also the heavy mixing of the translational, rotational and v_3 mode of the (AlO_4) unit. The vibrational modes at 543 and 556 cm^{-1} can be assigned as the v_2 mode of the (AlO_4) unit. These peaks are the internal stretching vibrations (v_1 and v_4) between aluminium ions and oxygen in the tetrahedral (AlO_4) unit.

The Nd^{3+} ions were substituted for Y^{3+} in YAG without the need for charge compensation. The larger size of the Nd^{3+} ions results in polyhedral sites with sides that are greater than those in Al^{3+} polyhedral site. That distorts the lattice and thus limits the maximum doping concentration to several atomic weight percent. Concentration of Nd^{3+} in our samples is, as a common for laser materials, 0.8 wt %. The lattice strains that are introduced by doping affect the properties of the optical spectra.

The optical spectra of YAG and Nd:YAG single crystals were recorded in far IR region at room temperature (298 K). The IR reflectance spectra of these crystals are shown in Fig. 7.

Seventeen of $18T_{1u}$ IR-active modes are visible in the near-normal reflectivity spectra of YAG and Nd:YAG crystals, as shown in Fig. 7. There are strong metal oxygen vibrations in region 650–800 cm^{-1} which are characteristics of Al–O bond: peaks at 784/854, 719/763 and 691/707 cm^{-1} correspond to asymmetric stretching vibrations in tetrahedral arrangement.

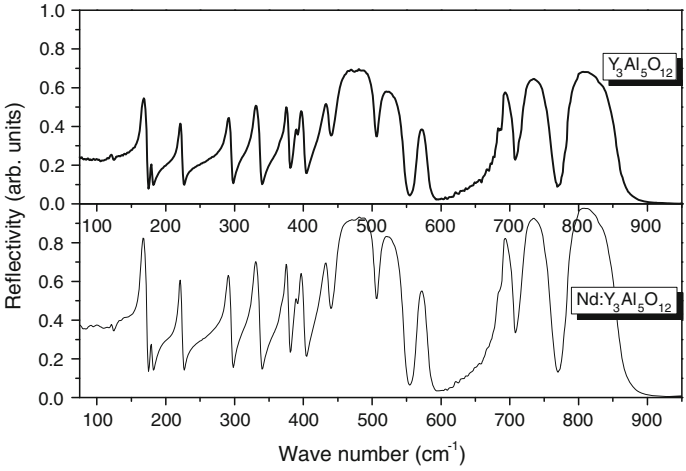

Fig. 7 IR spectra of YAG ($Y_3Al_5O_{12}$) and Nd:YAG ($Nd:Y_3Al_5O_{12}$) single crystals at room temperature

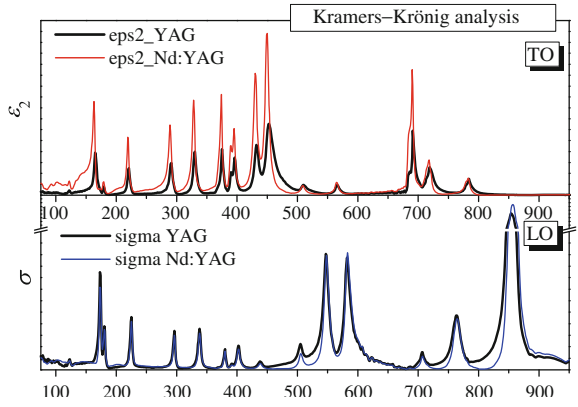

Fig. 8 TO and LO modes of YAG and Nd:YAG single crystals obtained by the Kramers–Krönig analysis

Peaks at 566/582, 510/547 and 477/505 cm^{-1} are asymmetric stretching vibrations, and 453/483 cm^{-1} is symmetric vibration of Al–O bond in octahedral arrangement of garnet structure. Lower energy peaks correspond to translation and liberation of cations in different coordination—tetrahedral, octahedral and dodecahedral in the case of four lowest modes [24].

Graphical presentation of the Kramers–Krönig analysis shows that with doping of YAG with Nd, *TO* modes undergo a red shift of 1–3 cm^{-1}, what is expected because of greater atomic mass of neodymium (144.2) related to yttrium (88.9) (Fig. 8). The values of these modes are presented in Table 2.

Table 2 Parameters fit the IR spectra of YAG and Nd:YAG single crystals and the transverse (*TO*) and the longitudinal (*LO*) frequency values obtained from Kramers–Krönig analysis (Peak Positions ε And σ)

	Single crystals		
	YAG	Nd:YAG	
	TO/LO	TO	Vibrations
Wave number (cm^{-1})	122/122.6	122	$T(+T_d)$ transl. of tetr. and dodecah. cation
	165/173	163	T_d transl. of dodecah. cation
	180/180	178	$T_d(+T)$ transl. of tetr. and dodecah. cation
	221/225	219	T_d transl. of dodecah. cation (translations of cations in YO_3 and AlO_4)
	291/296	289	T_0
	327/338	328	T transl of tetrah. cation
	375/380	374	R libr. of tetrah.
	390/392	389	T_0 transl. of octah.
	396/402	395	R libr. of tetrah.
	432/438	431	T_0 transl. of octah. (translations + liberation of cations in AlO_6 and AlO_4)
	453/483	449	v_2 symmetric
	477/505	475	v_4 symmetric
	510/547	509	v_4
	566/582	595	v_4 (symmetric and asymmetric stretching of Al–O in octahedrons)
	691/707	690	v_3
	719/763	717	v_3
	784/854	783	v_3 (asymmetric stretching of Al–O in tetrahedrons)

4 Conclusions

In conclusion, Czochralski technique has been used successfully to produce yttrium aluminium garnet (YAG) and yttrium aluminium garnet doped with neodymium (Nd:YAG) single crystal. The obtained crystals were studied by Raman and IR spectroscopy. We observed 15 Raman and 17 IR modes. The Raman and IR spectroscopy results are in accordance with X-ray diffraction analysis. The obtained YAG and Nd:YAG single crystals were without core and with good optical quality. The absence of a core was confirmed by viewing polished crystal slices. Also, it is important to emphasize that the obtained Nd:YAG single crystal has a concentration of 0.8 wt % Nd^{3+} that is the characteristic for laser materials.

Acknowledgment This research was financially supported by the Ministry of Education, Science and Technological Development of the Republic of Serbia through Project No. III45003.

References

1. T. Fukuda, K. Shimamura, V.V. Kochurikhin, V.I. Chani, B.M. Epelbaum, S.L. Buldochi, H. Takeda, A. Yoshikava, Crystal growth of oxide and fluoride materials for optical, piezoelectric and other applications. J. Mater. Sci.: Mater. Electron. **10**, 571–580 (1999)
2. D. Jun, D. Peizhen, X. Jun, The growth of Cr^{4+}, Yb^{3+}: yttrium aluminum garnet (YAG) crystal and its absorption spectra properties. J. Cryst. Growth **203**, 163–167 (1999)
3. A. Golubovic, S. Nikolic, R. Gajic, Z. Dohcevic-Mitrovic, A. Valcic, Growth and IR spectra of YAG and Nd:YAG single crystals. Metalurgija **10**, 363–370 (2004)
4. A. Golubovic, R. Gajic, Z. Dohcevic-Mitrovic, S. Nikolic, Nd pronounced anharmonicity in IR spectra of $CaWO_4$ single crystals. Sci. Sinter. **38**, 265–272 (2006)
5. C. Belouet, About crystalline perfection of Nd-doped YAG single crystals. J. Cryst. Growth **15**, 188–194 (1972)
6. V.J. Fratello, C.D. Brandle, Physical properties of a $Y_3Al_5O_{12}$ melt. J. Cryst. Growth **128**, 1006–1010 (1993)
7. Z. Galązka, H. Wilke, Influence of Marangoni convection on the flow pattern in the melt during growth of Y_3Al_5O12 single crystals by the Czochralski method. J. Cryst. Growth **216**, 389–398 (2000)
8. A. Golubović, S. Nikolić, R. Gajić, S. Đurić, A. Valčić, The growth of Nd:YAG single crystals. J. Serb. Chem. Soc. **67**, 291–300 (2002)
9. Y.M. Yu, V.I. Chani, K. Shimamura, T. Fukuda, Growth of $Ca(Li, Nb, Ga)(5)O^{-12}$ garnet crystals from stoichiometric melts. J. Cryst. Growth **171**, 463–471 (1997)
10. Y.M. Yu, V.I. Chani, K. Shimamura, K.T. Inaba, T. Fukuda, Growth of vanadium garnet fiber crystals and variations of lattice-parameter. J. Cryst. Growth **177**, 74–78 (1997)
11. R.S. Feigelson, Pulling optical fibers. J. Cryst. Growth **79**, 669–680 (1986)
12. R.S. Feigelson, Opportunities for research on single-crystal fibers. Mater. Sci. Eng. B **1**, 67–75 (1988)
13. R.S. Feigelson, *Tunable Solid State Lasers I*, ed. by P. Hammerling, A.B. Budgor, A. Pinto (Springer, Berlin, 1985), pp. 129–142
14. L. Dobrzycki, E. Bulska, D.A. Pawlak, Z. Frukacz, K. Wozniak, Structure of YAG crystals doped/substituted with erbium and ytterbium. Inorg. Chem. **43**(24), 7656–7664 (2004), pMID: 15554630
15. H. Saeedi, M. Asadian, Sh Enayati, N. Mirzaei, Cryst. Res. Technol. **46**, 1229–1234 (2011)
16. Z.Ž. Lazarević, P. Mihailović, S. Kostić, M.J. Romčević, M. Mitrić, S. Petričević, J. Radunović, M. Petrović-Damjanović, M. Gilić, N.Ž. Romčević, Opt. Mater. **34**, 1849–1859 (2012)
17. Z. Lazarević, S. Kostić, V. Radojević, M. Romčević, M. Gilić, M. Petrović-Damjanović, N. Romčević, Phys. Scr. **T157**, 014046 (2013)
18. Y. Peizhi, D. Peizhen, Y. Zhiwen, T. Yulian, The growth defects in Czochralski grown Yb: YAG crystal. J. Cryst. Growth **218**, 87–92 (2000)
19. S. Geller, L.D. Fullmer, P.B. Crandall, G.P. Espinosa, Thermal-expansion of some garnets. Mater. Res. Bull. **7**, 1219–1224 (1972)
20. J.P. Hurrell, P.S. Porto, I.F. Chang, S.S. Mitra, R.P. Bauman, Optical phonons of yttrium aluminium garnet. Phys. Rev. **173**, 851–856 (1965)
21. Y.F. Chen, P.K. Lim, S.J. Lim, Y.J. Yang, L.J. Hu, H.P. Chiang, W.S. Tse, Raman scattering investigation of Yb:YAG crystals grown by the Czochralski method. J. Raman Spectrosc. **34**, 882–885 (2003)
22. A. Lukowiak, R.J. Wiglusz, M. Maczka, P. Gluchowski, W. Strek, IR and Raman spectroscopy study of YAG nanoceramics. Chem. Phys. Lett. **494**, 279–283 (2010)
23. J. Su, Q. Zhang, S. Yin, D. Sun, S. Shao, Raman spectra analysis of Nd:YAG single crystal and its nano-powder. Spectrosc. Spectr. Anal. **29**, 1577–1580 (2009)
24. A.M. Hofmeister, K.R. Campbell, Infrared spectroscopy of yttrium aluminum, yttrium gallium, and yttrium iron garnets. J. Appl. Phys. **72**, 638–646 (1992)

Materials Research Bulletin 48 (2013) 404–415

Contents lists available at SciVerse ScienceDirect

Materials Research Bulletin

journal homepage: www.elsevier.com/locate/matresbu

Preparation and characterization of spinel nickel ferrite obtained by the soft mechanochemically assisted synthesis

Z.Ž. Lazarević [a,*], Č. Jovalekić [b], A. Rečnik [c], V.N. Ivanovski [d], A. Milutinović [a], M. Romčević [a], M.B. Pavlović [e], B. Cekić [d], N.Ž. Romčević [a]

[a] Institute of Physics, University of Belgrade, P.O. Box 68, Pregrevica 118, Zemun, Belgrade, Serbia
[b] The Institute for Multidisciplinary Research, University of Belgrade, Kneza Višeslava 1, Belgrade, Serbia
[c] Department for Nanostructured Materials, Jožef Stefan Institute, Ljubljana, Slovenia
[d] Institute of Nuclear Sciences Vinča, University of Belgrade, P.O. Box 522, 11001 Belgrade, Serbia
[e] Faculty of Electrical Engineering, University of Belgrade, Bulevar Kralja Aleksandra 73, Belgrade, Serbia

ARTICLE INFO

Article history:
Received 11 May 2012
Received in revised form 1 September 2012
Accepted 31 October 2012
Available online 16 November 2012

Keywords:
A. Magnetic materials
C. Mössbauer spectroscopy
C. Raman spectroscopy
C. X-ray diffraction

ABSTRACT

Nickel ferrite, $NiFe_2O_4$ has been prepared by a soft mechanochemical route from mixture of (1) $Ni(OH)_2$ and α-Fe_2O_3 and (2) $Ni(OH)_2$ and $Fe(OH)_3$ powders in a planetary ball mill for varying duration. Soft mechanochemical reaction leading to formation of the $NiFe_2O_4$ spinel phase was followed by X-ray diffraction, Raman and infrared spectroscopy, TGA, scanning and transmission microscopy. The spinel phase formation was first observed after 4 h of milling and its formation was completed after 25 h in the both cases. The synthesized $NiFe_2O_4$ ferrite has a nanocrystalline structure with a crystallite size of about 20 and 10 nm respectively for the cases (1) and (2). The final grain size in the system (1) is about twice as large as that in the system (2), what is a consequence of different reaction paths in these two processing routes. There are five Raman and four IR active modes. Mössbauer spectroscopy studies implied on the possible cation distribution between the tetrahedral and octahedral sites in formed $NiFe_2O_4$ spinel structure. We were able to estimate the degree of inversion at most 0.82 in the case (1) and 0.66 in the case (2).

1. Introduction

Cubic nanosized spinel ferrites with the general formula MFe_2O_4 are well known, important materials for applications such as high density information storage media, for drug delivery, medical diagnostics, ferrofluid technology, electronic devices, catalysts, sensor technology and microwave applications [1–5]. The interests for using of these material permanently increases because of their usability under extreme conditions. They possess unique magnetic, chemical and mechanical properties. It is well known that properties of ferrite materials strongly depend on the preparation conditions. One of the most interesting ferrites is nickel ferrite $NiFe_2O_4$.

Nickel ferrite bulk material is known to be a ferromagnetic ternary oxide that crystallizes with the cubic spinel type structure (a = 0.8433 nm), space group $Fd3m$ [6]. To emphasize the site occupancy at the atomic level, we may write $NiFe_2O_4$ as $(Fe^{3+})_A[Ni^{2+}Fe^{3+}]_BO_4^{2-}$, where A and B represent tetrahedral and octahedral sites, respectively [7]. Its magnetic properties depend upon the nature of the ions, their distribution among tetrahedral (A) and octahedral [B] sites [8]. It is widely appreciated that the cation distribution in $NiFe_2O_4$, upon which many physical and chemical properties depend, is a complex function of processing parameters and depends on the preparation method of the material [9].

Technological and scientific challenges coupled with environmental considerations have prompted a search for simple and energy-efficient synthesis and processing routes of nanocrystalline spinel ferrites [10]. Among the many types of preparation and processing techniques including, for example, hydrothermal reactions [11–14], coprecipitation [15,16], micelle technique [17], sol–gel method [18,19], solid-state reaction [20] and the nonconventional mechanochemical route [21] has been recognized as a powerful method for the production of novel, high-performance, and low-cost materials.

The mechanochemical synthesis can deliver the designed phases and structures by a single-step of the high-energy milling conducted in an enclosed activation chamber at room temperature [22]. Usually, the complete formation of spinel ferrites was obtained only after milling followed by sintering, i.e. by employing two processing steps. It is obvious that the combined mechanochemical-thermal treatment yields a well-ordered spinel phase in

* Corresponding author. Tel.: +381 11 37 13 035; fax: +381 11 3160 531.
E-mail addresses: lzorica@yahoo.com, lzorica@ipb.ac.rs (Z.Ž. Lazarević).

0025-5408/$ – see front matter © 2012 Elsevier Ltd. All rights reserved.
http://dx.doi.org/10.1016/j.materresbull.2012.10.061

ferrites at lower annealing temperatures and shorter durations than those required in conventional ceramic methods [23]. Of course, in such case the morphology of crystallite, agglomerate and particle is changed significantly.

For producing the nanocrystalline nickel ferrite by mechano-chemical synthesis two ways are used: (i) in the first one, the ferrite is formed in the nanocrystalline state by solid state reaction between precursors during milling [24,25]; (ii) in the second one, the polycrystalline nickel ferrite obtained by other methods is milled in order to reduce the grain size and to refine the structure [26,27]. Several studies where reported regarding the producing of nanocrystalline nickel ferrite by mechano-chemical route, but the results are very different depending on the experimental conditions. For example, the nickel ferrite phase was obtained after 8 h [28] or else after 35 h of milling [25]. For the sample milled 8 h a heat treatment was applied in order to increase the formation of nanoferrite [28]. Another study reported the obtaining of nickel ferrite in the nanocrystalline state by mechanical milling (with a crystallite size of 9 nm) from a mixture of oxides [23]. In the same article, it was observed that the magnetization is reduced by milling. A non-equilibrium distribution of cations and a spin canted effect have been reported by the same authors [23]. The cations inversion between the tetrahedral and octahedral sites into the spinel structure alongside of the spin canted effect and superparamagnetic behaviour was also reported by other authors [29,30]. The magnetization of nickel ferrite obtained in nanocrystalline state by mechanical milling is lower than the magnetization of nickel ferrite obtained by ceramic method [29]. Finally, it is worth to note that mechanical/reactive milling can be used to obtained nanostructures that have a non-equilibrium distribution of cations within the crystal structure.

Mechanochemical method, and particularly soft mechano-chemically procedure is very suitable for the activation or synthesis of inorganic precursors. This is reflected primarily in the simplicity of the procedure and equipment used [22,31]. In many cases, when it comes to classical synthesis reaction sintering process, requires high temperatures, which can present an additional problem in industrial production. Mechanochemical derived precursors exhibit significantly higher reactivity and thus lower the calcination and sintering temperature – even a few hundred degrees.

Mössbauer spectroscopy is a powerful tool for investigation of cations distribution. $NiFe_2O_4$ crystallizes in an inverse spinel ferrite structure with ionic bonding: $(Fe^{3+}\uparrow)[Ni^{2+}\downarrow Fe^{3+}\downarrow]O_4$ [32]. The parentheses denote the tetrahedral cation sites (A) whereas square brackets signify the octahedral sites [B]. Nickel ferrites were obtained in various crystallite sizes by solid-state reaction in a ball mill. Our measurements reveal differences in structural features of nanoparticles with respect to the bulk nickel spinel ferrite. One can estimate a new structural rearrangement described with the following expression: $(Ni^{2+}{}_{1-\lambda}Fe^{3+}{}_{\lambda})[Ni^{2+}{}_{\lambda}Fe^{3+}{}_{2-\lambda}]O_4$, where λ is a degree of inversion. Šepelák et al. [27] suggested that the degree of inversion λ $[A_{(A)}/A_{[B]} = f_{(A)}/f_{[B]} \times \lambda/(2-\lambda)]$ (where $f_{(A)}$, $f_{[B]}$ are corresponding occupation numbers) could be obtained with the known Mössbauer subspectral areas of both iron sites and assuming that the ratio of the recoil-less fraction is $f_{[B]}/f_{(A)} = 0.94$ at the room temperature and $f_{[B]}/f_{(A)} = 1$ at low temperatures [33].

Since the magnetic ions are distributed among the tetrahedral (A) and the octahedral [B] sites of the spinel structure, there are A–A, A–B and B–B antiferromagnetic exchange interactions. According to the Weiss model the strongest are octahedral A–B interactions between Ni^{2+} and Fe^{3+} ions [34,35]. It is worth to note that crystallite size influences spectral components and their appearance. The relaxation time τ is a measure of thermally induced energy fluctuation that changes magnetization direction and it is directly influenced by the nanoparticle volume. The Larmor precession time, τ_L denotes the precession of the nuclear magnetic moment in the local field. If τ is smaller then τ_L, only superparamagnetic doublet [36] will be observed (when particle size is of the order of 10 nm). If τ is of the order or somewhat bigger then τ_L, a collapsed and broadened sextet will appear in the spectra. On the other hand, when τ is large enough, a Zeeman sextet with narrow Lorentz lines will be observed.

In this article, we demonstrated the synthesis of nanocrystalline $NiFe_2O_4$ through soft mechanochemical treatment, via high-energy milling of binary oxide precursors, starting from a mixture of the (1) $Ni(OH)_2$ and α-Fe_2O_3 and (2) $Ni(OH)_2$ and $Fe(OH)_3$ powders in a planetary ball mill. In both cases, soft mechano-chemical reaction leading to formation of the $NiFe_2O_4$ spinel phase was followed by X-ray diffraction, Raman and IR spectroscopy, TGA (thermogravimetric analyses), electron microscopy (SEM and TEM). The Mössbauer spectroscopy at room temperature confirms the superparamagnetic character of these samples.

2. Experimental procedures

For mixtures of crystalline powders, denoted by (1) and (2), the starting material were: (1) nickel(II)-hydroxide ($Ni(OH)_2$, Merck 95% purity) and hematite (α-Fe_2O_3, Merck 99% purity) and (2) nickel(II)-hydroxide ($Ni(OH)_2$, Merck 95% purity) and $Fe(OH)_3$ in equimolar ratio. The $Fe(OH)_3$ powder was made by adding equimolar amounts of NaOH solution (25% mass), made from 99% purity NaOH (Merck) to the $FeCl_3$ solution (25% mass), made from 99% purity $FeCl_3 \times 6H_2O$ (Merck) [37]. Dark brown precipitate was filtrated, washed with large amounts of water and dried in a vacuum dessicator. Before milling, the $Fe(OH)_3 \times nH_2O$ powder was heated at 105 °C for 24 h. The material prepared by this way had 99.5% $Fe(OH)_3$. It was defined by potentiometric redox titration [37]. X-ray analysis confirmed that the sample was amorphous, with a small amount of crystalline phase.

Mechanochemical synthesis was performed in air atmosphere in planetary ball mill (Fritsch Pulverisette 5). A hardened-steel vial of 500 cm^3 volume, filled with 40 hardened steel balls with a diameter of 13.4 mm, was used as the milling medium. The mass of the powder was 20 g and the balls-to-powder mass ratio was 20:1. The milling was done in the air atmosphere without any additives. The angular velocity of the supporting disc and vial was about 32 and 40 rad s^{-1}, respectively. The intensity of milling corresponded to an acceleration of about 10 times the gravitation acceleration. All samples, with different starting compositions and milling times, were prepared and milled separately. At the expiration of the selected milling times (4, 10 and 25 h) the mill was stopped and a small amount of powder was removed from the vial for examination.

Characterization of the samples obtained after various milling times was carried out by:

- X-ray diffraction analysis of powders treated for various periods of milling times by a Philips PW 1050 diffractometer equipped with a PW 1730 generator (40 kV × 20 mA) using Ni filtered CuK_α radiation at the room temperature. Measurements were done in 2θ range of 10–80° with scanning step width of 0.05° and 10 s scanning time per step. After XRD measurements, the powder was placed back in a vial to obtain the same grinding conditions (balls to powder weight ratio);
- Raman measurements of mixture of powders and calcined samples were performed using Jobin-Ivon T64000 monochromator. An optical microscope with 100× objective was used to focus the 514 nm radiation from a Coherent Innova 99 Ar^+ laser on the sample. The same microscope was used to collect the backscattered radiation. The dispersed scattering light was detected by a charge-coupled device (CCD) detection system.

Room temperature Raman spectra are in spectral range from 100 to 800 cm^{-1}. The average power density on the sample was about 20 mW mm^{-2};

- The infrared (IR) measurements were carried out with a BOMMEM DA-8 FIR spectrometer. A DTGS pyroelectric detector was used to cover the wave number range from 50 to 700 cm^{-1};
- The thermal behaviour was investigated up to 1000 °C using an SDT Q600 TGA/DSC instrument (TA Instruments) at a heating rate of 20 °C min^{-1} under a dynamic (100 cm^3 min^{-1}) N_2 atmosphere;
- The morphology of powders and the size of soft mechano-synthesized ferrite crystallites were examined by scanning electron microscopy (SEM, Model TESCAN Vega TS130MM);
- For transmission electron microscopy (TEM) observations the powders were dispersed in ethanol. The suspension containing our sample was deposited onto the lacey carbon-coated TEM sample supports. TEM studies were performed using a 200 kV TEM (JEM-2100 UHR, Jeol Inc., Tokyo, Japan) equipped with an ultra-high resolution objective lens pole piece having a point-to-point resolution of 0.19 nm, being sufficient to resolve the lattice images of nanoparticles. Due to relatively small size of the nanoparticles selected area electron diffraction patterns (EDP) over the multiple nanocrystals was recorded to obtain the characteristic diffraction rings with structure-specific *d*-values. Electron energy dispersive X-ray spectroscopy was used to examine the chemical composition of the product;
- Mössbauer measurements were performed in transmission geometry with $^{57}Co(Rh)$ source at 294 K. The data analysis was performed by using WinNormos-Site [38] software on samples milled for 25 h with transmission integral correction for sample thickness. The data analysis for 4 h milled samples was performed using WinNormos-Dist [38] software that enables distribution of hyperfine parameters by histogram method and allows for Lorentz sextets and doublets on well-defined ion sites. The spectra calibrated by laser and isomer shifts are shown with respect to α-Fe.

3. Results and discussion

It is well known that physical and magnetic properties of ceramic materials are influenced primarily by their chemical composition, but also by their microstructure. Consequently, the process of synthesis may have considerable influence on the characteristics of materials. Therefore, we investigated the possibility of the formation of spinel ferrite phase trough soft mechanochemical treatment, starting from two different mixtures of materials. The two cases were:

- Case (1):
  step (a) milling time 0 h: $Ni(OH)_2 + \alpha\text{-}Fe_2O_3$
  step (b) milling time 4 h: $NiO + H_2O\uparrow$ (water vapour, at 380 °C) + $\alpha\text{-}Fe_2O_3$
  step (c) milling time 10 h: $Ni(OH)_2 + \alpha\text{-}Fe_2O_3 + NiFe_2O_4$
  step (d) milling time 25 h: $NiFe_2O_4$
- Case (2):
  step (a) milling time 0 h: $Ni(OH)_2 + 2Fe(OH)_3 \times nH_2O$
  step (b) milling time 4 h: $Ni(OH)_2 + 2Fe(OH)_3 + NiO + xH_2O$
  step (c) milling time 10 h → $Ni(OH)_2 + 2Fe(OH)_3 + xH_2O + NiO + H_2O\uparrow$ (water vapour, at 380 °C) + $Fe_2O_3 + 3H_2O\uparrow$ (at 500 °C) + $nH_2O + NiFe_2O_4$ and $NiO + H_2O$ (at 380 °C) + $Fe_2O_3 + 3H_2O\uparrow$ (at 500 °C) + $nH_2O + NiFe_2O_4$
  step (d) milling time 25 h: $NiFe_2O_4$

Chemical changes occurring in the system during soft mechanochemical treatment are visible in Fig. 1 showing X-ray diffraction patterns of (1) $Ni(OH)_2$ and $\alpha\text{-}Fe_2O_3$ and (2) $Ni(OH)_2$ and $Fe(OH)_3$ powders unmilled (0 h) and milled for the different intervals of time (4, 10 and 25 h). Before any mechanochemical treatment (milling time 0 h) only sharp peaks of the a small amount of crystalline $\alpha\text{-}Fe_2O_3$ phase and amorphous $Ni(OH)_2$ were present in the XRD pattern (Fig. 1a), expect for sample from the mixture of $Ni(OH)_2$ and $Fe(OH)_3$ powders, where X-ray analysis confirmed that both phases were amorphous (Fig. 1b).

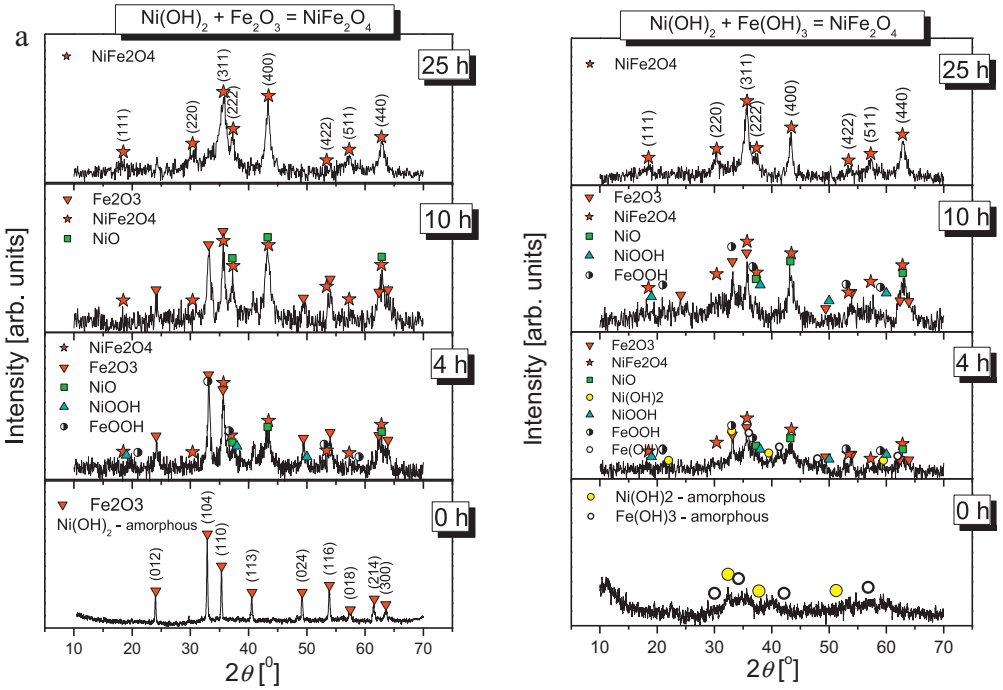

Fig. 1. X-ray diffraction pattern of the mixture of powders (a) $Ni(OH)_2$ and $\alpha\text{-}Fe_2O_3$ and (b) $Ni(OH)_2$ and $Fe(OH)_3$ after 4, 10 and 25 h milling time.

X-ray diffraction pattern of powders mechanochemically milled for 4 h was shown in Fig. 1a. In the case (a), $Ni(OH)_2$ quickly decomposed through $Ni(OH)_2 \rightarrow NiO + H_2O\uparrow$ (water vapour, at 350 °C), when the local temperature of collision between the balls and the material reached the decomposition temperature of $Ni(OH)_2$. Therefore, after 4 h there were no peaks corresponding to the starting compound $Ni(OH)_2$ (JCPDS card 74-2075). The most of the characteristic peaks of α-Fe_2O_3 (JCPDS card 89-8104), FeO(OH) (JCPDS card 89-6096), NiO peaks (JCPDS card 89-7101) and NiOOH (JCPDS card 06-0075) are present in the spectrum (Fig. 1). $Ni(OH)_2$ peaks could not be seen indicating that amorphisation of hydroxide had occurred. In the case (b) (Fig. 1b), in the full spectrum of $Ni(OH)_2$ (JCPDS card 74-2075) and $Fe(OH)_3$ (JCPDS card 22-0346) characteristic peaks were present, indicating that opposed to case (a), no decomposition of either of the starting components had occurred. The most probably it was the consequence of the presence and separation of the water from $Fe(OH)_3$ (via $Fe(OH)_3 \rightarrow FeO(OH) + H_2O$).

After 10 h of milling, in the case (1) and (2), again the spectrum of α-Fe_2O_3 characteristic peaks ware present. Broadening of the peaks was a consequence of the decrease in particle size and the appearance of a tension in the crystal lattice. The appearance of the new peak at $2\theta = 35.69°$, as well as the peaks at $2\theta = 43.38°$ and 63.023° clearly pointed to the formation of the new phase of $NiFe_2O_4$ (JCPDS card 89-4927). In the case (b), (Fig. 1b) again the full spectra of $Ni(OH)_2$ and $Fe(OH)_3$ characteristic peaks were present. The appearance of new peaks at $2\theta = 18.419°$, 35.69° and 63.023° here also pointed to the formation of the new phase of $NiFe_2O_4$. At the same time, the weak hematite peaks were detected in XRD pattern ($2\theta = 33.255°$ and 43.624°), indicating that decomposition of iron(III)-hydroxide to hematite and water had begun ($2Fe(OH)_3 \rightarrow Fe_2O_3 + 3H_2O\uparrow$ water vapour, at 500 °C) when the local temperature of collision between the balls and the material had reached the decomposition temperature of $Fe(OH)_3$. Decomposition of the nickel(II)-hydroxide to NiO and water was observed too, since NiO peaks could be seen indicating that amorphisation of nickel oxide had occurred.

X-ray diffraction patterns of powders (1) and (2) milled for 25 h were shown in Fig. 1. After 25 h in both cases of synthesis, all peaks detected at the $2\theta = 18.418°$, 30.298°, 35.690°, 43.380°, 53.827°, 57.384° and 63.023°, clearly pointed to the formation of the new phase of $NiFe_2O_4$ (JCPDS card 89-4927). The peaks are well indexed to the crystal plane of spinel ferrite (*k h l*) (1 1 1), (2 2 0), (3 1 1), (2 2 2), (4 0 0), (4 2 2), (5 1 1) and (4 4 0), respectively. This confirms that the mechanochemical synthesis of $NiFe_2O_4$ is feasible and complete after 25 h milling time. This is considerably less time compared with the time (35 h) for which the spinel $NiFe_2O_4$ obtained in the work by Jovalekić et al. [25].

In both cases, the conditions for soft milling existed since the synthesis took place in the presence of water (water vapour), which participates in the reaction as a damper of collisions between the balls and the material. Nevertheless, due to the small amount of water which separates from $Ni(OH)_2$ and $Fe(OH)_3$ during the synthesis $NiFe_2O_4$ (one water molecule per one decomposed molecule of $Ni(OH)_2$ in case (1) of synthesis, and three molecules of water per one decomposed molecule of $Fe(OH)_3$ gave four molecules of water in case (2)), and the periodic opening of the milling vessel to remove water vapour overpressure, the formation of the new phase of $NiFe_2O_4$ was accomplished.

The crystallite size (S) of $NiFe_2O_4$ powders treated mechanochemically for 25 h was calculated by means of Scherrer equation [39] using XRDP data as:

$$S = \frac{0.9\lambda}{B\cos\theta_B}$$

where S is the crystallite grain size, λ is the wavelength of the X-ray source, θ_B is the Bragg angle of the considered XRDP peaks. B

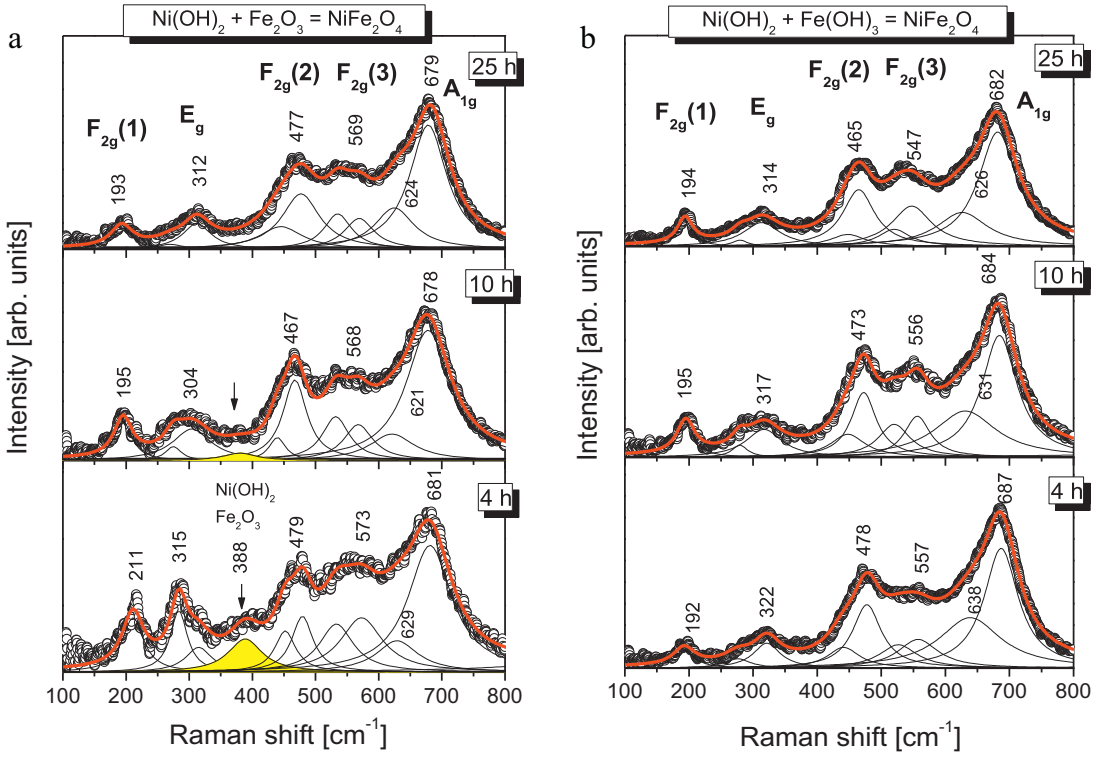

Fig. 2. Raman spectra at room temperature of the mixture of powders: (a) $Ni(OH)_2$ and α-Fe_2O_3 and (b) $Ni(OH)_2$ and $Fe(OH)_3$ after 4, 10 and 25 h milling time.

represents the FWHM line broadening (in the $2\theta_B$ units) obtained as follows [40]:

$$B^2 = B_m^2 - B_s^2$$

where B_m is the FWHM line broadening of the material and B_s represents the FWHM line broadening of the internal standard (α-Al_2O_3). The resulting value of the crystallite size, obtained from the (3 1 1) strongest reflections, is 18 and 14 nm respectively for cases denoted by (1) and (2) after 25 h milling times.

$NiFe_2O_4$ has inverse spinel structure (as Fe_3O_4) $(Fe^{3+})(Fe^{3+}Ni^{2+})O_4{}^{2-}$. Its crystal structure corresponds to $O_7{}^h$ ($Fd3m$) space group [41]. Group theory predicts 5 Raman active modes: $A_{1g} + E_g + 3F_{2g}$ and $4F_{1u}$ infrared active. In this structure the tetrahedral (A) sites are occupied by one half of the Fe^{3+} ions, while the other half of the Fe^{3+} and Ni^{2+} ions are distributed over the octahedral [B] sites. Except five allowed Raman modes, in Raman spectra is seen a number of additional peaks related to the presence of non-equivalent atoms at the [B] sites.

Fig. 2 shows Raman spectra for both cases of soft mechano-chemical synthesis. The A_{1g} mode is due to symmetric stretching of oxygen atoms along Fe–O bonds in the tetrahedral coordination. E_g is due to symmetric bending of oxygen with respect to Fe and $F_{2g}(3)$ is caused by asymmetric bending of oxygen. $F_{2g}(2)$ is due to asymmetric stretching of Fe and O. $F_{2g}(2)$ and $F_{2g}(3)$ correspond to the vibrations of octahedral group. $F_{2g}(1)$ is due to translational movement of the whole FeO_4 (Fe at tetrahedral site along with four oxygen atoms). There is a negligible displacement of Fe atoms in modes A_{1g}, E_g and $F_{2g}(3)$ [42].

All five Raman peaks are asymmetric, with shoulder on the low energy side. Each peak can be presented like a doublet. At a microscopic level the structure of $NiFe_2O_4$ can be considered as a mixture of two sublattices with Fe^{3+} and Ni^{2+}. It is supposed that Fe^{3+} and Ni^{2+} are ordered over the [B] sites. In nanocrystalline samples asymmetry is partly due to confinement and size-distribution of nanoparticles.

Raman spectra (Fig. 2) of samples, obtained by mixing of $Ni(OH)_2$ and $Fe(OH)_3$ and $Ni(OH)_2$ and α-Fe_2O_3 powders for 4, 10 and 25 h milling time are excited by Ar-laser line of 514 nm and power 20 mW. It can observed that after 4 h milling of starting compounds, Raman spectra shows features characteristic for $NiFe_2O_4$. Nanocrystalline samples have low thermal conductivity compared to crystal and thin film samples, and the higher laser power leads to heating of samples and to greater red shift of Raman modes. The position of the A_{1g} mode in a bulk sample spectra recorded for 0.1 mW is 703 cm^{-1} [42]. The energy shift obtained for A_{1g} mode after 25 h of the mixing of starting compounds (about 21–22 cm^{-1}) corresponds to value referred for nanocrystalline sample investigated in Ref. [41] in spectra exited by 20 mW laser power. Raman spectra are analyzed by deconvolution.

It can be concluded that all spectra have relatively low intensity. This is especially true for the spectrum of the sample that was obtained by milling a mixture of $Ni(OH)_2$ and α-Fe_2O_3 powders for 4 h. In the area of lower wave numbers, <450 cm^{-1}, where the modes of lower intensity are in the spectrum $NiFe_2O_4$, it can be seen the mode about 388 cm^{-1}, which comes from the superposition of modes $Ni(OH)_2$ and α-Fe_2O_3 [43–45]. It is obvious that the spinel modes $F(1)_{2g}$ and E_g are somewhat different, which is probably caused by interaction with the modes of the rest of the starting compounds, which did not react yet. In the spectrum of sample obtained after 10 h of milling, optional mode is reduced, and after longer milling times, this mode completely disappears.

It is obtained that practically all peaks, have red shift with the increase of mixing time. Red shift of peaks with the increase of mixing time indicates that nanoparticles of $NiFe_2O_4$ became smaller. Red shift is due to strain connected with increase of lattice parameter of nanoparticles. At the same time, the phonon confinement becomes more significant and contributes to the red shift.

In generally, the main modes in doublets became stronger because the structure of $NiFe_2O_4$ is a mixture of normal and inverse spinel structure and certain modes are superimposed. Raman

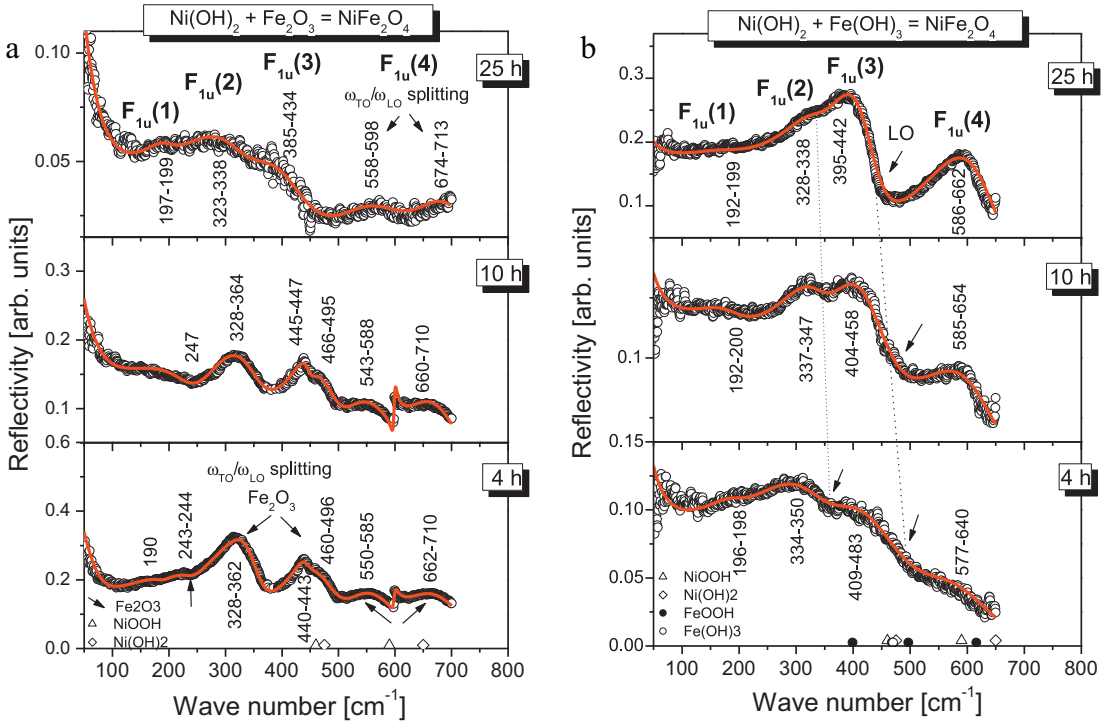

Fig. 3. IR spectra at room temperature of the mixture of powders: (a) $Ni(OH)_2$ and α-Fe_2O_3 and (b) $Ni(OH)_2$ and $Fe(OH)_3$ after 4, 10 and 25 h milling time.

measurements are very sensitive to atomic short-range order and it can be concluded that $NiFe_2O_4$ is already formed after 4 h of mixing. Prolongation of milling time leads to decrease of particle size and more uniform particle size distribution.

The IR reflectivity spectra of the samples, which were obtained by milling powders of nickel hydroxide $Ni(OH)_2$ and hematite (α-Fe_2O_3) (case (1)), undergo a striking change with prolongation of milling time of starting materials (Fig. 3a). At first glance, the obtained spectra for 4 h and 10 h of milling are similar to the spectra of α-Fe_2O_3. A more detailed analysis shows that they are created by superposition of phonons corresponding to the newly established $NiFe_2O_4$ spinel, the starting materials: $Ni(OH)_2$ and α-Fe_2O_3 and substances (products) obtained by conversion of $Ni(OH)_2$ to NiOOH and NiO. The presence of all these phases is confirmed by XRD-spectra.

Because of the great disorder of the system, selection rules are relaxed and in IR spectra are seen a hematite Raman active mode. It is also seen TO–LO splitting of strong IR active modes from hematite phase, as well as TO–LO splitting of $F_{1u}(4)$ modes from spinel phase. At about $\omega_{TO} = 190\ cm^{-1}$, after 4 h and 25 h milling, is poorly pronounced $F_{1u}(1)$ of $NiFe_2O_4$ mode. In the spectrum of the sample milled for 10 h this mode is not visible because it is screened by plasma. At $\omega_{TO} = 243\ cm^{-1}$ ($\omega_{LO} = 244\ cm^{-1}$) is a weak Raman-active mode E_g originating from α-Fe_2O_3 [43]. Mode at $\omega_{TO} = 328\ cm^{-1}$ ($\omega_{LO} = 362\ cm^{-1}$) is probably a combination of two modes: E_u mode of α-Fe_2O_3 (position of this mode in the pure hematite is 286–368 cm^{-1}) [46] and $F_{1u}(2)$ mode of $NiFe_2O_4$. Broad mode in the interval 440–496 cm^{-1} is E_u mode of α-Fe_2O_3 superimposed with a mode at 460 cm^{-1} originating from stretching of Ni–O bonds (a mode with approximately the same frequency occurs in $Ni(OH)_2$ and in NiOOH, also) [47]. It is assumed that the damped mode at 550–585 cm^{-1} is a combination of spinel $F_{1u}(4)$–TO mode and $F_{1u}(4)'$–LO mode, together with modes of the NiO phase at 580 cm^{-1} [46,47] and E_u(TO) mode of hematite at 525 cm^{-1} [45]. Mode with $\omega_{TO} = 662\ cm^{-1}$ and $\omega_{LO} = 710\ cm^{-1}$ is probably formed by superimposing spinel mode $F_{1u}(4)$(LO), E_u(LO) mode of hematite at about 659 cm^{-1} [43] and the deformation mode of the bond between Ni and OH^{-1}-group from $Ni(OH)_2$ at 650 cm^{-1} [47]. Mode at 599 cm^{-1} originates from NiOOH [47].

The features in the spectrum recorded after 25 h milling imply that spinel structure is dominant, although the broadness of the modes at frequencies 558–598 cm^{-1} and 674–713 cm^{-1}, leaves room for doubt that a certain amount of unreacted starting components is still present. XRD spectra of nanoparticles are generally of low intensity, with not well-defined peaks. That is the reason, why we dare to claim that it is possible that in the sample obtained after 25 h of milling, although in XRD spectrum except spinel peaks, peaks of other structures are not visible, however, may be present a small amount of residual hematite (which has the structural elements of the same symmetry as spinel, and the same positions of the corresponding peaks in the XRD spectrum).

It may be noted that for all samples obtained by milling of mixtures of hydroxides, $Ni(OH)_2$ and $Fe(OH)_3$ (case (2)) can be recognized the modes characteristic of $NiFe_2O_4$ spinel structure (Fig. 3b). One can see that already after 4 h of milling, $NiFe_2O_4$ spinel phase is dominant.

Somewhat modified values of TO and LO modes are due to superposition of modes of newly formed spinel structure and modes of initial hydroxides, or phases caused by conversion of hydroxides. With prolonged milling time the proportion of $NiFe_2O_4$ phase increases and the values of TO and LO modes become closer to the corresponding frequencies of modes in a crystal $NiFe_2O_4$ [48,49]. We did not use TO and LO frequencies estimated in [50], but we obtained TO and LO frequencies of crystal sample by fitting procedure and Kramers–Kronig analysis. Thus, the IR reflectivity analysis confirms that after 25 h of milling of corresponding hydroxides a pure phase of $NiFe_2O_4$ is formed.

It should be noted that in all IR reflectivity spectra plasma is visible as a result of a large number of surface defects. The samples are semiconducting at room temperature. It has already been explained that the $NiFe_2O_4$ was formed after 25 h milling time by soft mechanochemical synthesis starting from mixtures of powders in two ways (the case (1): $Ni(OH)_2 + \alpha\text{-}Fe_2O_3 \rightarrow NiFe_2O_4$ Fe_2O_4 and the case (2): $Ni(OH)_2 + Fe(OH)_3 \rightarrow NiFe_2O_4$). The positions of TO and LO modes, obtained by fitting procedure of IR reflectivity spectra of the samples for 25 h milling time (Fig. 3) have approximately the same values, except for isolated LO of $F_{1u}(4)$ mode in case (1). Although the corresponding modes have similar values, reflectivity spectra in case (1) and case (2), after 25 h of milling, looks very different what is a consequence of different values of the plasma frequencies and different damping of the modes.

In Fig. 4 are presented wave numbers of the modes directly connected with modes of spinel $NiFe_2O_4$. Modes that are the result of more complex superposition of spinel modes and modes of starting materials are omitted for better clarity of the graph.

In order to understand the thermal decomposition of the hydroxide precursor, thermogravimetry measurements (TG) has been done (Fig. 5). The weight loss of the samples obtained by milling for 25 h from the mixture of $Ni(OH)_2$ and α-Fe_2O_3 and of $Ni(OH)_2$ and $Fe(OH)_3$ powders in measured temperature range from 25 to 1000 °C is only 3.22% and 3.81%, respectively. Based on

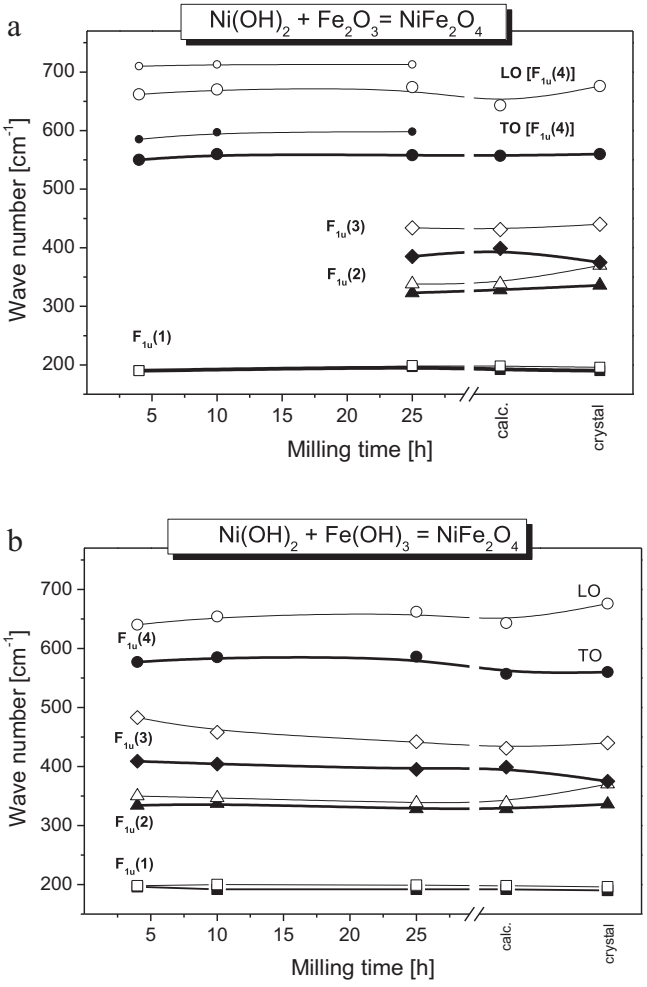

Fig. 4. Position of LO and TO infrared modes for both cases of soft mechanochemical synthesis.

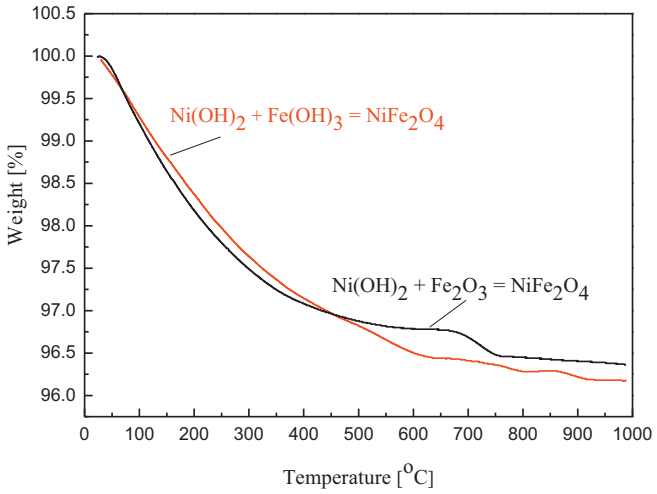

Fig. 5. TGA curves for the $NiFe_2O_4$ samples prepared from the mixture of powders: (case 1) $Ni(OH)_2$ and α-Fe_2O_3 and (case 2) $Ni(OH)_2$ and $Fe(OH)_3$ after 25 h of milling time, respectively.

the results from TGA, it can be concluded that the consequences of weight loss allocation (loss) of moisture and coordinated water from samples and is not due to dehydroxylation $Fe(OH)_3$ or $Ni(OH)_2$. The characteristic shape of the TG curve, which indicates dehydroxylation is not observed. Our results are in agreement with literature data [51,52].

The Raman spectra of samples after the calcination at selected intermediate temperature of 700 °C show five Raman modes typical of the spinel structure of $NiFe_2O_4$ (Fig. 6a). It is obvious that there is not a significant difference compared to the previously measured spectra of the samples obtained by milling a mixture of powders for 25 h. The modes of calcined samples have lower values of the full-width at half-maxima, as it was expected after the heat treatment. In this way is confirmed that obtained powder samples (after 25 h of milling time) can be attributed to the pure spinel $NiFe_2O_4$ structure according to a Refs. [40,53].

The fitting procedure of the IR spectra of the calcined samples (Fig. 6b) gave ω_{TO} and ω_{LO} wave numbers that converge to the values of crystal sample (Fig. 4). It is evident that in the case (1), Fig. 4a, the increase of ordering, caused by a heat treatment, leads to the changes in spectrum features, especially $F_{1u}(4)$ modes. In the case (2) changes are barely visible.

In both cases it is shown that after the heat treatment a disappearing of some modes that can be attributed to hematite or hydroxide precursors, does not happened. One can conclude that after 25 h milling time pure $NiFe_2O_4$ spinel is already formed.

Fig. 7 represents the scanning electron micrographs (SEM) of samples obtained from the mixture of (1) $Ni(OH)_2$ + α-Fe_2O_3 and (2) $Ni(OH)_2$ + $Fe(OH)_3$ powders by the soft mechanochemical synthesis after 4, 12 and 25 h milling time, respectively. The powder dissolved in kerosene was de-agglomerating in ultrasonic bath before analysis. The images show that agglomerate could not be completely destroyed. The tendency agglomerations increase with the milling time. The individual particle size was very difficult to determine due to indistinct image at higher magnification. The size of the powder particles of the starting powders mixture varied. As shown in Fig. 7 the surface morphology of the sample consists of the agglomerates, with relatively homogeneous grain distribution. The existence of agglomerates and changes in their size were confirmed. Powders milled for 4 h showed a wide distribution of particle agglomerates, while milled for 10 h showed a decrease in agglomerates size probably because during milling the primary agglomerates were destroyed. After that, secondary agglomeration starts and the agglomerates size increases resulting in a reduction of the specific surface area. The surface morphology of the sample as seen from the SEM consists of the grains, with relatively homogeneous grain distribution, with an average grain size varying from 1 to 3 μm.

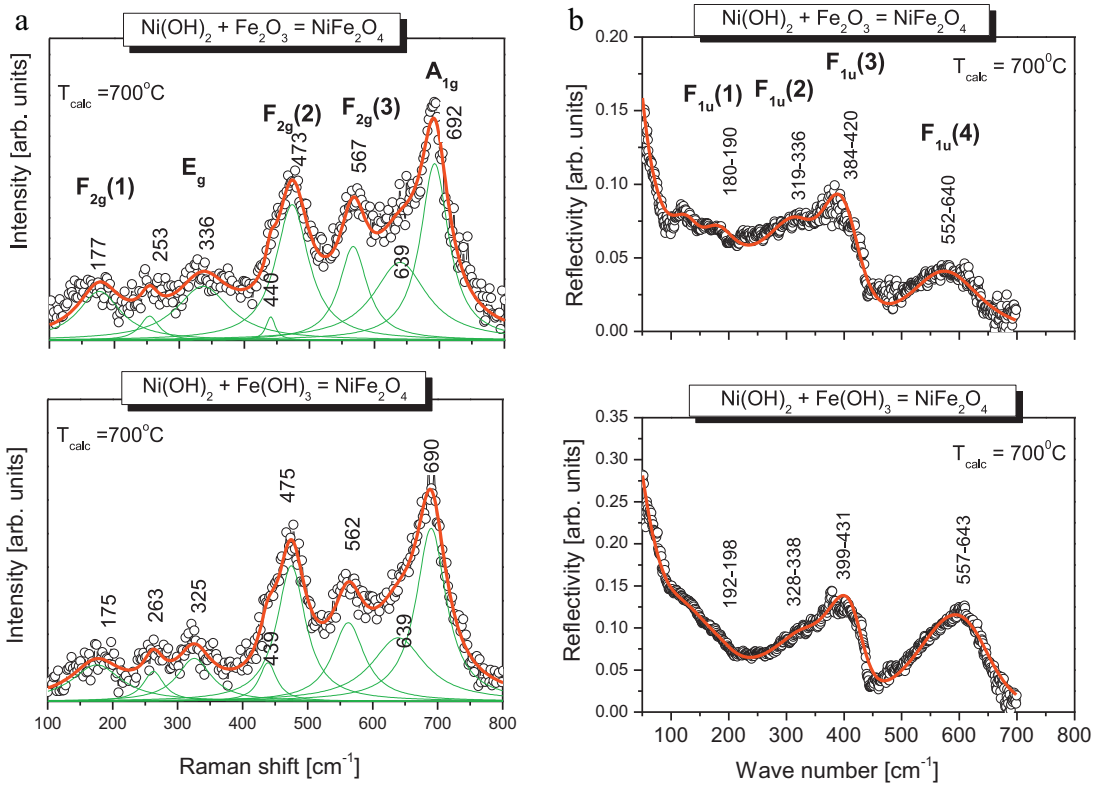

Fig. 6. (a) Raman and (b) IR spectra for the samples of $NiFe_2O_4$ calcined at 700 °C.

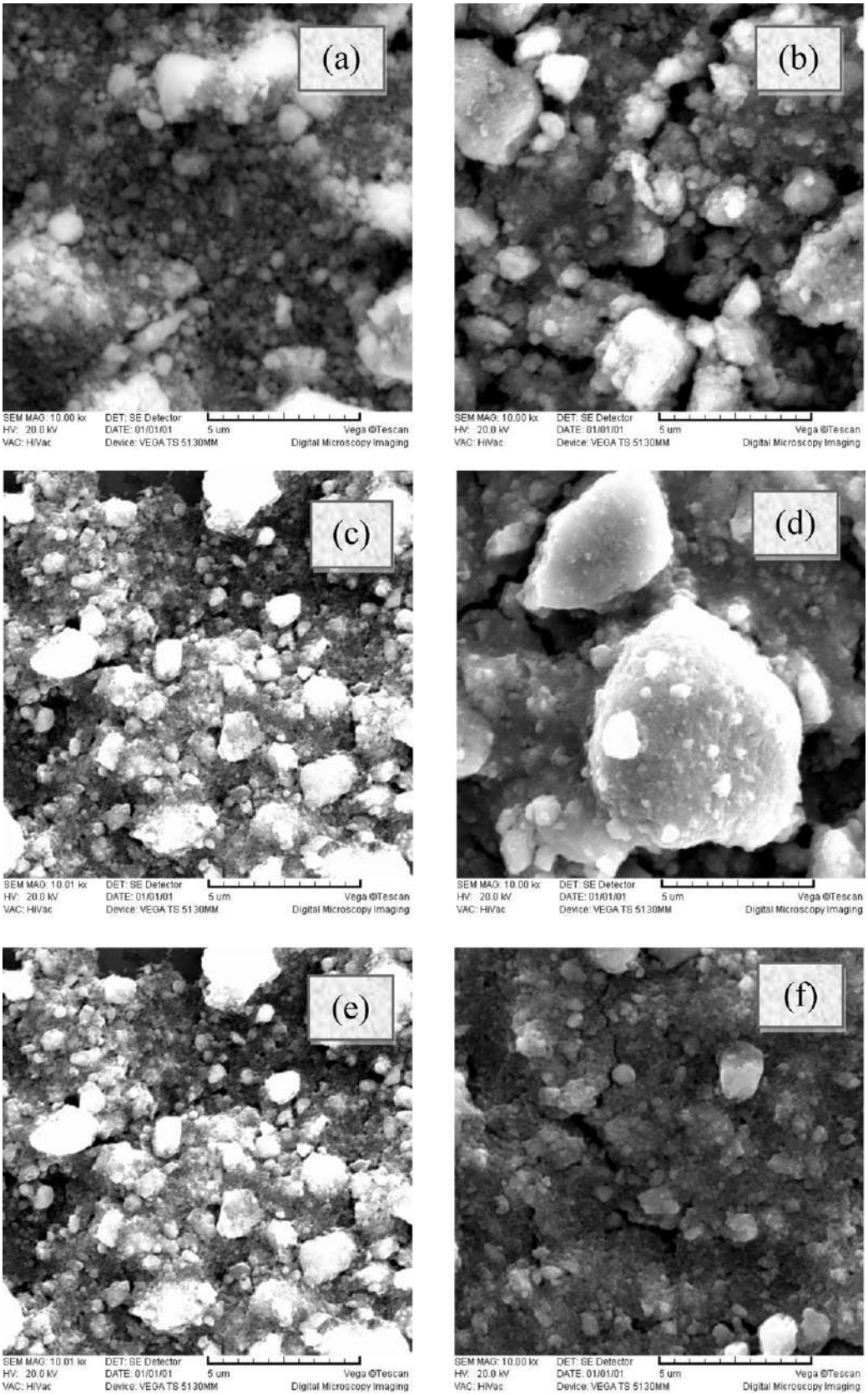

Fig. 7. SEM images of nanoscale mechanosynthesized of $NiFe_2O_4$ after 4, 10 and 25 h of milling of the mixture of powders: (case 1) $Ni(OH)_2$ and α-Fe_2O_3 (a, c, f) and (case 2) $Ni(OH)_2$ and $Fe(OH)_3$ (b, d, e), respectively.

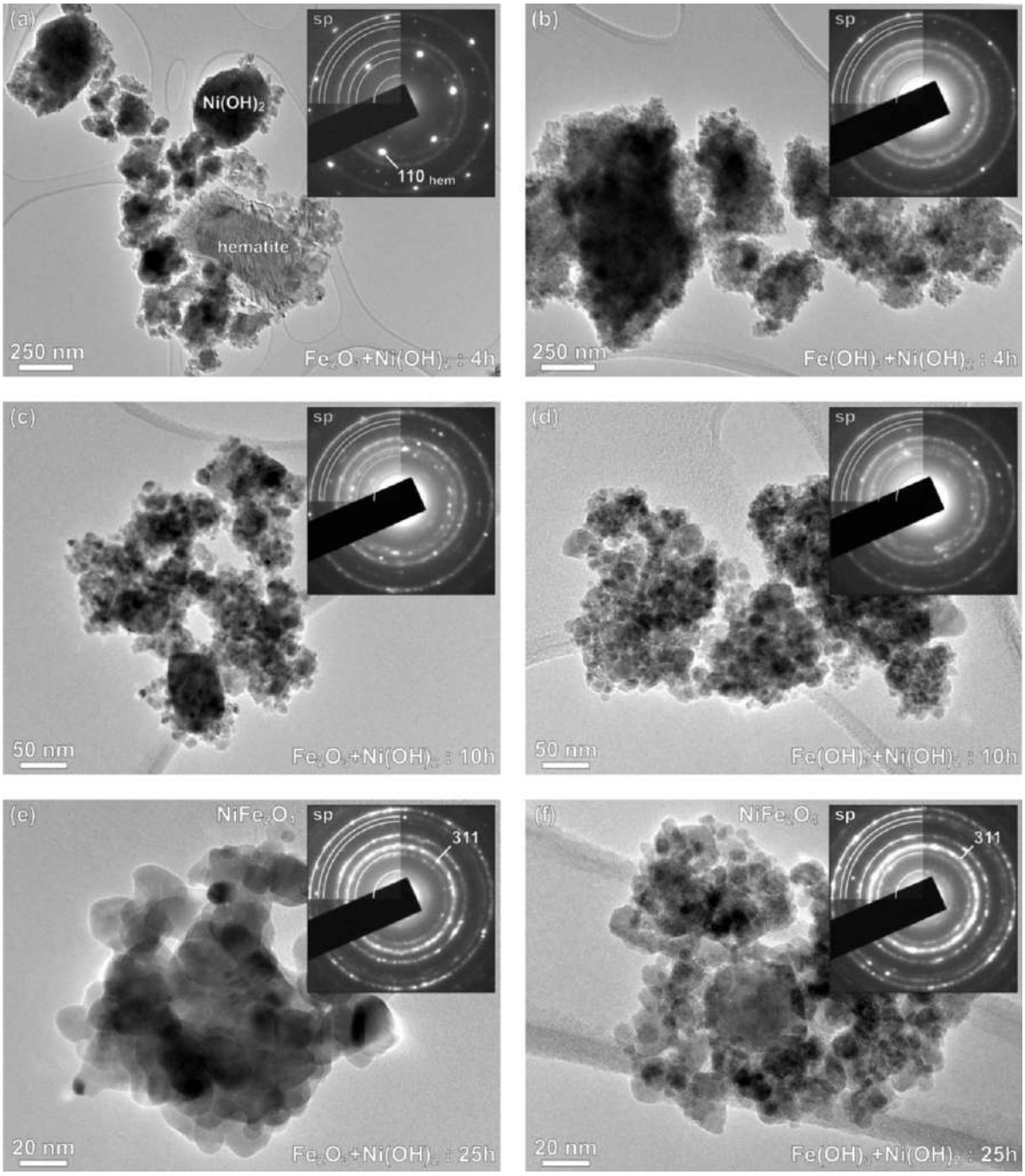

Fig. 8. TEM images with corresponding EDP (*insets* in the upper right corners) of mechano-chemically treated samples with starting compositions $Ni(OH)_2$ + α-Fe_2O_3 and $Ni(OH)_2$ + $Fe(OH)_3$ after processing for 4, 10 and 25 h. Lines in the upper-right quadrant of EDP indicate *d*-values for $NiFe_2O_4$ spinel phase (see Table 1) that fully evolves after 25 h of milling time.

$NiFe_2O_4$ is present in form of nanocrystalline particles in the mechanochemically treated samples after longer milling times. Fig. 8 shows TEM images of individual products after milling for 4, 10 and 25 h with corresponding electron diffraction patterns (EDP). In the samples milled for 4 h starting materials and intermediate reaction products dominate the EDP patterns. In the sample with starting composition α-Fe_2O_3 + $Ni(OH)_2$ we observe submicron large fragments of hematite and amorphous Ni-hydroxide globular particles, whereas $Fe(OH)_3$ + $Ni(OH)_2$ sample already shows some $NiFe_2O_4$ product in form of fine nanosized grains agglomerated in globules with primary hydroxide precursors. Spinel-type reflections become more pronounced after longer milling times, dominating the intensities of EDP patterns after 10 h of milling. Faint diffuse rings in EDP patterns belong to intermediate reaction products.

After 25 h of milling both processing routes yield pure spinel reflections belonging to $NiFe_2O_4$ phase. The final grain size in the $Ni(OH)_2$ + α-Fe_2O_3 system (average ~20 nm) is about twice as large as that in the $Ni(OH)_2$ + $Fe(OH)_3$ system (average ~10 nm), what is a consequence of different reaction paths in these two processing routes. These values of average grain size obtained from TEM are in good agreement with the size determination by Scherrer equation from XRD patterns. However the average size is not significantly different for powders synthesized by different methods [25,27]. Huo and Wei [13] was prepared $NiFe_2O_4$ ferrite with grain size distribution from 50 to 80 nm by hydrothermal

Table 1
Measured *d*-values [nm] for $NiFe_2O_4$ from EDP pattern (from Fig. 8e).

	D_1	D_2	D_3	D_4	D_5	D_6	D_7
Measured [nm]	0.481	0.295	0.250	0.209	0.171	0.161	0.148
JCPDF #89-4927	0.48133	0.29475	0.25137	0.20842	0.17017	0.16044	0.14737
Crystallogr. plane	{1 1 1}	{2 2 0}	{3 1 1}	{4 0 0}	{4 2 2}	{3 3 3}	{4 4 0}

synthesis. The formation of $NiFe_2O_4$ phase in the $Ni(OH)_2$ + α-Fe_2O_3 system started after longer milling times on sparse nucleation sites and therefore the final grain size is larger than in the $Ni(OH)_2$ + $Fe(OH)_3$ system where reactions started sooner and there were more nuclei for the spinel phase formation. The crystallites in both systems are rounded and tend to agglomerate into larger clusters with diameters of several hundred of nanometers. Measured *d*-values of $NiFe_2O_4$ from EDP pattern (from Fig. 8e) are listed in Table 1.

The composition of the product was analyzed by EDS measurements of several individual particles, as well as larger crystal clusters. The analyses show a constant Ni:Fe atomic ratio of 1:2, which corresponds to the $NiFe_2O_4$ phase. Fig. 9 shows a typical EDS spectrum, recorded on the sample obtained from mixture of $Ni(OH)_2$ + α-Fe_2O_3 powders milled for 25 h. The *inset* shows a HRTEM image of rounded $NiFe_2O_4$ nanoparticle with well resolved lattice fringes, characteristic for the spinel structure.

In order to understand better the whole process of phase formation and metal ion distribution, Mössbauer measurements were done. Fig. 10 shows the Mössbauer spectra for samples obtained at room temperature from the mixture of (1) $Ni(OH)_2$ + α-Fe_2O_3 and (2) $Ni(OH)_2$ + $Fe(OH)_3$ powders after 4 h and 25 h milling time. Subspectra corresponding to the nickel spinel ferrite nanoparticles are marked as *S*, *M* and *L* in Table 2. The sign *S* denotes superparamagnetic doublets, while the sign *M* is used for broadened sextets or sextets where it is not possible to differentiate resonant response from octahedral and the tetrahedral Fe^{3+} site. Such sextets have average values of isomer shift, broadened line width, lower magnitude of hyperfine field followed with higher value for quadrupole shift, because they come from nanoparticles of medium size where the structural and magnetic disorder of the surface atoms is dominant.

Measurement on the sample obtained at room temperature from the mixture of $Ni(OH)_2$/α-Fe_2O_3 powders after 4 h shows that 33% of total fitted area corresponds to the $NiFe_2O_4$ spinel (Fig. 10a). On the other hand, the $NiFe_2O_4$ spinel represents 42% of total area obtained on sample from 4 h milled mixed $Fe(OH)_3$/$Ni(OH)_2$ sample (Fig. 10c). Remained sextets are attributed to α-Fe_2O_3, γ-Fe_2O_3 and γ-FeOOH [54]. In both samples (Fig. 10a and c), hematite is described by distribution of hyperfine induction *B*. The distributions are characterized by sextets whose line widths were fixed to the value 0.24 mm s^{-1}. They are unimodal Gaussian like distribution (*see Insets* in Fig. 10). *Insets* (1) and (2) show a distribution of hyperfine field in samples (a) and (c) obtained for 4 h of milling for both cases of synthesis, respectively. The negative skew of the distribution −0.07 and −0.13, respectively, indicates that he left side tail of distribution is somewhat longer than the right hand side tail. The quadrupole shift of both samples is −0.17 mm s^{-1}. This is different from commonly reported in literature (−0.197 mm s^{-1}), probably due to superposition of hematite and larger crystalline $NiFe_2O_4$ quadrupole shifts.

The letter *L* marks sextets that arise from nanoparticles which have larger volume. They are recognized by narrow line width. In order to get good fit, we fixed some of *L*-sextets parameters for isomer shift: 0.25 mm s^{-1} and 0.36 mm s^{-1} for tetrahedral and

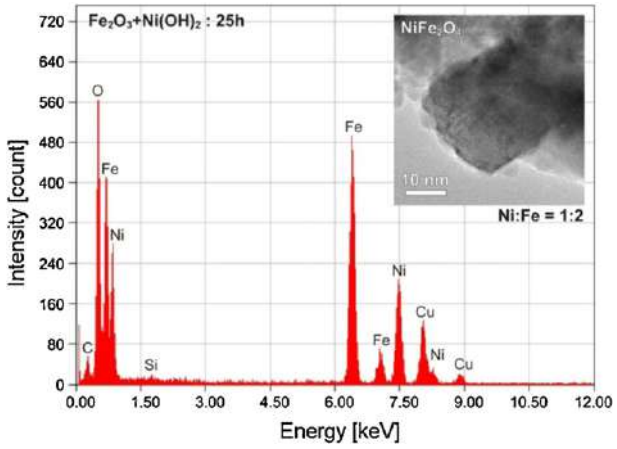

Fig. 9. EDS spectrum of the mixture $Ni(OH)_2$ + α-Fe_2O_3 powders after milling for 25 h shows the presence of single $NiFe_2O_4$ phase. The *inset* shows a HRTEM image of rounded $NiFe_2O_4$ nanoparticle with well resolved lattice fringes, characteristic for the spinel structure. *Cu* peak stems from the *Cu*-grid of the TEM specimen, whereas the minor peak of *Si* could not be explained.

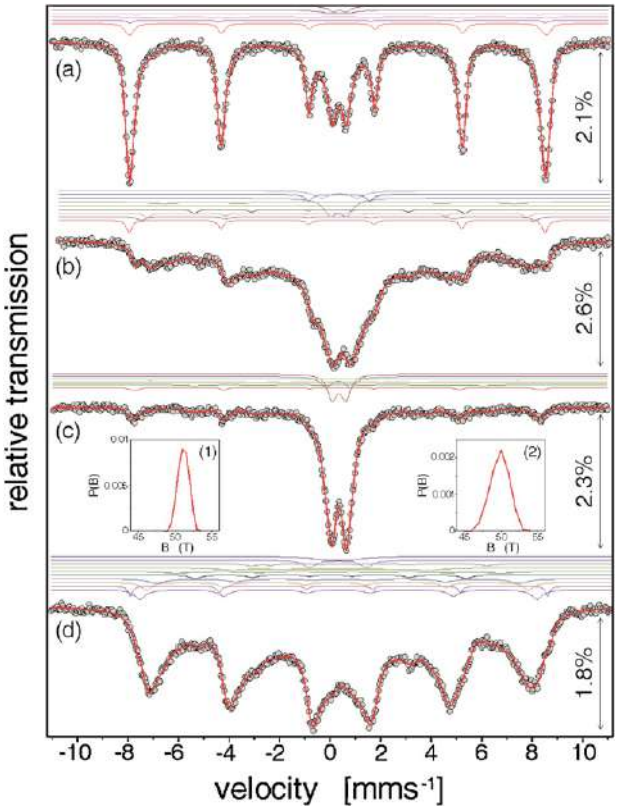

Fig. 10. Mössbauer spectra at room temperature of the mixture of powders $Ni(OH)_2$ and α-Fe_2O_3: (a) after 4 h milling time and (b) after 25 h milling time, and the mixture of powders $Ni(OH)_2$ and $Fe(OH)_3$: (c) after 4 h milling time and (d) after 25 h milling time. *Insets* (1) and (2) show a distribution of hyperfine field in samples (a) and (c), respectively.

Table 2
Mössbauer parameters: *A*-relative area fraction of component; Γ-line width (FWHM); δ-isomer shift with respect to α-Fe; Δ-quadruple splitting (2ε-shift) and *B*-hyperfine induction. Signs (*A*) and [*B*] denote tetrahedral and octahedral Fe^{3+} site occupancies respectively. Label *S*, *M*, and *L* classified particles by size. [f]Fixed value; *square bracket denotes the standard deviation of distribution.

Compound	Site	*A* [%]	Γ [mm s^{-1}]	δ [mm s^{-1}]	2ε or Δ [mm s^{-1}]	*Bhf* [T]
$NiFe_2O_4$ $Ni(OH)_2 + Fe_2O_3$, 4 h	M	5(1)	0.28(5)	0.47(1)	−0.34(2)	49.52(9)
	M	14(2)	0.91(9)	0.39(2)	0.04(5)	47.6(3)
	S	13(4)	0.85(8)	0.32(2)	0.8(1)	
α-Fe_2O_3		49(13)	0.24[f]	0.394(8)	−0.168(4)	51.13[0.73]*
γ-Fe_2O_3		8(2)	0.22(3)	0.308(8)	−0.03(2)	50.98(4)
γ-FeOOH		11(4)	0.39(5)	0.376(7)	0.51(2)	
$NiFe_2O_4$ $Ni(OH)_2 + Fe_2O_3$, 25 h	L (A)	3(1)	0.4(1)	0.25[f]	0.06(3)	46.6(2)
	L [B]	4(2)	0.4(1)	0.36[f]	−0.07(4)	48.3(2)
	M	46(9)	5.2(6)	0.35(4)	−0.1(1)	19(1)
	M	14(3)	1.3(1)	0.36(3)	−0.04(5)	43.0(4)
	S	16(4)	0.63(6)	0.333(8)	0.64(4)	
	S	2(1)	0.3(1)	0.36(2)	2.42(6)	
	S	9(5)	0.7(2)	0.38(1)	1.4(1)	
α-Fe_2O_3		4(1)	0.25(4)	0.37(1)	−0.17(2)	51.04(9)
α-Fe		2(1)	0.31(8)	−0.01(2)	−0.02(4)	33.2(1)
$NiFe_2O_4$ $Ni(OH)_2 + Fe(OH)_3$, 4 h	M	10(1)	1.1(2)	0.42(8)	−0.17(2)	35.5(3)
	M	6(1)	1.2(4)	0.2(1)	0.1(2)	20.3(7)
	M	2(1)	0.2(1)	0.26(3)	−0.20(6)	45.1(2)
	S	24(5)	0.53(3)	0.331(5)	0.97(5)	
α-Fe_2O_3		11(2)	0.24[f]	0.37(5)	−0.17(2)	49.82[1.24]*
γ-FeOOH		47(5)	0.44(2)	0.356(2)	0.54(2)	
$NiFe_2O_4$ $Ni(OH)_2 + Fe(OH)_3$, 25 h	L [B]	2(1)	0.21(5)	0.37(1)	−0.03(3)	51.22(9)
	L (A)	10(4)	0.50(7)	0.25[f]	0.08(2)	46.9(2)
	L [B]	17(5)	0.8(1)	0.36[f]	−0.09(2)	44.5(2)
	M	13(4)	1.3(2)	0.64(4)	−0.58(7)	39.8(4)
	M	21(4)	1.4(1)	0.17(2)	−0.30(3)	24.2(2)
	S	6(2)	0.56(8)	0.31(1)	2.25(3)	
	S	11(3)	1.2(2)	0.32(1)	1.0(1)	
γ-Fe_2O_3		13(4)	0.52(4)	0.33(1)	0.00(2)	48.7(1)
α-Fe		4(1)	0.50(9)	0.02(2)	0[f]	33.2(1)
Fe^{2+}		3(1)	0.6(1)	0.94(3)	1.20(7)	28.9(3)

octahedral sites, similar to Refs. [9,23]. Lower isomer shifts of (*A*) sites suggest that the Fe^{3+}–O^{2-} bonds on the tetrahedral site is more covalent then bonds on the octahedral sites. Iron ion on (*A*) site has *Td* point group symmetry, therefore there should be no electric field gradient (EFG). On the other hand, [*B*] site is trigonally distorted giving the significant quadrupole shift. As mentioned above, the more covalent iron–oxygen bonds of (*A*) sites contribute to distortion of 3d-electron density, which affects the polarization of 4*s*-electron density. This generates the hyperfine field of opposite sign than hyperfine field created by 1*s*, 2*s*, and 3*s*-electrons. Therefore, the sign of the hyperfine field with respect of direction of EFG is different for the (*A*) and the [*B*] site [34,55]. The opposite signs for the quadrupole shift were also obtained by Malik et al. [9].

The Mössbauer spectrum (Fig. 10b) of sample obtained from the mixture of the $Ni(OH)_2$ + α-Fe_2O_3 powders for 25 h of milling consists of over 94% fitted area and corresponds to the $NiFe_2O_4$ phase. There are at least 7% large size particles. The spectrum (Fig. 10d) of sample obtained from the mixture of the $Ni(OH)_2$ + $Fe(OH)_3$ powders by milling for 25 h shows about 80% fitted area and is associated with the main phase. At least 36% of total amount of the formed spinel ferrite consists of large particles. Knowing the subspectra's area of origin in large particles, we were able to estimate the degree of inversion which is at most 0.82 and 0.66, respectively. For the latter sample, low degree of inversion is confirmed by two sextets with Fe^{3+} in the octahedral sites. It is in good agreement with works of Šepelák and Siddique et al. [56,57]. The rest of hematite and formation of maghemite and lepidocrocite at Mössbauer spectra are expected based on the hydroxide transform scheme. The α-Fe and Fe^{2+} in high energy ball mill treatment are also observed by Menzel et al. [58].

4. Conclusions

$NiFe_2O_4$ ferrite powders have been prepared by soft mechanochemical synthesis starting from the mixture of (1) $Ni(OH)_2$ and α-Fe_2O_3 and (2) $Ni(OH)_2$ and $Fe(OH)_3$ powders. Single phase nanosized nickel-ferrite powder was synthesized by 25 h ball milling. X-ray diffraction of the prepared samples shows single phase cubic spinel structure. In recorded Raman and IR spectra are observed all five first-order Raman and four IR active modes. The intensity of the Raman modes during the formation of ferrite phase in both cases of synthesis is similar, but there are differences that indicate that milling leads to phase changes in the development of ferrite phase during application the soft mechanochemical method. TGA/DSC was used to confirm the complete conversion of the precursors to the $NiFe_2O_4$ ferrite. The Mössbauer spectra shows that the sample formed from oxide–hydroxide has a tendency to form larger size particles (at least 21%) than at least 7% spinel ferrite particles occurred from hydroxide–hydroxide. Knowing the subspectra's area originated from large particles, we were able to estimate the degree of inversion at most 0.82 and 0.66, respectively. This simple, low cost route should be applicable for the synthesis of other functional nanoparticles materials.

Acknowledgments

This research was financially supported by the Serbian Ministry of Education and Science through Projects No. III 45003, III 45015 and 171001.

References

[1] R.H. Kodama, J. Magn. Magn. Mater. 200 (2000) 359–372.

[2] H. Kavas, A. Baykal, M.S. Toprak, Y. Köseoğlu, M. Sertkol, B. Aktas, J. Alloys Compd. 479 (2009) 49–55.
[3] J.A.C. de Paiva, M.P.F. Graça, J. Monteiro, M.A. Macedo, M.A. Valente, J. Alloys Compd. 485 (2009) 637–641.
[4] A. Alarifi, N.M. Deraz, S. Shaban, J. Alloys Compd. 486 (2009) 501–506.
[5] A.M.M. Farea, S. Kumara, K.M. Batoo, A.Y.C.G. Lee, Alimuddin, J. Alloys Compd. 469 (2009) 451–457.
[6] Joint Committee on Powder Diffraction Standards (JCPDS) Powder Diffraction File (PDF), International Centre for Diffraction Data, Newton Square, PA, 2003.
[7] A. Goldman, Modern Ferrite Technology, Marcel Dekker, New York, 1993.
[8] C.V. Gopal Reddy, S.V. Manorama, V.J. Rao, Sens. Actuators B: Chem. 55 (1990) 90–95.
[9] R. Malik, S. Annapoorni, S. Lamba, V.R. Reddz, A. Gupta, P. Sharma, A. Inoue, J. Magn. Magn. Mater. 322 (2010) 3742–3747.
[10] M.A. Willard, L.K. Kurihara, E.E. Carpenter, S. Calvin, V.G. Harris, Int. Mater. Rev. 49 (2004) 125–170.
[11] F. Gözüak, Y. Köseoğlu, A. Baykal, H. Kavas, J. Magn. Magn. Mater. 321 (2009) 2170–2177.
[12] L. Wang, J. Ren, Y. Wang, X. Liu, Y. Wang, J. Alloys Compd. 490 (2010) 656–660.
[13] J. Huo, M. Wei, Mater. Lett. 63 (2009) 1183–1184.
[14] D. Chen, D. Chen, X. Jiao, Y. Zhao, M. He, Powder Technol. 133 (2003) 247–250.
[15] K. Maaz, A. Mumtaz, S.K. Hasanain, M.F. Bertino, J. Magn. Magn. Mater. 322 (2010) 2199–2202.
[16] P. Sivakumur, R. Ramesh, A. Ramanand, S. Ponnusamy, C. Muthamizhchelvan, Mater. Lett. 65 (2011) 483–485.
[17] A. Kale, S. Gubbala, R.D.K. Misra, J. Magn. Magn. Mater. 277 (2004) 350–358.
[18] D.H. Chen, X.R. He, Mater. Res. Bull. 36 (2001) 1369–1377.
[19] A.T. Raghavender, K. Zadro, D. Pajic, Z. Skoko, N. Biliskov, Mater. Lett. 64 (2010) 1143–1146.
[20] P.K. Roy, J. Bera, J. Mater. Process. Technol. 197 (2008) 279–283.
[21] V. Šepelák, U. Steinike, D.C. Uecker, S. Wissmann, K.D. Becker, J. Solid State Chem. 135 (1998) 52–58.
[22] E. Avvakumov, M. Senna, N. Kosova, Soft Mechanochemical Synthesis: A Basis for New Chemical Technologies, Kluwer Academic Publishers, Boston, 2001.
[23] V. Šepelák, I. Bergmann, A. Feldhoff, P. Heitjans, F. Krumeich, D. Menzel, F.J. Litterst, S.J. Campbell, K.D. Becker, J. Phys. Chem. C 111 (2007) 5026–5033.
[24] V. Šepelák, S. Indris, P. Heitjans, K.D. Becker, J. Alloys Compd. 434–435 (2007) 776–778.
[25] Č. Jovalekić, M. Zdujić, A. Radaković, M. Mitrić, Mater. Lett. 24 (1995) 365–368.
[26] C.N. Chinnasamy, A. Narayanasamy, N. Ponpandian, K. Chattopadhyay, K. Shinoda, B. Jeyadevan, K. Tohji, K. Nakatsuka, T. Furubayashi, I. Nakatani, Phys. Rev. B 63 (2007) 184108.
[27] V. Šepelák, D. Baabe, K.D. Becker, J. Mater. Synth. Process. 8 (2000) 333–337.
[28] H. Yang, X. Zhang, W. Ao, G. Qiu, Mater. Res. Bull. 39 (2004) 833–837.
[29] V. Šepelák, M. Menel, I. Bergmann, M. Wiebcke, F. Krumeich, K.D. Becker, J. Magn. Magn. Mater. 272–276 (2004) 1616–1618.
[30] T.F. Marinca, I. Chicinaş, O. Isnard, V. Pop, F. Popa, J. Alloys Compd. 509 (2011) 7931–7936.
[31] V.V. Boldyrev, Solid State Ionics 63–65 (1993) 537–543.
[32] R. Valenzuela, Magnetic Ceramics, Cambridge University Press, Cambridge, 1994
[33] G.A. Sawatzky, F. Van der Woude, A.H. Morrish, Phys. Rev. 187 (1969) 747–757.
[34] N.N. Greenwood, T.C. Gibb, Mössbauer Spectroscopy, Chapman and Hall Ltd., London, 1971, pp. 266–267.
[35] A. Ahlawat, V.G. Sathen, V.R. Reddy, A. Gupta, J. Magn. Magn. Mater. 323 (2011) 2049–2054.
[36] S. Mørup, in: G.J. Long (Ed.), Mössbauer Spectroscopy Applied to Inorganic Chemistry, vol. 2, Plenum Press, New York, 1987, pp. 89–123.
[37] Z.Ž. Lazarević, Č. Jovalekić, A. Recnik, V.N. Ivanovski, M. Mitrić, M.J. Romčević, N. Paunović, B.Đ. Cekić, N.Ž. Romčević, J. Alloys Compd. 509 (2011) 9977–9985.
[38] R.A. Brand, WinNormos Mössbauer fitting program. Universität Duisburg, 2008.
[39] Scherrer and Warren equations (B. E. Warren, X-ray Diffraction), Addison Wesley, Reading, MA, 1969.
[40] A. Baykal, N. Kasapoğlu, Y. Köseoğlu, M.S. Toprak, H. Bayrakdar, J. Alloys Compd. 509 (2008) 514–518.
[41] G. Dixit, J.P. Singh, R.C. Srivastava, H.M. Agrawal, Nucl. Instrum. Meth. B 269 (2011) 133–139.
[42] A. Ahlawat, V.G. Sathe, J. Raman Spectrosc. 42 (2011) 1087–1094.
[43] M.K. Nieuwoudt, J.D. Comins, I. Cukrowski, J. Raman Spectrosc. 42 (2011) 1335–1339.
[44] D. Bersani, P.P. Lottici, A. Montenero, J. Raman Spectrosc. 30 (1999) 355–360.
[45] J.L. Bantignies, S. Deabate, A. Righi, S. Rols, P. Hermet, J.L. Sauvajol, F. Henn, J. Phys. Chem. C 112 (2008) 2193–2201.
[46] A.M. Jubb, H.C. Allen, Appl. Mater. Interfaces 2 (2010) 2804–2812.
[47] A. Šurca, B. Orel, B. Pihlar, J. Sol–Gel Sci. Technol. 8 (1997) 743–749.
[48] R.D. Waldron, Phys. Rev. 99 (1955) 1727–1735.
[49] T. Shimada, T. Tachibana, T. Nakagawa, T.A. Yamamoto, J. Alloys Compd. 379 (2004) 122–126.
[50] H. Uchiyama, S. Tsutsui, A.Q.R. Baron, Phys. Rev. B 81 (2010) 241103.
[51] M. Senna, Solid State Ionics 63–65 (1993) 3–8.
[52] J. Temuujin, M. Aoyama, M. Senna, T. Masuko, C. Ando, H. Kishi, J. Solid State Chem. 1775 (2004) 3903–3908.
[53] Y. Shi, J. Ding, Z.X. Shen, W.X. Sun, L. Wang, Solid State Commun. 115 (2000) 237–241.
[54] E. Murad, Hyperfine Interact. 111 (1998) 251–259.
[55] G.A. Fatseas, G.A.R. Krishnan, J. Appl. Phys. 39 (1968) 1256–1257.
[56] V. Šepelák, I. Bergmann, S. Kipp, K.D. Becker, Z. Anorg. Allg. Chem. 631 (2005) 993–1003.
[57] M. Siddique, N.M. Butt, Physica B 405 (2010) 4211–4215.
[58] M. Menzel, V. Šepelák, K.D. Becker, Solid State Ionics 141–142 (2005) 663–669.

Nanodimensional spinel NiFe2O4 and ZnFe2O4 ferrites prepared by soft mechanochemical synthesis

Z. Ž. Lazarević, Č. Jovalekić, A. Milutinović, D. Sekulić, V. N. Ivanovski et al.

Citation: J. Appl. Phys. **113**, 187221 (2013); doi: 10.1063/1.4801962
View online: http://dx.doi.org/10.1063/1.4801962
View Table of Contents: http://jap.aip.org/resource/1/JAPIAU/v113/i18
Published by the American Institute of Physics.

Nanodimensional spinel $NiFe_2O_4$ and $ZnFe_2O_4$ ferrites prepared by soft mechanochemical synthesis

Z. Ž. Lazarević,[1,a)] Č. Jovalekić,[2] A. Milutinović,[1] D. Sekulić,[3] V. N. Ivanovski,[4] A. Rečnik,[5] B. Cekić,[4] and N. Ž. Romčević[1]
[1]*Institute of Physics, University of Belgrade, Pregrevica 118, Zemun, Belgrade, Serbia*
[2]*The Institute for Multidisciplinary Research, University of Belgrade, Kneza Višeslava 1, Belgrade, Serbia*
[3]*Faculty of Technical Sciences, University of Novi Sad, Novi Sad, Serbia*
[4]*Institute of Nuclear Sciences Vinča, University of Belgrade, P.O. Box 522, 11001 Belgrade, Serbia*
[5]*Department for Nanostructured Materials, Jožef Stefan Institute, Ljubljana, Slovenia*

(Received 3 October 2012; accepted 4 January 2013; published online 8 May 2013)

$NiFe_2O_4$ and $ZnFe_2O_4$ ferrites have been prepared by soft mechanochemical synthesis. The formation of spinel phase and crystal structure of sintered powders were analyzed by X-ray diffraction, Raman spectroscopy, and transmission microscopy. In order to confirm phase formation and cation arrangement, Mössbauer measurements were done. Investigation of the magnetization as a function of magnetic field confirms an expected change of the degree of inversion in the spinel structure with the sintering. The electrical DC/resistivity/conductivity was measured in the temperature range of 298-423 K. Impedance spectroscopy was performed in the wide frequency range (100 Hz-10 MHz) at different temperatures. © *2013 AIP Publishing LLC*
[http://dx.doi.org/10.1063/1.4801962]

I. INTRODUCTION

Cubic nanosized spinel ferrites with the general formula MFe_2O_4, where M is a divalent cation, belong to a family of magnetic materials that can be used in many areas, such as magnetic devices, switching devices, recording tapes, permanent magnets, hard disc recording media, flexible recording media, read-write heads, active components of ferrofluids, color imaging, magnetic refrigeration, detoxification of biological fluids, magnetically controlled transport of anti-cancer drugs, magnetic resonance imaging (MRI) contrast enhancement, and magnetic cell separation.[1] The interest for using of these materials permanently increases because of their usability under extreme conditions. It is well known that unique magnetic, chemical, and mechanical properties of ferrite materials strongly depend on the preparation conditions. One of the most interesting ferrite is $NiFe_2O_4$ and $ZnFe_2O_4$.

In normal spinel ferrites, all the divalent M^{2+} cations are on the tetrahedral sites and the trivalent Fe^{3+} cations on the octahedral sites. An example of normal spinel is a bulk $ZnFe_2O_4$ ferrite. The inverse spinel has the divalent cation occupying the octahedral sites and the trivalent cations are equally divided among the tetrahedral and remaining octahedral sites. $NiFe_2O_4$ ferrite is predominantly an inverse spinel. Spinel ferrites can be presented with general formula: $(M_{1-\lambda}Fe_\lambda)[M_\lambda Fe_{2-\lambda}]O_4$, where the cation distribution factor $\lambda = 0$ for normal spinels and $\lambda = 1$ for purely inverse spinel. As is common, parentheses and square brackets denote cation sites of tetrahedral and octahedral coordination, respectively.[2]

It is widely accepted that the cation distribution in MFe_2O_4 (M = Ni, Zn), which determines many physical and chemical properties, is a complex function of processing parameters and depends on the preparation method of the material.[3] Technological and scientific challenges coupled with environmental considerations have prompted a search for simple and energy-efficient synthesis and processing routes of nanocrystalline spinel ferrites.[4] Among many types of preparation and processing techniques (including, for example, hydrothermal reactions,[5,6] coprecipitation,[7–9] combustion synthesis,[10,11] the sol-gel method,[12,13] microwave processing,[14,15] micro emulsion procedures,[16,17] and chemical synthesis[18]), the nonconventional mechanochemical route[19] has been recognized as a powerful method for the production of novel, high-performance, and low-cost materials.

Novel approach to mechanochemical synthesis, based on reactions of solid acids, based hydrated compounds, crystal hydrates, basic and acidic salts, has been called soft mechanochemical synthesis.[20] The dissolved substances, compared to the same substances in the solid state, substantially change their nature. It can influence on the composition and properties of the final product. Peculiarities of soft mechanochemical reactions consist in the high reactivity of surface functional groups, notably, OH groups. Consequently, we investigated possibilities of synthesis of $NiFe_2O_4$ and $ZnFe_2O_4$ ferrites by soft mechanochemical technique and impact of this method on the properties significantly affected by particle size.

In this article, both ferrites have been prepared starting from a mixture of (1) $Ni(OH)_2$ and $Fe(OH)_3$ and (2) $Zn(OH)_2$ and $Fe(OH)_3$ powders in a planetary ball mill. The aim of this work is to apply a new synthesis route to prepare ultrafine ferrites and to investigate their structural, magnetic, and electrical properties.

II. EXPERIMENTAL PROCEDURE

For mixtures of crystalline powders, denoted by case (1) and (2), the starting materials were: (1) nickel(II)-hydroxide

[a)]Author to whom correspondence should be addressed. Electronic mail: lzorica@yahoo.com. Tel.: +381 11 37 13 035. Fax: +381 11 3160 531.

$(Ni(OH)_2$, Merck 95% purity) and $Fe(OH)_3$ and (2) zinc(II)-hydroxide ($Zn(OH)_2$, Merck 95% purity) and $Fe(OH)_3$ in equimolar ratio. Soft mechanochemical synthesis was performed in air atmosphere in planetary ball mill (Fritsch Pulverisette 5) for 25 h (case 1) and 18 h (case 2). Required milling times for obtaining a single-phase ferrites were determined experimentally, in earlier paper.[21,22] The powder mixture was pressed into pallet using a cold isostatic press (8 mm in diameter and ~3 mm thick). The powder mixtures were sintered at 1100 °C for 2 h (Lenton-UK oven) without pre-calcinations step. Heating rate was 10 °C min^{-1}, with nature cooling in air atmosphere.

The formation of phase and crystal structure of sintered powders of the $NiFe_2O_4$ and $ZnFe_2O_4$ were approved via the X-ray diffraction (XRD) measurements. Model Philips PW 1050 diffractometer equipped with a PW 1730 generator (40 kV × 20 mA) was used with Ni filtered CoKα radiation of 1.78897 Å at the room temperature. Measurements were done in 2θ range of 15°–80° with scanning step width of 0.05° and 10 s scanning time per step.

Raman measurements of mixture powder and sintered sample were performed using Jobin-Ivon T64000 monochromator. An optical microscope with 100× objective was used to focus the 514 nm radiation from a Coherent Innova 99 Ar^+ laser on the sample. The same microscope was used to collect the backscattered light. The scattering light dispersed was detected by a charge-coupled device (CCD) detection system. Room temperature Raman spectra are in spectral range from 100 to 800 cm^{-1}.

TEM studies were performed using a 200 kV TEM (JEM-2100 UHR, Jeol Inc., Tokyo, Japan) equipped with an ultra-high resolution objective lens pole piece having a point-to-point resolution of 0.19 nm, being sufficient to resolve the lattice images of nanoparticles. Due to relatively small size of the nanoparticles, selected area electron diffraction patterns (EDP) over the multiple nanocrystals were recorded to obtain the characteristic diffraction rings with structure-specific *d*-values.

The room temperature transmission ^{57}Fe Mössbauer experiments were carried out by constant acceleration mode using $^{57}Co(Rh)$ source. The spectra calibrated by laser and isomer shifts are shown with respect to the α-Fe. The data analysis was performed using WinNormos-Site[23] software including the transmission integral correction for sample thickness.

The magnetization measurements were done at room temperature using VSM 200 cryogenic magnetometer in magnetic field from 0 kOe to ± 80 kOe.

The electrical DC/resistivity/conductivity in the temperature range of 298-423 K was measured on a SourceMeter Keithley 2410. Impedance measurements were carried out in the frequency range 100 Hz to 10 MHz on a HP-4194A impedance/gain-phase analyzer using a HP-16048C test fixture at the temperature of 298-423 K.

III. RESULTS AND DISCUSSION

Figure 1 shows the XRD patterns of the synthesized $NiFe_2O_4$ and $ZnFe_2O_4$ nano powders for 25 h and 18 h of milling time and then sintered at 1100 °C for 2 h. All XRD peaks are indexed well with the standard pattern reported in PCPDF card for $NiFe_2O_4$ # 89-4927 and for $ZnFe_2O_4$ # 89-7412. The powder diffractograms present a series peaks

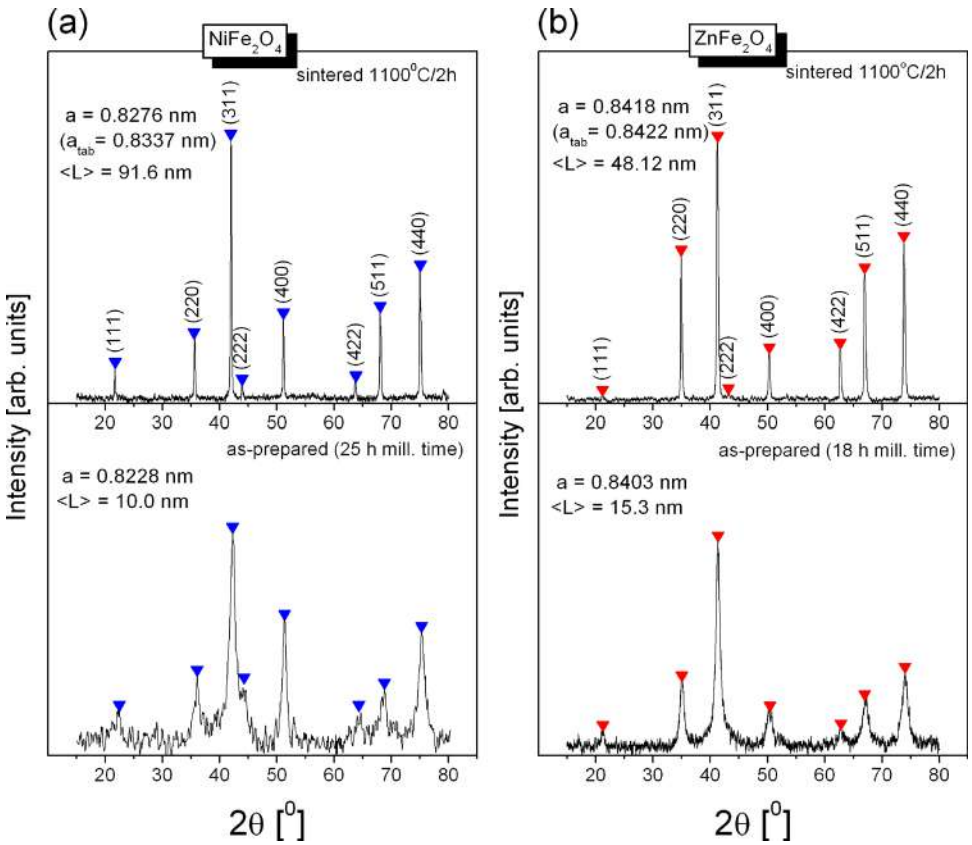

FIG. 1. X-ray diffraction **patterns of** the (a) $NiFe_2O_4$ and (b) $ZnFe_2O_4$ **powders** and sintered **samples** at 1100 °C for 2 h.

assigned to cubic spinel ferrite $NiFe_2O_4$ and $ZnFe_2O_4$ phases which mean single ferrite phases are formed after appropriate milling times. The average crystallite size has been calculated using Scherrer's formula $L = k_S\lambda_{Co}/\beta\cos\theta_{hkl}$, where L is the particle size, λ_{Co} is the wavelength of X-ray radiation (1.78897 Å for Co-K_α), β is the full width at half maximum (FWHM) reduced for instrumental broadening, and k_S is Scherrer constant.[24] The average calculated particle sizes have been found to be about 10 and 15 nm for the $NiFe_2O_4$ and $ZnFe_2O_4$ powders, respectively. The lattice parameters for powders (given in Fig. 1) computed according to the relation $a = \lambda_{Co}\,(h^2 + k^2 + l^2)^{1/2}/(2\sin\theta_{hkl})$ using respective (hkl) values are less than that of the bulk material. This reduction in lattice parameter may be attributed to surface tension which can lead to the distortion of the lattice and redistribution of cations. The diffraction peaks in sintered samples become sharper, which could be associated with the amount of significantly increased ferrite grains. It can be seen that there are no other diffraction peaks except peaks of spinel ferrites. The average grain sizes, calculated using Scherrer formula, are about 92 nm for $NiFe_2O_4$ and 48 nm for $ZnFe_2O_4$. The grains grow dramatically with the temperature, which indicates that selected sintering temperature is beneficial for ferrite crystallization.

Raman spectroscopy is a nondestructive material characterization technique sensitive to structural disorder. It provides an important tool to probe the structural properties of mechanochemically synthesized materials. Group theory predicts five first order Raman active modes ($A_{1g} + E_g + 3F_{2g}$) in the normal cubic spinel structure with symmetry $Fd3m$, and all these modes were observed as clear, symmetrical peaks in the spectrum of sintered $ZnFe_2O_4$ ferrite at ambient conditions, as shown in Fig. 2. In the case of the as-prepared powder sample of $ZnFe_2O_4$, as well as in the case of as-prepared powder and sintered $NiFe_2O_4$ samples, all five Raman peaks seem asymmetric, or even dissociated. Deconvolution of spectrum demonstrates that each peak can be presented like a doublet, which is a characteristic of the inverse spinel structure.[25,26] In the case of the as-prepared nanosized samples, a surface tension, characteristic for nano-particles, enables redistribution of the cations compared to stable bulk configuration. The octahedral sites are occupied by Zn(Ni) and by Fe ions. This results in a distortion of bond distances; owing to differences in ionic radii of Zn(Ni) and Fe ions, the metal-oxygen bond distance shows a substantial distribution. The symmetry becomes lower and the Raman spectra detect these changes very effectively. Inverse spinel belongs to $P4_322$ tetragonal space group, but it is common to assigned Raman modes as if they were in a normal spinel, for simplicity.

In the cubic ferrites, the strongest modes above 600 cm^{-1} correspond to symmetric stretching of oxygen in tetrahedral AO_4 groups, so the modes about 690 cm^{-1} in the case of $NiFe_2O_4$ (and 630 cm^{-1} in $ZnFe_2O_4$) can be considered as A_g symmetry. E_g at about 320 cm^{-1} (~250 cm^{-1}) is due to symmetric bending of oxygen with respect to cation in tetrahedral surrounding. $F_{2g}(2)$ at 470 cm^{-1} (~350 cm^{-1}) and $F_{2g}(3)$ at 570 cm^{-1} (~450 cm^{-1}) correspond to the vibrations of octahedral group: $F_{2g}(2)$ is due to asymmetric stretching and $F_{2g}(3)$ is caused by asymmetric bending of oxygen. $F_{2g}(1)$ at 180 cm^{-1} in the case of $NiFe_2O_4$, or ~160 cm^{-1} in the case of $ZnFe_2O_4$, is due to translational movement of the whole tetrahedron.

Figure 3 shows TEM images of $NiFe_2O_4$ and $ZnFe_2O_4$ nano ferrites obtained after appropriate milling time with

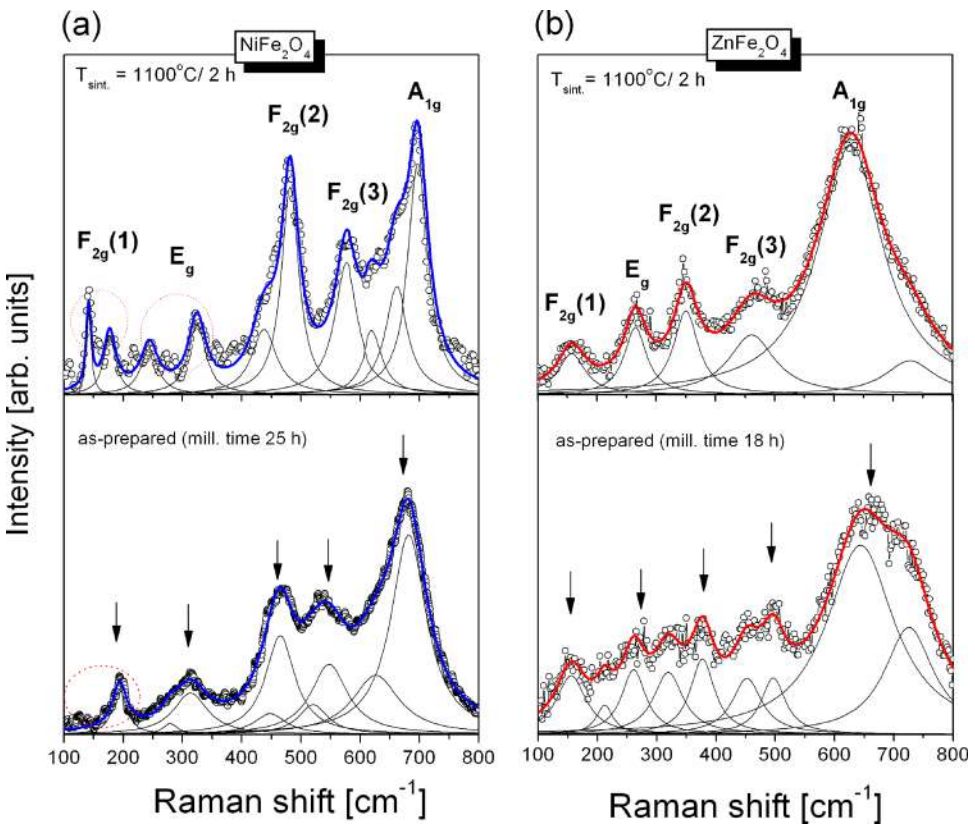

FIG. 2. Raman spectra of the (a) $NiFe_2O_4$ and (b) $ZnFe_2O_4$ powders and sintered samples at 1100 °C for 2 h.

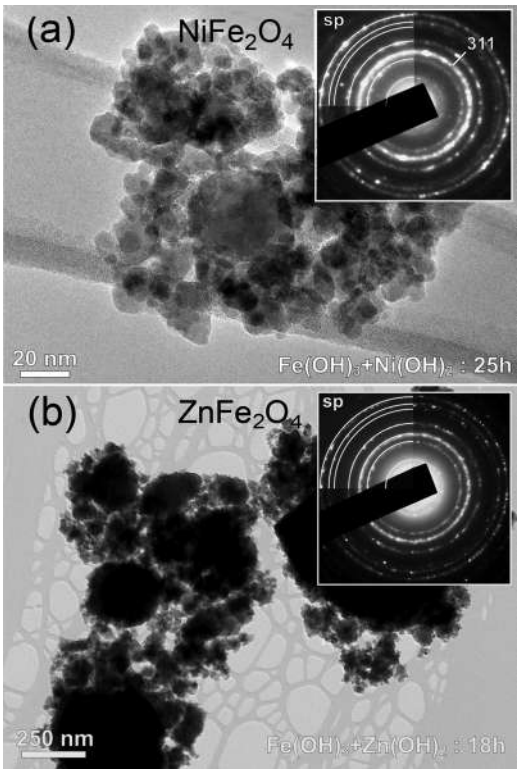

FIG. 3. TEM images with corresponding EDP (*insets* in the upper right corners) of mechanochemically prepared $NiFe_2O_4$ and $ZnFe_2O_4$ powders from starting compositions (a) $Ni(OH)_2 + Fe(OH)_3$ and (b) $Zn(OH)_2 + Fe(OH)_3$ after processing for 25 h and 18 h, respectively.

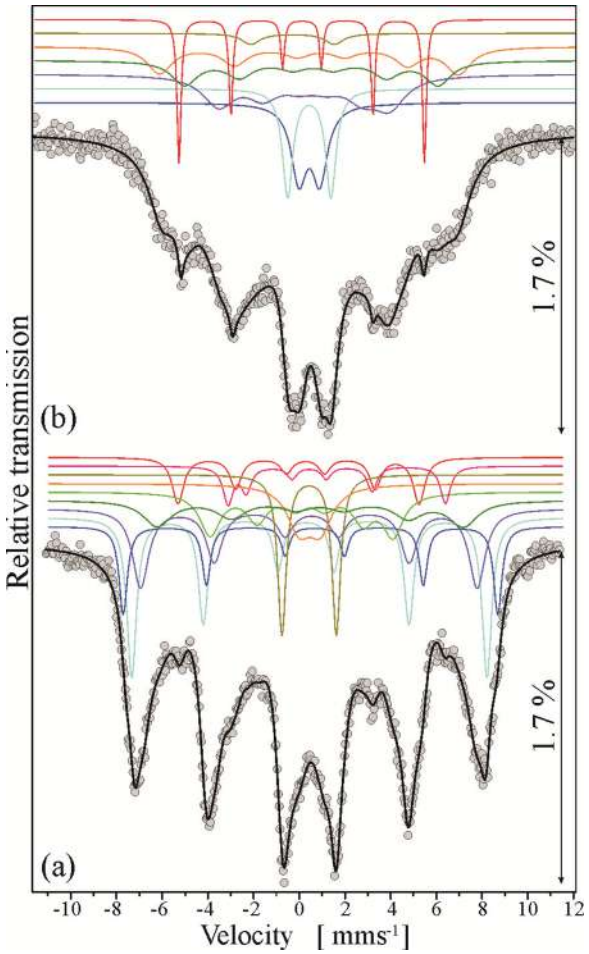

FIG. 4. Mössbauer spectra at room temperature of the mixture of powders (a) $Ni(OH)_2 + Fe(OH)_3$ and (b) $Zn(OH)_2 + Fe(OH)_3$ after processing for 25 h and 18 h, respectively. The values of relative absorption are shown. The subspectra are plotted above the main spectrum.

corresponding EDPs. The final grain size in the $NiFe_2O_4$ (average $\sim$ 10 nm) is about twice as large as that in the $ZnFe_2O_4$ (average $\sim$ 20 nm), which is a consequence of different reaction paths in these two ferrite processing routes. The formation of $NiFe_2O_4$ phase started after longer milling times on sparse nucleation sites and therefore the final grain size is lower than in the $ZnFe_2O_4$ system where reactions started sooner and there were more nuclei for the spinel phase formation. The crystallites in both systems are rounded and tend to agglomerate into larger clusters with diameters of several hundreds of nanometers. Measurements of the diffraction rings confirmed that they correspond to the crystal planes of spinel structure.

Mössbauer spectroscopy was used to investigate the synthesized $NiFe_2O_4$ and $ZnFe_2O_4$ nanopowders obtained after 25 h and 18 h of milling, respectively. The bulk $NiFe_2O_4$ has an inverse spinel ferrite structure with ionic bonding: $(Fe^{3+}\uparrow)_A[Ni^{2+}\downarrow Fe^{3+}\downarrow]_B O_4$.[27] The bulk $ZnFe_2O_4$ is a normal spinel with formula $(Zn^{2+})_A[Fe^{3+}\ Fe^{3+}]_B O_4$.[28] Marked ions in the parenthesis with sign (A) occupy tetrahedral sites, while ions inside square brackets as [B], and occupy octahedral sites. The obtained nanopowders $NiFe_2O_4$ and $ZnFe_2O_4$ spinels by soft mechanochemical synthesis in a ball mill, might crystallize in various sizes with cation redistribution described by the following formula $(M^{2+}{}_{1-\lambda}Fe^{3+}{}_{\lambda})[M^{2+}{}_{\lambda}Fe^{3+}{}_{2-\lambda}]O_4$. The parameter λ is a degree of inversion and M = Ni or Zn. Estimation of the parameter λ is the goal of this spectroscopy. Also, we could get more information about nanoparticles sizes.

The Mössbauer spectrum (Fig. 4) of $NiFe_2O_4$ consists of nine subspectra, precisely seven sextets and two doublets. According to the Mössbauer parameters (Table I), the sextets are divided into three types marked with letter L, M, and S. The sextets marked with L represent resonance response of ion ^{57}Fe from the large $NiFe_2O_4$ nanoparticles. The existence of magnetic ions on both (A) and [B] sites allows three types of antiferromagnetic exchange interactions: (A)-(A), (A)-[B], and [B]-[B]. The strongest interactions, according to the Weiss model, are between Ni^{2+} or Fe^{3+} ions at tetrahedral sites and Fe^{3+} ions at the octahedral sites.[29]

The first sextet in Table I for the $NiFe_2O_4$, with fixed value (0.25 mm s^{-1}) for the isomer shift, corresponding to the ^{57}Fe ion in tetrahedral site, includes both exchange interactions, (A)-(A) and (A)-[B], seen for tetrahedral site. The second subspectrum has fixed isomer shift, too, similar to Refs. 30 and 31 Its origin is in $[Fe^{3+}]$ at octahedral site.

The width of sextet (0.8(1) mm s^{-1}) indicates unregularly local environment occurred by cation rearrangement contributing change in magnitude of exchange interactions $[Fe^{3+}]$-O^{2-}- $[M^{2+}]$ and $[Fe^{3+}]$-O^{2-}-(M^{2+}). The lower isomer shifts of (A) sites suggest that the (Fe^{3+})-O^{2-} bonds on the tetrahedral site are more covalent than bonds on the octahedral sites. Such covalent bonds cause 3*d*-polarisation effects

TABLE I. Mössbauer parameters: A: relative area fraction of component; Γ: line width (FWHM); δ: isomer shift with respect to α-Fe; Δ: quadrupole splitting (2ε-shift), and B: hyperfine induction. Labels S, M, and L denote classified particles by their size. The fixed parameters in the fit are denoted by the superscript f. The superscript * denotes damaged $ZnFe_2O_4$.

			Mössbauer's parameters				
Sample	Compound	Size of particle	A (%)	Γ (mm s^{-1})	δ (mm s^{-1})	$\Delta/2\varepsilon$ (mm s^{-1})	B (T)
$Fe(OH)_3 + Ni(OH)_2 = NiFe_2O_4$	$NiFe_2O_4$	L	14(4)	0.51(5)	0.25^f	0.14(1)	48.22(9)
	$NiFe_2O_4$	L	19(7)	0.8(1)	0.36^f	−0.12(2)	45.7(2)
	$NiFe_2O_4$	L	6(1)	0.43(6)	0.46(1)	−0.19(2)	50.8(1)
	$NiFe_2O_4$	M	19(6)	1.5(2)	0.56(5)	−0.42(8)	41.5(6)
	$NiFe_2O_4$	M	17(3)	1.08(8)	0.17(2)	−0.37(3)	24.8(2)
	$NiFe_2O_4$	S	5(1)	0.45(5)	0.311(7)	2.38(2)	
	$NiFe_2O_4$	S	11(2)	1.3(2)	0.34(1)	0.94(7)	
	(Fe^{2+})		3(1)	0.51(8)	0.92(2)	1.21(5)	29.5(2)
	α-Fe		6(1)	0.61(9)	0.00(2)	−0.30(4)	32.7(1)
$Fe(OH)_3 + Zn(OH)_2 = ZnFe_2O_4$	$ZnFe_2O_4$	S	11(4)	0.8(1)	0.32(2)	0.9(1)	
	$ZnFe_2O_4$	S	7(4)	0.55(11)	0.32(2)	1.89(6)	
	$ZnFe_2O_4$*		2(1)	1.0(4)	−0.4(2)	3.6(3)	
	$ZnFe_2O_4$	M	38(10)	1.7(1)	0.27(4)	−0.37(6)	23.2(3)
	$ZnFe_2O_4$	M	19(8)	1.4(3)	0.44(6)	−0.1(1)	34.4(4)
	$ZnFe_2O_4$	M	20(7)	1.3(1)	0.57(4)	−0.53(7)	20(7)
	α-Fe		3(1)	0.20(7)	−0.01(2)	−0.01(3)	33.3(1)

on any 4s-electron density and create the hyperfine field of valence shell opposite in sign to that from the hyperfine field of core shell (1s, 2s, and 3s-electrons).[29,32] Taking into account that tetrahedral and octahedral sites have different point group of symmetry, (cubic) and [trigonal], we expect a different distribution of electron density at both sites, creating a different electric field gradient (EFG) and different orientation of principle axes of a EFG tensor with respect to the hyperfine field direction. In the tetrahedral site should be no EFG, and the presence of any quadrupole shift shows deviation from ideal structural ordering. Hence, one could recognize the site of iron ion in large nickel spinel ferrite nanoparticles by different sign of a quadrupole shift.[31,33]

The third sextet (Table I) the hyperfine field (B) and the quadrupole shift (2ε) are very similar to those of the γ-Fe_2O_3. Appearance of maghemite in the mixture is excluded by value of the isomer shift (δ) for this sextet. The origin of this interaction is therefore in octahedral positioned metallic ^{57}Fe ions, but in disturbed surrounding with vacancies like in maghemite.

The sign M denotes two sextets which originate from medium size nanoparticles. Due to the dominant structural and magnetic disorder of the surface, these sextets are broadened with average value of the isomer shift, larger quadrupole shift and smaller magnitude of hyperfine induction than at L-sextets. The sign S denotes superparamagnetic doublets which come from small volume nanoparticles. They are consequence of inability to observe a hyperfine field due to fluctuations of magnetization directions and it is directly influenced by the nanoparticle volume. Remaining two sextets do not belong to the $NiFe_2O_4$ phase. The 6% of total resonant absorption confirms the formation of α-Fe contaminated with Ni, and the three percent of total fitted area comes from Fe^{2+} in tetrahedral site.[34]

The Mössbauer spectroscopy of 25 h milled mixture $Fe(OH)_3/Ni(OH)_2$ reveals that more of 90% emergent iron containing powder is in the $NiFe_2O_4$ phase. Using a formula $[A_{(A)}/A_{[B]} = f_{(A)}/f_{[B]} \times \lambda/(2-\lambda)]$, where A is area of subspectrum, and assuming that the ratio of the recoil-less fraction is $f_{[B]}/f_{(A)} = 0.94$ at the room temperature, one could obtain λ.[35,36] According to the areas of measured sextets, only for large size particles, the estimated value for the degree of inversion is 70%, with uncertainty of 40%.

The Mössbauer spectrum (Fig. 4) of $ZnFe_2O_4$ obtained for 18 h milled mixture $Fe(OH)_3/Zn(OH)_2$ is composed of seven subspectra. Three of them are doublets. The bulk franklinite is normal spinel with weak superexchange interactions between Fe ions via oxygen anions on the octahedral sublattice. Hence, antiferromagnet ordering temperature is very low, about 10.5 K.[37] At room temperature, it behaves as paramagnet with the Mössbauer parameters: $\delta = 0.36(1)$ mm s^{-1} and $\Delta = 0.35(1)$ mm s^{-1}.[38] In the present work, the two doublets are characterized by $\delta = 0.32$ mm s^{-1}. Thus, obtained value indicates cations redistribution, so newly formed particles have to be described by some degree of inversion. Disjunction on tetrahedral and octahedral contribution is not possible. Large value of quadrupole splitting in both doublets is caused by changes in tetrahedral and octahedral bond lengths and angles incurred by milling process.[39] These two doublets describe small particles of $ZnFe_2O_4$. The third doublet (marked with an asterisk) has enormous quadrupole splitting value. Its origin is in formed oxygen vacancies. An outbreak of one oxygen anion at least induced more negative charge in iron nucleus, which is reflected on negative value of isomer shift for this doublet. Its relative abundance in whole fitted area is 2%.

Three remaining subspectra with origin in zinc spinel ferrite phase are sextets and probably correspond to particles

of the medium size. It is a well-known fact that zinc substitution by Fe increases with decreasing particle size.[40,41] Short-range AF correlation enables inter-lattice superexchange interaction of type (Fe^{3+})-$O^{2-}[Fe^{3+}]$. The line widths of all subspectra originating in $ZnFe_2O_4$ are broadened by different iron ions environment induced by site alteration of cations. Considering that there are no sextets that we can associate to A-sites doubtless, we were not able to estimate a degree of inversion in zinc ferrite nanoparticles. The Mössbauer spectroscopy of investigated mixture reveals that 97% of sample, which contains iron ions, makes $ZnFe_2O_4$ nanoparticles. The remainder of 3% is created α-Fe in ball mill process.

The magnetization curves of the nickel and zinc ferrites powder and sintered sample measured at room temperature are shown in Fig. 5. We have characterized the magnetic behavior of mechanochemical synthesized $NiFe_2O_4$ and $ZnFe_2O_4$ focusing on the study of the size-dependent magnetization. These measurements have revealed that the magnetic behavior of soft mechanochemical synthesized $NiFe_2O_4$ and

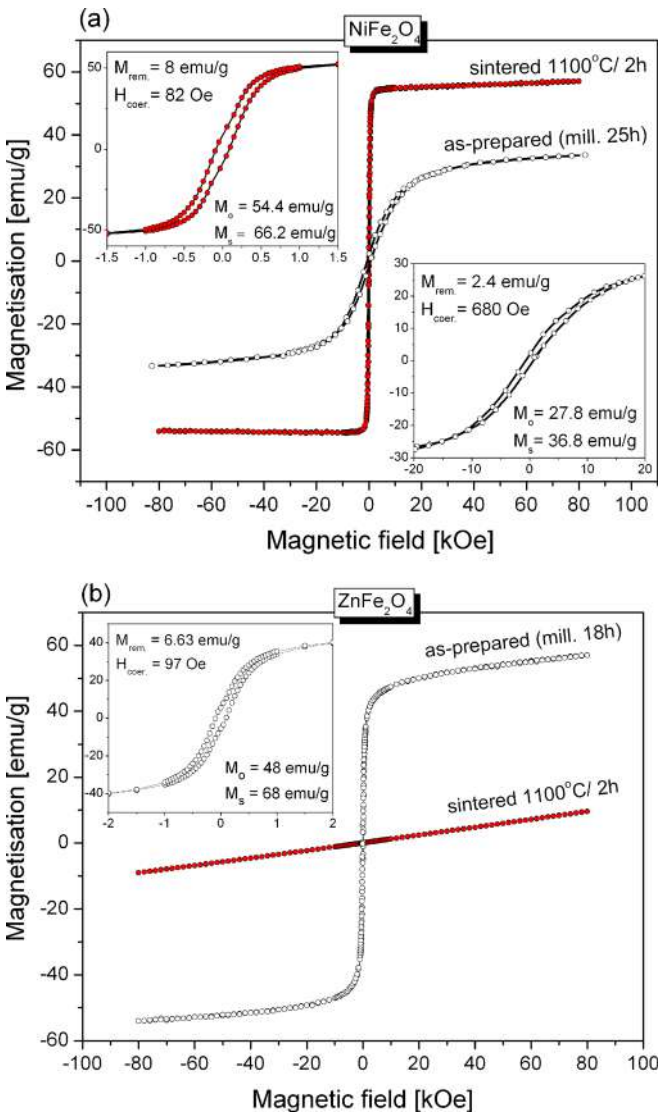

FIG. 5. The magnetic hysteresis curves of the (a) $NiFe_2O_4$ and (b) $ZnFe_2O_4$ powders and sintered samples at 1100 °C for 2 h. The insets show low magnetization behavior.

$ZnFe_2O_4$ is different from that of the powder prepared using the conventional ceramic method.

As can be seen (Fig. 5(a)), the magnetization of the mechanochemical synthesized sample does not saturate even at the maximum field attainable ($H_{ext} = 80$ kOe). This is in contrast to the magnetic behavior of the bulk (sintered) $NiFe_2O_4$, whose magnetization reaches a saturation value easily. An absence of saturation can be attributed to the effect of spin canting. Even in sintered mechanochemical synthesized nickel ferrite, the surface/volume ratio is rather great and the dangling bonds (uncompensated electrons) at the surface of the particles can contribute to magnetization.

The measurement of the coercivity warrants the determination of the magnetization response with better accuracy and resolution particularly at small applied fields. Hence, a separate set of hysteresis curves was showed for each sample with an applied field of −1500 to 1500 Oe at room temperature (the *inset M-H* curves in Fig. 5(a)). The hysteresis curve at low applied fields shows the values of the coercive field, $H_c \approx 80$ Oe for sintered sample and 36 Oe for as-prepared sample. The remnant magnetization is $M_r \approx 8$ emu/g and $M_r \approx 2.4$ emu/g for sintered and powder samples of $NiFe_2O_4$, respectively. The extrapolated magnetization M_0 measured on the spinel ferrite obtained by a soft mechanochemical synthesis is higher than that for spinel ferrites produced by other methods.[42] Lower value of magnetisation in the as-prepared sample of $NiFe_2O_4$ compared to sintered sample implies a lowering of a cation distribution factor in a nano-sized sample.

The magnetic properties of the $NiFe_2O_4$ with an inverse spinel structure can be explained in terms of the cations distribution and magnetization originates from Fe^{3+} ions at both tetrahedral and octahedral sites and Ni^{2+} ions in octahedral sites. Hysteresis loops in Fig. 5 for as-prepared samples are typical for soft magnetic materials and the "S" shape of the curves together with the negligible coercivity ($H_c \approx 80$ Oe) indicate the presence of small magnetic particles exhibiting super paramagnetic behaviors. In super paramagnetic materials, responsiveness to an applied magnetic field without retaining any magnetism after removal of the magnetic field is observed. This behavior is an important property for magnetic targeting carriers. In fact, the difference between ferromagnetism and superparamagnetism fabricates in the particle size. Literature data imply that when the diameter of particles is less than 50 nm, the particles show the character of superparamagnetism.

The magnetization curves of the zinc ferrite measured at room temperature are shown in Fig. 5(b). The curve has "S" shape with low coercivity ($H_c \approx 97$ Oe) and extremely small remanence magnetization. Sintered sample exhibits a paramagnetic behavior, which is expected in the case of bulk, or crystalline material with crystalline size of 100 nm order. Such material is practically without internal tensions and in the case of sintered $ZnFe_2O_4$ a normal spinel structure with fully populated antiferromagnetic tetrahedral [B] sites is established. ([B]–[B] super exchange interaction is weak and bulk $ZnFe_2O_4$ became antiferromagnetic at about 10 K.) On the other hand, in the as-prepared sample with nanosized crystallites can be recognized a super paramagnetic behaviour.[43,44]

The estimated value of saturation magnetization is $M_{sat} = 68$ emu/g which is a result of the inversion of cations. The largest super exchange interaction in spinel ferrites, in the case of $ZnFe_2O_4$ established between Fe^{3+} ions in (A) and [B] sites, generates such high value of magnetization. Nano powder of $ZnFe_2O_4$ in the as-prepared sample is predominantly of monodomen crystallites, which is confirmed by a small remanence magnetization, $M_{rem} = 6.63$ emu/g. Open hysteresis loop, with coercive field, $H_{coerc} = 97$ Oe (in combination with high magnetization), shows that ferromagnetic transition temperature is well above the room temperature. The fact that magnetization does not achieve a saturation in the magnetic fields up to ± 80 kOe implies a surface spin disorder. Ordering of these spins in a magnetic field contributes in the magnetic moment of the monodomen $ZnFe_2O_4$ crystallites, also.

The variations in electrical conductivity may be explained by Verwey's hopping mechanism.[45] According to Verwey, the electrical conductivity in ferrite is mainly due to hopping electron between ions of the same element present in more than one valance state, distributed randomly over crystallographically equivalent lattice sites. Ferrite structurally forms cubic close packed oxygen lattice with the cation at the octahedral, [B] and the tetrahedral, (A) sites. The distance between two metal ions on B sites is smaller than the distance between two metals ions on (A) and [B] sites; therefore, the hopping between A and B has very small probability compared with that for B-B hopping. The hopping between A-A sites does not exist, due to fact that there are only Fe^{3+} ions at (A) sites and any Fe^{2+} ions formed during processing preferentially occupy [B] sites only.[46] The hopping probability depends upon the separation between the ions involved and the activation energy. The charges can migrate under the influence of the applied field contributing to the electrical response of the system.

Pollak[47] has shown that the conductivity is an increasing function of frequency in the case of conduction by hopping and a decreasing function of frequency in case of band conduction. Generally, the total conductivity is the summation of the band and hopping parts[48]

$$\sigma = \sigma_{DC}(T) + \sigma_{AC}(\omega, T).$$

The first term represents the temperature dependent DC electrical conductivity due to the band conduction and it is frequency independent. The second term is frequency and temperature dependent pure AC conductivity due to the hopping processes at the octahedral site. It obeys the power law form.[48]

The DC conductivity on $NiFe_2O_4$ and $ZnFe_2O_4$ samples was measured as a function of temperature. The effect of the temperature on the electrical conductivity σ_{DC} for both ferrite samples is illustrated in Fig. 6. The plot of $\log(\sigma_{DC})$ versus $(1/T)$ shows that this dependence is linear for both sintered samples in a certain temperature range. The observed increase in the DC conductivity of sintered samples with temperature shows their semiconducting nature. This is confirmation of the negative temperature coefficient of resistance (NTCR)-type behavior of the pallets usually shown by semiconductors. The conductivity of ferrites is known to depend upon the purity of starting materials, sintering temperature and sintering time, which influence the microstructure and composition of the samples.[49]

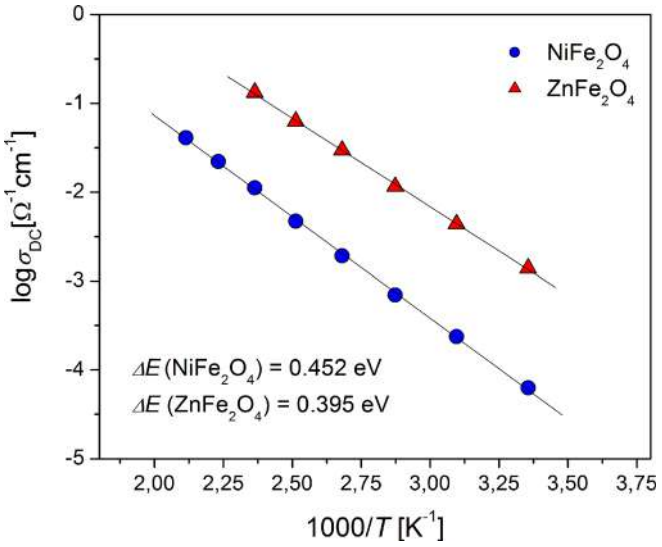

FIG. 6. Temperature dependence of DC electrical conductivity on $NiFe_2O_4$ and $ZnFe_2O_4$ samples.

The increase in electrical conductivity σ_{DC} with temperature is due to the increase in the thermally activated drift mobility of charge carriers according to the hopping conduction mechanism. The activation energy for the thermally activated hopping process was obtained by fitting the DC conductivity data with the Arrhenius relation[50]

$$\sigma_{DC}(T) = \sigma_0 \exp\left(-\frac{\Delta E}{kT}\right),$$

where σ_0 is the pre-exponential factor with the dimensions of $(\Omega\ \text{cm})^{-1}$ K, ΔE is the activation energy for DC conductivity, T is the absolute temperature, and k is the Boltzmann's constant. The slope of the $\log(\sigma_{DC})$ versus $(1/T)$ straight line is a measure of activation energy of the $NiFe_2O_4$ and $ZnFe_2O_4$ ferrites. Using Arrhenius equation, the determined values of the conduction activation energy ΔE are 0.395 eV and 0.452 eV for $ZnFe_2O_4$ and $NiFe_2O_4$, respectively. If we analyze the obtained values for the conduction activation energy, one can see that $NiFe_2O_4$ has a higher value compared to $ZnFe_2O_4$ sample. This showed that more energy is required for electron exchange between Fe^{2+} and Fe^{3+} ions for the $NiFe_2O_4$. As shown in Fig. 6, $NiFe_2O_4$ has the lower DC conductivity than the $ZnFe_2O_4$. It is in good accordance with the fact that the higher activation energy is associated with the lower electrical conductivity. Also, there is no remarkable change in the slope in the measured temperature range for both samples.

The variation of electrical AC conductivity of the both ferrites is plotted against the change in frequency for different temperatures and shown in Fig. 8. It is obvious that the $ZnFe_2O_4$ has a higher conductivity compared to $NiFe_2O_4$ at a certain temperature and at different frequencies. Also, it is seen that the AC conductivity of both ferrites shows a gradual rise at low frequencies, whereas at higher frequencies the

conductivity rises steeply. This behavior is more pronounced in the conductivity of $NiFe_2O_4$, especially at lower temperatures. The hopping of electron between Fe^{2+} and Fe^{3+} ions on the B, octahedral, sites is responsible for conduction mechanism in $ZnFe_2O_4$ and $NiFe_2O_4$ ferrites.[51] Also, various reports show that the hole hopping between Ni^{2+} and Ni^{3+} on B site also contributes to the electric conduction in $NiFe_2O_4$ as the inverse spinel.[52]

In general, the increase in conductivity with increase of frequency can be explained on the basis of Maxwell-Wagner theory.[53] According to this theory, dielectric structure was formed by two layers. First layer consists of ferrite grains of fairly well conducting, which is separated by a thin layer of poorly conducting substances, which forms the grain boundary. The non-conducting layer or grain boundary is formed by oxygen ions. Thus, each grain possesses oxygen rich layer on the surface as boundary. These grain boundaries are more active at lower frequencies; hence the hopping frequency of carriers between Fe^{2+} and Fe^{3+} ion is less at lower frequencies. As the frequency of the applied filed increases, the conductive grains became more active by promoting the hopping between Fe^{2+} and Fe^{3+} ions, thereby increasing the hopping frequency. Thus, we observe a gradual increase in conductivity with frequency.

On the other hand, the electrons in ferrites are localized and the electrical conductivity is increased with an increase in temperature due to the hopping of the charge carriers. As temperature increases, the mobility of hopping also increases thereby increasing conductivity. It is seen from Fig. 7 that the conductivity of $NiFe_2O_4$ and $ZnFe_2O_4$ increases with the increase in temperature which is a typical behavior of semiconductors.

It is well known that there are two types of polarons, small polarons and large polarons. In the small polaron model, the conductivity increases linearly with increase in frequency and in case of large polarons the conductivity decreases with increase in frequency.[54] For the present samples, the plots indicate small polaron type of conduction.

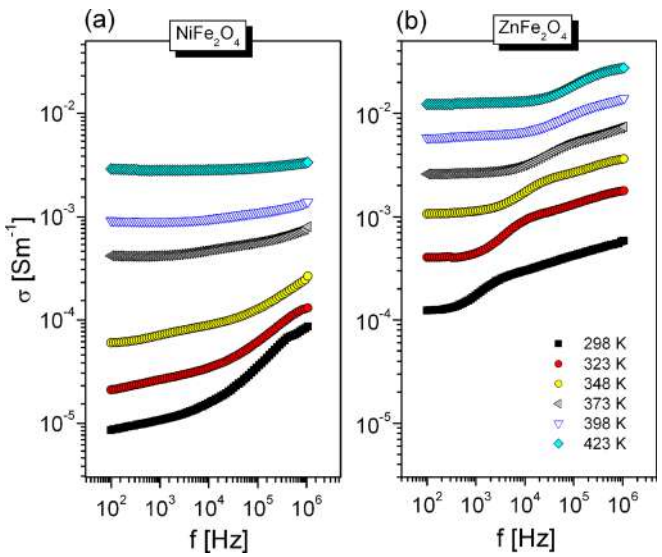

FIG. 7. Frequency dependent AC conductivity behavior of (a) $NiFe_2O_4$ and (b) $ZnFe_2O_4$ ferrites at different temperatures.

The complex impedance spectroscopy[55] is a powerful technique in solid states physics because of its ability to understand the electrical conduction mechanism of the synthesized materials. In the present analysis, the impedance spectroscopy has been used as well-developed tool to separate out the grain/bulk and grain boundary contribution to the total conductivity of $NiFe_2O_4$ and $ZnFe_2O_4$ ferrite. Depending on the electrical properties of the samples, the AC response can be modeled with two semi-circles in the impedance plane, the first in a low frequency domain represents the resistance of grain boundary. The second one obtained in a high frequency domain corresponds to the resistance of grain or bulk properties.[56]

Figure 8 shows the complex impedance plane plots of sintered $NiFe_2O_4$ and $ZnFe_2O_4$ ferrites as a function of frequency at different temperatures. Generally, two semicircles are observed in the *Cole-Cole* plots of both samples between the frequency range of 100 Hz-10 MHz. A larger one at low frequency represents the resistance of the grain boundary and a smaller one obtained at the higher frequency side corresponds to the resistance of grain of bulk properties. It is noticeable that the impedance spectra of $NiFe_2O_4$ and $ZnFe_2O_4$ ferrites include both grain and grain boundary effects. This

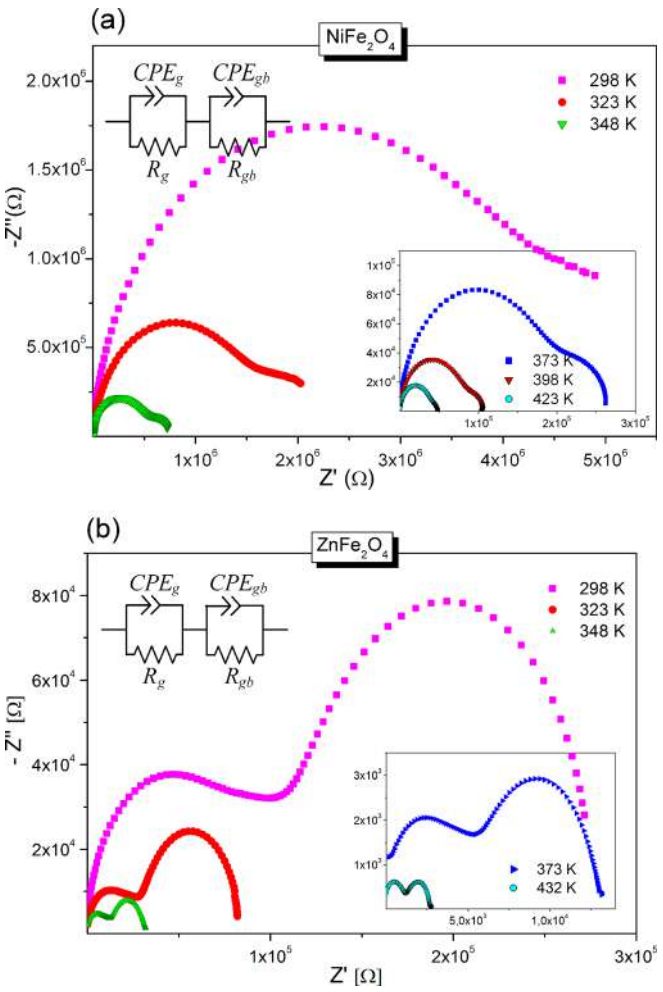

FIG. 8. *Cole-Cole* plots for the sample of the (a) $NiFe_2O_4$ and (b) $ZnFe_2O_4$ ferrites at different temperatures. *Inset*: proposed equivalent circuit model for analysis of the impedance spectroscopy data.

TABLE II. Impedance parameters calculated from the complex impedance plots at different temperatures.

Sample	T (K)	$R_g \times 10^4$ (Ω)	$C_g \times 10^{-11}$ (F)	n_g	$R_{gb} \times 10^6$ (Ω)	$C_{gb} \times 10^{-9}$ (F)	n_{gb}
$NiFe_2O_4$	298	239.77	4.487	0.881	3.789	4.912	0.688
	323	105.1	4.590	0.887	1.365	9.585	0.649
	348	29.1	4.525	0.892	471.9	8.101	0.713
	398	2.572	3.949	0.898	79.92	5.442	0.822
	423	1.043	3.104	0.921	37.97	7.682	0.789
$ZnFe_2O_4$	298	10.84	35.86	0.762	175.6	3.235	0.894
	323	2.904	35.86	0.774	54.76	4.071	0.905
	348	1.185	29.98	0.816	20.37	12.54	0.807
	398	0.2342	30.02	0.831	3.281	37.32	0.729
	423	0.1152	6.091	0.957	1.564	17.41	0.825

appearance of two semicircles indicates a phenomenon which is typically related to the presence of a distribution of relaxation time.

As one can see in impedance spectra of both ferrites, the diameters of the semicircles exhibit decreasing trends with the increase in temperature. It indicates that the conductivity increases with increase in temperature supporting the typical negative temperature coefficient of resistance behavior of $NiFe_2O_4$ and $ZnFe_2O_4$ usually shown by semiconductors. On impedance spectra is observed that $NiFe_2O_4$ has a higher impedance value of $ZnFe_2O_4$ at all temperatures, so it is in good accordance with the fact that the conductivity of $NiFe_2O_4$ is lower than conductivity of $ZnFe_2O_4$. The impedance value of both samples is decreased by two orders of magnitude, which is due to thermal activation mechanism. The rise of temperature brings with an enhanced conductivity, and hence, decreasing the impedance values.

In order to correlate the electrical properties of the $NiFe_2O_4$ and $ZnFe_2O_4$ sample with the microstructure of the material, an equivalent circuit model consisting of two serially connected parallel *R-CPE* elements, shown in the inset of Fig. 8, has been used to interpret the impedance spectra. Here, R_g and R_{gb} represent the grain and grain boundary resistance and CPE_g and CPE_{gb} are the constant phase elements for grain interiors and grain boundaries, respectively. The resistance of the circuit represents a conductive path and a given resistor in a circuit accounts for the bulk conductivity of the sample. The constant phase element *CPE* is used to accommodate the non-ideal behavior of the capacitance which may have its origin in the presence of more than one relaxation process with similar relaxation times. The impedance of a *CPE* can be described as[57]

$$Z_{CPE} = A^{-1}(j\omega)^{-n},$$

where ω is the angular frequency, A and n ($0 \leq n \leq 1$) are fitted parameters. When $n = 1$, then the *CPE* describes an ideal capacitor with $C = A$, while when $n = 0$ the *CPE* describes an ideal resistor with $R = 1/A$. The capacitances are generally associated with space charge polarization regions. The *CPE* elements in the equivalent circuit model have been used to describe non ideal Debye-like behavior[58] and enable taking into account phenomena occurring in the interface regions, associated with inhomogeneity and diffusion processes.[59]

Analysis and simulation of impedance spectra were performed using EIS Spectrum Analyzer software.[60,61] The different electrical parameters calculated from the complex impedance plots at selected temperatures are shown in Table II. In these types of ferrites, the value of the grain boundary resistance is generally larger than the resistance of the grain, $R_{gb} \geq R_g$. Additionally, the semicircle representing the grain boundaries lies on the lower frequency side since the relaxation time of the grain boundaries is much larger than that of the grains. Also, it is observed that the both resistances decrease with increasing temperature. It indicates that the conductivity of $NiFe_2O_4$ and $ZnFe_2O_4$ ferrites increases with increase in temperature. The higher values of resistance of both grain and grain boundary for the $NiFe_2O_4$ mean this ferrite has a lower conductivity than the $ZnFe_2O_4$. This decrease in the resistance of grains and grain boundaries has been suggested to be due to the thermal activation of the localized charges. Two types of thermal activations, i.e., carrier density in the case of band conduction and carrier mobility in case of hopping, are responsible for the reduction in the resistive properties with temperature.[52] For all the temperatures, the capacitance of the grain boundary is larger than that of the grain for both types of ferrite samples, which can be explained on the basis that capacitance is inversely proportional to the thickness of the media.

IV. CONCLUSIONS

In this paper, we obtained $NiFe_2O_4$ and $ZnFe_2O_4$ ferrite by soft mechanochemical synthesis starting from the mixture of appropriate powders and sintered at 1100 °C. It has been shown that mechanochemical treatment of mixture with starting materials leads to forming of the phase of $NiFe_2O_4$ and $ZnFe_2O_4$ after 25 and 18 h of milling time, respectively. In the Raman spectra is observed all of the group theory predicted first-order active modes characteristic for spinel structure. Raman modes of sintered $NiFe_2O_4$ and $ZnFe_2O_4$ are in the form characteristic for normal spinel structure, and in the case of powder, Raman spectra show a presence of cation inversion. The Mössbauer spectroscopy of the iron contained newly formed particles from mixture $Fe(OH)_3/Ni(OH)_2$ revealed that 94% is $NiFe_2O_4$. The degree of inversion, estimated from large particles, is 0.7. The sample formed from mixture $Fe(OH)_3/Ni(OH)_2$ contains $ZnFe_2O_4$ in 97%. The

certain degree of inversion apparent in Mössbauer subspectra cannot be resolved. It is confirmed that zinc substitution by Fe increases with decreasing particle size. Also, a high magnetization of a milled sample confirms cation inversion. Sintered sample has a normal spinel structure, as a consequence, paramagnetic behavior at 300 K. The higher values of resistance of both grain and grain boundary for the $NiFe_2O_4$ mean this ferrite has a lower conductivity than the $ZniFe_2O_4$. The values of the conduction activation energy ΔE are 0.395 eV and 0.452 eV for $ZnFe_2O_4$ and $NiFe_2O_4$, respectively. This decrease in the resistance of grains and grain boundaries has been suggested to be due to the thermal activation of the localized charges. The analysis of the complex impedance data shows that the capacitive and reactive properties of the sintered ferrites are mainly attributed due to the processes which are associated with the grain and grain boundary. Also, it is seen that the radius of curvature of *Cole-Cole* plots is decreased with increasing temperature, suggesting a mechanism temperature-dependent on relaxation.

ACKNOWLEDGMENTS

This research was financially supported by the Ministry of Education, Science and Technological Development of the Republic of Serbia through Project No. III 45003.

[1]Y. Köseoğlu, A. Baykal, M. S. Toprak, F. Gözüak, A. C. Başaran, and B. Aktaş, J. Alloys Compd. **462**, 209 (2008).
[2]J. Smit and H. P. Wijn, *Ferrites-Physical Properties of Ferrimagnetic Oxides in Relation to Their Technical Applications* (John Wiley and Sons, The Netherlands, 1959).
[3]V. Šepelák, D. Schultze, F. Krumeich, U. Steinike, and K. D. Becker, Solid State Ionics **141–142**, 677 (2001).
[4]M. A. Willard, L. K. Kurihara, E. E. Carpenter, S. Calvin, and V. G. Harris, Int. Mater. Rev. **49**, 125 (2004).
[5]J. Huo and M. Wei, Mater. Lett. **63**, 1183 (2009).
[6]S. H. Yu, T. Fujino, and M. Yoshimura, J. Magn. Magn. Mater. **256**, 420 (2003).
[7]K. Maaz, A. Mumtaz, S. K. Hasanain, and M. F. Bertino, J. Magn. Magn. Mater. **322**, 2199 (2010).
[8]P. Sivakumar, R. Ramesh, A. Ramanand, S. Ponnusamy, and C. Muthamizhchelvan, Mater. Lett. **65**, 483 (2011).
[9]B. Jeyadevan, K. Tohji, and K. Nakatsuka, J. Appl. Phys. **76**, 6325 (1994).
[10]J. Azadmanjiri, S. A. Seyyed Ebrahimi, and H. K. Salehani, Ceram. Int. **33**, 1623 (2007).
[11]S. Khorrami, F. Gharib, G. Mahmoudzadeh, S. Sadat Sepehr, S. Sadat Madani, N. Naderfar, and S. Manie, Int. J. Nano Dimen. **1**, 221 (2011).
[12]A. T. Raghavender, K. Zadro, D. Pajic, Z. Skoko, and N. Biliskov, Mater. Lett. **64**, 1144 (2010).
[13]S. H. Zhan, C. R. Gong, D. R. Chen, and X. L. Jiao, J. Dispersion Sci. Technol. **27**, 931 (2006).
[14]D. Chen and Y. Z. Zhang, Sci. China Technol. Sc. **55**, 1535 (2012).
[15]R. Sai, S. D. Kulkarni, K. J. Vinoy, N. Bhat, and S. A. Shivashankar, J. Mater. Chem. **22**, 2149 (2012).
[16]J. Fang, N. Shama, L. D. Tung, E. Y. Shin, C. J. O'Connor, K. L. Stokes, G. Caruntu, J. B. Wiley, L. Spinu, and J. Tang, J. Appl. Phys. **93**, 7483 (2003).
[17]S. Ozcan, B. Kaynar, M. M. Can, and T. Firat, Mater. Sci. Eng., B **121**, 278 (2005).
[18]J. L. Gunjakar, A. M. More, K. V. Gurav, and C. D. Lokhande, Appl. Surf. Sci. **254**, 5844 (2008).
[19]V. Šepelák, U. Steinike, D. C. Uecker, S. Wissmann, and K. D. Becker, J. Solid State Chem. **135**, 52 (1998).
[20]E. Avvakumov, M. Senna, and N. Kosova, *Soft Mechanochemical Synthesis: A Basis for New Chemical Technologies* (Kluwer Academic Publishers, Boston, 2001).
[21]Z. Ž. Lazarević, Č. Jovalekić, A. Rečnik, V. N. Ivanovski, A. Milutinović, M. Romčević, M. B. Pavlović, B. Cekić, and N. Ž. Romčević, Mater. Res. Bull. **48**, 404 (2013).
[22]Z. Lazarević, A. Milutinović, M. Romčević, N. Romčević, Č. Jovalekić, D. Sekulić, and M. Slankamenac, in *The USBs Electronic Conference Proceedings of ISAF ECAPD PFM 2012*, Aveiro, Portugal, No. 07, 2012.
[23]R. A. Brand, WinNormos Mössbauer Fitting Program, Universität Duisburg, 2008.
[24]B. E. Warren, "Scherrer and Warren equations," in *X-ray Diffraction* (Addison Wesley, Reading, MA, 1969).
[25]A. Ahlawat and V. G. Sathe, J. Raman Spectrosc. **42**, 1087 (2011).
[26]M. H. Sousa, F. A. Tourinho, and J. C. Rubim, J. Raman Spectrosc. **31**, 185 (2000).
[27]R. Valenzuela, *Magnetic Ceramics* (Cambridge University Press, Cambridge, 1994).
[28]B. D. Cullity, *Introduction to Magnetic Materials* (Addison-Wesley, Reading MA, 1971).
[29]N. N. Greenwood and T. C. Gibb, *Mössbauer Spectroscopy* (Chapman and Hall Ltd., London, 1971), pp. 266–267.
[30]V. Šepelák, I. Bergmann, A. Feldhoff, P. Heitjans, F. Krumeich, D. Menzel, F. J. Litterst, S. J. Campbell, and K. D. Becker, J. PhyS. Chem. C **111**, 5026 (2007).
[31]R. Malik, S. Annapoorni, S. Lamba, V. R. Reddy, A. Gupta, P. Sharma, and A. Inoue, J. Magn. Magn. Mater. **322**, 3742 (2010).
[32]G. A. Fatseas and R. Krishnan, J. Appl. Phys. **39**, 1256 (1968).
[33]A. Ahlawat, V. G. Sathe, V. R. Reddy, and A. Gupta, J. Magn. Magn. Mater. **323**, 2049 (2011).
[34]M. Menzel, V. Šepelák, and K. D. Becker, Solid State Ionics **141–142**, 663 (2001).
[35]V. Šepelák, D. Baabe, and K. D. Becker, J. Mater. Synth. Process. **8**, 333 (2000).
[36]G. A. Sawatzky, F. Van der Woude, and A. H. Morrish, Phys. Rev. **187**, 747 (1969).
[37]W. Schiessl, W. Potzel, H. Karzel, M. Steiner, G. M. Kalvius, A. Marti, M. K. Krause, I. Halevy, J. Gal, W. Schäfer, G. Will, M. Hillberg, and R. Wäppling, Phys. Rev. B **53**, 9143 (1996).
[38]G. F. Goya and H. R. Rechenberg, J. Magn. Magn. Mater. **196–197**, 191 (1999).
[39]V. Šepelák, K. Tkáčová, V. V. Boldyrev, S. Wißmann, and K. D. Becker, Physica B **234–236**, 617 (1997).
[40]M. R. Anantharaman, S. Jageatheesan, K. A. Malini, S. Sindhu, A. Narayanasamy, C. N. Chinnasamy, J. P. Jacobs, S. Reijne, K. Seshan, R. H. H. Smits, and H. H. Brongersma, J. Magn. Magn. Mater. **189**, 83 (1998).
[41]H. Ehrhardt, S. J. Campbell, and M. Hofmann, J. Alloys Compd. **339**, 255 (2002).
[42]A. Alarifi, N. M. Deraz, and S. Shaban, J. Alloys Compd. **486**, 501 (2009).
[43]E. C. Mendonça, C. B. R. Jesus, W. S. D. Folly, C. T. Meneses, J. G. S. Duque, and A. A. Coelho, J. Appl. Phys. **111**, 053917 (2012).
[44]C. Yao, Q. Zeng, G. F. Goya, T. Torres, J. Liu, H. Wu, M. Ge, Y. Zeng, Y. Wang, and J. Z. Jiang, J. Phys. Chem. C **111**, 12274 (2007).
[45]E. J. W. Verwey and J. H. de Boer, Recl. Trav. Chim. Pays-Bas **55**, 531 (1936).
[46]A. Lakshman, P. S. V. S. Rao, B. P. Rao, and K. H. Rao, J. Phys. D: Appl. Phys. **38**, 673–678 (2005).
[47]M. Pollak, in *Proceedings of the International Conference on Physics of Semiconductors, Exeter* (1962), p. 86.
[48]A. M. Abdeen, J. Magn. Magn. Mater. **185**, 199 (1998).
[49]P. A. Jadhav, R. S. Devan, Y. D. Kolekar, and B. K. Chougule, J. Phys. Chem. Solids **70**, 396 (2009).
[50]S. M. Savic, M. V. Nikolic, O. S. Aleksic, M. P. Slankamenac, M. B. Zivanov, and P. M. Nikolic, Sci. Sinter. **40**, 27 (2008).
[51]A. Pradeep, P. Priyadharsini, and G. Chandrasekaran, J. Alloys Compd. **509**, 3917 (2011).
[52]M. Younas, M. Nadeem, M. Atif, and R. Grossinger, J. Appl. Phys. **109**, 093704 (2011).
[53]C. G. Koops, Phys. Rev. **83**, 121 (1951).
[54]D. R. Patil and B. K. Chougule, Mater. Chem. Phys. **117**, 35 (2009).
[55]E. Barsoukov and J. R. Macdonald, *Impedance Spectroscopy: Theory, Experiment, and Applications*, 2nd ed. (John Wiley and Sons, 2005), pp. 205–343.
[56]W. Chen, W. Zhu, O. K. Tan, and X. F. Chen, J. Appl. Phys. **108**, 034101 (2010).
[57]R. Martinez, A. Kumar, R. Palai, J. F. Scott, and R. S. Katiyar, J. Phys. D: Appl. Phys. **44**, 105302 (2011).

[58]E. J. Abram, D. C. Sinclair, and A. R. West, J. Electroceram. **10**, 165 (2003).
[59]F. D. Morrison, D. J. Jung, and J. F. Scott, J. Appl. Phys. **101**, 094112 (2007).
[60]A. S. Bondarenko and G. A. Ragoisha, EIS Spectrum Analyser (*a freeware program for analysis and simulation of impedance spectra*), see http://www.abc.chemistry.bsu.by/vi/analyser/.
[61]G. A. Ragoisha and A. S. Bondarenko, Electrochim. Acta **50**, 1553 (2005).

Materials Research Bulletin 48 (2013) 4368–4378

Contents lists available at SciVerse ScienceDirect

Materials Research Bulletin

journal homepage: www.elsevier.com/locate/matresbu

Structural, electrical and dielectric properties of spinel nickel ferrite prepared by soft mechanochemical synthesis

Zorica Ž. Lazarević [a,*], Čedomir Jovalekić [b], Dalibor L. Sekulić [c], Aleksandra Milutinović [a], Sebastian Baloš [c], Miloš Slankamenac [c], Nebojša Ž. Romčević [a]

[a] Institute of Physics, University of Belgrade, P.O. Box 68, Pregrevica 118, Zemun, Belgrade, Serbia
[b] The Institute for Multidisciplinary Research, University of Belgrade, Kneza Višeslava 1, Belgrade, Serbia
[c] Faculty of Technical Sciences, University of Novi Sad, Trg Dositeja Obradovića 6, Novi Sad, Serbia

ARTICLE INFO

Article history:
Received 18 April 2013
Received in revised form 28 June 2013
Accepted 7 July 2013
Available online 13 July 2013

Keywords:
A. Magnetic materials
C. Impedance spectroscopy
C. Raman spectroscopy
D. Dielectric properties
D. Electrical properties.

ABSTRACT

Nickel ferrite, $NiFe_2O_4$ was prepared by a soft mechanochemical route from a mixture of (1) $Ni(OH)_2$ and α-Fe_2O_3 and (2) $Ni(OH)_2$ and $Fe(OH)_3$ powders in a planetary ball mill for 25 h. The powder samples were sintered at 1100 °C for 2 h and were characterized by X-ray diffraction (XRD), Raman spectroscopy and scanning electron microscopy (SEM). Impedance spectroscopy techniques were used to study the effect of grain and grain boundary on the electrical properties of the prepared samples. A difference in dielectric constant (ε) and dielectric loss tangent ($\tan\delta$) of $NiFe_2O_4$ samples obtained by the same methods but starting from different initial components was observed.

1. Introduction

Ferrites, MFe_2O_4 (M = Ni, Mn, Zn) have continued to attract attention over the years. As magnetic materials, ferrites cannot be replaced by any other magnetic material because they are relatively inexpensive, stable and have a wide range of technological applications in transformer core, high quality filters, high and very high frequency circuits and operating devices. The physical properties of ferrites are controlled by the preparation conditions, chemical composition, sintering temperature and time, type and amount of substitutions [1].

In recent years, nanostructured materials have drawn outstanding attention due to the unique mechanical, electrical, optical, and magnetic properties [2]. The unique properties of nanostructured materials are due to their changed electronic structure, close to that of an isolated atom or molecule. Among the nanoscale inorganic materials, the magnetic metal oxides and their composites are of particular interest due to their exciting applications in the areas of quantum computing, information storage media, magnetic resonance imaging, sensors, refrigeration, electromagnetic wave absorption and modulation [3].

The properties of the nanocrystalline materials are varied from those of corresponding bulk materials, due to their small grain size. In the nanocrystalline materials a large percentage of atoms are available at their grain boundaries and therefore there are more chances for interaction between the grains. Ferrites with AB_2O_4 formula crystallize in various spinel structures: a normal spinel structure, mixed or in a perfectly inverse spinel structure. In a normal spinel structure, the A^{2+} cations occupy the tetrahedral site, where as the B^{3+} cations occupy the octahedral site. In an inverse spinel structure, half of the octahedral coordination sites are occupied by A^{2+} cations and the remaining half as well as all the tetrahedral coordination sites are occupied by the B^{3+} cations. In the mixed spinels metal ions are distributed over both lattice sites. Generally, structural formula of cubic spinels can be written as: $(A^{2+}{}_{1-\lambda}B^{3+}{}_{\lambda})[A^{2+}{}_{\lambda}B^{3+}{}_{2-\lambda}]O_4$, where in the parentheses are cations in tetrahedral sites and the bracket denotes cations in octahedral sites. A symbol λ is a degree of the cation inversion. The crystallographic, electrical and magnetic properties of the spinel ferrites substantially depend on their method of preparation, chemical composition, sintering temperature, doping additives, and particle size etc. [4], which controls the microstructure forming of the high resistive boundaries between the constituent's grains. One of the most important members of ferrite systems is the nickel ferrite, which is a soft magnetic material with an inverse spinel structure. Ferrimagnetism originates from uncompensated

* Corresponding author. Tel.: +381 11 37 13 035; fax: +381 11 3160 531.
E-mail address: lzorica@yahoo.com (Z.Ž. Lazarević).

0025-5408/$ – see front matter © 2013 Elsevier Ltd. All rights reserved.
http://dx.doi.org/10.1016/j.materresbull.2013.07.012

magnetic moments of antiparallel spins between Fe^{3+} ions at tetrahedral sites and Fe^{3+} and Ni^{2+} ions at octahedral sites [5,6].

There is several different synthesis methods used to fabricate ferrites as reported in the literature such as solid state reaction [7–9], co-precipitation [10,11], hydrothermal [12–17], mechanochemical [18], reverse micelle technique [15] or sol–gel [19–22]. The mechanochemical synthesis can deliver the designed phases and structures by a single-step of the high-energy milling conducted in an enclosed activation chamber at room temperature [23,24]. Mechanochemical synthesis is the general name given to the process of milling of powders which is accompanied by chemical reactions. It was first developed for the preparation of intermetallic compounds and nano-crystalline alloys. Novel approach to mechanochemical synthesis, based on reactions of solid acids, based hydrated compounds, crystal hydrates, basic and acidic salts, has been called soft mechanochemical synthesis. The dissolved substances in the solid state substantially change their nature. It can influence on the comparison and properties of the final product. Peculiarities of soft mechanochemical reactions consist in the high reactivity of surface functional groups, notably, OH groups [24–26]. The major advantages of soft mechanochemical synthesis lie in the formation of reaction products at a room or a low temperature and the refinement of produced powders to a nanometer size range. This is reflected primarily in the simplicity of the procedure and equipment used. In many cases, when it comes to classical synthesis reaction sintering process, requires high temperatures, which can present an additional problem in industrial production. Mechanochemical derived precursors exhibit significantly higher reactivity and thus lower the sintering temperature.

There are a lot of studies of nanocrystalline nickel ferrite prepared by mechanochemical route, but the results are very different depending on the experimental conditions [27]. For example, $NiFe_2O_4$ ferrite phase was obtained after 8 h [28] or else after 35 h of milling [29]. For the sample milled 8 h a heat treatment was applied in order to increase the formation of nanoferrite [28]. Another study reported the obtaining of $NiFe_2O_4$ ferrite in the nanocrystalline state by mechanical milling (with a crystallite size of 9 nm) from a mixture of oxides [30]. In the same article, it was observed that the magnetization is reduced by milling. A non-equilibrium distribution of cations and a spin canted effect have been reported by the same authors [30]. The magnetization of $NiFe_2O_4$ ferrite obtained in nanocrystalline state by mechanical milling is lower than the magnetization of nickel ferrite obtained by ceramic method [31]. Finally, it is worth to note that mechanical/reactive milling can be used to obtained nanostructures that have a non-equilibrium distribution of cations within the crystal structure.

The aim of this work was synthesis of nanosized nickel ferrite by soft mechanochemical route from two different mixtures of starting powders. After the sintering, samples of $NiFe_2O_4$ ferrites were analyzed and their structural, electric and dielectric characteristics, as well as the influence of starting mixtures on that characteristic were discussed. It was shown that the impedance spectroscopy method is applicable for the better understanding of the electrical and dielectric properties of obtained ferrite.

2. Experimental procedures

$NiFe_2O_4$ samples were synthesized by soft mechanochemicaly from different mixtures of starting powders, which are described in detail elsewhere [32]. For mixtures of crystalline powders, denoted by (1) and (2), the starting material were: (1) nickel(II)-hydroxide ($Ni(OH)_2$, Merck 95% purity) and hematite (α-Fe_2O_3, Merck 99% purity) and (2) nickel(II)-hydroxide ($Ni(OH)_2$, Merck 95% purity) and $Fe(OH)_3$ in equimolar ratio. The $Fe(OH)_3$ powder was made by adding equimolar amounts of NaOH solution (25% mass), made from 99% purity NaOH (Merck) to the $FeCl_3$ solution (25% mass), made from 99% purity $FeCl_3{\cdot}6H_2O$ (Merck). Dark brown precipitate was filtrated, washed with large amounts of water and dried in a vacuum dessicator. Before milling, the $Fe(OH)_3{\cdot}nH_2O$ powder was heated at 105 °C for 24 h. The material prepared by this way had 99.5% $Fe(OH)_3$. It was defined by potentiometric redox titration [32]. Mechanochemical synthesis was performed in air atmosphere in planetary ball mill (Fritsch Pulverisette 5). The powders (0.3 g) were pressed into disk shaped samples. The thickness and diameter of each disk are 2.0 mm and 8.0 mm, respectively. All disk pellets were sintered at 1100 °C for 2 h. The densities of the sintered samples were measured by Archimedes method.

Characterization of the samples obtained for 25 h of milling time and after sintered at 1100 °C for 2 h were carried out by several methods:

- The formation of phase and crystal structure of $NiFe_2O_4$ in both cases of synthesis were approved using the X-ray diffractometer (XRD), Model Philips PW 1050 diffractometer equipped with a PW 1730 generator, 40 kV × 20 mA, using Ni filtered CoK_α radiation of 1.78897 Å at the room temperature. Measurements were done in 2θ range of 10–80° with scanning step width of 0.05° and 10 s scanning time per step.
- Raman measurements of mixture of powders and sintered samples were performed using Jobin-Ivon T64000 monochromator. An optical microscope with 100× objective was used to focus the 514 nm radiation from a Coherent Innova 99 Ar^+ laser on the sample. The same microscope was used to collect the backscattered radiation. The dispersed scattering light was detected by a charge-coupled device (CCD) detection system. Room temperature Raman spectra are in spectral range from 100 to 800 cm^{-1}. The average power density on the sample was about 20 mW mm^{-2}.
- The morphology and microstructural characterization of sintered samples soft mechanochemically synthesized $NiFe_2O_4$ ferrites were examined by scanning electron microscopy (SEM, Model JEOL JSM-6460LV).
- Several measurement techniques can be used for experimental determination of electrical properties of sintered $NiFe_2O_4$ ferrites depending on the frequency range. In this study, electrical DC conductivity in the temperature range 298 to 423 K was measured on a Source Meter Keithley 2410. The AC conductivity, dielectric and impedance spectroscopy measurements were carried out in the frequency range 100 Hz–1 MHz and in the temperature range 298–423 K. Specially prepared $NiFe_2O_4$ spinel ferrite samples, in the form of thick disk pellets, were placed between parallel electrodes, as illustrated in Fig. 1. This was done by applying silver paste on both sides of polished surfaces of $NiFe_2O_4$ pellets. In this way prepared samples with silver electrodes deposited on both sides can be considered electrically equivalent to a capacitance C_p in parallel with a resistance

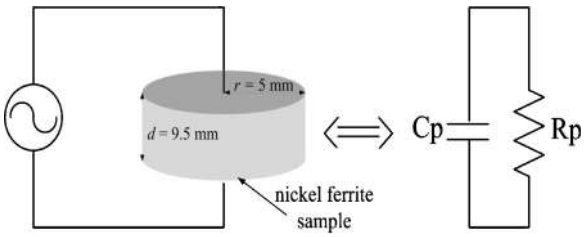

Fig. 1. Schematic diagram of electric circuit for measurement of the electric and dielectric properties of the prepared $NiFe_2O_4$ ferrite sample and equivalent circuit of a sample.

R_p. These values, C_p and R_p, were measured directly using an Impedance Analyzer HP-4194A and a HP-16048C test fixture. The important electrical parameters were determined using the following formulas:

$$\varepsilon' = \frac{C_p}{C_0} \quad (1)$$

$$\varepsilon'' = \frac{1}{\omega C_0 R_p} \quad (2)$$

$$\tan\delta = \frac{\varepsilon''}{\varepsilon'} \quad (3)$$

$$\sigma = \omega \varepsilon_0 \varepsilon'' \quad (4)$$

where C_0 represents the capacitance of the same structure only without the sample between the parallel electrodes, in vacuum, ω is the angular frequency of the applied field and ε_0 represents the permittivity of vacuum equal to 8.85×10^{-12} F^{-1} m. The capacitance C_0 is determined by plate area A and distance between the plates d, as follows $C_0 = A\varepsilon_0/d$.

- From the electrical measurements were obtained values for real (ε') and imaginary (ε'') parts of permittivity and the dielectric loss tangent of material was derived calculating from equation tan $\delta = \varepsilon''/\varepsilon'$.

3. Results and discussion

3.1. Structural characterization

Fig. 2 shows the X-ray diffractograms of the as-synthesized $NiFe_2O_4$ nano-powder samples after 25 h of milling time and the samples sintered at 1100 °C for 2 h. The formation of the $NiFe_2O_4$ inverse spinel structure in the two powder samples is confirmed by the powder XRD patterns shown in Fig. 2a and b (see the patterns in bottom part of this figure). No diffraction peaks of other impurities such as α-Fe_2O_3 or NiO or $Ni(OH)_2$ and $Fe(OH)_3$ hydroxides were observed. It is clearly showed that the reflection peaks on sintered samples become sharper and narrower, indicating the enhancement of crystallinity and good purity of the products. All the Bragg reflection peaks of the samples can be indexed to $NiFe_2O_4$, face centered cubic and *Fd*3*m* space group (the standard pattern reported in PCPDF card for $NiFe_2O_4$ #89-4927), where the diffraction peaks around 21.86°, 35.81°, 4169°, 43.63°, 50.89°, 63.42°, 67.66° and 74.73° are attributed to the reflections of (1 1 1), (2 2 0), (3 1 1), (2 2 2), (4 0 0), (4 2 2), (5 1 1) and (4 4 0) planes of the $NiFe_2O_4$, respectively. These diffraction lines confirm the formation of $NiFe_2O_4$. A standard XRD data is in the inset of the Fig. 2 (red dashes). It is good way to cross check the obtained data with the standard data for $NiFe_2O_4$. Displayed Bragg peak positions in powder diffraction patterns were obtained by Rietveld method. Data on the lattice constants and the positions Bragg reflection given in the standard (PCPDF card for $NiFe_2O_4$ #89-4927) refer to the much larger crystals and practically correspond positions in the sintered samples. The average crystallite size has been calculated using Scherrer's formula $L = k_S\lambda_{Co}/\beta\cos\theta_{h\,k\,l}$, where L is the particle size, k_S is Scherrer constant, $\lambda_{Co} = 1.78897$ Å the wavelength of X-ray sorce, β is the full width at half maximum (FWHM) of the peak ($h\,k\,l$) reduced for instrumental broadening and $\theta_{h\,k\,l}$ is a position of the corresponding Bragg peak [33]. The average calculated particles size for the powder samples are 7 nm for starting mixture (1): $Ni(OH)_2 + Fe_2O_3$ and 9 nm for mixture (2): $Ni(OH)_2 + Fe(OH)_3$. The mechanochemical synthesis of $NiFe_2O_4$ is feasible and complete after 25 h milling time. This is considerably less time compared with the time (35 h) for which the spinel $NiFe_2O_4$ obtained in the work by Jovalekić and co-authors [29]. Marinca and co-authors [27] were synthesized nanocrystalline $NiFe_2O_4$ in a high energy planetary mill. The obtained nickel ferrite has many inhomogeneities and a distorted spinel structure. The mean crystallites size at the final time of milling is 9 ± 2 nm and the lattice parameter increases with increase the milling time. It can once again confirm that our results are consistent with those found in the literature [27]. Our sintered samples have larger crystallites: 56 nm

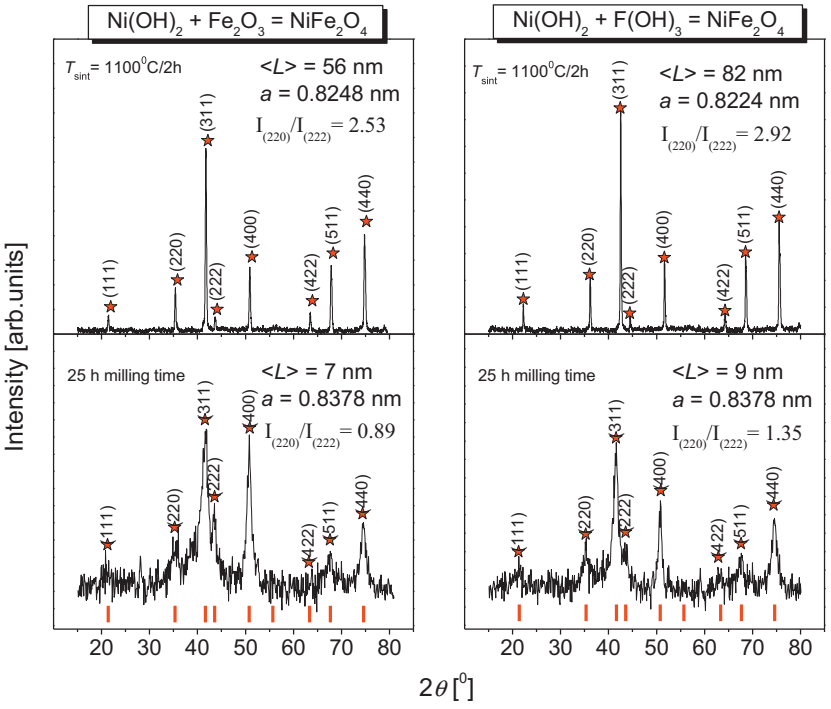

Fig. 2. X-ray diffraction patterns of the $NiFe_2O_4$ ferrite obtained from the mixture of powders: (a) $Ni(OH)_2$ and α-Fe_2O_3 and (b) $Ni(OH)_2$ and $Fe(OH)_3$ for 25 h milling time and after sintering at 1100 °C for 2 h, respectively. *Inset* showing the standard XRD pattern for $NiFe_2O_4$: PCPDF card #89-4927.

(case (1)) and 82 nm (case (2)). Huo and co-authors were prepared $NiFe_2O_4$ ferrite with grain size distribution from 50 to 80 nm by hydrothermal synthesis [34]. The grains were grown significantly with the temperature, what indicates that selected sintering temperature is favorable for ferrite crystallization. The lattice parameters of the powder samples 8.378 Å (given in Fig. 2) computed according to the relation $a = \lambda_{Co}(h^2 + k^2 + l^2)^{1/2}/(2\sin\theta_{h\,k\,l})$ using respective ($h\,k\,l$) values, are greater than for the sintered ones 8.248 Å and 8.224 Å (and the bulk material referred in PCPDF card). It is close to that of the reported values in the literature (JCPDS card No. 10-0325). This increase in lattice parameter of the powder samples is attributed to the increased surface tension which can lead to the distortion of the lattice and redistribution of cations. It is known that in cubic spinel structure Bragg reflection (2 2 0) depends exclusively on the cations occupying tetrahedral sites and intensity of the (2 2 2) reflection depends on cations in the octahedral sites [35]. Ratios of the intensities for diffraction lines (2 2 0) and (2 2 2) indicate that the sample with the highest $I(2\,2\,0)/I(2\,2\,2)$ has the highest degree of the cation inversion, too. It is obvious that all samples exhibit a mixed spinel structure and that the sintered sample obtained from mixture (1), with the greatest crystallite grains, is the closest to stable bulk perfectly inverse nickel ferrite.

Raman spectroscopy is a nondestructive characterization technique sensitive to structural disorder. It provides an important tool to check out the structural properties, including the inversion of cations, of mechanochemically synthesized materials. Group theory predicts five first order Raman active modes ($A_{1g} + E_g + 3F_{2g}$) in the normal cubic spinel structure with symmetry $Fd\bar{3}m$. In the case of the as-prepared powder samples of $NiFe_2O_4$, as well as in the case of sintered $NiFe_2O_4$ samples, all five Raman peaks are clearly visible (Fig. 3), but deconvolution of Raman spectra demonstrates that each peak can be presented like a doublet, which is a characteristic of the mixed or the inverse spinel structure [36,37]. In contrast to normal spinel ferrite structure, where M^{2+} cations are only in tetrahedral positions and Fe^{3+} exclusively in the octahedral sites, in the case of mixed spinels the both sites are occupied and by Ni^{2+} and by Fe^{3+} ions. This results in a distortion of bond distances. Owing to differences in ionic radii of Ni and Fe ions the metal–oxygen bond distance shows a substantial distribution. The symmetry become lower and the Raman spectroscopy detects these changes very well. Instead of five first order symmetric peaks like in the normal spinels, Raman spectra of the mixed or inverse spinel, like $NiFe_2O_4$, is more complicated. Inverse spinel belongs to $P4_322$ tetragonal space group [38], but it is common, for simplicity, to assign Raman modes as if they belong to a normal spinel.

In the cubic nickel ferrites, the strongest modes above 690 cm^{-1} correspond to symmetric stretching of oxygen in tetrahedral groups, and according to accepted convention, can be considered as A_g symmetry. E_g at about 320 cm^{-1} is due to symmetric bending of oxygen with respect to cation in tetrahedral surrounding. $F_{2g}(2)$ at 470 cm^{-1} and $F_{2g}(3)$ at 570 cm^{-1} correspond to the vibrations of octahedral group: $F_{2g}(2)$ is due to asymmetric stretching and $F_{2g}(3)$ is caused by asymmetric bending of oxygen. $F_{2g}(1)$ at 180 cm^{-1} is due to translational movement of the whole tetrahedron. The more expressed asymmetry and even dissociation of Raman modes in the sintered samples is a consequence of a greater degree of inversion. Except that, markedly better defined modes testify that these samples have greater crystallite size and more coherent structure.

A rather significant difference in sintered densities of $NiFe_2O_4$ ferrite *samples 1 and 2* obtained from two different mixtures of starting powders was noted. The density ($\rho_{II} = 4.43$ g cm^{-3}) of sintered $NiFe_2O_4$ ferrite obtained from mixture of $Ni(OH)_2$ and $Fe(OH)_3$ powders was higher, at least 82.45% of theoretical density (TD = 5.373 g cm^{-3}) comparing to $\sim$ 74.26% for the sintered $NiFe_2O_4$ ferrite obtained from mixture of $Ni(OH)_2$ and α-Fe_2O_3 powders ($\rho_I = 3.93$ g cm^{-3}).

SEM surface micrographs of both $NiFe_2O_4$ ferrites sintered at 1100 °C for 2 h are shown in Fig. 4. The images of microstructure of the $NiFe_2O_4$ samples clearly show the pronounced grain growth. In both cases of synthesis are formed the polygonal ferrite grains. It is noteworthy that in the case of sintered nickel ferrite obtained from $Ni(OH)_2$ and $Fe(OH)_3$ powders as starting the precursors, grain size

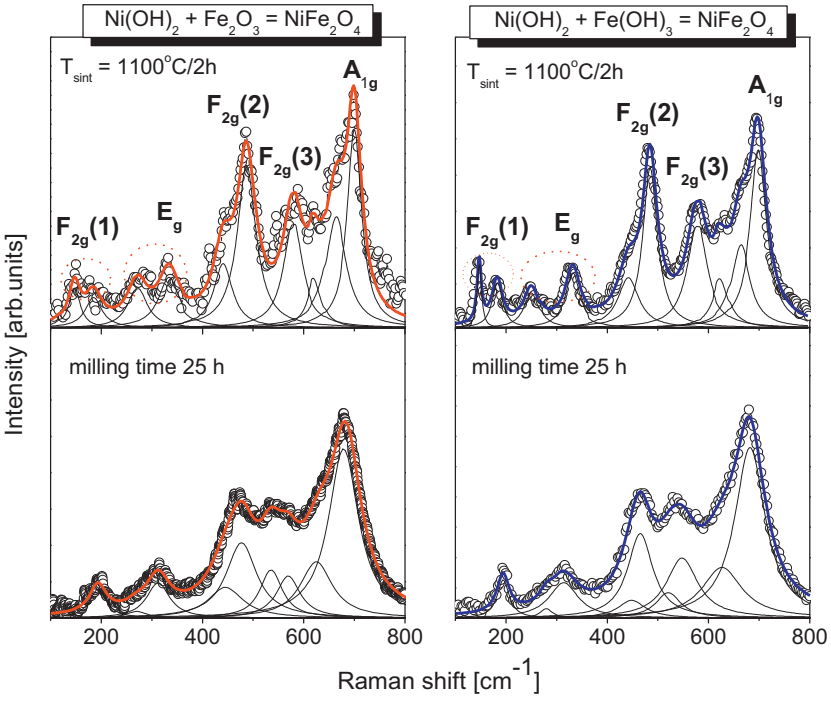

Fig. 3. Raman spectra of the $NiFe_2O_4$ ferrite obtained from the mixture of powders: (a) $Ni(OH)_2$ and α-Fe_2O_3 and (b) $Ni(OH)_2$ and $Fe(OH)_3$ for 25 h milling time and after sintering at 1100 °C for 2 h, respectively.

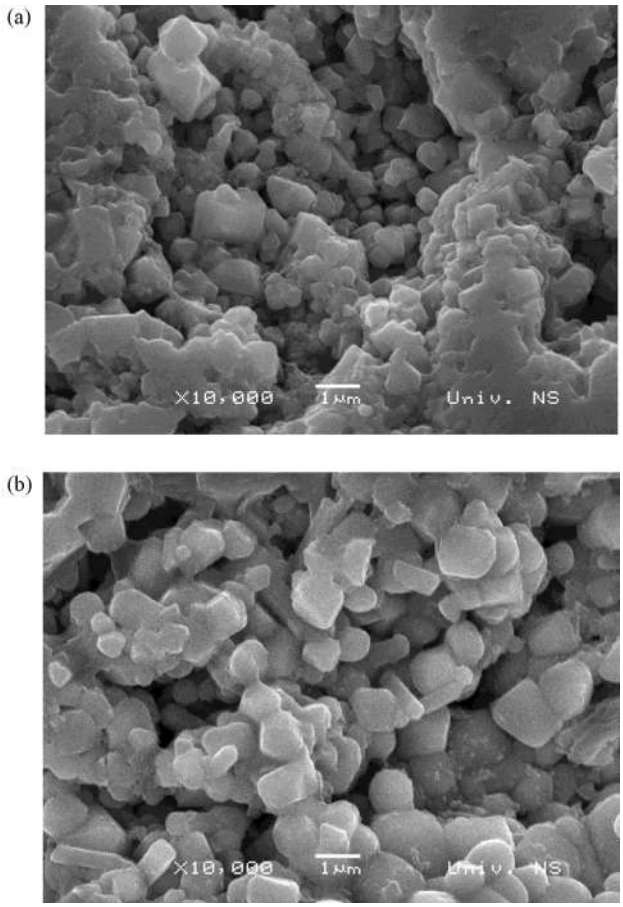

Fig. 4. SEM images of the $NiFe_2O_4$ ferrite obtained from the mixture of powders: (a) $Ni(OH)_2$ and α-Fe_2O_3 and (b) $Ni(OH)_2$ and $Fe(OH)_3$ for 25 h milling time and after sintering at 1100 °C for 2 h, respectively.

distribution is more uniform, ranging from 0.6 up to 1 μm (Fig. 4a), while in the sintered samples obtained from $Ni(OH)_2$ and α-Fe_2O_3 powders, grain size is in the range from 0.3 to 1.5 μm (Fig. 4b). It is obvious that this difference in the grain size is due to different starting precursors and not to the conditions of the synthesis process. Based on the micrographs it can be concluded that the sintered samples, in the case of the nickel ferrite mechanochemically synthesized from $Ni(OH)_2$ and $Fe(OH)_3$ powders have lower porosity than the nickel ferrite synthesized from $Ni(OH)_2$ and α-Fe_2O_3 powders, which is in agreement with the determined density based on Archimedes principle. The density is 3.93 g cm^3 and 4.43 g cm^3 for sintered samples obtained from the powders mixtures of $Ni(OH)_2$ and α-Fe_2O_3 and $Ni(OH)_2$ and $Fe(OH)_3$, respectively.

3.2. Electric properties of spinel nickel ferrites

3.2.1. Electrical conductivity

Electrical conductivity is the physical property of a material which characterizes the conducting power inside the material. Spinel ferrites have low electrical conductivities when compared to other magnetic materials and hence they find wide use at microwave frequencies. In general, these materials are semiconductors with their conductivity lying in between 10^2 and 10^{-11} Ω^{-1} cm^{-1}. The variations in conductivity may be explained by Verwey's hopping mechanism [39]. According to Verwey, the electrical conductivity in ferrites is mainly due to hopping electron between ions of the same element present in more than one valance state, distributed randomly over crystallographicaly equivalent lattice sites. Ferrite structurally from cubic close packed oxygen lattice with the cation at the octahedral [*B*] and the tetrahedral (*A*) sites. The distance between two metal ions on [*B*] sites smaller than the distance between two metals ions on [*B*] and (*A*) site, therefore the hopping between A and B has very small probability compared with that for [*B*]–[*B*] hopping. The hopping between (*A*)–(*A*) sites does not exist, because there are only Fe^{3+} ions at A sites and any Fe^{2+} ions formed during processing preferentially occupy [*B*] sites only [40]. The hopping probability depends upon the separation between the ions involved and the activation energy. The charges can migrate under the influence of the applied field contributing to the electrical response of the system.

Pollak [41] has shown that the conductivity is an increasing function of frequency in the case of conduction by hopping and a decreasing function of frequency in case of band conduction. Generally, the total conductivity is the summation of the band and hopping parts:

$$\sigma = \sigma_{DC}(T) + \sigma_{AC}(\omega, T) \quad (5)$$

The first term represents the temperature dependent DC electrical conductivity due to the band conduction and it is frequency independence. The second term is frequency and temperature dependent pure AC conductivity due to the hopping processes at the octahedral site. It obeys the power law form [42].

3.2.2. DC conductivity

The DC conductivity of prepared nickel ferrite samples was measured as a function of temperature. Fig. 5 and Table 1 show the effect of temperature on the electrical conductivity σ_{DC} for both $NiFe_2O_4$ samples. The studied both ferrite samples show a trend where electrical conductivity/resistivity increases/decreases with increasing temperature. It can be seen that the electrical conductivity of the ferrite obtained from mixture of $Ni(OH)_2$ and $Fe(OH)_3$ powders is higher in regard to the ferrite obtained from mixture of $Ni(OH)_2$ and α-Fe_2O_3 powders. We have already said that the $NiFe_2O_4$ (*sample* 2) obtained from $Ni(OH)_2$ and $Fe(OH)_3$ powders has a higher density and lower porosity compared to $NiFe_2O_4$ (*sample* 1) obtained from $Ni(OH)_2$ and α-Fe_2O_3 powders. The less numbers of pores in $NiFe_2O_4$ obtained from $Ni(OH)_2$ and $Fe(OH)_3$ powders leading to decrease in resistivity and increase in conductivity in comparison with $NiFe_2O_4$ obtained from $Ni(OH)_2$ and α-Fe_2O_3 powders. The plot of $\log(\sigma_{DC})$ versus (1/T) shows that this dependence is linear for sintered $NiFe_2O_4$ samples in the temperature range 298 to 473 K. The observed linear increase of DC conductivity with increasing temperature reflects semiconducting

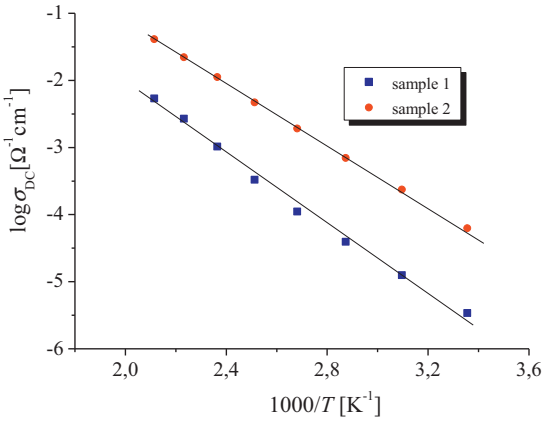

Fig. 5. Temperature dependence of DC electrical conductivity of sintered $NiFe_2O_4$ ferrite obtained from the mixture of the (a) $Ni(OH)_2$ and α-Fe_2O_3 and (b) $Ni(OH)_2$ and $Fe(OH)_3$ powder at different temperatures.

Table 1
DC conductivity and resistivity of sintered $NiFe_2O_4$ samples at selected temperatures.

Sample	T [K]	σ_{DC} [Ω^{-1} cm^{-1}]	$\rho \times 10^3$ [Ω cm]
(1)	293	3.68×10^{-6}	271.74
$Ni(OH)_2 + \alpha$-Fe_2O_3	373	1.112×10^{-4}	8.992
	473	5.384×10^{-3}	0.185
(2)	293	7.22×10^{-5}	13.85
$Ni(OH)_2 + Fe(OH)_3$	373	1.912×10^{-3}	0.523
	473	4.108×10^{-2}	0.024

nature of the $NiFe_2O_4$ ferrites. This is confirmation of the negative temperature coefficient of resistance (NTCR)-type behavior of the prepared pallets usually shown by semiconductors. Also, it is known that the conductivity of ferrites depends upon the purity of starting materials, sintering temperature and sintering time, which influence the microstructure and composition of the samples [43].

The increase in electrical conductivity σ_{DC} with temperature is due to the increase in the thermally activated drift mobility of charge carriers according to the hopping conduction mechanism. The activation energy for the thermally activated hopping process was obtained by fitting the DC conductivity data with the Arrhenius relation [44]:

$$\sigma_{DC}(T) = \sigma_0 \exp\left(\frac{-\Delta E}{kT}\right) \quad (6)$$

where σ_0 is the pre-exponential factor with the dimensions of $(\Omega\ \text{cm})^{-1}$ K, ΔE is the activation energy for DC conductivity, T is the absolute temperature and k_B is the Boltzmann's constant. The slope of the $\log(\sigma_{DC})$ versus $(1/T)$ straight line is a measure of activation energy of the nickel ferrites. In the present case, the activation energy was obtained by fitting the DC conductivity data with the Arrhenius relation (6). The determined values of the conduction activation energy ΔE are 0.653 eV and 0.452 eV for $NiFe_2O_4$ samples prepared from mixture of powders of $Ni(OH)_2$ and α-Fe_2O_3 (*sample* 1) and $Ni(OH)_2$ and $Fe(OH)_3$ (*sample* 2), respectively. If we analyze the obtained values for the conduction activation energy, one can see that *sample* 1 of the $NiFe_2O_4$ obtained from $Ni(OH)_2$ and α-Fe_2O_3 powders has a higher value compared to *sample* 2 of the $NiFe_2O_4$ obtained from $Ni(OH)_2$ and $Fe(OH)_3$ powders. This showed that more energy is required for electron exchange between Fe^{2+} and Fe^{3+} ions for *sample 1*. As shown in Fig. 5, *sample* 1 of the $NiFe_2O_4$ has the lower DC conductivity than *sample* 2 of the $NiFe_2O_4$ prepared from $Ni(OH)_2$ and $Fe(OH)_3$ powders at all temperatures. It is in good accordance with the fact that the higher activation energy is associated with the lower electrical conductivity. Also, there is no remarkable change in the slope in the measured temperature range for both $NiFe_2O_4$ samples. The electrical conductivity depends upon the activation energy, which is associated with the electrical energy barrier experienced by the electrons during hopping. The obtained values of the conduction activation energy ΔE (0.653 eV and 0.452 eV for our $NiFe_2O_4$ samples) could compared with value of the activation energy on the sample sintered in air (0.59 eV) increased obviously compared to those in nitrogen (0.23 eV) [9]. This showed that more energy was required for electron exchange between Fe^{2+} and Fe^{3+} ions for the samples sintered in air. It was in good accordance with the conclusion that the higher activation energy was associated with the lower electrical conductivity. Moreover, the conductivity of ferrites is closely related with the density and porosity [9].

3.2.3. AC conductivity

The variation of AC conductivity of sintered $NiFe_2O_4$ as a function of frequency for different temperatures is given in Fig. 6. It

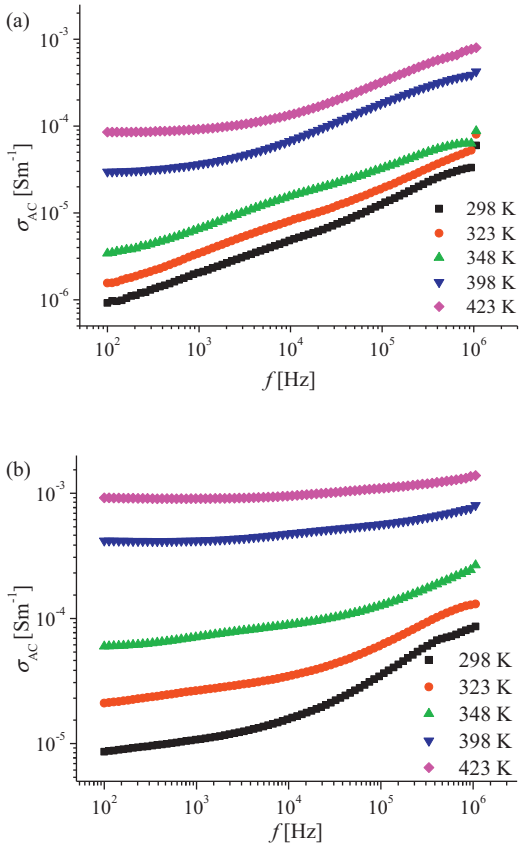

Fig. 6. Frequency dependent AC conductivity behavior of sintered $NiFe_2O_4$ ferrite obtained from the mixture of the (a) $Ni(OH)_2$ and α-Fe_2O_3 and (b) $Ni(OH)_2$ and $Fe(OH)_3$ powder at different temperatures.

is obvious that the $NiFe_2O_4$ (*sample* 2) obtained from the mixture of $Ni(OH)_2$ and $Fe(OH)_3$ powders has a higher conductivity compared to $NiFe_2O_4$ (*sample* 1) obtained from the mixture of $Ni(OH)_2$ and α-Fe_2O_3 powders at a certain temperature and at different frequencies. Also, one can see that the AC conductivity of both $NiFe_2O_4$ ferrites show a gradual rise at low frequencies, whereas at higher frequencies their conductivity rises steeply. This conductivity behavior can be explained by hopping of electron between Fe^{2+} and Fe^{3+} ions (n-type) on the B, octahedral, sites which is responsible for conduction mechanism in spinel $NiFe_2O_4$ ferrites [45]. Also, various reports show that the hole hopping between Ni^{2+} and Ni^{3+} (p-type) on B site also contribute to the electric conduction in $NiFe_2O_4$ as the inverse spinel ferrites [46].

In general, the increase in conductivity with increase of frequency can be explained on the basis of Maxwell–Wagner theory [47,48] and Koop's model [46,49]. According to this theory dielectric structure was formed by two layers. First layer consists of ferrite grains of fairly well conducting, which is separated by a thin layer of poorly conducting substances, which forms the grain boundary. The non-conducting layer or grain boundary is formed by oxygen ions. Thus each grain possesses oxygen rich layer on the surface as boundary. These grain boundaries are more active at lower frequencies, hence the hopping frequency of Fe^{2+} and Fe^{3+} ion is less at lower frequencies. As the frequency of the applied filed increases the conductive grains became more active by promoting the hopping between Fe^{2+} and Fe^{3+} ions, thereby increasing the hopping frequency. Thus, we observe a gradual increase in conductivity with frequency.

The linear increase in AC conductivity with the frequency confirms the polaron type of conduction [3]. It is well known that there are two types of polarons, small polarons and large polarons.

In the small polaron model the conductivity increases linearly with increase in frequency and in case of large polarons the conductivity decreases with increase in frequency [50]. For the prepared spinel $NiFe_2O_4$ ferrites the plots in Fig. 6 indicate small polaron type of conduction.

On the other hand, the charge carriers in ferrites are localized which as consequence has the increase of electrical conductivity with increasing temperature. This influence of temperature on conductivity can be explained by considering the mobility of charge carriers responsible for hopping. As temperature increases the mobility of hopping ions also increases there by increasing conductivity. One can see from Fig. 6 that the conductivity of both $NiFe_2O_4$ ferrites increases with the increase in temperature which is a typical behavior of semiconductors.

3.3. Dielectric properties of spinel $NiFe_2O_4$ ferrite

The dielectric properties can vary widely in ferrites as a function of temperature, frequency of applied electric field, crystal structure, humidity and other external factors. The dielectric response of ferrite materials can be described by the dielectric constant as a complex quantity made up of a real component and an imaginary component:

$$\varepsilon = \varepsilon' - j\varepsilon'' \quad (7)$$

where the first term ε' is the real part of dielectric constant representing the amount of energy stored in a dielectric material, while the second term ε'' is the imaginary part of dielectric constant which describes the dissipated energy. The real and imaginary parts of the dielectric constant have been calculated by the formulas (1) and (2).

3.3.1. Dielectric constant

Figs. 7 and 8 show the effects of frequency on dielectric constant for sintered spinel $NiFe_2O_4$ ferrites at different temperatures. It is clear that both prepared samples exhibit dielectric dispersion where both ε' and ε'' decrease with increasing frequency. The decrease of dielectric constant with increase of frequency as observed in the case of prepared nickel ferrites is a normal dielectric behavior of spinel ferrites. Generally, at low frequencies, in kHz region, the value of dielectric constant of ferrite samples range approximately in the order of 10^2–10^3. Hence, these nickel ferrites are good dielectric materials. The value of both real and imaginary part of dielectric constant is much higher at lower frequencies.

Same as with the electric resistivity/conductivity, the porosity of the ferrite samples also has an influence on the dielectric properties. It is well known that the higher density in sample causes an increase in the value of the dielectric constant. As a confirmation of this fact, the measured data for the dielectric constant of $NiFe_2O_4$ ferrites under investigation are given in Table 2. For example, the values of dielectric constant of samples $NiFe_2O_4$ obtained from the the mixture of $Ni(OH)_2$ and α-Fe_2O_3 powders (*sample* 1) and $Ni(OH)_2$ and $Fe(OH)_3$ powders (*sample* 2) measured at room temperature and a frequency of 1 kHz are ~70 and ~200, respectively, which is in agreement with the fact that the *sample* 2 of $NiFe_2O_4$ has the higher density.

The polarization in ferrites is through a mechanism similar to the conduction process. By electron exchange between Fe^{2+} and Fe^{3+}, the local displacement of electrons in the direction of the applied field occurs and these electrons determine the polarization. The decrease in the dielectric constant with increasing frequency is explained to be due to the decrease of polarization of the dipoles when electric field propagates with high frequency. In other words, beyond a certain frequency of electric field the electron exchange does not follow the alternating field. The large value of dielectric constant at lower frequency is due to the predominance of species like Fe^{2+} ions, oxygen vacancies, grain boundary defects, etc., while the decrease in dielectric constant with frequency is natural because of the fact that any species contributing to polarizability is found to show lagging behind the applied field at higher and higher frequencies [50].

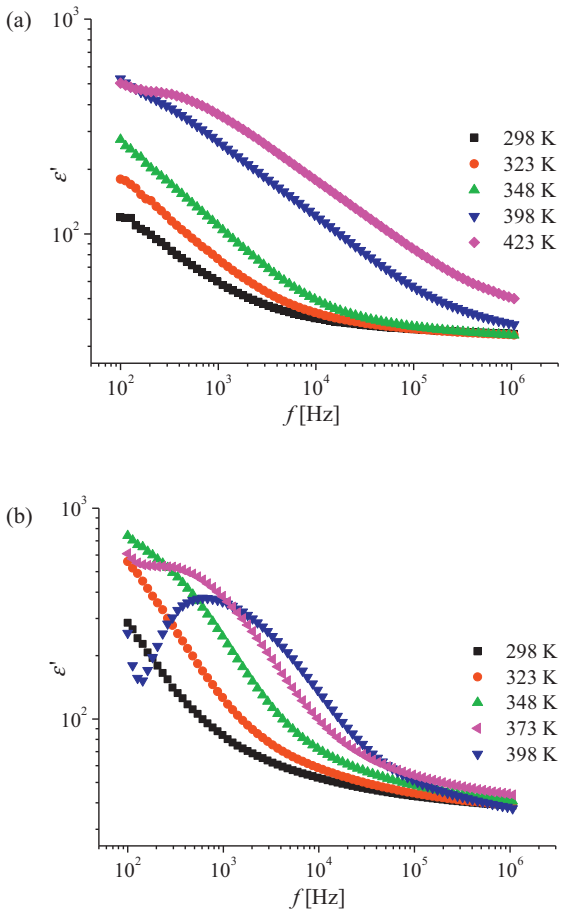

Fig. 7. Variation of the real part of dielectric constant (ε') with frequency for sintered $NiFe_2O_4$ ferrite obtained from the mixture of powders: (a) $Ni(OH)_2$ and α-Fe_2O_3 and (b) $Ni(OH)_2$ and $Fe(OH)_3$ at different temperatures.

It is also noticed from Figs. 7 and 8 that the dielectric constant increases with the increase in temperature. It is explained to be due to thermal activation which enhances the number of dipoles available for polarization when the sample is at a high temperature. The dielectric constant of sintered nickel spinel ferrites increases with the increase in temperature due to the increase in thermally activated charge carriers. This substantiates the normal semiconducting behavior of the spinel ferrites.

It is seen from Figs. 7 and 8 that there is a monotonous decrease in the values of imaginary part of the dielectric constant with increasing frequency. The curves show similar behavior to the real part of the dielectric constant but with slightly higher values for $NiFe_2O_4$ spinel ferrite samples. This can be explained by a correlation between the conduction mechanism (due to hopping of electrons between Fe^{2+} and Fe^{3+}) and dielectric properties of ferrites. The dielectric loss arises from the delay of the polarization behind the applied alternating electric field and is caused by the impurities and imperfections in the crystal lattice.

3.3.2. Dielectric loss tangent

The energy loss is usually characterized by the dielectric loss tangent, tanδ, which is expressed as the ratio of the imaginary part

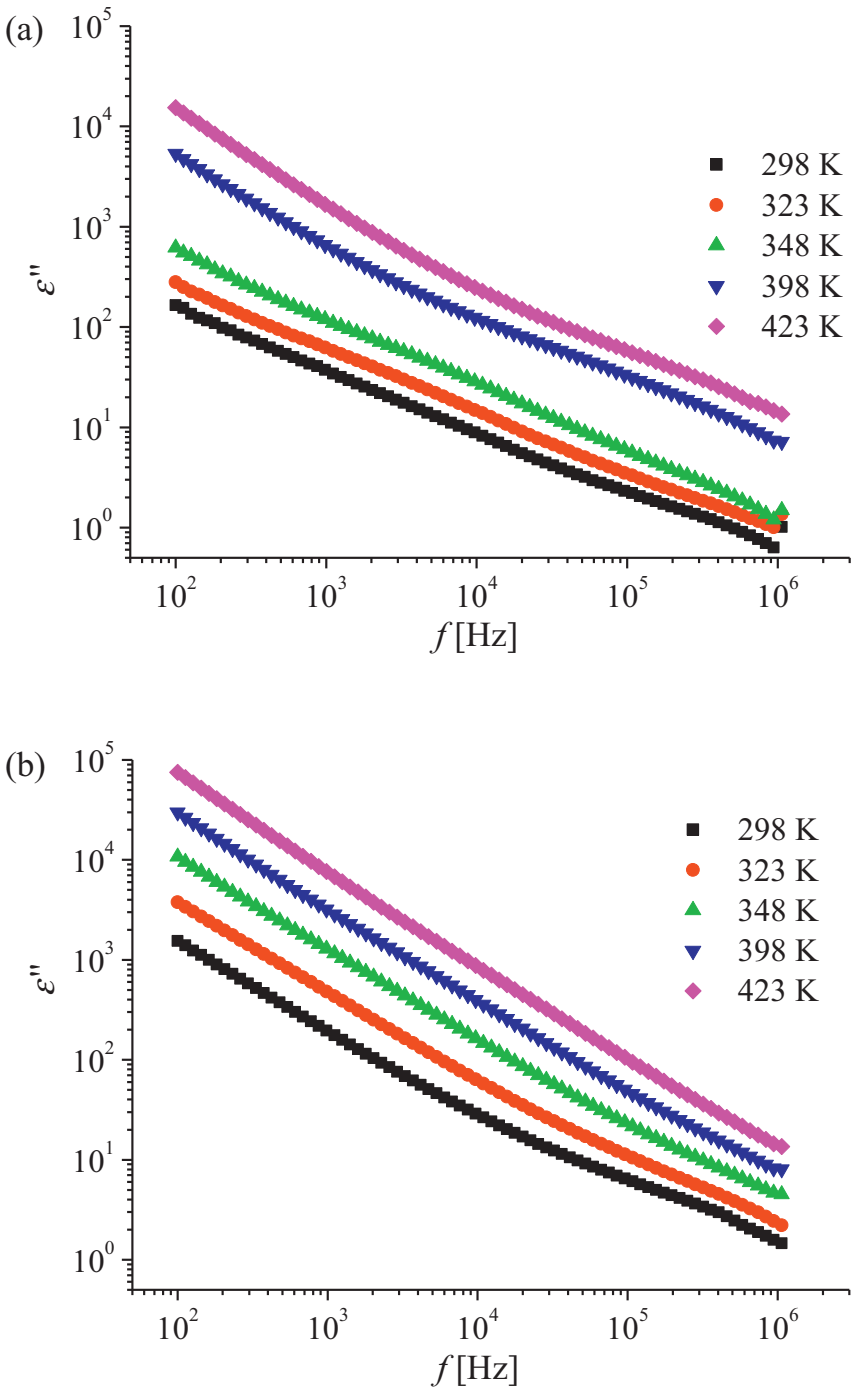

Fig. 8. Variation of the imaginary part of dielectric constant (ε'') with frequency for sintered $NiFe_2O_4$ ferrite obtained from the mixture of powders: (a) $Ni(OH)_2$ and α-Fe_2O_3 and (b) $Ni(OH)_2$ and $Fe(OH)_3$ at different temperatures.

of the dielectric constant to the real part, see formula (3). Dielectric loss arises when the polarization lag behind the applied alternating field which is caused by the impurities and imperfections in the crystal. The plots of dielectric loss versus frequencies for sintered nickel ferrites at different temperatures are shown in Fig. 9. It is observed that tan δ shows an increasing trend with rise in temperature. Also, it is obvious that the sample of $NiFe_2O_4$ prepared from $Ni(OH)_2$ and $Fe(OH)_3$ powders has a higher dielectric loss tangent compared to the sample of $NiFe_2O_4$ prepared from $Ni(OH)_2$ and α-Fe_2O_3 powders at a certain temperature and at different frequencies. From Fig. 9 it is noticed that the dielectric loss for both samples found to be greater at lower frequencies and decreases rapidly with the increase in frequency.

According to phenomenological Koop's theory [49], this is explained on the basis of the fact that in the low frequency region, where the resistivity is high and the grain boundary effect is dominant, more energy is required for electron exchange between Fe^{2+} and Fe^{3+} ions, as a result the loss is high. In the high frequency region, when the resistivity is low and grains themselves have a dominant role, a small energy is required for electron transfer between the two Fe ions at the octahedral site. The dielectric loss tangent shows its maximum value (Debye relaxation) when hopping frequency of charge carriers becomes approximately equal to the frequency of an externally applied field [51,52]. Also at lower frequencies, high dielectric loss may be because of impurities, crystal defects and moisture.

Table 2
Dielectric permittivity (ε', ε'') and dielectric loss tangent ($\tan\delta$) of sintered $NiFe_2O_4$ at selected frequencies.

Sample	Frequency (kHz)	298 K			348 K		
		ε'	ε''	$\tan\delta$	ε'	ε''	$\tan\delta$
(1)	0.1	119.64	165.41	1.384	257.32	616.63	2.239
$Ni(OH)_2 + \alpha\text{-}Fe_2O_3$	1	60.06	37.32	0.621	109.91	119.29	1.085
	10	40.16	8.24	0.205	48.30	26.43	0.547
	100	35.89	2.21	0.062	36.87	5.61	0.152
	1000	34.20	1.01	0.029	33.75	1.49	0.044
(2)	0.1	285.66	1545.73	5.411	740.42	10,766.68	14.541
$Ni(OH)_2 + Fe(OH)_3$	1	83.89	195.96	2.336	246.81	1292.35	5.236
	10	51.97	26.48	0.509	70.01	147.25	2.103
	100	42.79	6.09	0.142	48.05	21.51	0.447
	1000	38.72	1.46	0.038	40.75	4.51	0.111

Based on Figs. 7–9, Table 2 gives the values of dielectric constant (ε', ε'') and loss tangent ($\tan\delta$) of sintered nickel ferrites at selected frequencies. Results listed in table indicate that $NiFe_2O_4$ sintered sample obtained from the mixture of $Ni(OH)_2$ and α-Fe_2O_3 powders has the lower dielectric constant and tan δ compared to the $NiFe_2O_4$ sintered sample obtained from the mixture of $Ni(OH)_2$ and $Fe(OH)_3$ powders at all frequencies. In both nickel ferrites, the imaginary part of dielectric constant decreases more rapidly than the real part with increasing frequency, thus their dielectric loss tangent decreases rapidly. At low frequencies, the values of ε'' are higher than values of ε', especially in $NiFe_2O_4$ sample obtained from hydroxide powders, which results in its higher dielectric loss tangent values. This is more prominent at higher temperatures as one can see in Table 2.

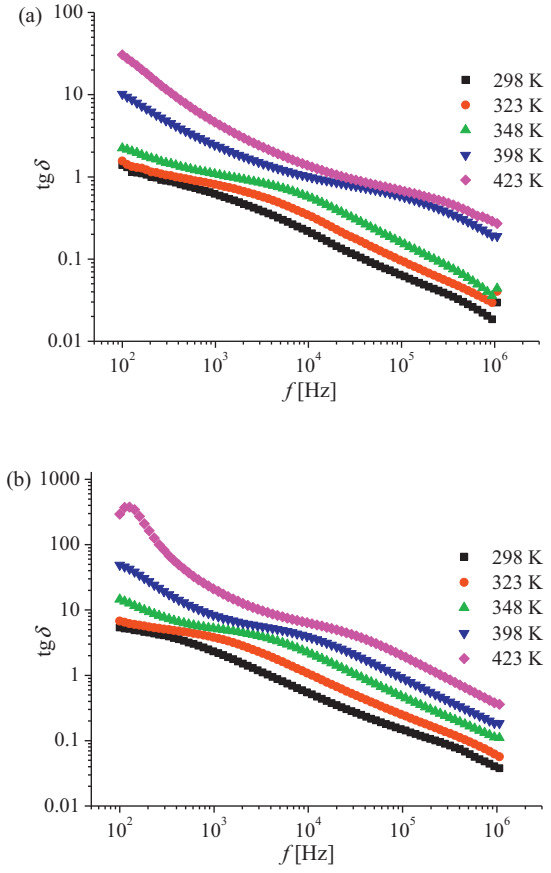

Fig. 9. Variation of the dielectric loss tangent ($\tan\delta$) with frequency for sintered $NiFe_2O_4$ ferrite obtained from the mixture of powders: (a) $Ni(OH)_2$ and α-Fe_2O_3 and (b) $Ni(OH)_2$ and $Fe(OH)_3$ at different temperatures.

3.3.3. Complex impedance analysis

The complex impedance spectroscopy is a powerful technique in the analysis of electrical properties of a material because it enables us to examine the correlation of properties (electrical conductivity, dielectric behavior, etc.) with microstructures (bulk material and grain boundary contributions, etc.) [53]. In the present analysis, the impedance spectroscopy [54] has been used as well-developed tool to separate out the grain/bulk and grain boundary contribution to the total conductivity of prepared nickel ferrites. Depending on the electrical properties of the materials, the AC response can be modeled with two semicircles in the impedance plane. The first semicircle in a low frequency domain represents the resistance of grain boundary and the second one obtained in a high frequency domain corresponds to the resistance of grain or bulk properties.

Fig. 10 shows the complex impedance plane plots (Z' vs Z') of the both samples of the sintered $NiFe_2O_4$ as a function of frequency at different temperatures. Generally, two semicircles are observed in the *Cole–Cole* plots of the sample $NiFe_2O_4$ prepared from $Ni(OH)_2$ and $Fe(OH)_3$ powders between the frequency range 100 Hz and

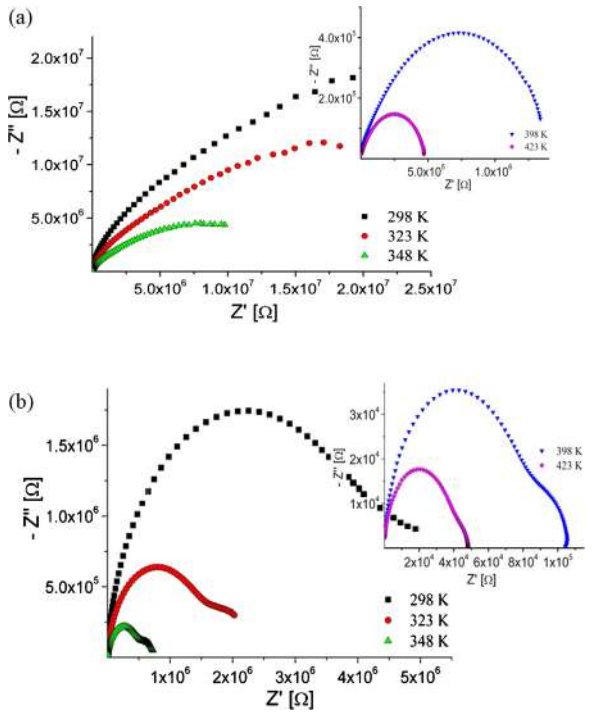

Fig. 10. *Cole–Cole* plots for sintered $NiFe_2O_4$ ferrite obtained from the mixture of powders: (a) $Ni(OH)_2$ and α-Fe_2O_3 and (b) $Ni(OH)_2$ and $Fe(OH)_3$ at different temperatures.

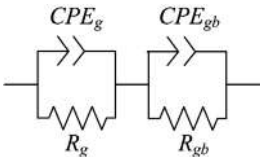

Fig. 11. Equivalent circuit model proposed while analyzing the impedance spectroscopy data.

1 MHz. A larger one at low frequency represents the resistance of the grain boundary and a smaller one obtained at the higher frequency side corresponds to the resistance of grain of bulk properties. It is noticeable that the impedance spectra of this $NiFe_2O_4$ ferrite include both grain and grain boundary effects. This appearance of two semicircles indicates a phenomenon which is typically related to the presence of a distribution of relaxation time. In Fig. 10 is obvious that the sample $NiFe_2O_4$ prepared from $Ni(OH)_2$ and α-Fe_2O_3 powders has a higher impedance compared to the sample $NiFe_2O_4$ prepared from $Ni(OH)_2$ and $Fe(OH)_3$ powders and the grain boundary effects are far more dominant at lower temperatures and noticeable than the bulk-grain effect at high frequencies. At higher temperatures, only one semicircle is observed in the complex impedance plane plots of the sample of $NiFe_2O_4$ prepared from $Ni(OH)_2$ and α-Fe_2O_3 powders in the measured frequency range.

As one can see in impedance spectra of both nickel ferrites, the diameters of the semicircles exhibit decreasing trends with the increase in temperature. It indicates that the conductivity increases with increase in temperature supporting the typical negative temperature coefficient of resistance behavior of both $NiFe_2O_4$ samples usually shown by semiconductors. On impedance spectra is observed that the $NiFe_2O_4$ sample prepared from $Ni(OH)_2$ and α-Fe_2O_3 powders has a higher impedance value than $NiFe_2O_4$ sample prepared from $Ni(OH)_2$ and $Fe(OH)_3$ powders at all temperatures, so it is in good accordance with the fact that the conductivity of $NiFe_2O_4$ *sample* 1 (from $Ni(OH)_2$ and α-Fe_2O_3 powders) is lower than conductivity of the $NiFe_2O_4$ *sample* 2 (from $Ni(OH)_2$ and $Fe(OH)_3$ powders). The impedance value of both samples is decreased by two orders of magnitude, which is due to thermal activation mechanism. The rise of temperature brings with an enhanced conductivity, and hence, decreasing the impedance values.

In order to correlate the electrical properties of the prepared $NiFe_2O_4$ spinel ferrites with the microstructure of these materials, an equivalent circuit model consisting of two serially connected parallel *R-CPE* elements, shown in Fig. 11, has been used to interpret the impedance spectra. Here R_g and R_{gb} represent the grain and grain boundary resistance and CPE_g and CPE_{gb} are the constant phase elements for grain interiors and grain boundaries, respectively. The resistance of the circuit represents a conductive path and a given resistor in a circuit account for the bulk conductivity of the sample. The constant phase element *CPE* is used to accommodate the non-ideal behavior of the capacitance which may have its origin in the presence of more than one relaxation process with similar relaxation times. The impedance of a *CPE* can be described as [46]:

$$Z_{CPE} = A^{-1}(j\varepsilon)^{-n} \quad (8)$$

where ω is the angular frequency, A and n ($0 \le n \le 1$) are fitted parameters. When $n = 1$, then the *CPE* describes an ideal capacitor with $C = A$, while when $n = 0$ the *CPE* describes an ideal resistor with $R = 1/A$. The capacitances are generally associated with space charge polarization regions. The *CPE* elements in the equivalent circuit model have been used to describe non-ideal Debye-like behavior and enable taking into account phenomena occurring in the interface regions, associated with inhomogeneity and diffusion processes [55].

Analysis and simulation of impedance spectra were performed using EIS Spectrum Analyzer software [56]. The different electrical parameters calculated from the complex impedance plots at selected temperatures are shown in Table 3. In the case of the $NiFe_2O_4$ sample prepared from $Ni(OH)_2$ and α-Fe_2O_3 powders the obtained values of grain and grain boundary resistivities are higher compared to the $NiFe_2O_4$ sample prepared from $Ni(OH)_2$ and $Fe(OH)_3$ powders. At lower temperatures, its grain boundary component dominates; the grain boundary resistivity is high. At higher temperatures (398 K and 423 K), we only determined the grain component in the higher frequency range. In the case of the $NiFe_2O_4$ sample prepared from $Ni(OH)_2$ and $Fe(OH)_3$ the proposed equivalent circuit could be applied in the complete measured temperature range.

In both types of $NiFe_2O_4$ spinel ferrites, the value of the grain boundary resistance is generally larger than the resistance of the grain, $R_{gb} \ge R_g$. Additionally, the semicircle representing the grain boundaries lies on the lower frequency side since the relaxation time of the grain boundaries ($\tau_{gb} = R_{gb}C_{gb}$) is much larger than that of the grains ($\tau_g = R_gC_g$). Also, it is observed that the both resistances decrease with increasing temperature. It indicates that the conductivity of sintered nickel ferrites increases with increase in temperature. The higher values of resistance of both grain and grain boundary for the $NiFe_2O_4$ sample from $Ni(OH)_2$ and α-Fe_2O_3 mean this ferrite has a lower conductivity than the $NiFe_2O_4$ sample prepared from $Ni(OH)_2$ and $Fe(OH)_3$ powders. This decrease in the resistance of grains and grain boundaries has been suggested to be due to the thermal activation of the localized charges. Two types of thermal activations, i.e., carrier density in the case of band conduction and carrier mobility in case of hopping, are responsible for the reduction in the resistive properties with

Table 3
The calculated resistance and *CPE* values from the complex impedance plots of $NiFe_2O_4$ ferrite at different temperatures.

Sample	T [K]	R_{gb} [Ω]	CPE1		R_g [Ω]	*C*PE2	
			C_{gb} [F]	n_{gb}		C_g [F]	n_g
(1)	298	5.657E7	1.248E−10	0.815	6.942E6	5.751E−11	0.913
$Ni(OH)_2 + \alpha$-Fe_2O_3	323	3.702E7	3.032E−10	0.748	4.459E6	1.159E−10	0.853
	348	1.449E7	5.835E−10	0.693	1.256E6	1.014E−10	0.897
	398	–	–		9.984E5	1.381E−9	0.664
	423	–	–		4.891E5	1.273E−9	0.695
(2)	298	3.789E6	4.912E−9	0.688	2.397E6	4.487E−11	0.881
$Ni(OH)_2 + Fe(OH)_3$	323	1.365E6	9.585E−9	0.649	1.051E6	4.590E−11	0.887
	348	4.719E5	8.101E−9	0.713	2.915E5	4.525E−11	0.892
	398	7.992E4	5.442E−9	0.822	2.572E4	3.949E−11	0.898
	423	3.797E4	7.682E−9	0.789	1.043E4	3.104E−11	0.921

temperature [45]. For all the temperatures the capacitance of the grain boundary is larger than that of the grain for both types of $NiFe_2O_4$ ferrite samples, which can be explained on the basis that capacitance is inversely proportional to the thickness of the media.

4. Conclusions

$NiFe_2O_4$ ferrite powders were prepared by soft mechanochemical synthesis starting from the mixture of (1) $Ni(OH)_2$ and α-Fe_2O_3 and (2) $Ni(OH)_2$ and $Fe(OH)_3$ powders. Single phase nanosized $NiFe_2O_4$ ferrite powder was formed for 25 h ball milling and then sintered at 1100 °C for 2 h. X-ray diffraction of the prepared samples shows single phase cubic spinel structure. In recorded Raman spectra are observed all first-order Raman active modes. Study of dielectric properties with frequency at different temperatures helps in understanding the electric behavior of the sintered samples. The phenomena of dielectric dispersion were explained in the light of Maxwell–Wagner two layer models and Koops phenomenological theory. The temperature and frequency dependence of dielectric properties showed that the AC conductivity and relaxation of the present nickel ferrites are dominated by hopping of charge carriers and dipoles respectively. Value of determined activation energy showed that conduction was due to electron hopping mechanism between Fe^{2+} and Fe^{3+}. The measured data clearly indicate that the apparent effect of the density/porosity $NiFe_2O_4$ ferrite samples on electrical resistivity/conductivity and dielectric constant. The analysis of the complex impedance data shows that the capacitive and the reactive properties of the nickel ferrites are mainly attributed to the processes that are associated with the grain and grain boundary. The grain and grain boundary resistances of sintered sample exhibit decreasing trends with the increase in temperature. It indicates that the conductivity increases with increase in temperature supporting the typical negative temperature coefficient of resistance (NTCR) behavior of the material usually shown by semiconductors.

Acknowledgment

This research was financially supported by the Ministry of Education, Science and Technological Development of the Republic of Serbia through Projects No. III 45003 and 45015.

References

[1] F.L. Zabotto, A.J. Gualdi, J.A. Eiras, A.J. Aparecido de Oliveira, D. Garcia, Mater. Res. 15 (2012) 428–433.
[2] A. Pui, D. Gherca, N. Cornei, Mater. Res. Bull. 48 (2013) 1357–1362.
[3] P. Sivakumar, R. Ramesh, A. Ramanand, S. Ponnusamy, C. Muthamizhchelvan, J. Alloys Compd. 537 (2012) 203–207.
[4] M.H. Alimuddin, S. Kumar, S.E. Shirsathc, R.K. Kotnala, J. Shah, R. Kumar, Ceram. Int. 9 (2013) 1807–1819.
[5] V. Šepelák, D. Baabe, D. Mienert, D. Schultze, F. Krumeich, F.J. Litterst, K.D. Necker, J. Magn. Magn. Mater. 257 (2003) 377–386.
[6] A.J. Moulson, J.M. Herbert, Electroceramics: Materials, Properties, and Applications, 2nd ed., John Wiley & Sons Ltd., Hoboken, 2003.
[7] Z. Zhang, Y. Liu, G. Yau, G. Zu, Y. Hao, Int. J. Appl. Ceram. Technol. 10 (2013) 142–149.
[8] T. Žák, V. Ćosović, A. Ćosović, B. David, N. Talijan, D. Živković, Sci. Sinter. 44 (2012) 103–112.
[9] B. Liu, K. Zhou, Z. Li, D. Zhang, L. Zhang, Mater. Res. Bull. 45 (2010) 1668–1671.
[10] J. Liu, H. He, X. Jin, Z. Hao, Z. Hud, Mater. Res. Bull. 36 (2001) 2357–2363.
[11] S. Ghatak, M. Sinha, A.K. Meikap, S.K. Pradhan, Mater. Res. Bull. 46 (2011) 1055–1064.
[12] K. Maaz, S. Karim, A. Mumtaz, S.K. Hasanain, J. Liu, J.L. Duan, J. Magn. Magn. Mater. 321 (2009) 1838–1842.
[13] P. Sivakumur, R. Ramesh, A. Ramanand, S. Ponnusamy, C. Muthamizhchelvan, Mater. Lett. 65 (2011) 483–485.
[14] J. Zhou, J. Ma, C. Sun, L. Xie, Z. Zhao, H. Tian, Y. Wang, J. Tao, X. Zhu, J. Am. Ceram. Soc. 88 (2005) 3535–3537.
[15] K.M. Reddy, L. Satyanarayana, S.V. Manorama, R.D.K. Misra, Mater. Res. Bull. 39 (2004) 1491–1498.
[16] S. Phumying, S. Labuayai, E. Swatsitang, V. Amornkitbamrung, S. Maensiri, Mater. Res. Bull. 48 (2013) 2060–2065.
[17] A. Baykal, N. Kasapoğlu, Y. Köseoğlu, M.S. Toprak, H. Bayrakdar, J. Alloys Compd. 464 (2008) 514–518.
[18] E. Manova, C. Estournès, D. Paneva, J.L. Rehspringe, T. Tsoncheva, B. Kunev, I. Mitov, Hyperfine Interact. 165 (2005) 215–220.
[19] D.H. Chen, X.R. He, Mater. Res. Bull. 36 (2001) 1369–1377.
[20] P. Sivakumar, R. Ramesh, A. Ramanand, S. Ponnusamy, C. Muthamizhchelvan, Mater. Res. Bull. 46 (2011) 2204–2207.
[21] P.K. Roy, J. Bera, J. Mater. Process. Technol. 197 (2008) 279–283.
[22] P. Sivakumar, R. Ramesh, A. Ramanand, S. Ponnusamy, C. Muthamizhchelvan, Mater. Res. Bull. 46 (2011) 2208–2211.
[23] V. Šepelák, U. Steinike, D.C. Uecker, S. Wissmann, K.D. Becker, J. Solid State Chem. 135 (1998) 52–58.
[24] E. Avvakumov, M. Senna, N. Kosova, Soft Mechanochemical Synthesis: A Basis For New Chemical Technologies, Kluwer Academic Publishers, Boston, 2001.
[25] M. Senna, Solid State Ionics 63–65 (1993) 3–9.
[26] V.V. Boldyrev, Solid State Ionics 63–65 (1993) 537–543.
[27] T.F. Marinca, I. Chicinaş, O. Isnard, V. Pop, F. Popa, J. Alloys Compd. 509 (2011) 7931–7936.
[28] H. Yang, X. Zhang, W. Ao, G. Qiu, Mater. Res. Bull. 39 (2004) 833–837.
[29] Č. Jovalekić, M. Zdujić, A. Radaković, M. Mitrić, Mater. Lett. 24 (1995) 365–368.
[30] V. Šepelák, I. Bergmann, A. Feldhoff, P. Heitjans, F. Krumeich, D. Menzel, F.J. Litterst, S.J. Campbell, K.D. Becker, J. Phys. Chem. C 111 (2007) 5026–5033.
[31] V. Šepelák, M. Menel, I. Bergmann, M. Wiebcke, F. Krumeich, K.D. Becker, J. Magn. Magn. Mater. 272–276 (2004) 1616–1618.
[32] Z.Ž. Lazarević, Č. Jovalekić, A. Rečnik, V.N. Ivanovski, A. Milutinović, M. Romčević, M.B. Pavlović, B. Cekić, N.Ž. Romčević, Mater. Res. Bull. 48 (2013) 404–415.
[33] B.D. Cullity, in: M. Cohen (Ed.), Elements of X-ray Diffraction, Addison-Wesley Publishing, San Diego, 1977.
[34] J. Huo, M. Wei, Mater. Lett. 63 (2009) 1183–1184.
[35] V. Šepelak, K. Tkáčova, Acta Montan. Slovaca 2 (1997) 266–272.
[36] A. Ahlawat, V.G. Sathe, J. Raman Spectrosc. 42 (2011) 1087–1094.
[37] M.H. Sousa, F.A. Tourinho, J.C. Rubim, J. Raman Spectrosc. 31 (2000) 185–191.
[38] C. Cheng, J. Magn. Magn. Mater. 325 (2013) 144–146.
[39] E.J.W. Verwey, J.H. de Boer, Rec. Travaux Chim. Pays-Bas 55 (1936) 531–540.
[40] A. Lakshman, P.S.V.S. Rao, B.P. Rao, K.H. Rao, J. Phys. D: Appl. Phys. 38 (2005) 673–678.
[41] M. Pollak, in: Proceedings of the International Conference on Physics of Semiconductors, Exeter, (1962), p. 86.
[42] A.M. Abdeen, J. Magn. Magn. Mater. 185 (1998) 199–206.
[43] P.A. Jadhav, R.S. Devan, Y.D. Kolekar, B.K. Chougule, J. Phys. Chem. Solids 70 (2009) 396–400.
[44] S.M. Savic, M.V. Nikolic, O.S. Aleksic, M.P. Slankamenac, M.B. Zivanov, P.M. Nikolic, Sci. Sinter. 40 (2008) 27–32.
[45] M. Younas, M. Nadeem, M. Atif, R. Grossinger, J. Appl. Phys. 109 (2011) 093704.
[46] K.S. Muthu, N. Lakshminarasimhan, Ceram. Int. 39 (2013) 2309–2315.
[47] J.C. Maxwell, Electricity and Magnetism, Oxford University Press, New York, 1973 p. 88.
[48] K.W. Wagner, Arch. Elektrotechn. 2 (1914) 371–387.
[49] C.G. Koops, Phys. Rev. 83 (1951) 121–124.
[50] D.R. Patil, B.K. Chougule, Mater. Chem. Phys. 117 (2009) 35–40.
[51] A.M.M. Farea, S. Kumara, K.M. Batoo, A. Yousef, C.G. Lee, Alimuddina, J. Alloys Compd. 464 (2008) 361–369.
[52] Z. Cvejic, S. Rakic, S. Jankov, S. Skuban, A. Kapor, J. Alloys Compd. 480 (2009) 241–245.
[53] K. Verma, S. Sharma, Ceram. Int. 38 (2012) 5957–5966.
[54] E. Barsoukov, J.R. Macdonald, Impedance Spectroscopy – Theory, Experiment and Applications, John Wiley & Sons, New Jersey, 2005.
[55] F.D. Morrison, D.J. Jung, J.F. Scott, J. Appl. Phys. 101 (2007) 094112.
[56] A.S. Bondarenko, G. Ragoisha, EIS Spectrum Analyser, http://www.abc.chemistry.bsu.by.

Materials Research Bulletin 48 (2013) 4759–4768

Contents lists available at ScienceDirect

Materials Research Bulletin

journal homepage: www.elsevier.com/locate/matresbu

The cation inversion and magnetization in nanopowder zinc ferrite obtained by soft mechanochemical processing

A. Milutinović [a], Z. Lazarević [a,*], Č. Jovalekić [b], I. Kuryliszyn-Kudelska [c], M. Romčević [a], S. Kostić [a], N. Romčević [a]

[a] Institute of Physics, University of Belgrade, Pregrevica 118, Zemun, Belgrade, Serbia
[b] Institute for Multidisciplinary Research, University of Belgrade, Belgrade, Serbia
[c] Institute of Physics, Polish Academy of Sciences, Al. Lotników 32/46, 02-668 Warsaw, Poland

ARTICLE INFO

Article history:
Received 7 March 2013
Received in revised form 2 August 2013
Accepted 16 August 2013
Available online 28 August 2013

Keywords:
A. Magnetic materials
A. Nanostructures
C. Raman spectroscopy
C. X-ray diffraction
D. Magnetic properties

ABSTRACT

Two zinc ferrite nanoparticle materials were prepared by the same method – soft mechanochemical synthesis, but starting from different powder mixtures: (1) $Zn(OH)_2/\alpha$-Fe_2O_3 and (2) $Zn(OH)_2$/$Fe(OH)_3$. In both cases a single phase system was obtained after 18 h of milling. The progress of the synthesis was controlled by X-ray diffractometry (XRD), Raman spectroscopy, TEM and magnetic measurements. Analysis of the XRD patterns by Rietveld refinement allowed determination of the cation inversion degree for both obtained single phase $ZnFe_2O_4$ samples. The sample obtained from mixture (1) has the cation inversion degree 0.3482 and the sample obtained from mixture (2) 0.400. Magnetization measurements were confirmed that the degrees of the inversion were well estimated. Comparison with published data shows that used method of synthesis gives nano powder samples with extremely high values of saturation magnetizations: sample (1) 78.3 emu g^{-1} and sample (2) 91.5 emu g^{-1} at $T = 4.5$ K.

1. Introduction

The spinel ferrites are a large group of oxides that have the structure of the natural spinel $MgAl_2O_4$. The structure of spinel was first investigated by William Henry Bragg [1,2] and independently Shoji Nishikawa [3] in far 1915 year. The ideal structure consists of cubic close-packed oxygen anions; with a unit cell that containing eight formula units. The space group is *Fd*-3*m*, number 227 in the International Tables. Between the oxygen atoms there are 96 interstices. Among 64 interstices with tetrahedral coordination only eight special positions 8*a* (point symmetry $\bar{4}3m$) are occupied with the "A" cations. Remaining 32 positions are octahedral coordinated and a half of them, with positions 16*d* (point symmetry *m*3*m*), are occupied with "B" cations. Oxygen positions are labeled with 32*e* in Wyckoff notation. Spinel structure is called normal $(A)[B_2]O_4$ when 2^+ cations are only in tetrahedral positions and Fe^{3+} in octahedral sites. The oxygen atoms are not in the ideal f.c.c. positions, depending on the difference in the effective ionic radii of "A" and "B" cations. Except that, spinel structures can be partially or completely inverse, with general formula $(A_{1-\delta}B_\delta)[A_\delta B_{2-\delta}]O_4$, where δ is a degree of inversion, i.e. part of cations from octahedral positions that "had settled" in tetrahedral sites. Degree of inversion, δ can vary from 0 for normal to 1 for the perfectly inverse spinel. For $\delta = 2/3$ arrangement is completely random and corresponds to maximum of the configurationally entropy. The oxygen usually displace along a [1 1 1] direction to accommodate the ionic radii of the cations in both sites causing an enlargement of the tetrahedral polyhedron at the expense of the octahedral radius and leading to change in symmetry of octahedral site to $\bar{3}m$. For precise definition of the spinel unit cell, except length of a unit cell *a*, it is necessary to know an oxygen (or deformation) parameter *u*, also. If the origin of the unit cell is taken at the occupied tetrahedral site: A(0, 0, 0), then cation in octahedral site is in position B(0.625, 0.625, 0.625), and $u = 3/8 = 0.375$, i.e. position of oxygen in relation to the origin of the unit cell is: O(0.375, 0.375, 0.375) in the ideal *f.c.c.* symmetry.

Cation to anion distances are given by [4]:

$$R_{tet} = a\sqrt{3}(u - 1/4) \quad (1)$$

* Corresponding author. Tel.: +381 11 37 13 035; fax: +381 11 31 60 531.
E-mail address: lzorica@yahoo.com (Z. Lazarević).

0025-5408/$ – see front matter © 2013 Elsevier Ltd. All rights reserved.
http://dx.doi.org/10.1016/j.materresbull.2013.08.020

$$R_{oct} = a[3u^2 - 2.75u + 43/64]^{1/2} \sim a(5/8 - u)^* \quad (2)$$

At[1] the other side, these distances are the sum of the oxygen anion radius r_O and the radius of the corresponding cation:

$$R_{tet} = \langle r_A \rangle + r_O \quad (3)$$

$$R_{oct} = \langle r_B \rangle + r_O \quad (4)$$

The mean ionic radii of the tetrahedral and octahedral site for the mixed or inverse spinels are

$$\langle r_A \rangle = (1 - \delta) r_A + \delta r_B \quad (5)$$

$$\langle r_B \rangle = 1/2[\delta r_A + (2 - \delta) r_B] \quad (6)$$

Value of lattice parameter can be calculated according to the relation:

$$a_{calc} = 8/3\left[\frac{(\langle r_A \rangle + r_O)}{\sqrt{3}} + (\langle r_B \rangle + r_O)\right] \quad (7)$$

Effective ionic radii in tetrahedral and octahedral coordination and oxygen anion radius are given in Ref. [5]. For Zn^{2+} in tetrahedral position effective radius is 0.58 Å, and in octahedral site radius is 0.73 Å. For Fe^{3+} in tetrahedral position effective radius is 0.485 Å, and in octahedral site radius is 0.645 Å. Oxygen's radius is 1.38 Å.

There are two methods for the preparation of magnetic nanoparticles: physical and chemical. The methods of generation of magnetic nanoparticles in the gas or solid phase using high-energy treatment of the material are usually called physical, while the nanoparticle syntheses, which are often carried out in solutions at moderate temperatures are chemical methods. Different routes have become an essential focus of the related research and development activities. Various fabrication methods to prepare nanosize spinel ferrites have been reported, e.g., sol–gel methods [6], the ball-milling technique [7–9], co-precipitation [10,11], polymeric assisted route [12] the hydrothermal method [13,14], the reverse micelles process and the micro-emulsion method [15–22]. Various precipitation agents have been used to produce specific size and shape spinel ferrites nanocrystals, e.g., metal hydroxide in the co-precipitation method, surfactant and ammonia in the reverse micelles process and various micro-emulsion methods, and organic matrices in the sol–gel method. Most of these methods have achieved particles of the required sizes and shapes, but they are difficult to employ on a large scale because of their expensive and complicated procedures, high reaction temperatures, long reaction times, toxic reagents and by-products, and their potential harm to the environment. Mechanochemical synthesis is the general name given to the process of milling of powders which is accompanied by chemical reactions. Novel approach to mechanochemical synthesis, based on reactions of solid acids, based hydrated compounds, crystal hydrates, basic and acidic salts, has been called soft mechanochemical synthesis. The soft mechanochemical reactions consist in the high reactivity of surface functional groups, notably, OH groups [23]. The major advantages of soft mechanochemical synthesis lie in the formation of reaction products at a room or a low temperature and the refinement of produced powders to a nanometer size range. This is reflected primarily in the simplicity of the procedure and equipment used. Also, this method is inexpensive in comparison with other method of synthesis.

It is well known that different methods of preparation greatly affect the strain, shape and size of obtained nanoparticles what results in a significant change of the lattice constant, oxygen parameter and the degree of inversion. A correlation between particle size and the inversion degree can be established only for samples obtained by the same synthesis method. Changes in structural parameters surely change all physical characteristics, particularly magnetic and electric properties of nano spinels.

In spinel ferrites disorder in the cation distribution between A and B sites can affects the value of saturation magnetization M_{sat}, exchange interactions and ferromagnetic ordering temperatures. Magnetic properties can be used as a probe of disorder in ferromagnetic spinels. This particularly applies for zinc ferrite which is a paramagnetic at room temperature in a form of bulk, but in the form of nanoparticles has a significant magnetization.

In recent years, spinel ferrite nanoparticles have been extensively investigated because, owing to chemical stability, mechanical hardness and especially of their magnetic and electrical properties, they can be used for recording media, spintronics, magnetic refrigeration, ferro fluids, magnetic resonance imaging, the delivery of drugs to specific areas of the body, etc. [24–28]. Understanding of the crystal chemistry of spinel nanoparticles is essential for controlling their magnetic properties, because of the close connections between their magnetic properties and their crystal chemistry and structures. The cation distribution in nanomaterials can be estimated by X-ray diffraction, nuclear magnetic resonance, neutron diffraction [29,30], Mössbauer analysis, electron energy loss spectroscopy EELS [31], EXAFS [32], and usually by combination of several methods for greater reliability [33]. Magnetic nanoparticles with dimensions ranging from a few nanometers up to tens of nanometers, thanks to their comparable or smaller size than proteins, cells or viruses, are able to interact with (bind to or penetrate into) biological entities of interest. These size advantages of magnetic nanoparticles together with their sensing, moving and heating capabilites based on the unique nanometer-scale magnetic and physiological properties give them the possibility to be used in biomedical applications such as magnetic resonance imaging (MRI), targeted drug delivery and hyperthermia [34–37]. Rana et al. investigated the reverse micelle and chemical hydrolysis techniques had been successfully combined to synthesize composite nanoparticles consisting of a photocatalytic shell of titania and a magnetic core of ferrite. The nature of titania shell, i.e. anatase or brookite, depends on the TiO_2 and ferrite molar ratio. The work presented here describes the photo catalytic and anti-microbial activity of the composite nanoparticles together with the magnetic characteristics of the nickel ferrite core. The TiO_2-coated ferrite nanoparticles retain the magnetic characteristics of uncoated nanocrystalline ferrites (superparamagnetism; absence of hysteresis, remanence and coercivity at 300 K) encouraging their application as removable anti-microbial photocatalyst nanoparticles that could be extracted from the sprayed surface (human body or environment) after exposure [36].

In the present work we investigated zinc ferrite nanoparticle materials prepared by the same method - soft mechanochemical synthesis, but starting from two different mixtures. In both cases we obtained a single phase system after 18 h of milling [38]. The progress of the synthesis is controlled by X-ray diffractometry, Raman spectroscopy and magnetic measurements. Analysis of the results of used methods allows estimating the degree of the inversion for both obtained single phase $ZnFe_2O_4$ samples.

[1] If the origin of the unit cell is chosen in the (vacant octahedral site) then A site is in 8*f* in Wyckoff notation and *A*(0.125, 0.125, 0.125), B site is 16*c*, *B*(0.5, 0.5, 0.5) and oxygen is in 32*e*, but with relative coordinate $u^* = 0.250$ for ideal f.c.c. lattice. In that case cation to anion distances are $R_{tet} = a(u^* - 1/8)$ and $R_{oct} = a[3u^{*2} - 2u^* + 3/8]^{1/2}$.

2. Experimental

Starting compounds used for synthesizing of two types zinc ferrite nanopowders were

(1) Zinc-hydroxide ($Zn(OH)_2$, Merck 95% purity) and hematite (α-Fe_2O_3, Merck 99% purity) and (2) zinc-hydroxide ($Zn(OH)_2$, Merck 95% purity) and $Fe(OH)_3$ in equimolar ratio.

Soft mechanochemical synthesis was performed in air atmosphere in planetary ball mill (Fritsch Pulverisette 5) for 4, 10 and 18 h. The powder mixtures were pressed into pallets using a cold isostatic press (8 mm in diameter and ~3 mm thick).

X-ray diffraction (XRD) measurements were performed on Philips PW 1050 diffractometer with Ni filtered Co$K\alpha$ radiation of 1.78897 Å at room temperature. Measurements were done in 2θ range of 15–80° with scanning step width of 0.05° and 10 s scanning time per step.

The microstructural characteristics (crystallite size, strain and cation inversion) were obtained from the Rietveld analysis of the XRD data by means of the *FullProf Suite* [39] and *PowderCell 2.4 Program* [40], simultaneously, in order to verify the accuracy of more simple, but "user friendly" *PowderCell 2.4 Program*. The *Joint Committee on Powder Diffraction Standards* (JCPDS) *Powder Diffraction File* (PDF) database was used for phase identification [41].

Raman measurements of mixture of powders and sintered samples were performed using Jobin-Ivon T64000 monochromator. An optical microscope with 100× objective was used to focus the 514 nm radiation from a Coherent Innova 99 Ar^+ laser on the sample. The same microscope was used to collect the back-scattered radiation. The dispersed scattering light was detected by a charge-coupled device (CCD) detection system. Room temperature Raman spectra are in spectral range from 100 to 800 cm^{-1}. The average power density on the sample was about 20 mW mm^{-2};

TEM studies were performed using a 200 kV TEM (JEM-2100 UHR, Jeol Inc., Tokyo, Japan) equipped with an ultra-high resolution objective lens pole piece having a point-to-point resolution of 0.19 nm, being sufficient to resolve the lattice images of nanoparticles. Due to relatively small size of the nanoparticles, selected area electron diffraction patterns (EDP) over the multiple nanocrystals were recorded to obtain the characteristic diffraction rings with structure-specific *d*-values. Electron energy dispersive X-ray spectroscopy (EDS) was used to examine the chemical composition of the product.

The magnetization measurements were done at Cryogenic vibrating sample magnetometer (VSM) in magnetic field from 0 kOe to ±80 kOe.

3. Results and discussion

X-ray diffractograms of two different starting mixtures after 4, 10 and 18 h of milling time are presented in Fig. 1. It is well seen that spinel phase is already present after 4 h milling. In the case (2) mechanochemical activation takes place faster and after 10 h of milling the presence of unreacted compounds is smaller than in the case (1). According to Rietveld refinement we estimated that the spinel phase in the case (1) is 94.3% and in the chase (2) more than 98.0%. We have to remark that in these cases, when diffractograms are poorly defined, Rietveld results can be considered with a certain caution. Namely, powder patterns after 10 h of milling time are characterized by a low crystallinity what results in high discrepancy factors, R_{wp} (R-weighted differences between measured and calculated patterns), over 30%.

After 18 h of milling a single spinel phase is achieved in both systems. Samples are still of low crystallinity, but in this case Rietveld refinement of diffractograms was carried out very

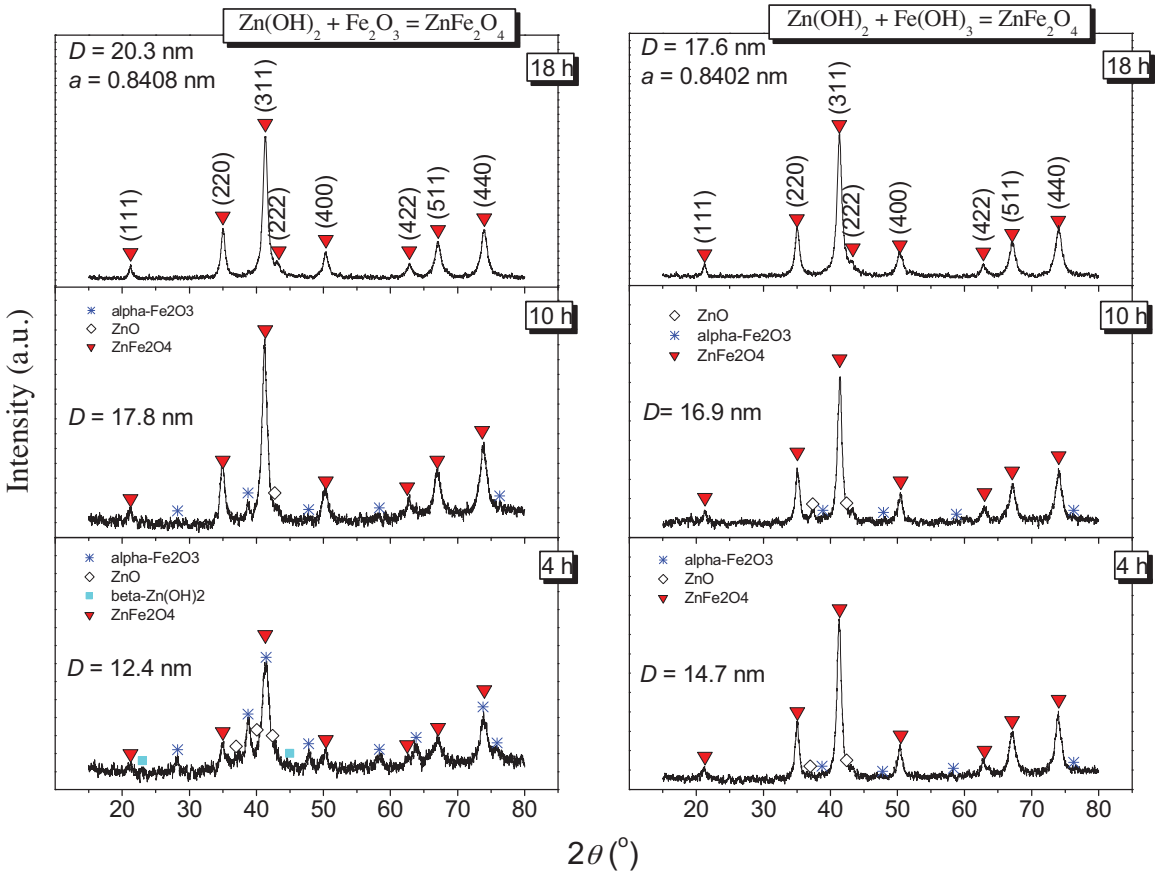

Fig. 1. X-ray diffractograms of the samples obtained after 4, 10 and 18 h milling time of (a) zinc hydroxide and hematite and (b) zinc hydroxide and ferric hydroxide powders.

carefully in order to reduce the R_{wp} and determine the structural parameters of zinc ferrite nanomaterials as precise as possible. Diffraction intensities observed experimentally were compared with diffractions calculated for a large number of hypothetical crystals structures.

In the first step the global parameters (2θ-zero, background and specimen displacement) were refined. Due to the observed peak broadness we did not deconvolute an instrumental profile, which is more than ten times smaller. In the next step, the structure parameters (lattice constant, oxygen parameter, specimen's profile breadth parameter and site occupancy) were refined sequentially. The site occupancy in the two positions, octahedral and tetrahedral, was limited in order to keep the sum of the same cations in the two sites in its stoichiometric value. The criteria for the most probable distributions should be the lowest values of the agreement factors.

In the last cycle, when the R-weighted profile, R_{wp}, has reached its minimum value, all the parameters - global and structural were refined simultaneously. The goodness of fit, $\chi^2 = {R_{wp}}^2/{R_{exp}}^2$, where R_{exp} is expected value, i.e. the best possible R_{wp} factor, is >1. It is known that high values of R_{wp} and χ^2 can be the effect of too good counting statistics (for instance, long scanning time per step), despite the profile problems are minor. A general advice is to judge quality from a plot of the fit [42]. Rietveld analysis of the XRD by means of the *FullProf Suite* and *PowderCell 2.4 Program* gives comparable results (for the data we needed in our analyses), but *PowderCell 2.4 Program* for the refining of the same diffraction pattern obtains higher discrepancy factors R_{wp} and goodness of fit χ^2. Results of Rietveld refinement of XRD spectra of samples obtained after 18 h milling time are presented in Fig. 2.

Structural parameters and discrepancy factors derived by Rietveld refinement of X-diffractograms of two $ZnFe_2O_4$ nanopowder samples are listed in Table 1. Sample denoted with "o-h" is obtained by mechanochemical activation of the hematite powder and zinc hydroxide powder for 18 h milling, and sample "h-h" by milling zinc- and ferric hydroxide for 18 h, also. Crystal lattice constant is calculated from diffractograms (values marked with the # in Table 1) and a_{calc} using relation (7). Average crystallite size, D, and strain, ε_{str}, are derived from Williams-Hall plot for approximately Lorentzian peak shape:

$$w_{hkl} \cdot \cos\theta_{hkl} = \frac{\lambda_{Co}}{D} + 4\varepsilon_{str} \cdot \sin\ \theta_{hkl} \qquad (8)$$

where λ_{Co} = 1.78897 Å is wavelength of used Co$K\alpha$ – X-ray source, w_{hkl} observed line broadening of diffraction line at θ_{hkl} Bragg angle. We get a linear fit to the data and extract the crystallite size from the y-intercept of the fit, and the strain from the slope of the fit. The calculated values of crystallite size are slightly higher than values obtained by Rietveld refinement. Calculated strain from Williams-Hall plot in "o-h" sample was $28(4) \times 10^{-4}$ and $25(2) \times 10^{-4}$ in "h-h" sample. From Rietveld refinement, by peak profile analysis (pseudo-Voigt function), it was obtained $21(1) \times 10^{-4}$ for "o-h" and $23(1) \times 10^{-4}$ for "h-h" sample. Considering that the refined data are more credible than calculation on the basis of the raw diffractogram, it can be concluded that in the sample obtained by milling of hydroxides a little greater micro strain occurs.

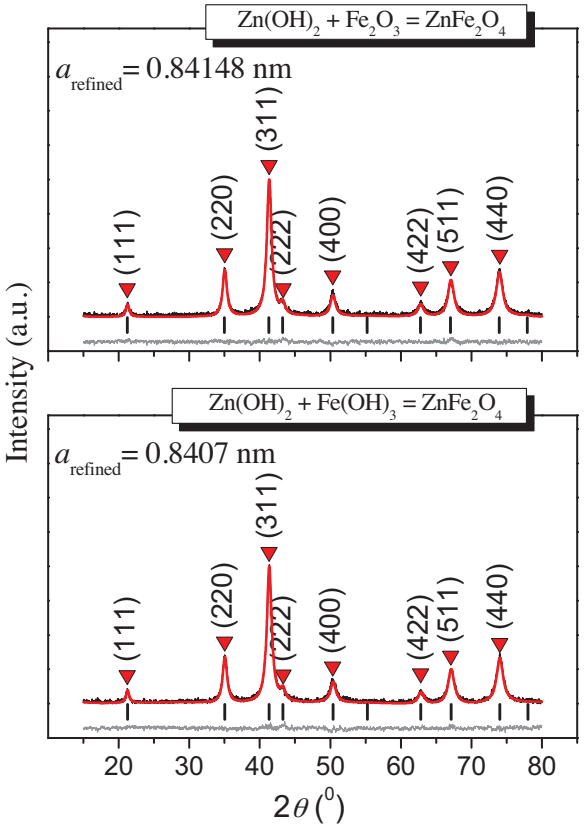

Fig. 2. Rietveld refinement of XRD spectra of the ferrite samples obtained after 18 h milling time.

$R_t(R_{tet})$ and $R_o(R_{oct})$ are cation–anion bond length in tetrahedral and octahedral sites, respectively, obtained by Rietveld refinement (and calculated by the relations (3) and (4)). Since we have chosen the refinement parameters that gave minimal differences between measured and calculated diffractogram patterns, we observed that all theoretical values calculated with δ obtained by Rietveld refinement and deviations from the refined values were in the limit of error of evaluating effective ionic radii, except for tetrahedral cation–anion bond length, especially for "o-h" sample. At the same time, value of lattice parameter of "o-h" sample obtained by Rietveld refinement was somewhat smaller than parameter calculated directly from diffractogram, using the relation $a = \lambda_{Co}(h^2 + k^2 + l^2)^{1/2}/(2\ \sin\theta_{hkl})$. In the new attempt of the refinement we firstly fixed lattice constant of "o-h" sample on a calculated value, higher than obtained by the previous refinement. It turned out that we get better agreement of the refined and theoretically calculated parameters at a cost of increasing the discrepancy factor R_{wp} for less than 1%.

Table 1
Structural parameters calculated from diffractograms (values denoted #), by Rietveld refinement and according to theoretical relations (3)–(7) (in brackets).

Sample	a (a_{calc}), (Å)	u	δ	D (Nm)	R_t ($R_{tet.}$) (Å)	R_o (R_{oct}) (Å)	R_{wp} (%)	R_{exp} (%)	χ^2
(1) "o-h"	8.4081# 8.4148 (8.41)	0.38214	0.3482	20.3# 16.8	1.9259 (1.93)	2.0454 (2.04)	12.04	2.34	17.2
(2) "h-h"	8.4019# 8.4038 (8.39)	0.38082	0.4000	17.6# 15.6	1.9097 (1.92)	2.0502 (2.03)	14.22	2.28	27.4

Table 2
Ratios of the intensities for selected diffraction lines.

Sample	$I_{(2\,2\,0)}/I_{(2\,2\,2)}$	$I_{(2\,2\,0)}/I_{(4\,4\,0)}$	$I_{(4\,0\,0)}/I_{(4\,4\,0)}$
"o-h"	3.74	0.72	0.38
"h-h"	3.60	0.70	0.39

Independently of this "intervention", structural parameters obtained by Rietveld refinement have already shown a complete consistency. The sample obtained by milling of zinc and ferric hydroxides for 18 h has a smaller crystal constant, smaller oxygen parameter and smaller dimension of tetrahedrons what means that larger zinc cations were moved into the octahedral sites in a greater number and that the degree of the conversion must be higher than in the case of the zinc ferrite sample denoted with "o-h".

It is known that in cubic spinel structure Bragg reflection (2 2 0) depends exclusively on the cations occupying tetrahedral sites and intensity of the (2 2 2) reflection depends on cations in the octahedral sites [43]. Ratios of the intensities for diffraction lines (2 2 0) and (2 2 2) indicate that the zinc ferrite sample with the highest $I_{(2\,2\,0)}/I_{(2\,2\,2)}$ has the lowest degree of the cation inversion [44]. With the increase of the degree of inversion it is expected that the intensity of Bragg reflection (2 2 0) decrease, (4 0 0) increase and (4 4 0) stays unchanged [45]. Therefore it is convenient to compare the relative intensity ratios for these selected reflections with the aim to assess the values of the cation inversion parameters, Table 2.

Based on calculated ratios of the diffraction lines intensity, Table 2, it has been confirmed that the sample "h-h" had a little higher cation inversion parameter.

Raman spectra of the nanopowder samples obtained after 4, 10 and 18 h milling of starting compounds are presented in Fig. 3. It is seen that even after 4 h of milling, a spinel structure is dominant. As it is usual, for the sake of simplicity, Raman modes are assigned as in normal cubic spinel ($A_{1g} + E_g + 3F_{2g}$), even though spectra of nanopowder samples with asymmetric – doubled, or even dissociated peaks are characteristic for inverse and partially inverse ("mixed") spinel structure. (Inverse spinel belongs to $P4_322$ tetragonal space group). Recorded spectra support the conclusions of XRD analysis that mechanochemical activating in the case of mixing hydroxides at the beginning (after 4 and 10 h) progresses more rapidly, nevertheless a single phase $ZnFe_2O_4$ in both cases of starting mixtures is achieved after the same milling time. After 10 h of milling in the Raman spectra of the sample obtained from zinc hydroxide + hematite starting mixture the mode of hematite, superponed on the *Eg* spinel mode, is still emphasized. Except that, the multiphonon features at about 1000 and 1300 cm^{-1} are extremely exaggerate. This is a symptom of very disturbed structure.

Deconvolution of spectra recorded on single phase samples (obtained after 18 h of milling) gives information about distribution of cations over tetrahedral and octahedral sublattices. The high frequency first order mode A_{1g} is due to symmetric stretching of oxygen atoms along Fe–O and Zn–O bonds in the tetrahedral coordination [46,47]. A much more pronounced mode at 634 cm^{-1} in the "o-h" sample (or 647 cm^{-1} in "h-h" sample) is related with stretching along Zn–O bonds in tetrahedrons. A smaller mode, at 717 cm^{-1} (718 cm^{-1}), corresponds to A_{1g} mode of magnetite (i.e. stretching along Fe–O bonds in tetrahedrons). It can be observed that this mode in "h-h" sample is more intensive than in "o-h" sample, what implies that more Fe^{3+} ions are in tetrahedral sites, i.e. that "h-h" sample has higher cation inversion parameter.

Modes $F_{2g}(2)$ and $F_{2g}(3)$ correspond to the vibrations of the octahedral group. These modes are not very strong and because of rather high level of noise we could not estimate the inversion

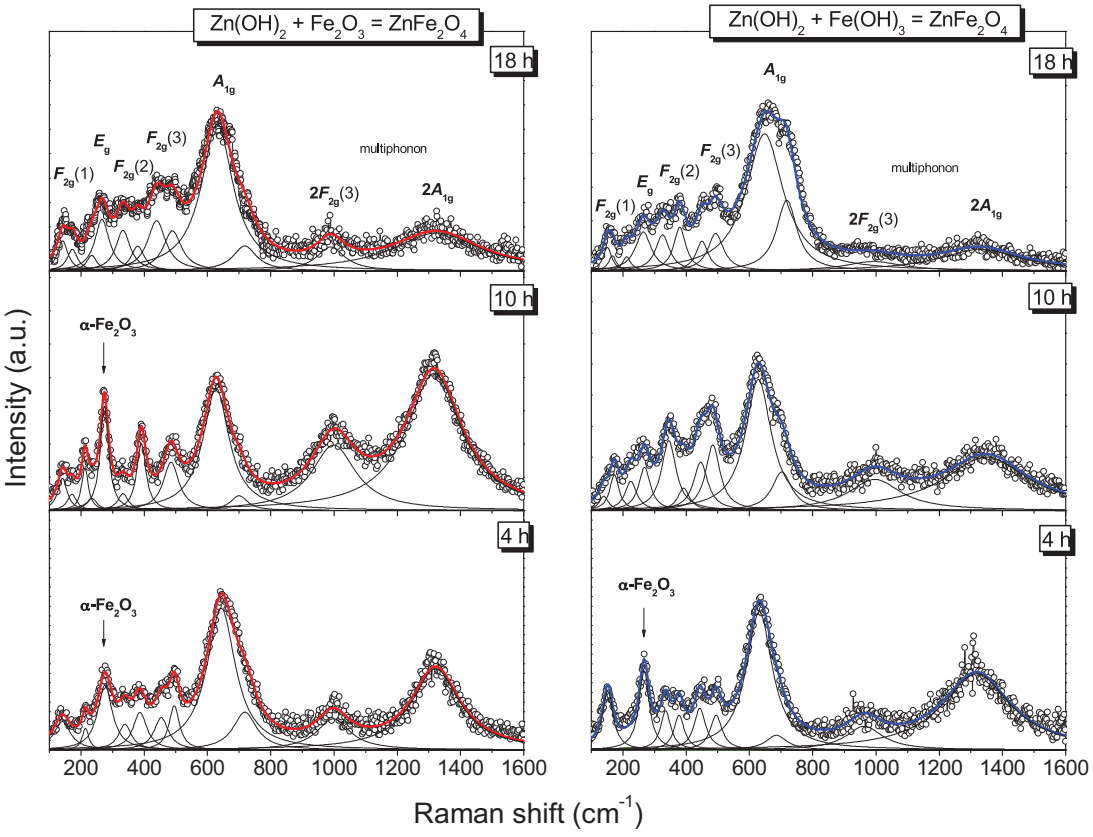

Fig. 3. Raman spectra of two starting powder mixtures after 4, 10 and 18 h of milling time.

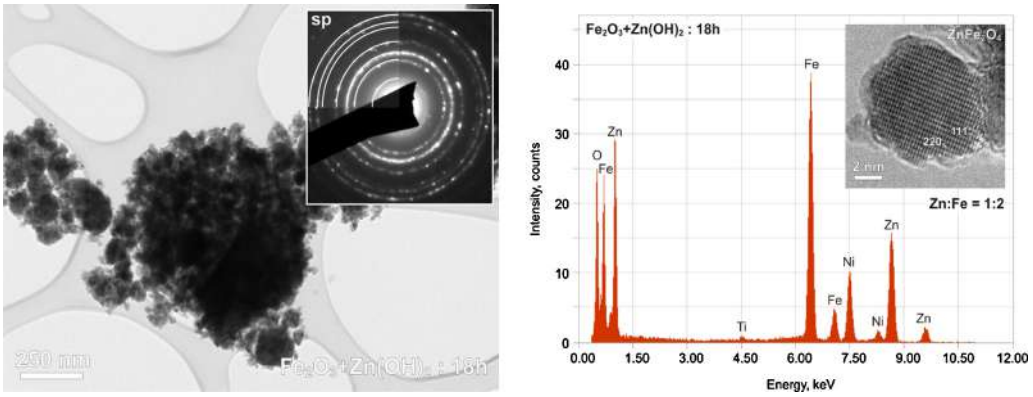

Fig. 4. TEM image with corresponding EDP (*inset* in the upper right corners) and EDS spectra of mechanochemically treated sample with starting compositions $Zn(OH)_2/\alpha$-Fe_2O_3 after processing for 18 h. Lines in the upper-right quadrant of EDP indicate *d*-values for $ZnFe_2O_4$ spinel phase that fully evolves after 18 h of milling time. The *inset* in EDS shows a HRTEM image of rounded $ZnFe_2O_4$ nanoparticle oriented close to the [11–0] zone axis with well resolved lattice fringes, characteristic for the spinel structure.

parameter from the ratio of their intensities. We only dare to say that octahedral sublattice seems to be less ordered than tetrahedral one.

Fig. 4 shows TEM image with corresponding EDPs of individual products and EDS after milling of 18 h of the mixture of $Zn(OH)_2/Fe_2O_3$ powders. Particle size distribution for obtained spinel $ZnFe_2O_4$ prepared from mixture of $Zn(OH)_2/Fe_2O_3$ powders is in range between 3 and 20 nm. The crystallites are rounded, show highly activated non-equilibrium surfaces and tend to agglomerate into larger clusters with diameters of several hundred of nanometers. In the initial stages of mechanochemical reaction particles are covered by few nanometers thick amorphous layers, which disappear after 18 h. After longer times of milling both processing routes produce pure spinel reflections belonging to $ZnFe_2O_4$ phase. Measurements of the diffraction rings confirmed that they correspond to the crystal planes of spinel structure. The composition of the products milled for 18 h was analyzed by EDS measurements on several individual particles, as well as larger crystal clusters. The analyses show a constant Zn:Fe atomic ratio of 1:2, which corresponds to the $ZnFe_2O_4$ phase. Fig. 4 shows a typical EDS spectrum, recorded on the $Zn(OH)_2/Fe_2O_3$ sample milled for 18 h. Ni-peak present in the EDS spectrum stems from the Ni-grid of the TEM specimen, whereas the minor peak of Ti probably originates from ilmenite impurities in the Fe_2O_3 precursor.

Ferrimagnetic couplings in systems with magnetic cations on tetrahedral – A and octahedral – B sites can involve antiferromagnetic exchange interactions between A–A, B–B and A–B cations as first proposed by Néel. According to Néel's assumptions that interaction between collinear A and B sublattice is dominant and that the other interactions can be neglected in the first approximation, net dipole moment per formula unit, M^{N}_{calc}, in Bohr magnetons μ_B ($\mu_B = 9.27 \times 10^{-24}\,J\,T^{-1}$) is obtained as follows:

$$M^{N}_{calc} = M_{[B]} - M_{(A)} = [(2-\delta)N_B + \delta N_A] - ((1-\delta)N_A + \delta N_B) \qquad (9)$$

where $N_{A,B}$ is a number of magnetons of corresponding magnetic ion. It was shown that this relation is valid only for naturally inverse spinels and for their nano counterparts bat only for a small deviations from a perfect inverse structure ($\delta = 1$). Deviation from this simple linear dependence for $\delta < 0.8$ is a consequence of fluctuations in the super exchange interaction due to the compositional and structural irregularities caused by cation redistribution and to the existence of noncollinear, so called Yafet-Kittel, spin structures [48].

In the case of normal spinel structure, as bulk zinc ferrite with nonmagnetic Zn^{2+} ions with $M_{A(Zn)} = 0\mu_B$ and $M_{B(Fe)} = 5\mu_B$, relation (8), from which follows: $M^{N}_{calc} = 10(1-\delta)$, is obviously quite incompatible with experimental facts for small degrees of the inversion. (According to this relation, a minimal δ would cause a maximal magnetization $\approx 10\ \mu_B$.)

Judge to some experimental data, in zinc ferrite, except a long-range order, could be very significant a short-range antiferromagnetic order. Schiessel et al. [49] at 100 K by neutron diffraction, muon-spin rotation/relaxation and ^{57}Fe and ^{67}Zn Mössbauer spectroscopy confirmed developing and existence of numerous small regions with short-range antiferromagnetic order. Such regions coexists with long-range antiferromagnetic order even below $T_N = 10.5$ K. This result refers to perfectly normal zinc ferrite and could be an intrinsic property of $ZnFe_2O_4$ in the opinion of authors.

In the partially inverse $ZnFe_2O_4$, the Fe^{3+} situated on A-sites forms a cluster with its $(12 - x)$ next nearest neighbors (*nnn*) at B-sites through antiferromagnetic coupling. A number of nnn Fe^{3+} depends on the cation distribution (x is a number of nonmagnetic Zn^{2+} ions among nn neighbors on B-sites). Thereby, Fe^{3+} ions situated on A sites are mutually collinear as have been shown by Mössbauer spectra in the presence of an applied magnetic field, while a number of Fe^{3+} ions situated on B sites are noncollinear (canted) [50]. In Ref. [51] the LEIS (low energy ion scattering) results together with the Mössbauer analysis and the magnetic measurements at room temperature lead to the conclusion that the magnetization exhibited by ultra-fine particles of zinc ferrite is certainly due to partial inversion of cations, but is followed by short range ordering, also. Soliman et al. [52] have used a local density approximation in their ab initio calculation to examine the electronic structure and magnetic properties of different allowed symmetries and cation distributions in the $ZnFe_2O_4$ spinel. It is confirmed that $ZnFe_2O_4$ cannot be treated as a correlated system only and that deformation of the octahedral site have to be taken into consideration together with the degree of inversion.

Stewart et al. [33] estimated the variation of saturation magnetization, M_{sat} in the function of the inversion parameter assuming a random distribution of super exchange interactions, as proposed by Gilleo [53]. The degree of cation inversion obtained by EXAFS for different stoichiometric $ZnFe_2O_4$ samples was in good agreement with proposed model. In Ref. [54] was examined dependence of magnetization on the degree of cation inversion, also. The cation inversion was determined by neutron diffraction.

Based on the results presented in references [33] and [54] it is obvious that dependence M_{sat} on the degree of the inversion δ for $\delta < 0.4$ is almost linear. The contribution of octahedral sublattice in magnetization is negligible, i.e. antiferromagnetic interaction between (nearly) equivalent *B*1 and *B*2-sites in octahedral

sublattice and, especially, the presence of short-range antiferromagnetic regions makes $M_{[B]} \approx 0$. At the other side, a number of magnetic ions in A sublattice for small δ is diluted and A–B interaction must be weak and comparable with B–B interaction. With increasing a number of Fe^{3+} in tetrahedral positions exchange interactions in $ZnFe_2O_4$ lattice are changing. The spins from A sites hold all neighbor spins from B sites almost antiparallel (a stronger A–B interaction disturbs weaker antiferromagnetic interaction between $B1$ and $B2$ sub-sublattices). Except that, with increasing a number of Fe^{3+} in tetrahedral positions, in the octahedral sublattice, due to reduction of Fe^{3+} ions, stay corrupted or modified super exchange "connections". Within the B-sublattice, $B1$ and $B2$ sub-sublattices are no longer equivalent and magnetic moment $M_{[B]}$ becomes nonzero. This leads to a reduction of a net magnetization. Therefore relation (9) takes on meaning in nano $ZnFe_2O_4$ with increasing δ.

The interplay between competing exchange interactions for ions on different sublattices allows for new, noncollinear magnetization of sublattices. Yafet-Kittel model [48] includes Néel model as special case and can be applied in nano systems for any value of inversion coefficient. We can suppose, on the basis of references listed above, that the main difference arise in octahedral B-sublattices. It is supposed that magnetic moments of $B1$ and $B2$ sublattices have the same intensity, but they are not collinear. Their resultant is antiparallel to the saturation magnetization of the spins on the A site. Mössbauer measurements confirm that the angle between $A1$ and $A2$ sub-sublattices is 0°. Applying Néel's two-sublattice model of ferrimagnetism with included Yafet-Kittel effect of spin canting, the calculated magnetic moment, n_{calc}, per unit formula, in simplified form is expressed as:

$$n_{calc.} = M_{[B]}\cos\psi_{YK} - M_{(A)} \quad (10)$$

where $M_{(A)}$ and $M_{[B]}$ are the A and B sublattice magnetic moments ($M_{(A1)} = M_{(A2)}$, $M_{[B1]} = M_{[B2]}$) and ψ_{YK} is Yafet-Kittel angle ($2\psi_{YK}$ is angle between directions of $M_{[B1]}$ and $M_{[B2]}$ and $M_{[B]}\cdot\cos\psi_{YK}$ is a projection of octahedral sub-sublattice magnetic moment on the direction of tetrahedral magnetic moment).

Important consequence of Yafet-Kittel concept is that the canting of one sublattice is a result of dilution of the other sublattice. Gilleo assumed that Fe^{3+} ions with even one nonmagnetic nearest neighbor would not contribute to the spontaneous magnetization. The net magnetic moment per molecule, according to this model is:

$$n(k_A, k_B) = n_B(k_A, k_B) - n_A(k_A, k_B) \quad (11)$$

where $n_B = n_B{}^0(1 - k_B)[1 - E_B(k_A)]$, $n_A = n_A{}^0(1 - k_A)[1 - E_A(k_B)]$, $E_B(k_A) = 6k_A{}^5 - 5k_A{}^6$, $E_A(k_B) = 12k_B{}^{11} - 11k_B{}^{12}$, $n_B{}^0$ and $n_A{}^0$ are undiluted magnetons per molecule, but left as variables because of usual varying of ionic spin values in spinel system (for Fe^{3+} is average spin, $\langle S\rangle$ <5/2, i.e. $n_A{}^0 < 5\ \mu_B$ and $n_B{}^0 < 2 \times 5\ \mu_B$). Parameters $k_A = 1 - \delta$ and $k_B = \delta/2$ are degrees of nonmagnetic ions on corresponding sites. The values $E_{A,B}$ are sublattice canting probabilities from opposite sublattice dilution as determined from random probability theory.

It remained to check weather the saturation magnetizations for the two samples support the observed differences in the cation inversion coefficients. It remained to check weather the saturation magnetizations of our samples support the observed differences in the cation inversion coefficients. We were primarily interested in the value of magnetization at low temperatures which is directly related to the degree of inversion. At the same time, magnetic measurements allow us to monitor the process of the synthesis and the characteristics of the obtained single phase nano powder $ZnFe_2O_4$.

Hysteresis loops of ferromagnetic $ZnFe_2O_4$ powders obtained after different milling times are shown in Fig. 5 for low values of magnetic field. These measurements were done at 4.5, 30 and 300 K.

In Fig. 6a and b are shown magnetizations for high magnetic fields - only for single phase samples obtained after 18 h of milling time from different starting compounds.

It can be observed that magnetization does not saturate even at fields of 80 kOe. The observed resultant magnetic moment is due also to spin disorder at the surface (owing to broken exchange bonds and broken symmetry) and may be explained by means of core–shell model. Ferrimagnetically aligned core spins are coupled by exchange interactions and surrounded by a magnetically disordered shell [55]. After all the core moments are completely aligned in a magnetic field, further increase in the magnetization is affected only by uncompensated spins in the shell. In this case "saturation magnetization" is value obtained from the graph of $M = f(1/H)$ when $1/H = 0$.

As it can be seen in Figs. 5 and 6, saturation magnetization increases with milling time in both starting mixtures. In the case of mixture (1) magnetic remanence after 10 h of milling time passes through a maximum value 6.7 emu g^{-1}, and then falls to 4.5 emu g^{-1} after 18 h. In the case of mixture (2), the remanence uniformly increases from 4.3 emu g^{-1} to 5.5 emu g^{-1} after 18 h of milling. Coercive field in mixture (1) after 10 h milling has a small increase and after 18 h reaches 103 Oe. In the mixture (2) coercive field decreases uniformly from 118 Oe and attains value about 87 Oe for single phase $ZnFe_2O_4$ obtained after 18 h milling time. The deviations of remanence and coercivity values in mixture (1) after 10 h milling are probably connected with existence of hematite registered by XRD, also. Magnetic measurements confirmed that starting from mixture (2) it is obtained a single phase zinc ferrite with the smaller nano particles and that the process of mechano-chemical synthesis leads to single phase zinc ferrite more uniformly.

High saturation magnetizations and small coercive fields at 300 K suggest a superparamagnetic-like behavior, but in all samples ratio M_{rem}/M_{sat} is of order10^{-1}, and these samples have to be considered as mixtures of superparamagnetic grains, single domain and multidomain grains [56,57]. It is more obvious from magnetizations on low temperatures (4.5 K), Figs. 5 and 6, where the great coercive fields, about 330 Oe, and remanences >20 emu g^{-1} show that the contribution of larger particles (when thermal energy is not enough to overcome the crystalline anisotropy energy), is not negligible. (To remind: anisotropy energy for a given material is dependent on crystallite size, but beyond the characteristic threshold size particles become superparamagnetic at all temperatures.)

Magnetization data taken at $T = 4.5$ K show that the hysteresis loop remains open up to about 6 kOe, demonstrating that magnetization is irreversible below this field value. At 300 K hysteresis is open up to 1.5 kOe in both single phase samples.

It was shown that saturation magnetization at 300 K for "h-h" sample is 65.1 emu g^{-1} and for "o-h" sample 54.2 emu g^{-1} (Fig. 6). At 4.5 K saturation magnetization is 91.50 emu g^{-1} for "h-h" and 78.26 emu g^{-1} g for "o-h" sample. In the paper of Yao at al. [58] have been listed previously reported values of saturation magnetization M_{sat} for zinc ferrite nanoparticles prepared by various methods (16 papers). The broad range of magnetization $M_{sat} \sim$ 12–88 emu g^{-1} shows that M_{sat} strongly depends on the synthesis method and thermal treatment after the process of synthesis. The values of magnetization obtained in our work at 4.5 K are probably the highest referred until now.

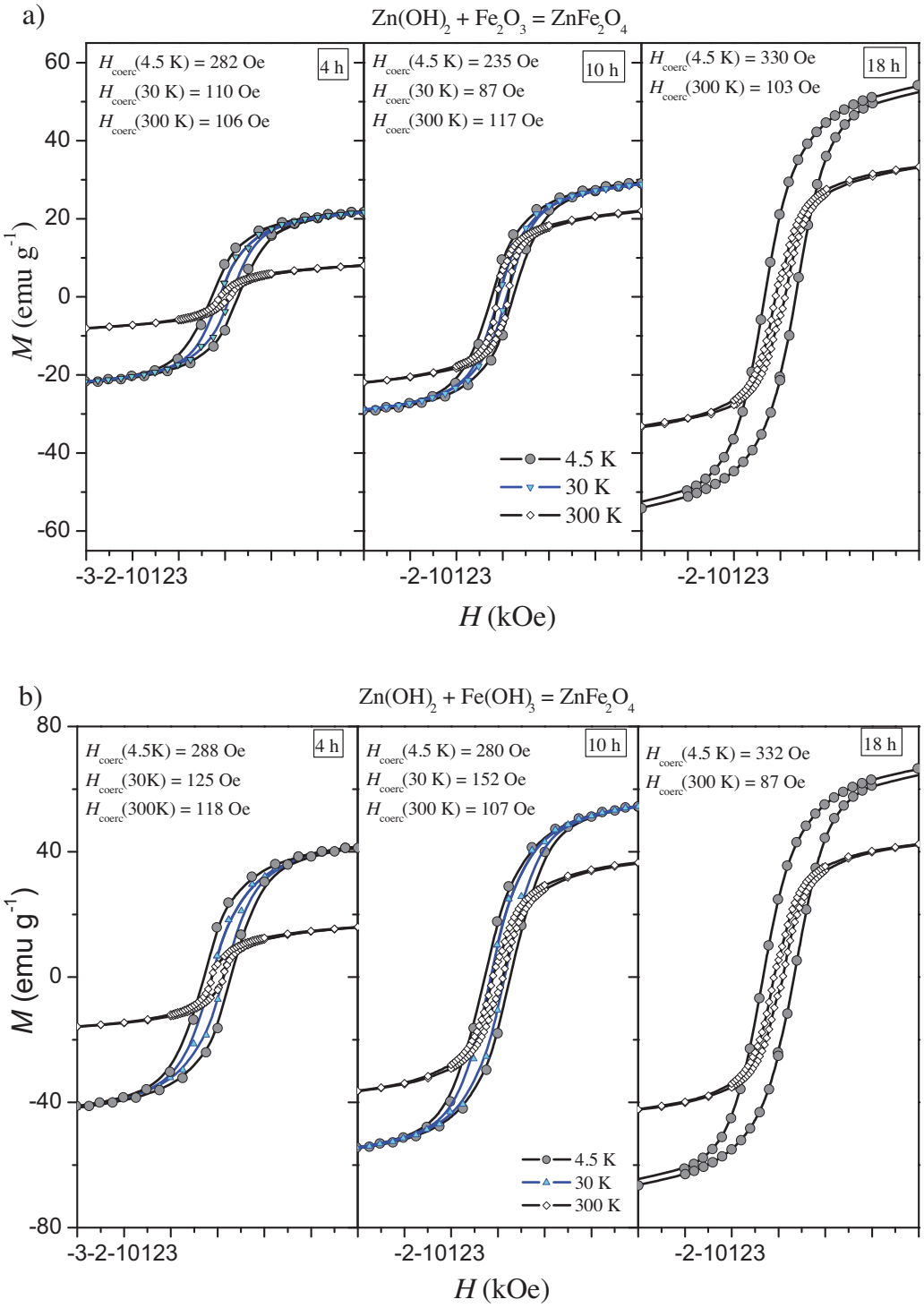

Fig. 5. Hysteresis loops of the samples obtained after 4, 10 and 18 h milling time of (a) zinc hydroxide and hematite and (b) zinc hydroxide and ferric hydroxide powders, measured at 4.5, 30 and 300 K in low magnetic fields.

The observed magneton number (n_{obs}) is proportional to magnetization, M_{sat}:

$$n_{obs} = M(ZnFe_2O_4) \cdot \frac{M_{sat}}{\mu_B N_A} = M(ZnFe_2O_4) \cdot \frac{M_{sat}}{5585} \quad (12)$$

where $M(ZnFe_2O_4)$ is molecular weight, μ_B Bohr magneton and N_A Avogadro's number. Magnetization calculated by relation (8), observed saturation magnetization, corresponding number of Bohr magnetons and Yafet-Kittel angle at 4.5 K (when thermal disorder of sublattices is minimal) are given in Table 3.

The reduction of the canting angle, compared to the bulk angle 90° in $ZnFe_2O_4$, is an effective contribution of nanosize dimension of particles. Thus it is evident that spin canting is also the cause for the deviation between observed and theoretical values of magnetic moment in the nano ferrite. The reduction of ψ_{YK} with increasing of the cation inversion coefficient shows an enhancement of the B-sublattice magnetization contribution in the total magnetization.

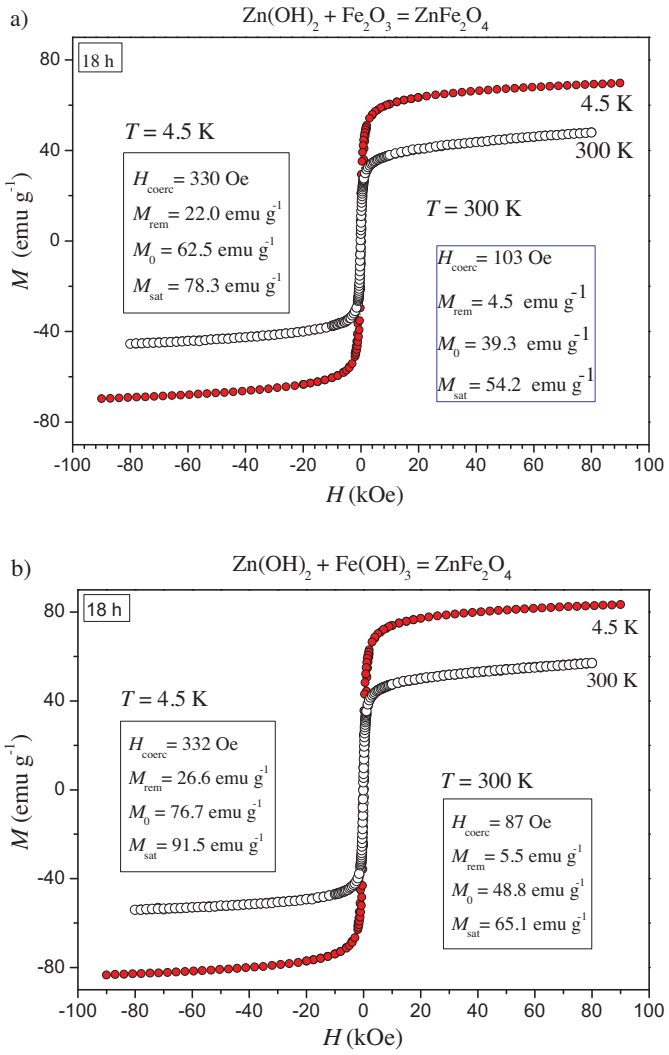

Fig. 6. Magnetizations in high magnetic fields for single phase ferrite samples obtained after 18 h of milling of (a) zinc hydroxide and hematite and (b) zinc hydroxide and ferric hydroxide powders.

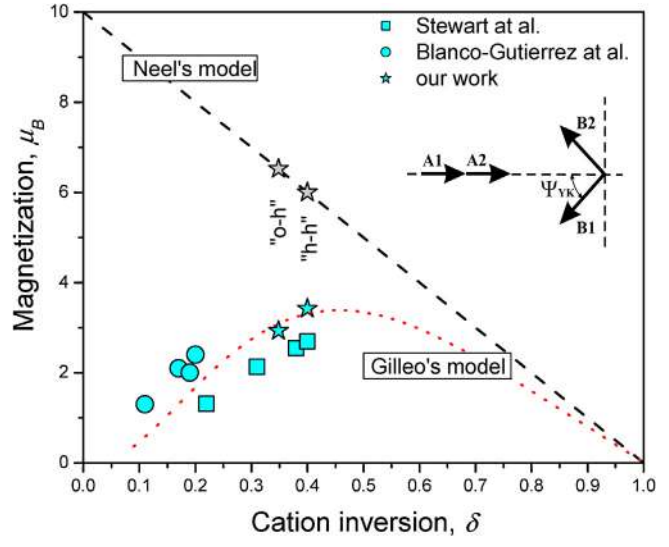

Fig. 7. Dependence of magnetization, M_{sat}, on the degree of the inversion. Squares present data taken from Ref. [15] and circles are data from Ref. [32] obtained at 5 K; stars are values obtained in this paper. The curved line presents Gilleo's model, with $n_A^0 = 4\ \mu_B$; straight line is Néel's model. *Inset*: configuration of sublattices in Yafet-Kittel model.

Table 3
Magnetization and Yafet-Kittel angle at 4.5 K.

Sample	M^N_{calc} [μ_B]	M_{sat} 300 K [emu g^{-1}] (n_{obs} [μ_B])	M_{sat} 4.5 K [emu g^{-1}] (n_{obs} [μ_B])	ψ_{YK} 4.5 K
(1)"o-h"	6.52	54.2 (2.03)	78.3 (2.93)	55.49°
(2)"h-h"	6.00	65.1 (2.44)	91.5 (3.42)	47.35°

Saturation magnetizations from references [33] and [54] as a function of the degree of inversion are shown in Fig. 7 together with results obtained in our work. It is obvious that our values of the degree of inversion obtained by Rietveld refinement are in very good agreement with results of other authors. Gilleo's graph with $n_A^0 = 4\mu_B$ (and $n_B^0 = 2 \times 4\mu_B$) is a good fit for all measured magnetizations.

4. Conclusions

Spinel ferrite nanoparticles have been extensively investigated especially owing to their magnetic properties that are very important for a number of their applications. In this paper were investigated synthesis of nano zinc ferrite by mechanochemical method and influence of starting precursors on the structural characteristics (quality of nanocrystallites, their size and cation inversion) and on the achieved magnetizations. Examination was performed by XRD, Raman, TEM and magnetization measurements. It is confirmed that Raman spectroscopy is a good and quick method for monitoring a synthesis process and for determining existence of cation inversion in zinc ferrite samples. All used methods show that nanopowder samples obtained by mechanochemical activation, starting from powders of zinc and ferric hydroxide, have more uniform synthesis flow, smaller grains and a slightly greater inversion degree ($\delta = 0.40$). This resulting in higher values of saturation magnetization (91.5 emu g^{-1} at $T = 4.5$ K), among the highest registered so far. At the same time it was confirmed that the combination of XRD analysis and magnetization measurements gives a reliable way for ordering of a degree of cation inversion, particularly in nano zinc ferrite.

Acknowledgments

This research was financially supported by the Ministry of Education, Science and Technological Development of the Republic of Serbia through Projects No. III 45003 and research project under the agreement of scientific collaboration between Polish Academy of Science and Institute of Physics Belgrade.

References

[1] W.H. Bragg, Nature 95 (1915) 561.
[2] W.H. Bragg, Philos. Mag. 30 (1915) 305–315.
[3] N. Shoji, Proc. Math. Phys. Soc. Tokyo 8 (1915) 199–209.
[4] R. Valenzuela, Magnetic Ceramics, Cambridge University Press, Cambridge, 2005.
[5] H.C. O'Neill, A. Navrotsky, Am. Miner. 68 (1983) 181–194.
[6] M. Atif, S.K. Hasanain, M. Nadeem, Solid State Commun. 138 (2006) 416–421.
[7] V. Šepelák, L. Wilde, U. Steinike, K.D. Becker, Mater. Sci. Eng. A 375–377 (2004) 865–868.
[8] P.M. Botta, E.F. Aglietti, J.M. Porto López, Mater. Res. Bull. 41 (2006) 714–723.
[9] G.F. Goya, H.R. Rechenberg, J. Magn. Magn. Mater. 203 (1999) 141–142.
[10] R. Klimkiewicz, J. Wolska, A. Przepiera, K. Przepiera, M. Jabłoński, S. Lenart, Mater. Res. Bull. 44 (2009) 15–20.
[11] C.A. Ladole, Int. J. Chem. Sci. 10 (2012) 1230–1234.
[12] M. Gharagozlou, J. Alloy. Compd. 486 (2009) 660–665.
[13] L. Nalbandian, A.V. Delimitis, T. Zaspalis, E.A. Deliyanni, D.N. Bakoyannakis, E.N. Peleka, Micropor. Mesopor. Mater. 114 (2008) 465–473.
[14] G.-Y. Zhang, Y.-Q. Sun, D.-Z. Gao, Y.-Y. Xu, Mater. Res. Bull. 45 (2010) 755–760.
[15] D.O. Yener, H. Giesche, J. Am. Ceram. Soc. 84 (2001) 1987–1995.
[16] S. Gubbala, R.D.K. Misra, Mater. Sci. Technol. 22 (2006) 845–851.
[17] H. Nathani, R.D.K. Misra, Mater. Sci. Eng. B 113 (2004) 228–235.
[18] H. Nathani, S. Gubbala, R.D.K. Misra, Mater. Sci. Eng. B 121 (2005) 126–136.
[19] H. Nathani, S. Gubbala, R.D.K. Misra, Mater. Sci. Eng. B 111 (2004) 95–100.

[20] S. Rana, A. Gallo, R.S. Srivastava, R.D.K. Misra, Acta Biomater. 3 (2007) 233–242.
[21] A. Kale, S.R. Gubbala, D.K. Misra, J. Magn. Magn. Mater. 277 (2004) 350–358.
[22] J.P. Hochepied, J.F. Bonville, M.P. Pileni, J. Phys. Chem. 104 (2000) 905–912.
[23] E. Avvakumov, M. Senna, N. Kosova, Soft Mechanochemical Synthesis: A Basis for New Chemical Technologies, Kluwer Academic Publishers, Boston, 2001.
[24] R.H. Kodama, J. Magn. Magn. Mater. 200 (2000) 359–372.
[25] H. Kavas, A. Baykal, M.S. Toprak, Y. Köseoğlu, M. Sertkol, B. Aktas, J. Alloy. Compd. 479 (2009) 49–55.
[26] J.A.C. de Paiva, M.P.F. Graça, J. Monteiro, M.A. Macedo, M.A. Valente, J. Alloy. Compd. 485 (2009) 637–641.
[27] A. Alarifi, N.M. Deraz, S. Shaban, J. Alloy. Compd. 486 (2009) 501–506.
[28] A.M.M. Farea, S. Kumara, K.M. Batoo, A.Y.C.G. Lee, Alimuddin, J. Alloy. Compd. 469 (2009) 451–457.
[29] J.H. Shim, S. Lee, J.H. Park, S.-J. Han, Y.H. Jeong, Y.W. Cho, Phys. Rev. B 73 (2006) 064404.
[30] M. Hofmann, S.J. Campbell, H. Ehrhardt, R.J. Feyerherm, J. Mater. Sci. 39 (2004) 5057–5065.
[31] Z.J. Zhang, Z.L. Wang, B.C. Chakoumakos, J.S. Yin, J. Am. Chem. Soc. 120 (1998) 1800–1804.
[32] V. Blanco-Gutiérrez, F. Jiménez-Villacorta, P. Bonville, J. María, R. Torralvo-Fernández, Sáez-Puche, J. Phys. Chem. C 115 (2011) 1627–1634.
[33] S.J. Stewart, I.A. Al-Omari, F.R. Sives, H.M. Widatallah, J. Alloy. Compd. 495 (2010) 506–508.
[34] J. Zhang, R.D.K. Misra, Acta Biomater. 3 (2007) 838–850.
[35] A. Lascialfari, C. Sangregorio, Chem. Today 29 (2) (2011) 20–23.
[36] S. Rana, J. Rawat, R.D.K. Misra, Acta Biomater. 1 (2005) 691–703.
[37] J. Rawat, S. Rana, R. Srivastava, R.D.K. Misra, Mater. Sci. Eng. C 27 (2007) 540–545.
[38] Z. Lazarević, A. Milutinović, M. Romčević, N. Romčević, Č. Jovalekić, D. Sekulić, M. Slankamenac, ISAF ECAPD PFM 2012, Aveiro, Portugal, in: the USBs electronic conference Proceedings, No 07 (2012) and IEEE Conference Publications, 2012, http://dx.doi.org/10.1109/ISAF.2012.6297730.
[39] T. Roisnel, J. Rodriguez-Carvajal, http://www.ill.eu/sites/fullprof, version: September 2012.
[40] W. Kraus, G. Nolze, PowderCell for Windows, version 2.4, Federal Institute for Materials Research and Testing, Berlin, Germany, 2000.
[41] Joint Committee on Powder Diffraction Standards (JCPDS), Powder Diffraction File (PDF), International Centre for Diffraction Data, Newtown Square, PA, 2004.
[42] B.H. Toby, Powder Diffr. 21 (2006) 67–70.
[43] V. Šepelak, K. Tkáčova, Acta Montan. Slovaca 2 (1997) 266–272.
[44] M. Mozaffari, M. Eghbali Arani, J. Amighian, J. Magn. Magn. Mater. 322 (2010) 3240–3244.
[45] K. Tkáčova, V. Šepelak, N. Števulová, J. Solid State Chem. 123 (1996) 100–108.
[46] Z. Wang, D. Schiferl, Y. Zhao, H.St.C. O'Neill, J. Phys. Chem. Solids 64 (2003) 2517–2523.
[47] G. Dixit, J.P. Singh, R.C. Srivastava, H.M. Agrawal, Nucl. Instrum. Methods B 269 (2011) 133–139.
[48] Y. Yafet, C. Kittel, Phys. Rev. 87 (1952) 290–294.
[49] W. Schiessel, W. Potzel, H. Karzel, M. Steiner, G.N. Kalvius, A. Martin, N.K. Karause, I. Halevy, J. Gal, W. Schafer, G. Will, M. Hillberg, R. Wappling, Phys. Rev. B 53 (1996) 9143–9152.
[50] E.J. Choi, Y. Ahn, K.-C. Song, J. Magn. Magn. Mater. 301 (2006) 171–174.
[51] M.R. Anantharaman, S. Jagatheesan, K.A. Malini, S. Sindhu, A. Narayanasamy, C.N. Chinnasamy, J.P. Jacobs, S. Reijne, K. Seshan, R.H.H. Smits, H.H. Brongersma, J. Magn. Magn. Mater. 189 (1998) 83–88.
[52] S. Soliman, A. Elfalaky, G.H. Fecher, C. Felser, Phys. Rev. B 83 (2011) 0852051–852056.
[53] M.A. Gilleo, J. Phys. Chem. Solids 13 (1960) 33–36.
[54] V. Blanco-Gutierrez, E. Climent-Pascual, M.J. Torralvo-Fernandez, R. Saez-Puche, M.T. Fernandez-Diaz, J. Solid State Chem. 184 (2011) 1608–1613.
[55] R.H. Kodama, A.E. Berkowitz, E.J. McNiff Jr., S. Foner, Phys. Rev. Lett. 77 (1996) 394–397.
[56] R. Day, M.D. Fuller, V.A. Schmidt, Phys. Earth Planet. Inter. 13 (1977) 260–267.
[57] L. Tauxe, T.A.T. Mullender, T. Pick, J. Geophys. Res. 101 (1996) 571–584.
[58] C. Yao, Q. Zeng, G.F. Goya, T. Torres, J. Liu, H. Wu, M. Ge, Y. Zeng, Y. Wang, J.Z. Jiang, J. Phys. Chem. C 111 (2007) 12274–12278.

J Mater Sci: Mater Electron (2015) 26:1291–1303
DOI 10.1007/s10854-014-2491-0

Temperature-dependent complex impedance, electrical conductivity and dielectric studies of MFe$_2$O$_4$ (M = Mn, Ni, Zn) ferrites prepared by sintering of mechanochemical synthesized nanopowders

Dalibor L. Sekulic · Zorica Z. Lazarevic · Miljko V. Sataric · Cedomir D. Jovalekic · Nebojsa Z. Romcevic

Received: 17 September 2014 / Accepted: 6 November 2014 / Published online: 23 January 2015

Abstract Effect of temperature on electrical and dielectric properties of MFe$_2$O$_4$ (M = Mn, Ni, Zn) ferrites has been investigated in a wide frequency range 100 Hz to 1 MHz. Ferrite ceramics under study were successfully fabricated by a conventional sintering of nanosized powders (1100 °C/2 h) synthesized by soft mechanochemical processing. The structural studies have been carried out using the transmission electron microscopy, X-ray diffraction and scanning electron microscopy. Direct current (DC) resistivity of all samples decreases with increasing temperature, while drift mobility increases, exhibiting the typical semiconductor-like behaviour. Activation energy is calculated by using Arrhenius type resistivity plots. The analysis of experimental data indicates that alternating current (AC) conductivity is mainly due to the hopping mechanism, which is discussed in terms of Maxwell–Wagner two-layer model. The dielectric behaviour is explained by using the mechanism of polarization process, which is correlated to that of electron exchange interaction. Ni-ferrite possesses the lowest value of conductivity of 10^{-7} $(\Omega\text{cm})^{-1}$, whereas Zn-ferrite has the highest dielectric constant value of 2,641 at frequency of 1 kHz and room temperature. The complex impedance spectroscopy was used to study the effect of microstructures on the electrical properties of sintered ferrites using equivalent circuits. It was found that the electrical resistivity is predominantly controlled by the grain boundaries.

D. L. Sekulic (✉) · M. V. Sataric
Faculty of Technical Sciences, University of Novi Sad, Trg Dositeja Obradovića 6, Novi Sad, Serbia
e-mail: dalsek@uns.ac.rs

Z. Z. Lazarevic · N. Z. Romcevic
Institute of Physics, University of Belgrade, P.O. Box 68, Pregrevica 118, Zemun, Belgrade, Serbia

C. D. Jovalekic
The Institute for Multidisciplinary Research, University of Belgrade, Kneza Višeslava 1, Belgrade, Serbia

1 Introduction

Since their discovery, the design and synthesis of ferrites have been the focus of intense fundamental and applied research with special emphasis on improvement of their physical properties. Ferrite materials are widely used in many electronic devices and various electromagnetic applications because of their multifunctional features: rich electrical and magnetic properties, high chemical and thermal stability, mechanical hardness, reasonable cost, easy preparation etc. [1]. They possess high resistivity up to 10^9 Ωcm at room temperature which contributes to very low losses at high frequency needed for microwave devices, transformer core and inductors [2].

The spinel ferrites can be represented by general formula MFe$_2$O$_4$, where M (M = Mn, Ni, Zn etc.) is a divalent metal cation. The distribution of divalent M^{2+} and trivalent Fe^{3+} cations between the tetrahedral (A) and octahedral [B] sites can be expressed with formula $(M_\delta Fe_{1-\delta})[M_{1-\delta}Fe_{1+\delta}]O_4$, where δ is the so-called inversion degree defined as the fraction of the (A) sites occupied by Fe^{3+} cations [3]. The cation arrangement can vary between two extreme cases. One is the normal spinel structure with $\delta = 0$, where all the divalent M^{2+} cations occupy (A) sites and all the trivalent Fe^{3+} cations occupy [B] sites. The other one is the inverse spinel with $\delta = 1$, where all M^{2+} ions occupy [B] sites and Fe^{3+} cations are equally distributed between (A) and [B] sites. In a mixed spinel structure with δ between 1 and 0, both the

tetrahedral and octahedral sublattice sites are occupied by divalent and trivalent ions [4]. It is well known that nickel and zinc have very strong preference for the tetrahedral (A) and octahedral [B] sites, respectively, making Ni-ferrite a model inverse ferrite and Zn-ferrite a model normal ferrite [5]. However, nanosized Ni- and Zn-ferrite are known to exist as mixed spinel structures [6]. On the other hand, earlier studies have shown that Mn-ferrite is a partial inverse spinel ferrite, where in the bulk form it was about 20 % inverse, but a higher inversion up to 60 % was reported in nanosized manganese ferrite [7]. Also, the introduction of different metal cations M^{2+} into the spinel structure of $M\mathrm{Fe_2O_4}$ ferrites leads to significant change in their electrical properties [8].

The electrical properties are of great importance for ferrites, not only from the application point of view, but also from the fundamental point of view. It is well established that these properties of ferrites are strongly dependent on the method of preparation, sintering temperature, chemical composition and particle size [9]. Hence, it is important to investigate electrical properties at different frequencies, temperatures and chemical compositions which may provide valuable information about the kind and amount of additives required to obtain high quality ferrites for various applications in electronics. As a result, the study of these properties provides valuable information regarding the behavior of localized charge carriers under an alternating field. It gives the evidences of their mobility, the mechanism of conduction, and enables greater understanding of the mechanism of dielectric polarization of ferrites [10]. It is well known that electrical conductivity in spinel ferrites is due to the transfer of charge carriers (electrons or holes) between cations occupying the octahedral sites. The transfer of charge carrier is possible when a metal ion possesses more than one valence state [3].

Attempts towards improving the technological performance of ferrites and requirements for their different electrical properties have prompted the development of several novel methods of synthesis, such as co-precipitation [5, 11], sol–gel method [12, 13], chemical synthesis [14], reverse micelle technique [15] and other techniques that have been proposed in recent years. Most of these methods have achieved particles of the required sizes and shapes, but they are difficult to employ on a large scale because of their expensive and complicated procedures, high reaction temperatures, long reaction times, toxic reagents and by-products, and their potential harm to the environment. Novel approach to mechanochemical synthesis, based on reactions of solid acids, based hydrated compounds, crystal hydrates, basic and acidic salts, has been called soft mechanochemical synthesis [16]. The peculiarity of soft mechanochemical reactions consists in the high reactivity of surface functional groups, notably, OH groups. Unlike the other methods mentioned above, this technique is a low-cost, novel and effective method of producing a wide range of nanopowders. The major advantages of soft mechanochemical synthesis lie in the formation of reaction products at room or low temperatures and the refinement of produced powders to a nanometer size range. This is reflected primarily in the simplicity of the procedure and equipment used. Also, this method is inexpensive in comparison with other method of synthesis.

The objective of this comparative study is to investigate how introduction of different metal cations M^{2+} (M = Mn, Ni, Zn) into the spinel structure of $M\mathrm{Fe_2O_4}$ leads to significant change in electrical and dielectric properties of the ferrites obtained by the same method. All three samples were prepared by a conventional sintering of nanosized powders synthesized by soft mechanochemical processing that is environmentally friendly, does not require expensive starting materials or extremely high temperature. In order to provide valuable information for the potential electronic application of obtained ferrites, we have carried out a detailed study about electrical resistivity/conductivity, complex impedance and dielectric constant of $M\mathrm{Fe_2O_4}$ (M = Mn, Ni, Zn) over a wide range of frequencies as a function of temperature.

2 Experimental procedures

2.1 Synthesis

The $M\mathrm{Fe_2O_4}$ (M = Mn, Ni, Zn) ferrites under study were successfully fabricated from different mixtures of starting nanosize powders prepared by soft mechanochemical route. Starting compounds used for synthesizing of Mn-, Ni- and Zn-ferrite nanopowders were respectively:

- manganese(II)-hydroxide ($\mathrm{Mn(OH)_2}$, Merck 95 % purity) and hematite (α-$\mathrm{Fe_2O_3}$, Merck 99 % purity);
- nickel(II)-hydroxide ($\mathrm{Ni(OH)_2}$, Merck 95 % purity) and hematite (α-$\mathrm{Fe_2O_3}$, Merck 99 % purity) and
- zinc(II)-hydroxide ($\mathrm{Zn(OH)_2}$, Merck 95 % purity) and hematite (α-$\mathrm{Fe_2O_3}$, Merck 99 % purity)

in equimolar ratio. The starting hydroxides were amorphous, while hematite was crystalline. Mechanochemical synthesis was performed in air atmosphere in planetary ball mill (Fritsch Pulverisette 5). A hardened-steel vial of 500 $\mathrm{cm^3}$ volume, filled with 40 hardened steel balls with a diameter of 13.4 mm, was used as the milling medium. The mass of the powder was 20 g and the balls-to-powder mass ratio was 20:1. The milling was done in the air atmosphere without any additives. The angular velocity of the supporting disc and vial was about 32 and 40 rad/s, respectively. The intensity of milling corresponded to an acceleration of about ten times

the gravitation acceleration. At the expiration of the selected milling times the mill was stopped and a small amount of powder was removed from the vial for examination. Required milling times for obtaining a single-phase ferrites were determined experimentally. It was found that spinel phase was completed after 18 h for Zn-ferrite, and 25 h for Mn- and Ni-ferrite. Thus synthesized nanopowders were pressed into pallet using a cold isostatic press. All disk-shaped pallets were sintered at 1,100 °C for 2 h (Lenton—UK oven) without pre-calcinations step. Heating rate was 10 °C/min, with nature cooling in air atmosphere. The thickness and diameter of each sintered samples are 2.0 and 8.0 mm, respectively.

2.2 Characterization

TEM studies were performed using a 200 kV TEM (Model JEOL JEM-2100 UHR) equipped with an ultra-high resolution objective lens pole piece having a point-to-point resolution of 0.19 nm, being sufficient to resolve the lattice images of nanoparticles. For transmission electron microscopy observations the synthesized ferrite powders were dispersed in ethanol. Due to relatively small size of the nanoparticles selected area, electron diffraction patterns (EDP) over the multiple nanocrystals was recorded to obtain the characteristic diffraction rings with structure-specific d values. The formation of phase and crystal structure of sintered $M\mathrm{Fe_2O_4}$ (M = Mn, Ni, Zn) ferrites were verified via the X-ray diffraction measurements (XRD). Model Philips PW 1050 diffractometer equipped with a PW 1730 generator (40 kV × 20 mA) was used with Ni filtered CoKα radiation of 1.78897 Å at the room temperature. Measurements were done in 2θ range of 15–80° with scanning step width of 0.05° and 10 s scanning time per step. The microstructures of sintered ferrites were recorded at room temperature using scanning electron microscope (Model JEOL JSM-6460 LV) applied on a gold coated surface of samples. The sintered (bulk) density of the samples was measured by applying Archimedes' principle at room temperature using toluene as an immersion liquid.

In this study, the sintered ferrite pallets used for electrical measurements were coated with silver paste to ensure good ohmic contacts. Thus prepared samples with silver electrodes deposited on both sides can be considered electrically equivalent to a capacitance C_p in parallel with a resistance R_p, see Fig. 1. These alternating current (AC) parameters were measured directly in the frequency range 100 Hz to 1 MHz at different temperatures using an Impedance Analyzer HP-4194A with a set of temperature control equipment. In this measurement setup, a personal computer with in-house-built software implemented by LabVIEW was used for acquisition of measured data. The AC conductivity was determined using the following relation:

$$\sigma_\mathrm{AC} = \omega\varepsilon_0\varepsilon'', \tag{1}$$

where $\varepsilon'' = (\omega R_\mathrm{p} C_0)^{-1}$, $\omega = 2\pi f$ is the angular frequency of the applied field and ε_0 represents the permittivity of vacuum equal to 8.85×10^{-12} F/m. The capacitance C_0 is determined by area of electrode A and distance between the electrodes d, as follows $C_0 = A\varepsilon_0/d$. The dielectric constant of the ferrites under study was determined by using the following relation:

$$\varepsilon' = \frac{C_\mathrm{p}}{C_0}. \tag{2}$$

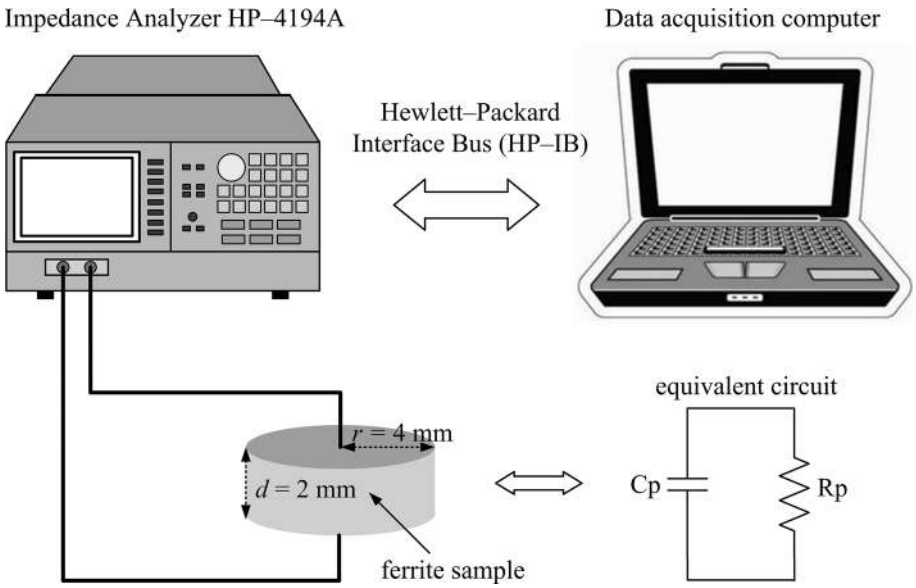

Fig. 1 Schematic diagram of the experimental setup for measuring the electrical properties of ferrites and equivalent circuit of prepared sample

The direct current (DC) resistivity of the synthesized ferrites was measured by simple two-probe method within temperature range 298–448 K. A Source Meter Keithley 2410 was used for the said purpose. The DC resistivity was calculated by using the following formula:

$$\rho_{DC} = \frac{RA}{d}, \tag{3}$$

where R is the measured resistance, A is area of electrode and d is the thickness of the sample.

3 Results and discussion

3.1 Structural study

The shape, size and morphology of mechano-synthesized $M\mathrm{Fe_2O_4}$ (M = Mn, Ni, Zn) nanopowders are characterized by direct observation via transmission electron microscope. The representative TEM images with corresponding EDPs of powder samples obtained after appropriate milling time are depicted in Fig. 2. Bright-field TEM reveals the nanoscale nature of synthesized ferrite particles, mostly in the size ranges between 10–60 nm. The shape of the majority of the nanoparticles is nearly spherical. The crystallites in all three systems are rounded and tend to agglomerate into larger clusters with diameters of several hundreds of nanometers. Measurements of the diffraction rings confirmed that they correspond to the crystal planes of spinel structure.

Figure 3 shows the X-ray diffraction patterns of sintered $M\mathrm{Fe_2O_4}$ (M = Mn, Ni, Zn) spinel ferrites. It is evident from obtained XRD results of all three samples that the spinel phase, with characteristic Bragg reflections, was formed during the soft mechanochemical process followed by sintering at 1,100 °C for 2 h. The sintered ferrites show a sharp XRD peak indicating the crystalline nature of the samples. The average crystallite sizes D_c were determined from the characteristic diffraction peak of spinel cubic structure belonging to (311) Miller plane using the Scherrer's formula [9]:

$$D_c = \frac{0.9\lambda}{\beta \cos\theta}, \tag{4}$$

where λ is wavelength of used X-ray source (1.78897 Å), β represents full-width at half-maximum of peak, and parameter θ is the Bragg angle of diffraction. The determined values of crystallite size are 45, 49 and 54 nm for appropriate Ni-, Mn- and Zn-ferrite, respectively. Based on the measured positions of diffraction peaks, lattice constant a was calculated by well-known relation [4]:

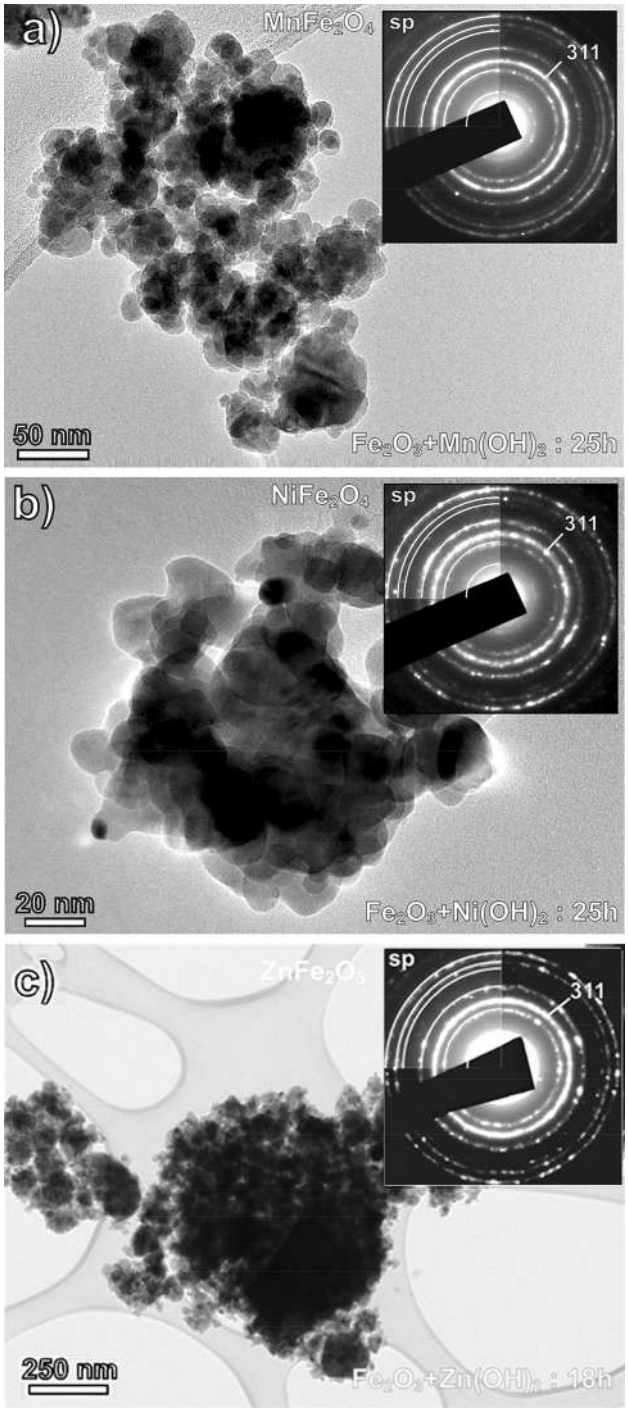

Fig. 2 TEM images with corresponding EDPs (*insets* in *the upper right corners*) of mechano-synthesized $\mathrm{MnFe_2O_4}$ (**a**), $\mathrm{NiFe_2O_4}$ (**b**) and $\mathrm{ZnFe_2O_4}$ (**c**) ferrite nanoparticles

$$a = \frac{\lambda}{2\sin\theta} \times \sqrt{h^2 + k^2 + l^2}, \tag{5}$$

Related lattice constants are 8.339, 8.421 and 8.418 Å for sintered Ni-, Mn- and Zn-ferrite, respectively. The visible shift of Bragg reflections towards higher 2θ-angles

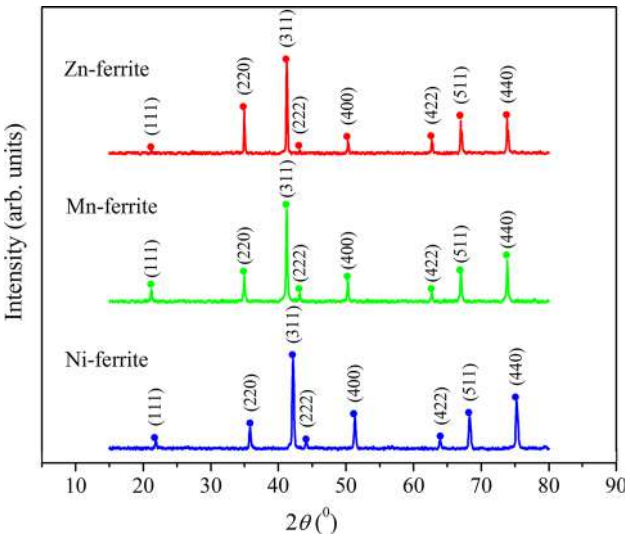

Fig. 3 X-ray diffraction patterns of the MFe_2O_4 (M = Ni, Mn, Zn) ferrites sintered at 1,100 °C/2 h

in the case of Ni-ferrite corresponds to the smallest lattice constant.

Zn^{2+} ions, with the greatest ionic radii, occupie tetrahedral (A) sites forming a normal spinel structure (paramagnetic in the case of sintered $ZnFe_2O_4$). Through the process of the inversion some of Fe^{3+} cations from octahedral [B] sites occupy free (A) sites (forbidden at equilibrium conditions in normal spinels) and the M^{2+} cations pass into octahedral vacancies. The changes in the cation sublattice are accompanied by a lattice contraction resulting mainly in the alteration of the bond angles in the octahedrals. This shifting of cations causes changes in XRD pattern also.

It is known that in cubic spinel structure Bragg reflection (220) depends exclusively on the cations occupying tetrahedral sites and intensity of the (222) reflection depends on cations in the octahedral sites [17]. As the amount of iron ions in [B] sites decreases, the intensity of the (222) peak decreases. Ratios of the intensities for diffraction lines (220) and (222) indicate that the ferrite sample with the highest $I_{(220)}/I_{(222)}$ has the lowest degree of the cation inversion [18]. At the first sight, it is visible that the relative intensity ratios $I_{(200)}/I_{(222)}$ of reflections in the investigated ferrites increase from totally inversion in $NiFe_2O_4$ spinel structure ($I_{(200)}/I_{(222)} = 2.7$) towards mixed inverse $MnFe_2O_4$ ($I_{(200)}/I_{(222)} = 3.2$) to normal $ZnFe_2O_4$ spinel structure ($I_{(200)}/I_{(222)} = 7.4$). Figure 3 not only shows that single phase ferrites are formed, but it presents an evidence of their cation distribution.

The microstructures of MFe_2O_4 (M = Mn, Ni, Zn) samples sintered at 1,100 °C for 2 h are given in Fig. 4. Room temperature SEM images clearly show the presence of conducting grains (A) separated from each other by the

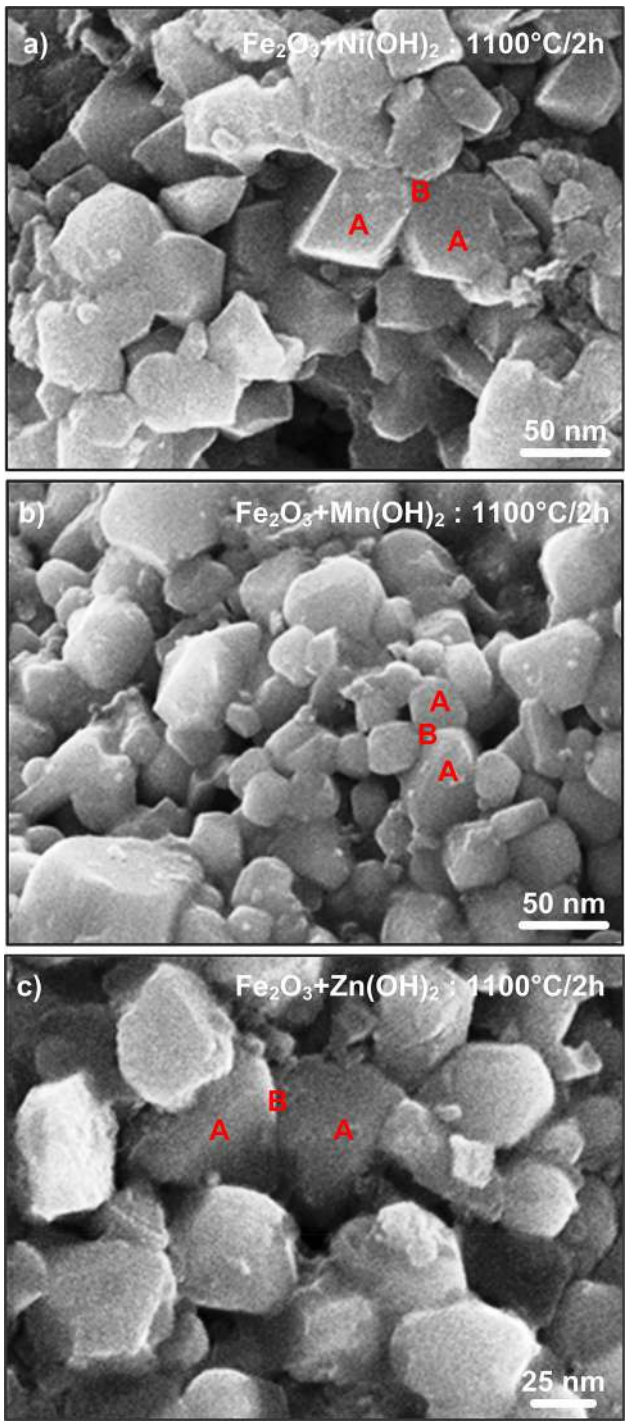

Fig. 4 SEM micrographs of $NiFe_2O_4$ (**a**), $MnFe_2O_4$ (**b**) and $ZnFe_2O_4$ (**c**) ferrite samples sintered at 1,100 °C for 2 h. The *A* and *B* marks denote grain and grain boundaries, respectively

well-defined grain boundaries (B). These two main components comprise the microstructure of ferrites under study and the correspondence between them is important in understanding the overall properties of these materials. The grain boundaries control the electrical and dielectric properties of the ferrites, especially in the case of

Table 1 Structural characteristics of MFe_2O_4 (M = Mn, Ni, Zn) ferrite samples sintered at 1,100 °C for 2 h

Ferrite sample	Lattice constant (Å)	Crystallite size (nm)	Sintered density (g/cm^3)
$NiFe_2O_4$	8.339	45	3.93
$MnFe_2O_4$	8.421	49	4.21
$ZnFe_2O_4$	8.418	54	4.86

nanocrystalline ferrites [7]. By using an Archimedes experimental method, the sintered (bulk) density ρ_s was determined by applying the relationship [19]:

$$\rho_s = \rho_b \frac{w_a}{w_a - w_b}, \quad (6)$$

where ρ_b is the density of the buoyant, w_a and w_b are the sample weights in air and the buoyant, respectively. The experiment was repeated five times and the estimated error in density measurement for all three samples is $\pm$ 3.5 $\times$ 10^{-3} g cm^{-3}. The bulk density values and other crystallographic data for sintered MFe_2O_4 (M = Mn, Ni, Zn) ferrites are presented in Table 1.

3.2 DC electrical resistivity

The DC electrical resistivity is one of the most important properties of ferrite ceramics; usually high resistivity is prerequisite for most electronic applications that require negligible eddy currents which degrade the ferrite performance. The electrical resistivity of the MFe_2O_4 (M = Mn, Ni, Zn) ferrites under investigation was measured by two-probe method as a function of temperature. The variation of DC resistivity as a function of temperature is shown in Fig. 5. It is noticed that temperature dependent electrical resistivity of ferrites decreases with increase in temperature indicating the semiconducting nature of all sintered samples [20]. This effect can be explained by the enhancement in thermally activated drift mobility of charge carriers, which is in accordance with the hopping conduction mechanism [21].

In this study, the variation of electrical DC resistivity ρ_{DC} with absolute temperature T can be expressed by the Arrhenius equation as [22]:

$$\rho_{DC}(T) = \rho_0 \exp\left(\frac{\Delta E}{k_B T}\right), \quad (7)$$

where ρ_0 is the pre-exponential factor with the dimensions of (Ωcm), k_B is the Boltzmann's constant and ΔE is the activation energy in (eV) which is needed for electron hopping from one metallic ion to the next. In the measured temperature range, the value of the activation energy for each sample was calculated from the slope of the linear plots of DC resistivity and obtained results are presented in

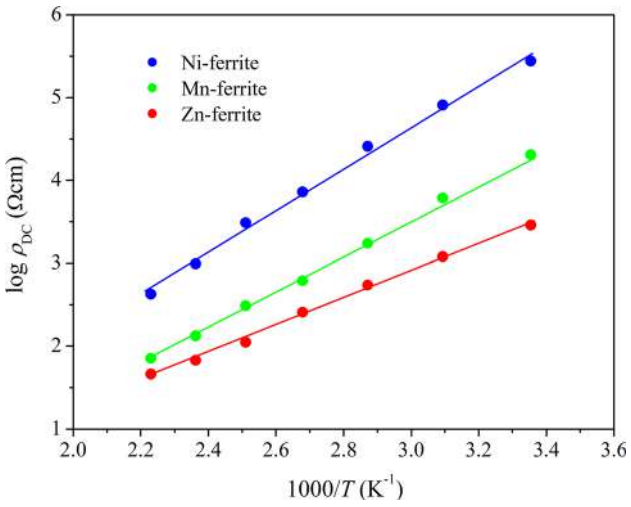

Fig. 5 Variation of DC electrical resistivity with temperature for MFe_2O_4 (M = Mn, Ni, Zn) ferrites

Table 2 The values of activation energy, DC electrical resistivity and drift mobility at room temperature for the MFe_2O_4 (M = Mn, Ni, Zn) ferrite samples

Ferrite sample	ΔE (eV)	ρ_{DC} (Ωcm) at 298 K	μ_d (cm^{2}V^{-1}s^{-1}) at 298 K
$NiFe_2O_4$	0.653	2.72 $\times$ 10^5	1.14 $\times$ 10^{-9}
$MnFe_2O_4$	0.408	2.01 $\times$ 10^4	1.32 $\times$ 10^{-8}
$ZnFe_2O_4$	0.331	2.81 $\times$ 10^3	1.06 $\times$ 10^{-7}

Table 2. The determined activation energies for the investigated ferrites range from 0.331 to 0.653 eV, which suggest that the conduction mechanism in these ferrites is due to hopping of charge carriers according to Klinger [23].

Comparison of the DC resistivity and activation energy shows a good agreement in the sense that samples with higher resistivity have higher value of activation energy and vice versa. The measured resistivity of the sintered MFe_2O_4 (M = Mn, Ni, Zn) ferrites at room temperature was found to vary from 2.81 $\times$ 10^3 to 2.72 $\times$ 10^5 Ωcm as given in Table 2. Among the present samples, it is observed that Ni-ferrite has the highest value of the DC resistivity, what makes it as a good candidate for electronic devices applications that require negligible eddy currents.

3.3 Drift mobility

The drift mobility μ_d was determined by the DC electrical resistivity ρ_{DC} using the following relation [24]:

$$\mu_d(T) = \frac{1}{ne\rho_{DC}(T)}, \quad (8)$$

where e is the charge of electron and n is the concentration of charge carrier that can be calculated from the well-known equation:

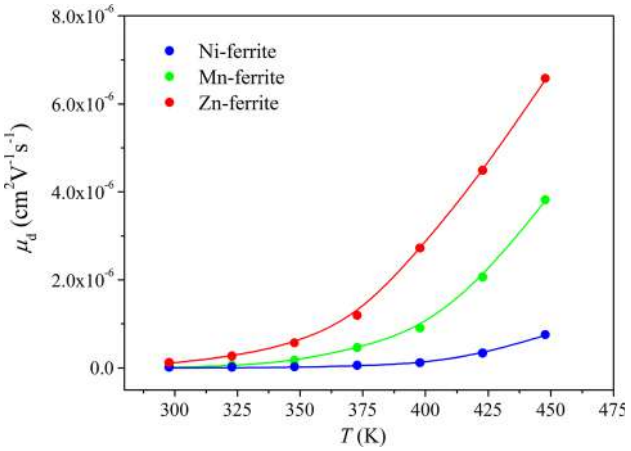

Fig. 6 Temperature dependence of drift mobility of sintered MFe_2O_4 (M = Mn, Ni, Zn) ferrites

$$n = \frac{N_A \rho_s Q}{M}, \tag{9}$$

where N_A is the Avogadro's number, ρ_s the measured bulk density of sintered sample, Q the number of iron atoms in the chemical formula of the ferrite and M is the molar mass of the sample.

From the measured DC electrical resistivity data, the temperature dependence of the drift mobility of MFe_2O_4 (M = Mn, Ni, Zn) ferrite samples is determined and it is shown in Fig. 6. It is observed that variation of the drift mobility shows an opposite behaviour in comparison to the DC resistivity; it increases with increasing temperature. The increase in drift mobility represents enhanced mobility of the charge carriers due to thermal activation. It may be because of the fact that as the temperature increases, the charge carriers start hopping from one site to another; hence the conduction process increases [25]. Also, data given in Table 2 show that the studied ferrites with higher value of DC resistivity have lower value of drift mobility and vice versa.

3.4 AC conductivity

Spinel ferrites possess low electrical conductivity when compared to other magnetic materials, and hence they find wide use at microwave frequencies. In order to understand the conduction mechanism and type of charge carriers responsible for this process, the AC electrical conductivity of the sintered MFe_2O_4 (M = Mn, Ni, Zn) ferrites was investigated as a function of frequency at different temperatures. Generally, electrical conductivity is an increasing function of frequency if it takes place by hopping of charges and it is a decreasing function of frequency if the band conduction is used [26]. Figure 7 shows the dependence of AC conductivity on the frequency at selected

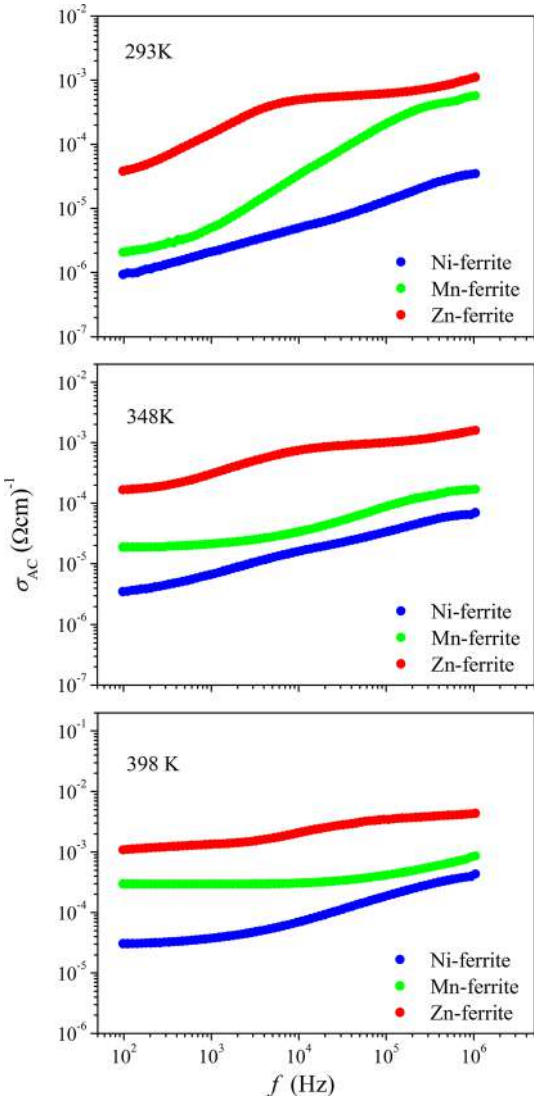

Fig. 7 Frequency dependent AC electrical conductivity of MFe_2O_4 (M = Mn, Ni, Zn) ferrites at different temperatures

measuring temperatures. It is observed that AC conductivity of all studied samples increases with increasing frequency of the applied field. It is well known that this conductivity behavior can be explained on the basis of Maxwell–Wagner two-layer model [27, 28] and Koop's phenomenological theory [29], which assumes that the ferrites consist of conductivity grains separated by highly resistive thin layers known as grain boundaries as illustrated in Fig. 4. The grain boundaries are the region of mismatch between the energy states of adjacent grains and hence act as a barrier to the flow of electrons [10]. According to this model, the grain boundaries are much more active than grain at lower frequencies, resulting that the hopping probability of charge carriers is less. As the frequency of the applied filed increases, the ferrite grains became more active by promoting the hopping of the

electrons between Fe^{2+} and Fe^{3+} ions (n-type) on the octahedral [B] sites in accordance with Verwey de Boer conduction mechanism [30]. As a result, the AC conductivity of all ferrites under investigation increases. But, various reports have shown that the hole hopping between Ni^{2+} and Ni^{3+} (p-type) on the [B] site can also contribute to the electric conduction in the case of Ni-ferrites as inverse spinel structures [31, 32]. This type of hopping depends upon the Ni^{2+} concentration at the octahedral [B] site [31, 33]. Considering the low value of the conductivity of sintered Ni-ferrite of about 9.1×10^{-7} $(\Omega cm)^{-1}$ at room temperature, the hole hopping ($Ni^{3+} \leftrightarrow Ni^{2+} + e^{+}$) is weak compared to electron hopping ($Fe^{2+} \leftrightarrow Fe^{3+} + e^{-}$), hence n-type is assumed to be the dominant conduction mechanism [34]. However, a clear understanding of the conduction mechanism in this mechano-synthesized Ni-ferrite needs further investigation.

In present study, frequency dependent AC conductivity of the synthesized ferrites varies from 10^{-7} to 10^{-3} $(\Omega cm)^{-1}$ and the conductivity behavior for all samples is analogous with each other. The plots of conductivity are almost linear, indicating that the conduction of the MFe_2O_4 (M = Mn, Ni, Zn) ferrites is due to small polarons. For ionic solids, it has been shown that the concept of small polaron is valid [21, 35]. Similar type of electrical conduction mechanism in terms of electron and polaron hopping has been elaborated in detail by Austin and Mott [36]. On the other hand, one can note that obtained measurement data of AC conductivity obey the power law given by the empirical formula proposed by Jonscher [22]:

$$\sigma_{AC}(\omega, T) = A(T)\omega^{n}, \tag{10}$$

where $A(T)$ is the temperature dependent parameter and it has the unit of electrical conductivity; n is dimensionless exponent and generally it is less than or equal to one. For $n = 0$, the electrical conduction is frequency independent (DC conduction), while for $n \leq 1$ the conduction is frequency dependent (AC conduction) [37]. The value of exponent n for each sample was calculated from the slope of $\log(\sigma_{AC})$ versus $\log(\omega)$ at room temperature. In the present study, the values of exponent n are found to be 0.342, 0.411 and 0.698 for Zn-, Ni- and Mn-ferrite, respectively. The obtained values suggest that the conduction phenomena in studied samples follow hopping conduction.

It is also evident from Fig. 7 that AC conductivity of studied ferrites increases with increasing temperature, which is in good agreement with the well-established information that ferrites can be categorized as semiconductors. This influence of temperature on conductivity is mostly associated with the temperature dependent drift mobility of the thermally activated super-exchange interaction between Fe^{2+}–O–Fe^{3+} ions in the octahedral sites. [38]. The density of ferrite materials also plays an important role in the variation of electrical properties. Higher density causes an increase in the value of AC conductivity. As a confirmation of this fact, Zn-ferrite with the highest value of sintered density possesses the highest value of conductivity in comparison to the other two ferrites under study.

3.5 Complex impedance analysis

The complex impedance spectroscopy [39] is very useful and powerful technique that enables to determine the correlation of the electrical properties of a ferrite with its microstructures. In the analysis of impedance data, this method helps us to separate grain and grain-boundary contributions of polycrystalline ferrites to the total electrical conductivity over wide frequency range. The experimental data for the complex impedance (Z) provide information on the resistive (real part, Z') and reactive (imaginary part, Z'') components. The frequency dependence of the impedance ($Z = Z' + jZ''$) at selected temperatures is plotted in Fig. 8. One can note that values of Z decrease with the increase of applied frequency indicating an increase in AC electrical conductivity with frequency for all ferrite samples. Among the three present ferrites under study, Zn-ferrite shows lower values of impedance at each selected temperature. This fact is in good agreement with the obtained conductivity results which show that the Zn-ferrite has the highest value of conductivity in comparison with the other two samples, Mn- and Ni-ferrites. In the case of Zn-ferrite, it can be observed two dispersions, that of the grains and that of the grain boundaries, which are marked in Fig. 8. The behavior of complex impedance of other two ferrites is different than in Zn-ferrite and it shows only one dispersion, probably due to a limited frequency range used in this study (100 Hz–l MHz) [40]. With increasing temperature, these individual dispersion regions are shifted to a higher frequency. In general, the impedance values of all samples decrease by two orders of magnitude in the measurement range, which is due to thermal activation mechanism. As one can see from the Fig. 8, the temperature dependent complex impedance of sintered ferrites, especially in the case of Mn-ferrite, shows a plateau from low frequency side at 348 K, which is followed by a nearly negative slope at high frequency side. This segment of nearly constant impedance becomes predominated with increasing temperature, suggesting strengthened relaxation behaviour [41]. In addition, the decreasing trend of impedance means increasing loss in resistive property of investigated ferrites, i.e. negative temperature coefficient of resistance (NTCR) type behaviour like that of semiconductors [22].

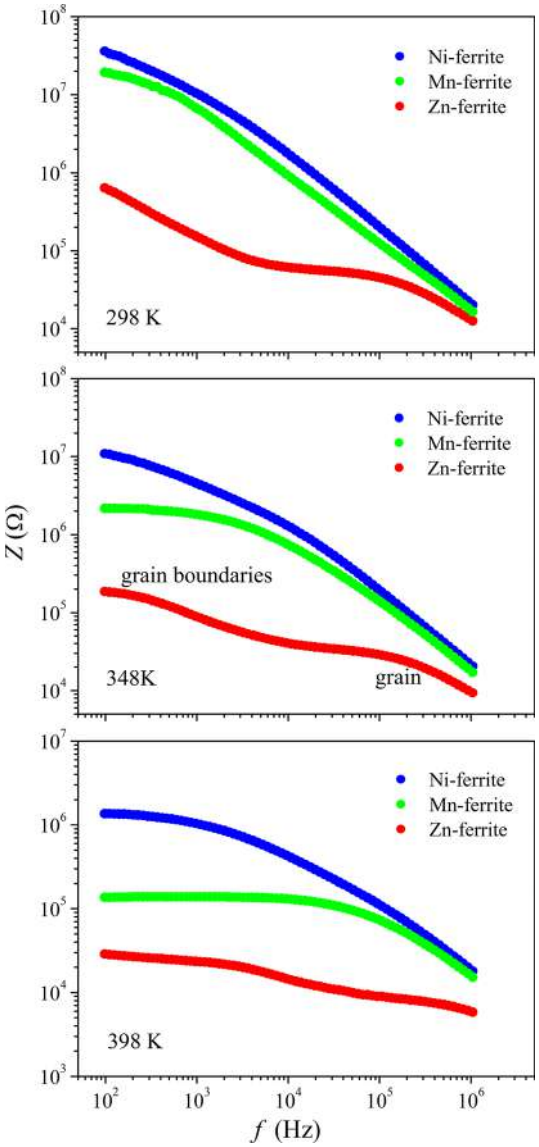

Fig. 8 Variation of complex impedance of MFe_2O_4 (M = Mn, Ni, Zn) ferrites with frequency at different temperatures

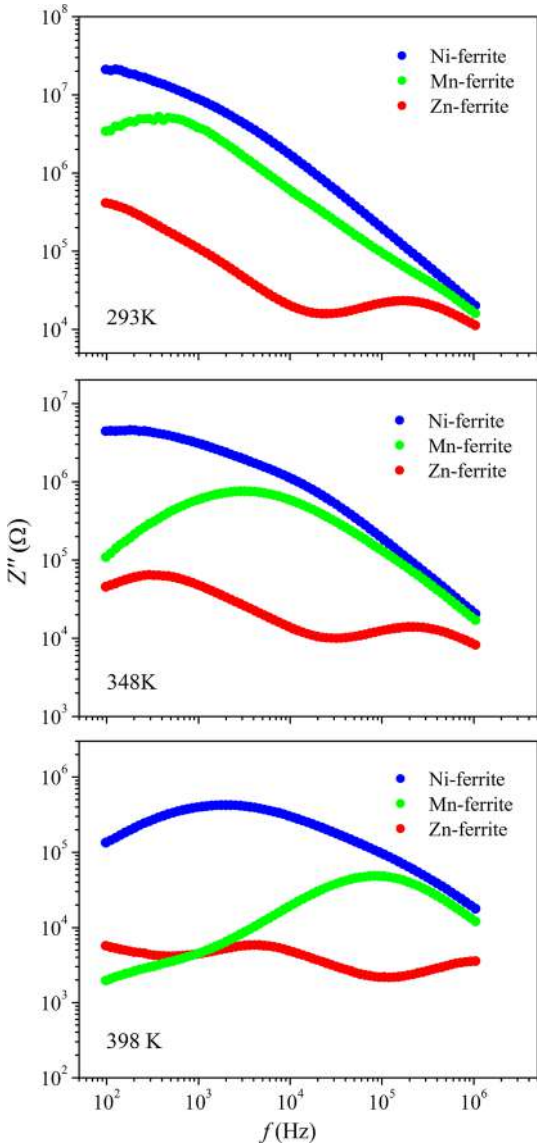

Fig. 9 Frequency dependence of imaginary part of impedance of MFe_2O_4 (M = Mn, Ni, Zn) ferrites at selected temperatures

The variation of the imaginary part of the impedance (Z'') with frequency at selected temperatures is presented in Fig. 9. In the case of Ni- and Mn-ferrites, the curves show that the Z'' value increases initially, reaches the maximum value (Z''_{max}) at particular frequency and then it decreases continuously with increasing frequency for given temperatures of measurement. The appearance of one peak indicates single relaxation process in these two synthesized ferrites [42]. Similar behaviour of reactive part of the impedance is observed in present Zn-ferrite, but two peaks appear in the values of Z'' at all temperatures. This suggests the coexistence of two relaxation effects which can be attributed to grain and grain boundary responses [43]. In all three ferrites under study, the maximum values of Z'' shift to high frequency side with increasing temperature, which corresponds to plateau relaxations observed earlier in complex impedance [41]. Also, it is evident that Z''_{max} decreases with increasing temperature, which reveals the decrease in the resistance of sintered ferrite samples.

To get more insight into electrical process occurring within the samples, the impedance spectra of MFe_2O_4 (M = Mn, Ni, Zn) ferrites were studied in the frequency range from 100 Hz to 1 MHz at different temperatures. The complex impedance spectrum, known as Cole–Cole or Nyquist plot, is characterized by the appearance of semi-circle arcs whose pattern changes, but not its shape, when the temperature measurement increases [44]. It is well known that the arc at lower frequencies corresponds to the

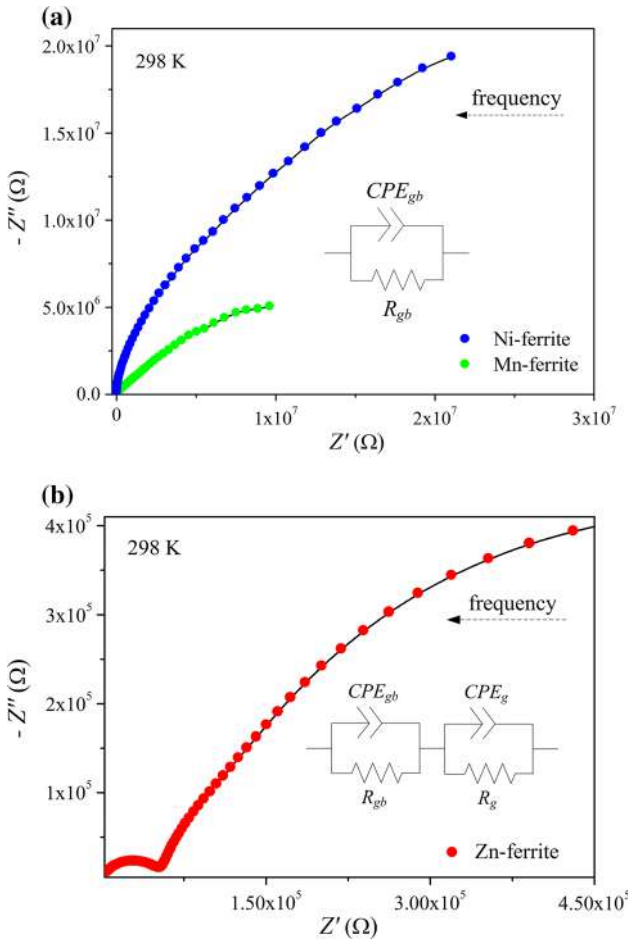

Fig. 10 Impedance spectra for (**a**) Ni-and Mn-ferrites and (**b**) Zn-ferrite at room temperatures. *Inset* shows the proposed equivalent circuit model for analysis of the impedance data

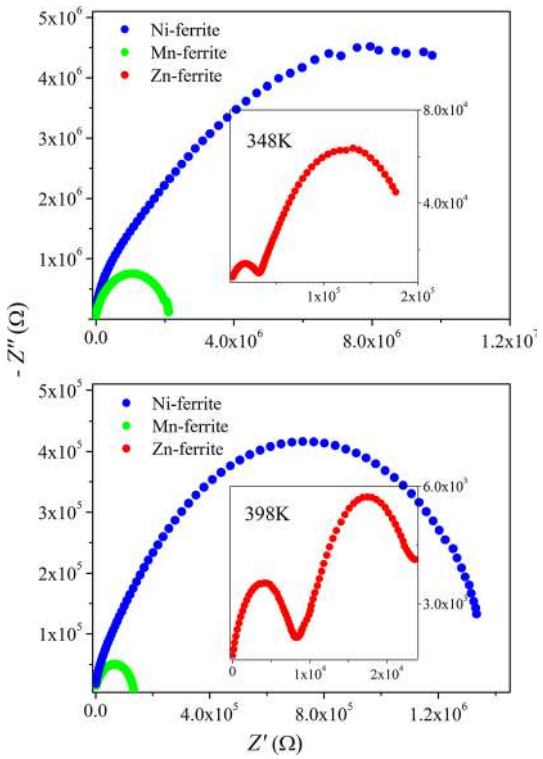

Fig. 11 Impedance spectra of MFe$_2$O$_4$ (M = Mn, Ni, Zn) ferrites at some selected temperatures

grain boundaries, while the high frequency arc represents the grain. Impedance spectra of studied samples synthesized by soft mechanochemical method are presented in Figs. 10 and 11. In the impedance spectra of Ni- and Mn-ferrites only one semicircle at selected temperatures is observed, indicating just one dominant relaxation phenomenon. These results suggest that conduction takes place predominantly through the grain boundary and that contribution from the grain is not resolved for these samples. This may be due to a limited frequency range used in this study (100 Hz–l MHz) or the grain boundary contribution cannot be separated from the grain contribution by the impedance spectroscopy [40]. On the other hand, the impedance spectra obtained for Zn-ferrite have two semicircle arcs, including both grain and grain boundary effects at all temperatures. This appearance of two arcs in Cole–Cole plots at each temperature indicates the presences of two types of relaxation phenomena with sufficiently different relaxation times [31]. The diameters of these semicircles correspond to the resistances: a larger one at low frequency represents the resistance of the grain boundary and a smaller one obtained at the higher frequency side corresponds to the grain made resistance [45]. Figures 10 and 11 show that Cole–Cole plots are temperature dependent, since the diameters of these semicircles exhibit decreasing trends with increasing temperature. This indicates decrease in relaxation time [46] and increase in conductivity with rise in temperature, supporting typical semiconducting behavior observed in all three sintered ferrite samples.

Impedance spectrum provides information about the electrical process occurring within the samples and their correlation with the sample microstructure, when it is modelled in terms of an electrical equivalent circuit [47]. The proposed electrical models, shown in the inset of Fig. 10, has been used to interpret the impedance response of MFe$_2$O$_4$ (M = Mn, Ni, Zn) ferrites. Here R_{gb} and R_g represent the grain boundary and grain resistance, while CPE_{gb} and CPE_g are the constant phase elements for grain boundaries and grain interiors, respectively. The CPE is used to accommodate the non-ideal Debye-like behavior of the capacitance which is given by relation $C = Q^{1/n}R^{(1-n)/n}$, where the value of parameter n is 1 for a pure capacitor and it has a value of zero for pure resistive behavior [4, 31, 47]. The electrical parameters of proposed equivalent circuits were obtained by analyzing the impedance data using EIS Spectrum Analyzer software [48]. The calculated values of

Table 3 The electrical parameters of proposed equivalent circuits calculated from impedance response of the MFe_2O_4 (M = Mn, Ni, Zn) ferrite samples at selected temperatures

Sample	Temperature (K)	R_{gb} (kΩ)	C_{gb} (F)	n_{gb}	R_g (kΩ)	C_g (F)	n_g
$NiFe_2O_4$	298	66,075.1	1.72×10^{-10}	0.723	–	–	–
	348	16,431.5	7.61×10^{-10}	0.628	–	–	–
	398	1,453.3	1.28×10^{-9}	0.663	–	–	–
$MnFe_2O_4$	298	12,842.5	1.08×10^{-10}	0.775	–	–	–
	348	2,185.3	2.19×10^{-10}	0.734	–	–	–
	398	137.4	3.18×10^{-10}	0.756	–	–	–
$ZnFe_2O_4$	298	1,173.4	7.13×10^{-9}	0.807	54.3	1.44×10^{-10}	0.839
	348	177.1	1.36×10^{-8}	0.785	34.2	3.00×10^{-10}	0.811
	398	65.3	3.87×10^{-8}	0.726	24.5	1.66×10^{-10}	0.850

these impedance parameters are given in Table 3. It has been found that values of the grain boundary resistance are generally larger than the resistances of the grain ($R_{gb} > R_g$) in the case of Zn-ferrite. This can be ascribed to the fact that the atomic arrangement near the grain boundary region is disordered, resulting in a serious increase in electron scattering [49]. The higher grain boundary resistance also arises from other factors such as a decrease in Fe^{2+} ion content in this region [50]. Also, for Zn-ferrite sample the capacitance of grain boundary is larger than that of the grain, which is explained on basis that the capacitances are inversely proportional to the thickness of the media [51]. Additionally, the relaxation time of the grain boundaries ($\tau_{gb} = R_{gb}C_{gb}$) is much larger than that of the grains ($\tau_g = R_gC_g$), since the semicircle representing the grain boundaries lies on the lower frequency side. Among all three ferrites synthesized by soft mechanochemical method, the Ni-ferrite exhibits the highest value of resistances which means lower polarizability for this ferrite. The higher value of resistance for sintered Ni-ferrite sample retards electron hopping, which is known to be a mechanism for both conduction and polarization in ferrites [52]. Based on the above, the trends observed in the electrical conductivity and complex impedance of present MFe_2O_4 (M = Mn, Ni, Zn) ferrites are in good agreement with each other. Also, it can be concluded that the effect of grain boundaries is the dominant for the electrical behavior of all mechano-synthesized ferrites in frequency range used in this study (100 Hz–l MHz).

3.6 Dielectric constant

The frequency dependence of the dielectric constant of MFe_2O_4 (M = Mn, Ni, Zn) ferrites under study at selected temperatures is represented in Fig. 12. It is clear from the analysis of the graphs that Zn-ferrite exhibits the highest dielectric constant at low frequencies when compared to other two samples. The dielectric constant of Mn-ferrite exceeds that of Ni-ferrite at room temperature. For example, the values of dielectric constant of Ni-, Mn- and Zn- ferrites are 67, 132 and 2,641 at frequency of 1 kHz and room temperature, respectively. In general, the dielectric constant of all three samples decreases with the increase in frequency, which is the normal dielectric behaviour of spinel ferrites. More dielectric dispersion is observed at low frequency region and it remains almost independent of applied external field at high frequency region. Such behaviour, observed in a number of ferrite materials, is mainly due to the Maxwell–Wagner type of interfacial polarization [27, 28] which is a result of inhomogeneous nature of the dielectric structure in the samples. It is formed by large number of well conducting grains separated by thin poorly conducting intermediate grain boundaries as shown in Fig. 4. Such a type of heterogeneous structure is understood to be formed at the time of sintering [19].

According to Rabinkin and Novikova [53], it is observed that the mechanism of dielectric polarization is similar to the mechanism of electrical conduction in ferrites. It is known that ferrites are dipolar materials due to the presence of majority Fe^{3+} ions and minority Fe^{2+} ions in them. Fe^{2+} ions are usually formed due to partial reduction of Fe^{3+} ions during the process of synthesis. The electron exchange between Fe^{3+} and Fe^{2+} ions gives local displacement in the direction of applied electric field, thus determining the polarization in ferrites. Polarization decreases with the rise in frequency and then attains a constant value. It is because of the fact that beyond a certain value of frequency of external field, the electron exchange between Fe^{2+} and Fe^{3+} ions cannot follow the alternating field [54]. On the other hand, Fig. 12 shows that the dielectric constant of all tree ferrites increases with the increase in temperature due to the increase in thermally activated charge carriers. This substantiates the normal dielectric behaviour of the samples under study as magnetic semiconductor ferrites [11].

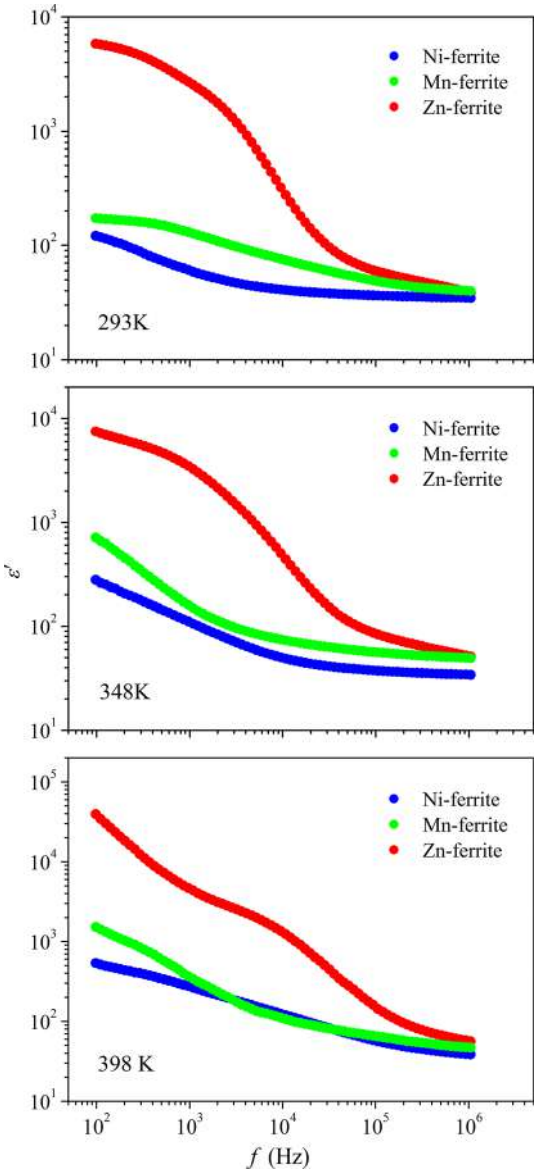

Fig. 12 Frequency dependent dielectric constant of MFe_2O_4 (M = Mn, Ni, Zn) ferrites at different temperatures

4 Conclusions

Comparative study of the temperature and frequency dependence of electrical and dielectric properties of MFe_2O_4 (M = Mn, Ni, Zn) ferrites, fabricated by a conventional sintering of nanosized powders (1,100 °C/2 h) synthesized by soft mechanochemical technique, is presented in this paper. The decrease in the value of DC resistivity of all samples with increasing temperature suggests the negative temperature coefficient of resistance behavior usually shown by semiconducting materials. In addition, the DC resistivity well obeys the Arrhenius law and the activation energies are calculated from the slope of electrical resistivity plots. The AC electrical conductivity of the present samples is explained in the light of the hopping mechanism by means of Maxwell–Wagner model in consonance with Koop's phenomenological theory. The complex impedance spectra of Ni- and Mn-ferrites show the presence of only one semicircle at all selected temperatures, suggesting a dominant role of the grain boundary contribution. In the case of Zn-ferrite, impedance spectrum includes both grain and grain boundary effects corresponding to two semicircles. The analysis of impedance data using an equivalent circuit indicates that the capacitive and resistive properties of the mechano-synthesized ferrites are mainly attributed to the processes that are associated with the grain boundaries in frequency range used in this study. A decrease in dielectric constant with increasing frequency in sintered samples revealed the presence of Maxwell-Wagner type interfacial polarization. In view of the studied electrical and dielectric properties, Ni-ferrite has the highest value of resistivity, the lowest value of conductivity, and appreciable value of the dielectric constant, making it very suitable for electronic devices applications at high frequencies.

Acknowledgments This research was financially supported by the Ministry of Education, Science and Technological Development of the Republic of Serbia through Projects No. III43008 and III45003.

References

1. S.M. Chavan, M.K. Babrekar, S.S. More, K.M. Jadhav, J. Alloy Compd. **507**, 21 (2010)
2. A.B. Gadkari, T.J. Shinde, P.N. Vasambekar, Mater. Res. Bull. **48**, 476 (2013)
3. A. Sutka, G. Mezinskis, A. Lusis, Phys. Scr. **87**, 025601 (2013)
4. Z.Z. Lazarevic, C. Jovalekic, A. Milutinovic, D. Sekulic, V.N. Ivanovski, A. Recnik, B. Cekic, N.Z. Romcevic, J. Appl. Phys. **113**, 187221 (2013)
5. I.H. Gul, W. Ahmed, A. Maqsood, J. Magn. Magn. Mater. **320**, 270 (2008)
6. C.N. Chinnasamy, A. Narayanasamy, N. Ponpandian, Phys. Rev. B **63**, 184108 (2001)
7. E.V. Gopalan, K.A. Malini, S. Saravanan, D.S. Kumar, Y. Yoshida, M.R. Anantharaman, J. Phys. D Appl. Phys. **41**, 185005 (2008)
8. H. Anwar, A. Maqsood, Mater. Res. Bull. **49**, 426 (2014)
9. M. Pavlovic, C. Jovalekic, A.S. Nikolic, D. Manojlovic, N. Sojic, J. Mater. Sci. Mater. Electron. **20**, 782 (2009)
10. S.F. Mansour, M.A. Elkestawy, Ceram. Int. **37**, 1175 (2011)
11. G. Sathishkumar, C. Venkataraju, R. Murugaraj, K. Sivakumar, J. Mater. Sci. Mater. Electron. **23**, 243 (2012)
12. A. Chatterjee, D. Das, S.K. Pradhan, D. Chakravorty, J. Magn. Magn. Mater. **127**, 214 (1993)
13. S.R. Kulkarni, P.U. Londhe, N.B. Chaure, J. Mater. Sci. Mater. Electron. **24**, 4186 (2013)
14. T. Hyeon, Chem. Commun. **9**, 927 (2003)
15. C.R. Vestal, Z.J. Zhang, Nano Lett. **3**, 1739 (2003)
16. E. Avvakumov, M. Senna, N. Kosova, *Soft mechanochemical synthesis: a basis for new chemical technologies* (Kluwer Academic Publishers, Boston, 2001)
17. V. Sepelak, K. Tkacova, Acta Montan. Slovaca **2**, 266 (1997)

18. M. Mozaffari, M.E. Arani, J. Amighian, J. Magn. Magn. Mater. **322**, 3240 (2010)
19. A. Bhaskar, S.R. Murthy, J. Mater. Sci. Mater. Electron. **24**, 3292 (2013)
20. P.P. Hankare, N.M. Patil, R.P. Patil, D.R. Patil, S.D. Delekar, J. Mater. Sci. Mater. Electron. **24**, 4028 (2013)
21. S.P. Yadav, S.S. Shinde, A.A. Kadam, K.Y. Rajpure, J. Alloy Compd. **555**, 330 (2013)
22. P. Dhak, D. Dhak, M. Das, P. Pramanik, J. Mater. Sci. Mater. Electron. **22**, 1750 (2011)
23. M.I. Klinger, J. Phys. C Solid State Phys. **8**, 3595 (1975)
24. U. Ghazanfar, S.A. Siddiqi, G. Abbas, Mater. Sci. Eng. B **118**, 132 (2005)
25. M.A. Khan, M.U. Islam, M. Ishaque, I.Z. Rahman, Ceram. Int. **37**, 2519 (2011)
26. M. Hashim, S. Alimuddin, B. Kumar, H. Koo, S.E. Shirsath, E.M. Mohammed, J. Shah, R.K. Kotnala, H.K. Choi, H. Chung, R. Kumar, J. Alloy. Compd. **11**, 518 (2012)
27. J.C. Maxwell, *Electricity and magnetism* (Oxford University Press, New York, 1973)
28. K.W. Wagner, Arch. Elektrotechnol. **2**, 371 (1914)
29. C.G. Koop, Phys. Rev. **83**, 121 (1951)
30. E.J.W. Verwey, J.H. de Boer, Rec. Trav. Chim. Pays-Bas. **55**, 531 (1936)
31. M. Younas, M. Nadeem, M. Atif, R. Grossinger, J. Appl. Phys. **109**, 093704 (2011)
32. B. Senthilkumar, R.K. Selvan, P. Vinothbabu, I. Perelshtein, A. Gedanken, Mater. Chem. Phys. **130**, 285 (2011)
33. S. Mahalakshmi, K.S. Manja, J. Alloy Compd. **457**, 522 (2008)
34. B. Baruwati, K.M. Reddy, S.V. Manorama, R.K. Singh, O. Parkash, Appl. Phys. Lett. **85**, 2833 (2004)
35. K.K. Patankar, S.S. Joshi, B.K. Chougule, Phys. Lett. A **346**, 337 (2005)
36. I.G. Austin, N.F. Mott, Adv. Phys. **18**, 41 (1969)
37. M.A.E. Hiti, J. Phys. D Appl. Phys. **29**, 501 (1996)
38. R.P. Mahajan, K.K. Patankar, M.B. Kothale, S.A. Patil, Bull. Mater. Sci. **23**, 273 (2000)
39. E. Barsoukov, J.R. Macdonald, *Impedance spectroscopy—theory, experiment and applications* (Wiley, New Jersey, 2005)
40. R.K. Kotnala, M.A. Dar, V. Verma, A.P. Singh, W.A. Siddiqui, J. Magn. Magn. Mater. **322**, 3714 (2010)
41. W. Chen, W. Zhu, O.K. Tan, X.F. Chen, J. Appl. Phys. **108**, 034101 (2010)
42. S.S. Shinde, A.V. Moholkar, J.H. Kim, K.Y. Rajpure, Surf. Coat. Technol. **205**, 3567 (2011)
43. A. Srivastava, A. Garg, F.D. Morrison, J. Appl. Phys. **105**, 054103 (2009)
44. S.S. Shinde, K.Y. Rajpure, J. Solid State Chem. **183**, 2886 (2010)
45. H. Anwar, A. Maqsood, J. Magn. Magn. Mater. **333**, 46 (2013)
46. O. Subohi, L. Shastri, G.S. Kumar, M.M. Malik, R. Kurchania, Mater. Res. Bull. **49**, 651 (2014)
47. M.V. Nikolic, M.P. Slankamenac, N. Nikolic, D.L. Sekulic, O.S. Aleksic, M. Mitric, T. Ivetic, V.B. Pavlovic, P.M. Nikolic, Sci. Sinter. **44**, 307 (2012)
48. A. S Bondarenko, G. A. Ragoisha, EIS Spectrum Analyser (a freeware program for analysis and simulation of impedance spectra), http://www.abc.chemistry.bsu.by/vi/analyser/
49. K.M. Batoo, F.A. Mir, M.S.A. El-sadek, M.D. Shahabuddin, N. Ahmed, J. Nanopart. Res. **15**, 2067 (2013)
50. D. Arcos, M. Vazquez, R. Valenzuela, M. Vallet-Regi, J. Mater. Res. **14**, 861 (1999)
51. A.M.M. Farea, S. Kumar, K.M. Batoo, A. Yousef, C.G. Lee, Alimuddin, J. Alloy. Compd. **464**, 361 (2008)
52. R.K. Kotnala, R. Gupta, J. Shah, M.A. Dar, J. Sol-Gel. Sci. Technol. **64**, 149 (2012)
53. I.T. Rabinkin, Z.I. Novikova, *Ferrites* (Izv Acad. Nauk USSR, Minsk, 1960)
54. M. Ajmal, A. Maqsood, Mater. Sci. Eng. B **139**, 164 (2007)

Materials Research Bulletin 63 (2015) 80–87

Contents lists available at ScienceDirect

Materials Research Bulletin

journal homepage: www.elsevier.com/locate/matresbu

Study of structural and optical properties of YAG and Nd:YAG single crystals

S. Kostić [a], Z.Ž. Lazarević [a,*], V. Radojević [b], A. Milutinović [a], M. Romčević [a], N.Ž. Romčević [a], A. Valčić [b]

[a] Institute of Physics, University of Belgrade, P.O. Box 68, Pregrevica 118, Zemun, Belgrade, Serbia
[b] Faculty of Technology and Metallurgy, University of Belgrade, Belgrade, Serbia

ARTICLE INFO

Article history:
Received 22 May 2014
Received in revised form 9 October 2014
Accepted 14 November 2014
Available online 18 November 2014

Keywords:
Single crystal
Nd:YAG
Optical materials
Crystal growth

ABSTRACT

Yttrium aluminum garnet (YAG, $Y_3Al_5O_{12}$) and yttrium aluminum garnet doped with neodymium (Nd:YAG) single crystals were grown by the Czochralski technique. The critical diameter and the critical rate of rotation were calculated. Suitable polishing and etching solutions were determined. As a result of our experiments, the transparent YAG and pale pink Nd:YAG single crystals were produced. The obtained crystals were studied by X-ray diffraction, Raman and IR spectroscopy. The crystal structure was confirmed by XRD. The 15 Raman and 17 IR modes were observed. The Raman and IR spectroscopy results are in accordance with X-ray diffraction analysis. The obtained YAG and Nd:YAG single crystals were without core and of good optical quality. The absence of a core was confirmed by viewing polished crystal slices. Also, it is important to emphasize that the obtained Nd:YAG single crystal has a concentration of 0.8 wt.% Nd^{3+} that is characteristic for laser materials.

1. Introduction

Oxide materials are very interesting and they are being used more and more. They are used as laser materials, in nonlinear optics, acousto optics, for memorizing optical data and magnetic memories, wave guides, etc. [1,2].

Yttrium aluminum garnet (YAG, $Y_3Al_5O_{12}$) and yttrium aluminum garnet doped with neodymium (Nd:YAG) are the most famous kind of oxide crystals widely used as the active medium in solid state lasers [3,4]. The dopant, triply ionized neodymium, Nd (III), typically replaces a small fraction of the yttrium ions in the host crystal structure of the yttrium aluminum garnet. It is the neodymium ion which provides the leasing activity in the crystal. Nd:YAG lasers typically emit light with a wavelength of 1064 nm, in the infrared. However, there are also transitions near 940, 1120, 1320, and 1440 nm. Nd:YAG lasers operate in both pulsed and continuous mode. Nd:YAG crystals are usually grown by the conventional Czochralski (CZ) technique [5–7]. Besides that, for miniature laser sources Nd:YAG can by the micro-pulling-down technique and by the crucibles laser heating pedestal method [8].

The Czochralski technique has great advantages for growth of the high quality and large size YAG and Nd:YAG single crystals for usage as medium – in high power efficient lasers. A stable and equilibrant process of crystal growth with CZ technique is necessarily controlled by many different growth parameters. Each fluctuation in growth parameters could make the system unstable and directly affect on the crystal quality [9,10]. The temperature gradient adjusted by thermal shields, growth atmosphere and cooling system is the most important growth parameter in the furnace. This parameter influences the crystal perfection by effect on the fluid dynamic and kinetics of a growing crystal [5]. On the other hand, an improper thermal gradient during the growth cause the change of the convexity of solid–liquid interface, reduce/enlarge the size of central core, create large thermal stress and cracks in the crystal [5,9]. The temperature gradient has to be stable during the growth of the crystal. In fact, instability of the temperature gradient leads to increase in the fluctuations of growth rate. Constitutional undercooling may occur due to the fluctuations and cause the change of the morphology of the liquid/solid interface [5,13]. High fluctuations of the water flow rate in the cooling system of growth furnace – wall and induction coil, even for short duration, remarkably affect the growth process of oxide crystals. None of the mentioned references has investigated these fluctuations during the growth process particularly. The aim of the current research is experimental investigation of the effect of intensity and time duration of thermal shocks induced by cooling system on the growth process and crystal quality of Nd:YAG grown by CZ technique [14].

* Corresponding author: Tel.: +381 11 37 13 035; fax: +381 11 31 60 531.
E-mail address: lzorica@yahoo.com (Z.Ž. Lazarević).

http://dx.doi.org/10.1016/j.materresbull.2014.11.033

Owing to the specific characteristics of the method of crystal growth from the high temperature melt (~2273 K) and the required characteristics of a YAG crystal, there are a number of factors that can affect the quality of the resulting crystals: constitutional undercooling, thermal stress, temperature fluctuations and the appearance of the flat crystallization front.

Segregation of impurities that may be present in the starting materials (Y_2O_3), or in the materials added as dopants (Nd_2O_3), can cause a positive gradient of undercooling, leading to the appearance of instability forms of the liquid/solid interface.

The occurrence of constitutional undercooling during the growth of YAG crystals, can lead to the appearance of non-stoichiometry composition of the melt. In this case, the excess of added components also causes segregation and leads to the same effects as in the case of present impurities.

The shape of the liquid/solid interface in crystal growth can have an exceptionally large influence on the crystals properties, and the homogeneous distribution of dopant, strains and dislocation concentration greatly depends on it.

YAG crystal structure is a complex cubic structure containing three different oxygen polyhedral (Fig. 1) [14]. Y^{+3} ions occupy dodecahedral sites and Al^{3+} ions are in octahedral and tetrahedral sites in the ratio of 2:3. This arrangement is the consequence of the differences in the ionic radii: O^{-2}(1.4 Å), Y^{+3}(1.281 Å), Al^{3+}(0.51 Å). Since the ionic radii of Y^{+3} ions and ions of rare-earth are relatively close [11,13,15], trivalent ions of rare earth can replace Y^{+3} ions to a certain small degree. The most frequently used is Nd^{+3} (1.323 Å) ion. For laser gain applications, YAG is typically doped with Nd^{3+} at the 0.2–1.4% atomic weight percent. Lower doped material (0.5–0.8%) is better to steady-state laser performance where optical beam quality is important. Concentration of Nd^{3+} in our samples is, as a common for steady-state laser materials, 0.8 wt.% [16]. It is important to point out that the growth of YAG crystals, which contain Nd^{+3} ions, it is very important coefficient of neodymium in the system $Y_{3-x}Nd_xAl_5O_{12}$ melt – $Y_{3-y}Nd_yAl_5O_{12}$ crystal. Due to the differences in ionic radii between Y^{+3} and Nd^{3+} ions, Nd^{3+} ions are difficult to incorporate into the structure and the coefficient segregation is small, K = 0.2 [17].

In addition, it was noted that the effective coefficient of segregation at a certain rate of rotation is equal to the equilibrium, at a growth temperature i.e., that the growth rate and the rotation does not affect the segregation. In order to obtain the desired concentration of Nd^{3+} ions at the beginning of the crystals, it is necessary that the melt has five times the required concentration of Nd^{3+} ions (K = 0.2). The concentration C_s of Nd^{3+} ions along the crystal change the equation:

$$C_s = KC_{10}(1-y)^{k-1} \quad (1)$$

where is: y-crystallized part, C_{10} – the initial concentration of Nd^{3+} ions in the melt.

During the crystals growth process it is possible, according to the Czochralski's method, to influence the shape of the liquid/solid interface through the growth parameters, such as both the growth and the crystal rotation rate, as well as the temperature gradient. It should be certainly mentioned that growth and rotation rates are rather constant, while the temperature distribution in a melt changes during the process of crystal growth, as the amount of the melt decreases. That gradual reduction of the melts depth, requires the change of the stirring conditions in order to keep stable temperature distribution when lower depths are involved.

Although the seed orientation was , it was noticed that in the initial state of the process of YAG crystal growth, on the liquid/solid interface were formed some (211) and (110) facets. The mechanism of crystal growth can differ depending on whether facets exist on central crystal spots or not. Those spots are characterized by different lattice parameters, thus causing strains in the crystals. The above mentioned reasons require new conditions in which the formation of facets is reduced to the lowest possible degree. Laser rods of high quality can be obtained by cutting crystals large in diameter from those parts that are stress-free. Another approach to this problem involves the establishing of conditions under which the whole liquid/solid interface would be covered by facets. Thus the strains resulting from a difference existing in lattice parameters will be eliminated completely.

To avoid facets formation at the liquid/solid interface it is necessary, according to literature data [18,19], that the rotation rate of a crystal be 150 rpm. But on the other hand such crystals frequently have a high concentration of dislocations.

Other authors are of the opinion [20] that a liquid/solid interface can be completely covered with facets if the rotation rate of a crystal is small (6 rpm). In any case, the rotation rate is not the only factor that has a strong influence on the liquid/solid interface. Such a conclusion can be also made on the basis of the experiments we performed. The most recent investigations (with other crystals) [11,12] proved that a rapid change in the shape of the liquid/solid

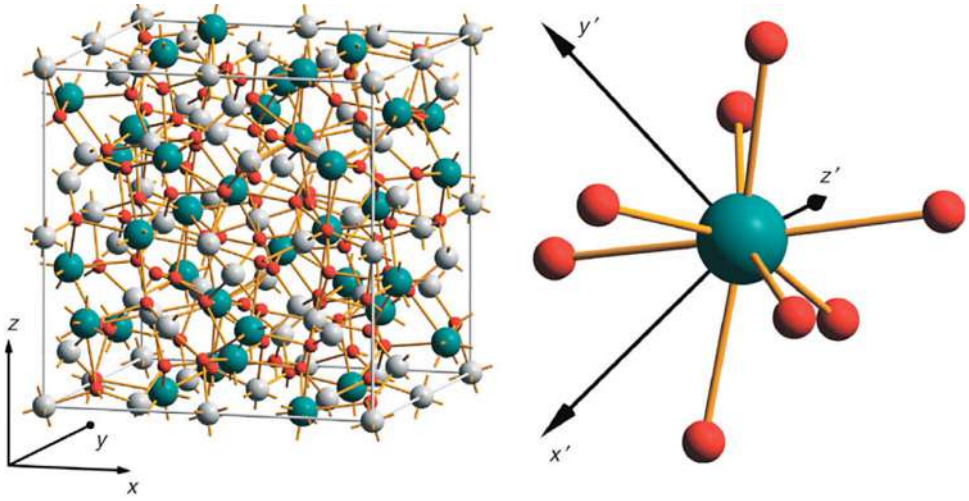

Fig. 1. Unit cell of YAG crystal. Green, white and red sites are occupied by yttrium, aluminium and oxygen, respectively. All together, the unit cell contains eight molecular units $Y_3Al_5O_{12}$. Neodymium occupies yttrium sites substitutionally. The local surrounding of one yttrium site. (For interpretation of the references to color in this figure legend, the reader is referred to the web version of this article.)

interface i.e., inversion, is caused at the very moment when a crystals diameter reaches its critical value for a particular rate of the rotation. This phenomena is the result of changes in the melts movements. At the same time a certain part of a crystal is being remelted and facets are removed. The liquid/solid interface, convex till then, become almost flat with respect to the melt.

Inversion is carried out at the moment when the liquid movements caused by the crystal rotation overcome the natural convexity [21], i.e., when a critical Reynold's number is exceeded. The Reynold's number is as follows:

$$\mathrm{Re} = \frac{\pi \rho D^2 \omega}{2\eta} \tag{2}$$

where is ρ – density of the melt, D – diameter of a crystal, ω – crystal rotation rate and η – viscosity of the melt. Takagi and co-authors [21] established an expression for the diameter of inversion, D_c, which is:

$$D_c = \left(\frac{2}{\pi}\right)^{1/2} \left(\frac{\mathrm{Re}\eta}{\rho}\right)^{1/2} \omega^{-1/2} \tag{3}$$

or

$$D_c \approx \mathrm{K}\omega^{-1/2} \tag{4}$$

This simplified equation is valid only when all parameters of growth remain unchanged. Experimental results show that D_c depends on temperature gradient, growth rate, depth of melt, i.e., diameter of a crucible, and height of meniscus between crystal and melt. D_c grows together with the increase in temperature gradient and decreases with growth rate and rotation. Having used the Grashof's and Reynold's number, Carruthers [22] gave a somewhat more complete equation comprising both the influence of the crucibles dimensions and temperature gradient.

$$D_c = \left(g\alpha \Delta T R^3 \pi^{-2}\right)^{1/4} \omega^{1/2} \tag{5}$$

where is g – gravitation, α – coefficient of thermal expansion of a melt, ΔT – radial difference of temperature in a melt, R – radius of crucible and ω – crystal rotation rate.

Having started from the fact that inversion is determined by Reynold's number, Brice together with Whiffin [23] established the dependence of a critical value $(\mathrm{Re})_c$ on previously mentioned parameters of growth and gave the following equation for the radius of inversion R_c.

$$R_c^2 = \frac{\mathrm{A}G^{1/3}}{\left(1 - R_c^2/R^2\right)\left(1 + \mathrm{B}R_c^2 f\right)} \tag{6}$$

where A and B are constants which are to be experimentally determined, f – growth rate, G – temperature gradient. This equation can be applied only when a melt depth out of which a crystal is pulled, is great. When a melt is shallow the value $(\mathrm{Re})_c$ is higher due to a greater influence of the bottom of the crucible on the mixing process.

In the CZ process, the liquid/solid interface shape is dictated by crystal thermal history. When the interface shape is curved, the thermal field becomes non-uniform along the radial direction, which may result in non-uniformities in mechanical, optical, and electrical properties. Therefore, it is important to keep the interface shape as flat as possible during the single crystal growth. The importance of the interface shape and its role in the single crystal qualities have been emphasized by previous researchers in a review paper published by Dupret and Van Den Bogaert [24]. Control of liquid/solid interface shape is the most important problem in the CZ crystal growth process. Having a high-quality crystal, it is necessary to keep the liquid/solid interface flat or nearly flat which depends on the operating parameters [25]. Numerous research work have been performed to understand the parameters affecting the interface shape and to find out the critical parameters controlling the growth rate at which the interface shape becomes nearly flat. Cockayne et al. [26] determined the interface shape by measuring both the crystal weight and the melt temperature near the interface. They realized that the interface shape is dependent upon the crystal rotation rate. An increase of rotation rate leads to a concave interface with respect to crystal while the convex shape is obtained as a result of low rotation rate. Thus, a lower rotation rate is favorable for obtaining a nearly flat interface. Various researchers studied the effects of different parameters on the shape of crystal interface both numerically and experimentally [27,28]. In almost all these research work, it was found that the rotation rate of the crystal plays a critical role on the liquid/solid interface shape. Kobayashi et al. [29] studied numerically to obtain the critical crystal Reynold's number at which the interface inversion occurs. This phenomenon basically depends on the melt flow structure composed of free and forced convection caused by the crystal rotation rate [30].

The aim of our work was to produce YAG single crystals with and without dopant Nd^{3+} and without a core, the growth parameters and annealing condition investigate, by applying both theoretical and experimental treatment. The structural and optical properties obtained single YAG and Nd:YAG crystals were characterized using XRD, Raman and IR spectroscopy.

2. Experimental

Single YAG and Nd:YAG crystals have been grown using the standard Czochralski technique. Both crystals (Fig. 2) were grown by the Czochralski technique using a MSR 2 crystal puller controlled by a Eurotherm. The atmosphere used was argon. The starting materials were powdered Y_2O_3, Al_2O_3 and Nd_2O_3 (all Koch&Light) all of 4N purity. Powdered ZrO_2 (Koch&Light) of 4N purity was used for isolation. The purity of argon (Tehnogas) was 4N. The iridium crucible (40 mm diameter, 40 mm high) was placed into an alumina vessel surrounded by ZrO_2 wool isolation. Double walls were used to protect the high radiation. To decrease the radial temperature gradient in the melt, alumina was mounted around all the system. The best results were obtained with a pull rate of 2–3 mm h^{-1} for YAG and 1 mm h^{-1} for Nd:YAG crystals

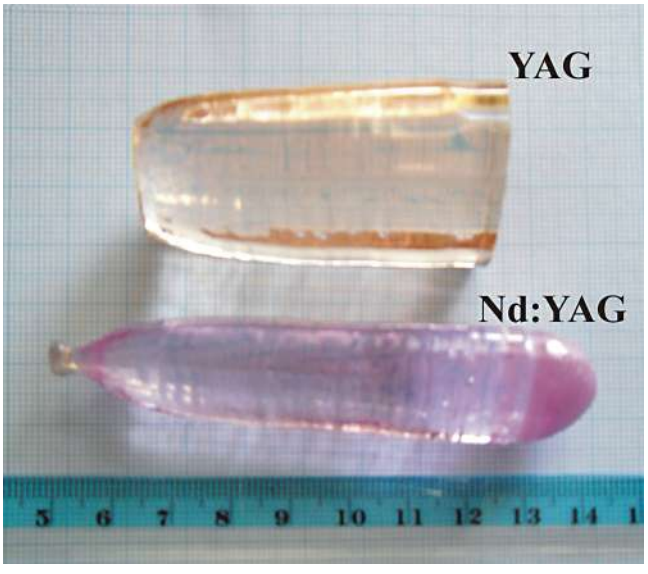

Fig. 2. A view of an obtained: (a) YAG and (b) Nd:YAG single crystals plate.

(Fig. 2). The crystal rotation rates were between 6 and 100 rpm (YAG). The best results were obtained with a crystal rotation of 100 rpm (YAG) and 20 rpm (Nd:YAG). The diameters of crystals were between 10 and 20 mm. The crucible was not rotated during the growth. After the growth run, the crystal boule was cooled at a rate of about 50 K h^{-1} down to room temperature.

Such obtained YAG and Nd:YAG crystals were cut either transversal to the growth axis, or along or parallel to the plane (1 1 0). Then they were polished, smoothed and observed in polarized light.

In order to study the influence of rotation on strains existing in YAG crystal, three series of crystal pulling, of orientation , were performed.

In the first series of experiments, YAG crystals with diameters of about 10 mm were pulled with 3 mm h^{-1} pulling rate. Rotation rate was rapidly changed after a particular crystal length was reached. As with the one crystal, for example, the rotation was changed from 12 to 100 rpm. Within the range of 12–60 rpm no significant influence of rotation on a core has been perceived (Fig. 3). But when the rotation increases to 100 rpm it can be clearly noticed that the core rapidly reduces, and that at that very place some small bubbles appear, while a considerable blurring is noticed.

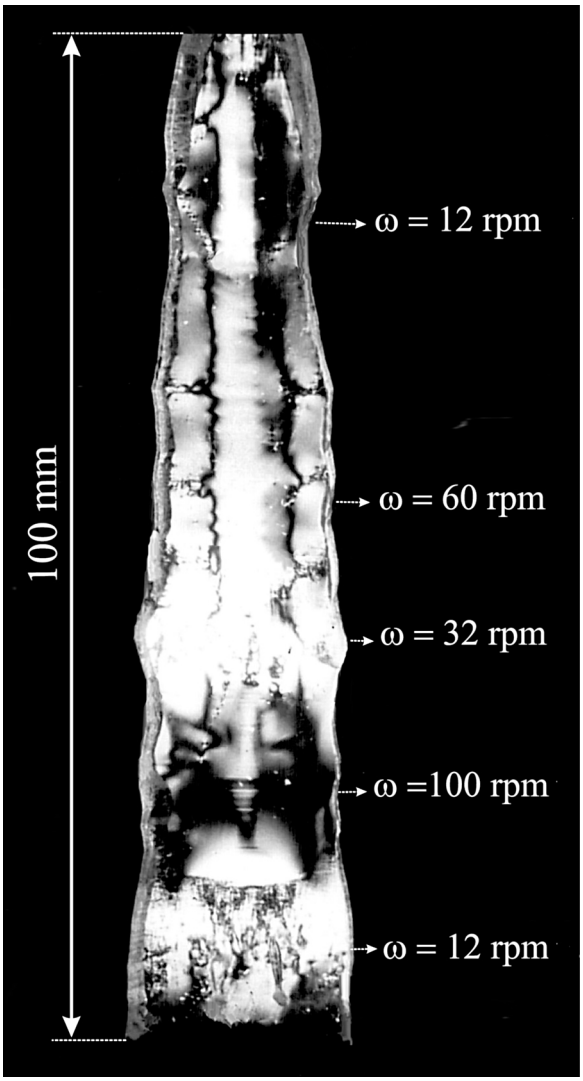

Fig. 3. YAG crystal grown with different rotation rates ω = 12, 60, 32, 100 and 12 rpm.

Rotation of 100 rpm caused melting of the central part of a crystal and a somewhat more rapid growth at the periphery of the same crystal. When rotation is reduced, relative disturbances are far greater as the liquid/solid interface, being almost plain becomes convex with respect to the melt, which causes a rapid increase in growth rate. Similar conclusions can be derived when analyzing the behaviour of other crystals from the same series.

The second group of experiments dealt with crystals, of diameters 15–20 mm, which were pulled at a rate of 2 mm h^{-1}. The rotation during the crystal growth was not changed. Fifteen crystals were pulled with different rotation rates ranging from 6 to 100 rpm.

It can be said on the basis of the results obtained that in crystals rotated at smaller rates (up to 60 rpm) strains, being caused by simultaneous action of two different growth mechanisms, can be noticed (Fig. 4). The core existing in the center of a crystal, which is the result of facet formations, does not essentially depend on rotation rate.The qualitative change appears when a crystal reaches a critical diameter D_c for a particular rotation. The core vanishes under these conditions. It should certainly be pointed out that the core vanishes at the moment when a critical diameter is obtained, but some lesser strains extend along the crystal to a length of about 10 mm. The dependence of type: $D_c = K\omega_c^{-1/2}$ as expected by theoretical postulate, is valid.

In the third series of experiments, the crystals that grew under the same conditions as in second series, were separated from the melt. Thus, we were able to find out immediately the shape of the liquid/solid interface for different rotations and to see the part that was covered with facets. The liquid/solid interface is rather convex with respect to the melt when slow rotations are involved, while it is almost even with faster rotations (90 rpm).

Crystal slices with <111> orientation were cut from the as-grown crystal boule and the slices were subsequently polished on both sides with diamond paste. The mechanically polished slices were chemically polished in liquid H_3PO_4 [15]. Various solutions of H_3PO_4 at different temperatures and for various exposure times were tried for chemical polishing and etching. For chemical polishing, exposure to a concentrated (85%) solution of H_3PO_4 at 603 K (330 °C) for 20 min was confirmed to be suitable. Exposure for 1 h to an 85% solution of H_3PO_4 at 493 K (220 °C) after was found to be a suitable for etching [9,15].

The observations relating to the dislocation were recorded by observing an etched surface of YAG and Nd:YAG crystals, using a Metaval of Carl Zeiss Java metallographic microscope with magnification of 270× and 200×, respectively.

All the obtained crystal YAG plates were observed in polarized light to visualize the presence of a core and/or striations. The absence of a core was confirmed by viewing both polished crystal slices in normal light.

3. Results and discussion

Eq. (5) holds if all other growth parameters are unchanged. Experiments have shown that D_c depends on R,G, melt depth, i.e., the vessel diameter and the meniscus height the crystal and the melt. On the basis of our experimental results it may be concluded that the crystals growing at higher rotation rates, when the inversion of the crystallization front from convex to planar has occurred, do not contain a core and the strains in them are considerably (Figs. 3 and 4).

In the case of YAG crystals with Nd^{3+} ions, after inversion useless crystals with bubbles and opaque regions were obtained. Therefore, investigations were directed at obtaining Nd:YAG crystals with the smallest possible core (1–2 mm).

Investigations that were carried out with YAG not containing Nd^{3+} ions helped us a lot in our studies of YAG containing Nd^{3+} ions.

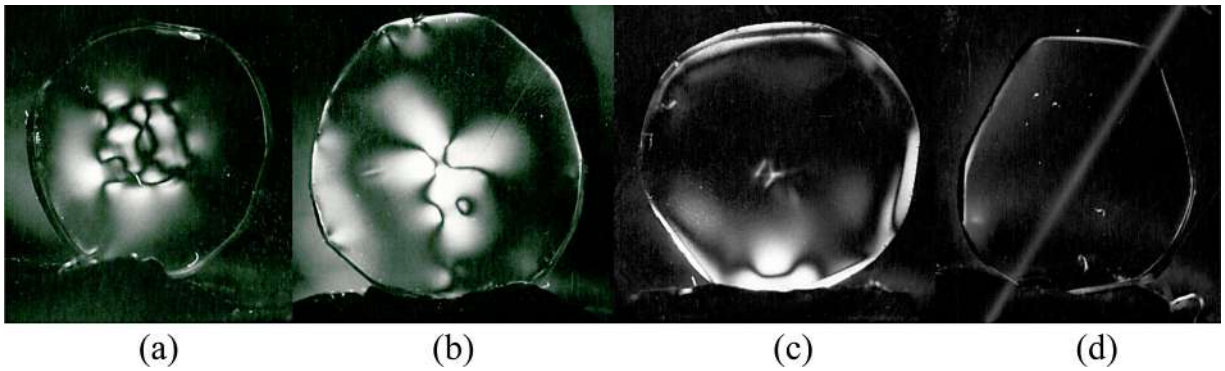

Fig. 4. Cross section of signal YAG crystals grown with different rotation rates under crossed polarizers: (a) 7 rpm, (b) 15 rpm, (c) 60 rpm and (d) 100 rpm.

When investigating YAG containing no Nd^{3+} ions we noticed that after the performed inversion of the liquid/solid interface the crystals obtained did not have cores. On the contrary, when we analyzed YAG containing Nd^{3+} ions we immediately saw that the whole system was far more sensitive, due to the presence of Nd^{3+} ions, to any charge in growth conditions and all our attempts to obtain crystals without a core caused the blurring of the crystals.

In recent years, studies on laser crystals show that YAG crystal has nearly optimal properties that are required of materials for lasers. However, a factor that partially restricts all potential possibilities of this crystal is the difficulty in obtaining single crystals containing a higher concentration of activator (neodymium), while at the same crystal contains all the necessary optical quality. This difficulty is caused by the significant difference of the ionic radii of Nd^{3+} compared to Y^{3+} which in turn makes it difficult to isomorphic substitution of more than 1% (atomic) Nd^{3+} in YAG crystal. Therefore, many studies in order to obtain Nd:YAG crystals oriented in the direction of getting other elements (for example lutenium – Lu), whose ionic radius much smaller than Y^{3+}, so their embedding in the crystal lattice of YAG achieves the effect of compensation between such ions and ions Nd^{3+} and crystal lattice parameter remains approximately 12.01 Å. The main defects of the crystal structure, not counting dislocations, which are the proper conduct of the process of crystal growth may keep a level of 100 dislocations per cm^2 are also inhomogeneous incorporation of Nd^{3+} due to the appearance of (2 1 1) flat in the center of the crystal orientation (1 1 1) zone of the stress in the direction (1 1 0) on the plane (1 1 1) and furrows caused by impurity character of the interface crystal-melt during the process of crystal growth. From the Fig. 5 it can be observed dislocations on YAG and Nd^{3+}:YAG single crystals, respectively. Etch pits have the shape of a three-sided pyramid. Number of dislocations is of the order of 10^4 per cm^2. Most of the crystals were no dislocation.

The works of the oxide crystal material have shown that thermal stress in the crystal, which may be cooled to cause the occurrence of dislocations. These errors reduce the crystallographic and optical perfection of the crystals. Their occurrence can be prevented by using an annealing which thermal stresses can be limited to values that are lower than the limits of the critical stress for a given crystal. The occurrence of flat at the front of crystallization leads to the appearance of stress in a crystal YAG and also uneven incorporation of Nd^{+3} ions. Fluctuations in temperature cause a change in the growth rate which leads to stress in the crystals and uneven incorporation of Nd^{+3} ions. Tests in polarized light showed that the index of refraction in the crystal YAG we received has not the same value of the cross section. Difference in refractive index are due to the crystallization front partially covered with a flatbed and partly not.

The mechanism of the crystal growth is not the same when it is growing with a flat surface (flat across) rise than when roughened surface. This leads to the crystal have parts that have different lattice parameters, the local saturation with oxygen vacancies. Removal of stress annealing may be performed in argon, to the air, in vacuum and the oxidation atmosphere [15,17,31]. Since the transition from brittle to ductile state in YAG at 1350 °C, annealing, we performed in 1600, 1700 and 1800 °C. Annealing was performed in the same unit in which they are drawn crystals. The average speed of raising and lowering the temperature ranged from 1 to

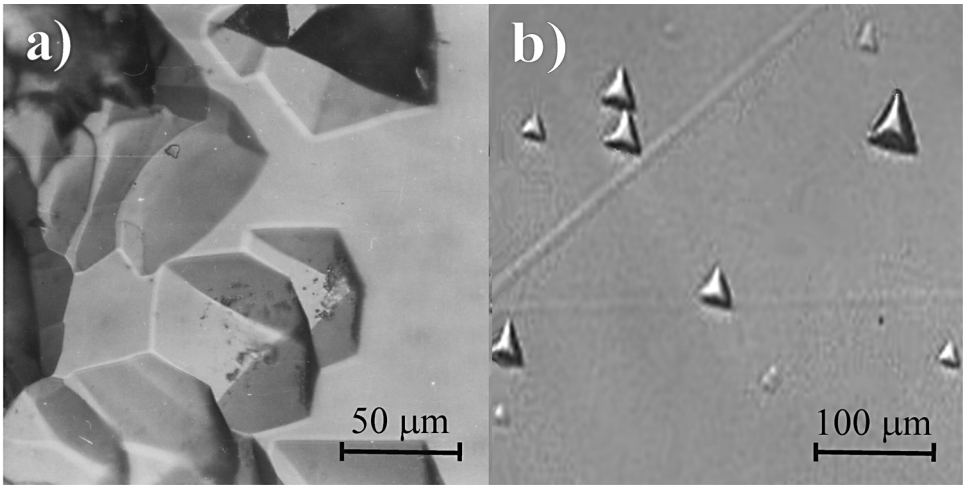

Fig. 5. The microscopic image of the surface YAG Nd:YAG single crystals plate etched with H_3PO_4 in the direction (1 1 1). Magnification of 270× and 200×, respectively.

1.5 °C min^{-1}. After annealing was done observing the polarized light. Based on the obtained data, it was concluded that prolonged heating at 1800 °C able to mitigate the difference in refractive index. When testing centers scattering of light we concluded that if the crystal pull rate of 0.9 mm h^{-1} there is no scattering centers. At speeds of 1–1.3 mm h^{-1} is little shimmer, while at higher speeds shimmer is more intense (refers to Nd: YAG).

The existence of centers of scattering of light due to the presence of very small bubbles, inclusions, etc., in the obtained crystals was carried out using a He–Nd laser beam. Number of dislocation is very small. Frequently there are none. Mosaic blocks were not detected.

3.1. Structural and spectroscopic characterization

The structural properties were obtained using X-ray diffraction analysis of powdered single crystal samples. The X-ray diffraction (XRD) curves for powdered YAG and Nd:YAG is shown in Fig. 6. Diffractions correspond to JCPDS 79-1892. The unit cell of YAG and Nd:YAG is calculated by the least square method using 15 reflections. In Fig. 6, all the reflections correspond to YAG crystals and not any other phase was found. The calculated result reveals that the crystals have body-centered cubic Bravais lattice with space group Ia3d. The lattice parameter for YAG is a = 11.9538 Å, and for Nd:YAG a = 11.9677 Å, what is slightly less than the published data [9,17] (12.011 Å). The cell parameter of Nd:YAG crystal is 0.12% larger than that of YAG crystal. The radius of Nd^{3+} ion (1.249 Å) is larger than the radius of Y^{3+} ion (1.159 Å), and the difference of about 7.8% not only makes the incorporation of Nd^{3+} into the Y^{3+} site of the crystal lattice hard, but also results in larger cell parameter. It causes a shift of diffractions in the spectra of Nd:YAG towards smaller 2θ – angles. Obtained differences are presented in Table 1.

The FWHM of [1 1 1] symmetric rocking curve measured by X-ray double-crystal diffractometry is equal to 0.5183. Compared with research of Chani by Czochralski method (FWHM = 0.381°) [32] and Zhang by the horizontal directional solidification – HDS method (FWHM = 0.2631°) [17], the value of FWHM demonstrates the good crystallinity of the Nd:YAG crystal.

The large number of atoms in the primitive cell leads to 240 (3×80) possible normal modes which can be classified according to the irreducible representation of the O_h group as follows: $3A_{1g} + 5A_{2g} + 8E_g + 14T_{1g} + 14T_{2g} + 5A_{1u} + 5A_{2u} + 10E_u + 18T_{1u} + 16T_{2u}$. The 25 modes having symmetries A_{1g}, E_g, and T_{2g} are Raman active while the 18 having T_{1u} symmetry are IR active [33–35]. The 16 of the 25 Raman active vibrational modes can be observed in the Raman spectrum from 100 to 900 cm^{-1}. The Raman spectrum of rare earth doped YAG compounds can be divided into two different parts: the high frequency region (500–900 cm^{-1}) and the low frequency region (<500 cm^{-1}). The high frequency region accounts to the ν_1 (breathing mode), ν_2 (quadruple) and ν_4 molecular internal modes associated with the (AlO_4) group, whilst the low frequency region is due to: (i) translational motion of the rare earth ions, (ii) rotational and translational motion of the AlO_4 units, and (iii) the ν_3 molecular mode of the AlO_4 [33,34].

The Raman spectra of YAG and Nd:YAG single crystals have been recorded in 100–900 cm^{-1} spectral range at room temperature (Fig. 7). The differences in the Raman spectra of the pure YAG crystal and Nd^{3+} doped YAG crystal are in slightly blue shifting of modes in doped crystal, Table 2, and in the shape of some peaks, also. It is observable that some peaks show a doublet structure, and that some weak modes in the low energy side of regular modes

Table 1
Positions of the diffractions observed in XRD spectra of YAG and Nd:YAG powder and their mutual difference (Δ) caused by doping.

(*hkl*)	YAG 2θ(°)	Nd:YAG 2θ(°)	Δ (°)
−211	18.139	17.99	0.149
−220	21.03	20.81	0.22
−321	27.876	27.75	0.126
−400	29.916	29.68	0.236
−420	33.475	33.367	0.108
−422	36.774	36.65	0.124
−431	38.393	38.222	0.171
−521	41.333	41.155	0.178
−440	42.712	42.69	0.022
−611	46.831	46.6	0.231
−541	–	49.455	–
−631	51.83	51.67	0.16
−444	52.989	52.74	0.249
−640	55.379	55.167	0.212
−552	56.528	56.322	0.206
−642	57.868	57.454	0.414
−651	60.947	60.75	0.197
−800	61.9	61.77	0.13
−820	–	64.055	–
−660	66.146	65.97	0.176
−743	67.426	–	–
−840	70.285	70.023	0.262
−842	72.324	72.078	0.246
−655	73.29	73.09	0.2
−664	74.385	74.056	0.329
−932	77.143	76.949	0.194
−844	–	79.122	–
	a (Å)	a(Å)	
	11.9538	11.9677	

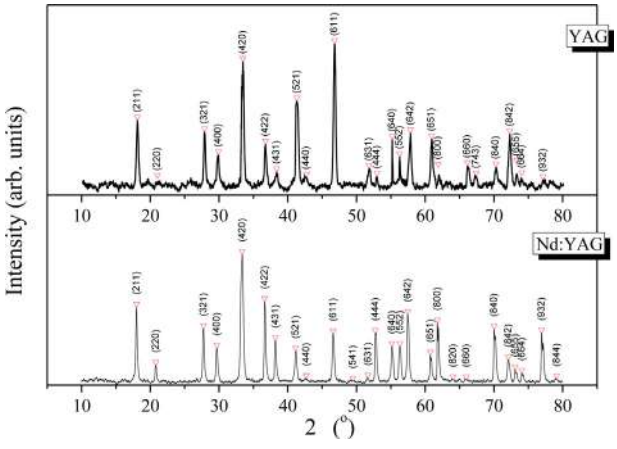

Fig. 6. X-ray diffraction patterns of the: (a) YAG and (b) Nd^{3+}:YAG powdered sample.

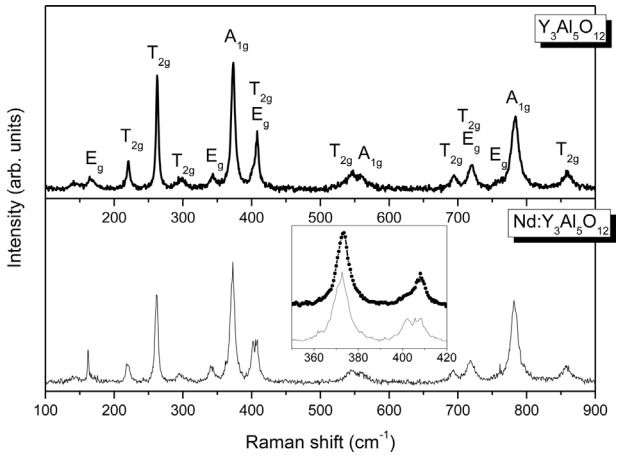

Fig. 7. Raman spectra of YAG and Nd:YAG single crystals at room temperature.

Table 2
Position (cm^{-1}) of the modes in the Raman spectra and symmetries of lines of YAG Nd:YAG single crystals.

Symmetry type	Experimental frequency (cm^{-1})		Vibrations
	YAG	Nd:YAG	
E_g	164	162	Y or Nd
T_{2g}	219	221	Translation
T_{2g}	263	263	Translation + Rotation + $\nu_3(AlO_4)$
T_{2g}	294	295	
E_g	340	343	
A_{1g}	373	373	
T_{2g}	403	409	
E_g	–	407	
T_{2g}	544	548	ν_2 (AlO_4)
A_{1g}	556	557	
T_{2g}	690	693	$\nu_1 + \nu_4$ (AlO_4)
E_g	720	720	
T_{2g}	720	720	
A_{1g}	784	783	
T_{2g}	857	858	

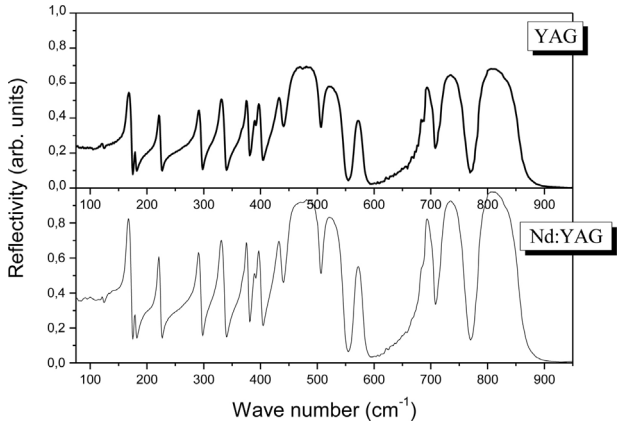

Fig. 8. IR reflectance spectra of YAG and Nd:YAG single crystals at room temperature.

become visible, Fig. 7, insert. These new features in the Raman spectra are not a consequence of increasing disorder, but indicate a regular substituting of Y^{3+} by heavier Nd^{3+}-ions.

According to work by Su et al., on Nd:YAG [36], the peaks at 161, 219, 263, 340, 373, 402 and 407 cm^{-1} (Fig. 7 and Table 2) have been attributed to the translatory motion of the Y^{3+} or Nd^{3+}-ions within the distorted cube with eight oxygen ions at the corners, and also the heavy mixing of the translational, rotational, and ν_3 mode of the (AlO_4) unit. The vibrational modes at 543 and 556 cm^{-1} can be assigned as the ν_2 mode of the (AlO_4) unit. These peaks are the internal stretching vibrations (ν_1 and ν_4) between aluminum ions and oxygen in the tetrahedral (AlO_4) unit.

The Nd^{3+} ions substitute for Y^{3+} in YAG without the need for charge compensation. The larger size of the Nd^{3+} ions results in polyhedral with sides that are greater than those in Al^{3+} polyhedral. That distorts the lattice and thus limits the maximum doping concentration a few atomic weight percent. Concentration of Nd^{3+} in our samples is, as a common for laser materials, 0.8 wt.%. The lattice strains that are introduced by doping affect the properties of the optical spectra.

The reflectivity spectra of YAG and Nd:YAG single crystals were recorded in far-IR and mid-IR region at room temperature (298 K). The IR reflectance spectra of these crystals are shown in Fig. 8. The seventeen of $18T_{1u}$ IR-active modes are visible in the near normal reflectivity spectra of YAG and Nd:YAG crystals, Fig. 8. There are strong metal oxygen vibrations in region 650–800 cm^{-1} which are characteristics of Al—O bond: peaks at 784/854, 719/763 and 691/707 cm^{-1} correspond to asymmetric stretching vibrations in tetrahedral arrangement. Peaks at 566/582, 510/547 and 477/505 cm^{-1} are asymmetric stretching vibrations and 453/483 cm^{-1} is symmetric vibration of Al—O bond in octahedral arrangement of garnet structure. Lower energy peaks correspond to translation and vibration of cations in different coordination – tetrahedral, octahedral and dodecahedral in the case of four lowest modes (Table 3) [37].

Graphical presentation of the Kramers–Krönig analysis shows that with doping of YAG with Nd^{3+}, TO modes undergo a red shift of 1–3 cm^{-1}, what is expected because of greater atomic mass of neodymium (144.2) related to yttrium (88.9) (Fig. 9). The values of these modes are presented in Table 3.

Table 3
Parameters of fit the IR spectra of YAG and Nd:YAG single crystals and the transverse (TO) and the longitudinal (LO) frequencies values obtained from Kramers–Krönig analysis (peak positions ε_2 and σ).

YAG TO/LO wave number (cm^{-1})	Nd:YAG TO wave number (cm^{-1})	Vibrations
122/122.6	122	$T(+T_d)$ transl. of tetr. and dodecah. cation
165/173	163	T_d transl. of dodecah. cation
180/180	178	$T_d(+T)$ transl. of tetr. and dodecah. cation
221/225	219	T_d transl. of dodecah. cation (translations of cations in YO_3 and AlO_4)
291/296	289	T_0
327/338	328	T transl of tetrah. cation
375/380	374	R libr. of tetrah.
390/392	389	T_0 transl. of octah.
396/402	395	R libr. of tetrah.
432/438	431	T_0 transl. of octah. (translations + libration of cations in AlO_6 and AlO_4)
453/483	449	ν_2 symmetric
477/505	475	ν_4 symmetric
510/547	509	ν_4
566/582	595	ν_4 (symmetric and asymmetric stretching of Al–O in octahedrons)
691/707	690	ν_3
719/763	717	ν_3
784/854	783	ν_3 (asymmetric stretching of Al–O in tetrahedrons)

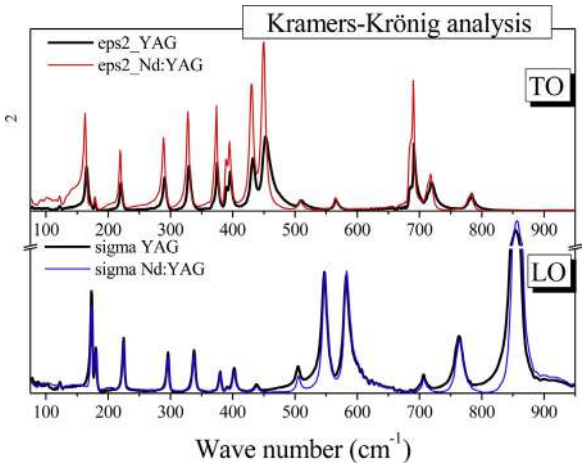

Fig. 9. TO and LO modes of YAG and Nd:YAG single crystals obtained by the Kramers–Krönig analysis.

4. Conclusions

In this paper, we used the Czochralski method to obtain good quality YAG and Nd:YAG crystals. The investigations were based on the growth mechanisms and the shape of the liquid/solid interface on the crystal properties and incorporation of Nd^{3+} ions. The obtained single YAG and Nd:YAG crystals were studied by use of X-ray diffraction, Raman and IR spectroscopy. There are strong metal oxygen vibrations in region 650–800 cm^{-1} which are characteristics of Al—O bond: peaks at 784/854, 719/763 and 691/707 cm^{-1} correspond to asymmetric stretching vibrations in tetrahedral arrangement. Peaks at 566/582, 510/547 and 477/505 cm^{-1} are asymmetric stretching vibrations and 453/483 cm^{-1} is symmetric vibration of Al—O bond in octahedral arrangement of garnet structure. Lower energy peaks correspond to translation and libration of cations in different coordinations – tetrahedral, octahedral and dodecahedral in the case of the lowest modes.

Acknowledgments

This research was financially supported by the Ministry of Education, Science and Technological Development of the Republic of Serbia through Project No. III45003.

References

[1] D. Jun, D. Peizhen, X. Jun, J. Cryst. Growth 203 (1999) 163–167.
[2] A.K. Pradhan, K. Zhang, G.B. Loutts, Mater. Res. Bull. 39 (2004) 1291–1298.
[3] M. Yadegari, M. Asadian, H. Saeedi, Y. Khodaei, N. Mirzaei, J. Cryst. Growth 367 (2013) 57–61.
[4] M. Katsurayama, Y. Anzai, A. Sugiyama, M. Kokie, Y. Kato, J. Cryst. Growth 229 (2001) 193–198.
[5] H. Saeedi, M. Yadegari, S. Enayati, M. Asadian, M. Shojaee, Y. Khodaei, N. Mirzaei, I. Mashayekhi Asl, J. Cryst. Growth 363 (2013) 171–175.
[6] M.H. Tavakoli, E. Mohammad-Manesh, S. Omid, Cryst. Res. Technol. 45 (2010) 1117–1122.
[7] C. Belouet, J. Cryst. Growth 15 (1972) 188–194.
[8] J.H. Mun, A. Novoselov, A. Yoshikawa, G. Boulon, T. Fukuda, Mater. Res. Bull. 40 (2005) 1235–1243.
[9] A. Golubovic, S. Nikolic, R. Gajic, S. Djuric, A. Valcic, J. Serb. Chem. Soc. 67 (2002) 291–300.
[10] H. Saeedi, M. Asadian, Sh. Enayati, N. Mirzaei, Cryst. Res. Techn. 46 (2011) 1229–1234.
[11] Z.Ž. Lazarević, P. Mihailović, S. Kostić, M.J. Romčević, M. Mitrić, S. Petričević, J. Radunović, M. Petrović-Damjanović, M. Gilić, N.Ž. Romčević, Opt. Mater. 34 (2012) 1849–1859.
[12] Z. Lazarević, S. Kostić, V. Radojević, M. Romčević, M. Gilić, M. Petrović-Damjanović, N. Romčević, Physica Scripta T157 (2013) 14046.
[13] E. Kanchanavaleerat, D. Cochet-Muchy, M. Kokta, J. Stone-Sundberg, Opt. Mater. 26 (2004) 337–341.
[14] R. Kolesov, K. Xia, R. Reuter, R. Stöhr, A. Zappe, J. Meijer, P.R. Hemmer, J. Wrachtrup, Nat. Commun. 3 (2012) 1029, doi:http://dx.doi.org/10.1038/ncomms2034.
[15] Y. Peizhi, D. Peiyhen, Y. Yhiwen, T. Yulian, J. Cryst. Growth 218 (2000) 87–92.
[16] A. Golubovic, S. Nikolic, R. Gajic, Z. Dohcevic-Mitrovic, A. Valcic, Metalurgija 10 (2004) 363–370.
[17] M. Zhang, H. Guo, J. Han, H. Zhang, C. Xu, J. Cryst. Growth 340 (2012) 130–134.
[18] B. Cockayne, J.M. Roslington, A.W. Vere, J. Mater. Sci. 8 (1973) 382–384.
[19] B. Cockayne, J. Cryst. Growth 3–4 (1968) 60–70.
[20] C. Belouet, J. Cryst. Growth 15 (1972) 188–194.
[21] K. Takagi, T. Fukazawa, M. Ishii, J. Cryst. Growth 32 (1976) 89–94.
[22] J.R. Carruthers, J. Cryst. Growth 36 (1976) 212–214.
[23] J.C. Brice, P.A.C. Whiffin, J. Cryst. Growth 38 (1977) 245–248.
[24] F. Dupret, N. Van den Bogaert, in: D.T.J. Hurle (Ed.), Handbook of Crystal Growth, Elsevier, North-Holland, Amsterdam, 1994, pp. 875.
[25] P.W. Mokruchnikov, Cryst. Res. Technol. 34 (1999) 1169–1173.
[26] B. Cockayne, B. Lent, J.M. Roslington, J. Mater. Sci. 11 (1976) 259–263.
[27] J.H. Jeong, I.S. Kang, J. Cryst. Growth 218 (2000) 294–312.
[28] A. Hirata, M. Tachibana, Y. Okano, T. Fukuda, J. Cryst. Growth 128 (1993) 195–200.
[29] M. Kobayashi, T. Tsukada, M. Hozawa, J. Cryst. Growth 180 (1997) 157–166.
[30] M. Asadian, S.H. Seyedein, M.R. Aboutalebi, A. Maroosi, J. Cryst. Growth 311 (2009) 342–348.
[31] M. Świrkowicz, M. Skórczakowski, J. Jabczyński, A. Bajor, E. Tymicki, B. Kaczmarek, T. Lukasiewicz, Opto-Electron. Rev. 13 (2005) 213–220.
[32] V.L. Chani, A. Yoshikawa, Y. Kuwano, J. Cryst. Growth 204 (1999) 155–162.
[33] J.P. Hurrell, P.S. Porto, I.F. Chang, S. Mitra, R.P. Bauman, Phys. Rev. 173 (1965) 173–851.
[34] Y.F. Chen, P.K. Lim, S.J. Lim, Y.J. Yang, L.J. Hu, H.P. Chiang, W.S. Tse, J. Raman Spectrosc. 34 (2003) 882–885.
[35] A. Lukowiak, R.J. Wiglusz, M. Maczka, P. Gluchowski, W. Strek, Chem. Phys. Lett. 494 (2010) 279–283.
[36] J. Su, Q. Zhang, S. Yin, D. Sun, S. Shao, Spectrosc. Spect. Anal. 29 (2009) 1577–1580.
[37] A.M. Hofmeister, K.R. Campbell, J. Appl. Phys. 72 (1992) 638–646.

Materials Research Bulletin 63 (2015) 239–247

Contents lists available at ScienceDirect

Materials Research Bulletin

journal homepage: www.elsevier.com/locate/matresbu

Spectroscopy investigation of nanostructured nickel–zinc ferrite obtained by mechanochemical synthesis

Zorica Ž. Lazarević [a,*], Aleksandra N. Milutinović [a], Čedomir D. Jovalekić [b], Valentin N. Ivanovski [c], Nina Daneu [d], Ivan Mađarević [c], Nebojša Ž. Romčević [a]

[a] Institute of Physics, University of Belgrade, P.O. Box 68, Pregrevica 118, Zemun, Belgrade, Serbia
[b] The Institute for Multidisciplinary Research, University of Belgrade, Kneza Višeslava 1, Belgrade, Serbia
[c] Institute of Nuclear Sciences Vinča, University of Belgrade, P.O. Box 522, 11001 Belgrade, Serbia
[d] Department for Nanostructured Materials, Jožef Stefan Institute, Ljubljana, Slovenia

ARTICLE INFO

Article history:
Received 18 July 2014
Received in revised form 21 November 2014
Accepted 2 December 2014
Available online 4 December 2014

Keywords:
A. Magnetic materials
C. Infrared spectroscopy
C. Mössbauer spectroscopy
C. Raman spectroscopy
C. X-ray diffraction

ABSTRACT

Nano crystalline samples of nickel–zinc ferrite, $Ni_{0.5}Zn_{0.5}Fe_2O_4$ were prepared by mechanochemical route in a planetary ball mill starting from two mixtures of the appropriate quantities of the powders: case (1) oxide powders: NiO, ZnO and α-Fe_2O_3 in one case, and in the second case (2) hydroxide powders: $Ni(OH)_2$, $Zn(OH)_2$ and $Fe(OH)_3$. In order to monitor the progress of chemical reaction and confirm phase formation, powder samples obtained after 5 h and 10 h of milling were characterized by X-ray diffraction (XRD), transmission electron microscopy (TEM), Raman, IR and Mössbauer spectroscopy. It is shown that the soft mechanochemical method, *i.e.* mechanochemical activation of hydroxides, produces high quality single phase $Ni_{0.5}Zn_{0.5}Fe_2O_4$ samples in much more efficient way. From the IR spectroscopy of single phase samples it is obvious that energy of modes depends on the ratio of cations. The deconvolution of Raman spectra allows to separate contributions of different cations to a particular type of vibration and to estimate the degree of inversion.

1. Introduction

The ideal crystal structure of cubic spinel ferrites $M^{2+}Fe^{3+}{}_2O^{2-}{}_4$ (M=Mg, Mn, Fe, Co, Ni, Zn) has a face centered cubic unit cell of 32 oxygen anions with cations in 24 of possible 96 interstitial sites: 8 tetrahedral (A-sites) (1/8 of the total tetrahedral sites number) and 16 octahedral [B-sites] (1/2 of total number) [1,2]. Cations Fe^{3+} and M^{2+}, could be arranged in both sites: $(M^{2+}{}_{1-\delta}Fe^{3+}{}_{\delta})[M^{2+}{}_{\delta}Fe^{3+}{}_{2-\delta}]O^{2-}{}_4$ and, therefore, ferrites are classified according to cations degree of inversion δ (positioning between normal ($\delta=0$) and inverse ($\delta=1$) extreme patterns). The space group symmetry of normal cubic spinels is *Fd3m* [3]. The most of cubic ferrites at the nanosized scale have partially inverse (or "mixed") structure. Cubic ferrites may also contain a mixture of divalent metal ions: $M1_{1-x}M2_xFe_2O_4$. These quaternary compounds have interesting magnetic and magnetooptical properties that depend on the chemical composition (x), but are considerably affected by the cation distribution δ, also.

Among quaternary cubic spinel ferrites, nickel–zinc ferrites (NZF) are possibly the most important because they are extensively used as soft magnetic materials for applications in the field of telecommunications. NZF are used for antenna rods, loading coils, microwave devices, core material for power transformers etc. due to their high electrical resistivity, high saturation magnetization, high effective permeability in combination with low magnetic coercivity and low eddy current loss [4–7].

The zinc concentration and distribution among A and B sites in a NZF has a crucial influence on the material's microstructure, dielectric and magnetic properties [8]. It was referred that nano crystalline $Ni_{1-x}Zn_xFe_2O_4$ was prepared by ball milling of oxide mixture [9,10], by co-precipitation method [11], solid-state reaction [8], by thermal decomposition/combustion [12], citrate precursor [13], citrate gel method [14], sol–gel method [15,16]. To the best of our knowledge it is not referred on soft mechanochemical method of the NZF nano powder synthesis.

The aim of this work was the synthesis of nanosized nickel–zinc ferrite by ball milling of two different starting powder mixtures: (1) oxide mixture and (2) hydroxide mixture under the same conditions. The efficiencies of mechanochemical activating in these two cases, are compared. The "conventional mechanochemical route" hereinafter will mean a mechanochemical activating of

* Corresponding author. Tel.: +381 11 37 13 035; fax: +381 11 3160 531.
E-mail address: lzorica@yahoo.com (Z.Ž. Lazarević).

http://dx.doi.org/10.1016/j.materresbull.2014.12.005
0025-5408/

oxide mixture. According to Avvakumov et al. [17], the phrase "soft mechanochemical route" will be used for the reaction of hydroxides. Progress of the reaction and characterization of NZF nano powder samples are investigated by XRD, TEM, Raman, IR and Mössbauer spectroscopy.

It was shown that the high quality single phase $Ni_{0.5}Zn_{0.5}Fe_2O_4$ samples can be produced by soft mechanochemical method in more efficient way. The obtained single phase samples were analysed by Raman and IR spectroscopy with particular attention to origin of the observed modes.

2. Experimental procedures

Starting materials for the conventional and soft mechanochemical synthesis of $Ni_{0.5}Zn_{0.5}Fe_2O_4$ samples were: Merck oxides NiO, ZnO and Fe_2O_3 with 99% purity and Merck zinc and nickel hydroxides with 95% purity. Ferric-hydroxide was made in laboratory. NaOH solution (25% mass), made from 99% purity NaOH (Merck) was added to the $FeCl_3$ solution (25% mass), made from 99% purity $FeCl_3 \times 6H_2O$ (Merck) [18]. Obtained hydrated ferric-hydroxide ($Fe(OH)_3 \times nH_2O$) in the form of dark brown precipitate was filtrated, washed with large amounts of water and dried in a vacuum dessicator. Before milling, the $Fe(OH)_3 \times nH_2O$ powder was heated at 105 °C for 24 h. The material prepared in this way had 99.5% $Fe(OH)_3$. It was confirmed by potentiometric redox titration.

Mechanochemical synthesis was performed in air atmosphere in planetary ball mill Fritsch Pulverisette 5. Balls-to-powder mass ratio was 20:1. The angular velocity of the supporting disc and vial was 32 and 40 rad s^{-1}, respectively. The powders obtained after milling were pressed into disc shaped samples with thickness of 2.0 mm and diameter 8.0 mm.

For XRD analysis the X-ray diffractometer, Model Philips PW 1050, equipped with a PW 1730 generator (40 kV × 20 mA) was used. X-ray source was Ni filtered CoKα radiation of 1.78897 Å. Measurements were done at room temperature in 2θ range of 10–80° with scanning step width of 0.05° and 10 s scanning time per step.

Transmission electron microscopy studies were performed using a JEOL JEM-2100F Microscope (Jeol Inc., Tokyo, Japan) with maximum acceleration voltage of 200 kV equipped with an ultra-high resolution objective lens pole piece having a point-to-point resolution of 0.19 nm, being sufficient to resolve the lattice images of nanoparticles. Electron diffraction patterns (EDP) of nano crystals were recorded to obtain the diffraction rings with specific structure *d*-values and in that way verify the crystal structure.

Electron energy dispersive X-ray spectroscopy (EDS), as part of transmission electron microscopy, was used to examine the chemical composition of selected crystallites.

The Raman scattering measurements of NZF nano powder samples were performed in the backscattering geometry at room temperature in the air using a Jobin-Yvon T64000 triple spectrometer, equipped with a confocal microscope (100x) and a nitrogen-cooled charge coupled device detector (CCD). The spectra have been excited by a 514.5 nm line of Coherent Innova 99 Ar^+–ion laser with an output power of less than 20 mW to avoid local heating due to laser irradiation. Spectra were recorded in the range from 100 cm^{-1} to 800 cm^{-1}

The reflectivity measurements were carried out with a BOMMEM DA-8 spectrometer. A DTGS pyroelectric detector was used to cover the wave number range from 50 cm^{-1} to 700 cm^{-1}.

The Mössbauer spectra were collected at the room temperature in the transmission mode with a constant acceleration, using a ^{57}Co/Rh source. The calibrations of spectra were done by laser. The isomer shift (IS) values were in agreement with values for a standard α-Fe foil at 300 K. Least squares fits were calculated using the SITE option of the WINNORMOS software. Line width corrections were carried out by the transmission integral. The DIST/ISO option of the program, based on the histogram method, was used to perform distributions of Mössbauer's lines [19].

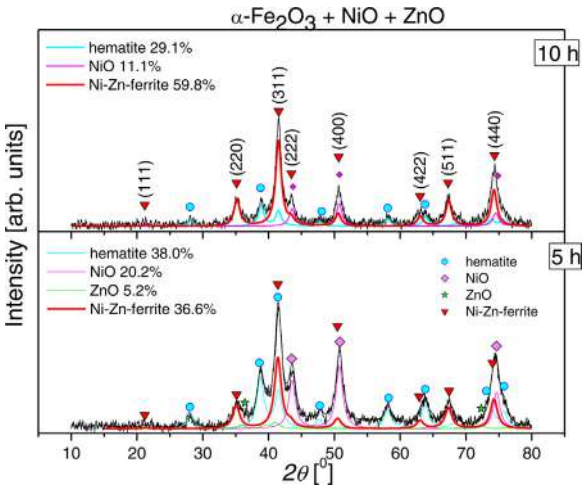

Fig. 1. XRD spectra of the mixture of starting NiO, ZnO and α-Fe_2O_3 powders after milling for 5 h and 10 h.

3. Results and discussion

3.1. Structural characterization

Figs. 1 and 2 show the X-ray diffractograms of partially, or completely, reacted powders after 5 h and 10 h of mechanochemical treatment. In the oxide mixture after 5 h of milling the reaction begins and the spinel peaks become observable in the corresponding diffractogram, Fig. 1. Considering that the starting oxide materials have crystallites with average sizes ~50 nm ZnO to ~90 nm α-Fe_2O_3, there is still a lot of unreacted starting oxides after 5 h, but in the form of smaller nano crystallites. The Rietveld analysis suggests that there are 36.6% of spinel NZF phase, 38.0% of hematite, 20.2% nickel oxide and 5.2% of zinc oxide with crystallites smaller than 13 nm. After 10 h of milling, Fig. 1, in the diffractogram dominate spinel peaks (about 60% of NZF phase), but diffraction peaks of hematite and nickel oxide are still present. A conventional mechanochemical reaction between anhydrous starting oxides

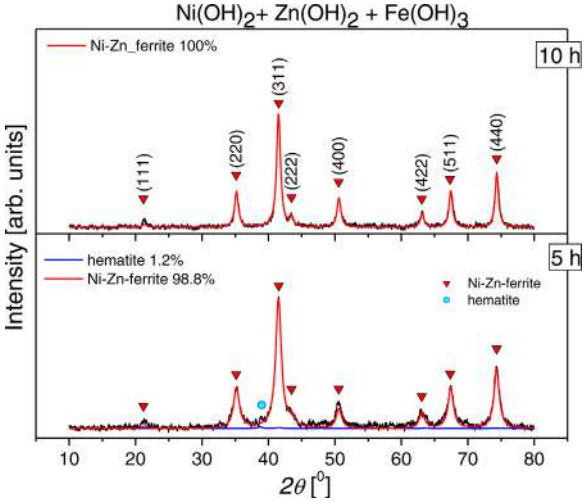

Fig. 2. XRD spectra of the mixture of starting $Ni(OH)_2$, $Zn(OH)_2$ and $Fe(OH)_3$ powders after milling for 5 h and 10 h.

Table 1
Estimated lattice constants, crystallite sizes and cation distributions in NZF phase.

Starting mixture	Milling time (h)	a (Å)	$<L>$ (nm)	Cation distribution
(1) Oxides	5	8.3780	12.6	$(Ni_{0.39}Zn_{0.49}Fe_{0.09})[Ni_{0.12}Zn_{0.02}Fe_{1.72}]O_4$
	10	8.3962	16.2	$(Ni_{0.19}Zn_{0.29}Fe_{0.50})[Ni_{0.24}Zn_{0.14}Fe_{1.50}]O_4$
(2)	5	8.3803	13.8	$(Zn_{0.49}Fe_{0.50})[Ni_{0.50}Zn_{0.02}Fe_{1.50}]O_4$
Hydroxides	10	8.3721	24.1	$(Ni_{0.31}Zn_{0.48}Fe_{0.17})[Ni_{0.22}Zn_{0.04}Fe_{1.86}]O_4$

was used in Refs. [9,10], also. A precise comparison is not possible because milling conditions were not the same (a speed of the vials and ball-to-powder mass ratio), but it was shown that a milling time longer than 10 h is needed for the obtaining a single phase NZF, as evidenced by our experiment, as well.

NZF can be obtained directly from oxide mixture at about 500 °C (this temperature is achieved locally by the collision and friction during the process of the high energy milling):

$$NiO + ZnO + 2\alpha\text{-}Fe_2O_3 \rightarrow 2Ni_{0.5}Zn_{0.5}Fe_2O_4$$

The reaction becomes possible after a certain activation time, as milling reduces the particle size, thoroughly mixes the components, and increases the number of chemically active defect sites [20]. Obviously, due to a great size and hardness of the oxide crystallites, for the formation of pure phase of NZ-ferrite (under the used milling conditions) a more time is required.

The starting hydroxides are amorphous and very reactive which facilitates the chemical reaction [17] and after 5 h of milling the reaction was almost complete, Fig. 2. Rietveld analysis shows that there is 98.8% NZF in the form of small nano crystallites (about 14 nm) and only 1.2% of hematite. After 10 h of milling, Fig. 2, there are no traces of starting materials, *i.e.* any other intermediate reaction product.

In the case of starting hydroxide mixture the synthesis occurred in two stages. The first of the two stages was followed by the evolution of water vapor. For instance, the ferric-hydroxide Fe $(OH)_3$ can be easily transformed in hematite during milling through thermal decomposition [18]:

$$2Fe(OH)_3 \rightarrow \alpha\text{-}Fe_2O_3 + 3H_2O$$

All hydroxides undergo the similar reaction at about 300–350 °C [17]. The second step in the synthesis of NZF is a direct synthesis of the obtained amorphous NiO, ZnO and α-Fe_2O_3 oxides. The extremely small dimensions of the obtained oxide crystallites (amorphous) provide a better adhesion between particles (what is a prerequisite for a faster reaction at lower temperature). A occurrence of substantial amount of water that is formed during soft mechanochemical reactions between hydroxides, in comparison with a much smaller amount of physically adsorbed water that can liberated from pores of oxide crystallites, contributes to better energy transfer from milling media to reacting materials and to acceleration of the formation rate. All stated above are well known advantages of the soft mechanochemical synthesis what is discussed in detail in Refs. [17], [21] and [22].

In Figs. 1 and 2, for 10 h of milling, the positions of NZF diffractions are indicated. Positions of the peaks and their intensities correspond to the reference PCPDFWIN data (PDF #52-0278) for $Ni_{0.5}Zn_{0.5}Fe_2O_4$-spinel ferrite Bragg reflections. The lattice constant depends not only to chemical composition, but to

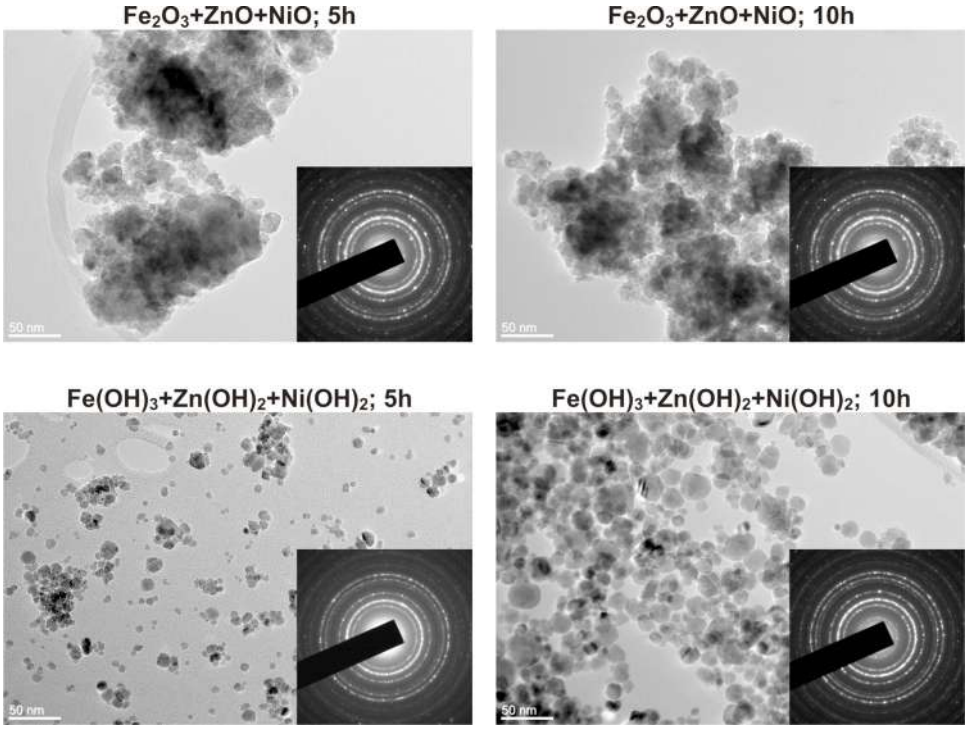

Fig. 3. TEM images with corresponding electron diffraction patterns (EDP *insets* in the lower right corners) of the samples obtained from the mixtures of NiO, ZnO and α-Fe_2O_3 oxide and the mixture of $Ni(OH)_2$, $Zn(OH)_2$ and $Fe(OH)_3$ hydroxide powders for 5 h and 10 h of milling time.

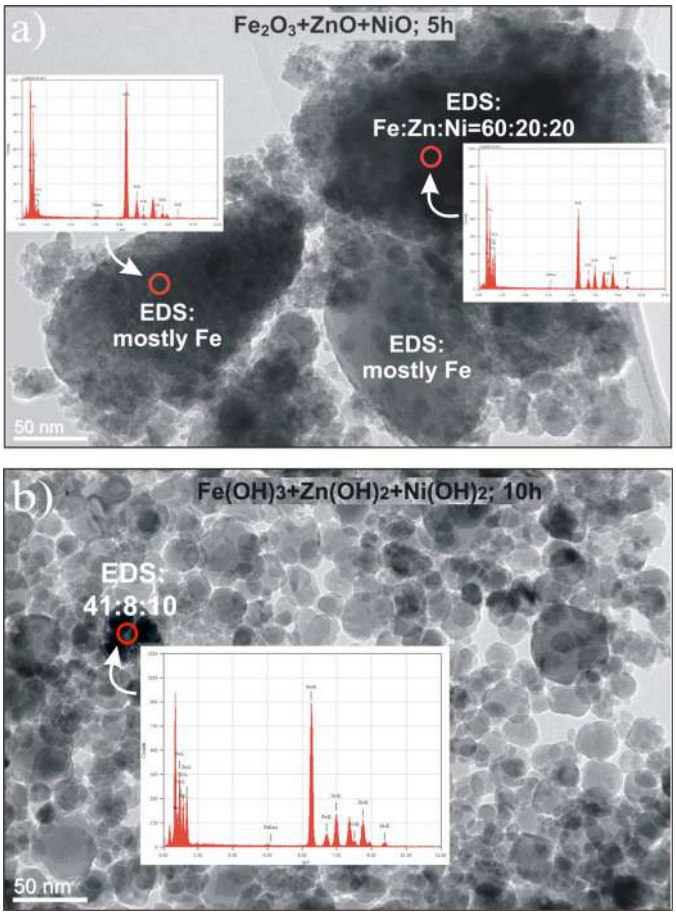

Fig. 4. TEM images with corresponding EDS of selected grains in the case of (a) a sample obtained after 5 h milling of starting oxides and (b) a single-phase sample obtained after 10 h milling of starting hydroxides.

the crystallite size and cation distribution, also. The lattice constants of obtained NZF (a), average crystallite sizes ($<L>$) in various samples and the distribution of cations over tetrahedral and octahedral sites, which gives the best fit to observed diffractograms, are estimated by Rietveld refinement. The results are given in Table 1. In the samples originated from oxide mixture a and $<L>$ are calculated for the NZF participation in the mixture. It should be noted that peaks profile in diffractograms of samples obtained by milling of hydroxides for 10 h are fitted by *Pseudo-Voight2* function and for other samples the Lorentz profile was more convenient.

The XRD – analysis of the powder samples obtained after 5 h and 10 h milling of starting mixtures shows that the soft mechanochemical activation (*i.e.* milling of amorphous hydroxides) gives practically pure NZF phase after 5 h. During further milling process the crystallites continue to growth and their cation distribution changes. In the case of the oxide mixture the formation of NZF phase is much slower.

TEM analysis, Fig. 3, revealed that all samples are composed of nanosized particles (around 20 nm). The size of the particles in the samples prepared form oxides is similar after 5 h and 10 h, whereas in the samples prepared from hydroxides, the size of the particles is larger in the 10 h sample. The particles in the oxide samples (5 h and 10 h) have irregular shape and are highly agglomerated, while the particles in the hydroxide samples (5 h and 10 h) are roundish and less agglomerated.

Electron energy dispersive X-ray spectra (EDS) were measured in each sample on several nanosized particles. Obtained spectra

Table 2
Values of characteristic interplanar distances and relative intensities of Debye–Sherrer rings for Ni–Zn-ferrite sample obtained by milling of starting hydroxides for 10 h.

Experimental			Theoretical	Exp./theor.	
Ring no.	(*hkl*)	*d* (nm)	$Ni_{0.5}Zn_{0.5}Fe_2O_4$	Int.	Diff. (%)
1	(1 1 1)	0.4841	0.4860	17	−0.4
2	(2 2 0)	0.2959	0.2964	38	−0.2
3	(3 1 1)	0.2531	0.2524	100	0.3
4	(2 2 2)	0.2412	0.2419	10	−0.3
5	(4 0 0)	0.2093	0.2087	26	0.3
6	(4 2 2)	0.1707	0.1714	25	−0.4
7	(5 1 1)	0.1619	0.1614	33	0.3
8	(4 4 0)	0.1482	0.1483	41	−0.1

illustrate a progress of the reaction in milling powders. In Fig. 4a is a TEM image of a sample obtained after 5 h milling of crystalline oxides with inserted EDS of two selected grains. It is obvious that in this sample a number of large particles of the precursor oxides is present. In Fig. 4b is presented a TEM image of single phase sample obtained after 10 h milling of starting hydroxides with EDS of one chosen grain. The similar chemical composition ratios are achieved in all tested grains of this sample. Large remnant precursor particles were much rarer in the "oxide" sample after 10 h milling, whereas precursor particles were not observed in the samples prepared from hydroxides.

The analysis of electron diffraction patterns (EDP) confirms that after 10 h milling of hydroxides a single phase of NZF is obtained. Table 2 shows experimental and theoretical interplanar distances (d-values) for a single phase sample (see Fig. 5). The corresponding values are not the same to all 4 decimal numbers, but the compliance is good enough to identify the major phase. The result is in agreement with XRD analysis. From Table 2 it is obvious that the values of interplanar distances and relative intensities of Debye–Sherrer rings fit perfectly to the $Ni_{0.5}Zn_{0.5}Fe_2O_4$ phase. Diffraction spots or rings from no other phase are observed.

3.2. Raman and IR spectroscopy

Mechanochemically produced nano powder samples of nickel–zinc ferrite have mixed spinel structure and belongs to $P4_322$

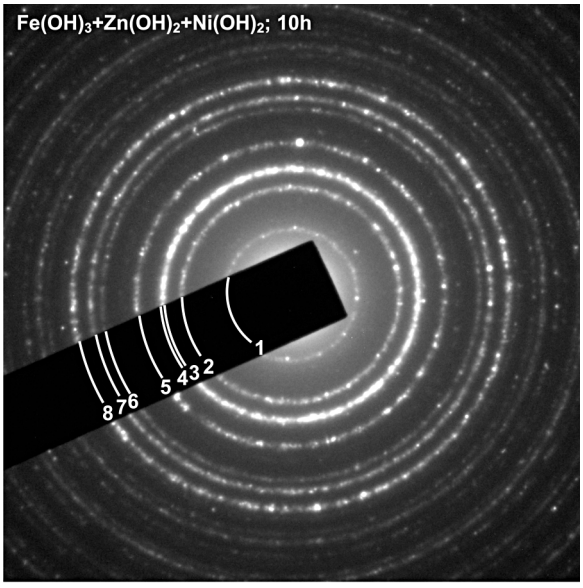

Fig. 5. Electron diffraction patterns (Debye–Sherrer rings) of Ni–Zn-ferrite sample obtained from the mixture of $Ni(OH)_2$, $Zn(OH)_2$ and $Fe(OH)_3$ hydroxides powders by milling for 10 h.

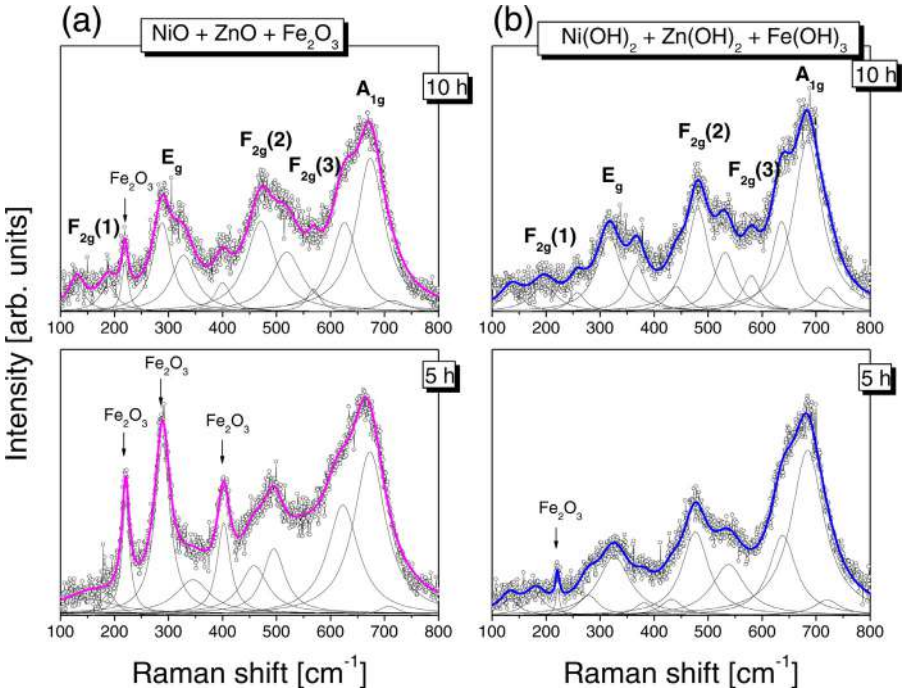

Fig. 6. Raman spectra of the samples obtained from the mixtures of starting (a) NiO, ZnO and α-Fe_2O_3 oxide powders and (b) $Ni(OH)_2$, $Zn(OH)_2$ and $Fe(OH)_3$ hydroxide powders after mechanochemical treatment for 5 h and 10 h. Arrows indicate peaks of unreacted hematite.

tetragonal space group [23]. However, it is usual, for the sake of simplicity, to assign Raman and IR modes as in normal cubic spinel, as the symmetry group is $Fd\bar{3}m$. The factor group analysis predicts 5 Raman active mode: $A_{1g}+E_g+3F_{2g}$ and 4 IR active modes $4F_{1u}$ from the center of Brillouin zone in the normal spinel.

The Raman spectra recorded on the samples obtained during mechanochemical activation of oxide and hydroxide starting mixtures are presented in Fig. 6. The characteristic features of spinel ferrite are recognizable in Raman spectrum already after 5 h of milling oxide mixture, although XRD and TEM suggest that it must be present a lot of unreacted starting oxides in the samples. The strong modes of hematite (indicated by arrows in Fig. 6a) are superposed to spinel modes. Hematite modes are still clearly visible in the oxide sample obtained after 10 h of milling. In the spectrum of the sample made from hydroxides after 5 h of milling a narrow hematite peak testifies that the amount of hematite is very small. After 10 h there is no traces of any other phase in NZF hydroxide sample.

It is obvious that all samples have more than 5 Raman active modes predicted by group theory in the normal spinel structure. Deconvolution of measured spectra allows one to conclude that all complex bands in the spectra are made of individual peaks with the intensities that vary from spectrum to spectrum. In order to determine the origin of the peaks, we have compared the Raman spectra of previously investigated $NiFe_2O_4$ and $ZnFe_2O_4$ [24], with the spectrum of single phase NZF, Fig. 7. On the example of single phase sample of $Ni_{0.5}Zn_{0.5}Fe_2O_4$ obtained by milling of hydroxides for 10 h it is visible that modes originated from vibrating of different cations (in Ni-ferrite, or Zn-ferrite) are reproduced in Raman spectra of mixed NZF.

The high frequency first order mode A_{1g} is due to symmetric stretching of oxygen atoms along Zn—O, Fe—O and Ni—O bonds in the tetrahedral coordination [25]. The mode at 637 cm^{-1} is related with stretching along Zn—O bonds in tetrahedrons [26,27]. The mode at 670 cm^{-1} is related with Fe—O bonds stretching [28], at 689 cm^{-1} with Ni—O bonds [18,29] and a small mode at 721 cm^{-1} corresponds to A_{1g} mode of maghemite, *i.e.* to oscilations of Fe—O in uncompleted tetrahedrons (with oxygen vacancies) [30]. In principle, modes $F_{2g}(2)$ and $F_{2g}(3)$ correspond to the vibrations of the octahedral group, but it seems that components of these modes can hardly be resolved in the Raman spectra of NZF. At about 370 cm^{-1} is the Zn-component of $F_{2g}(2)$ mode, at 480 cm^{-1} is Ni–$F_{2g}(2)$ and between them Zn-component of $F_{2g}(3)$ mode, Fig. 7. These modes are not very strong and the possible fitting error can be too high because of rather high level of noise. For that reason we

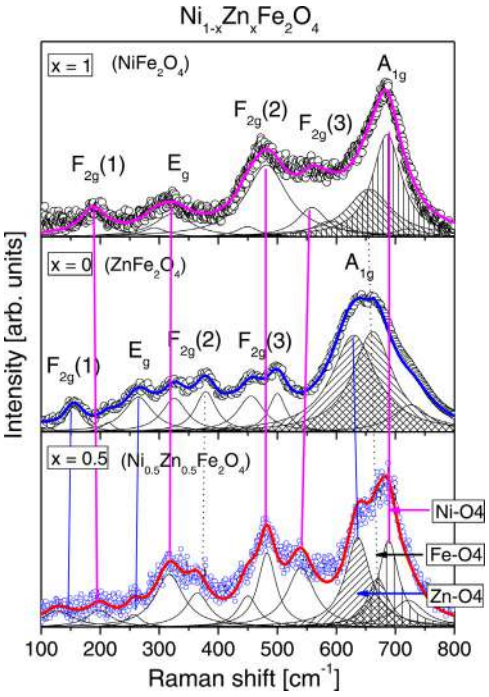

Fig. 7. Raman spectra of the $Ni_{1-x}Zn_xFe_2O_4$, for different values of *x*.

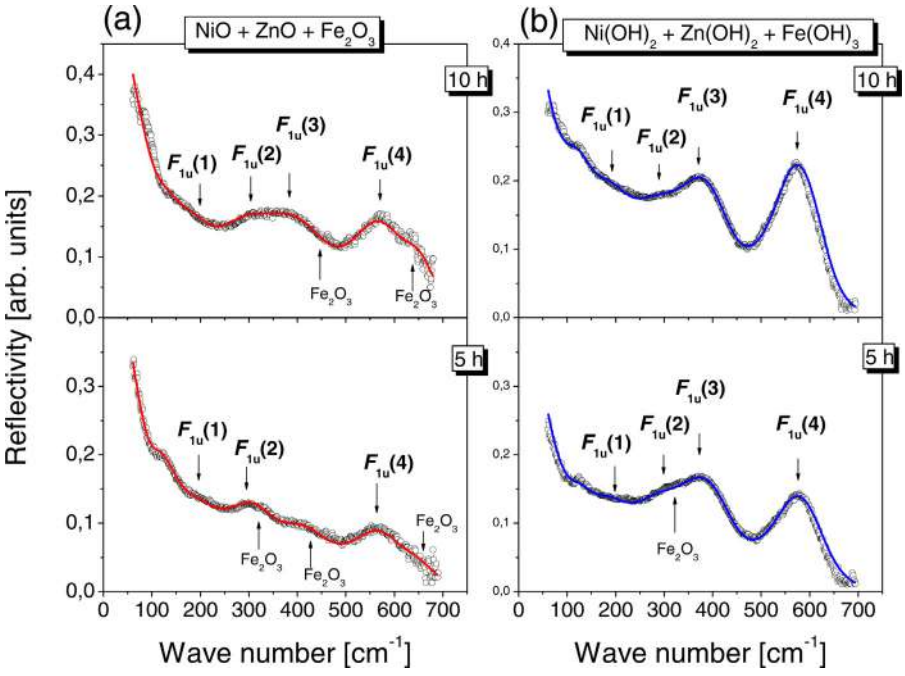

Fig. 8. IR reflectivity spectra of the samples obtained from the mixtures of starting (a) NiO, ZnO and α-Fe_2O_3 oxide powders and (b) $Ni(OH)_2$, $Zn(OH)_2$ and $Fe(OH)_3$ hydroxide powders after mechanochemical treatment for 5 h and 10 h.

tried to analyze the most exaggerate A_{1g} mode and to estimate the inversion parameter from the ratio of the intensities of A_{1g} components. The integrated intensity of certain component of A_{1g} mode is proportional approximately to the contribution of the corresponding cations in A-sites. The participation of Zn^{2+} in A-sites should be: $x_{Zn}(A) = I_{Zn}/(I_{Zn} + I_{Ni} + I_{Fe} + I_{Fe^*})$. In the exact formula intensities of Lorentzians are multiplied by corresponding force constants. We can suppose that the force constant in the case of "maghemite" oscillation is much smaller than the force constants of other vibrations (in regular surrounding) and to neglect its contribution. In this approximation, for hydroxide sample, Fig. 7, we obtained: $Fe_{0.20}Ni_{0.35}Zn_{0.44}$, what is roughly like the result of Rietveld analysis (Rietveld analysis gives: $Fe_{0.17}Ni_{0.31}Zn_{0.48}$).

FIR spectra of the nano powder samples obtained after 5 h or 10 h milling of starting compounds are given in Fig. 8. Milling of hydroxides $Ni(OH)_2$, $Zn(OH)_2$ and $Fe(OH)_3$ in stoichiometric amounts after 5 h already leads to the formation of pure spinel structure with clearly observable all four F_{1u} modes predicted by

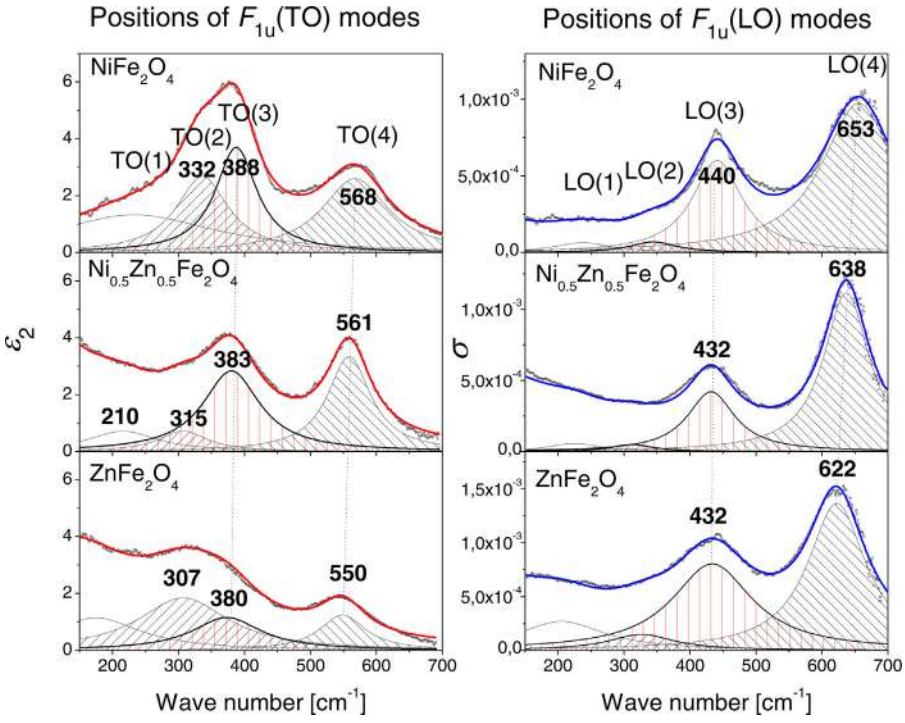

Fig. 9. Comparison of the results of Kramers-Krönig analysis of IR spectra Ni-ferrite, Zn-ferrite and single phase mixed $Ni_{0.5}Zn_{0.5}Fe_2O_4$ ferrite.

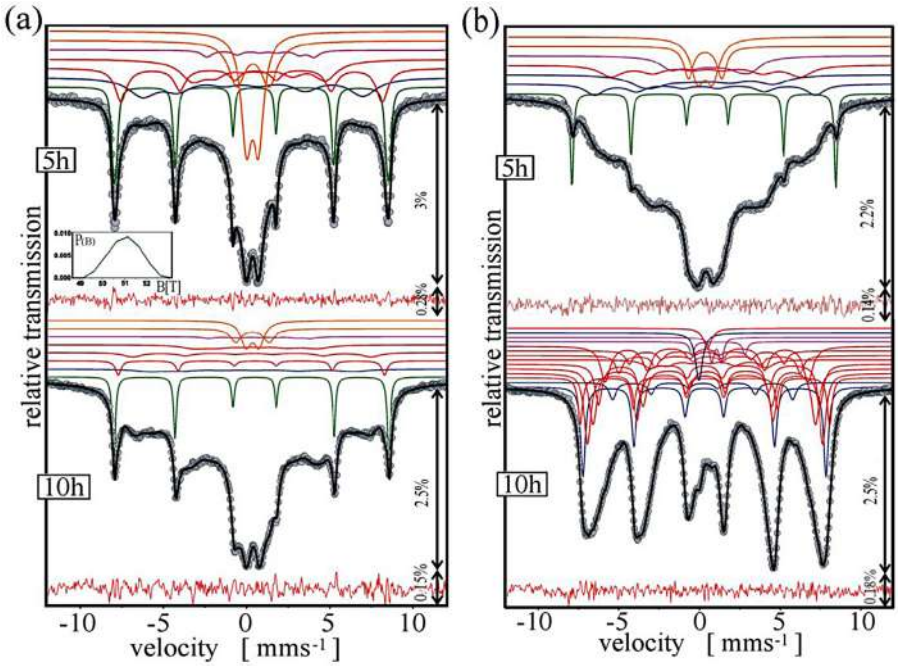

Fig. 10. Mössbauer spectra at room temperature after 5 h and 10 h milling time of the mixture (a) NiO/ZnO/α-Fe_2O_3 and (b) $Ni(OH)_2$/$Zn(OH)_2$/$Fe(OH)_3$. *Inset* shows a distribution of hyperfine field in the "oxide" sample obtained after 5 h of milling. The experimental values of relative transmission are shown by the grey circles. The fitted lines of subspectra are plotted above the main spectra fits.

the group theory. These modes are only more pronounced after 10 h of milling.

In the case of the oxide starting mixture, FIR spectra recorded on the samples obtained after 5 h and even 10 h milling of NiO, ZnO and Fe_2O_3 show spinel modes superposed with modes of non-reacting amounts of hematite (Fig. 8a). After 10 h milling the spinel peaks become more pronounced, but hematite modes are still present. Broad peaks of low intensity imply that these nano powders have smaller crystallites than the samples made by milling of hydroxide starting compounds.

Reflectivity spectra of the single phase "hydroxide" samples have two strong rather well defined TO/LO infrared bands: at 561/635 cm^{-1} and 383/432 cm^{-1}; at 312 cm^{-1} is a very weak band, and about 210 cm^{-1} is one more, hardly visible band (Fig. 8b). Waldron [31] investigated vibrational properties of ferrites and explained their or igin and force constants of oscillations by a semiclassical approach.

In the case of mixed nano ferrites with three different cations, obtained mechanochemically, it is clear that modes will be broad and weak. In the tetrahedral, as well as in the octahedral positions, can be all three types of cations.

In Fig. 9 are compared the results of Kramers–Krönig analysis of three FIR spectra: Ni-ferrite, Zn-ferrite and mixed $Ni_{0.5}Zn_{0.5}Fe_2O_4$ ferrite. Spectra of Ni and Zn ferrites are from Refs. [18,32]. It is visible that the positions of both TO and LO modes shift to lower wave numbers with increasing of total mass of divalent cations. Considering that in literature could be found various values of frequencies even for sintered ferrites, we can not expect accurate estimation of cation distribution in nano powders on the basis of FIR measurements. But there is no doubt that FIR technique could show the presence of small amounts of unreacted starting compounds.

3.3. Mössbauer spectroscopy

The Mössbauer spectra show distributions of hyperfine fields. In order to investigate valence and coordination number (CN) of iron cations in the spinel, distributions are partitioned on disjunct subspectra based on Lorentzian lines. The Mössbauer spectrum of the sample obtained from the mixture of NiO/ZnO/α-Fe_2O_3 powders milled for 5 h, is divided into seven subspectra (see Fig. 10a). The initial hematite is present, however fits with the characteristic sextet (IS = 0.37 mm s^{-1}; $\Delta = -0.197$ mm s^{-1}; B_{hf} = 51.75 T) are somewhat ambiguous. We resorted to the use of distribution of hyperfine fields. This yields a Gaussian–like distribution with centroid at 51.03 T and with the standard deviation of 0.68 T. The average isomer shift (IS) has value of 0.383(5) mm s^{-1}. The quadrupole shift has value of −0.180 (2) mm s^{-1}. The parameters of distribution suggest that a superposition of resonant signal occurs from hematite and ^{57}Fe at the octahedral site of the larger crystalline spinel ferrite. In order to simplify the calculation of the relative amount of phases in the sample from the areas of subspectra, we estimate that the factors of recoilless fraction are equal for all iron sites. The distribution covers 16.7(1.4)% of the total fitted area (see Table 3).

Generally, the bond length of Fe^{3+}—O^{2-} at the tetrahedral site is smaller than the similar length at the octahedral site, allowing larger overlapping of orbitals and respectively more covalent bond at the tetrahedral site. The consequence is smaller value for the isomer shift. That explains why the sextet A1 is associated with the tetrahedral site, and B1 and B2 with the octahedral site. The large value of the quadrupole shift (2ε) at the combined interaction, sextet A1, and large line width (Γ) show that this sextet occurs in response to overall changes in the [B]-sublattice. Overall changes include all combinations of iron, zinc, and nickel ions and holes intra [*B*]-sites that interact *via* the four oxygen anions, lowering the cube point symmetry (T_d) at the place of interaction and reducing the magnitude of hyperfine interaction (B_{hf}). By comparing the data from our previous work on the nickel ferrite nanopowder spinel, we conclude that sextet B1 belongs to the octahedral site [18]. The negative signs of the quadrupole shifts of these sextets are only consequences of the orientation of direction of B_{hf} relative to the principle axis of the electric field gradient tensor. The sextet B2 is assigned to the octahedral site as well. The low value of

Table 3
Mössbauer parameters: A – relative area fraction of component; Γ – line width (FWHM); *IS* – isomer shift with respect to α-Fe; Δ – quadruple splitting (2ε-shift) and *B* – hyperfine induction. Square bracket denotes the standard deviation of distribution. Labels A_i and B_i denote tetrahedral and octahedral Fe^{3+} site occupancies, respectively. Labels SPD_i and SPS_i denote the superparamagnetic doublets and singlets, respectively.

Mixture	Phase	Site	Mössbauer parameters				
			A (%)	Γ ($mm\,s^{-1}$)	IS ($mm\,s^{-1}$)	Δ or 2ε ($mm\,s^{-1}$)	*B* (*T*)
NiO + ZnO + α-Fe_2O_3 (5 h)	α-Fe_2O_3		16.7(1.4)		<0.383>(5)	−0.180(2)	<51.03>(068)
		A1	18.1(1.5)	2.0(1)	0.03(3)	0.68(6)	41.2(2)
		B1	13.8(0.8)	0.83(4)	0.417(8)	−0.24(1)	48.7(1)
		B2	16.3(1.4)	1.7(1)	0.58(2)	0.31(4)	24.8(3)
	Fe^{2+}	B	2.5(0.7)	0.8(1)	1.07(4)	−0.47(9)	20.0(3)
		SPD1	12.8(1.4)	1.19(8)	0.384(9)	1.93(7)	
		SPD2	19.8(1.0)	0.75(2)	0.358(2)	0.72(1)	
NiO + ZnO + α-Fe_2O_3 (10 h)	α-Fe_2O_3		8(1)	0.20(1)	0.381(1)	−0.195(3)	51.25(2)
		A1	24(4)	2.2(1)	−0.06(4)	0.72(7)	37.9(4)
		B1	4(1)	0.37(4)	0.401(6)	−0.23(1)	49.6(1)
		B2	14(4)	1.3(1)	0.38(1)	−0.15(3)	44.5(1)
		B3	24(3)	1.8(1)	0.46(3)	0.23(4)	22.8(2)
	Fe^{2+}	B	3(1)	0.9(2)	1.00(6)	−0.4(2)	19.0(3)
		SPD1	9(1)	0.78(4)	0.347(9)	2.00(3)	
		SPD2	14(2)	0.74(2)	0.358(3)	0.72(2)	
$Ni(OH)_2 + Zn(OH)_2 + Fe(OH)_3$ (5 h)	α-Fe_2O_3		3(1)	0.21(2)	0.388(5)	−0.21(1)	50.74(3)
		A1	12(3)	1.3(1)	0.21(3)	0.30(6)	42.5(3)
		A2	27(9)	2.2(3)	0.1(1)	0.9(3)	25.0(4)
		B1	21(8)	1.7(2)	0.46(3)	−0.12(7)	36.4(3)
		B2	19(9)	1.6(2)	0.85(4)	−0.27(5)	15.4(3)
		SPD1	5(1)	0.7(1)	0.36(1)	2.07(5)	
		SPD2	13(3)	1.01(8)	0.36(1)	0.92(6)	
		A1	10(1)	0.34(2)	0.307(4)	0.021(7)	46.69(7)
$Ni(OH)_2 + Zn(OH)_2 + Fe(OH)_3$ (10 h)		A2	4(1)	0.48(6)	0.21(2)	−0.03(3)	34.6(1)
		B1	5(1)	0.34(2)	0.356(6)	−0.03(1)	47.92(8)
		B2	16(5)	0.49(3)	0.360(6)	0.005(9)	45.20(8)
		B3	17(4)	0.56(5)	0.39(1)	−0.20(2)	42.7(1)
		B4	11(3)	0.52(6)	0.46(1)	0.30(3)	42.58(9)
		B5	16(4)	0.70(5)	0.425(9)	0.05(2)	39.0(1)
		B6	5(1)	0.54(8)	0.57(2)	0.13(2)	34.8(1)
		B7	3(1)	0.52(7)	0.43(1)	0.03(2)	29.7(1)
		B8	7(1)	0.98(8)	0.33(3)	0.47(6)	22.4(2)
		SPD1	1(1)	0.34(7)	1.17(2)	3.29(6)	
		SPD2	1(1)	0.32(3)	1.06(2)	0.58(4)	
		SPSA	3(1)	0.50(4)	−0.03(1)		
		SPSB	2(1)	0.6(1)	0.50(3)		

magnetic strength might be explained by the presence of a diamagnetic Zn^{2+} ($3d^{10}$) at the both sites, lowering the strong antifferomagnetic coupling. The volume size should also be taken into account. There is a sextet which has 1.07(4) $mm\,s^{-1}$ isomer shift (IS) and B_{hf} = 20.0(3) T. It is assigned to Fe^{2+} with CN = 6. Its existence might be explained by the magnetite structure where [Fe^{3+}] is replaced by another cation or a hole, breaking down the Verwey's electron exchange. The relative amount of this sextet is 2.5(0.7)%, as seen previously [18,33]. The doublet SPD1 indicates superparamagnetism, occurring in the limitation on $KV << k_BT$, where V is the volume of particle and K is the magnetic anisotropy constant [34]. The value of IS = 0.384(9) $mm\,s^{-1}$ should not be interpreted as the value of the bulk spinel ferrite, since the nanoparticle values (for IS) are always somewhat bigger. Hence, we consider that this value is the average of both sites [35]. The high value of the quadrupole splitting is due to chemical disorder. The large amount of the relative area, 19.8(1.0)%, belongs to the second doublet, SPD2. Its Mössbaer's parameters, IS = 0.358(2) $mm\,s^{-1}$ and Δ = 0.72(1) $mm\,s^{-1}$ are identical to the parameters of the natural ferrihydrite obtained by Coey and Readman [36]. Likewise, they are similar to parameters of the synthetic iron oxide gels [37]. The line width of SPD2 is much larger than width of lines at the cited samples. Hence, SPD2 is assigned to another superparamagnetic doublet.

The relative amount of the hematite in the same mixture, but now milled for 10 h, is 8(1)%. The sextet from Fe^{2+} has 3(1)% of total fitted area. The superparamagnetic phase of spinel totals 23(3) percent. All three sextets represent the response from the octahedral sites and have the combined value of 42(3)% of the total fitted area. According to known subspectral areas of both iron sites and using the formula $A_{(A)}/A_{[B]} = f_{(A)}/f_{[B]} \times \delta(2-\delta)$ we can estimate δ, the degree of inversion [38]. By taking the ratio of recoil-less fractions to be 0.94, as is estimated for the magnetite at ambient temperature [39] and calculating the degree of inversion only from representation of large particles, we obtain δ = 0.76(11). The error is estimated from the weighted error of summed areas.

The Mössbauer spectrum of the sample obtained from the mixture of $Ni(OH)_2/Zn(OH)_2/Fe(OH)_3$ powders milled for 5 h consists of seven subspectra (Fig. 10b). It reveals spinel structure of the sample, excluding the formed hematite in amounts of 3(1) percent of the total fitted area.

The Mössbauer spectrum of the sample obtained from the mixture of $Ni(OH)_2/Zn(OH)_2/Fe(OH)_3$ powders after 10 h of milling is fitted by 10 sextets, two superparamagnetic doublets and two singlets (Fig. 10b). Two sextets with the smallest isomer shift are referred to tetrahedral A-site with different occupation numbers and the other sextets are referred to B-site surrounded with different number of magnetic ions or disturbed in other way. Two doublets

(SPD), with high isomer shift, could be connected with Fe^{3+} ions in very small superparamagnetic nano particles. There are also two superparamagnetic singlets (SPS), which could be assigned to the tetrahedral (SPSA) and to the octahedral (SPSB) site. All subspectra correspond to the pure spinel ferrite phase. We find that the degree of inversion estimated for the single phase nickel–zinc ferrite sample obtained during 10 h milling of starting hydroxides is $\delta = 0.36(3)$. The presented analysis of the Mössbauer spectra of all NZ-ferrite samples is in good agreement with conclusions of previous measurements (XRD, EDP, EDS, Raman and FIR).

4. Conclusions

This study shows that under the laboratory conditions it is simple to prepare the good quality nanosized $Ni_{0.5}Zn_{0.5}Fe_2O_4$ ferrite powders by (soft) mechanochemical synthesis. It was examined evolution of the synthesis of nano $Ni_{0.5}Zn_{0.5}Fe_2O_4$ starting from two mixtures of powders milled in different duration time. The starting materials were: case (1) mixture of NiO/ZnO/α-Fe_2O_3 oxide and case (2) mixture of $Ni(OH)_2/Zn(OH)_2/Fe(OH)_3$ hydroxide powders. The samples obtained after 5 and 10 h of milling time are compared and investigated using various characterization methods. The X-ray diffractogram of the sample obtained after 10 h milling time in case (2) shows single phase cubic spinel structure. TEM analysis revealed that all samples are composed of more or less agglomerated nanosize particles. The average size of nano crystallites is ~20 nm. Crystallites are smaller after 5 h of milling and grow with milling time. This result is in agreement with the results of XRD analysis. The degree of the cation inversion of NZF is estimated for spinel fraction in all samples by Rietveld analysis. In the Raman and IR spectra are observed all of first-order Raman and IR active modes. In the spectra of the single phase "hydroxide" samples it is visible that the energy position and intensity of modes is dependent on the composition and cation distribution. It was shown that the modes in Raman spectra of nickel–zinc-ferrite that originate from vibrating of different cations (Ni-ferrite-like, Zn-ferrite-like, or magnetite-like) could be clearly distinguished. From the ratio of intensities of the A_{1g} -type Raman modes, it is possible to estimate the inversion of cations. The Mössbauer spectra of samples were fitted by several subspectra and according to known subspectral areas of both iron sites the degree of inversion was calculated, also. In the case of single phase sample obtained from the mixture of appropriate hydroxide powders for 10 h milling the cation inversion is $\delta = 0.36(3)$.

Acknowledgment

This research was financially supported by the Ministry of Education, Science and Technological Development of the Republic of Serbia through Projects no. III 45003, 45015 and 45018.

References

[1] M. Mohapatra, S. Anand, Int. J. Eng. Sci. Technol. 2 (2010) 127–146. www.ijest-ng.com.
[2] A.R. Tanna, H.H. Joshi, World Acad. Sci. Eng. Technol. 7 (2013) 70–77.
[3] W.H. Bragg, Philos. Mag. 30 (1915) 305–315.
[4] B. Aktaş, L. Tagirov, F. Mikailov, Magnetic Nanostructures, eight ed., Springer, Berlin, 2007.
[5] E.S. Murdock, R.F. Simmons, R. Davidson, IEEE Trans. Magn. 28 (1992) 3078–3083.
[6] K. Kondo, T. Chiba, S. Yamada, J. Magn. Magn. Mater. 254–255 (2003) 541–543.
[7] D. Stoppels, J. Magn. Magn. Mater. 160 (1996) 323–328.
[8] Q. Liu, L. Lv, J.P. Zhou, X.M. Chen, X.B. Bian, P. Liu, J. Ceram. Process. Res. 13 (2012) 110–116.
[9] S. Bid, S.K. Pradhan, Mater. Chem. Phys. 84 (2004) 291–301.
[10] M. Jalaly, M.H. Enayati, P. Kameli, F. Karimzadeh, Physics B 405 (2010) 507–512.
[11] E. Manova, D. Paneva, B. Kunev, E. Rivière, C. Estournès, I. Mitov, J. Phys. Conf. Ser. 217 (2010) 12102, doi:http://dx.doi.org/10.1088/1742-6596/217/1/012102.
[12] K. Suresh, K.C. Patil, J. Solid State Chem. 99 (1992) 12–17.
[13] A. Verma, T.C. Goel, R.G. Mendiratta, Mater. Sci. Technol.-London 16 (2000) 712–715.
[14] K.R. Krishna, K.V. Kumar, C. Ravindernathgupta, D. Ravinder, Adv. Mater. Phys. Chem. 2 (2012) 149–154. http://dx.doi.org/10.4236/ampc.2012.23022.
[15] A. Chatterjee, D. Das, S.K. Pradhan, D. Chakravorty, J. Magn. Magn. Mater. 127 (1993) 214–218.
[16] A.T. Raghavender, N. Biliškov, Ž. Skoko, Mater. Lett. 65 (2011) 677–680.
[17] E. Avvakumov, M. Senna, N. Kosova, Soft Mechanochemical Synthesis: A Basis for New Chemical Technologies, Kluwer Academic Publishers, Boston, 2001.
[18] Z.Ž. Lazarević, Č. Jovalekić, A. Rečnik, V.N. Ivanovski, A. Milutinović, M. Romčević, M.B. Pavlović, B. Cekić, N. Ž. Romčević, Mater. Res. Bull. 48 (2013) 404–415.
[19] R.A. Brand, WinNormos Mössbauer Fitting Program, Universität Duisburg, 2008.
[20] L. Takacs, Prog. Mat. Sci. 47 (2002) 355–414.
[21] P. Baláž, M. Achimovičová, M. Baláž, P. Billik, Z. Cherkezova-Zheleva, J. Manuel Criado, F. Delogu, E. Dutková, E. Gaffet, F. José Gotor, R. Kumar, I. Mitov, T. Rojac, M. Senna, A. Streletskii, K. Wieczorek-Ciurowa, Chem. Soc. Rev. 42 (2013) 7571–7637.
[22] V.V. Boldyrev, Russ. Chem. Rev. 75 (2006) 177–189.
[23] V.G. Ivanov, M.V. Abrashev, M.N. Iliev, M.M. Gospodinov, J. Meen, M.I. Aroyo, Phys. Rev. B 82 (2010) 024104.
[24] Z.Ž. Lazarević, Č. Jovalekić, A. Milutinović, D. Sekulić, V.N. Ivanovski, A. Rečnik, B. Cekić, N.Z. Romčević, J. Appl. Phys. 113 (2013) 187221.
[25] Z.W. Wang, P. Lazor, S.K. Saxena, G. Artioli, J. Solid State Chem. 165 (2002) 165–170.
[26] M. Maletin, E.G. Moshopoulou, A.G. Kontos, E. Devlin, A. Delimitis, V.T. Zaspalis, L. Nalbandian, V.V. Srdić, J. Eur. Ceram. Soc. 27 (2007) 4391–4394.
[27] A. Milutinović, Z.Ž. Lazarević, Č. Jovalekić, I. Kuryliszyn-Kudelska, M. Romčević, S. Kostic, N.Ž. Romčević, Mater. Res. Bull. 48 (2013) 4759–4768.
[28] O.N. Shebanova, P. Lazor, J. Raman Spectrosc. 34 (2003) 845–852.
[29] A. Ahlawat, V.G. Sathe, J. Raman Spectrosc. 42 (2011) 1087–1094.
[30] Ž. Cvejić, S. Rakić,, A. Kremenović, B. Antić, Č. Jovalekić, P. Colomban, Solid State Sci. 8 (2006) 908–915.
[31] R.D. Waldron, Phys. Rev. 99 (1955) 1727–1735.
[32] Z.Ž. Lazarević, Č. Jovalekić, V.N. Ivanovski, A. Rečnik, A. Milutinović, B. Cekić, N.Ž. Romčević, J. Phys. Chem. Solids 75 (2014) 869–877.
[33] M. Menzel, V. Šepelák, K.D. Becker, Solid State Ionics 141–142 (2001) 663–669.
[34] S. Morup, J. Magn. Magn. Mater. 37 (1983) 39–50.
[35] N.N. Greenwood, T.C. Gibb, Mössbauer Spectroscopy, Chapman and Hall Ltd., London, 1971.
[36] J.M.D. Coey, P.W. Readman, Earth Planet Sci. Lett. 21 (1973) 45–51.
[37] E. Murad, U. Schwertmann, Am. Mineral. 65 (1980) 1044–1049.
[38] V. Šepelák, D. Baabe, K.D. Becker, J. Mater. Synth. Process. 8 (2000) 333–337.
[39] G.A. Sawatzky, F. Van der Woude, A.H. Morrish, Phys. Rev. 187 (1969) 747–757.

Journal of Alloys and Compounds 649 (2015) 375–379

Contents lists available at ScienceDirect

Journal of Alloys and Compounds

journal homepage: http://www.elsevier.com/locate/jalcom

Far-infrared spectroscopy of $Zn_{1-x}Mn_xGeAs_2$ single crystals: Plasma damping influence on plasmon – Phonon interaction

N. Romcevic [a, *], M. Romcevic [a], W.D. Dobrowolski [b], L. Kilanski [b], M. Petrovic [a], J. Trajic [a], B. Hadzic [a], Z. Lazarevic [a], M. Gilic [a], J.L. Ristic-Djurovic [a], N. Paunovic [a], A. Reszka [b], B.J. Kowalski [b], I.V. Fedorchenko [c, d], S.F. Marenkin [c, d]

[a] Institute of Physics, University of Belgrade, Pregrevica 118, 11080 Belgrade, Serbia
[b] Institute of Physics, Polish Academy of Science, 02-668 Warsaw, Poland
[c] Kurnakov Institute of General and Inorganic Chemistry RAS, 119991 Moscow, Russia
[d] National Institute of Science and Technology, MISiS, Moscow, Russia

ARTICLE INFO

Article history:
Received 12 June 2015
Received in revised form
8 July 2015
Accepted 10 July 2015
Available online 13 July 2015

Keywords:
Semiconductors
Electron–phonon interactions
Light absorption and reflection

ABSTRACT

The interest in thorough description of $Zn_{1-x}Mn_xGeAs_2$ arises from its suitability for application in the field of non-linear optics. The room temperature far-infrared reflectivity spectra of single crystals $Zn_{1-x}Mn_xGeAs_2$, where $0 \leq x \leq 0.078$, were measured in the spectral range from 80 cm^{-1} to 500 cm^{-1}. The spectra were analyzed by fitting procedure using a dielectric function which includes interaction between a plasmon and two different phonons. The detected phonons are in excellent agreement with the theoretical predictions. The MnAs cluster phonons are detected, as well.

1. Introduction

Ternary semiconductors of the form II-IV-V_2 are crystal-chemicals that are electrical twins of semiconductors of the form III-V. Ordered replacement of the atom III in a semiconductor by the atoms II and IV in a ternary semiconductor causes doubling of the unit cell size in the direction of the *c*-axis and consequent reduction of symmetry from the cubic to the tetragonal. For example, a representative of this group of materials, $ZnGeAs_2$ with the twin semiconductor GaAs, crystallizes in the chalcopyrite structure.

A diluted magnetic semiconductor whose Curie temperature is as high as 300 K can be obtained by doping $ZnGeAs_2$ with Mn [1,2]. The non-linear optical coefficients of the resulting alloy, i.e., of $Zn_{1-x}Mn_xGeAs_2$, are large [3], and its direct energy gap corresponding to $T = 300$ K at the Γ point of the Brillouin zone is $E_g = 1.15$ eV [4]. Due to these characteristics, the described material is suitable for application in the non-linear optics; hence the interest for its other attributes.

The plasmons of free carriers and the longitudinal-optical (LO) phonons interact through their macroscopic electric fields, and the result is appearance of the coupled LO phonon-plasmon modes (CPPMs). The vast majority of published studies are devoted to the *n*-type semiconductors and the interaction of a single phonon with effective plasmons. The studies involving the influence of the plasmon damping on the CPPM followed somewhat later [5]. For example, for low damping rates in the *n*-type GaAs, the coupled modes can be classified in an upper L_+ branch and a lower L_- branch. With the increase in the carrier density, i.e., plasma frequency, the nature of the upper mode changes in energy from the LO phonon-like to a plasmon-like. The change in the lower frequency mode occurs the other way around, reaching the transverse-optical (TO) phonon energy for large plasmon energy. The distinction between the upper and lower mode becomes meaningless for large plasmon dumping. In this case, one mode is more phonon-like with energy ω_{LO} for $\omega_P = 0$ and ω_{TO} for $\omega_P >> \omega_{LO}$, with nearly pure phonon damping in both cases, whereas the other mode is an overdamped plasmon mode. Further, it is the plasma with high mobilities and low effective masses of the carriers that is often considered, in which case is enabled the detection of low, L_-, and high, L_+, energy branch of the CPPM [6,7].

Despite the early theoretical prediction of the interaction between two phonons and a plasmon [8], experimental confirmations are rare [9–11]. As for the influence of the plasmon damping on the

* Corresponding author.
E-mail address: romcevi@ipb.ac.rs (N. Romcevic).

http://dx.doi.org/10.1016/j.jallcom.2015.07.087
0925-8388/

interaction between a plasmon and two different phonons, i.e. on the coupled plasmon-two-phonons modes, CP2PM, to the best of our knowledge it has not been considered so far.

Our intention is to use far-infrared spectroscopy to study the fundamental properties of the coupled plasmon-two-phonons modes in the *p*-type materials, as well as to further investigate these coupled modes under different plasmon damping conditions. The Raman spectra measurements performed on the $Zn_{1-x}Mn_xGeAs_2$ system [12] offer additional justification for the intended course of research.

2. Experimental technique, methods, and groundwork

The studied samples of $Zn_{1-x}Mn_xGeAs_2$ were grown from a stoichiometric ratio of high purity powders of $ZnAs_2$, Ge, and Mn, using the direct fusion method. The chemical composition was within the interval $0 \leq x \leq 0.078$. The technology of sample preparation is explained in detail in Ref. [13].

The preliminary studies of characteristics of $Zn_{1-x}Mn_xGeAs_2$ samples were undertaken and the results were presented in Refs. [2,14,15]. Using the X-ray diffraction spectra of powdered samples it was found that samples contain two main phases. These are solid solutions of Mn in $ZnGeAs_2$ and in $Zn_2Ge_{11}As_4$ compound, with chalcopyrite and zinc-blade cubic crystal structure, respectively. The magnetic properties of the alloy depend on the presence of Mn in the composition. Low Mn content produces a paramagnetic material, whereas larger amounts of Mn cause a ferromagnetic alignment of the alloy. From the results of the Hall measurements given in Table 1 it can be observed that the samples with relatively high density of the *p*-type free carrier, i.e. samples with $x = 0$, 0.013, and 0.047, have rather low mobility, whereas high mobility is associated with low density of the free carrier in samples with $x = 0.0028$, 0.053, and 0.078.

The presence of MnAs clusters in our $Zn_{1-x}Mn_xGeAs_2$ crystals was done with the use of a scanning electron microscope (SEM) coupled with energy dispersive x-ray spectrometer system (EDX). We used the field emission Hitachi SU-70 Analytical UHR FE-SEM SEM equipped with Thermo Scientific NSS 312 EDX system equipped with silicon drift detector. The samples surface was prepared prior to the SEM measurements including was mechanical polishing and chemical cleaning. The purpose of the sample preparation was to reduce the surface roughness and remove unintentional dirt and impurities. Our equipment allowed simultaneous use of the SEM and EDX techniques which in turn enabled to obtain images of the sample surface and the measurements of the localized elemental information at selected surface spots. A series of SEM maps was obtained for the $Zn_{1-x}Mn_xGeAs_2$ samples with different chemical composition. In agreement with our previous results [2] the SEM data showed no clustering for the samples with $x < 0.07$. For $x = 0.078$ the presence of MnAs clusters was observed (see Fig. 1).

The EDX results indicate the presence of MnAs clusters with diameter of about 10 μm. The stoichiometry of the $ZnGeAs_2$ equals 1:1:2 and the chemical content of MnAs inclusions is also close to 1:1.

The study of the CP2PM in *p*-type $Zn_{1-x}Mn_xGeAs_2$ was performed by measuring the far-infrared (FIR) reflection spectra at room temperature in the spectral range of 80 cm^{-1}–500 cm^{-1}, using BOMEM DA 8 spectrometer.

Table 1
Results of Hall measurements for $Zn_{1-x}Mn_xGeAs_2$.

x(Mn)	0	0.0028	0.013	0.047	0.053	0.078
p(10^{19} cm^{-3})	8.1	1.9	10.5	10.2	3.3	5.2
μ(cm^2/Vs)	19.1	67.8	14.9	15.3	44.1	28.7

3. Results and analysis

The far-infrared reflection spectra of single crystal samples of $Zn_{1-x}Mn_xGeAs_2$ are shown in Fig. 2. Each experimentally obtained data point is marked with a circular symbol. Two different spectra types are clearly visible. The samples with low free carrier density, i.e., samples corresponding to $x = 0.0028$, 0.053, and 0.078, show significant phonon structure. For the sample with $x = 0.0028$ the following features are distinguishable: the two dominant structures, clearly separated and located one in section 235 cm^{-1}–245 cm^{-1} and the other in 270 cm^{-1}–290 cm^{-1}, two phonons at about 210 cm^{-1} and 260 cm^{-1}, as well as the weakly expressed structures at approximately 120 cm^{-1} and 190 cm^{-1}. Note that stabilization of tetragonal structures occurred in this sample, according to the results of the X-ray measurements. The described features are visible in the spectra corresponding to $x = 0.053$ and $x = 0.078$, as well, however, in much less pronounced form. In these two cases it would be more appropriate to state that only the two most dominant structures are clearly visible.

When the free carrier density increases, i.e., for the samples corresponding to the remaining three values of *x*, the spectra take a completely different shape. Only the outlines of formerly clear structures can now be distinguished within a single wide shape, which should rather be described as a structure of slightly wavy shape. The most pronounced spectra from this group corresponds to $x = 0.047$. The phonon located at about 210 cm^{-1} and the structure positioned between 235 cm^{-1} and 245 cm^{-1} are broadened, merged, and spread up to 270 cm^{-1}, which is the lower limit of the most pronounced structure in previously described spectra and is now practically hidden by the electrons. The most pronounced became the structures located at about 180 cm^{-1} and 260 cm^{-1}, as well as the phonon positioned at approximately 90 cm^{-1}. The global minimum is shifted to above 320 cm^{-1}. Compared to the samples with low free carrier density, a noticeable reflectivity increase is registered in this area, as well.

A theoretical model of the bulk dielectric function has been discussed by several authors [6,16]. The low-frequency dielectric properties of single crystals are described by classical oscillators corresponding to the TO-modes, to which the Drude part is superimposed to take into account the free carrier contribution:

$$\varepsilon_S(\omega) = \varepsilon_\infty + \sum_{k=1}^{l} \frac{\varepsilon_\infty\left(\omega_{LOk}^2 - \omega_{TOk}^2\right)}{\omega_{TOk}^2 - \omega^2 - i\gamma_{TOk}\omega} - \frac{\varepsilon_\infty\omega_P^2}{\omega(\omega + i\Gamma_P)}, \quad (1)$$

where ε_∞ is the bound charge contribution and it is assumed to be a constant, ω_{LOk} and ω_{TOk} are the longitudinal and transverse optical-phonon frequencies, ω_P the plasma frequency, γ_{LOk} and γ_{TOk} indicate the damping of uncoupled modes of the host crystal, and Γ_P is the plasmon mode damping coefficient.

Our previous works [17–19] support the opinion that the structures located in the regions 235 cm^{-1}–245 cm^{-1} and 270 cm^{-1}–290 cm^{-1}, are a consequence of the combined plasmon-LO phonon modes, ω_{lj}. Therefore, we consider these two structures as good candidates for verification of CP2PM. The outcomes of the coupling between a single phonon and a plasmon, CPPM, for the various values of plasma damping Γ, are given in Fig. 3. The phonon is taken to be the E^2 phonon in $Zn_{1-x}Mn_xGeAs_2$, which in Eq. (1) corresponds to $l = 1$, $\omega_{TO} = 268$ cm^{-1}, and $\omega_{LO} = 273$ cm^{-1}, whereas ω_P defines the plasmon. The positions of the coupled mode were obtained from the real part of Eq. (1) as the solution of the equation $\mathrm{Re}\{\varepsilon_S\} = 0$ for $l = 1$. The obtained result is in excellent agreement with the GaAs case described in Ref. [5]. Further, each of the two structures taken as an example can be explained using the approach illustrated in Fig. 3, i.e., for the both cases the appropriate

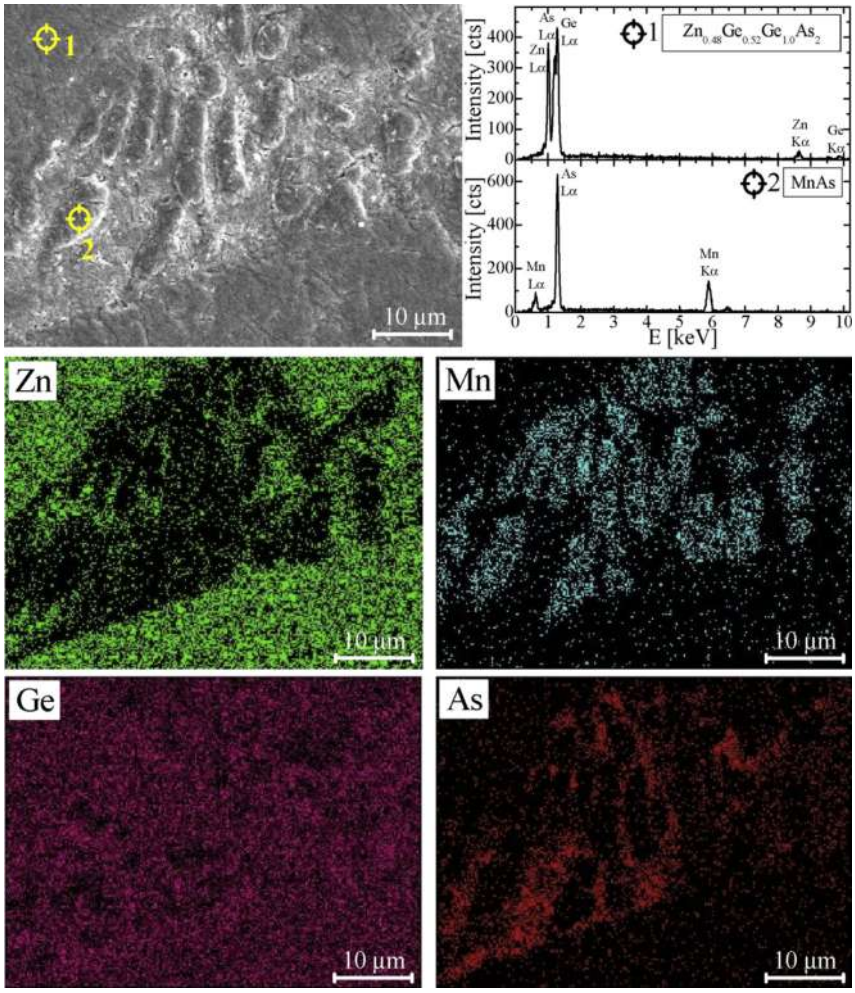

Fig. 1. Exemplary SEM image (top left) and EDX microprobe results including the detailed chemical content measurement (top right) and the maps of the distribution of the alloying elements obtained for the $Zn_{1-x}Mn_xGeAs_2$ sample with $x = 0.078$.

values of plasma frequency and damping can be determined to provide full description of the given structure. However, the dielectric function formed in such a way to account for the interaction of each individual phonon with the plasma, would lead to difficulties in understanding the nature of the multicomponent plasma. Several studies are dedicated to this issue [7–11].

With the intention to avoid the discussed difficulties and to establish better model of reflectivity spectra of $Zn_{1-x}Mn_xGeAs_2$, we used the dielectric function that includes in its initial form the interaction between two different LO phonons and a plasmon, i.e., the plasmon-two-phonons interaction [8,11], namely:

$$\varepsilon(\omega) = \varepsilon_\infty \frac{\prod_{j=1}^{3}\left(\omega^2 + i\gamma_{lj}\omega - \omega_{lj}^2\right)}{\omega(\omega + i\Gamma_P)\prod_{i=1}^{2}\left(\omega^2 + i\gamma_{ti}\omega - \omega_{ti}^2\right)} \times \prod_{k=1}^{s}\frac{\omega^2 + i\gamma_{LOk}\omega - \omega_{LOk}^2}{\omega^2 + i\gamma_{TOk}\omega - \omega_{TOk}^2}. \quad (2)$$

The first term in Eq. (2) represents coupling of a plasmon and two phonons, whereas the second term accounts for all s uncoupled modes of the crystal. The parameters ω_{lj} and γ_{lj} in the numerator of the first part are eigenfrequencies and damping coefficients of the longitudinal (LO) component of the plasmon-two-phonons waves, respectively. The parameters ω_{tj} and γ_{tj} in the denominator of the first part correspond to the corresponding characteristics of the transverse (TO) vibrations. The second factor represents uncoupled crystal modes, where ω_{LOk} and ω_{TOk} are the longitudinal and transverse frequencies, while γ_{LOk} and γ_{TOk} are the damping coefficients of the k-th crystal mode.

The dielectric function given with Eq. (2) was used to obtain the theoretical prediction of the experimental spectra shown in Fig. 2. The agreement between the experimental data shown as circles and the theoretical spectra given as solid lines is excellent.

The number of uncoupled phonons, s, depends on the manganese concentration, x, and will be discussed latter. In order to better understand the obtained results, the influence of the plasma damping on the positions of coupled plasmon-two-phonons modes is shown in Fig. 4. As explained earlier, the coupled mode positions are defined as the solutions of the real part of Eq. (1), i.e., $\mathrm{Re}\{\varepsilon_S\} = 0$; however, now under the condition $l = 2$.

The values of frequencies ω_{TO1} and ω_{TO2}, obtained as the best fit to experimental data, are 236 cm^{-1} and 268 cm^{-1} for E^3 and E^2, respectively. Ten values of the parameter Γ were considered, namely $\Gamma = 0$, 40, 60, 80, 100, 120, 140, 160, 180, and 250 cm^{-1}. The obtained dependence of the coupled modes positions depicted in Fig. 4 is qualitatively different from the one given in Fig. 3, which is expected since the number of coupled modes is different. For $\Gamma = 0$,

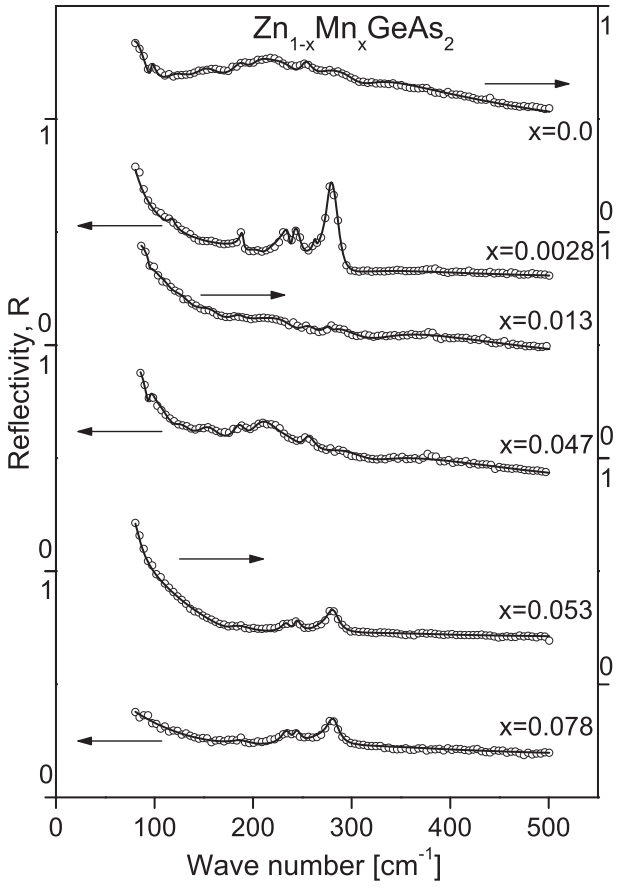

Fig. 2. Far-infrared reflection spectra of $Zn_{1-x}Mn_xGeAs_2$ single crystals. The experimentally obtained data points are depicted by circles. The theoretical spectra obtained with the model defined by Eq. (2) and fitting procedure are given as solid lines. Six different samples were considered with six values of manganese concentration $x = 0$, 0.0028, 0.013, 0.047, 0.053, and 0.078.

here as well as in Fig. 3, the lower branch starts as a plasmon and ends in TO1 phonons, whereas the upper branch begins as a phonon and ends in plasmon tail. The new branch, absent in Fig. 3, begins as LO1 phonon and approaches TO2 phonon at high values

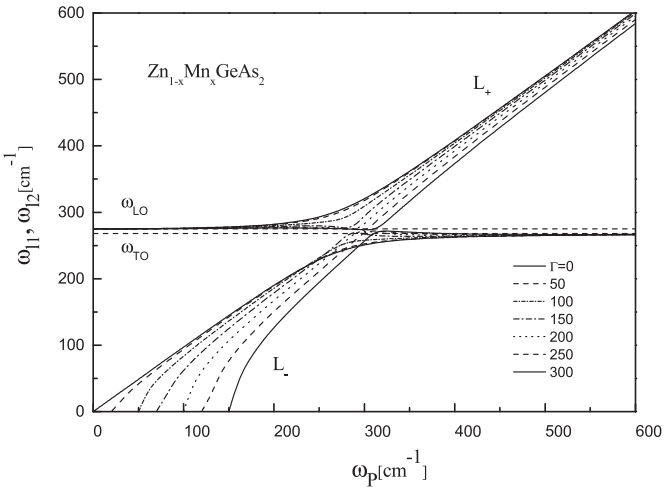

Fig. 3. Eigenfrequencies of plasmon–phonon modes for single crystal $Zn_{1-x}Mn_xGeAs_2$. The solid lines are spectra calculated from $Re\{\varepsilon_S\} = 0$, where ε_S is given by Eq. (1) whose parameter l is set to 1. Seven different values of plasma damping were considered, i.e., $\Gamma = 0$, 50, 100, 150, 200, 250, and 300 cm^{-1}.

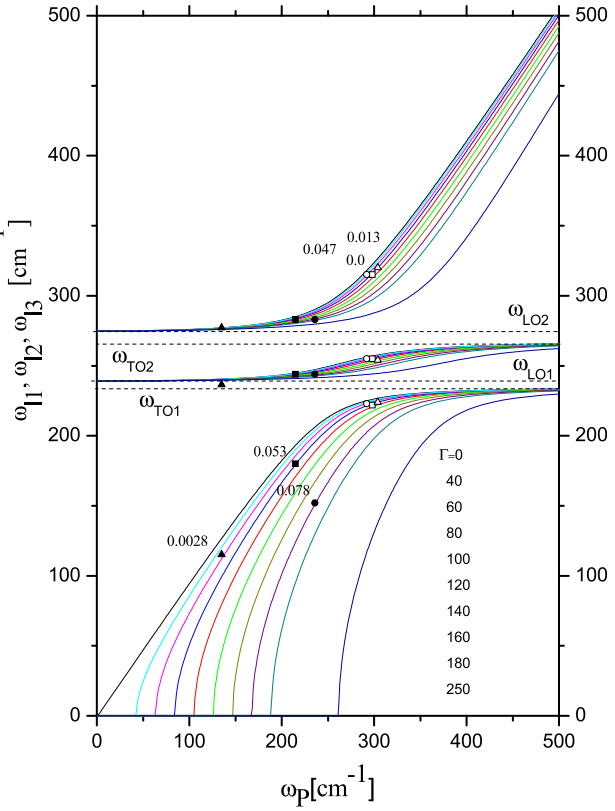

Fig. 4. Eigenfrequencies of plasmon-two-phonon modes for single crystal $Zn_{1-x}Mn_xGeAs_2$. The solid lines are spectra calculated from $Re\{\varepsilon_S\} = 0$, where ε_S is given by Eq. (1) whose parameter l is set to 2. Ten different values of plasma damping were considered, i.e., $\Gamma = 0$, 40, 60, 80, 100, 120, 140, 160, 180, and 250 cm^{-1}. Values obtained with Eq. (2) as the best fit to the experimental data in Fig. 1 are represented by solid symbols for samples with low free carrier density and open symbols for high free carrier density.

of plasma frequency. The values of LO phonon frequencies are obtained from Fig. 4 as a results of best fit. The nature of the branches does not change with the increase of plasma damping up to relatively large value of $\Gamma = 250$ cm^{-1}; instead, each branch is shifted within its range. The regions between TO1 and LO1, as well as between TO2 and LO2 are branch-free, as was the case with the TO–LO region in Fig. 3 for the LO phonon-plasmon interaction.

Results obtained as the best fit to the experimental data are in Fig. 4 denoted by different symbols for different values of x. The obtained values of plasma frequencies follow the change in free carrier density, N, which was expected since ω_P^2 is proportional to N. The most pronounced spectrum from each of the two groups, i.e., the one with $x = 0.0028$ and $x = 0.047$, correspond to the smallest value of plasma damping within its group.

There are three groups of uncoupled phonons. The first group contains the phonons that originated from $ZnGeAs_2$ and were detected in all spectra. These are the phonons located at around 101 cm^{-1}, 117 cm^{-1}, 161 cm^{-1}, and 210 cm^{-1}, with the B^3_1, E^5, E^4, and A_1 symmetry, respectively, as well as the group of phonons in the vicinity of 275 cm^{-1} whose symmetry is of the E^1 and B^1_2 type. These phonons are described in detail in Ref. [20].

The weak phonons around 180 cm^{-1} for $x = 0.053$ and 0.078, and above 320 cm^{-1} for $x = 0.013$ and 0.047, probably correspond to another detected phase, i.e., to $Zn_2Ge_{11}As_4$, or to the surface modes.

The most interesting is the third group of phonons at about 170 cm^{-1} which correspond to $x = 0.013$ and 0.047. Although their presence was noticeable in these two spectra, we did not observe

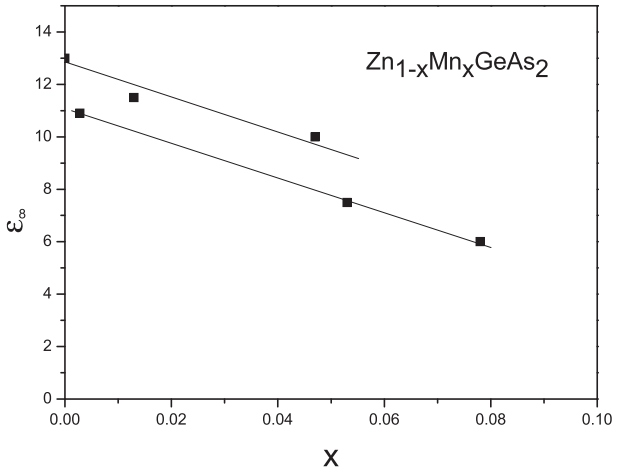

Fig. 5. Dependence of ε_∞ on manganese concentration.

these phonons in the spectra of the basic material. The calculated values of the MnAs clusters are positioned at these frequencies, as well [19]. Note that the Raman spectra measurements offer much more distinguished results. On the other hand, given the number of clusters and high free carrier density, for IR spectra it can be concluded with certainty only that it would not be possible to completely reproduce the spectra if these phonons were not taken into account.

The dependence of ε_∞ on the concentration of Mn is given quantitatively in Fig. 5. It was clear from Fig. 1 that ε_∞ decreases with the increase in Mn concentration. In addition to confirming this conclusion numerically, Fig. 5 shows that the dependence is linear within each of the two groups of samples that were established with respect to the free carrier density, i.e. for the group of samples with high as well as with low carrier density. The carrier density does not influence the shape of the dependence, i.e., the linearity; however, the group of samples with high carrier density has larger ε_∞ compared to the group with low carrier density.

4. Conclusion

We used far-infrared reflectivity measurements to investigate the influence of plasma damping on the interaction between a plasmon and two different phonons in $Zn_{1-x}Mn_xGeAs_2$. The specific nature of the behavior of the coupled phonons frequency is determined. At high plasma damping values entrance of phonons into the region between TO and LO frequencies is not observed for the plasmon-two-phonons interaction, unlike was the case with the plasmon-phonon interaction. Existence of MnAs clusters is confirmed and relation between free carrier concentration and optical parameters is determined.

Acknowledgments

This work was supported under the Agreement of Scientific Collaboration between Polish Academy of Science and Serbian Academy of Sciences and Arts. The work in Serbia was supported by the Serbian Ministry of Education, Science and Technological Development through Project 45003, and in Poland by National Science Center under granted decision No. DEC-2011/01/B/ST5/06602.

References

[1] S. Choi, G.B. Cha, S.C. Hong, S. Cho, Y. Kim, J.B. Ketterson, S.Y. Jeong, G.C. Yi, Solid State Commun. 122 (2002) 165.
[2] L. Kilanski, M. Gorska, W. Dobrowolski, E. Dynowska, M. Wojcik, B.J. Kowalski, J.R. Anderson, C.R. Rotundu, D.K. Maude, S.S. Varnavskiy, I.V. Fedorchenko, S.F. Marenkin, J. Appl. Phys. 108 (2010) 073925.
[3] W. Dobrowolski, J. Kossut, T. Story, Handbook of Magnetic Materials, Elsevier, Amsterdam, 2002.
[4] S. Picozzi, Nat. Mater 3 (2004) 349.
[5] G. Irmer, M. Wenzel, J. Monecke, Phys. Rev. B 56 (15) (1997) 9524.
[6] G. Abstreiter, M. Cardona, A. Pinczuk, in: M. Cardona, G. Guntherodt (Eds.), Light Scattering in Solids, IV, Springer-Verlag, Berlin, 1984.
[7] R.T. Holm, J.W. Gibson, E.D. Palik, J. Appl. Phys. 48 (1977) 212.
[8] A.A. Kukharski, Solid State Commun. 8 (1970) 1275.
[9] J. Trajić, N. Romčević, M. Romčević, V.N. Nikiforov, Mater. Res. Bull. 42 (2007) 2192–2201.
[10] J. Trajić, N. Romčević, M. Romčević, D. Stojanović, R. Rudolf, T.A. Kuznetsova, D.R. Khokhlov, J. Alloys Compd. 493 (2010) 41–46.
[11] M. Petrovic, N. Romcevic, J. Trajic, W.D. Dobrowolski, M. Romcevic, B. Hadzic, M. Gilic, A. Mycelski, Infrared Phys. Technol. 87 (2014) 323–326.
[12] M. Romčević, N. Romčević, W. Dobrowolski, L. Kalinski, J. Trajić, D.V. Timotijević, E. Dynowska, I.V. Fedorchenko, S.F. Marenkin, J. Alloys Compd. 548 (2013) 33–37.
[13] V.M. Novotortsev, V.T. Kalinnikov, L.I. Koroleva, R.V. Demin, S.F. Marenkin, T.G. Aminov, G.G. Shabunina, S.V. Boichuk, V.A. Ivanov, Russ. J. Inorg. Chem. 50 (2005) 429.
[14] V.M. Novovotortsev, S.F. Marenkin, S.A. Varnavskii, L.I. Koroleva, T.A. Kupriyanova, R. Szymcak, L. Kilanski, B. Krzmanska, Russi. J. Inorg. Chem. 53 (2008) 22.
[15] L.I. Koroleva, V.Yu Pavlov, D.M. Zashhchirinskii, S.F. Marenkin, S.A. Varnavskii, R. Szimczak, W. Dobrowolski, L. Kilanski, Phys. Solid Sate 49 (2007) 2121.
[16] E. Burstein, A. Pinczuk, R.F. Wallis, in: D.L. Carter, R.T. Bate (Eds.), The Phys. Of Semimetals and Narrow-Gap Semicon, 1971. Pergamon, New York.
[17] M. Romcevic, L. Kilanski, N. Romcevic, B. Hadzic, W. Dobrowolski, I.V. Fedorchenko, S.F. Marenkin, Mater. Res. Bull. 59 (2014) 300–304.
[18] J. Trajić, N. Romčević, M. Romčević, D. Stojanović, L.I. Ryabova, D.R. Khokhlov, J. Alloys Compd. 602 (2014) 300–305.
[19] N. Romčević, J. Trajić, T.A. Kuznetsova, M. Romčević, B. Hadžić, D.R. Khokhlov, J. Alloys Compd. 442 (2007) 324–327.
[20] F.W. Ohrendorf, H. Haeuseler, Cryst. Res. Technol. 34 (1999) 339–349.

Raman spectroscopy of bismuth silicon oxide single crystals grown by the Czochralski technique

2013 Phys. Scr. 2013 014046

(http://iopscience.iop.org/1402-4896/2013/T157/014046)

Phys. Scr. **T157** (2013) 014046 (4pp) doi:10.1088/0031-8949/2013/T157/014046

Raman spectroscopy of bismuth silicon oxide single crystals grown by the Czochralski technique

Z Lazarević[1], S Kostić[1], V Radojević[2], M Romčević[1], M Gilić[1], M Petrović-Damjanović[1] and N Romčević[1]

[1] Institute of Physics, University of Belgrade, Belgrade, Serbia
[2] Faculty of Technology and Metallurgy, University of Belgrade, Belgrade, Serbia

E-mail: lzorica@yahoo.com

Received 24 August 2012
Accepted for publication 16 December 2012
Published 15 November 2013
Online at stacks.iop.org/PhysScr/T157/014046

Abstract
In this work, single crystals of bismuth silicon oxide (BSO; $Bi_{12}SiO_{20}$) have been grown by the Czochralski method. The growth conditions were studied. The critical diameter and the critical rate of rotation were calculated. Suitable polishing and etching solutions were determined. The structure of the $Bi_{12}SiO_{20}$ has been investigated by x-ray diffraction (XRD), and Raman and Fourier transform infrared spectroscopy (FTIR) spectroscopy. The results obtained are discussed and compared with the published data. The pale yellow $Bi_{12}SiO_{20}$ single crystals prepared were without cores. Using spectroscopic measurements 19 Raman and 5 IR modes were observed.

PACS numbers: 81.10.−h, 78.30.−j, 61.72.Ff

(Some figures may appear in color only in the online journal)

1. Introduction

Cubic crystals with the sillenite-type structure are described by the general formula $Bi_{12}M^{+n}O_{20\pm\delta}$, where M is an element of groups II–V of the periodic table (M = Si, Ge, Ti, etc). Bismuth silicon oxide (BSO; $Bi_{12}SiO_{20}$) belongs to the group of sillenite single crystals (with the space group $I23$) [1]. These exhibit many interesting properties such as photoconductivity, the electro-optic effect, piezoelectricity and photorefractivity [1–3]. Such properties make these materials attractive for technological application in the fields of optical memories, holography and optical phase-conjugating devices [1–5]. Many of the important properties of selenite exploited for different applications are either determined or affected by impurities.

$Bi_{12}SiO_{20}$ single crystals were grown by a laser-heated pedestal growth (LHPG) method [6], the hydrothermal growth technique [7] and the sol–gel process [8]. Also, mechanical alloying has been used successfully to produce nanocrystalline powders of BSO [9]. Films of these compounds can be produced by liquid phase epitaxy (LPE), physical sputtering, chemical vapor transport and solution growth [5]. $Bi_{12}SiO_{20}$ crystals have been produced mainly by the Bridgman method [10], by the floating-zone technique [11], and recently also by the Czochralski technique [12–16]. A question of major importance in the melt growth of sillenite compounds is the optical homogeneity of single crystals [9]. The two most typical 'optical' defects in sillenite-type crystals are second-phase inclusions and regions differing in optical absorption. Increased-absorption regions in bismuth silicate crystals may appear as striations and a so-called central core, which is seen as a dark area in the central part of cross-sections. It is commonly believed [13, 17] that the central core and selective decoration in the shape of a Maltese cross for the ⟨100⟩ and ⟨110⟩ growth directions or in the shape of a three-bladed propeller for the ⟨111⟩ growth direction are associated with growth rate anisotropy and the difference in the distribution coefficient of 'photochromic' impurities between the polar and nonpolar facets of the growth interface. If the interface has the form of a flat ⟨100⟩ facet (usually in faceted growth at fast crystal rotation rates), there is no central core [18, 19]. This is the main reason why it is very much necessary to find optimal conditions for growth, so that this does not happen [5, 20]. Most $Bi_{12}SiO_{20}$ single

crystals for acoustic and optical applications were grown by Czochralski pulling. Using this technique, BSO single crystals 50–70 mm in diameter and up to 400 mm in length have been grown. The stoichometric melt composition for BSO crystal growth is Bi_2O_3: $SiO_2 = 6:1$. The Raman spectra of the $Bi_{12}M^{+n}O_{20\pm\delta}$ crystals were studied in [21, 22]; the *M*-cations in these compounds are characterized by the oxidation degree 4^+, which determines the existence of only insignificant differences between crystal lattices that are associated, first of all, with the occupancy of the *M*-positions. However, these compounds do not exhaust the broad spectrum of synthesized single crystals with the sillenite structure.

In this paper, we have studied the growth of $Bi_{12}SiO_{20}$ single crystals and characterized them by Raman spectroscopy. $Bi_{12}SiO_{20}$ single crystals were grown which produced growth by the Czochralski technique. The yellow $Bi_{12}SiO_{20}$ crystal was characterized using Raman spectroscopy.

2. Experimental procedure

The experimental conditions of crystal growth are presented in earlier works [16, 20]. $Bi_{12}SiO_{20}$ single crystals were grown by the Czochralski technique using an MSR 2 crystal puller controlled by a Eurotherm. This system kept the crucible temperature constant to within 0.2 °C. The melt was contained in a platinum crucible (Ø = 40 mm, 40 mm depth). To decrease the radial temperature gradient in the melt, alumina was mounted on all of the system. All crystals were grown from synthesized Bi_2O_3 and SiO_2. The starting materials were mixed together in the stoichiometric ratio 6 : 1. The best results were obtained with a pull rate of 5–6 mm h^{-1}. The critical crystal rotation was calculated to be 20 rpm. The critical diameter of the crystals was calculated to be 15 mm. A solution of $HCl + HNO_3 + H_2O$ in the ratio 1 : 1 : 5 was found to be suitable for the chemical polishing of the bismuth silicon oxide crystals. Etching solutions of $HF + HNO_3$ in the ratio 2 : 1; NaOH 0.1 M; and $HCl + H_2O$ in the ratio 1 : 5 was satisfactory.

$Bi_{12}SiO_{20}$ single crystals were grown by the Czochralski technique along the ⟨111⟩ direction. Part of a polished slice of a $Bi_{12}SiO_{20}$ single crystal with etched pits of dislocations is shown in figure 1(a). For the examination of the dislocations in the crystals a Metaval of a Carl Zeiss Java metallographic microscope was used with a magnification of 600×. The absence of a core was confirmed by viewing polished crystal slices in both normal and polarized light. Also, in figure 1(a) can be observed the appearance of a regular pyramid, approximate orientation ⟨111⟩ with distinctive peaks.

The x-ray diffraction (XRD) data for $Bi_{12}SiO_{20}$ single crystals were measured using Cu Kα radiation and a monochromator (model Philips PW 1710 diffractometer) under the following experimental conditions: 40 kV and 20 mA, $20^\circ < 2\theta < 80^\circ$, with a step of 0.02° for 0.5 s. Figure 1(b) presents the XRD pattern of $Bi_{12}SiO_{20}$. The diffractometer was used in the 2θ range from 20° to 80°. XRD indicates that all peaks belong to the $Bi_{12}SiO_{20}$ phase that is in good agreement with JCPDF card no. 37–0485. The unit cell of $Bi_{12}SiO_{20}$ was calculated by the least squares method using all 21 reflections including more Kα_2 for five

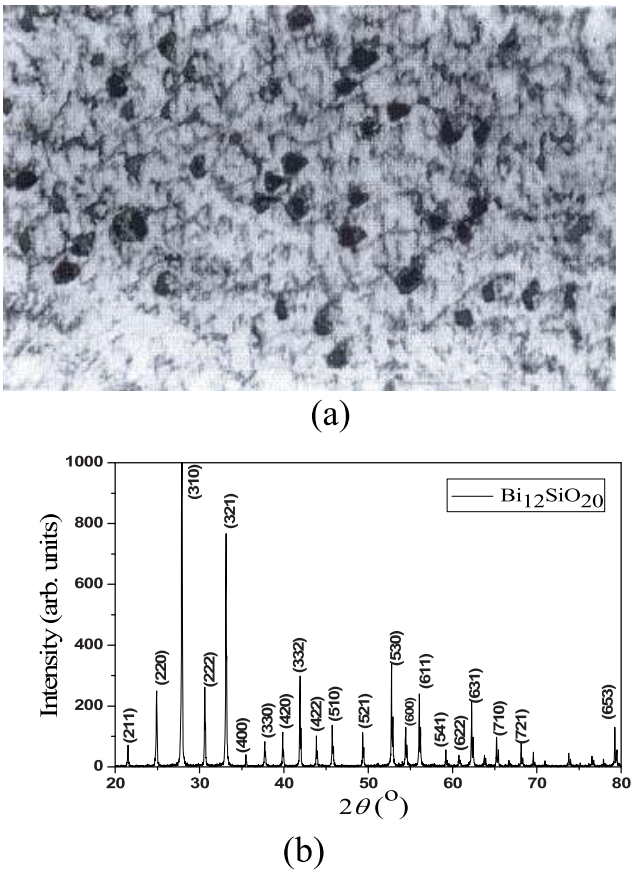

Figure 1. (a) A view of an etched plate of $Bi_{12}SiO_{20}$ crystals with triangles of dislocations. Magnification: 600×. (b) XRD pattern of $Bi_{12}SiO_{20}$ single crystals.

reflections. Many of the reflections correspond to $Bi_{12}SiO_{20}$ crystals with the parameter of the cubic *I*-centered cell $a = 1.01067$ nm, and $x = 12$. Our calculated result for the lattice parameter is $a = 1.0096$ nm, which is in good agreement with the published data. It should also be mentioned that a value of $x = 12$ for $Bi_xSiO_{1.5x+2}$ crystals where diameters of 10–12 mm for a crucible diameter of about 40 mm have been reported in the literature [12]. This is in accord with the dimensions of the crystals obtained in this work.

Raman spectra in the spectral range from 50 to 900 cm^{-1}, in back scattering geometry, were obtained by the micro-Raman analyzed using a Jobin–Yvon T64000 spectrometer equipped with a nitrogen cooled charge-coupled device detector. As the excitation source the 514 nm line of an Ar-ion laser was used. The measurements were made at 20 mW.

The infrared (IR) spectrum of the powder was obtained with Fourier transform infrared (FTIR) transmission–KBr disk spectroscopy (Hartmann and Braun, MB-series). The scanning range of FTIR was between 2000 and 400 cm^{-1}.

3. Results and discussion

The Raman spectra of $Bi_{12}SiO_{20}$ single crystals formed by the Czochralski technique, in the spectral range from 50 to 900 cm^{-1} at room temperature, are shown in figure 2. Raman spectra are often analyzed with the help of Lorentzian and Gaussian curves. Our interest is in quantitative analysis with

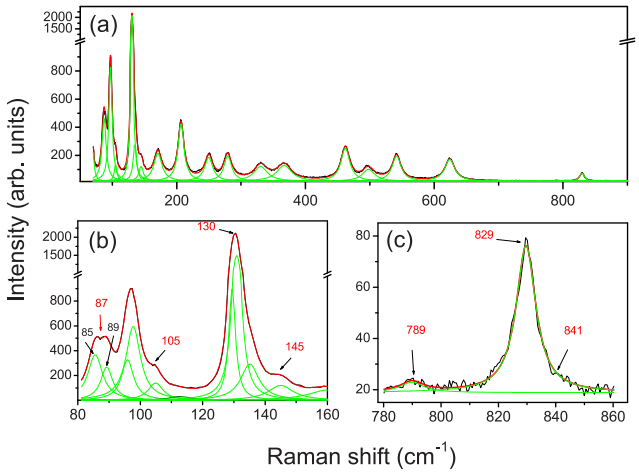

Figure 2. Raman spectra of $Bi_{12}SiO_{20}$ single crystals at room temperature.

a partial discussion of the trend, and we assume that all lines are of Lorentzian type. Solid lines in figure 2 were obtained by adding 19 different profiles. For BSO, group-theoretical analysis gives: $\Gamma = 8A + 8E + 25F$. The triply degenerated oscillations ($F \equiv TO + LO$, TO, LO) are manifested in the Raman and IR spectra, and the nondegenerated (A) and doubly degenerated (E) oscillations are manifested in the Raman spectra. Because all these oscillations are manifested in the Raman spectra, these spectra give the most complete information on the internal crystal oscillations. These spectra contain 19 Raman modes of different relative intensities, indicated as strong, medium and weak. The spectrum of $Bi_{12}SiO_{20}$ exhibits intense modes at about 87.1, 97.1, 104.26, 129.29, 134.9, 144.28, 170.8, 206.7, 249.7, 279.3, 330.3, 366.9, 461.9, 497.9, 541.5, 624.1 and 829.6 cm^{-1} (figure 2(a)). In the low-frequency region, the Raman spectra of sillenites together with the spectra of other complex oxide compounds of bismuth are similar to the Raman spectra of the α-Bi_2O_3. Among numerous intense lines in the spectra of $Bi_{12}SiO_{20}$ narrow lines are observed which coincide with an accuracy of several cm^{-1} with the lines at 87 and 130 cm^{-1} in the Raman spectra of sillenites. The oscillations in the region $\omega < 150\,cm^{-1}$ in the Raman spectrum of α-Bi_2O_3 are related to the external oscillations of the Bi atom. The oscillations of O lie in the region $\omega > 150\,cm^{-1}$. The internal modes should be sought in the range from 200 to 600 cm^{-1}. This fact confirms once more that the main contribution to the vibration spectrum of sillenites in the region $\omega < 650\,cm^{-1}$ is given by excitations of the bismuth–oxygen sublattice.

At the same time, for a number of oscillations, especially in the high-frequency region ($\omega > 650\,cm^{-1}$), an opposite situation occurs. The frequencies of these oscillations depend substantially on the mass of the atom M. The main contribution to these oscillations of the crystal lattice is given by oscillations of the tetrahedral $[MO_4]$. In accord with the structural data, the tetrahedron $[MO_4]$ is surrounded by 12 heavy atoms of bismuth, and its oscillations do not cause notable displacements. Indeed, the calculation of the normal oscillation frequencies for the complex molecule $M[O_4(Bi)_3]_4$ (M = Ge, Si, Ti) shows that the values of these frequencies are in good agreement with the experimentally measured ones and are close to the values of the corresponding frequencies of the group $[MO_4]^{4-}$. Registered modes in figure 2 are shown: $6A$, $5E$ and $8F$ ($3TO$, $1LO$ and $4(TO + LO)$). The intensity modes at about 144, 171, 280, 330, 541 and 789 cm^{-1} belong to the symmetry type A. These modes are characterized by the type of vibration, which shows 'breathing' of Bi and O atoms [23]. Also, these vibrations are combinations of bending and stretching modes in Bi_3O_4, Bi–O stretching, O–Bi–O bending, O–Si bending, symmetric Si–O stretching. The modes at about 87, 130, 250, 462* and 624 cm^{-1} belong to the symmetry type E and show Bi and O vibrations elongating the cluster along either ⟨100⟩ or ⟨001⟩, ⟨100⟩ or ⟨010⟩, respectively. These modes can be present in combinations of bending and stretching modes in Bi_3O_4, Bi–O stretching, O–Bi–O bending, and O–Si bending. The mode at about 462 cm^{-1} shows at the same time symmetry types E and F. The mode at about 87 cm^{-1} is very interesting because it is not so simple. This mode has already been registered in the literature. In our case the mode at 87 cm^{-1} is divided into two modes, whose positions are 85 and 89 cm^{-1}. The mode is clearly shown in figure 2(b). Also, the modes at about 97, 135, 207, 367, 462*, 498 and 830 cm^{-1} belong to the symmetry type F. The symmetry type (TO) has modes at about 97, 207, 462* and 830 cm^{-1}. They describe the vibrations in the SiO_4 (MO_4) unit: rocking of SiO_4, asymmetric stretching mode in SiO_4. The modes at about 105, 135, 367 and 498 cm^{-1} can be presented by symmetry type (TO+LO). The mode at about 367 cm^{-1} can be described as rotation of the SiO_4 unit. The mode at 789 cm^{-1} (symmetry type A), or modes at 830 cm^{-1} (symmetry type TO) and 841 cm^{-1} (symmetry type LO) are characteristic of symmetric stretching of the Si–O bond, or the asymmetric stretching SiO_4 unit, respectively. It may be noted that there are three new modes (104.26 ≅ 105, 129.29 ≅ 130 and 144.28 ≅ 145 cm^{-1}), which have not been shown in the literature so far (figure 2(b)). The modes at about 789 and 841 cm^{-1} are weakened, but still can be registered, as can be seen in figure 2(c). The very strong mode at 829 cm^{-1} can be seen in the same figure. Also, it should be noted that the frequency of the asymmetric stretching mode of the MO_4 tetrahedral is lower than that of the symmetric one. This is due to the strong influence of the Bi–O framework on the vibration behavior of the MO_4 tetrahedral in sillenites. It is characteristic of MO_4 structure. This is in agreement with the literature data.

Figure 3 has the IR spectra of samples of $Bi_{12}SiO_{20}$. The IR absorption spectra of $Bi_{12}SiO_{20}$ could be directly associated with the spectra of Bi_2O_3. We expect to have good agreement with the Raman and IR spectra of the crystalline BSO. Also, the IR spectrum is in good agreement with the data reported in the literature [24]. The major lines BSO was identified in our $Bi_{12}SiO_{20}$ single crystal. Five IR active modes are observed (figure 3). All modes are TO symmetry. The FTIR spectrum shows well-defined peaks located at 832, 606, 577, 528 and 468 cm^{-1}. The peak located at 832 cm^{-1} is due to the stretching vibration mode of Bi–O–Si bonds. In the present case, in the Bi–O–Si bonds, when the vibrations of the Bi–O and Si–O are in phase, the absorption is located at 840 and 812 cm^{-1}. The shift observed in the bands location can be associated with the difference in the atomic masses of silicon and bismuth atoms.

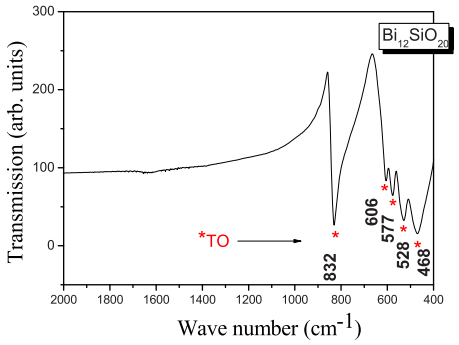

Figure 3. FTIR transmittance spectra of $Bi_{12}SiO_{20}$ single crystals at room temperature.

The peak at 606 cm^{-1} is related to cationic vibrations in the network or Bi–O vibration. The peak located at 577 cm^{-1} is associated with the bending vibration mode of the distorted tetrahedron formed by $(SiO_4)^{4-}$ groups. The band located at 528 cm^{-1} is assigned to deformation vibration of isolated $(SiO_4)^{4-}$ groups. The band located at 468 cm^{-1} is related to Si–O bond rocking and interaction by $[BiO_6]$ polyhedron.

4. Conclusion

In conclusion, the Czochralski technique has been used successfully to produce $Bi_{12}SiO_{20}$ single crystals. The obtained crystal was studied by XRD, Raman and FTIR spectroscopy. The single-crystal structure $Bi_{12}SiO_{20}$ was confirmed by XRD. We observed 19 Raman and 5 IR modes. The Raman and FTIR spectroscopy results are in accordance with XRD analysis. The Czochralski technique has become an important method for the growth and production of $Bi_{12}SiO_{20}$ single crystals without cores and with good optical quality. The absence of a core was confirmed by viewing polished crystal slices.

Acknowledgment

This work was financially supported by the Ministry of Education, Science and Technological Development of the Republic of Serbia through project no. III45003.

References

[1] Stepanov S I 1994 *Rep. Prog. Phys.* **57** 39–110
[2] Nolte D D and Melloch M R 1995 *Photorefractive Effects and Materials* ed D D Nolte (Dordrecht: Kluwer) pp 373–451
[3] Frejlich J and Garcia P M 2000 *Opt. Laser Eng.* **32** 515–27
[4] Blistanov A A, Bondarenko V S, Parelomova N V, Strizhevskaia F N, Chkalova V V and Shaskol'skaya M P 1982 Akusticheskie kristally, Spravochnik *Acoustic Crystals: A Handbook* ed M P Shaskol'skaya (Moscow: Nauka) p 632
[5] Skorikov V M, Kargin Yu F, Egorysheva A V, Volkov V V and Gospodinov M 2005 *Inorg. Mater.* **41** 24–46
[6] Chen J C, Liu L T and Young C C 1999 *J. Cryst. Growth* **198–199** 476–81
[7] Harris M, Larkin J, Cormier J E and Armington A F 1994 *J. Cryst. Growth* **137** 128–31
[8] Veber A, Kunej S and Suvorov D 2010 *Ceram. Int.* **36** 245–50
[9] Vasconcelos I F, De Figueiredo R S, Lima S J and Sombra A S B 1999 *J. Mater. Sci. Lett.* **18** 1871–4
[10] Xu X, Liao J, Shen B, Shao P, Chen X and He C 1993 *J. Cryst. Growth* **133** 267–72
[11] Lan C W, Chen H J and Tsai C B 2002 *J. Cryst. Growth* **245** 56–62
[12] Brice J C, Bruton T M, Hill O F and Whiffin F A C 1974 *J. Cryst. Growth* **24–25** 42–431
[13] Aggarwal M D, Wang W S, Choi J, Cochrane J C and Wang Z Y 1994 *J. Cryst. Growth* **137** 132–5
[14] Gopalakrishnan R, Krishnamurthy D, Arivuoli D and Ramasamy P 1994 *Mater. Chem. Phys.* **37** 90–3
[15] Santos M T, Rojo J C, Cintas A, Arizmendi L and Diguez E 1995 *J. Cryst. Growth* **156** 413–20
[16] Golubović A, Nikolić S, Gajić R, Djurić S and Valčić A 1999 *J. Serb. Chem. Soc.* **64** 553–61
[17] Rojo J C, Dieguez E and Derby J J 1999 *J. Cryst. Growth* **200** 329–34
[18] Picone P J 1988 *J. Cryst. Growth* **87** 421–4
[19] Santos M T, Arizmendi L, Bravo D and Diguez E 1996 *Mater. Res. Bull.* **31** 389–96
[20] Golubović A, Nikolić S, Gajić R, Djurić S and Valčić A 2002 *J. Serb. Chem. Soc.* **67** 279–89
[21] Venugopalan S and Ramdas A K 1972 *Phys. Rev.* B **5** 4065–79
[22] Vasconcelos I F, Pimenta M A and Sombra A S B 2001 *J. Mater. Sci.* **36** 587–92
[23] Wojdowski W 1985 *Phys. Status Solidi* B **130** 121–30
[24] Capelletti R, Beneventi P, Kovacs L and Fowler W B 2002 *Phys. Rev.* B **66** 174307

Journal of Physics and Chemistry of Solids 75 (2014) 869–877

Contents lists available at ScienceDirect

Journal of Physics and Chemistry of Solids

journal homepage: www.elsevier.com/locate/jpcs

Characterization of partially inverse spinel $ZnFe_2O_4$ with high saturation magnetization synthesized via soft mechanochemically assisted route

Zorica Ž. Lazarević [a,*], Čedomir Jovalekić [b], Valentin N. Ivanovski [c], Aleksander Rečnik [d], Aleksandra Milutinović [a], Božidar Cekić [c], Nebojša Ž. Romčević [a]

[a] Institute of Physics, University of Belgrade, P.O. Box 68, Pregrevica 118, Zemun, Belgrade, Serbia
[b] The Institute for Multidisciplinary Research, University of Belgrade, Kneza Višeslava 1, Belgrade, Serbia
[c] Institute of Nuclear Sciences Vinča, University of Belgrade, P.O. Box 522, 11001 Belgrade, Serbia
[d] Department for Nanostructured Materials, Jožef Stefan Institute, Ljubljana, Slovenia

ARTICLE INFO

Article history:
Received 31 October 2013
Received in revised form
1 March 2014
Accepted 6 March 2014
Available online 15 March 2014

Keywords:
A. Magnetic materials
C. Infrared spectroscopy
C. Mössbauer spectroscopy
C. Raman spectroscopy
D. Magnetic properties

ABSTRACT

$ZnFe_2O_4$ was prepared by a soft mechanochemical route from two starting combinations of powders: (1) $Zn(OH)_2$/α-Fe_2O_3 and (2) $Zn(OH)_2$/$Fe(OH)_3$ mixed in a planetary ball mill. The mechanochemical treatment provoked reaction leading to the formation of the $ZnFe_2O_4$ spinel phase that was monitored by XRD, TEM, IR and Raman spectroscopy. The spinel phase was first observed after 4 h of milling and its formation was completed after 18 h in both the cases of starting precursors. The synthesized $ZnFe_2O_4$ has a nanocrystalline structure with a crystallite size of about 20.3 and 17.6 nm, for the cases (1) and (2), respectively. In the far-infrared reflectivity spectra are seen four active modes. Raman spectra suggest an existence of mixed spinel structure in the obtained nanosamples. In order to confirm phase formation and cation arrangement, Mössbauer measurements were done. Estimated degree of inversion is about 0.58 for both starting mixtures. The magnetic properties of the prepared $ZnFe_2O_4$ powders were also studied. The results show that the samples have a typical superparamagnetic-like behavior at room temperature. Higher values of magnetization in the case of samples obtained with starting mixture (2) suggest somewhat higher degree of cation inversion.

1. Introduction

Spinel ferrites belong to a kind of magnetic materials that can be used in many areas, such as magnetic devices and switching devices [1–3]. Zinc ferrite ($ZnFe_2O_4$) is of interest not only to basic research in magnetism and electrical properties [4], but also has great potential in technological applications, such as magnetic materials, gas sensors, catalysts, photocatalysts, and absorbent materials [5–11]. Spinel ferrites described by the general formula $(A_{1-\lambda}B_{\lambda})[B_{2-\lambda}A_{\lambda}]O_4$, possess the cubic structure, have tetrahedral and octahedral cation sites in a face-centred cubic oxygen anion sublattice, denoted by ( ) and [ ], respectively. The letter A/B indicates cation that is originally placed in tetrahedral/octahedral site. For bulk paramagnetic $ZnFe_2O_4$ prepared by the conventional ceramic method, the inversion parameter λ is zero (normal spinel) [12,13]. Bulk $ZnFe_2O_4$ has a normal spinel structure with non-magnetic Zn^{2+} ions in the A-site and magnetic Fe^{3+} ions in the B-sites (in two antiparallel sublattices) and can be described by the formula $(Zn^{2+})[Fe^{3+}\uparrow Fe^{3+}\downarrow]O_4$. However, in contrast to bulk compound, the nanocrystalline $ZnFe_2O_4$ system always shows up as a mixed spinel structure in which Zn^{2+} and Fe^{3+} ions are distributed over the A and B-sites. This cationic rearrangement leads to the formation of two magnetic sublattices, which is responsible for the enhanced magnetization displayed when compared with normal $ZnFe_2O_4$ [4,14–18].

The synthesis of spinel $ZnFe_2O_4$ ferrite nanoparticles has been intensively studied in the recent years and the principal role of the preparation conditions on the morphological and structural features of the ferrites is discussed. The properties are strongly influenced by the composition and microstructure of ferrite particles, which are sensitive to the preparation methodology used in their synthesis. Many types of methods including ceramic synthesis [19,20], co-precipitation method [21–24], tartrate precursor method [25], hydro-thermal [26,27], combustion [28], auto-combustion [29], polymeric

* Corresponding author. Tel.: +381 11 37 13 035; fax: +381 11 3160 531.
E-mail address: lzorica@yahoo.com (Z.Ž. Lazarević).

http://dx.doi.org/10.1016/j.jpcs.2014.03.004
0022-3697/

precursor route [30], solvothermal [31], sol-gel [15,32–34] and ball-milling technique [20,35–37] have been used for the preparation of zinc ferrite nanoparticles.

Mechanochemical treatment has been recognized as a powerful technique for synthesis of a wide range of materials. New approach to mechanochemical synthesis, based on reactions of solid acids and bases, crystal hydrates, basic and acidic salts, which react with each other releasing water, has been called soft mechanochemical synthesis [38]. As the hardness of these compounds is 3–4 times lower than that of anhydrous oxides, it is easier to activate a reaction among them mechanochemically.

The aim of this paper is to show that under the laboratory conditions it is simple to prepare the good quality nano-$ZnFe_2O_4$ ferrite by soft mechanochemical synthesis. The evolution of the synthesis of nano-$ZnFe_2O_4$ starting from the two mixtures of powders milled in different time durations was examined. The starting materials were (1) mixture of $Zn(OH)_2$/α-Fe_2O_3 and (2) mixture of $Zn(OH)_2$/$Fe(OH)_3$ powders. The samples obtained after 4, 10 and 18 h of milling time are compared and investigated using various characterization methods.

2. Experimental procedures

For mixtures of crystalline powders, denoted by (1) and (2), the starting material were (1) zinc(II)-hydroxide ($Zn(OH)_2$, Merck 95% purity) and hematite (α-Fe_2O_3, Merck 99% purity) and (2) zinc(II)-hydroxide and iron-hydroxide ($Fe(OH)_3$) in equimolar ratio [4]. The $Fe(OH)_3$ powder was made by adding equimolar amounts of NaOH solution (25% mass), made from 99% purity NaOH (Merck) to the $FeCl_3$ solution (25% mass), made from 99% purity $FeCl_3 \cdot 6H_2O$ (Merck) [39]. Dark brown precipitate was filtrated, washed with large amounts of water and dried in a vacuum dessicator. Before milling, the $Fe(OH)_3 \cdot nH_2O$ powder was heated at 105 °C for 24 h. The material prepared by this way had 99.5% $Fe(OH)_3$. It was defined by potentiometric redox titration [39]. The starting hydrohides were amorphous, while hematite was crystalline.

Mechanochemical synthesis was performed in air atmosphere in planetary ball mill (Fritsch Pulverisette 5). A hardened-steel vial of 500 cm^3 volume, filled with 40 hardened steel balls with a diameter of 13.4 mm, was used as the milling medium. The mass of the powder was 20 g and the balls-to-powder mass ratio was 20:1. The milling was done in the air atmosphere without any additives. The angular velocity of the supporting disc and vial was about 32 and 40 rad s^{-1}, respectively. The intensity of milling corresponded to an acceleration of about 10 times the gravitation acceleration. All samples, with different starting compositions and milling times, were prepared and milled separately. At the expiration of the selected milling times (4, 10 and 18 h) the mill was stopped and a small amount of powder was removed from the vial for examination.

Characterization of the samples obtained after various milling times was carried out by

- X-ray diffraction analysis of powders treated for various periods of milling times by a Philips PW 1050 diffractometer equipped with a PW 1730 generator (40 kV × 0 mA) using Ni filtered CoK_α radiation at the room temperature. Measurements were done in 2θ range of 15–80° with scanning step width of 0.05° and 10 s scanning time per step. After XRD measurements, the powder was placed back in a vial to obtain the same grinding conditions (balls to powder weight ratio).
- For transmission electron microscopy (TEM) observations the powders were dispersed in ethanol. The suspension containing our sample was deposited onto the lacey carbon-coated TEM sample supports. TEM studies were performed using a 200 kV TEM (JEM-2100 UHR, Jeol Inc., Tokyo, Japan) equipped with an ultra-high resolution objective lens pole piece having a point-to-point resolution of 0.19 nm, being sufficient to resolve the lattice images of nanoparticles. Due to relatively small size of the nanoparticles selected area electron diffraction patterns (EDP) over the multiple nanocrystals was recorded to obtain the characteristic diffraction rings with structure-specific *d*-values. Electron energy dispersive X-ray spectroscopy (EDS) was used to examine the chemical composition of the product.
- The infrared (IR) measurements were carried out with a BOMMEM DA-8 FIR spectrometer. A DTGS pyroelectric detector was used to cover the wave number range from 50 to 700 cm^{-1}.
- Raman measurements of mixture of powders were performed using Jobin-Yvon spectrometer. An optical microscope with 100 × objective was used to focus the 514 nm radiation from a Coherent Innova 99 Ar^+ laser on the sample. The same microscope was used to collect the backscattered radiation. The dispersed scattering light was detected by a charge-coupled device (CCD) detection system. Room temperature Raman spectra are in spectral range from 100 to 1600 cm^{-1}. The average power density on the sample was about 20 mW mm^{-2}.
- The ^{57}Fe Mössbauer spectra were obtained by constant acceleration in transmission mode using ^{57}Co(Rh) source, at room temperature. The spectra calibrated by laser and isomer shifts, are shown with respect to the α-Fe. The data were analyzed by the WinNormos-Site software based on the least squares method [40]. The correction for sample thickness was done by the transmission integral.
- Magnetic measurements were done at Cryogenic vibrating sample magnetometer (VSM) in the magnetic field from 0 kOe to ± 80 kOe.

3. Results and discussion

We investigated the possibility of the formation of spinel $ZnFe_2O_4$ ferrite phase trough the soft mechanochemical treatment, starting from two different mixtures of materials. The two cases were

- Case (1):
  Step (a) milling time 0 h: $Zn(OH)_2 + \alpha\text{-}Fe_2O_3$.
  Step (b) milling time 4 h: $ZnO + H_2O\uparrow$ (water vapor, at 100 °C) + α-Fe_2O_3 + β-$Zn(OH)_2$ + $ZnFe_2O_4$.
  Step (c) milling time 10 h: $ZnO + \alpha\text{-}Fe_2O_3 + ZnFe_2O_4$.
  Step (d) milling time 18 h: $ZnFe_2O_4$.
- Case (2):
  Step (a) milling time 0 h: $Zn(OH)_2 + 2Fe(OH)_3 \times nH_2O$.
  Step (b) milling time 4 h: $ZnO + H_2O\uparrow$ (water vapor, at 100 °C) + α-Fe_2O_3 + $ZnFe_2O_4$.
  Step (c) milling time 10 h → $ZnO + H_2O\uparrow$ (water vapor, at 100 °C) + α-Fe_2O_3 + $ZnFe_2O_4$.
  Step (d) milling time 18 h: $ZnFe_2O_4$.

Fig. 1 shows the X-ray diffraction patterns of (1) $Zn(OH)_2$ and α-Fe_2O_3 and (2) $Zn(OH)_2$ and $Fe(OH)_3$ powders milled during different time (4, 10 and 18 h). In mechanochemically treated samples a spinel $ZnFe_2O_4$ phase is present in form of nanocrystalline particles already after shortest milling times. With increasing milling time, the diffraction peaks corresponding to the simple oxide and hydroxide gradually disappear. After 18 h of milling, in both cases of precursors, only a single phase nano-zinc ferrite is obtained. During 4 h mechanochemical treatment of mixture (1), Fig. 1a, the characteristic peaks for β-$Zn(OH)_2$ (JCPDS card 89-0138) ZnO (JCPDS card 89-7102), α-Fe_2O_3 (JCPDS card 89-8103) and

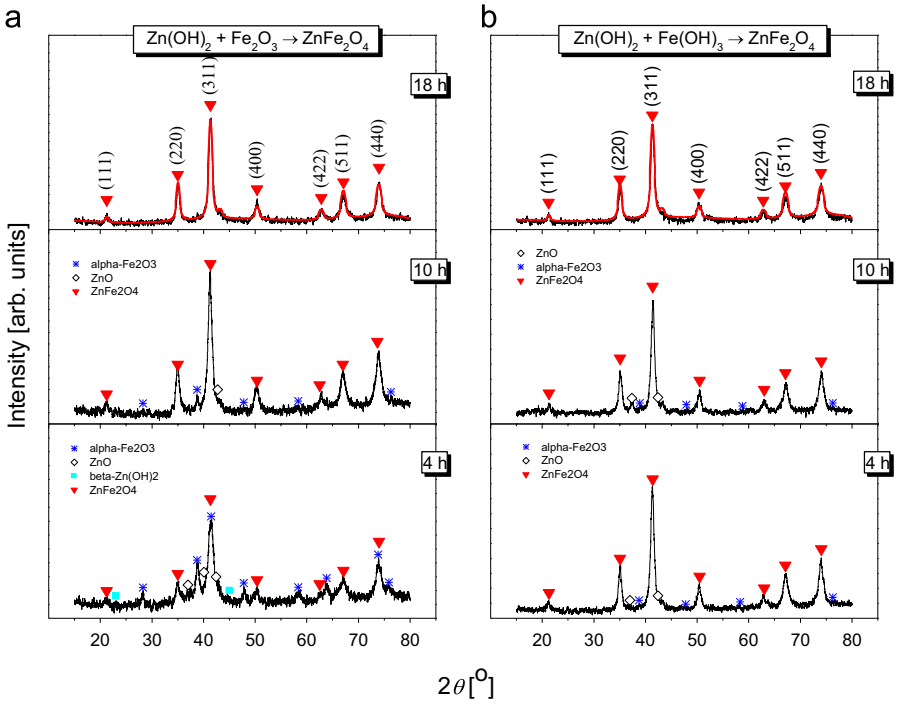

Fig. 1. X-ray diffraction pattern of the mixture of powders (a) $Zn(OH)_2/\alpha$-Fe_2O_3 and (b) $Zn(OH)_2/Fe(OH)_3$ after 4, 10 and 18 h milling time.

$ZnFe_2O_4$ (JCPDS card 89-7412) [41] are visible. In the XRD spectrum of mixture (2), Fig. 1b, ZnO, α-Fe_2O_3 and $ZnFe_2O_4$ reflections are present. It can be observed that the sample obtained after 4 h milling of the mixture hydroxide/oxide powders exhibits somewhat lower intensity of the ferrite phase peaks compared to the spectrum obtained from the mixture of hydroxide/hydroxide powder. With prolongation of milling to 10 h in both the cases of synthesis, the characteristic peaks of the ferrite phase become more pronounced and sharper and the secondary phases that can be seen after 4 h of grinding almost disappear. It can be noticed that the major peaks of the ferrite phase were continuously increasing with the milling time. It is important to note that after milling of the mixtures of powders even for 4 h in both mixtures $ZnFe_2O_4$ phase (JCPDS card 89-7412) is dominant. The main reason for this phenomenon is a rapid decomposition of $Zn(OH)_2$ ($Zn(OH)_2 \rightarrow ZnO + H_2O$), so that after 10 h of milling there are no peaks corresponding to the starting compound $Zn(OH)_2$. It is known that the milling process leads to overheating of the vessel, and at temperatures higher than 100 °C results in the evolution of water vapor. Opening of the container allows partial evaporation of water. It might be noted that the hydroxides transform into oxides and in XRD spectra the characteristic oxide peaks can be observed. Overpressure of gasses in the vessel, especially water vapor, reduces the efficiency of milling and to some extent slows down the creation of a new phase. Further milling up to 18 h leads to full synthesis of a new phase. All peaks are well indexed to the crystal planes of spinel ferrite (k h l): (111), (220), (311), (400), (422), (422), (511) and (440). This confirms that the mechanochemical synthesis of $ZnFe_2O_4$ is feasible and complete for 18 h milling time. Compared to other synthesis routes, the soft mechanochemical process used here represents a more favorable, high-yielding, low-temperature and low-cost procedure for synthesis of nanocrystalline $ZnFe_2O_4$ [14,21,22].

Crystallite size, S of powders treated mechanochemically for 18 h were calculated using XRD data by means of the Scherrer equation [42]:

$$S = 0.9\lambda/(B_m \cos \theta_B)$$

where λ is the wavelength of the X-ray source and θ_B is the Bragg angle of the considered XRD peaks. B_m represents the FWHM line broadening for investigated material, obtained for Lorentz profile of peaks, as follows:

$$B_m = B_{obs} - B_s$$

where B_{obs} is the FWHM line broadening of the observed peak, and B_s represents the FWHM line broadening of the internal standard (α-Al_2O_3) [42]. The resulting value of the crystallite size, obtained from the strongest reflections (311) is 20.3 and 17.6 nm, respectively, for cases denoted by (1) and (2) after 18 h milling time.

Fig. 2 shows TEM images with corresponding EDPs of individual products after milling for 4 and 18 h (Fig. 3). In the samples milled for 4 h spinel-type reflections of $ZnFe_2O_4$ already dominate the EDPs, while weak lines corresponding to starting materials are still present. Measured d-values of $ZnFe_2O_4$ are listed in Table 1. In the sample with starting composition of $Zn(OH)_2/Fe_2O_3$ few of the stronger reflections of hematite are present in EDPs, whereas $Zn(OH)_2/Fe(OH)_3$ sample shows remnants of Fe-rich hydroxide, Fig. 3. In general, both synthesis routes produced a substantial amount of nanosized $ZnFe_2O_4$ particles already after 4 h of milling, that is consistent with our XRD data. According to EDPs measurements chemical compositions of nanocrystalline clusters have a slightly lower scatter intensity when Fe_2O_3 is used instead of Fe $(OH)_3$ as a starting material. Particle size distribution is in both processing routes are comparable and ranges between 3 and 25 nm. The crystallites in both systems are rounded, show highly activated non-equilibrium surfaces and tend to agglomerate into larger clusters with diameters of several hundred of nanometers. In the initial stages of mechanochemical reaction particles are covered by few nanometers thick amorphous layers, which disappear after 18 h. After 18 h milling time, both processing routes produce pure spinel reflections belonging to the $ZnFe_2O_4$ phase.

The composition of the products milled for 18 h was analyzed by EDS measurements on several individual particles, as well as on large crystal clusters. The analyses show a constant Zn:Fe atomic ratio of 1:2, which corresponds to the $ZnFe_2O_4$ phase. Fig. 3 shows a typical EDS spectrum, recorded on the $Fe_2O_3/Zn(OH)_2$ sample

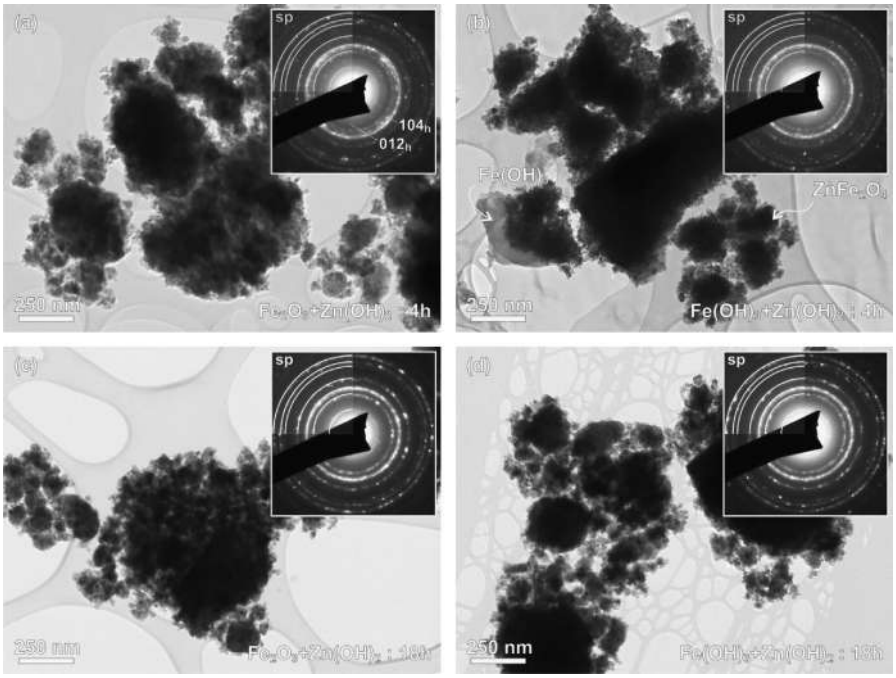

Fig. 2. TEM images with corresponding EDP (insets in the upper right corners) of mechano-chemically treated samples with starting compositions $Zn(OH)_2/\alpha$-Fe_2O_3 and $Zn(OH)_2/Fe(OH)_3$ after processing for 4 and 18 h. Lines in the upper-right quadrant of EDP indicate *d*-values for $ZnFe_2O_4$ spinel phase (see Table 1) that fully evolves after 18 h of milling time.

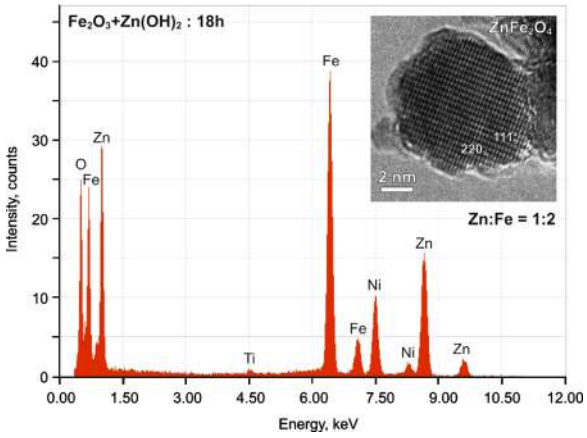

Fig. 3. EDS spectrum of $Zn(OH)_2/\alpha$-Fe_2O_3 after milling for 18 h shows the presence of single $ZnFe_2O_4$ phase. The inset shows a HRTEM image of rounded $ZnFe_2O_4$ nanoparticle oriented close to the $[1\bar{1}0]$ zone axis with well resolved lattice fringes, characteristic for the spinel structure.

milled for 18 h (see Fig. 2c). Ni-peak present in the EDS spectrum stems from the Ni-grid for the TEM specimens, whereas the minor peak of Ti probably originates from ilmenite impurities in the Fe_2O_3 precursor.

Far infrared reflectivity (FIR) spectra of the synthesized $ZnFe_2O_4$ ferrite were recorded in the range of 50–700 cm^{-1}, where all the group theory predicted spinel modes (4 F_{1u}) are expected to be, Fig. 4. It is known that the band at $\sim$600 cm^{-1} corresponds to the vibrations of cation–oxygen bonds in tetrahedral site and the lower band at $\sim$350 cm^{-1} is attributed to the vibrations of the cation–oxygen bond in octahedral site. The different values of the energy position for these modes are due to different values of metal ion–O^{2-} distances for octahedral and tetrahedral sites. In reflectivity spectra of $ZnFe_2O_4$ obtained after 4 h and 10 h milling of the mixture (1) and in the case of 4 h milled mixture (2), it is obvious that hematite modes are superposed to $F_{1u}(2)$ and $F_{1u}(3)$ spinel modes. It is visible in Fig. 5, where fitted values of TO and LO modes are also presented. Values of the $ZnFe_2O_4$ spinel modes in the powder samples are expectedly modified in comparison with a bulk due to superposition of bulk and surface effects.

Raman spectra of samples obtained from the two mixtures of nanopowders: (1) $Zn(OH)_2/\alpha$-Fe_2O_3 and (2) $Zn(OH)_2/Fe(OH)_3$ after various milling times are analyzed by deconvolution (Fig. 6). Already after 4 h of milling a spinel phase is prevalent as evidenced by the characteristic features in Raman spectra. In the spectra of both the samples obtained after 4 h milling time and after 10 h in the case of mixture (1), a more intensive mode can be seen at about 290 cm^{-1} superposed with a hematite mode. This is consistent with the results of XRD and FIR reflectivity analysis. At the same time, the samples listed above, have the multiphonon parts of spectra with intensities comparable with active spinel modes what suggests an increased structure irregularities. After 18 h milling time both type of samples become a single phase. All samples have more than 5 Raman active modes predicted by the group theory in the normal spinel structure: $A_{1g}+E_g+3F_{2g}$. Raman spectra of $ZnFe_2O_4$ nanocrystalline samples, obtained by the mechanochemical method have visible doublets and it could be concluded that spinel structure of these samples is partially inversed [43].

Deconvolution of spectra recorded on single phase samples (obtained after 18 h of milling) gives information about distribution of cations over tetrahedral and octahedral sublattices. The high frequency first order mode A_{1g} is due to symmetric stretching of oxygen atoms along cation–oxygen bonds in the tetrahedral coordination [44,45]. Double modes in the milled samples imply that ordered sublattice of Zn ions exist together with analogous sublattice of Fe-ions. The strongest modes above 600 cm^{-1}, with A_g symmetry, correspond to symmetric stretching of oxygen in tetrahedral AO_4 groups, so the modes at about 630 cm^{-1} can be considered as stretching of oxygen in the environment of heavier Zn-cation and the mode at about 720 cm^{-1} originated from FeO_4 tetrahedron (like in Fe_3O_4). It is similar with other doubled modes. E_g pair is due to symmetric bending of oxygen with respect to

Table 1
Measured *d*-values [nm] for $ZnFe_2O_4$ from EDP pattern (from Fig. 2c).

	D_1	D_2	D_3	D_4	D_5	D_6	D_7
Measured [nm]	0.4866	0.2998	0.2535	0.2112	0.1726	0.1618	0.1489
JCPDF #89-7412	0.48687	0.29815	0.25426	0.21082	0.17213	0.16229	0.14907
Crystallogr. plane	{111}	{220}	{311}	{400}	{422}	{333}	{440}

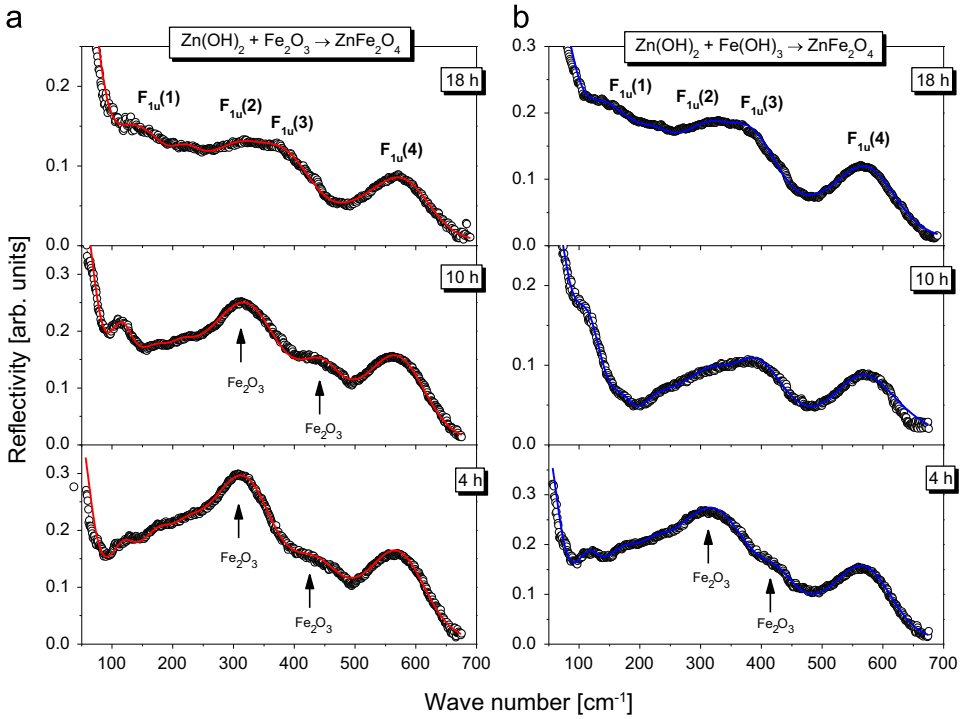

Fig. 4. IR spectra at room temperature of the mixture of powders: (a) $Zn(OH)_2/\alpha$-Fe_2O_3 and (b) $Zn(OH)_2/Fe(OH)_3$ after 4, 10 and 18 h milling time.

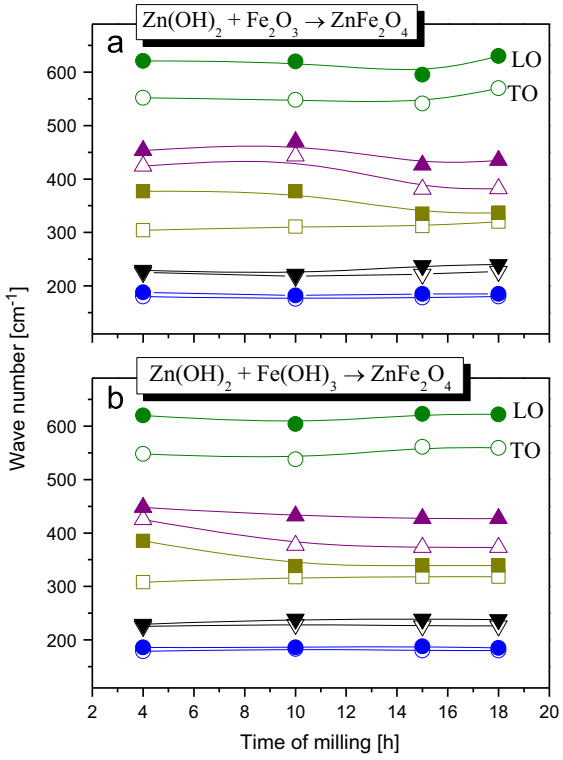

Fig. 5. Position of LO and TO infrared modes for both cases of soft mechanochemical synthesis.

cations in tetrahedral surrounding. $F_{2g}(2)$ and $F_{2g}(3)$ correspond to the vibrations of octahedral group. $F_{2g}(1)$ is due to translational movement of the whole tetrahedron.

According to more exaggerated A_{1g} mode originated from vibrating of FeO_4 tetrahedrons in the case of single phase sample obtained from mixed hydroxides it can be supposed that this sample must have a little higher degree of inversion.

Mössbauer spectroscopy was performed in order to get more information on metal cation redistribution in the nanocrystalline ferrite powders $ZnFe_2O_4$. As it is already been mentioned, the mechanochemically synthesized powders $ZnFe_2O_4$, both obtained from mixtures $Zn(OH)_2/\alpha$-Fe_2O_3 and $Zn(OH)_2/Fe(OH)_3$ in planetary ball mill, might have distribution of cations in the zinc spinel ferrites described by the general formula $(Zn^{2+}_{1-\lambda}Fe^{3+}_{\lambda})[Zn^{2+}_{\lambda}Fe^{3+}_{2-\lambda}]O^{2-}_4$. Knowing the ratio of areas (A) of Mössbauer subspectra of both iron sites (tetrahedral A) and [octahedral B], the inversion parameter λ could be estimated from equation: $A_{(A)}/A_{[B]}=\lambda/(1-\lambda)$ [46]. It is worth to note this equation is obtained by assumption that the ratio of the recoil-less fraction is $f_{[B]}/f_{(A)}=1$ at the room temperature [47].

Room temperature Mössbauer measurements of the bulk $ZnFe_2O_4$ with normal spinel structure shows a paramagnetic doublet with quadrupole splitting $\Delta=0.35$ mm s^{-1}and isomer shift $\delta=0.36$ mm s^{-1} [48]. There are two reasons for the appearance of Zeeman's hyperfine field sextets in spectra of nano-$ZnFe_2O_4$. Both of them are based on displacement of Zn^{2+} cations to octahedral sites and Fe^{3+} cations into tetrahedral sites, induced by preparation conditions, in our case, mechanical treatment. The cations redistribution leads to decrease of unit cells and oxygen parameter, causing the deviation of the $[Fe^{3+}]$–O^{2-}–$[Fe^{3+}]$ bond

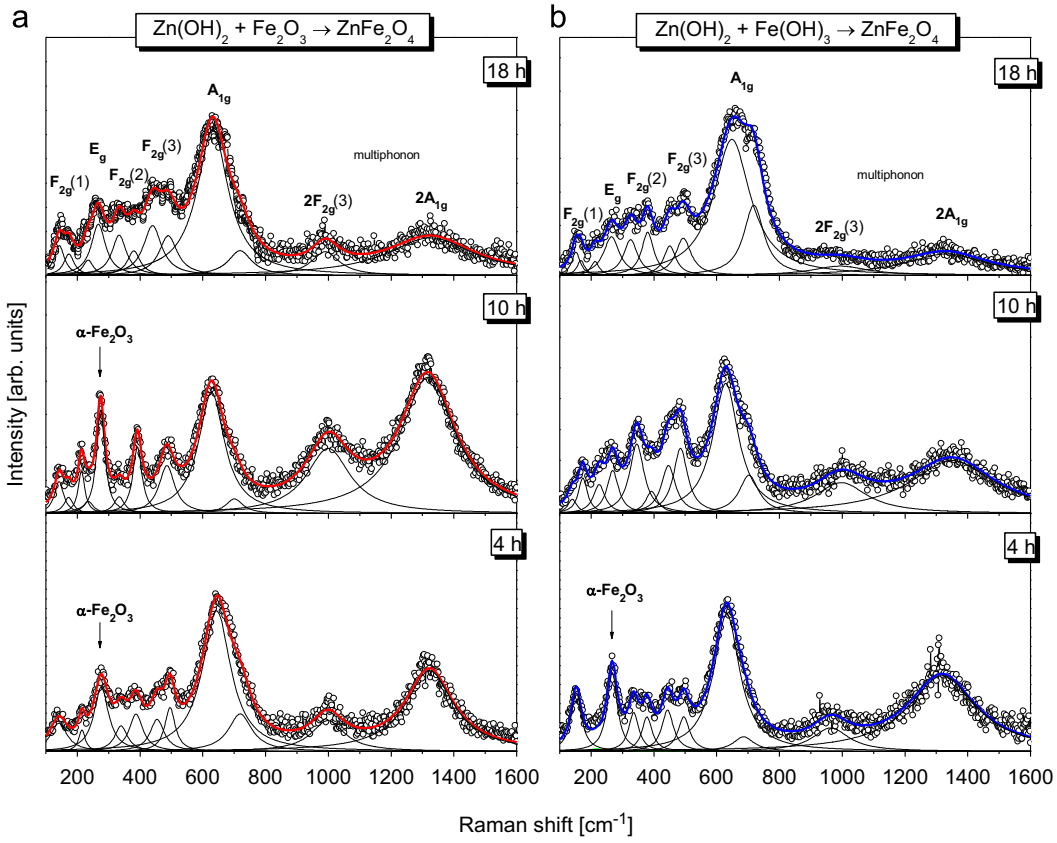

Fig. 6. Raman spectra at room temperature of the mixture of powders: (a) $Zn(OH)_2/\alpha$-Fe_2O_3 and (b) $Zn(OH)_2/Fe(OH)_3$ after 4, 10 and 18 h milling time.

angle and the intensity of the superexchange interaction [49]. A distorted octahedron would cause a large value of the quadruple shift (2ε) for combined hyperfine interaction. The much stronger superexchange interaction rises from tetrahedral site where substituted (Fe^{3+}) magnetic ion coupling with 12 [Fe^{3+}] nearest neighbors in the second coordination sphere via four oxygen anions from the first coordination sphere. The number of formed clusters in this way increases with decreasing nanoparticle size [50].

The Mössbauer spectrum (Fig. 7a) of the sample formed from $Zn(OH)_2$ and α-Fe_2O_3 milled in 4 h, is fitted with two sextets and two doublets. It was concluded that sample exhibits existence of a large amount of hematite versus formed zinc spinel ferrite. The hematite sextet in Mössbauer measurements might be recognized by the following parameters: isomer shift $\delta=0.376$ mm s^{-1}, quadruple shift $2\varepsilon=-0.197$ mm s^{-1}, and hyperfine field $B_{hf}=51.75$ T. The initial hematite makes 43% of the total fitted area, obtained by the very sharp line characterized by FWHM: $\Gamma=0.21$ mm s^{-1} (Table 2). The second sextet in the measured spectra originates from ferrite, 24% of the total fitted area, with disturbed octahedral environment. The higher value of the line width $\Gamma=0.54$ mm s^{-1} is incurred by a distribution of hyperfine fields as consequence of the hyperfine field sensitivity to the changes of of Fe–O distance. A paramagnetic doublet's presence in the measured sample with $\delta=0.352(5)$ mm s^{-1}, and $\Delta=0.551(9)$ mm s^{-1}, represents 19% of the total resonant signal. The measured isomer shift is typical for Fe^{3+} in octahedral environment, while somewhat higher values for Δ and Γ show that environment is disordered by milling. Hence, oxygen's structure parameters deviate from the ideal value 0.375 disturbing symmetry of the octahedral site. The point group of the *B* site transformed from cubic symmetry to trigonal symmetry, causes the appearance of large value for Δ. That signal, obviously, comes from larger Zn in octahedral surrounding in the case of very small, super-paramagnetic nanoparticles. The second doublet, represented with 14% of the total resonant signal, has the isomer shift $\delta=0.26$ mm s^{-1} as same as isomer shift's values for Fe^{3+} in the tetrahedral site. The significantly large value for quadruple splitting, $\Delta=1$ mm s^{-1} does not match the cubic symmetry on the tetrahedral site. It has originated as repercussion of changes in tetrahedral and octahedral bond lengths and positions, that is happening with nanoparticles whose size is below 10 nm [51]. As a confirmation for this kind of disorder, there is a large value for the line width $\Gamma=1.02$ mm s^{-1}.

On the other hand, the sample obtained from $Zn(OH)_2/Fe(OH)_3$ milled in 4 h, consists of only 6% hematite observed by the Mössbauer spectroscopy (Fig. 7c). The second sextet, with 18% of the total fitted area, corresponds to $ZnFe_2O_4$ and measures value of 20 T of hyperfine field. The remaining subspectra are the two super-paramagnetic doublets that originate from very small nanoparticles of zinc ferrite. They are created by signals from Fe^{3+} ions in octahedral surroundings.

Investigation of the sample formed from $Zn(OH)_2/\alpha$-Fe_2O_3 milled in 18 h by Mössbauer spectroscopy reveals three Zeeman's sextets and four paramagnetic doublets (Fig. 7b). Only 2.2% of whole fitted area belongs to the remained hematite. The two other sextets have the origin from tetrahedral positioned (Fe^{3+}) ions in $ZnFe_2O_4$. Also, these all paramagnetic doublets have got origin in the zinc ferrite spinel. These signals come from [Fe^{3+}] ions in octahedral sites, but from particles with different sizes. The whole fitted area from A-sites is $A_{(A)}=57(15)$%, and from B-sites $A_{[B]}=40.8(13.2)$. Hence, we could calculate that sample obtained after 18 h milling of $Fe_2O_3/Zn(OH)_2$ powders has zinc ferrite spinel structure with the inversion parameter $\lambda=0.58(32)$.

The Mössbauer spectrum taken from 18 h milled $Zn(OH)_2/Fe(OH)_3$ sample consists of three sextets and three doublets (Fig. 7d). The parameters of one sextet with relative abundance of 2.9% refer

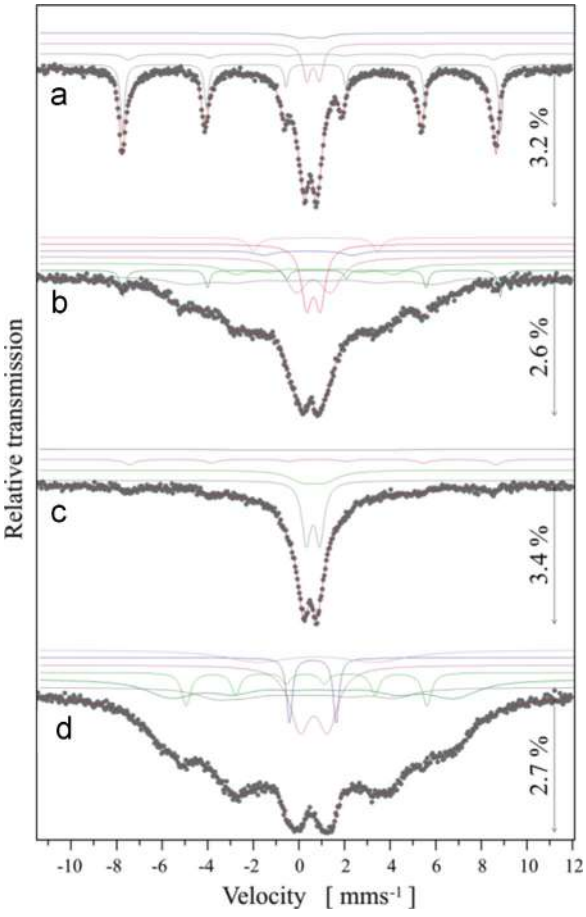

Fig. 7. Mössbauer spectra at room temperature: (a) of the mixture of $Zn(OH)_2$/α-Fe_2O_3 after 4 h milling time; (b) of the mixture of $Zn(OH)_2$/α-Fe_2O_3 after 18 h milling time, and (c) of the mixture of $Zn(OH)_2$/$Fe(OH)_3$ after 4 h milling time; (d) of the mixture of $Zn(OH)_2$/$Fe(OH)_3$ after 18 h milling time. The values of relative absorption are shown. The fitted lines of subspectra are plotted above the main spectrum with fitted line.

on the presence of α-Fe. The resonant signals make sextets having the origin from iron ions on tetrahedral sites. On the other side, the doublets are created by signals from octahedral standing iron ions. For this sample the inversion parameter λ is 0.58(63). The λ is calculated by data, based on following total fitted area: $A_{(A)}=56$ (32) and $A_{[B]}=41.1(18.7)$.

There is a possibility to arise changes in tetrahedral and octahedral bond lengths and angles or to form oxygen vacancies during the milling process. The consequences are large and enormously large values are obtained for Δ or 2ε and value changes for an isomer shift. Also, a line width is sensitive to this structure changes, too. Different iron ions environment produced by cations redistribution, produces different subspectra and also contributes to broadening of the corresponding line width.

The magnetization curves of the samples obtained from (1) $Zn(OH)_2$/α-Fe_2O_3 and (2) $Zn(OH)_2$/$Fe(OH)_3$ mixture of powders milled during different time (4, 10 and 18 h) measured at room temperature are shown in Fig. 8. The curves have "S" shape with low coercivity and very small remanence magnetization. In the case of pure phase $ZnFe_2O_4$ samples obtained after 18 h of milling coercivity is $H_c=103$ Oe and 87 Oe and remanence magnetization is $M_{rem}=4.5$ emu g^{-1} and 5.5 emu g^{-1} (Fig. 8a and b).

The estimated values of saturation magnetization for 18 h of milling are $M_{sat}=54.2$ emu g^{-1} and 65.1 emu g^{-1}, respectively, which is a result of the inversion of cations (Fig. 8). Super exchange interaction between Fe^{3+} ions in (A) and [B] sites, causes such a high value of magnetization. The small remanence magnetization in the $ZnFe_2O_4$ powder samples confirms that nanocrystallites are mostly single domain. Open hysteresis loop, with coercive field $H_c \neq 0$, (in combination with high magnetization), shows that ferromagnetic transition temperature is well above the room temperature. The magnetization does not achieve a saturation in the magnetic fields up to ± 80 kOe that indicates a surface spin disorder. Ordering of these spins in a magnetic field contributes in the magnetic moment of the predominantly monodomen $ZnFe_2O_4$ crystallites, also. As it can be seen in Fig. 8a and b, saturation magnetization increases with milling time in both starting mixtures. In the case of single phase sample obtained from mixture

Table 2
Mössbauer parameters: A-relative area fraction of component, Γ-line width (FWHM), δ-isomer shift with respect to the α-Fe, Δ-quadrupole splitting (2ε-quadrupole shift) and B-hyperfine induction. Labels (A) and [B] denote the tetrahedral and octahedral sites, respectively. The fixed parameters in the fit are denoted by the superscript *f*.

Mixture		Compound	Site	Mössbauer parameters				
				A **[%]**	***Γ*** **[mms^{-1}]**	***δ*** **[mms^{-1}]**	***Δ/2ε*** **[mms^{-1}]**	***B*** **[T]**
$Fe_2O_3+Zn(OH)_2=ZnFe_2O_4$	4 h	α-Fe_2O_3		43(7)	0.21(1)	0.376(2)	−0.198(4)	51.45(2)
		$ZnFe_2O_4$	[B]	24(5)	0.54(5)	0.364(9)	−0.22(2)	49.6(2)
		$ZnFe_2O_4$	[B]	19(2)	0.41(2)	0.352(5)	0.551(9)	
		$ZnFe_2O_4$	(A)	14(2)	1.02(6)	0.26(2)	1.0(1)	
	18 h	α-Fe_2O_3		2.2(2)	0.255^f	0.39(2)	−0.23(4)	51.3(1)
		$ZnFe_2O_4$	(A)	21(5)	1.3(2)	0.43(8)	0.0(1)	21.6(4)
		$ZnFe_2O_4$	(A)	36(10)	2.03(9)	0.15(6)	0.1(1)	33.5(2)
		$ZnFe_2O_4$	[B]	11(5)	0.55(9)	0.36(1)	0.60(4)	
		$ZnFe_2O_4$	[B]	25(7)	1.1(2)	0.36(2)	1.5(1)	
		$ZnFe_2O_4$	[B]	2.8(2)	1.0(5)	0.1(1)	3.9(2)	
		$ZnFe_2O_4$	[B]	2(1)	0.5(2)	0.45(4)	5.45(9)	
$Fe(OH)_3+Zn(OH)_2=ZnFe_2O_4$	4 h	α-Fe_2O_3		6(3)	0.52(9)	0.43(3)	−0.20(5)	49.8(2)
		$ZnFe_2O_4$	(A)	18(10)	2.6(1.0)	0.3(2)	0.1(2)	20(1)
		$ZnFe_2O_4$	[B]	28(19)	0.46(8)	0.346(5)	0.59(2)	
		$ZnFe_2O_4$	[B]	48(34)	1.5(1)	0.37(1)	1.0(3)	
	18 h	α-Fe		2.9(8)	0.45(9)	0.03(2)	0.05(4)	32.7(1)
		$ZnFe_2O_4$	(A)	42(22)	2.6(2)	0.37(7)	−0.1(2)	38.5(2)
		$ZnFe_2O_4$	(A)	14(10)	2.0(4)	−0.2(1)	0.4(2)	24(1)
		$ZnFe_2O_4$	[B]	13(2)	1.0(1)	0.38(1)	1.21(8)	
		$ZnFe_2O_4$	[B]	1.1(7)	0.3(1)	0.34(2)	2.05(4)	
		$ZnFe_2O_4$	[B]	27(16)	3.6(8)	0.50(9)	5.2(4)	

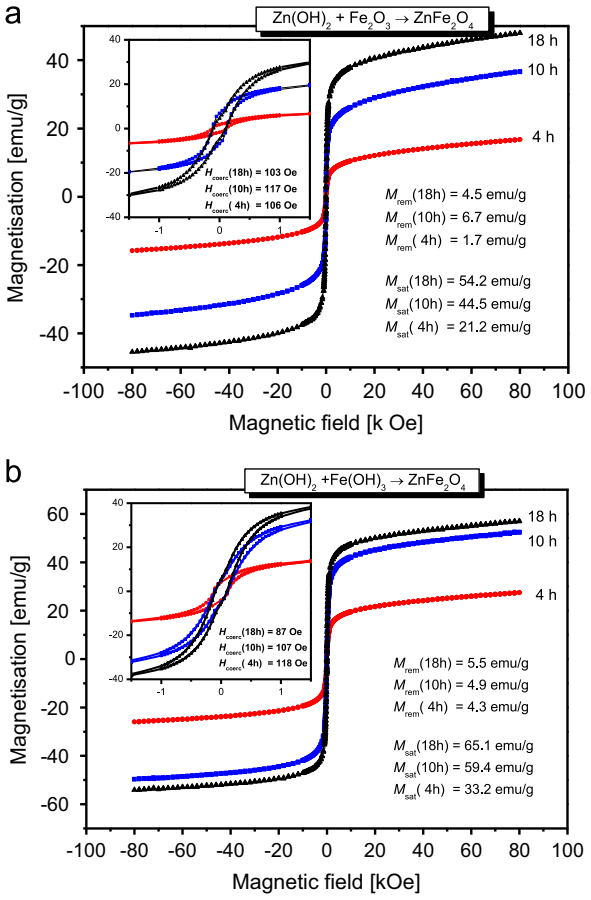

Fig. 8. The magnetic hysteresis curves of the mixture of powders (a) $Zn(OH)_2$/α-Fe_2O_3 and (b) $Zn(OH)_2$/$Fe(OH)_3$ after 4, 10 and 18 h milling time. The insets show low magnetization behavior.

(1) magnetic remanence and saturation magnetization stay about 18% lower in comparison with sample obtained from mixture (2). At the same time, coercive field in mixture (1), for 18 h, is higher for about 18%.

All these facts imply that starting from mixture (2) a single phase zinc ferrite is obtained with a little smaller average size of the nanoparticles and, as a consequence, higher magnetization and the degree of inversion.

Generally, small values of the coercive fields and remanence magnetization at 300 K suggest a superparamagnetic-like behavior of the $ZnFe_2O_4$ samples obtained by the soft mechanochemical method.

4. Conclusions

Nanosize $ZnFe_2O_4$ ferrite was obtained by soft mechanochemical synthesis in planetary mill. It has been shown using XRD analysis that mechanochemical treatment of mixtures in the case (1) after 4 h of milling leads to the amorphization of the starting powders and to their partial reaction, producing a mixture of β-$Zn(OH)_2$, ZnO, α-Fe_2O_3 and $ZnFe_2O_4$, after 10 h a mixture of ZnO, α-Fe_2O_3 and $ZnFe_2O_4$, and finally after 18 h single $ZnFe_2O_4$ phase is obtained. In the case (2), after 4 h milling of starting powders the presence of ZnO, α-Fe_2O_3 and $ZnFe_2O_4$ also can be observed, after 10 h of milling in the mixture the uppermost $ZnFe_2O_4$ and a very little amount of ZnO and α-Fe_2O_3 is present, and after 18 h stay pure spinel $ZnFe_2O_4$ phase is observed. The crystallite sizes in pure $ZnFe_2O_4$ samples are about 20.3 nm for case (1) and 17.6 nm for case (2). It could be concluded that mechanochemical treatment leads to the successful formation of ultrafine powders of $ZnFe_2O_4$ ferrite.

In the FIR spectra recorded after 4 and 10 h of milling it is visible that the FIR modes are superposed from the modes of spinel and are unreacted or partially reacted starting materials. After 18 h of milling, spectra correspond to pure phase of $ZnFe_2O_4$ nanopowder, that is in accordance with results of XRD analysis.

In the Raman spectra it is observed that all of the group theory predicted first-order active modes characteristic for spinel structure. The intensity and frequencies of the Raman modes during the formation of ferrite phase by the soft mechanochemical method in both mixtures have very close values, but there are some differences which indicate that milling leads to faster development of $ZnFe_2O_4$ ferrite in the case (2). Mössbauer spectroscopy studies implied the substantial cation distribution between the tetrahedral and octahedral sites in formed $ZnFe_2O_4$ spinel structure. It is found out that amount of Zn^{2+} at tetrahedral site reduces as size of particles decrease. The magnetic measurements after 18 h of milling show high magnetization values of 54.2 emu g^{-1} and 65 1 emu g^{-1}. Higher value of magnetization corresponds to smaller particle size in samples obtained from hydroxides mixture. It was shown that although the conditions of synthesis were the same, even after 18 h of milling the starting precursors affected the characteristics of the obtained $ZnFe_2O_4$ nanoferrite samples. In conclusion, it is confirmed that soft mechanochemical synthesis is the simple, low cost method applicable for the synthesis of good quality $ZnFe_2O_4$ powders.

Acknowledgments

This research was financially supported by the Ministry of Education, Science and Technological Development of the Republic of Serbia through Projects no. III 45003, 45015 and 45018.

References

[1] Y. Xu, Y. Liang, L. Jiang, H. Wu, H. Zhao, D. Xue, J. Nanomater. (2011), http://dx.doi.org/10.1155/2011/525967(article ID 525967).
[2] R.W. Chantrell, K. O'Grady, The magnetic properties of fine particles, in: R. Gerber, C.C. Wright, G. Asti (Eds.), Applied Magnetism, Kluwer Academic Publishers, Dordrecht, 1994, pp. 113–164.
[3] H. Ehrhardt, S.J. Campbell, M. Hofmann, Scr. Mater. 48 (2003) 1141–1146.
[4] Z.Ž. Lazarević, Č. Jovalekić, A. Milutinović, D. Sekulić, V.N. Ivanovski, A. Rečnik, B. Cekić, N.Ž. Romčević, J. Appl. Phys. 113 (2013) 187221-1–187221-11.
[5] K. Tanaka, M. Makita, Y. Shimizugawa, K. Hirao, N. Soga, J. Phys. Chem. Solids 59 (1998) 1611–1618.
[6] A. Kundu, C. Upadhyay, H.C. Verma, Phys. Lett. A 311 (2003) 410–415.
[7] S. Bid, S.K. Pradhan, Mater. Chem. Phys. 82 (2003) 27–37.
[8] X. Niu, W. Du, W. Du, Sens. Actuators B: Chem. 99 (2004) 405–409.
[9] J.A. Toledo-Antonio, N. Nava, M. Martínez, X. Bokhimi, Appl. Catal. A: Gen. 234 (2002) 137–234.
[10] J. Qiu, C. Wang, M. Gu, Mater. Sci. Eng. B: Adv. 112 (2004) 1–4.
[11] F. Tomás-Alonso, J.M.P. Latasa, Fuel Process. Technol. 86 (2004) 191–203.
[12] V. Šepelák, M. Zatroch, K. Tkacova, P. Petrovic, S. Widmann, K.D. Becker, Mater. Sci. Eng. A 22 (1997) 226–228.
[13] S.A. Oliver, V.G. Harris, H.H. Hamdeh, J.C. Ho, Appl. Phys. Lett. 76 (2000) 2761–2763.
[14] C. Yao, Q. Zeng, G.F. Goya, T. Torres, J. Liu, H. Wu, M. Ge, Y. Zeng, Y. Wang, J.Z. Jiang, J. Phys. Chem. C 111 (2007) 12274–12278.
[15] M. Atif, S.K. Hasanain, M. Nadeem, Solid State Commun. 138 (2006) 416–421.
[16] C. Upadhyay, H.C. Verma, V. Sathe, A.V. Pimpale, J. Magn. Magn. Mater. 312 (2007) 271–279.
[17] S. Nakashima, K. Fujita, K. Tanaka, K. Hirao, J. Phys. Condens. Matter 17 (2005) 137–149.
[18] R. Nawathey, R.D. Vispute, S.M. Chaudhari, S.M. Kanetkar, S.B. Ogale, A. Mitra, S.K. Date, J. Appl. Phys. 65 (1989) 3197–3204.
[19] C.N. Chinnasamy, A. Narayanasamy, N. Ponpandian, J. Phy. Condens. Matter 12 (2000) 7795–7806.
[20] P.M. Botta, E.F. Aglietti, J.M. Porto López, Mater. Res. Bull. 41 (2006) 714–723.
[21] R. Klimkiewicz, J. Wolska, A. Przepiera, K. Przepiera, M. Jabłoński, S. Lenart, Mater. Res. Bull. 44 (2009) 15–20.
[22] C.A. Ladole, Int. J. Chem. Sci. 10 (2012) 1230–1234.

[23] D. Makovec, A. Kodre, I. Arcon, M. Drofenik, J. Nanopart. Res. 13 (2011) 1781–1790.
[24] M. Maletin, E.G. Moshopoulou, A.G. Kontos, E. Devlin, A. Delimitis, V.T. Zaspalis, L. Nalbandian, V.V. Srdic, J. Eur. Ceram. Soc. 27 (2007) 4391–4394.
[25] J.M. Yang, K.L. Yang, J. Nanopart. Res. 11 (2009) 1739–1750.
[26] L. Nalbandian, A.V. Delimitis, T. Zaspalis, E.A. Deliyanni, D.N. Bakoyannakis, E. N. Peleka, Microporous Mesoporous Mater. 114 (2008) 465–473.
[27] Guo-Ying Zhang, Ya-Qiu Sun, Dong-Zhao Gao, Yan-Yan Xu, Mater. Res. Bull. 45 (2010) 755–760.
[28] M. Sertkol, Y. Köseoğlu, A. Baykal, H. Kavas, M.S. Toprak, J. Magn. Magn. Mater. 322 (2010) 866–871.
[29] M.R. Barati, S.A.S. Ebrahimi, A. Badiei, J. Non-Cryst. Solids 354 (2008) 5184–5185.
[30] M. Gharagozlou, J. Alloys Compd. 486 (2009) 660–665.
[31] S. Yáñez-Vilar, M. Sánchez-Andújar, C. Gómez-Aguirre, J. Mira, M.A. Señarís-Rodríguez, S. Castro-García, J. Solid State Chem. 182 (2009) 2685–2690.
[32] M. Veith, M. Haas, V. Huch, Chem. Mater. 17 (2005) 95–101.
[33] B. Zhang, J. Zhang, F. Chen, Res. Chem. Intermed 34 (2008) 375–380.
[34] O.M. Lemine, Int. J. Phys. Sci. 8 (2013) 380–387.
[35] J.J. Thomas, A.B. Shinde, P.S.R. Krishna, N. Kalarikkal, Mater. Res. Bull. 48 (2013) 1506–1511.
[36] H. Yang, X. Zhang, C. Huang, W. Yang, G. Qiu, J. Phys. Chem. Solids 65 (2004) 1329–1332.
[37] V. Šepelák, L. Wilde, U. Steinike, K.D. Becker, Mater. Sci. Eng. A 375–377 (2004) 865–868.
[38] E. Avvakumov, M. Senna, N. Kosova, Soft Mechanochemical Synthesis: A Basis For New Chemical Technologies, Kluwer Academic Publishers, Boston, 2001.
[39] Z.Ž. Lazarević, Č. Jovalekić, A. Rečnik, V.N. Ivanovski, A. Milutinović, M. Romčević, M.B. Pavlović, B. Cekić, N.Ž. Romčević, Mater. Res. Bull. 48 (2013) 404–415.
[40] R.A. Brand, WinNormos Mössbauer fitting program, Universität Duisburg, 2008.
[41] Joint Committee on Powder Diffraction Standards (JCPDS) Powder Diffraction File (PDF), International Centre for Diffraction Data, Newton Square, PA, 2003.
[42] B.E. Warren, X-ray Diffraction, Addison-Wesley Pub. Co., Reading, MA, 1969.
[43] M.H. Sousa, F.A. Tourinho, J.C. Rubim, J. Raman Spectrosc. 31 (2000) 185–191.
[44] Z. Wang, D. Schiferl, Y. Zhao, H. St., C. O'Neill, J. Phys. Chem. Solids 64 (2003) 2517–2523.
[45] G. Dixit, J.P. Singh, R.C. Srivastava, H.M. Agrawal, Nuclear Instrum. Methods B 269 (2011) 133–139.
[46] V. Nachbaur, G. Tauvel, T. Verdier, M. Jean, J. Juraszek, D. Houvet, J. Alloys Compd. 473 (2009) 303–307.
[47] G.A. Sawatzky, F. Van der Woude, A.H. Morrish, Phys. Rev. B 187 (1968) 747–757.
[48] G.F. Goya, H.R. Rechenberg, J. Magn. Magn. Mater. 196–197 (1999) 191–192.
[49] V. Šepelák, U. Steinike, D.C. Uecker, S. Wiβmann, K.D. Becker, J. Solid State Chem. 135 (1998) 52–58.
[50] M.R. Anantharaman, S. Jagatheesan, K.A. Malini, S. Sindhu, A. Narayanasamy, C.N. Chinnasamy, J.P. Jacobs, S. Reijne, K. Seshan, R.H.H. Smits, H.H. Brongersma, J. Magn. Magn. Mater. 189 (1998) 83–88.
[51] H. Enharrdt, S.J. Campbell, M. Hofmann, J. Alloys Compd. 339 (2002) 255–260.

Far-infrared investigations of the surface modes in CdS thin films

2014 Phys. Scr. 2014 014031

(http://iopscience.iop.org/1402-4896/2014/T162/014031)

IOP Publishing | Royal Swedish Academy of Sciences Physica Scripta

Phys. Scr. **T162** (2014) 014031 (4pp) doi:10.1088/0031-8949/2014/T162/014031

Far-infrared investigations of the surface modes in CdS thin films

J Trajić[1], M Gilić[1], N Romčević[1], M Romčević[1], G Stanišić[1], Z Lazarević[1], D Joksimović[3] and I S Yahia[2]

[1] Institute of Physics, University of Belgrade, Belgrade, Serbia
[2] Nano–Science & Semiconductor Laboratories, Department of Physics, Faculty of Education, Ain Shams University, Roxy, Cairo, Egypt
[3] Megatrend University, Belgrade, Serbia

E-mail: jelena@ipb.ac.rs

Received 12 September 2013
Accepted for publication 3 March 2014
Published 19 September 2014

Abstract

The properties of Cadmium sulphide (CdS) thin films were investigated by applying atomic force microscopy (AFM) and far–infrared spectroscopy. CdS thin films were prepared using thermal evaporation technique under a base pressure of 2×10^{-5} torr. The quality of these films was investigated by AFM spectroscopy. We apply far–infrared spectroscopy to investigate the optical properties of CdS thin films, and reveal the existence of a surface optical phonon (SOP) mode at 297 cm^{-1}. For the first time, the dielectric function of CdS thin film is modeled as a mixture of homogenous spherical inclusions in air by the Maxwell–Garnet formula. In the analysis of the far–infrared reflection spectra, a numerical model for calculating the reflectivity coefficient for a system which includes films and substrates has been applied.

Keywords: CdS thin films, AFM, Raman spectroscopy, far-infrared spectroscopy

(Some figures may appear in colour only in the online journal)

1. Introduction

Thin film polycrystalline semiconductors have attracted great interest due to an expanding variety of applications in various electronic and optoelectronic devices. The technological interest in polycrystalline based devices is mainly due to their very low production costs. Thin films now occupy a prominent place in basic research and solid state technology.

Among the II–VI semiconductors, CdS polycrystalline thin film is a representative material. Cadmium sulphide (CdS) is a very useful optoelectronic [1, 2], piezo–electronic [3], and semiconducting material. As CdS has a wide direct band gap (2.42 eV) it has been used as a window material, together with several semiconductors such as CdTe, Cu_2S and $CuInSe_2$ [4].

The deposition of CdS films has been explored by different techniques: sputtering, thermal evaporation, chemical bath deposition, and molecular beam epitaxy [5–9]. In each of these methods polycrystalline, uniform and hard films are obtained, and their electrical properties are very sensitive to the method of preparation.

In the case of real crystals, when their dimensions are relatively small, surface modes and the effects of dimension will also be manifested, in addition to the normal mode of an infinite lattice. When their dimensions become extremely small (nanocrystals), only the surface mode persists [10].

Surface modes play an important role in determining the different physical properties of nanocrystals. For a plane wave propagating in the x–direction in a bulk crystal, the temporal and spatial variation of the wave is described by the factor exp $[i(kx - \omega t)]$, where $k = (\omega/c)\sqrt{\varepsilon(\omega)}$ is the wavevector and $\varepsilon(\omega)$ is the dielectric constant of the crystal. In the frequency range between bulk longitudinal (ω_{LO}) and transverse (ω_{TO}) optical mode frequencies, $\varepsilon(\omega)$ has a negative value, and accordingly k is imaginary. Therefore, in this frequency range the wave decays exponentially in the medium, i.e. it cannot propagate in bulk crystals and only surface modes exist [11].

In this work we investigated the optical properties of CdS thin films, evaporated by thermal evaporation technique, using far-infrared spectroscopy. Far-infrared spectra were analyzed using a numerical model for calculating the

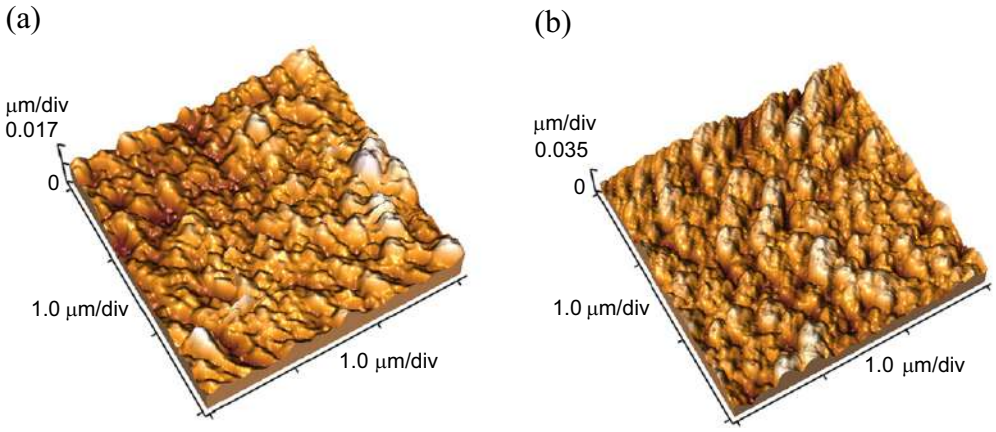

Figure 1. AFM surface image of CdS thin films of different thicknesses on glass substrate: (a) d = 1.6 μm, and (b) d = 2.2 μm.

reflectivity coefficient for complex systems, which include films and substrates. The dielectric function of a CdS thin film is modeled as a mixture of homogenous spherical inclusions in air, by the Maxwell–Garnet formula. We analyzed films of thicknesses 1.6, 1.8, 2.0 and 2.2 lm. The sample's characterization was performed using atomic force microscopy (AFM).

2. Samples: preparation and characterization

CdS powder with high purity was purchased from the Sigma–Aldrich Company. CdS thin films of different thicknesses were deposited onto highly pre–cleaned glass substrates, using thermal evaporation at room temperature. A high vacuum coating unit (Edwards, E–306 A) was used under base pressure 2×10^{-5} torr. The distance between the evaporation source (molybdenum boat) and the substrate holder was about 21 cm to avoid any heating flow from the heating source to the substrates. The rate of deposition was 10 nm s^{-1} and the film thickness was controlled using a quartz crystal thickness monitor (FTM4, Edwards).

The morphology of CdS thin films was investigated by AFM. AFM images of the investigated CdS samples are presented in figure 1.

For all samples, hillocks with heights of about 30 nm were observed (table 1). Surface topology, values of average roughness (R_a), and root mean squared (*RMS*) roughness were analyzed. According to the obtained results, presented in table 1, the employed surfaces at a micro scale are relatively smooth and uniform (with the exception of a few scratches). AFM images show that all CdS samples present well defined nanosized grains, with relatively small roughness values ranging from 3.84 nm to 5.84 nm, as shown in table 1.

Table 1. Average height, average roughness (R_a) and root mean squared (*RMS*) roughness for different CdS thin films thicknesses.

d [μm]	Average height [nm]	Ra [nm]	RMS [nm]
1.6	30.09	3.87	5.4
1.8	25.14	3.84	4.76
2.0	28.67	5.84	7.27
2.2	30.07	5.56	6.99

3. Results and discussion

The far–infrared measurements were carried out with a BOMEM DA–8 FIR spectrometer. A DTGS pyroelectric detector was used to cover the wave number range from 40 to 600 cm^{-1}. The penetration depth of the infrared electromagnetic waves into a nontransparent crystal is approximately 3 μm. As the thicknesses of our films varies from 1.6 μm to 2.2 μm, so the reflectivity spectra contain information about the CdS films, together with information about the substrate. Accordingly, our model of the reflectance considers a three–layer structure, where medium 1 is air with dielectric function ε_1 ($\varepsilon_1 = 1$), medium 2 is the thin bulk CdS crystal layer with corresponding dielectric function ε_2, and medium 3 is the substrate (glass) with dielectric function ε_3. In this case:

$$R_A = \frac{A_r}{A_i} = \frac{\mathbf{r}_{12}e^{-i\alpha} + \mathbf{r}_{23}e^{i\alpha}}{e^{-i\alpha} + \mathbf{r}_{12}\mathbf{r}_{23}e^{i\alpha}}, \quad (1)$$

where A_i and A_r are amplitudes of the incident and reflection beams,

$r_{ij} = (n_i - n_j)\Big/\left(n_i + n_j\right) = \left(\sqrt{\varepsilon_i} - \sqrt{\varepsilon_j}\right)\Big/\left(\sqrt{\varepsilon_i} + \sqrt{\varepsilon_j}\right)$ are Fresnel coefficients, n is the complex indices of refraction, ε is the dielectric constant, and $\alpha = 2\pi\omega d(\varepsilon_2)^{1/2}$ is the complex phase change related to the absorption in the crystal layer with the thickness d. The corresponding reflectance (R) is:

$$R = \left|R_A\right|^2 \quad (2)$$

The dielectric function of the glass substrate is:

$$\varepsilon_s(\omega) = \varepsilon_{\infty\,\mathrm{sup}}\,\frac{\omega_{LO}^2 - \omega^2 + i\gamma_{LO}\omega}{\omega_{TO}^2 - \omega^2 + i\gamma_{TO}\omega}, \quad (3)$$

where ω_{TO} and ω_{LO} are the transversal and longitudinal optical vibrations, and γ_{TO} and γ_{LO} are damping parameters.

We consider phonons in the thin bulk CdS crystal layer as surface optical phonons. Surface phonon modes are observed for particle sizes smaller then the wavelength of the exciting laser light inside the particles. Usually these modes of small particles appear in polar crystals [12]. The dielectric function for the case of a polar semi-insulating semiconductor:

$$\varepsilon(\omega) = \varepsilon_\infty \prod_{i=1}^{n} \frac{\omega_{LOi}^2 - \omega^2 - i\omega\gamma_i}{\omega_{TOi}^2 - \omega^2 - i\omega\gamma_i}, \quad (4)$$

describes its optical properties in the IR region. The bulk phonons in small particles have properties similar to those of the corresponding phonons in infinite crystals; however their wave functions are adapted to the geometry of small particles.

When visible light interacts with semiconducting nanoparticles (characteristic size L, dielectric function ε_2) which are distributed in a medium with the dielectric constant ε_1 in the limit $\lambda \gg L$, the heterogeneous composite can be treated as a homogeneous medium, and a so–called effective medium theory applies.

There are many mixing models for the effective dielectric permittivity of such a mixture [13]. Since all our samples are well defined and separated nanosized grains we decided to use the Maxwell–Garnet model for the present case.

For the spherical inclusions case, the prediction of the effective permittivity of mixture ε_{eff} according to the Maxwell–Garnet mixing rule reads [14, 15]:

$$\varepsilon_{ff} = \varepsilon_1 + 3f\varepsilon_a \frac{\varepsilon_b - \varepsilon_a}{\varepsilon_b + 2\varepsilon_a - f(\varepsilon_a - \varepsilon_b)}. \quad (5)$$

Here, spheres of permittivity ε_b are located randomly in the homogeneous environment ε_a and occupy a volume fraction f.

The far–infrared reflection spectra of CdS thin films are presented in figure 2. The experimental data are presented by circles, while the solid lines are calculated spectra obtained by a fitting procedure based on the previously presented model.

The far infrared–reflectivity spectrum of the glass substrate is shown in figure 2(f). The calculated spectrum, presented by a solid line, was obtained using the dielectric function given by equation (3). As a result of the best fit, we obtained two modes, whose characteristic frequencies are $\omega_{TO1} = 438\ \mathrm{cm}^{-1}$, $\omega_{LO1} = 439\ \mathrm{cm}^{-1}$ and $\omega_{TO2} = 471\ \mathrm{cm}^{-1}$, $\omega_{LO2} = 523\ \mathrm{cm}^{-1}$. Frequency values of these modes remained the same during the fitting procedure for all CdS thin film samples.

Far–infrared spectra of the bulk CdS crystal is shown in figure 2(a). The calculated spectrum, presented by a solid line, was obtained using the dielectric function given by equation (4). Characteristic phonon frequencies obtained by analysis of this spectrum and their symmetries are: transverse mode at $234\ \mathrm{cm}^{-1}$ (A_1), longitudinal at $305\ \mathrm{cm}^{-1}$ (E_1) and modes at $70\ \mathrm{cm}^{-1}$ (E_2^2), $170\ \mathrm{cm}^{-1}$ (B_2^2), $214\ \mathrm{cm}^{-1}$ (B_2^1), $263\ \mathrm{cm}^{-1}$ (E_2^1), which is in agreement with literature data [16–18].

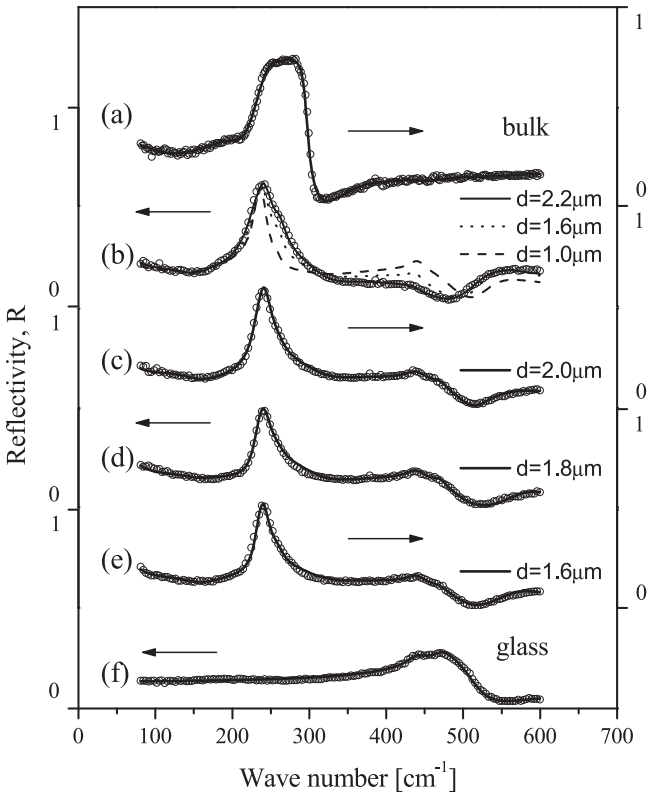

Figure 2. Far–infrared reflection spectra of: (a) a bulk CdS single crystal; CdS thin films with thicknesses of (b) 2.2 μm, (c) 2.0 μm, (d) 1.8 μm, (e) 1.6 μm; and a glass substrate (f).

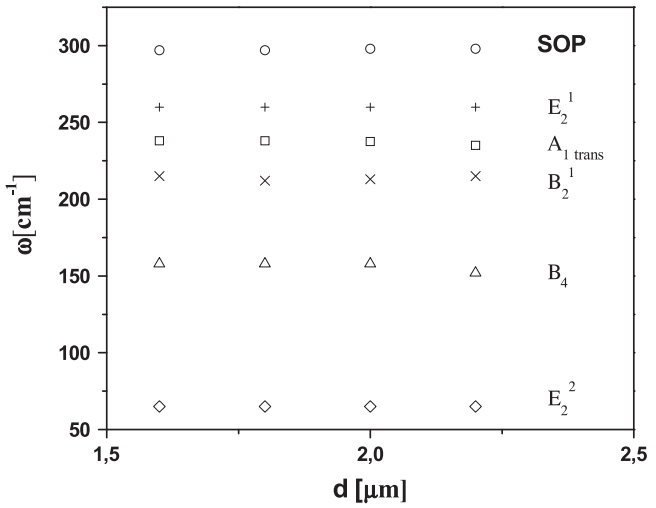

Figure 3. Characteristic frequency as a function of the samples thickness.

Far infrared reflection spectra for different thicknesses of CdS thin films on glass substrates are shown in figures 2(b)–(e). Calculated spectra, obtained using the fitting procedure given by equations (1)–(3) and (5), and are presented by solid lines. The observed samples' characteristic frequencies correspond to bulk CdS crystal phonon modes, except for in the longitudinal optical mode. The only disagreement was observed in the case of the mode at $304\ \mathrm{cm}^{-1}$,

where we registered a shift from 304 cm^{-1} to 297 cm^{-1}. This slight shift to a lower frequency is attributed to the SOP mode effect [10, 19].

In figure 3, frequency modes depending on the samples thickness are presented. As one can see from the figure, CdS thin mode frequencies do not distinctly vary with the thickness of samples.

Samples thickness is revealed by FIR measurements. Figure 2(b) represents the calculated spectra for different film thicknesses. The calculated spectrum for the CdS film of thickness 1.0 μm is presented by the dashed line, for 1.6 μm by the dotted line and for 2.2 μm by the solid line. The figure shows that for different thickness there is a significant variance in the calculated spectra. For small values of film thickness, the thin film calculated spectra is comparable to the glass substrate's reflectivity spectra; with increasing film thickness, spectra increasingly resemble the spectrum of the CdS bulk crystal.

4. Conclusion

In this paper, we present the results of our investigations of CdS thin films with different thicknesses. We determined that all of the samples' surfaces are relatively smooth and uniform, having well defined nanosized grains with relatively small roughness values. Far–infrared spectra measurements reveal, besides characteristic CdS modes and their multiphonon combinations, the existence of surface optical phonon modes. A numerical model for calculating the reflectivity coefficient of a complex system, which includes films and substrate, has been applied. We treat the CdS thin film as a mixture of homogenous spherical inclusions in air, modeled by the Maxwell–Garnet formula. Besides characteristic cadmium sulphide modes, we registered the existence of SOP modes.

Acknowledgements

This research was supported by the Serbian Ministry of Education and Science (No. 45003).

References

[1] Iyechika Y, Wigner G, Jager D, Witt A and Klingshirn C 1988 *SPIE Opt. Comput.* **88** 103
[2] Bogdanov S V and Lyssenko V G 1988 *Phys. Status Solidi* **B150** 593–8
[3] Stefko V V 1991 *Sov. J. Commun. Technol. Electron.* **36** 13
[4] Mahdi M A, Kasem S J, Hassen J J, Swadi A A and Al–Ani S K J 2009 *Int. J. Nanoelectron. Mater.* **2** 163
[5] V´azquez J G, Zehe A and Zelaya O 1999 *Cryst. Res. Technol.* **34** 949
[6] Su B and Choy K L 2000 *Thin Solid Films* **359** 160
[7] Ashour A, El–Kadry N and Mahmoud S A 1995 *Thin Solid Films* **269** 117
[8] Mahmoud S A, Ibrahim A A and Riad A S 2000 *Thin Solid Films* **372** 144
[9] Oliva A I, Solis–Canto O, Castro–Rodŕıguez R and Quintana P 2001 *Thin Solid Films* **391** 28
[10] Chuu D S, Dai C M, Hsieh W F and Tsai C T 1991 *J. Appl. Phys.* **69** 12
[11] Singha A, Satpati B, Satyam P V and Roy A 2005 *J. Phys.: Condens. Matter* **17** 5697–708
[12] Irmer G 2007 *J. Raman Spectrosc.* **38** 634
[13] Karkkainen K, Saviola A and Nikoskinen K 2001 *IEEE Trans. Geosci. Remote Sensors* **39** 1013
[14] Garnett J C M 1904 *Trans. R. Soc.* **CCIII** 385
[15] Sihvola A and Lindell I V 1992 *Dielectric properties of heterogeneous materials* (*PIER 6 Progress Electromagnetic Research*) ed A Priou (Amsterdam: Elsevier) pp 101–51
[16] Nusimovici M A and Balkanski M 1970 *Phys. Rev.* B **1** 595
[17] Nusimovici M A and Birman J L 1967 *Phys. Rev.* **156** 925
[18] Marshal R and Mitra S S 1964 *Phys. Rev.* **134** A1019
[19] Azhniuk Y M, Yu H, Lopushanski V V, Milekhin A G and Gomonnai A V 2009 *Phys. Stat. Sol.* C **6** 2039

Spectroscopic characterization of YAG and Nd:YAG single crystals

2014 Phys. Scr. 2014 014026

(http://iopscience.iop.org/1402-4896/2014/T162/014026)

IOP Publishing | Royal Swedish Academy of Sciences Physica Scripta

Phys. Scr. **T162** (2014) 014026 (5pp) doi:10.1088/0031-8949/2014/T162/014026

Spectroscopic characterization of YAG and Nd:YAG single crystals

S Kostić[1], Z Lazarević[1], M Romčević[1], V Radojević[2], A Milutinović[1], G Stanišić[1] and M Gilić[1]

[1] Institute of Physics, University of Belgrade, Belgrade, Serbia
[2] Faculty of Technology and Metallurgy, University of Belgrade, Belgrade, Serbia

E-mail: lzorica@yahoo.com

Received 10 September 2013
Accepted for publication 12 February 2014
Published 19 September 2014

Abstract

In this paper, we used the Czochralski method to obtain good quality yttrium aluminium garnet (YAG, $Y_3Al_5O_{12}$) and yttrium aluminium garnet doped with neodymium (Nd:YAG) crystals. The investigations were based on the growth mechanisms and the shape of the liquid/solid interface crystallization front on the crystal properties and incorporation of Nd^{3+} ions. The obtained single YAG and Nd:YAG crystals were studied by use of x-ray diffraction, Raman and IR spectroscopy. There are strong metal oxygen vibrations in the region of 650–800 cm^{-1} which are characteristics of Al-O bond: peaks at 784/854, 719/763 and 691/707 cm^{-1} correspond to asymmetric stretching vibrations in tetrahedral arrangement. Peaks at 566/582, 510/547 and 477/505 cm^{-1} are asymmetric stretching vibrations and 453/483 cm^{-1} is the symmetric vibration of the Al-O bond in octahedral arrangements of the garnet structure. Lower energy peaks correspond to translation and vibration of cations in different coordinations—tetrahedral, octahedral and dodecahedral in the case of the lowest modes.

Keywords: crystal growth, YAG, Nd:YAG, Czochralski technique, optical material, Raman lasers, infrared and Raman spectra

1. Introduction

Garnets are a fascinating palette for study. The unique crystal chemistry of the garnets with eight-, six- and four-coordinate crystallographic sites can lead to seemingly endless compositional combinations of alkaline earth metals, rare earth elements, transition metals and main group elements such as aluminium, silicon, gallium and germanium, both in nature and in the laboratory [1, 2]. As a result, and also owing to some favorable physical and optical properties, garnet-based materials (such as single crystals and transparent ceramics) have found great favour for use as solid-state laser materials. While the field of optics has advanced at a rapid pace to develop and improve such lasers it would seem that the crystal growth of garnets has not advanced quite at the same pace. Though the Czochralski and flux growth of YAG have enjoyed several advances (in particular the understanding of compositional variations, interface shape and diameter control), YAG crystals are still grown much in the same way as they were in the early days of laser materials research some 40–50 years ago [1].

Yttrium aluminium garnet (YAG) and yttrium aluminium garnet doped with neodymium (Nd:YAG) are two of the most popular crystals used in solid-state laser technology [2–5]. Good optical quality, high mechanical strength as well as good chemical stability have made them standard materials in industrial, medical and scientific applications [6, 7]. Since the Czochralski (CZ) technique is the conventional method for growing Nd:YAG single crystals [8, 9], it is very important to investigate the defects of the crystal formed during this growth technique. The formation of this defect has adverse effects on the optical homogeneity of the active medium [10] and causes a large area of the grown crystal to become useless.

During the crystals growth process it is possible, according to the CZ method, to influence the shape of the liquid/solid interface through the growth parameters, such as both the growth and crystal rotation rate, as well as the temperature gradient. It should be certainly mentioned that growth and rotation rates are rather constant, while the temperature distribution in a melt changes during the process of

crystal growth, as the melt level decreases. That causes gradual reduction of the melt depth, which on the other hand, can change the stirring conditions and consequently the temperature distribution when lower depths are involved.

In this work, YAG and Nd:YAG single crystals were produced. YAG single crystals with and without dopant Nd^{3+} without cores were characterized by XRD, Raman and IR spectroscopy.

2. Experimental procedure

YAG and Nd:YAG single crystals were grown by the CZ technique using a MSR 2 crystal puller controlled by a Eurotherm. The atmosphere of argon was used. The starting materials were powdered Y_2O_3, Al_2O_3 and Nd_2O_3 (all Koch&Light) all of 4N purity. Powdered ZrO_2 (Koch&Light) of 4N purity was used for isolation. The purity of argon (Tehnogas) was 4N. The iridium crucible (40 mm diameter, 40 mm high) was placed into an alumina vessel surrounded by ZrO_2 wool isolation. Double walls were used to protect the high radiation. To decrease the radial temperature gradient in the melt, alumina was mounted around all of the system. The pull rates were generally in the range 0.8–3 mm h^{-1}, and the best results were obtained with a pull rate of 1 mm h^{-1}. The crystal rotation rates were between 6 and 100 rpm. The best results were obtained with a crystal rotation of 20 rpm. The diameters of crystals were between 10 and 20 mm. The crucible was not rotated during the growth. After the growth run, the crystal boule was cooled at a rate of about 50 K h^{-1} down to room temperature.

Various concentrations of solutions of H_3PO_4 at different temperatures and for various exposure times were tried for chemical polishing and etching. For chemical polishing, exposure to a concentrated (85%) solution of H_3PO_4 at 603 K for 20 min was confirmed to be suitable. Exposure for 1 h to an 85% solution of H_3PO_4 at 493 K after was found to be convenient for etching [6, 10].

All the obtained crystal plates were observed in polarized light to visualize the presence of a core and/or striations. The absence of a core was confirmed by viewing both of the polished crystal slices in normal light (figure 1).

The crystal structure of YAG and Nd:YAG single crystals were approved using the x-ray diffractometer (XRD, Model Philips PW 1050) diffractometer equipped with a PW 1730 generator, 40 kV × 20 mA, using CuKα radiation of 1.540 598 Å at room temperature. Measurements were done in the 2θ range of 10–80° with a scanning step width of 0.05° and 10 s scanning time per step.

The Raman spectra in a spectral range from 100 to 900 cm^{-1}, in back scattering geometry, were obtained by the micro-Raman Jobin Yvon T64000 spectrometer, equipped with a nitrogen cooled charge-coupled device detector. As the excitation source we used the 514 nm line of an Ar-ion laser. The measurements were performed at 20 mW.

The infrared (IR) measurements were carried out with a BOMMEM DA-8 FIR spectrometer. A DTGS pyroelectric detector was used to cover the wave number range from 50 to 900 cm^{-1}.

3. Results and discussion

Investigations that were carried out with YAG not containing Nd^{3+} ions helped us a lot in our studies of YAG containing Nd^{3+} ions. When investigating YAG containing no Nd^{3+} ions we noticed that after the performed inversion of the liquid/solid interface the crystals obtained did not have cores. On the contrary, when we analyzed YAG containing Nd^{3+} ions we immediately saw that the whole system was far more sensitive, due to the presence of Nd^{3+} ions, to any change in growth conditions and all our attempts to obtain crystals without a core caused a blurring of the crystals.

The structural properties were obtained using x-ray diffraction analysis of powdered single samples. An x-ray diffraction for powdered Nd:YAG is given in figure 2(a). The unit cell of Nd:YAG is calculated by the least square method using 15 reflections including more Kα_2 for 1 reflection. In figure 2, all the reflections correspond to the Nd:YAG crystal and not any other phase was found.The calculated result reveals the Nd:YAG crystal crystallizes in cubic with space group *Ia3d* and the lattice parameter is $a = 12.0138$ Å, which is consistent with the published data (Ref. [6, 11] (12.011 Å)). The little divergence can be explained by the fact that x-ray powder diffraction analysis gives a statistical result. The cell parameter is much larger than that of the YAG crystal. The radius of the Nd^{3+} ion (1.12 Å) is larger than the radius of the Y^{3+} ion (1.01 Å), and the difference of about 10.9% not only makes it complicated to incorporate it into the Y^{3+} site of the crystal lattice, but also results in a larger cell parameter.

The x-ray diffraction (XRD) curve of the [111] Nd:YAG is shown in figure 2(b). The FWHM of [111] symmetric rocking curve measured by x-ray double-crystal diffractometry is equal to 0.335 42. Compared with the research of Chani by the CZ method (FWHM = 0.381) [12] and Zhang by the horizontal directional solidification—HDS method (FWHM = 0.2631) [11], the value of FWHM demonstrates the good crystallinity of the Nd:YAG crystal.

YAG is one of the garnet family compounds. The garnets usually have a general formula of $[A]_3\{B\}_2(C)_3O_{12}$, where [ ], { }, and ( ) denote dodecahedral, octahedral, and tetrahedral coordinations, respectively. YAG and Nd:YAG have a cubic structure with O_h^{10}—*Ia3d* space group symmetry with eight units in the unit cell. Three different sites are available in the lattice. The dodecahedral site *c* with local symmetry D_2, is normally occupied by the large Y^{3+} ions surrounded by eight O^{2-} ions, the octahedral site a (local symmetry C_{3i}) is normally occupied by Al^{3+} surrounded by six O^{2-} ions and the tetrahedral site *d* (local symmetry S_4) is occupied by Al^{3+}. The Al^{3+} cations occupy eight octahedral sites of C_{3i} symmetry and twelve tetrahedral sites of S_4 symmetry. Nd^{3+} ions usually replace Y^{3+} cations placed in twelve dodecahedral sites of D_2 symmetry [13]. Figure 3 shows the crystal structure of YAG, where Y^{3+} is coordinated with eight oxygen ions, some Al^{3+} are six-fold coordinated and others are four-fold coordinated. Each AlO_6 octahedron is connected to six AlO_4 tetrahedrons, and each AlO_4 tetrahedron is connected to four AlO_6 octahedrons by sharing the corners. Y^{3+} locates at the

Figure 1 A view of an obtained (a) YAG and (b) Nd:YAG single crystals plate.

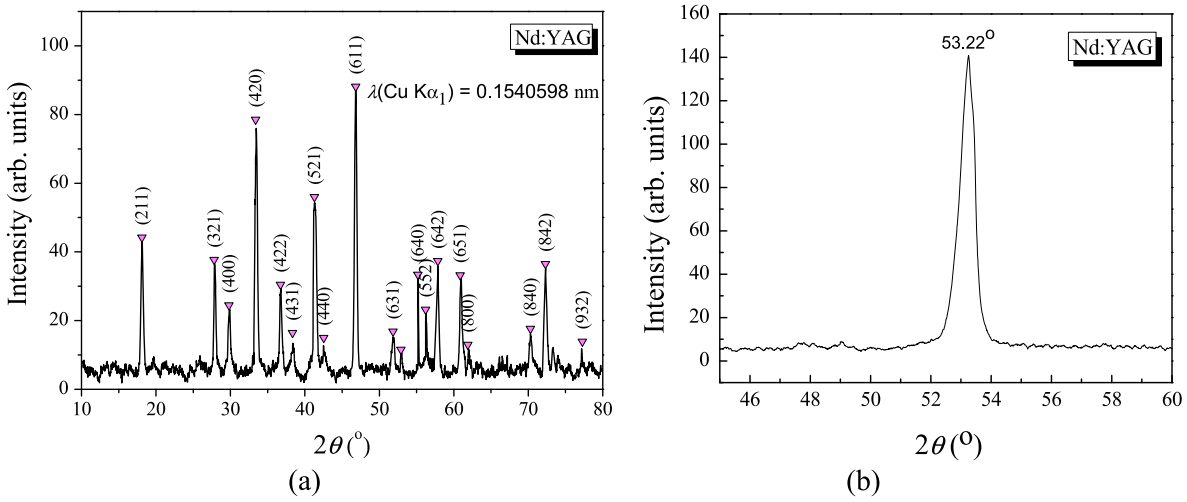

Figure 2. X-ray diffraction patterns (a) of the powdered sample Nd^{3+}:YAG and (b) of the [111] Nd:YAG crystal.

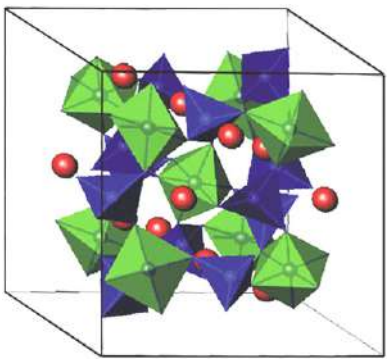

Figure 3. Crystal structure of YAG. Red, green, blue polyhedrons represent YO_8 dodecahedrons, AlO_6 octahedrons, and AlO_4 tetrahedrons, respectively. The corners are shared between AlO_6 and AlO_4.

space inside the AlO_x framework. The Nd^{3+} replaces the Y^{3+} of the Y-O dodecahedron in the Nd^{3+} doped YAG crystal.

The large number of atoms in the primitive cell leads to 240 (3×80) possible normal modes which can be classified according to the irreducible representation of the O_h group as follows: $3A_{1g} + 5A_{2g} + 8E_g + 14T_{1g} + 14T_{2g} + 5A_{1u} + 5A_{2u} + 10E_u + 18T_{1u} + 16T_{2u}$. The 25 modes having symmetries A_{1g}, E_g., and T_{2g} are Raman active while the 18 having T_{1u} symmetry are IR active [14–16]. 16 of the 25 Raman active vibrational modes can be observed in the Raman spectrum from 100 to 900 cm^{-1}. The Raman spectrum of rare earth doped YAG compounds can be divided into two different parts: the high frequency region (500–900 cm^{-1}) and the low frequency region (<500 cm^{-1}). The high frequency region accounts to the ν_1 (breathing mode), ν_2 (quadrupolar) and ν_4

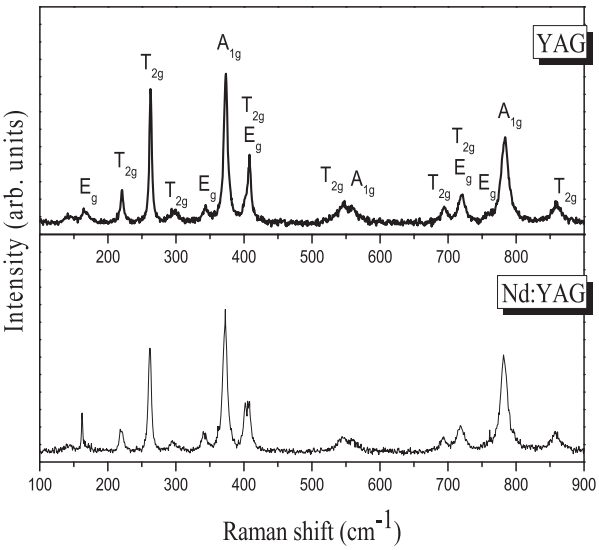

Figure 4. Raman spectra of YAG and Nd:YAG single crystals at room temperature.

Table 1. Position (cm^{-1}) of the modes in the Raman spectra and symmetries of lines of YAG Nd:YAG single crystals.

Symmetry type	Experimental frequency (cm^{-1}) YAG	Nd:YAG	Vibrations
E_g	164	162	Y or Nd
T_{2g}	219	221	Translation
T_{2g}	263	263	
T_{2g}	294	295	Translation +
E_g	340	343	Rotation +
A_{1g}	373	373	ν_3 (AlO_4)
T_{2g}	403	409	
E_g	—	407	
T_{2g}	544	548	
A_{1g}	556	557	ν_2 (AlO_4)
T_{2g}	690	693	
E_g	720	720	
T_{2g}	720	720	$\nu_1+\nu_4$ (AlO_4)
A_{1g}	784	783	
T_{2g}	857	858	

molecular internal modes associated with the (AlO_4) group, whilst the low frequency region is due to: (i) the translational motion of the rare earth ions, (ii) the rotational and translational motion of the AlO_4 units, and (iii) the ν_3 molecular mode of the AlO_4 [14, 15].

The Raman spectra of YAG and Nd:YAG single crystals have been recorded in the 100–900 cm^{-1} spectral range at room temperature (figure 4). The difference in the Raman spectral shape is indeed observed from the pure YAG crystal to Nd^{3+} doped YAG.

This clearly indicates that Nd-doping does replace ions in the crystal, thus changing the original YAG vibrational modes toward the Nd:YAG Raman spectrum. We believe that the

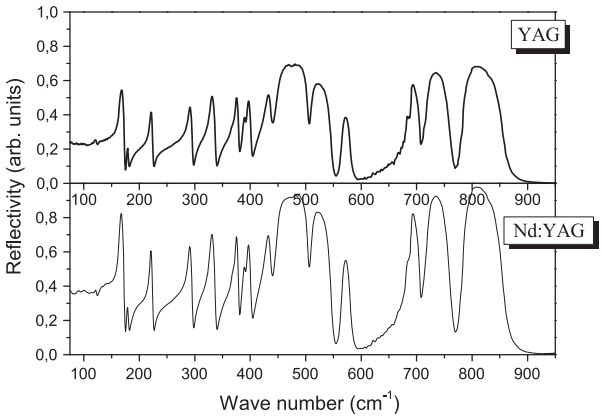

Figure 5. IR reflectance spectra of YAG and Nd:YAG single crystals at room temperature.

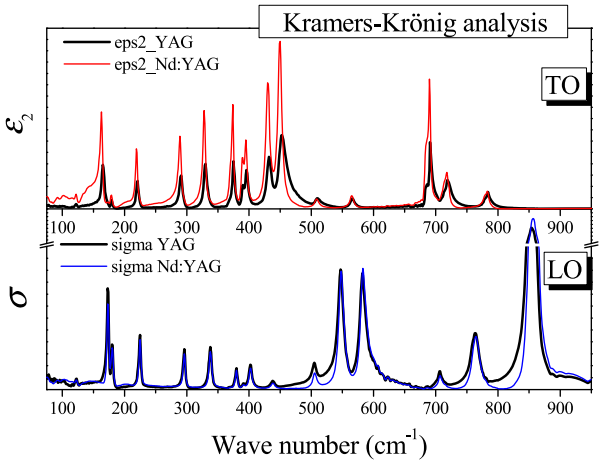

Figure 6. *TO* and *LO* modes of YAG and Nd:YAG single crystals obtained by the Kramers–Krönig analysis.

replaced ions are centred instead of aluminium ions in the tetrahedrons and octahedrons. According to work by Su *et al* on Nd:YAG [17], the peaks at 161, 219, 263, 340, 373, 402 and 407 cm^{-1} in figure 4 and table 1 have been attributed to the translatory motion of the Y or Nd ions within the distorted cube with eight oxygen ions at the corners, and also the heavy mixing of the translational, rotational, and ν_3 mode of the (AlO_4) unit. The vibrational modes at 543 and 556 cm^{-1} can be assigned as the ν_2 mode of the (AlO_4) unit. These peaks are the internal stretching vibrations (ν_1 and ν_4) between aluminium ions and oxygen in the tetrahedral (AlO_4) unit.

The Nd^{3+} ions substitute for Y^{3+} in YAG without the need for charge compensation. The larger size of the Nd^{3+} ions results in a polyhedral with sides that are greater than those in the Al^{3+} polyhedral. That distorts the lattice and thus limits the maximum doping concentration to several atomic weight percent. The concentration of Nd^{3+} in our samples is, as is common for laser materials, 0.8 wt.%. The lattice strains that are introduced by doping affect the properties of the optical spectra.

The optical spectra of YAG and Nd:YAG single crystals were recorded in far IR region at room temperature (298 K).

Table 2. Parameters of fit for the IR spectra of YAG and Nd:YAG single crystals and the transverse (*TO*) and the longitudinal (*LO*) frequencies values obtained from Kramers–Krönig analysis (peak positions $\varepsilon 2$ and σ).

YAG	Nd:YAG	
TO/*LO* wave number (cm^{-1})	*TO* wave number (cm^{-1})	Vibrations
122/122.6	122	$T(+T_d)$ transl. of tetr. and dodecah.cation
165/173	163	T_d transl. of dodecah. cation
180/180	178	$T_d(+T)$ transl. of tetr. and dodecah. cation
221/225	219	T_d transl. of dodecah. cation (translations of cations in YO_3 and AlO_4)
291/296	289	T_0
327/338	328	*T* transl of tetrah. cation
375/380	374	*R* libr. of tetrah.
390/392	389	T_0 transl. of octah.
396/402	395	*R* libr. of tetrah.
432/438	431	T_0 transl. of octah. (translations + libration of cations in AlO_6 and AlO_4)
453/483	449	ν_2 symmetric
477/505	475	ν_4 symmetric
510/547	509	ν_4
566/582	595	ν_4 (symmetric and asymmetric stretching of Al-O in octahedrons)
691/707	690	ν_3
719/763	717	ν_3
784/854	783	ν_3 (asymmetric stretching of Al-O in tetrahedrons)

The IR reflectance spectra of these crystals are shown in figure 5.

Seventeen of $18T_{1u}$ IR-active modes are visible in the near normal reflectivity spectra of YAG and Nd:YAG crystals, figure 5. There are strong metal oxygen vibrations in region 650–800 cm^{-1} which are characteristics of the Al-O bond: peaks at 784/854, 719/763 and 691/707 cm^{-1} correspond to asymmetric stretching vibrations in a tetrahedral arrangement. Peaks at 566/582, 510/547 and 477/505 cm^{-1} are asymmetric stretching vibrations and 453/483 cm^{-1} is the symmetric vibration of the Al-O bond in an octahedral arrangement of garnet structure. Lower energy peaks correspond to translation and libration of cations in different coordinations—tetrahedral, octahedral and dodecahedral in the case of the four lowest modes (table 2) [18].

The graphical presentation of the Kramers–Krönig analysis shows that the doping of YAG with Nd, *TO* modes undergo a red shift of 1–3 cm^{-1}, which is expected because of the greater atomic mass of neodymium (144.2) related to yttrium (88.9) (figure 6). The values of these modes are presented in table 2.

4. Conclusion

In conclusion, the Czochralski technique has been used successfully to produce yttrium aluminium garnet (YAG) and yttrium aluminium garnet doped with neodymium (Nd:YAG) single crystals. The obtained crystals were studied by x-ray diffraction, Raman and IR spectroscopy. The crystal structure was confirmed by XRD. We observed 15 Raman and 17 IR modes. The Raman and IR spectroscopy results are in accordance with x-ray diffraction analysis. The obtained YAG and Nd:YAG single crystals were without cores and with good optical quality. The absence of a core was confirmed by viewing polished crystal slices. Also, it is important to emphasize that the obtained Nd:YAG single crystal has a concentration of 0.8 wt.% Nd^{3+} that is characteristic for laser materials.

Acknowledgment

This research was financially supported by the Serbian Ministry of Education, Science and Technological Development through project no. III45003.

References

[1] McMillen C D, Mann M, Fan J, Zhu L and Kolis J W 2012 *J. Cryst. Growth* **356** 58–64
[2] Yadegari M, Asadian M, Saeedi H, Khodaei Y and Mirzaei N 2013 *J. Cryst. Growth* **367** 57–61
[3] Saeedi H, Yadegari M, Sh E, Asadian M, Shojaee M, Khodaei Y, Mirzaei N and Mashayekhi A I 2013 *J. Cryst. Growth* **363** 171–5
[4] Katsurayama M, Anzai Y, Sugiyama A, Kokie M and Kato Y 2001 *J. Cryst. Growth* **229** 193–8
[5] Mazur K and Wierzchowski W 1995 *J. Cryst. Growth* **148** 345–54
[6] Golubović A, Nikolić S, Gajić R, Djurić S and Valčić A 2002 *J. Serb. Chem. Soc.* **67** 291–300
[7] Kanchanavaleerat E, Cochet-Muchy D, Kokta M, Stone-Sundberg J, Sarkies P, Ju S and Jo S 2004 *Opt. Mater.* **26** 337–41
[8] Brandle C D 2004 *J. Cryst. Growth* **264** 593–604
[9] Golubović A, Nikolić S, Gajić R, Dohčević-Mitrović Z and Valčić A 2004 *Metalurgija* **10** 363–70
[10] Peizhi Y, Peizhen D, Zhiwen Y and Yulian T 2000 *J. Cryst. Growth* **218** 87–92
[11] Zhang M, Guo H, Han J, Zhang H and Xu C 2012 *J. Cryst. Growth* **240** 130–4
[12] Chani V L, Yoshikawa A and Kuwano Y 1999 *J. Cryst. Growth* **204** 155–62
[13] Geller S, Fullmer L D, Crandall P B and Espinosa G P 1972 *Mater. Res. Bull.* **7** 1219–24
[14] Hurrell J P, Porto P S, Chang I F, Mitra S and Bauman R P 1965 *Phys. Rev.* **173** 851–173
[15] Chen Y F, Lim P K, Lim S J, Yang Y J, Hu L J, Chiang H P and Tse W S 2003 *J. Raman Spectrosc.* **34** 882–5
[16] Lukowiak A, Wiglusz R J, Maczka M, Gluchowski P and Strek W 2010 *Chem. Phys. Lett.* **494** 279–83
[17] Su J, Zhang Q L, Yin S T, Sun D L and Shao S F 2009 *Spectrosc. Spect. Anal.* **29** 1577–80
[18] Hofmeister A M and Campbell K R 1992 *J. Appl. Phys.* **72** 638–46

Science of Sintering, **46** (2014) 235-245

doi: 10.2298/SOS1402235S

UDK 532.74; 665.7.035.8

The Comparative Study of the Structural and the Electrical Properties of the Nano Spinel Ferrites Prepared by the Soft Mehanochemical Synthesis

D. L. Sekulić[1], Z. Ž. Lazarević[2,*)], Č. Jovalekić[3], A. Rečnik[4], M. Romčević[2], B. Hadžić[2], N. Ž. Romčević[2]

[1]Faculty of Technical Sciences, University of Novi Sad, Novi Sad, Serbia
[2]Institute of Physics, University of Belgrade, Pregrevica 118, Zemun, Belgrade, Serbia
[3]The Institute for Multidisciplinary Research, University of Belgrade, Belgrade, Serbia
[4]Department for Nanostructured Materials, Jožef Stefan Institute, Ljubljana, Slovenia

Abstract:

Nano spinel ferrites MFe_2O_4 (M= Ni, Mn, Zn) were obtained by soft mechanochemical synthesis in a planetary ball mill. The appropriate mixture of oxide and hydroxide powders was used as initial compounds. All of this mixture of powders was mechanically activated, uniaxial pressed and sintered at 1100℃/2h. The phase composition of the powders and sintered samples were analyzed by XRD and Raman spectroscopy. Morphologies were examined by SEM. In this study, the AC-conductivity and DC-resistivity of sintered samples of MFe_2O_4 (M= Ni, Mn, Zn) ferrites were measured at different frequencies and at room temperature. The values of the electrical conductivities show an increase with increasing temperature, which indicated the semiconducting behavior of the studied ferrites. The conduction phenomenon of the investigated samples could be explained on the basis of hopping model. The complex impedance spectroscopy analysis was used to study the effect of grain and grain boundary on the electrical properties of all three obtained ferrites.

Keywords: *Ferrites, Raman spectroscopy, DC conductivity, Complex impedance.*

1. Introduction

Ferrites are homogeneous materials composed of various oxides containing iron oxide (Fe_2O_3) as their main constituent [1]. Spinel ferrites have been investigated in recent years for their useful electrical and magnetic properties, and applications in several important technological fields such as ferrofluids, magnetic drug delivery and magnetic high-density information storage [1-4]. The synthesis and magnetic structure characterization of spinel metastable nano-ferrites have been investigated with much interest. Among these spinel ferrites, the inverse type is particularly interesting due to its high magnetocrystalline anisotropy, high saturation magnetization from a typical crystal and magnetic structure. The properties of the synthesized materials are influenced by the composition and microstructure, which are sensitive to the preparation methodology used in their synthesis.

*) **Corresponding author**: lzorica@ipb.ac.rs

In recent years, a number of chemical and physical methods have been attempted to produce nanosize ferrites. Some of the main physical methods include mechanical milling [5-7], severe plastic deformation consolidation and inert gas condensation [8]. The widely used chemical methods are electro-deposition [9], hydrothermal reaction [10-12], co-precipitation [13-15], organic precursor method [16], sonochemical decomposition [17] and sol-gel synthesis technique [18-20]. Aggregation and coarsening of particles at elevated temperatures is a critical obstacle in majority of the above mentioned synthesis techniques.

Mechanochemical treatment has been recognized as a powerful technique for synthesis of a wide range of materials. New approach to mechanochemical synthesis, based on reactions of solid acids and bases, crystal hydrates, basic and acidic salts, which react with each other releasing water, has been called soft mechanochemical synthesis [21]. In many cases, when it comes to classical synthesis reaction sintering process, requires high temperatures, which can present an additional problem in industrial production. Mechanochemical derived precursors exhibit significantly higher reactivity and thus lower the calcination and sintering temperature.

In present work, nanosized nickel, manganese and zinc ferrites were synthesized using the soft mechanochemical treatment. The soft mechanochemical reaction leading to formation of the spinel phase was followed by X-ray diffraction and Raman spectroscopy. Scanning electron microscopy was used to analyze microstructure of the sintered sample. The electrical character of obtained ferrites was confirmed by measurements of electrical AC-conductivity and DC-resistivity at different frequencies and at room temperature.

2. Experimental

In present work $MnFe_2O_4$, $NiFe_2O_4$ and $ZnFe_2O_4$ ferrites were prepared from appropriate mixture of powders $Mn(OH)_2/\alpha$-Fe_2O_3, $Ni(OH)_2/\alpha$-Fe_2O_3 and $Zn(OH)_2/\alpha$-Fe_2O_3 by soft mechanochemical synthesis in a planetary ball mill for 25 h, 25 h and 18 h, respectively. The obtained ferrite powders were pressed into pallets and sintered at 1100 °C/2h. Heating rate was 10 °C min^{-1}, with nature cooling in air atmosphere. The formation of phase and crystal structure of ferrites was approved using the X-ray diffractometer (XRD, Model Philips PW 1050 diffractometer). Raman measurements of sintered samples were performed using Jobin-Ivon T64000 monochromator. Room temperature Raman spectra are in spectral range from 100 to 800 cm^{-1}.

TEM studies were performed using a 200 kV TEM (JEM-2100 UHR, Jeol Inc., Tokyo, Japan) equipped with an ultra-high resolution objective lens pole piece having a point-to-point resolution of 0.19 nm, being sufficient to resolve the lattice images of nanoparticles.

The morphology and microstructure of sintered samples were examined using scanning electron microscope (SEM, Model JEOL JSM-6460LV). The sintered samples in the disc shape were prepared for microstructure examination and electrical properties by polishing to thickness of 1 mm with silicon carbide and alumina powder and cleaning in an ultrasonic bath in ethanol.

In this study, the ferrite samples used for electrical measurements were coated with silver paste to ensure good ohm contacts. Thus prepared samples with silver electrodes deposited on both sides can be considered electrically equivalent to a capacitance C_p in parallel with a resistance R_p. These AC parameters were measured directly in the frequency range 100 Hz to 1 MHz at room temperature using an Impedance Analyzer HP-4194A. The AC conductivity was determined using the following relation:

$$\sigma_{AC} = \omega \varepsilon_0 \varepsilon'' \quad (1)$$

where $\varepsilon'' = (\omega R_p C_0)^{-1}$, $\omega = 2\pi f$ is the angular frequency of the applied field and ε_0 represents the permittivity of vacuum equal to 8.85×10^{-12} F m^{-1}. The capacitance C_0 is determined by area of electrode A and distance between the electrodes d, as follows $C_0 = A\varepsilon_0/d$. The DC resistivity of the synthetized ferrites was measured at room temperature by simple two-probe method. A Source Meter Keithley 2410 was used for the said purpose. The DC resistivity was calculated by using the following formula:

$$\rho_{DC} = \frac{RA}{d} \tag{2}$$

where R is the measured resistance, A is area of electrode and d is the thickness of the sample.

3. Results and discussions

Formations mechanisms of materials from nanopowders by soft mechanically assisted synthesis (mechanochemical synthesis) are complex have not been fully understood yet. During the ferroelectric materials formation, the process passes through few steps. Generally, it starts with the decrease in particle and grain size of starting materials following by the nucleation and crystallization of target compound. As the result of mechanically assisted synthesis, nanocrystalline powders can be obtained directly from their oxide/hydroxide mixtures after milling.

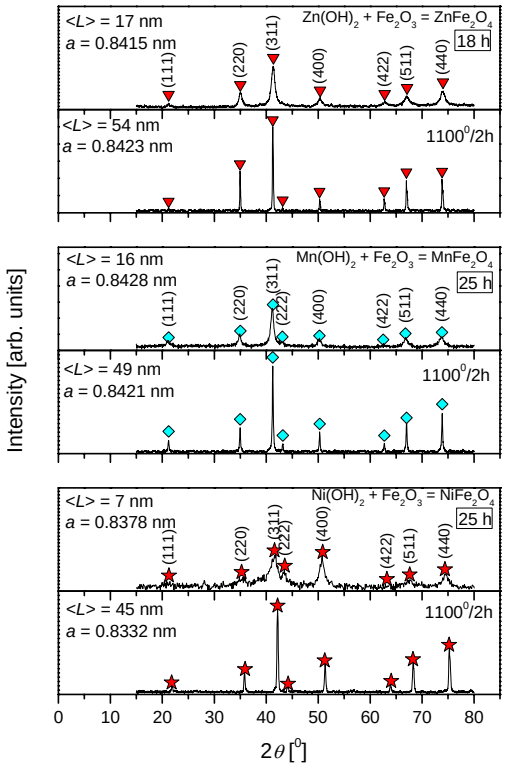

Fig. 1. X-ray diffraction patterns of the MFe_2O_4 (M= Ni, Mn, Zn) powders and sintered samples at 1100 °C/2h.

The Fig. 1 shows the X-ray diffraction spectra of $NiFe_2O_4$, $MnFe_2O_4$ and $ZnFe_2O_4$ powders and appropriate ferrite samples after sintering at 1100 ºC/2h. All peaks detected at

about the 2θ = 22º, 36º, 42º, 44º, 51º, 64º, 68º and 75º clearly pointed to the formation of the new phase of $NiFe_2O_4$ (JCPDS card 89 4927), $MnFe_2O_4$ (JCPDS card 74-2403) and $ZnFe_2O_4$ (JCPDS card JCPDS card 89-7412). The peaks are well indexed to the crystal plane of spinel ferrite (k h l) (111), (220), (311), (222), (400), (422), (511) and (440), respectively. This confirms that the mechanochemical synthesis of $NiFe_2O_4$ and $MnFe_2O_4$ are feasible and complete after 25 h milling time of the mixture of the $Ni(OH)_2/\alpha$-Fe_2O_3 and $Mn(OH)_2/\alpha$-Fe_2O_3 and sintered at 1100 °C/2h. The mechanochemical synthesis of $ZnFe_2O_4$ from mixture of the $Zn(OH)_2/\alpha$-Fe_2O_3 was completed after 18 h of milling time, than sintered at same temperatures as $NiFe_2O_4$, $MnFe_2O_4$. The size crystallite is calculated by Scherrers equation:

$$L = \lambda_{Co} / [w_{(2\theta)} \cdot \cos\theta]$$

where $w_{(2\theta)}$ is peak width in radians, 2θ is peak position and λ_{Co} = 1.78897 Å wavelength of used X-ray source. The mean size is L = 49, 45 and 54 nm for $NiFe_2O_4$, $MnFe_2O_4$ and $ZnFe_2O_4$, respectively.

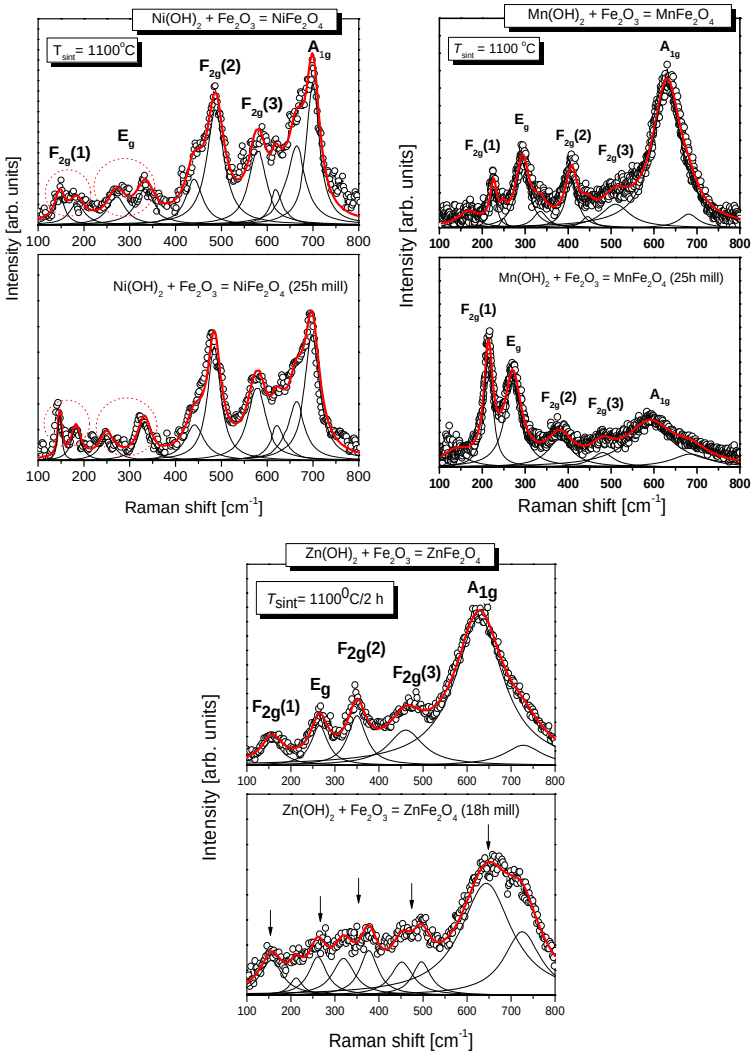

Fig. 2. Raman spectra for the sample of the MFe_2O_4 (M= Ni, Mn, Zn) sintered at 1100 °C/2h.

The Fig. 2 shows Raman spectra for the $NiFe_2O_4$, $MnFe_2O_4$ and $ZnFe_2O_4$ prepared by the soft mechanochemical synthesis. To simplify, peaks are assigned as for normal spinel

structure. But, all five Raman peaks are asymmetric (or dissociated). Each peak can be presented like a doublet, what is a characteristic of the inverse spinel structure. At a microscopic level the structure of MFe_2O_4 (M= Ni, Mn, Zn) can be considered as a mixture of two sublattices with Fe^{3+} and M^{2+}. It is supposed that Fe^{3+} and M^{2+} are ordered over the A and B-sites.

The A_{1g} mode is due to symmetric stretching of oxygen atoms along Fe-O (and M-O) bonds in the tetrahedral coordination. E_g is due to symmetric bending of oxygen with respect to the metal ion and $F_{2g}(3)$ is caused by asymmetric bending of oxygen. $F_{2g}(2)$ is due to asymmetric stretching of Fe (Ni, Mn or Zn) and O. $F_{2g}(2)$ and $F_{2g}(3)$ correspond to the vibrations of octahedral group. $F_{2g}(1)$ is due to translational movement of the tetrahedron (metal ion at tetrahedral site together with four oxygen atoms). There is a negligible displacement of metal atoms in modes A_{1g}, E_g and $F_{2g}(3)$ [22].

All five Raman peaks are asymmetric, with shoulder on the low energy side. Each peak can be presented like a doublet. At a microscopic level the structure of MFe_2O_4 (M= Ni, Mn, Zn) can be considered as a mixture of two sublattices with Fe^{3+} and M^{2+} (M= Ni, Mn, Zn). It is supposed that Fe^{3+} and M^{2+} are ordered over the B-sites. In nanocrystalline samples asymmetry is partly due to confinement and size-distribution of nanoparticles.

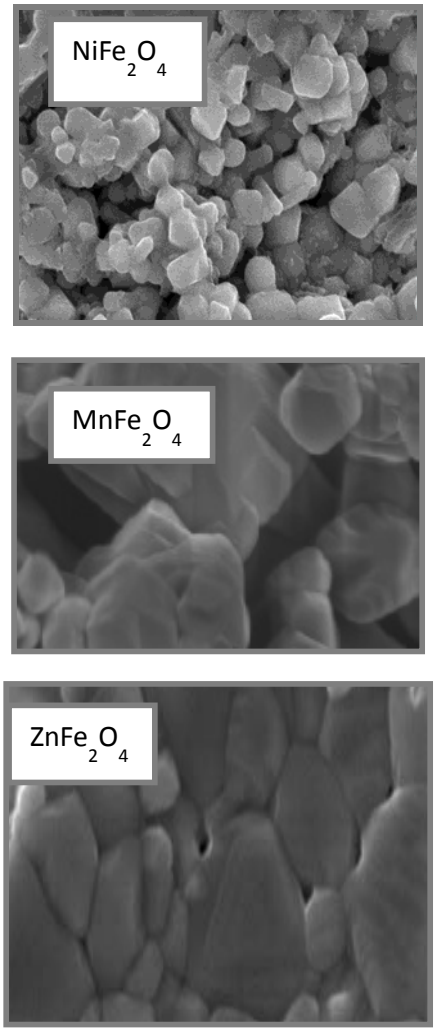

Fig. 3. SEM micrograph pattern of the MFe_2O_4 (M= Ni, Mn, Zn) sintered at 1100 °C/2h.

Fig. 3 shows SEM images of $NiFe_2O_4$, $MnFe_2O_4$ and $ZnFe_2O_4$ ferrites sintered at 1100 °C/2h. Relatively uniform distribution of grain size polygonal shape was formed. In the case of sintered nickel-ferrite grain size in the range of 0.3-1.5 μm, while in the sintered samples of manganese- and zink- ferrites grain size are in the range of 0.3-1.2 μm and 0.2-1.0 μm, respectively (Fig. 3). It is obvious that this difference in the grain size is due to different starting precursors and not to the conditions of the synthesis process. Based on the micrographs it can be concluded that the sintered samples, in the case of the $ZnFe_2O_4$ ferrite has lower porosity than the $NiFe_2O_4$ and $MnFe_2O_4$ ferrite, which is in agreement with the determined density based on Archimedes principle. The density are 3.93 g cm^{-3}, 4.2 g $cm^{-3}$and 5.58 g cm^{-3} for $NiFe_2O_4$, $MnFe_2O_4$ and $ZnFe_2O_4$ ferrite sintered samples, respectively. Density can be attributed to the difference in specific cations of the ferrite components, as NiO (6.72 g cm^{-3}) is heavier than MnO (5.28 g cm^{-3}) and ZnO (5.60 g cm^{-3}).

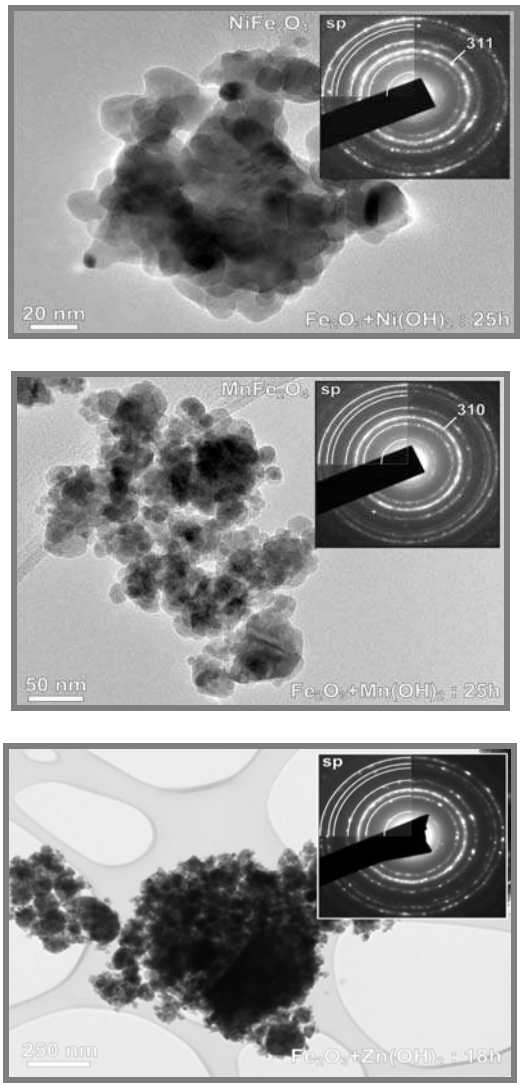

Fig. 4. TEM images with corresponding EDP (insets in the upper right corners) of mechano-chemically treated samples with starting compositions $Ni(OH)_2/\alpha$-Fe_2O_3, $Mn(OH)_2/\alpha$-Fe_2O_3 and $Zn(OH)_2/\alpha$-Fe_2O_3 after processing for 25 and 18h.

All of the synthesized ferrite samples are also characterized by transmission electron microscope. For this the powder samples are dispersed in methyl alcohol and a drop of these dispersions are allowed to dry on the transmission electron microscopy grids. The micrographs thus obtained are shown in insets of Fig. 4. Particle size distribution for all tree ferrites is in ranges between 5-20 nm. This is in agreement with XRD analysis, where particle size for $NiFe_2O_4$, $MnFe_2O_4$ and $ZnFe_2O_4$ are about 7, 16 and 17 nm respectively.

In order to understand the conduction mechanism and the hopping of charge carriers responsible for the conduction mechanism, the variation of electrical AC conductivity of ferrites under investigation is determined from measurement data using the relations (1). Generally, conductivity is an increasing function of frequency if it takes place by hopping of charges and it is a decreasing function of frequency if the band conduction is used [23].

The variation of AC conductivity is represented as a function of frequency in the range 100 Hz to 1 MHz at room temperatures. It is observed that electrical conductivity of all sintered samples increases with increasing frequency of the applied field. This behavior could be explained on the basis of Maxwell-Wagner model and Koops phenomenological theory [24], which assumes that the ferrites consist of conductivity grains separated by highly resistive thin layers (grain boundaries). As the frequency of the applied filed increases, the conductive ferrite grains became more active by promoting the hopping of the electrons between Fe^{2+} and Fe^{3+} ions (n-type) on the octahedral (B) sites [25, 26]. As a result, the AC conductivity of all ferrites under study increases. But, various reports show that the hole hopping between Ni^{2+} and Ni^{3+}. (p-type) on B site also contribute to the electric conduction in the case of $NiFe_2O_4$ferrites [25, 27].

In our present case, frequency dependent AC conductivity of samples under study varies from 10^{-7} to 10^{-3} $(\Omega cm)^{-1}$ and the conductivity behavior for all ferities is analogous with each other. From the Fig. 5, one can see that the $ZnFe_2O_4$ has the highest values of AC conductivity compared to the $NiFe_2O_4$ and $MnFe_2O_4$ at different frequencies and at room temperature. The measured values of DC resistivity of present MFe_2O_4 (M= Ni, Mn, Zn) ferrites are given in the Table 1. It is observed that $NiFe_2O_4$ has the highest value of the DC resistivity compared to the other two ferrite samples, which is in good agreement with results of AC conductivity. The high value of electrical resistivity makes $NiFe_2O_4$ ferrite good candidate for microwave devices applications that require negligible eddy currents.

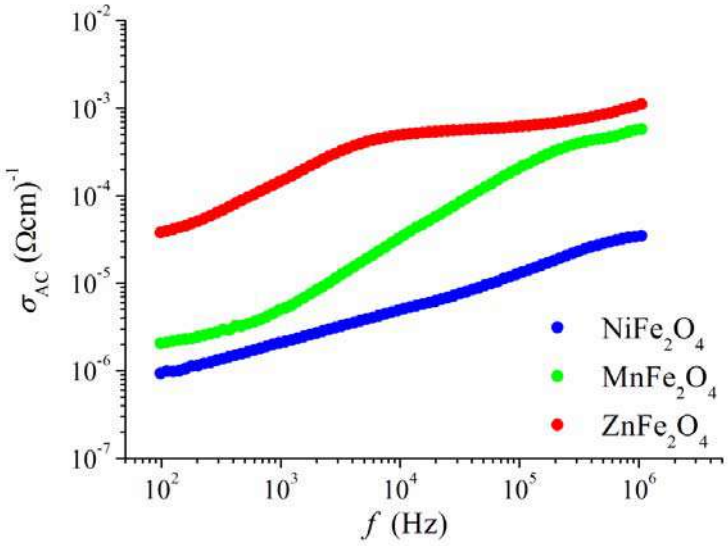

Fig. 5. Variation of AC conductivity with frequency for MFe_2O_4 (M= Ni, Mn, Zn) ferrites at room temperature.

Tab. I. The values of DC resistivity at room temperature for the MFe_2O_4 (M=Mn, Ni, Zn) samples.

sample	ρ_{DC} (Ωcm)
$NiFe_2O_4$	2.72×10^5
$MnFe_2O_4$	2.01×10^4
$ZnFe_2O_4$	2.81×10^3

In the present study, the complex impedance spectroscopy [28] as well-developed tool has been used to separate out the grain boundary and grain contribution to the total electrical conductivity of sintered ferrites. In this regard, impedance spectra (Cole-Cole plots) have been drawn in the frequency range from 100 Hz to 1 MHz at room temperature. It is evident from Fig. 6(a) that one semicircle are obtained in the impedance spectra of $NiFe_2O_4$ and $MnFe_2O_4$ ferrites indicating one dominant relaxation phenomenon and suggesting a dominant role of the grain boundary contribution. But, if we analyze the impedance response measured for $ZnFe_2O_4$ ferrite, it is noticeable that the impedance spectrum includes both grain and grain boundary effects (see Fig. 6b)). The diameters of these semicircles correspond to the resistance: a larger one at low frequency represents the resistance of the grain boundary and a smaller one obtained at the higher frequency side corresponds to the resistance of grain properties [29].

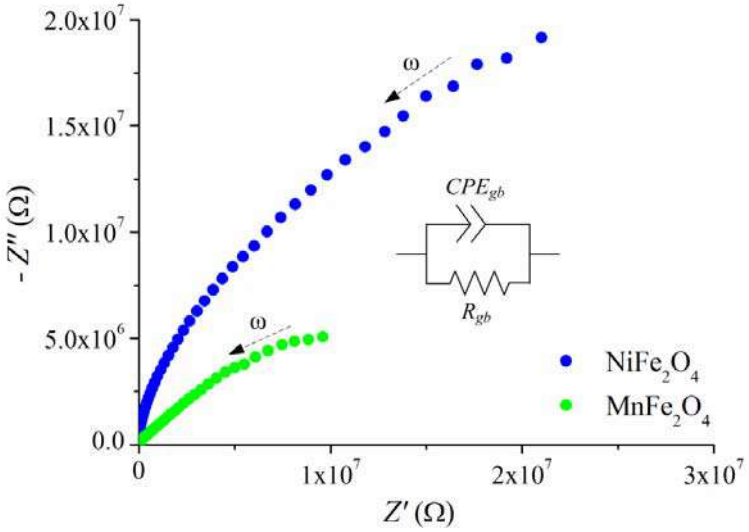

Fig. 6. Impedance spectra for (a) $NiFe_2O_4$ and $MnFe_2O_4$ ferrites and (b) $ZnFe_2O_4$ ferrite at room temperatures. Insets: proposed equivalent circuits model for analysis of the impedance data.

Tab. II. Impedance parameters for MFe_2O_4 (M=Mn, Ni, Zn) ferrites calculated from their impedance response at room temperature.

sample	R_{gb} (kΩ)	C_{gb} (F)	n_{gb}	R_g (kΩ)	C_g (F)	n_g
$NiFe_2O_4$	66075.1	1.72E–10	0.723	–	–	–
$MnFe_2O_4$	12842.5	1.08 E–10	0.775	–	–	–
$ZnFe_2O_4$	1173.4	7.13E–9	0.807	54.3	1.44E–10	0.839

In order to correlate the electrical properties of MFe_2O_4 (M= Mn, Ni, Zn) samples with the microstructure of these ferrites, the equivalent circuit models shown in the insets of Fig. 6 have been used to interpret their impedance response. In the proposed models, R_{gb} and R_g represent the grain boundary and grain resistance, while CPE_{gb} and CPE_g are the constant phase elements for grain boundaries and grain interiors, respectively [30]. The CPE is used to accommodate the non-ideal Debye-like behavior of the capacitance which is given by relation $C = Q^{1/n}R^{(1-n)/n}$, where the value of parameter n is 1 for a pure capacitor [25, 27, 30, 31]. The electrical parameters of equivalent circuits were obtained by analyzing the impedance data using EIS Spectrum Analyzer software [32]. The calculated values of these impedance parameters are given in Table 2. In the case of $ZnFe_2O_4$ ferrite, it is observed that resistance and capacitance have higher values for the grain boundary than for the grain. Higher value of capacitance can be explained by the fact that capacitance is inversely proportional to the thickness of the media [30]. Among all prepared samples, the $ZnFe_2O_4$ exhibits the lowest value of resistances which means greater polarizability for this ferrite. The lower total resistance at $ZnFe_2O_4$ promotes rate of electron hopping, which is the sole process for both conduction and polarization in ferrites [33]. Thus, the trend observed in both the electrical conductivity and complex impedance of present MFe_2O_4 (M= Ni, Mn, Zn) ferrites are in good agreement with each other.

4. Conclusions

MFe_2O_4 (M=Mn, Ni, Zn) ferrite powders and sintered samples were prepared by soft mechanochemical synthesis. Single phase nanosized $NiFe_2O_4$ and $MnFe_2O_4$ ferrite were synthesized by 25 h ball milling, while the $ZnFe_2O_4$ ferrite powder was obtained after 18 h of milling. All three samples obtained ferrites were sintered at the same temperature (1100 °C) and for the same time (2 h). X-ray diffraction of the prepared samples shows single phase cubic spinel structure. All of five first-order Raman active modes characteristic for spinel structure were observed in obtained Raman spectra. The obtained sintered ferrite samples have polygonal grains. The value of AC conductivity of the $ZnFe_2O_4$ is higher than the values of the $MnFe_2O_4$ and $NiFe_2O_4$ at different frequencies and at room temperature. Also, the values of DC resistivity are 2.72×10^5, 2.01×10^4 and 2.81×10^3 for sintered MFe_2O_4 (M= Ni, Mn, Zn) ferrites, respectively. Based on impedance measurements it can be concluded that the dominant role of the grain boundary contribution is characteristic for both $NiFe_2O_4$ and $MnFe_2O_4$ ferrites. On the other hand, one can see that the impedance spectrum of $ZnFe_2O_4$ ferrite includes both grain and grain boundary effects.

Acknowledgments

This research was financially supported by the Ministry of Education, Science and Technological Development of the Republic of Serbia through Project No. III 45003.

5. References

1. K. J. Standley, Oxide Magnetic Materials, 2nd ed., Clarendon Press, Oxford (1972).
2. M. Mohapatra, S. Anand, Int. J. Eng. Sci. Tech. 2 (2010) 127-146.
3. S. S. Yattinahalli, S. B. Kapatkar, N. H. Ayachit, S. N. Mathad, International Journal of Self-Propagating High-Temperature Synthesis, 22 (2013) 147-150.
4. T. Žák, V. Ćosović, A. Ćosović, B. David, N. Talijan, D. Živković, Sci. Sinter. 44 (2012) 103-112.
5. J. J. Thomas, A. B. Shinde, P. S. R. Krishna, N. Kalarikkal, Mater. Res. Bull. 48 (2013) 1506-1511.
6. V. Šepelák, L. Wilde, U. Steinike, K. D. Becker, Mater. Sci. Eng. A 375-377 (2004) 865-868.
7. V. Sepelak, I. Bergmann, A. Feldhoff, P. Heitjans, F. Krumeich, D. Menzel, F. J. Litterst, S. J. Campbell, K.D. Becker, J. Phys. Chem. C 111 (2007) 5026-5033.
8. R. D. K. Misra, A. Kale, B. J. Kooi, J. Th. M. De Hosson, Mater. Sci. Tech. 19 (2003) 1617-1621.
9. U. Erb, Nanostruct. Mater. 6 (1995) 533-538.
10. A. Baykal, N. Kasapoğlu, Y. Köseoğlu, M. S. Toprak, H. Bayrakdar, J. Alloys Compd. 464 (2008) 514-518.
11. L. Zhen, K. He, C.Y. Xu, W.Z. Shao, J. Magn. Magn. Mater. 320 (2008) 2672-2675.
12. Guo-Ying Zhang, Ya-Qiu Sun, Dong-Zhao Gao, Yan-Yan Xu, Mater. Res. Bull. 45 (2010) 755-760.
13. S. Ghatak, M. Sinha, A. K. Meikap, S. K. Pradhan, Mater. Res. Bull. 46 (2011) 1055-1064.
14. J. P. Chen, C. M. Sorensen, K. J. Klabunde, G. C. Hadijpanayis, E. Devlin, A. Kostikas, Phys. Rev. B 54 (1996) 9288-9296.
15. C. A. Ladole, Int. J. Chem. Sci. 10 (2012) 1230-1234.
16. M. Rajendran, A. K. Bhattacharya, D. Das, S. N. Chintalpudi, C. K. Majumdar, Int. J. Mod. Phys. B 15(2001) 305-312.
17. K. V. P. M. Shafi, Y. Koltypin, A. Gedanken, R. Prozorov, J. Balogh, J. Lendvai, I. Felner,J. Phys. Chem. B 101 (1997) 6409-6414.
18. P. Sivakumar, R. Ramesh, A. Ramanand, S. Ponnusamy, C. Muthamizhchelvan, Mater. Res. Bull. 46 (2011) 2204-2207.
19. D. M. Schleich, Y. Zhang, Mater. Res. Bull. 30 (1995) 447-452.
20. M. Atif, S. K. Hasanain, M. Nadeem, Solid State Commun. 138 (2006) 416-421.
21. E. Avvakumov, M. Senna, N. Kosova, Soft Mechanochemical Synthesis: A Basis For New Chemical Technologies, Kluwer Academic Publishers, Boston, 2001.
22. A. Ahlawat, V. G. Sathe, J. Raman Spectrosc. 42 (2011) 1087-1094.
23. M. Hashim, Alimuddin, S. Kumar, B. H. Koo, S. E. Shirsath, E. M. Mohammed, J. Shah, R. K. Kotnala, H. K. Choi, H. Chung, R. Kumar, J. Alloys Compd. 518 (2012) 11-18.
24. C. G. Koops, Phys. Rev. 83 (1951) 121-124.
25. Z. Z. Lazarevic, C. Jovalekic, A. Milutinovic, D. Sekulic, V. N. Ivanovski, A. Recnik, B. Cekic, N. Z. Romcevic, J. App. Phys. 113 (2013) 187221.
26. A. S. Fawzi, A. D. Sheikh, V. L. Mathe, J. Alloys Compd. 502 (2010) 231-237.
27. M. Younas, M. Nadeem, M. Atif, R. Grossinger, J. Appl. Phys. 109 (2011) 093704.

28. E. Barsoukov, J. R. Macdonald, Impedance Spectroscopy: Theory, Experiment, and Applications, 2nd ed., John Wiley and Sons (2005) 205-343.
29. H. Anwar, A. Maqsood, J. Magn. Magn. Mater. 333 (2013) 46-52.
30. Z. Z. Lazarevic, C. Jovalekic, D. Sekulic, M. Slankamenac, M. Romcevic, A. Milutinovic, N. Z. Romcevic, Sci. Sinter. 44 (2012) 331-339.
31. M. V. Nikolic, M. P. Slankamenac, N. Nikolic, D. L. Sekulic, O. S. Aleksic, M. Mitric, T. Ivetic, V. B. Pavlovic, P. M. Nikolic, Sci. Sinter. 44 (2012) 307-321.
32. A. S. Bondarenko, G. A. Ragoisha, EIS Spectrum Analyser, http://www.abc.chemistry.bsu.by/vi/analyser/.
33. K. M. Batoo, S. Kumar, C. G. Lee, Alimuddin, Curr. Appl. Phys. 9 (2009) 1397-1406.

Садржај: *Нано спинел ферити MFe_2O_4 (M= Ni-никал, Mn-манган, Zn-зинк) су били добијени софт механохемијском синтезом у планетарном млину са куглама. Мешавине одговарајућих прахова оксида и хидроксида су коришћене као полазне компоненте. Свака од ових смеша је механички активирана, затим пресована и синтерована на 1100 °C током 2 часа. Фазни састав праха и синтерованих узорака анализиран је ренгено структурном анализом (XRD) и Раман спектроскопијом. Морфологије су биле прегледане на скенирајућем електронском микроскопу. У овом раду, AC- проводности и DC-отпорности на синтерованим узорцима MFe_2O_4 (M= Ni-никал, Mn-манган, Zn-зинк) ферита су мерене на различитим фреквенцијама и на собној температури. Вредности електричне проводности показују раст са повећањем температуре, што указује на проводно понашање испитиваних ферита. Феномен проводности испитиваних узорака може бити објашњен на основу модела скока. Анализа комплексном импедансном спектроскопијом је била коришћена за проучавање ефекта зрна и границе зрна на електричне особине код сва три добијена ферита.*

Кључне речи: *Ферити, Раман спектроскопија, DC проводност, комплексна импеданса.*

Journal of Physics and Chemistry of Solids 89 (2016) 120–127

Contents lists available at ScienceDirect

Journal of Physics and Chemistry of Solids

journal homepage: www.elsevier.com/locate/jpcs

Optical properties of layered III–VI semiconductor γ-InSe:M (M=Mn, Fe, Co, Ni)

Aleksandra Milutinović [a], Zorica Ž. Lazarević [a,*], Milka Jakovljević [a], Branka Hadzić [a], Milica Petrović [a], Martina Gilić [a], Witold Daniel Dobrowolski [b], Nebojša Ž. Romčević [a]

[a] Institute of Physics, University of Belgrade, P.O. Box 68, Pregrevica 118, Zemun, Belgrade, Serbia
[b] Institute of Physics, Polish Academy of Science, 02-668 Warsaw, Poland

ARTICLE INFO

Article history:
Received 26 August 2015
Received in revised form
30 October 2015
Accepted 31 October 2015
Available online 5 November 2015

Keywords:
Layered compounds
Crystal growth
X-ray diffraction
Raman spectroscopy
Electronic structure

ABSTRACT

Indium selenide belongs to layered III–VI semiconductors with highly anisotropic optical and electronic properties. Energy gap of 1.32 eV makes this material very attractive for solar energy conversion. We investigated the influence of 1% 3-d transition metals M=Mn, Fe, Co, Ni, used as dopants, on energy levels of InSe:M in the range 1.4–6.5 eV and especially in the range of energy gap <1.4 eV by means of ellipsometric measurements. It was concluded that at ambient temperature foregoing dopants, all di-valent, with $4s^2$ valent electrons, in the similar way influenced on blue-shift of energy levels in valent zone, but did not influence on the fundamental energy gap. Photoluminescence measurements confirmed blue-shift of the valent zone energy levels and an existence of deep impurity levels.

1. Introduction

Layered semiconductors are of great interest because they have highly anisotropic optical and electronic properties and relatively inert basal planes. Because of these properties, layered semiconductors are often used as photochemical electrodes. Indium selenide, with its direct energy gap in near infrared energy range [1,2], is an attractive material for solar energy conversion. Absence of dangling bonds on the (0 0 1) plane is an additional advantage for application as heterojunction device with a low density of interface states.

The layers of InSe crystals consist of covalently bonded Se–In–In–Se sheets with three Se atoms coordinated to one In atom. Covalent In–In bonds are oriented perpendicular to the layers. The bonding between the layers is weak, predominantly of Van der Waals type and, as in the other layered III–VI semiconductors, there exist several crystals polytypes.

There are three most common polytpes which differ by the stacking sequences of the layers. They are described as β- (space group $P6_3mmc$), ε-(P-6m2) and γ-polytypes ($R3m$). The β- and ε-polytypes belong to the hexagonal system and each unit cell contains eight atoms extended over two layers. The γ-polytype has rhombohedral symmetry and its unit cell contains four atoms. When the unit cell is transformed to the hexagonal system for the comparison with other polytypes, the non-primitive unit cell contains twelve atoms extended over three layers. There is also multiplied hexagonal modification δ-($P6_3mc$), as well as multiplied rhombohedral 9R and 12R modifications [3–5].

The Bridgman-grown InSe crystals are usually of γ-polytype with rhombohedral (trigonal) symmetry. At low temperatures photoluminescence (*PL*) spectra of pure InSe has two visible bands usually: one, at higher energy, very exaggerate band corresponds to a direct transition and the second, weaker band presents an indirect transition. In some InSe crystals an indirect transition can be dominant [6,7]. The presence of large concentrations of native donors and acceptors, results in the existence of corresponding levels in the InSe energy gap. Complicated structure of *PL* spectra, especially at temperatures higher of 100 K, is due to the presence of energy levels of various natures in the InSe energy gap. *PL* spectra of different samples show various *PL* spectra structure. The quality of the samples affects the structure of PL spectra. In Ref. [8] is investigated the temperature dependence of various *PL* bands that appear in the range of 100 to 295 K. At T=295 K the direct and indirect energy gaps are E_g^d=1.324 eV and E_g^i=1.270 eV, respectively. The binding energies of the free direct and indirect excitons are E_X^d=16.9 meV and E_X^i=13.0 meV.) The energy depths of the donor level below the conduction band bottom and acceptor level above the valence band top are E_D=26 meV and E_A=60 meV, respectively.

Doping impurities in InSe mainly segregate in interlayer

* Corresponding author. fax: +381 11 3160 531.
E-mail address: lzorica@yahoo.com (Z.Ž. Lazarević).

http://dx.doi.org/10.1016/j.jpcs.2015.10.020
0022-3697/

spacing forming planar defects, like stacking faults or interlayer precipitates. These planar defects do not affect the carrier mobility along the layers [9,10]. For rather high concentration of doped impurities, the effective number of charge carriers never exceeds 10^{16} cm^{-3}, which is close to concentration for the pure InSe.

Doping of *n*-InSe with two-valence Zn, Cd, and Hg leads to transforming of *n*-InSe in *p*-InSe and to appearing new photoluminescence (*PL*) bands. Zn-doping activates *PL* band at 1.17 eV [11]. In Cd-doped samples two hole-trapping levels, at 0.42 eV and 0.48 eV above the valence band are detected [12]. A broad emission band at 1.237 eV, that is $< E_g$, in Hg-doped InSe is due to transition between a shallow donor level and a deep acceptor level at 0.07 eV (424.55 cm^{-1}) above the valence band [12].

In Ref. [13] was shown that in InSe doped with GaS exciton energy has a blue-shift. With increasing of dopant quantity over 2.5 ppm the excitonic energy does not change. Doping of *n*-type InSe by trivalent Er [14], Ho [15] and Dy [16] shows an effect on crystal band width. The absorption measurements show a red shift of band gap.

This paper is intended to be a contribution to the study of the influence of impurities on the γ-InSe optical properties, concerning possible impact on band gap. Firstly it was confirmed that our crystals represent the γ-modification and then we investigated the influence of divalent 3-d transition metals Mn, Fe, Co and Ni on the energy band gap and excitons in doped crystals. 3-d metals have magnetic moments, but properties of magnetically doped γ-InSe will be a point of some other paper. Exciton-phonon interactions are very interesting for photon absorption characteristics of solar cell materials. We investigated the dopant influence on higher energy levels of γ-InSe, also.

2. Experiment

InSe single crystals were grown in *Institute of Physics, Polish Academy of Sciences,* using Bridgman method. The dopants were added to the starting melt in crystal growth procedure. The melting point of the InSe is 660 ± 5 °C. The obtained ingots had no cracks or voids on the surface. Samples were cleaved from ingots parallel to the layers. No polishing or cleaning treatments were needed because of the natural mirror-like cleavage faces.

The distribution of dopant along the ingot is inhomogeneous. In the first 60% of the ingot length the concentration of dopant is very small (~0%) and at the end of the ingot the concentration achieves a few atomic percents. (We used only samples with concentration of dopants about 1 at%).

For XRD analysis the Philips PW 1050 X-ray diffractometer was used. X-ray source was Ni filtered Cu*K*α radiation of 1.54056 Å. Measurements were done at room temperature in 2θ range of 5–80° with scanning step width of 0.01° and 10 s scanning time per step.

Raman and photoluminescent spectra were excited by Ar-ion laser line of 514.5 nm at room temperature and 488 nm at 20 K and recorded by a Joben-Yvon U1000 spectrometer in the back scattering geometry. Low-temperature spectra were measured using Leybold closed-cycle helium cryostat.

Absorption measurements at ambient temperature were carried out on high resolution variable angle spectroscopic ellipsometer SOPRA GES5-IRSE. The quantity measured in ellipsometry is complex reflectance ratio $\rho(\omega, \psi) = r_p(\omega, \psi)/r_s(\omega, \psi)$, where r_p and r_s are Fresnel reflection coefficients in p- and s-polarised light; ψ is an angle of incidence-in our case fixed at 70°. The inversion of $\rho(\omega, \psi)$ gives the complex dielectric function:

$$\varepsilon(\omega, \psi) = N^2 = \{1 + \tan^2\psi \cdot [(1 - \rho(\omega, \psi))/(1 + \rho(\omega, \psi))]^2\} \cdot \sin^2\psi$$

N is a complex refractive index: $N = n + i \cdot k$. The absorption coefficient α is calculated from coefficient of extinction, k, as:

$$\alpha = 4\pi \cdot k/\lambda$$

where λ is wavelength of incident photon.

3. The band structure of γ-InSe

Energy bands of InSe have three-dimensional (3D) character. It is confirmed theoretically, by band-structure calculation, and experimentally, by cyclotron resonance measurements [17]. Various theoretical approaches were used to generate band structure for (layered) γ-InSe: empirical pseudopotential method [18] with or without spin-orbit splitting, *ab initio* band structure calculation under pressure, total energy calculations using the linear augmented plane wave method with relativistic corrections and spin-orbit coupling [19,20]. Energy of fundamental gap is underestimated in all calculations. Gomes da Costa et al. [18] used "scissor operator" that set gap to the experimental value 1.35 eV. The valence band maximum and conduction band minimum of γ-InSe are at the *Z*-point of the Brillouin zone (BZ). *Z*-point is at the zone boundary in the direction perpendicular to the crystal layers. (For β-InSe gap is at the Γ-point, in the center of BZ.) The top of valence band and the bottom of the conduction band are mainly formed by 5*s* indium orbitals mixed with $4p_z$ orbitals of selenium atoms. Bonding-antibonding repulsion of these orbitals splits energy level and forms valence band and conduction band. Interlayer interaction of Se p_z orbitals produced splitting of formed bands, also. Below the top of the twofold degenerate valence band edge at *Z*-point there are 4 bands arise from two $p_{x,y}$-like states which are split by spin-orbit interaction. In Ref. [18] calculated spin-orbit splitting is 0.32 eV for the both doublets. In Ref. [20] is estimated a lower value of splitting for the second doublet. However, according to Gomes da Costa et al. [18], the oscillator strength for the other spin-orbit split pair is weak and it is expected that this transitions could be hardly visible. It is confirmed by Schottky-barrier electroreflectance spectroscopy [21] where only the first doublet bands, E_1 and E_1', were clearly observed.

Between -6.5 eV and -12.5 eV there is another gap that separates the deep Se 4 s band from In 5*s*, 5*p* orbitals.

4. Results and discussion

The X-ray diffraction spectra recorded on the crystal sample of pure InSe, perpendicular to (0 0 1) growth direction, is presented in Fig. 1. When XRD is recorded in the growth direction, *i.e.* direction of crystal layers (0 0 1), spectrum is reduced to (0 0 *l*) Bragg reflections, where $l = 3n$ in the case of rhombohedral modification, or $l = 2n$ in the case of hexagonal modification [22,23]. Due to similar positions of (0 0 3*n*) and (0 0 2*n*) diffractions in the XRD spectra of rhombohedral and hexagonal InSe crystals, respectively, it is difficult to conclude which modification is in question only on the basis of a XRD spectra recorded in the growth direction. But, an existence of the "undesirable" diffraction at $2\theta = 29.00°$, confirms that crystal structure has rhombohedral symmetry. (Reflection at that Bragg angle exists only in powder XRD of rhombohedral modification of InSe.)

Therefore, the peak positions in Fig. 1 are consistent with γ-polytype of the InSe crystal structure with rhombohedral *R*3m (C_{3v}^5) symmetry, space group number 160. Crystal cell constants are $a = b = 4.0568$ Å, $c = 24.8500$ Å, what is obtained for the best fit of spectrum (by comparing experimental spectrum with spectra generated by PCW 2.4 programme). Coordinates of four atoms

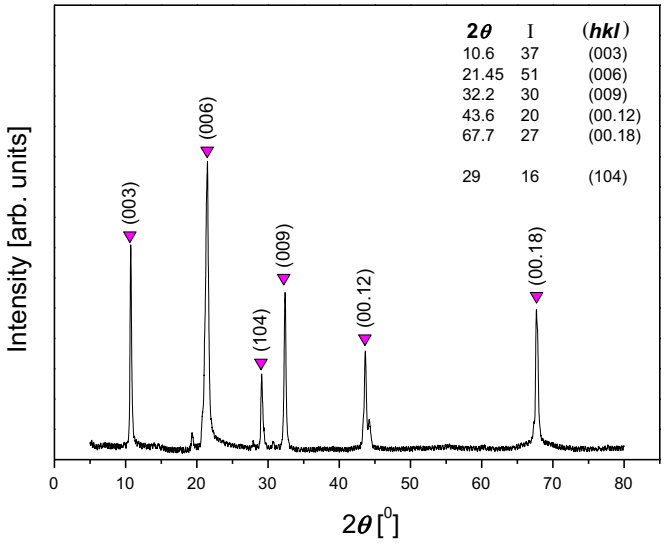

Fig. 1. XRD spectrum of the crystal sample of pure InSe recorded perpendicular to (0 0 1) growth direction.

with Wickoff symbols **3a** are In1: 0, 0, 0; In2: 0, 0, 0.1100; Se1: 0, 0, 0.6223 and Se2: 0, 0, 0.8201. Existence of only one additional (1 0 4) reflection is a confirmation of a satisfactory quality of layered crystal. Unequal intensity of reflections suggests the presence of a certain extent of different crystal polytypes, *i.e.* different stacking sequences, formed during crystal growth.

Raman spectra reflect the symmetry of the nearest surrounding and verify a crystal arrangement. The observed phonon frequencies in various modifications of InSe are rather close, as is reported in the literature. Phonons mainly involve vibrations of atoms within the $(InSe)_2$ bilayer, and therefore are not too sensitive to the stacking of the bilayers. Raman spectra of pure InSe and InSe doped with 1% *M* (*M*=Mn, Fe, Co, Ni) excited by 514.5 nm (2.41 eV) Ar-ion laser line, recorded in the range of 70–550 cm^{-1} at room temperature, are presented in Figs. 2 and 3. Fifteen modes are registered. Positions of the observed modes correspond to first, second and third-order phonons of γ-polytype InSe. Modes are assigned like in Refs. [24–27]. As γ-InSe belongs to the C_{3v}^5 space group, with four atoms per primitive rhombohedral unit cell, there are twelve normal modes of vibration. According to theoretical group considerations, the normal modes are presented as:

$$\Gamma = 4A_1 + 4E$$

Modes A_1^1 and E^1 are acoustic and other modes are optical. Optical modes are both Raman and infrared active. All atoms take part in each vibration, A_1 modes perpendicular to the layers, E modes parallel with layers [24,25]. The Coulomb interaction cancels the degeneracy of some optical modes and produces the splitting between LO and TO phonons. (There are no IR active optical modes in Raman spectra of hexagonal InSe modifications.)

At about 40 cm^{-1} is the first optical E bending mode (outside the range of our measurement). The first visible peak in our experimental spectra (Fig. 2) is at 115 cm^{-1} and corresponds to A_1 stretching mode. In these two modes the In–Se bond does not play a significant role because covalently bonded In and Se vibrate in phase, Fig. 4. Restoring forces are mainly provided by interlayer interactions and by either In–In bond bending (E), or stretching (A_1). So these low frequency modes are affected by interlayer interaction and stacking sequences. At 176.9 cm^{-1} is E and at 226.9 cm^{-1} is A_1 mode. Marked with an arrow is A_1(LO) mode at 199 cm^{-1}. Stretching of In–Se bond play an important role in nonpolar E (176.9 cm^{-1}) and polar A_1(LO) (199 cm^{-1}). These vibrations do not depend on interlayer interactions. In the non-polar

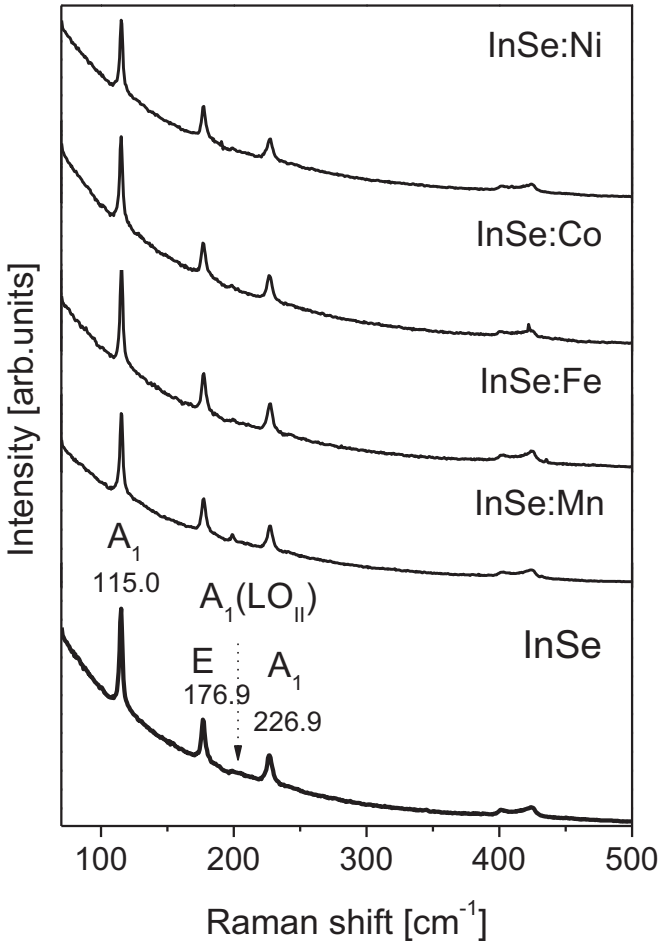

Fig. 2. Raman spectra of pure and doped InSe crystals, recorded at room temperature.

A_1 mode at 226.9 cm^{-1} all bonds provide restorative stretching force and its frequency is affected by interlayer interaction and stacking sequences. For the A_1 modes at 115 cm^{-1} and 227 cm^{-1} the layers move against each other in the z direction.

According to high intensity and enormous Rayleigh tail, recorded Raman spectra, Fig. 2, are near-resonant. (Rayleigh tail is mainly due to luminescence of the first energy transition above the lowest energy gap.)

Deconvolution of spectra clearly shows low-intensity IR modes, Fig. 3 (left side). IR modes exist only in Raman spectra of rhombohedral γ-InSe. Their frequencies are in accordance with far-infrared reflectivity measurements.

Weak peaks starting from 243 cm^{-1} up to 519 cm^{-1} (Fig. 3, right) are second and third order modes. At 243 cm^{-1} can be a combination of $A_{1(277)}$ and a acoustic mode at 17 cm^{-1}. At 385 cm^{-1} is $A_1(TO_{II}+LO_{II})$ mode, at 402 cm^{-1} is $2A_1(LO_{II})$ mode and at 424 cm^{-1} is $2E(LO_{\perp})$ mode. A broad mode at 417 cm^{-1} can be a combination of $2A_1(LO_{II})$ and a acoustic mode (Ac.) at 19 cm^{-1}. At 453 cm^{-1} is a second harmonic of $A_{1(227)}$ mode and at 519 cm^{-1} a third harmonic of $E_{(117)}$.

It is not observable any shift of modes in doped crystals. Raman spectra of pure and doped InSe crystals confirm that all our crystal samples obtained by Bridgman method have rhombohedral $R3m$ (C_{3v}^5) symmetry.

The absorption coefficients α of pure and doped γ-InSe are derived from ellipsometric measurements at 300 K in the energy range 0.77–6.5 eV. Wide energy range includes energy gap, as well as higher energy transitions. Results are presented in two distinct

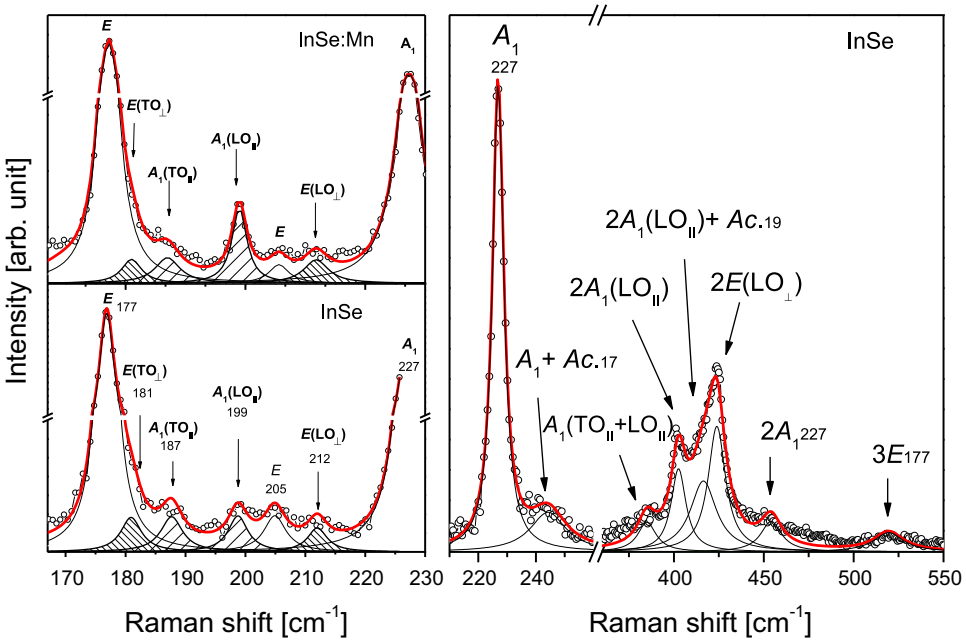

Fig. 3. Deconvolution of the Raman spectra: IR modes (left side) and the second-, or the third-order modes (right) are stressed by arrows.

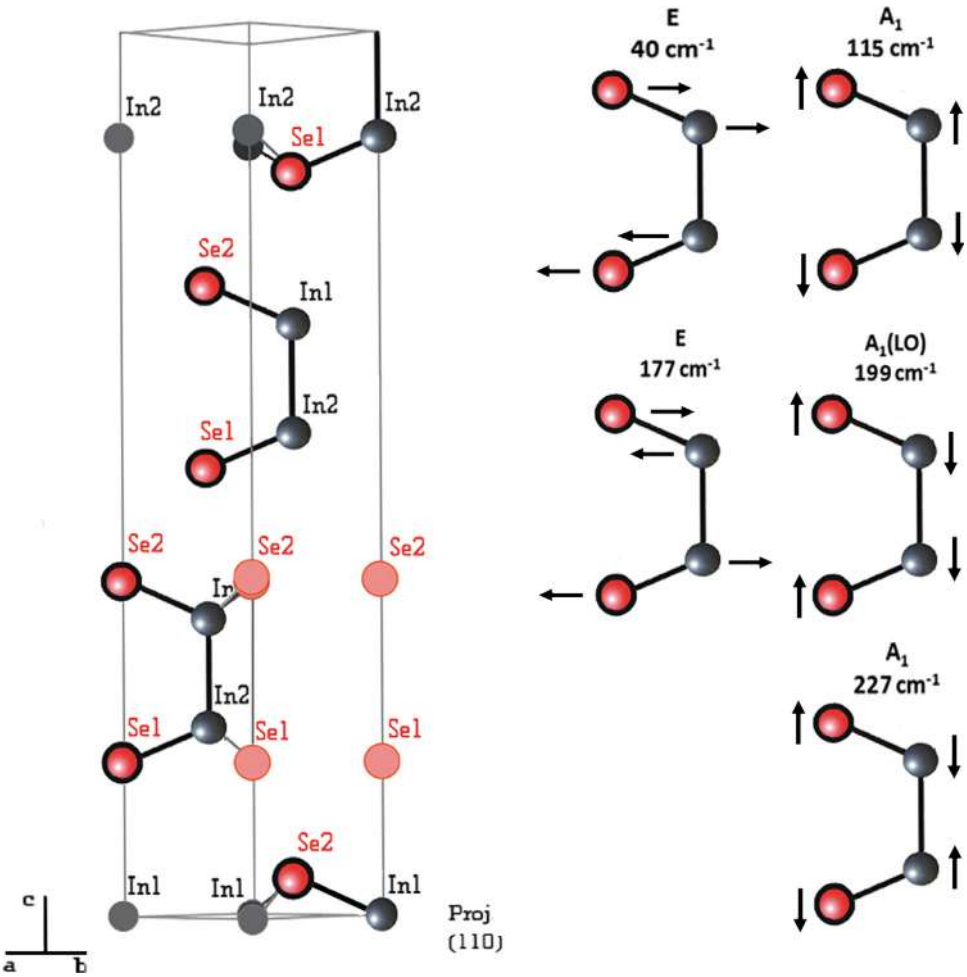

Fig. 4. The non-primitive unit cell of γ-InSe (transformed to the hexagonal system) with twelve atoms extended over three bilayers and schemes of oscillating for the strongest modes in our Raman spectra.

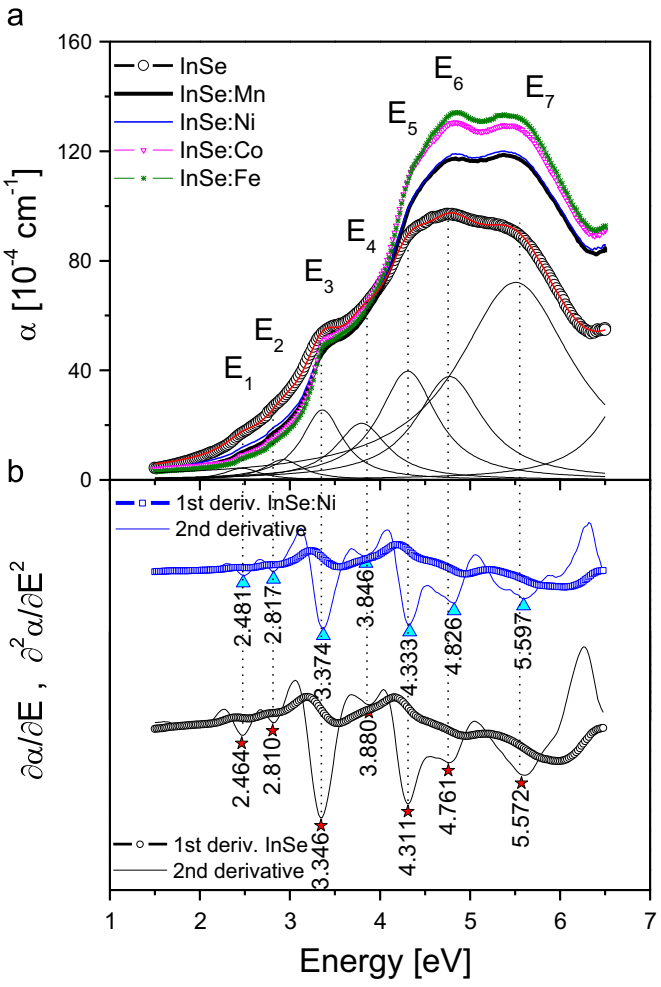

Fig. 5. (a) Absorption coefficient of pure InSe and doped InSe:*M* (*M*=Mn, Fe, Co, Ni) in energy range 1.5–6.5 eV; (b) the first and the second derivative of the absorption coefficient are given only for InSe and InSe:Ni for the sake of clarity.

figures because the intensities of the absorption spectra in the low energy range of intragap transitions are more than ten times weaker than in the range of high-energy transitions. Energies of higher transitions, Fig. 5, were compared with the results of mostly theoretical Refs. [18,20,21], and intragap transitions with *PL* measurements [8,12,28] electroreflectance and the results of absorption spectroscopy [2,15,29,30]. Energy band structure taken from Ref. [18] is given in Fig. 6 together with schematically presented energy transitions obtained in this paper.

The absorption spectra in the energy range 1.5–6.5 eV, presented in Fig. 5, show that spectra of doped samples have a higher intensity and a blue-shift (in average) of energy bands in comparison to spectrum of the undoped sample. The transition energies are estimated by deconvolution of the absorption spectra and registered energy bands (marked with E_i, $i=1, 2, 3\ldots$) are assigned as in above mentioned papers [18,20,21].

Therefore, weak bands E_1 and E_2 of pure InSe with energies 2.464 eV and 2.810 eV, respectively, correspond to the first of the split Se $p_{x,y}$-like bands (E_1 and E_1') from the *Z*-point of BZ. In Ref. [21] is shown that the corresponding bands (observed at the similar energies) have the same behaviour under the pressure, what is the proof of the same origin. According to energy band calculations, the second of Se $p_{x,y}$-like doublets should be $E_2 \approx E_1'$ and $E_2' \approx 3.0$ eV, but these transitions was not registered neither in Ref. [21], nor in our measurements. An analyse of the absorption spectra shows that E_1 and E_2 in the case of pure InSe are separated by 0.346 eV, what is in good agreement with values predicted in Ref. [20] and measured in Ref. [21] for E_1 and E_1'.

The forthcoming assignation of experimentally obtained energy transitions gives a satisfactory agreement with the calculated energy band structure of γ-InSe given in Fig. 6. The bands E_3 (3.346 eV), E_4 (3.880 eV) and E_5 (4.311 eV) correspond to transitions from *D*-point of BZ. Band E_6 (4.761 eV) seem to be from Γ-point. Feature at 5.572 eV, E_7, corresponds to direct energy transition from *Z*-point from In 5*s*, 5*p* band. The high energy side of the measured spectra can be properly fitted only if band at about 7.4 eV (*Z*-point), originated from splitting of In 5*s*, 5*p* band, is included.

The energies of bands of doped InSe and their shift in correspondence to undoped InSe are presented in the Table 1. The covalent radii of dopants are given, in addition [31].

From Fig. 5 and Table 1, it can be seen that influence of dopants is visible in the whole investigated energy range from 1.5 eV to

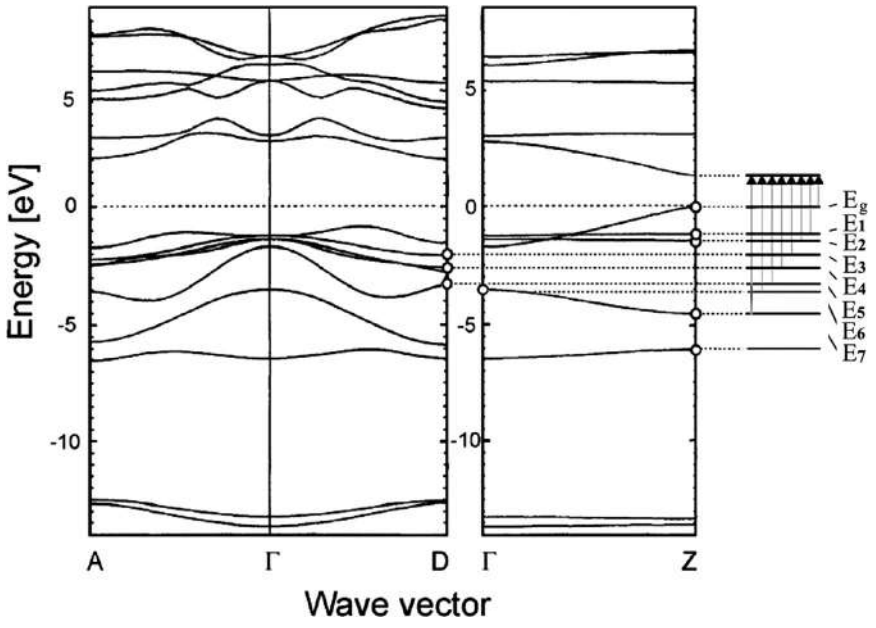

Fig. 6. Energy band structure taken from Ref. [18]. The energy transitions obtained in this paper are indicated at the right side of the figure.

Table 1
Experimentally obtained values of energy bands in pure and doped InSe. (Energy shift of doped InSe is given in brackets.)

	E_1 [eV] (Δ [meV])	E_2 [eV] (Δ [meV])	E_3 [eV] (Δ [meV])	E_4 [eV] (Δ [meV])	E_5 [eV] (Δ [meV])	E_6 [eV] (Δ [meV])	E_7 [eV] (Δ [meV])
InSe	2.464	2.810	3.346	3.880	4.311	4.761	5.572
InSe:Mn	2.480 (16)	2.819 (9)	3.357 (11)	3.873 (−7)	4.325 (14)	4.754 (−7)	5.624 (52)
InSe:Fe	2.471 (7)	2.831 (21)	3.357 (11)	3.942 (62)	4.317 (6)	4.815 (54)	5.617 (45)
InSe:Co	2.485 (21)	2.818 (18)	3.363 (17)	3.960 (80)	4.323 (12)	4.795 (34)	5.589 (17)
InSe:Ni	2.481 (17)	2.817 (7)	3.374 (28)	3.846 (-34)	4.333 (22)	4.826 (65)	5.597 (25)

Covalent radii (Å): ^{25}Mn = 1.39, ^{26}Fe = 1.32, ^{27}Co = 1.26, ^{28}Ni = 1.24, ^{49}In = 1.42 Å, ^{34}Se = 1.20.

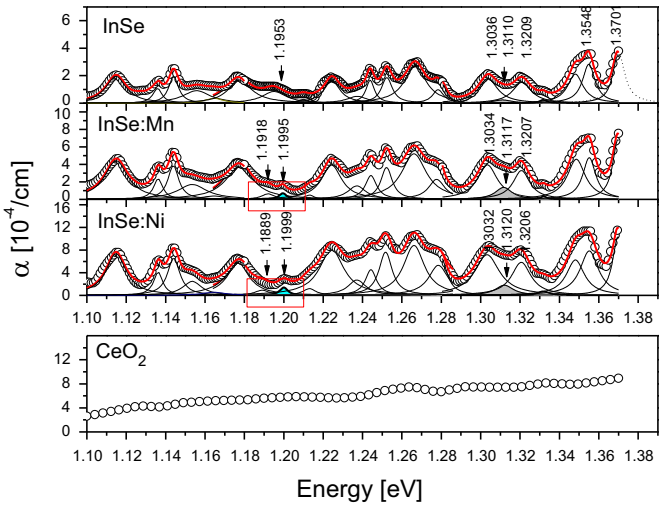

Fig. 7. Intragap absorption of pure and doped InSe samples in energy range 0.7–1.37 eV. Spectra are obtained by ellipsometric measurements at room temperature under angle of 70°. Selected part of the intra-gap absorption spectra in: pure InSe, InSe:Mn and InSe:Ni are deconvoluted. (Because of surprising likeness of investigated spectra, a spectrum of sintered CeO_2 sample recorded under the same conditions is given at the bottom of the picture.)

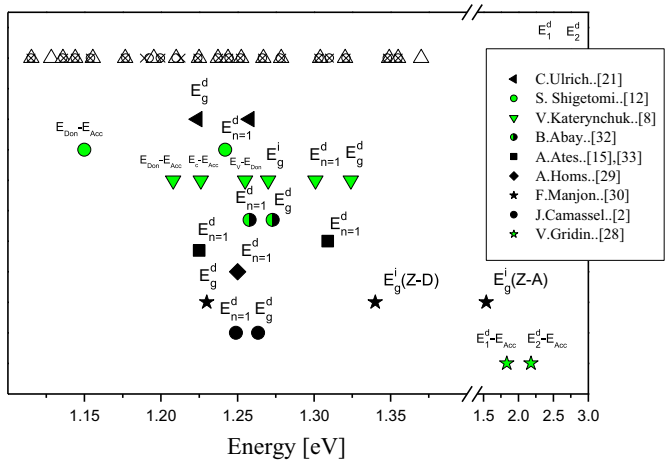

Fig. 8. "Graphically" presented results of other authors: obtained by *PL* spectroscopy – green symbols; electroreflectance and absorption measurements – solid black symbols (see text). All data are related to pure InSe at 300 K. The data from this paper are in the first row: transitions in pure InSe are indicated with open triangles, InSe doped with Mn is presented with open circles and InSe doped with Ni is presented with crosses. (For interpretation of the references to color in this figure legend, the reader is referred to the web version of this article.)

6.5 eV. Systematic changes of the blue-shift with changes of dopants atomic masses, or covalent radii are not registered. It is obvious that the bands E_4, E_5, E_6 and E_7 are noticeably broader and probably have more complex structure as a result of superposition of several energy transitions. The derivatives of these broad bands clearly indicate an existence of the additional local maxima.

In energy range < 1.4 eV the obtained spectra are extremely rich. Deconvolution of spectra shows that almost analogous Lorentzians are presented in all samples. In Fig. 7 is presented a part of fitted spectra (range 1.10–1.37 eV) where some dissimilarities are observed between pure InSe and doped InSe samples. In the available literature we did not find any transition data outside the selected area. Dissimilarities are stressed by arrows.

Energies of the corresponding transitions in the intraband range are practically the same in all samples. In doped samples only, instead of the peak at 1.1953 eV, two small additional peaks appear. One, in InSe:Mn is at 1.1995 eV and in InSe:Ni at 1.1999 eV, and the other peak is at 1.1918 eV in InSe:Mn and 1.1889 eV in InSe:Ni, Fig. 7. Relative intensities of intraband transitions vary slightly from sample to sample, but generally, intensity of spectra of doped samples is higher. This is noticeable in Fig. 5 for high energy transitions, as well as in intraband region. Analyse of spectra reveals that some peaks in doped samples become more intensive, as in the case of the peak at about 1.31 eV.

Energies of energy gaps: direct and indirect, of free excitons and another transitions measured by other authors on 300 K (or extrapolated to 300 K) are very different to each other, despite the fact that all samples are obtained by the standard Bridgman method and with pure starting components, Fig. 8. Available literature data do not facilitate our attempt to assign a great number of intragap modes [2,8,12,15,21,28,29,30,32,33]. A lot of native donors and acceptors are unintentionally integrated in pure InSe creating their own energy levels. Various defects like stacking faults and antisite defects are surely present in the structure. (In the case of InSe, antisite defects are created when group-VI Se substitutes for group-III In.)

Based on the general form of spectra and energy difference between particular transitions and their intensities we suppose that at 1.3209 eV (in pure InSe) is a direct energy gap E_g^d. Peak at 1.3036 eV corresponds to free exciton ($n=1$). Energy difference of 17.3 meV is close to previously published values of the Rydberg energy (*i.e.* free exciton binding energy): $R^d = 14.5$ meV [2], 16.9 meV [8] and 14.3 meV [34].

A pair of peaks at about 1.33 eV and 1.31 eV (small Lorentzians coloured in grey) could be associated with the direct gap energy and energy of the free exciton in the regions of samples where the stacking sequence of layers is different. A number of such stacking faults probably increases with doping and these pair of peaks become a little more intensive in doped samples.

A peak at 1.278 eV corresponds to indirect band-to-band transition ("vertical", Z–Z) E_g^i, that takes place with participation of phonons. Energy of phonons is about 43 meV, *e.g.* 346 cm^{-1}. In Ref. [8] phonon energy is 44 meV. Peak at 1.2667 eV can correspond to electron transition from principal, $n=1$ energy level of the indirect free exciton to valence band. Obtained binding energy of indirect exciton would be 11.3 meV, what is close to energy obtained in Ref. [8].

A group of bands 1.2523 eV, 1.2439 eV, 1.2368 eV and maybe 1.2245 eV corresponds to energy transition between donor states at 25.7 meV, 34.1 meV, 41.2 meV and 53.5 meV, respectively, and valence band.

Weak peaks at about 1.2 eV surely belong to acceptor-to-conduction band transitions. Energy of the "central" peak in InSe is 78 meV above the valence band. According to usual acceptor energies, 70 meV [35], peaks at 1.1776 and 1.2098 eV can match to acceptor-to-conduction band transitions, also. In Ref. [35] is shown that the same acceptor level exists in undoped InSe samples and in InSe samples doped with Hg. Therefore, corresponding transition is connected with the same type of center (or centers).

Bands grouped around the peak at 1.1439 eV correspond to donor-acceptor recombination. Band at 1.115 eV can be connected with deep acceptor-to-conduction band transition.

At energies higher than band-gap a pair of rather strong transitions is observed. We suppose that these bands at about 1.352 eV and 1.37 eV can be indirect transitions from some local minimum of conduction band to the top of the valence band. In Ref. [30] for bands at 1.34 eV and 1.542 eV was suggested that could be indirect transitions from the local minimums at *D* and *A* points of Brilouin zone, to the top of the valence band in the *Z*-point. Since the energy difference between our bands is only about 20 meV, we suppose that these bands, seen in our spectra, are probably in relation with *D*–*Z* transition only. One peak could be band-to-band ("non-vertical") transition and the other band-to-shallow acceptor level above the valence band.

The results from Ref. [28], presented by stars in Fig. 8, are obtained from photoluminescent measurements of InSe doped with tin (Sn). Measured *PL* bands at 1.839 eV and 2.178 eV, correspond to direct transitions (*Z*–*Z*) from high energy bands E_1 and E_2 to acceptor level. Estimated acceptor level is at about 600 meV above the valence band. *PL* bands are asymmetric and very broad. We estimate (from Fig. 1 of Ref. [28]) that FWHM is about 200 meV. Reason could be an existence of more than one acceptor level.

In Ref. [11] in all samples of InSe, undoped and doped with various amounts of Zn at 77 K in *PL* spectra were registered free excitons at 1.32 eV and two weak transitions at about 1.225 eV and 1.28 eV. The existence and the origin of these weak transitions were not discussed. A transition at 1.28 eV can be a deep donor level at about 54 meV, and another weak band at 1.225 eV, could be donor-to-acceptor transition for acceptor level at about 60 meV (or band-to-acceptor transition for acceptor level about 100 meV). Except these bands, in Zn-doped samples is seen a broad *PL* band centred at 1.17 eV. This band was identified as the localized electronic transition from the excited state of a vacancy to the ground state of a Zn acceptor level. It is estimated that Zn-acceptor level is 160 meV above the valence band. In the same paper it was referred from Hall-effect measurements and deep-level transient spectroscopy (DLTS) that at 600 meV is another, deep acceptor level. This deep acceptor level was associated with the defects or defect complexes formed by Zn atoms in the interlayers. By the characteristics of layer crystals (weak interlayer bonds), unintended dopant atoms tend to precipitate in the interlayer spaces and form defects and defect complexes. In that way deep trapping levels are formed in the forbidden zone.

An existence of deep acceptor levels, as is supposed in Refs. [11,28], could be an explanation for part of low-energy transitions observed in our ellipsometric measurements, also.

The photoluminescence (*PL*) spectra of pure InSe and InSe doped with Ni, both recorded at 20 K in the energy range 1.550–2.533 eV, are given In Fig. 9. Doped InSe crystal has a wide *PL* band centred at about 2.11 eV that can be deconvoluted in several subbands. Energy of the observed band corresponds to direct transition from energy level E_1, that is excited by energy of used laser line 488 nm (2.54 eV), to the group of acceptor levels. In the energy range of the broad *PL* band a few narrow bands are visible in both spectra: in pure InSe at 1.636 eV (in doped InSe:Ni at 1.648 eV), 2.019 eV (2.058 eV), 2.270 eV (2.283 eV) and at 2.348 eV (2.360 eV). An average blue-shift of *PL* bands in doped crystal is 19 meV. Deconvolution of *PL* spectra in the range 2.44–2.533 eV, Fig. 9-right, shows that the energy of the first band in valent zone of InSe:Ni, E_1 is 2.5423 eV at 20 K. In pure InSe this energy is E_1 =2.5391 eV at 20 K. Calculated energies of the acceptor levels are in the range of about 260 meV to 890 meV above the valence band.

Sharp peaks at the higher energies are γ-InSe phonons. At 2.48810 eV and 2.49001 eV are the second- and the third-order phonons $2E(LO_{\perp})$ and $2A_1(LO_{\parallel})+Ac$ (426 cm^{-1} and 411 cm^{-1}). At 2.5128 eV is a first order A_1 mode (227 cm^{-1}); at 2.51513 eV is *E* (209.6 cm^{-1}); at 2.51641 eV is $A_1(LO_{\parallel})$ (198 cm^{-1}); at 2.52699 eV is A_1 (112.85 cm^{-1}) [24–27]. A strong $A_1(LO_{\parallel})$ IR mode confirms the rhombohedral structure, *i.e.* γ-modification of InSe. The obtained near-resonant Raman spectra shows that more intensity spectrum of the pure InSe, with more exaggerated polar IR-modes is excited

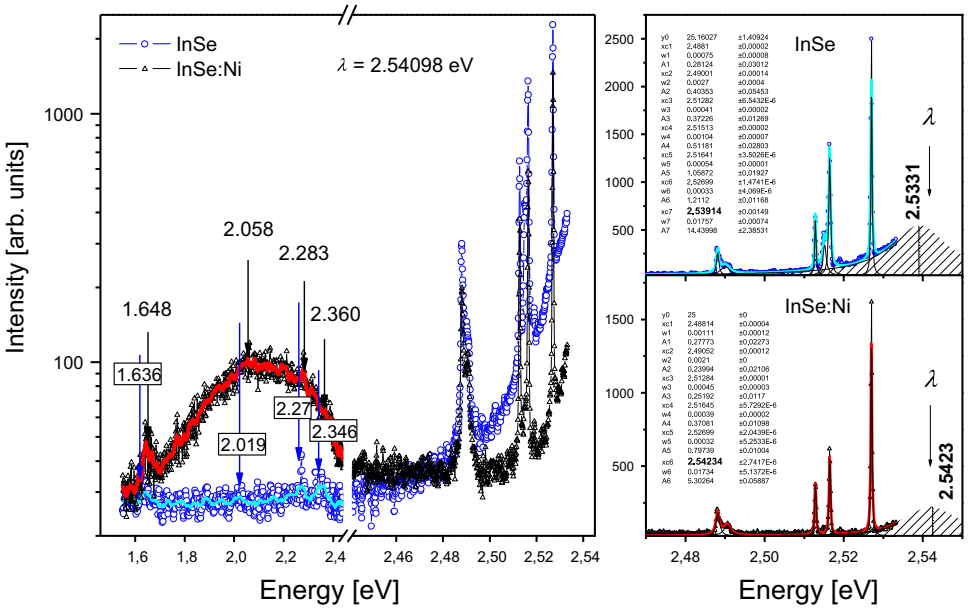

Fig. 9. The photoluminescence spectra of pure InSe crystal and crystal doped with 1% Ni recorded at 20 K. Acceptor levels (left side of the figure) and the first electron energy level E_1 (right) are stressed by arrows.

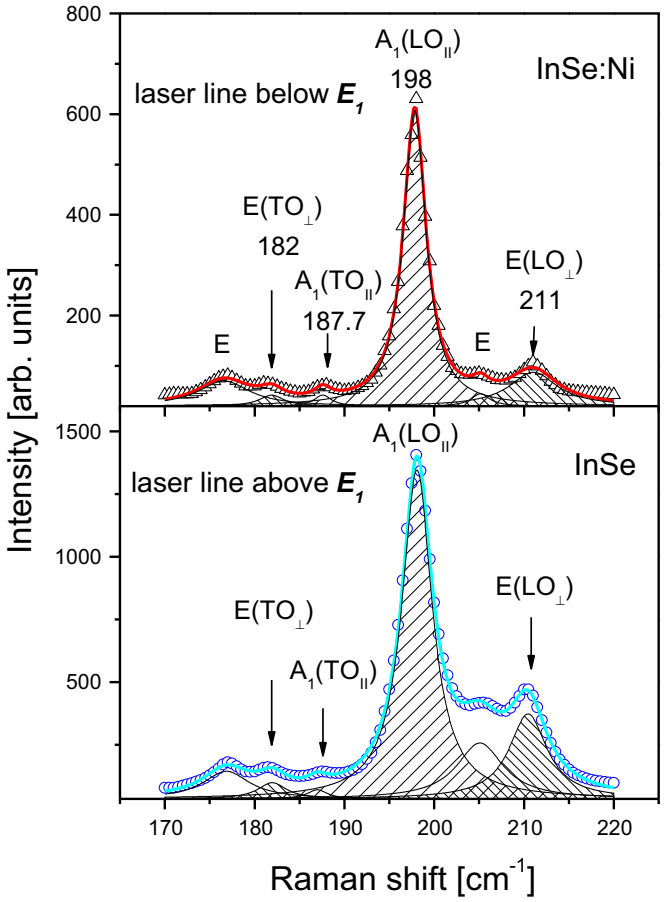

Fig. 10. Part of Raman spectra with first order polar modes, extracted from the photoluminescence spectra, excited by 488 nm laser line at 20 K and recorded in the back scattering geometry $Z(X_Y^X)Z$.

by laser line 2.54098 eV which is above energy transition due to resonant luminescence. In the doped InSe, the used dopants cause a blue-shift of energy levels above the lowest energy gap and the laser line stays below the energy transition which contributes to near-resonant Raman spectra and a little weaker polar modes. A relevant part of Raman spectra excited by 488 nm laser energy at 20 K is presented in Fig. 10.

In the case of the near-resonant Raman spectra excited by laser line 514.5 nm (2.41 eV) at room temperature, energy transition E_1 is higher (2.464 eV for InSe to 2.485 eV for InSe:Co, Table 1) and polar modes are considerably weaker. Anyway, the presence of IR modes in Raman spectra is proof that InSe has a rhombohedral $R3m$ symmetry [25].

PL measurements proved the existence of deep impurity levels and a blue-shift of energy levels in the doped InSe.

5. Conclusion

XRD analysis and Raman spectroscopy confirm that InSe crystals obtained by Bridgman method are of γ-modification, *i.e.* with rhombohedral $R3m$ symmetry.

Energy transitions of pure γ-InSe and γ-InSe doped with 1% M (M=Mn, Fe, Co, Ni) are investigated by ellipsometric measurements in the range of energy gap (<1.4 eV) and in the range of higher energy levels (1.5–6.5 eV). Measured absorption is higher in doped crystals in both energy ranges. It is shown that in energy range <1.4 eV exists a great number of transitions connected with defect and impurity levels. Energies of all transitions in this range are practically the same in pure and doped crystals. Direct energy gap is at $E_g^d=1.3209$ eV, free exciton energy $E_{n=1}^d=1.3036$ eV, indirect gap is at $E_g^i=1.2780$ eV and indirect free exciton energy at $E_{n=1}^i=1.2667$ eV. Obtained binding energies are 17.3 meV for direct free exciton and 11.3 meV for indirect free exciton. In the higher energy range a blue energy shift is observed in doped samples. Exhibited blue-shift is more pronounced in the case of higher energy levels.

PL spectra of γ-InSe and γ-InSe:Ni confirm the existence of deep impurity levels and a blue-shift of E_1 energy.

Acknowledgments

This research was financially supported by the Ministry of Education, Science and Technological Development of the Republic of Serbia through Project no. III 45003.

References

[1] Landolt-Börnstein, Group III Condens. Matter 41C (1998) 1–3.
[2] J. Camassel, P. Merle, H. Mathieu, A. Chevy, Phys. Rev. B 17 (1978) 4718–4725.
[3] C. De Blasi, D. Manno, A. Rizzo, J. Cryst. Growth 100 (1990) 347–353.
[4] A. Chevy, J. Cryst. Growth 51 (1981) 157–163.
[5] P.A. Likforman, D. Carré, J. Etienne, B. Bachet, Acta Crystallogr. B 31 (1975) 1252.
[6] G. Saintonge, J.L. Brebner, Phys. Rev. B 30 (1984) 1957–1961.
[7] A. Cingolani, M. Ferrara, M. Lugarà, F. Lévy, Phys. Rev. B 25 (1982) 1174–1178.
[8] V.M. Katerynchuk, M.Z. Kovalyuk, M.V. Tovarnitskii, Semicond. Phys. Quantum Electron. Optoelectron. 9 (2006) 36–39.
[9] A. Segura, F. Pomer, A. Cantarero, W. Krause, A. Chevy, Phys. Rev. B 29 (1984) 5708–5717.
[10] A. Segura, B. Mari, J. Martinez-Pastor, A. Chevy, Phys. Rev. B 43 (1991) 4953–4965.
[11] S. Shigetomi, H. Ohkubo, T. Ikari, H. Nakashima, J. Appl. Phys. 66 (1989) 3647–3650.
[12] S. Shigetomi, T. Ikari, H. Nakashima, H. Ohkubo, Phys. Status Solidi A 115 (1989) K43–K45.
[13] M. Zolfaghari, K.P. Jain, H.S. Mavi, M. Balkanski, C. Julien, A. Chevy, Mater. Sci. Eng. B – Adv. 38 (1996) 161–170.
[14] B. Gürbulak, M. Yildrim, A. Ateş, S. Dogan, Y.K. Yoğurtçu, Jpn. J. Appl. Phys. 38 (1999) 5133–5136.
[15] A. Ateş, M. Yildrim, B. Gürbulak, Opt. Mater. 28 (2006) 488–493.
[16] B. Gürbulak, Solid State Commun. 109 (1999) 665–669.
[17] E. Kress-Rogers, R.J. Nicholas, J.C. Portal, A. Chevy, Solid State Commun. 44 (1982) 379–383.
[18] P. Gomes da Costa, R.G. Dandrea, R.F. Wallis, M. Balkanski, Phys. Rev. B 48 (1993) 14135–14141.
[19] M.O.D. Camara, A. Mauger, I. Devos, Phys. Rev. B 65 (2002) 125206–125218.
[20] D. Olguín, A. Cantarero, C. Ulrich, K. Syassen, Phys. Status Solidi B 235 (2003) 456–463.
[21] C. Urlich, D. Olguín, A. Cantarero, A.R. Gõni, K. Syassen, A. Chevy, Phys. Status Solidi B 221 (2000) 777–787.
[22] Z.D. Kovalyuk, O.M. Sydor, OA. Sydor, V.G. Tkachenko, I.M. Maksymchuk, V. I. Dubinko, P.M. Ostapchuk, J. Mater. Sci. Eng. A 2 (2012) 537–543.
[23] In-Hwan Choi, J. Korean Phys. Soc. 59 (2011) 80–84.
[24] F.E. Faradev, N.M. Gasanly, B.N. Mavrin, N.N. Melnik, Phys. Status Solidi B 85 (1978) 381–386.
[25] N. Kuroda, Y. Nishina, Solid State Commun. 28 (1978) 439–443.
[26] N. Kuroda, Y. Nishina, H. Iwasaki, Y. Watanabe, Solid State Commun. 38 (1981) 139–142.
[27] J.F. Sánchez-Royo, G. Muñoz-Matutano, M. Brotons-Gisbert, J.P. Martínez-Pastor, A. Segura, A. Cantarero, R. Mata, J. Canet-Ferrer, G. Tobias, E. Canadell, J. Marqués-Hueso, B.D. Gerardot, Nano Res. 7 (2014) 1556–1568.
[28] V.V. Gridin, C. Kasl, J.D. Comins, R. Beserman, J. Appl. Phys. 71 (1992) 6069–6072.
[29] A.A. Homs, B. Mari, J. Appl. Phys. 88 (2000) 4654–4659.
[30] F.J. Manjón, A. Segura, V. Muñoz-Sanjosé, G. Tobías, P. Ordejón, E. Canadell, Phys. Rev. B 70 (2004) 125201–125212.
[31] B. Cordero, V. Gómez, A.E. Platero-Prats, M. Revés, J. Echeverría, E. Cremades, F. Barragán, S. Alvarez, Dalton Trans. 21 (2008) 2832–2838.
[32] B. Abay, H. Efeoğlu, Y.K. Yoğurtçu, Mater. Res. Bull. 33 (1998) 1401–1410.
[33] A. Ateş, M. Kundakci, Y. Akaltun, B. Gurbulak, M. Yildirim, Phys. E 36 (2007) 217–220.
[34] A. Goni, A. Cantarero, U. Schwarz, K. Syassen, A. Chevy, Phys. Rev. B 45 (1992) 4221–4226.
[35] S. Shigetomi, T. Ikari, H. Nakashima, Phys. Status Solidi B 209 (1998) 93–99.

Science of Sintering, **48** (2016) 17-28

doi: 10.2298/SOS1601017S

UDK 621.315.612; 665.7.035.8

Impedance Spectroscopy of Nanocrystalline $MgFe_2O_4$ and $MnFe_2O_4$ Ferrite Ceramics: Effect of Grain Boundaries on the Electrical Properties

Dalibor L. Sekulić[1*)], Zorica Z. Lazarević[2], Čedomir D. Jovalekić[3], Aleksandra N. Milutinović[2], Nebojša Z. Romčević[2]

[1]Faculty of Technical Sciences, University of Novi Sad, Trg Dositeja Obradovića 6, Novi Sad, Serbia

[2]Institute of Physics, University of Belgrade, P.O. Box 68, Pregrevica 118, Zemun, Belgrade, Serbia

[3]The Institute for Multidisciplinary Research, University of Belgrade, Kneza Višeslava 1, Belgrade, Serbia

Abstract:

Two ferrite ceramic materials, $MgFe_2O_4$ and $MnFe_2O_4$, were successfully fabricated by a conventional sintering of nanosized powders (at 1373 K for 2 h) synthesized by soft mechanochemical route. The particle size and morphology of powders were studied using X–ray diffraction (XRD) and transmission electron microscopy (TEM). XRD analysis was carried out for the determination of phase purity, crystal structure and average crystallite size of sintered ferrites. Both mechanosynthesized ferrite samples show mean crystallite sizes in the nm–range. Over the frequency range of 100 Hz to 1 MHz, impedance spectra of prepared ferrite ceramics are investigated at and above room temperature. Changes in the impedance plane plots with temperature have been discussed and correlated to the microstructure of materials. An equivalent circuit model is applied to explore the electrical parameters (resistance and capacitance) associated with grains and grain boundaries. Complex impedance analysis indicates the dominance of grain boundary effects which control the overall electrical behaviour of studied ferrites. The decrease in grain boundary resistance with temperature suggests a thermally activated conduction mechanism.

Keywords: *Ferrite ceramics; Impedance spectroscopy; Electrical properties; Grain boundaries.*

1. Introduction

Spinel ferrites MFe_2O_4, where M^{2+} is a divalent metal cation, are an important class of magnetic materials, which have been intensively investigated over the last few decades due to good combination of electrical and magnetic properties. These materials are technologically interesting because of high electrical resistivities and consequently low eddy current losses, as well as high dielectric constant, high initial permeability and moderate saturation magnetization [1]. Polycrystalline ferrites are widely used in electronic applications in a range of frequencies extending from microwave to radio frequency.

Most of the ferrospinels form cubic spinel–type structure with the distribution of

*) **Corresponding author**: dalsek@uns.ac.rs or dalsek@yahoo.com

cations between two different coordinated interstitial lattice sites, tetrahedral (A) and octahedral [B] sublattices. The divalent metal cation M^{2+} can occupy the either (A) or [B] sites or both sites of the spinel structures. Generally, the structura of spinel ferrites could be described with the $(M_{1-\lambda}Fe_{\lambda})[M_{\lambda}Fe_{2-\lambda}]O_4$ formula, where λ is the so–called inversion degree defined as the fraction of tetrahedral (A) sites occupied by trivalent Fe^{3+} cations and its value depends on the method of preparation [2]. Typically two extreme type of spinel structure can be found, normal and inverse spinel, but in practice a mixed spinel structure are often observed, especially in the case of nanocrystalline ferrites. If metal cation M^{2+} occupies only the (A) sites, the spinel is normal (λ=0); but in the case when it occupies only the [B] sites, the spinel is inverse (λ=1). The mixed spinel structure has the cations distributed in a combined mode, M^{2+} occupying both (A) and [B] sites. In addition, the magnetic, dielectric and electrical properties of spinel ferrites can be varied systematically by changing the identity of the divalent M^{2+} cations (M= Ni, Zn, Mn, Mg, Co etc.) without changing the spinel crystal structure [3].

Among spinel ferrites, the magnesium ($MgFe_2O_4$) and manganese ($MnFe_2O_4$) ferrites are soft magnetic semiconducting materials characterized by low dielectric losses and high resistivity due to their dielectric nature. Previous experimental studies have shown that $MnFe_2O_4$ belongs to the partially inverse spinel, where in the bulk form 20% of the Mn^{2+} cations residing on the octahedral sublattice, while a higher inversion up to 60% were reported in nanostructured manganese ferrite [4]. Also, it has been reported that the spinel structure of $MgFe_2O_4$ bulk material is nearly inverse with 90% of Mg^{2+} cations distributed over [B] sites, and that inversion factor decreases to about 70% for the magnesium ferrite nanoparticles [5]. Electrical as well as magnetic properties of spinel ferrites strongly depend on the cation distribution at the different sites as well as method of preparation, sintering temperature, particle size, doping of additives etc. [6]. Currently, the synthesis of reproducible ferrites is being carried out by various techniques in order to improve their physical properties and widen the scope of their applications. Several methods such as co–precipitation [4, 6, 7], sol–gel [8, 9], combustion [5, 8], ball milling [10, 11] etc. have been used for successful preparation of magnesium and manganese ferrites in recent years.

In the present paper, we have reported the electrical properties of $MgFe_2O_4$ and $MnFe_2O_4$ ferrites prepared by a conventional sintering of nanosized powders synthesized by soft mechanochemical processing that is environmentally friendly, does not require expensive starting materials or extremely high temperature [12]. In order to understand the conduction mechanism, electrical properties associated with grains and grain boundaries in these synthetized nanocrystalline ceramic materials were studied as a function of frequency and temperature using complex impedance spectroscopy technique.

2. Complex impedance formalism

Complex impedance spectroscopy [13] is a non–destructive and widely used testing method for analysing the electrical processes occurring in materials on the application of small AC signal as input perturbation. To understand the overall properties of electroceramics, electrical information associated with its microstructures is very important. Impedance spectroscopy has the capability to resolve the effect of grains and grain boundaries, two main components which comprise the microstructure of ceramics. In this technique, the real and imaginary parts of complex electrical parameters (impedance, modulus or dielectric permittivity) are measured as a function of frequency and temperature. Generally, the complex impedance can be expressed by using the classical Debye expression [14]

$$Z^*(\omega) = \frac{Z_0}{1 + j\omega\tau} = Z'(\omega) - jZ''(\omega), \quad (1)$$

where ω and τ are the angular frequency and the relaxation time, respectively. Here, Z' and Z'' represent the real component of impedance and imaginary component of impedance, respectively.

The charge transport behavior of the electroceramics and its relation to the different microstructures (phases) are studied by means of the impedance spectra. The impedance spectrum, known as Cole–Cole plot, is usually represented as Z'' against Z'. The Cole–Cole plot of polycrystalline material commonly gives two semicircles depending upon the electrical properties of investigated material. The first semicircle at low frequency represents the resistance of grain boundary, while the second one obtained for high frequency domain corresponds to the resistance of grain or bulk properties [15]. It is well–known that the behaviour of characteristic impedance spectra is usually interpreted in terms of equivalent circuit model. From the microstructural point of view, each of ceramic components (i.e. grains and grain boundaries) may be represented by a R–C element (resistor R and capacitor C in parallel combinations), and the simplest appropriate equivalent circuit is a series array of parallel R–C elements [16], see Fig 1a. In accordance with this approach known as brick layer model, total complex impedance is given by

$$Z^*(\omega) = \left(\frac{1}{R_{\mathrm{gb}}} + j\omega C_{\mathrm{gb}}\right)^{-1} + \left(\frac{1}{R_{\mathrm{g}}} + j\omega C_{\mathrm{g}}\right)^{-1}, \quad (2)$$

where R_g and R_{gb} represent the grain and grain boundary resistance, while C_g and C_{gb} are the grain and the grain boundary capacitance, respectively.

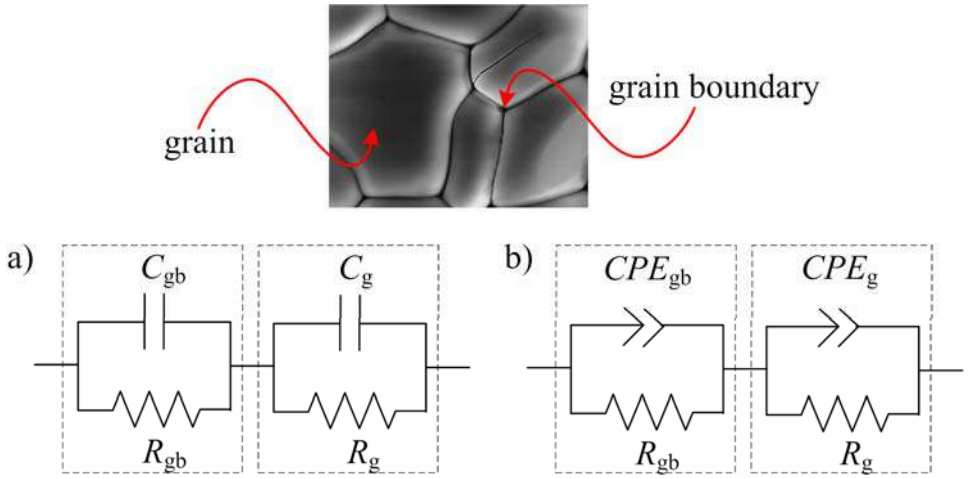

Fig. 1. Equivalent electrical circuits of two–phase electroceramic materials according to *brick layer model*: (a) two parallel R–C elements; (b) two parallel R–CPE elements.

In many electroceramics, the resistance of grain boundaries exceeds that of the grains [17]. This can be ascribed to the fact that the atomic arrangement near the grain boundary region is disordered, resulting in a serious increase in electron scattering. The higher boundary resistance also arises from other factors such as a decrease in Fe^{2+} ion content in this region [18] Also, the capacitance of grain boundary is usually larger than that of the grain, which is explained on basis that the capacitances are inversely proportional to the thickness of the media. In such system, these two components of ceramic microstructure indicate two distinct relaxation phenomena with sufficiently different relaxation times: $\tau_g = R_gC_g$ and $\tau_{gb} = R_{gb}C_{gb}$ [19]. Additionally, the relaxation time of the grain boundaries τ_{gb} is much larger than that of the grains τ_g, since the semicircle representing the grain boundaries lies on the lower frequency side. In general, all these quantities can be treated as fitting parameters whose values can be evaluated from the best fit to the impedance spectrum. The fitting is relatively

unambiguous since the elements of equivalent circuits dominate in different frequency regions.

It is important to note that a proposed circuit, two parallel RC elements connected in series, refers to the ideal Debye–like behaviour in ceramic materials. But in practice, the most electroceramics exhibit non–ideal Debye–like behaviour, so that a constant phase element (CPE) is used in the equivalent circuit to illustrate more fully the deviation from an ideal capacitor [15], as shown Fig 1b. The CPE has impedance defined as [20]

$$Z^*_{\mathrm{CPE}}(\omega) = \left[A(j\omega)^n\right]^{-1}, \tag{3}$$

where parameter A is independent of frequency, and n is the measure of non–ideal behavior having value between 1 and 0 ($0 \le n \le 1$). The CPE describes an ideal capacitor with C = A for n = 1 and an ideal resistor with R = 1/A for n = 0. Based on that, total complex impedance reads as follows [16]

$$Z^*(\omega) = \left(\frac{1}{R_{\mathrm{gb}}} + A_{\mathrm{gb}}(j\omega)^{n_{\mathrm{gb}}}\right)^{-1} + \left(\frac{1}{R_{\mathrm{g}}} + A_{\mathrm{g}}(j\omega)^{n_{\mathrm{g}}}\right)^{-1}. \tag{4}$$

Using the above equation, the equivalent circuit elements can be fitted from the experimental data of impedance spectrum for various materials.

3. Experimental details

3.1. Preparation

The $MgFe_2O_4$ and $MnFe_2O_4$ ferrite nanoparticles were prepared by means of soft mechanochemical route using a mixture of:

- magnesium(II)–hydroxide ($Mg(OH)_2$, Merck 95% purity) and hematite (α–Fe_2O_3, Merck 99% purity), and
- manganese(II)–hydroxide ($Mn(OH)_2$, Merck 95% purity) and hematite (α–Fe_2O_3, Merck 99% purity)

in equimolar ratio, respectively. The starting hydroxides were amorphous, while hematite was crystalline. Mechanochemical synthesis was carried out with planetary ball mill (Fritsch Pulverisette 5) in air atmosphere. Eperimentally determined milling times were 15 h and 25 h for $MgFe_2O_4$ and $MnFe_2O_4$, respectively, depending upon the progress of formation of spinel ferrite phase. Thus obtained nanosize powders were pressed into disk–shaped pallets using a cold isostatic press. The pellets were then sintered at 1373 K for 2 h (Lenton–UK oven) without pre–calcinations step. Heating rate was 10°C/min, with nature cooling in air atmosphere. The thickness and diameter of sintered samples used for further characterizations are 2.0 mm and 10.0 mm, respectively.

3.2. Characterization

The particle size and morphology of soft mechanochemical synthetized powders were investigated using a 200 kV transmission electron microscope (TEM, Model JEOL JEM–2100 UHR). The phase purity and crystal structure of the powder and sintered samples have been characterized using X–ray diffractometer (Model Philips PW 1050) at room temperature. The XRD data was collected using CoKα radiation (λ = 1.78897 Å) at 40 kV and 20 mA (PW 1730 generator) in a wide range of Bragg's angles 2θ ($15° \le 2\theta \le 80°$) with a scanning step size of 0.05° in a 10 s per step of counting time. The lattice parameter and crystallite (grain) size of the sintered ferrites were calculated from XRD data.

In order to study the electrical properties of $MgFe_2O_4$ and $MnFe_2O_4$ ferrite ceramics by means of complex impedance spectroscopy, both the flat and parallel surfaces of the

samples were polished and contacts were made by high quality silver paste on opposite sides of the pallets. The electrical parameters of sintered ferrites, parallel resistance (R_p) and parallel capacitance (C_p), were measured in a wide frequency range (100 Hz – 1 MHz) at different temperatures (298 K – 398 K) using a computer–controlled Impedance Analyzer HP–4194A with a laboratory set of temperature control equipment. The experimentally measured parallel values of the resistance and the capacitance were converted and displayed in the form of complex impedance as follows:

$$Z^*(\omega) = Z'(\omega) - jZ''(\omega) = \left(\frac{1}{R_p} + j\omega C_p\right)^{-1}. \quad (5)$$

The details of this measurement procedure are same as presented in [15]. For fitting and analysis of the impedance data, EIS Spectrum Analyzer software [21] was used with about 2% of fitting errors.

4. Results and discussion

4.1. Structural analysis

XRD patterns of synthesized $MgFe_2O_4$ and $MnFe_2O_4$ ferrite nanopowders are shown in Fig. 2. It is evident that the cubic spinel structure was formed during the soft mechanochemical processing. The appearance of a peak at 2θ = 35.50°, as well as of peaks at 2θ = 18.24°, 30.14° , 43.13°, 53.63°, 57.00° and 62.66°, clearly points to the formation of the new phase of $MgFe_2O_4$ (JCPDS card 88–1943) (Fig. 2 left). The peaks are well indexed to the crystal plane of spinel ferrite (k h l) (311) for the most intense peak at 2θ = 35.50°, and (k h l) (111), (220), (400), (422), (511) and (440) for other peaks, respectively. The peaks at 2θ = 18.28 °, 29.96 °, 35.25 °, 42.92 °, 53.22 °, 56.46 °, 62.13 ° and 73.74 °, clearly confirm the spinel phase $MnFe_2O_4$ (JCPDS card 74–2403) (Fig. 2 right). The peaks are well indexed to the crystal plane of spinel ferrite (k h l) (111), (220), (311), (400), (422), (333), (440) and (533), respectively. The diffraction peaks are fairly broad, which is caused by nanometer size of the crystallites. The average crystallite sizes were calculated from the most intense peak (311) using Scherer's formula [20]. The average particle sizes have been found to be 12 nm and 16 nm for magnesium and manganese ferrites, respectively.

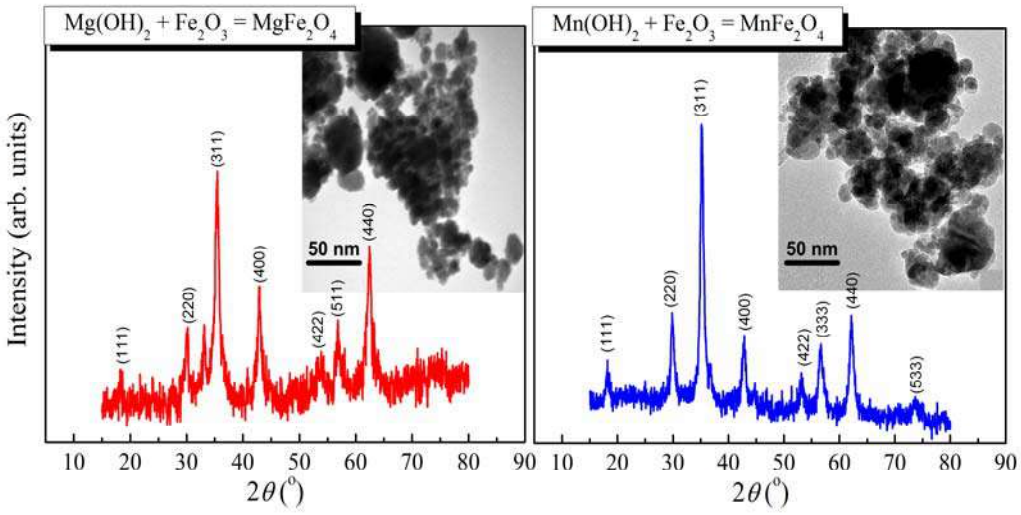

Fig. 2. The experimental XRD patterns of $MgFe_2O_4$ and $MnFe_2O_4$ ferrite nanopowders, recorded at room temperature. Insets show TEM images of ferrite nanoparticles.

The representative TEM images of powders obtained after appropriate milling time are depicted in the inset of Fig. 2. It can be seen that the particles have an almost spherical morphology with size distribution between 5 – 15 nm and 10 – 25 nm for $MgFe_2O_4$ and $MnFe_2O_4$, respectively, which is in close agreement with the crystallite size obtained from XRD data. TEM micrographs confirm nanoscale nature of as–prepared ferrite particles which tend to agglomerate because of the dipolar field of each crystallite.

Fig. 3. shows the room temperature X–ray diffraction spectra of $MgFe_2O_4$ and $MnFe_2O_4$ ferrite ceramics sintered at 1373 K for 2 h. The relative intensities of all diffraction peaks match well with the reported cubic spinel ferrite and sharp XRD peaks indicate the polycrystalline nature of sintered samples.

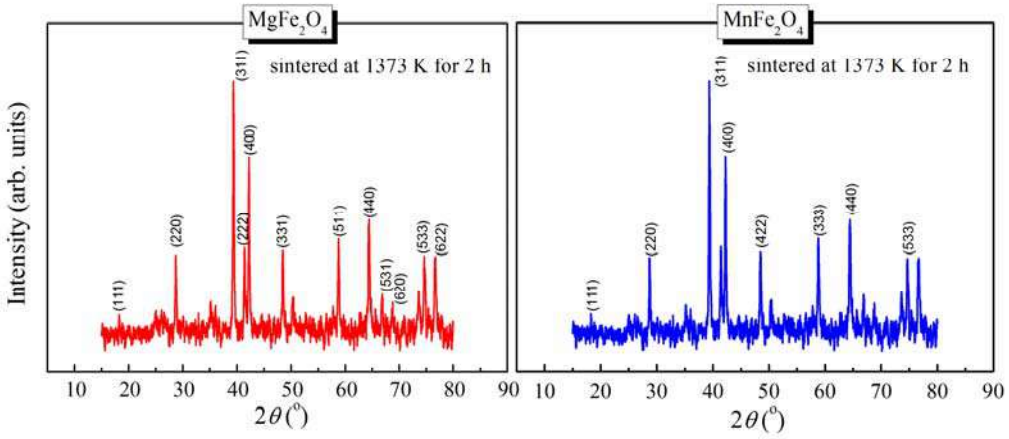

Fig. 3. XRD spectra of nanocrystalline $MgFe_2O_4$ and $MnFe_2O_4$ ceramic ferrites sintered at 1373 K for 2 h.

The values of crystallite size and lattice parameters deduced from experimental X–ray data are summarized in Tab. I. The lattice constants were calculated using data of inter–planar spacing and corresponding Miller indices (hkl) [15]. Also, Tab. I shows the values of the sintered (bulk) density of the samples which were measured by applying Archimedes' principle at room temperature.

Tab. I Some structural parameters of $MgFe_2O_4$ and $MnFe_2O_4$ ferrite samples sintered at 1373 K for 2h.

ferrite sample	lattice constant (Å)	crystallite size (nm)	sintered density (g/cm^3)
$MgFe_2O_4$	8.371	41	4.53
$MnFe_2O_4$	8.421	49	4.21

4.2. Complex impedance analysis

The frequency dependence of imaginary part of impedance Z", usually called as loss spectrum, at selected temperatures is shown in Fig. 4. In the case of both samples can be seen that the – Z" value increases initially, reaches the maximum value ($Z"_{max}$) at particular frequency and then it decreases continuously with increasing frequency for given temperatures. The appearance of only one peak in loss spectra at characteristic frequency ($\omega_{max} = 2\pi f_{max}$) suggests an existence of single relaxation process in $MgFe_2O_4$ and $MnFe_2O_4$ ferrites under study. Observed relaxation peaks are due to the existence of the space charge relaxation that dominates when the material is composed of grain and grain boundaries [22]. In both samples, these peaks shift towards the higher frequency side possibly due to an

increase in the rate of hopping of charge carriers with the rise of temperature. The shifting of peaks in Z'' also indicates to the decreasing relaxation time of mobile charge carriers with the increase of temperature [16]. A lower relaxation time implies faster movement of mobile carriers and vice versa. Also, it is evident that the magnitude of Z'' maxima decreases with increase in temperature, indicating increasing loss in the resistive property of prepared samples [23].

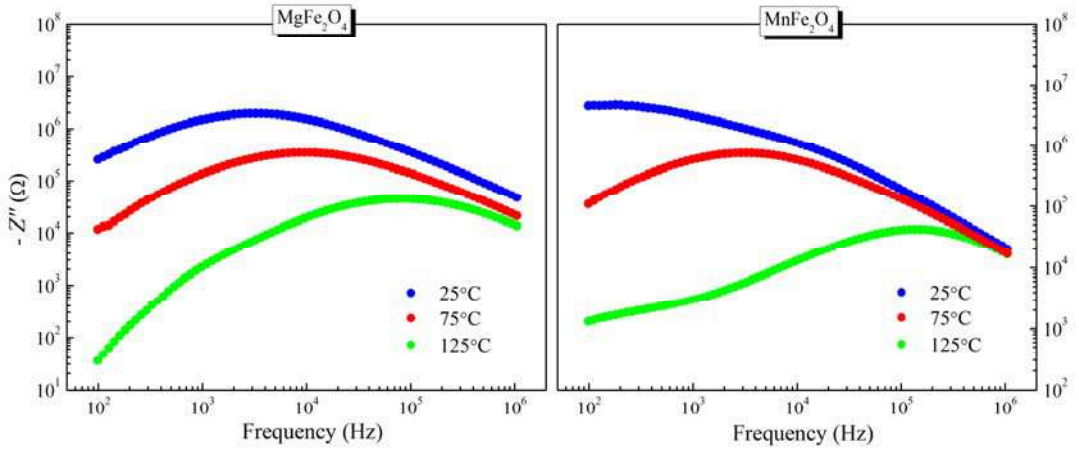

Fig. 4. Variation of imaginary parts of impedance with frequency for $MgFe_2O_4$ and $MnFe_2O_4$ ferrites at and above room temperature.

Generally, the impedance loss spectra were used to evaluate the relaxation time τ of the electrical phenomena occurring in ferrites using the following relation [24]

$$\tau = \omega_{\max}^{-1} = \frac{1}{2\pi f_{\max}}, \quad (6)$$

where f_{max} is characteristic frequency maximum known as relaxation frequency which depends on temperature. Variation of corresponding values τ with inverse of absolute temperature is given in Fig 5. A decrease in relaxation time with temperature can be noted for both ferrites. Also, these graphics follow the Arrhenius dependence [4]

$$\tau = \tau_0 \exp(\frac{\Delta E}{k_B T}), \quad (7)$$

where τ_0 is the pre–exponential factor, ΔE represents the activation energy and k_B is Boltzmann's constant. From the Arrhenius plots, the activation energies are found to be 0.361 eV and 0.406 eV for $MgFe_2O_4$ and $MnFe_2O_4$ samples, respectively. Since $\tau = (2P)^{-1}$, where P is the hopping probability, the decrease in relaxation time with temperature results in an increase in hopping probability of charge carriers with temperature [4]. The pre–exponential factor τ_0 has been calculated from the results of fitting and its values are 6.35×10^{-11} s and 1.49×10^{-13} s for $MgFe_2O_4$ and $MnFe_2O_4$, respectively.

In order to correlate the electrical properties of synthetized ferrites with their microstructures, the impedance spectra were studied in the wide frequency range from 100 Hz to 1 MHz at several temperatures (298 K – 398 K). Fig. 6 shows the measured complex impedance plane plots for $MgFe_2O_4$ and $MnFe_2O_4$ at selected temperatures. It is evident that Cole–Cole plots clearly show evidence of the existence of only one semicircle, which indicates that the contribution to electrical conductivity arises mainly from the grain boundary and that contribution from the grain is not resolved for both samples within the measuring range up to 1MHz. In the cases of nanocrystalline ferrites, the similar behaviour of impedance spectra with single semicircle was observed by other authors [25, 26]. These results suggest

that the grain boundary volume in nanostructured ferrited is high because of the small grain sizes and hence conduction takes place predominantly through the grain boundary [27]. In addition, it is obvious that obtained impedance spectra of $MgFe_2O_4$ and $MnFe_2O_4$ are temperature dependent, since the diameters of semicircles exhibit decreasing trends with increasing temperature. This indicates decrease in relaxation time and increase in conductivity with rise in temperature.

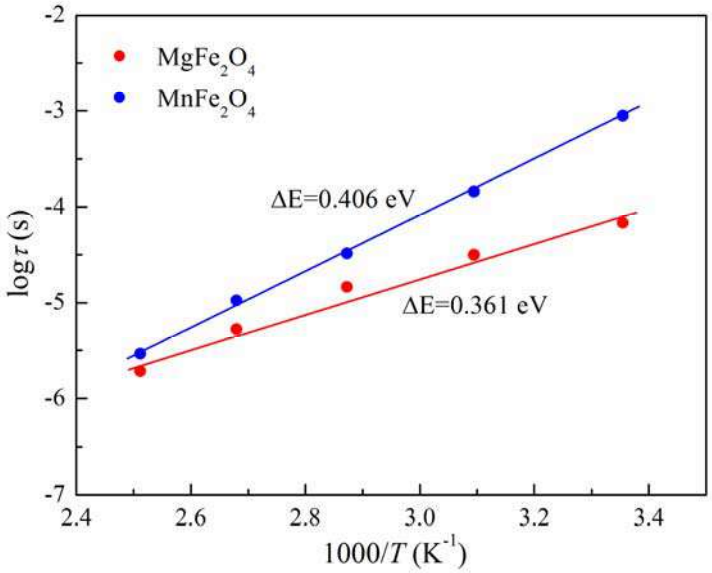

Fig. 5. Variation of relaxation times with inverse of temperature.

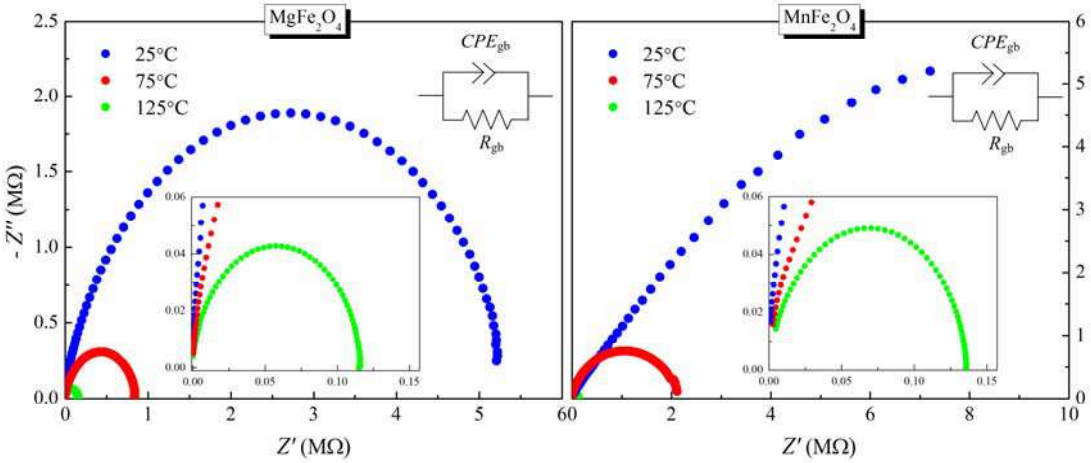

Fig. 6. Impedance spectra of $MgFe_2O_4$ and $MnFe_2O_4$ ferrites at and above room temperature.

It is usual to the impedance response is interpreted in terms of equivalent circuit model. The shape of the impedance plane plots for ferrites under study suggests that the impedance data can be approximately modelled by an equivalent circuit based on only one parallel R–CPE element shown in the inset of the Fig. 6. Here, R_{gb} and CPE_{gb} are the resistances and the constant phase elements for grain boundaries, respectively. The parameters R_{gb}, C_{gb} and n_{gb} have been derived by fitting the impedance spectra (within 0.5 – 2% fitting errors).

The variation of the fitted parameters is depicted as a function of temperature in Fig. 7. Evaluated R_{gb} for $MgFe_2O_4$ and $MnFe_2O_4$ show a strong similarity in their temperature dependence and their values decrease as the temperature increased. This kind of behaviour

suggests that the both ferrites possess a negative temperature coefficient of resistance (NTCR) [16], implying a thermal activated conductivity of these materials. Also, this substantial drop in the R_{gb} provides a clear and unambiguous evidence of grain boundary conduction resulting from reduction in the barrier facilitating thereby mobility of charge carriers with rise in temperature [24]. Further, Fig. 7 right implies the slight variations in parameters C_{gb} and n_{gb} with temperature. The n_{gb} has a slow decreasing trend in the measured temperature range and its values are between 0.835 and 0.817 for $MgFe_2O_4$, i.e. between 0.775 and 0.735 for $MnFe_2O_4$. This tend signifies that the grain boundary capacitance deviates from ideal behaviour as the temperature is increased. The observed decrease in the capacitance of the grain boundaries with increasing temperature may be due to the delocalization of the charge carriers from traps followed by the accumulation of these charges at the grain boundaries, thereby increasing its capacitance as well as space charge polarization effects [28]. Similar results for this behaviour of the grain boundaries capacitance were found by others authors [2, 28].

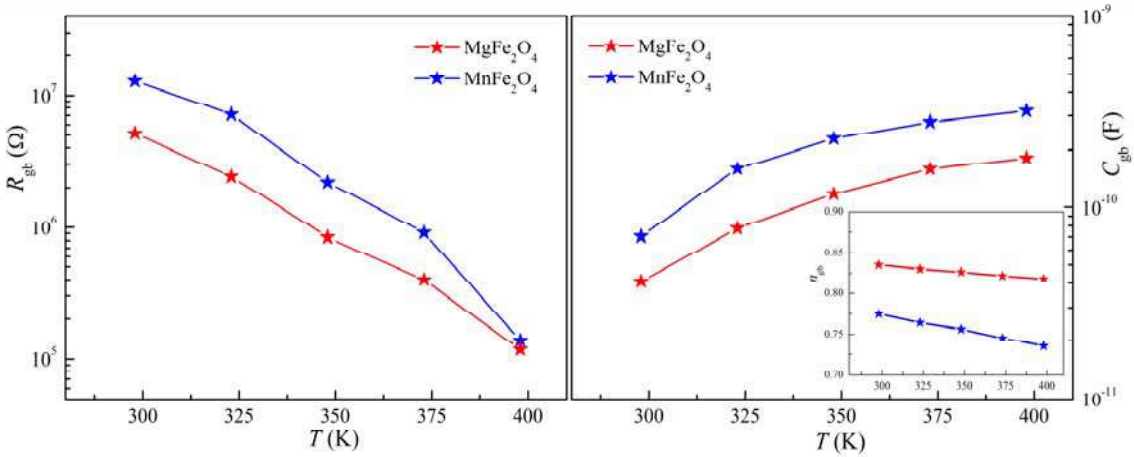

Fig. 7. Variation of grain boundary resistance R_{gb} with temperature (left), and variation of grain boundary capacitance C_{gb} and deviation parameter n_{gb} with temperature (right) for nanocrystalline $MgFe_2O_4$ and $MnFe_2O_4$ ferrites.

In the present study, the DC conductivity for grain boundary contribution is calculated using the expression [24]

$$\sigma_{DC} = \frac{d}{R_{gb}A}, \tag{8}$$

where R_{gb} is the resistance values of the grain boundary which is evaluated from impedance spectra of nanocrystalline ferrites under study. Parameters d and A represent the thickness of sample and area of the electrode deposited on the sample, respectively. Fig. 8 shows the temperature dependence of σ_{DC}. It can be clearly noticed that the nature of the variation is linear and well obeys the Arrhenius relation that is defined by equation [20]:

$$\sigma_{DC} = \sigma_0 \exp(-\frac{E_a}{k_B T}), \tag{9}$$

where σ_0, E_a and k_B are the pre–exponential factor, the activation energy of the carriers for conduction and Boltzmann's constant, respectively. In the cases of both ferrites, the DC conductivity increases with rise in temperature showing a typical semiconductor behaviour with negative temperature coefficient of resistance (NTCR) characteristics [29]. Using this Arrhenius plot of grain boundary conductivity, the corresponding activation energies for the thermally activated charge carriers in $MgFe_2O_4$ and $MnFe_2O_4$ were determined from the slope

of the $\log\sigma_{DC}$ versus 1000/T curves and were found to be 379 meV and 392 meV, respectively.

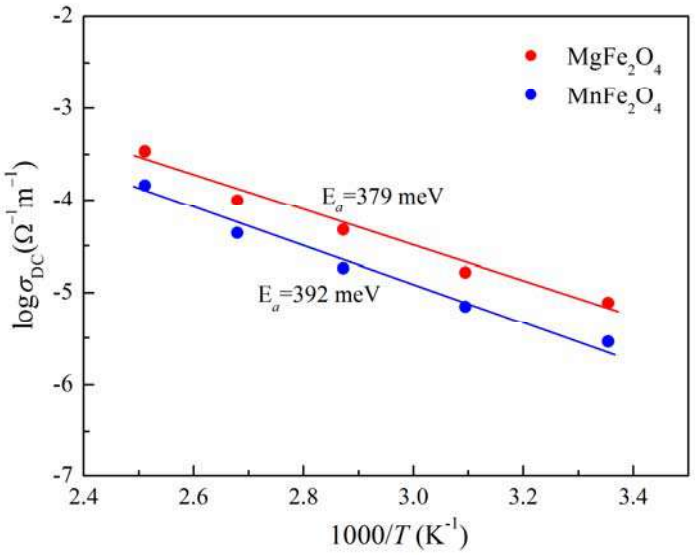

Fig. 8. Variation of DC conductivity of grain boundary with inverse of temperature.

Comparison of evaluated DC conductivity for grain boundary contribution and activation energy shows a good agreement in the sense that the sample with lower conductivity has higher value of activation energy and vice versa. The grain boundary conductivity in sintered nanocrystalline $MgFe_2O_4$ and $MnFe_2O_4$ was found to be 7.83×10^{-6} $\Omega^{-1}m^{-1}$ and 2.82×10^{-6} $\Omega^{-1}m^{-1}$ at room temperature, respectively.

5. Conclusions

In summary, nanocrystalline $MgFe_2O_4$ and $MnFe_2O_4$ spinel ferrites have been synthesis using a soft mechanochemical route and then the powders were sintered at 1373 K for 2 h. The X–ray diffraction analysis confirmed the cubic spinel structure of sintered samples and the average crystallite sizes in the nm–range were determined on the basis of XRD data. Complex impedance spectroscopy was used to characterize the electrical properties of these materials. In the studied frequency range, the impedance spectra of sintered ferrites show the presence of only one semicircle at and above room temperatures. The analysis of impedance data using an equivalent circuit indicates that the electrical properties of the synthetized ferrites are mainly attributed to the processes that are associated with the grain boundaries. The decrease in value of grain boundaries' resistance on increasing temperature suggests the negative temperature coefficient of resistance behavior usually shown by semiconducting materials. In the case of both ferrites, the imaginary part of impedance clearly confirms only one relaxation processes due to grain boundaries. It was found that the relaxation time decreases with temperature and follows Arrhenius dependence.

Acknowledgments

This research was financially supported by the Ministry of Education, Science and Technological Development of the Republic of Serbia through Projects No. III43008 and III45003.

6. References

1. A. Goldman, Modern Ferrite Technology (Springer, New York, 2006).
2. M. Younas, M. Nadeem, M. Atif, R. Grossinger, J. Appl. Phys.109 (2011) 093704.
3. E. Sentürk, Y. Köseoglu, T. Sasmaz, F. Alan, M. Tan, J. Alloy. Compd. 578 (2013) 90–95.
4. E. V. Gopalan, K. A. Malini, S. Saravanan, D. S. Kumar, Y. Yoshida, M. R. Anantharaman, J. Phys. D: Appl. Phys. 41 (2008) 185005.
5. A. Franco M. S. Silva, J. Appl. Phys. 109 (2011) 07B505.
6. S. F. Mansour, J. Magn. Magn. Mater. 323 (2011) 1735–1740.
7. M. J. Akhtar, M. Younas, Solid Stat. Sci. 14 (2012) 1536–1542.
8. M. A. Ahmed, N. Okasha, S. I. El–Dek, Nanotechnology 19 (2008) 065603.
9. C. P. Liu, M. W. Li, Z. Cui, J. R. Huang, Y. L. Tian, T Lin, W. B. Mi, J. Mater. Sci. 42 (2007) 6133–6138.
10. S. K. Pradhan, S. Bid, M. Gateshkia, V. Petkov, Mater. Chem. Phys. 93 (2005) 224–230.
11. M. H. Mahmoud, H. H. Hamdeh, J. C. Ho, M. J. O'Shea, J. C. Walker, J. Magn. Magn. Mater. 220 (2000) 139–146.
12. D. L. Sekulić, Z. Ž. Lazarević, Č. Jovalekić, A. Rečnik, M. Romčević, B. Hadžić, N. Ž. Romčević, Sci. Sinter. 46 (2014) 235–245.
13. E. Barsoukov, J. R. Macdonald, Impedance Spectroscopy – Theory, Experiment and Applications (John Wiley & Sons, New Jersey, 2005).
14. J. S. Kim, B. C. Choi, J. H. Jeong, J. Korean Phys. Soc. 55 (2009) 879–883.
15. Z. Ž. Lazarević, Č. Jovalekić, D. L. Sekulić, A. Milutinović, S. Baloš, M. Slankamenac, N. Ž. Romčević, Mater. Res. Bull. 48 (2013) 4368–4378.
16. R. Martínez, A. Kumar, R. Palai, J. F. Scott, R. S. Katiyar, J. Phys. D: Appl. Phys. 44 (2011) 105302.
17. E. J. Abram, D. C. Sinclair, A. R. West, J. Electroceram. 10 (2003) 165–177.
18. D. Arcos, M. Vazquez, R. Valenzuela, M. Vallet–Regi, J. Mater. Res. 14 (1999) 861–865.
19. Z. V. Mocanu, M. Airimioaei, C. E. Ciomaga, L. Curecheriu, F. Tudorache, S. Tascu, A. R. Iordan, N. M. Palamaru, L. Mitoseriu, J. Mater. Sci. 49 (2014) 3276–3286.
20. Z. Ž. Lazarević, Č. Jovalekić, D. Sekulić, M. Slankamenac, M. Romčević, A. Milutinović, N. Ž. Romčević, Sci. Sinter. 44 (2012) 331–339.
21. A. S Bondarenko, G. A. Ragoisha, EIS Spectrum Analyser (a freeware program for analysis and simulation of impedance spectra), http://www.abc.chemistry.bsu.by/vi/analyser/.
22. M. Azizar Rahman, A. K. M. Akther Hossain, Phys. Scr. 89 (2014) 025803.
23. S. Dutta, R. N. P. Choudhary, P. K. Sinha, A. K. Thakur, J. Appl. Phys. 96 (2004) 1607– 1613.
24. P. Dhak, D. Dhak, M. Das, P. Pramanik, J. Mater. Sci.: Mater. Electron. 22 (2011) 1750–1760.
25. G. Kumar, S. Sharma, R. K. Kotnala, J. Shah , S. E. Shirsath, K. M. Batoo, M. Singh, J. Mol. Struct. 1051 (2013) 336–344.
26. K. M. Batoo, S. Kumar, C. G. Lee, Alimuddin, Curr. Appl. Phys. 9 (2009) 1072–1078.
27. K. M. Batoo, S. Kumar, C. G. Lee, Alimuddin, Curr. Appl. Phys. 9 (2009) 826–832.
28. M. J. Akhtar, M. Younas, Solid State Sci. 14 (2012) 1536–1542.
29. A. Mohapatra, P. R. Das, R. N. P. Choudhary, J. Mater. Sci.: Mater. Electron. 25 (2014) 1348–1353.

Садржај: *Два феритна керамичка материјала, $MgFe_2O_4$ и $MnFe_2O_4$, успешно су фабрикована помоћу конвенционалног синтеровања нанопрахова (на 1373 K за 2 сата) синтетисаних soft механохемијским путем. Величина честице и морфологија прахова је испитана коришћењем рендгенске дифракције (XRD) и трансмисионог електронског микроскопа (TEM). XRD анализа је употребљена за одређивање чистоће фазе, кристалне структуре и просечне величине кристала синтерованих ферита. Оба механо–хемијском реакцијом синтетисана феритна узорка поседују средњу величину кристала у nm–опсегу. У широком опсегу фреквенција од 100 Hz до 1 M Hz, импедансни спектри феритних керамика су испитани на и изнад собне температуре. Промене на импедансним дијаграмима са порастом температуре су дискутоване и доведене у корелацију са микроструктуром материјала. Примењен је модел еквивалентног електричног коло ради одређивања електричних параметара (отпорност и капацитивност) везаних за зрна и границе зрна. Анализа комплексне импедансе указала је на доминацију ефекта граница зрна који контролише електричне особине испитиваних ферита. Смањење отпорности границе зрна са температуром указује на механизам провођења активиран температуром.*

Кључне речи: *феритна керамика; импедансна спектроскопија; електрична својства; границе зрна*

Science of Sintering, **48** (2016) 333-341

doi: 10.2298/SOS1603333E

UDK 535.375; 543.4

The Bridgman Method Growth and Spectroscopic Characterization of Calcium Fluoride Single Crystals

Hana Ibrahim Elswie[1, 2], Zorica Ž. Lazarević[3*)], Vesna Radojević[1], Martina Gilić[3], Maja Rabasović[3], Dragutin Šević[3], Nebojša Ž. Romčević[3]

[1]Faculty of Technology and Metallurgy, University of Belgrade, Belgrade, Serbia
[2]Faculty of Science, Department of Science, Tripoli University, Tripoli, Libya
[3]Institute of Physics, University of Belgrade, Pregrevica 118, Zemun, Belgrade, Serbia

Abstract:

It must be noted that the main objective of this study was to obtain single crystals of calcium fluoride - CaF_2, and after that the crystals were characterized with various spectroscopic methods. The crystals were grown using the Bridgman technique. By optimizing growth conditions, <111> oriented CaF_2 crystals up to 20 mm in diameter were grown. Number of dislocations in CaF_2 crystals was 5×10^4 - 2×10^5 per cm^2. Selected CaF_2 single crystal is cut into several tiles with the diamond saw. The plates were polished, first with the silicon carbide, then the paraffin oil, and finally with a diamond paste. The obtained crystal was studied by Raman and infrared -IR spectroscopy. The crystal structure is confirmed by X-ray diffraction (XRD). One Raman and two IR optical modes predicted by group theory are observed. A low photoluminescence testifies that the concentration of oxygen defects within the host CaF_2 is small. All performed investigations show that the obtained CaF_2 single crystal has good optical quality, which was the goal of this work.

Keywords: *CaF_2, Raman spectroscopy, IR spectroscopy, Photoluminescence.*

1. Introduction

Single crystals, especially calcium fluoride (CaF_2) single crystals, are required as starting materials for optical components in DUV-photolithography, such as steppers or excimer lasers. They are conventionally used as lenses or prisms [1, 2]. They are especially used to optically copy fine structures into integrated circuits, computer chips and/or photo-lacquer-coated wafers [3, 4]. Crystals, in principle, can be grown from the gas phase, the melt, from solution and even from a solid phase by recrystallization or solid body diffusion [5]. Different processes for crystal growth are described in text books for crystal growth, such as the 1088 page work of Wilke and Bohm [6].

For excellent optical quality, intense studies have been undertaken on each stage of producing CaF_2 crystal, from raw materials purification [7, 8], growth parameters optimization [9], growth technique innovation [10-12], annealing [13] and surface machining improvement [14]. Among these stages, crystal growth technique is the most radical and crucial. The main techniques for CaF_2 single crystal growth are the Czochralski [15], Bridgman-Stockbarger [11], and gradient solidification methods [10], which all possess

*) **Corresponding author:** lzorica@yahoo.com

respective advantages and drawbacks. It seems significant to find a more effective method for high-quality and large-dimension CaF_2 crystals. However single crystals for industrial applications are usually grown by solidification from a melt [16]. The so-called Stockbarger-Bridgeman and the vertical gradient freeze processes are used for industrial manufacture of single crystals [17]. The crystals are grown in a drawing oven and in a vacuum of 10^{-4} to 10^{-5} mbar in the Stockbarger-Bridgeman method. A crystalline raw material is melted, so that a homogeneous single crystal is obtained with exacting control of temperature. CaF_2 single crystals of more than 10 inches in diameter are required for the lens materials. Such large CaF_2 single crystals are grown by the Czochralski method [18, 19] or the vertical Bridgman method [20, 21].

CaF_2 is an ionic crystal with the fluorite structure [22]. Unit cell of CaF_2 is presented in Fig. 1. The crystal lattice is a face centered cubic (fcc) structure with three sublattices. The fluorite structure, seen in calcium fluoride, has the calcium ions in a face centered cubic array with the fluoride ions in all (8) of the tetrahedral holes. The fluoride ions have a coordination number 4, and the calcium ions have a coordination number 8. The natural cleavage plane of the crystal is the <111> surface. In Fig. 1, the four possible <111> planes are defined by F^--ion Ca^{2+}-ion a respective triple of the four Ca^{2+} ions [23]. The melting point of CaF_2 is at 1347 °C. At a temperature of 1147 °C, a maximum of the specific heat is observed that is caused by melting of the fluorine sublattice. The fluorine ions are randomly distributed over the normal lattice sites (tetrahedral coordinated) and the interstitial sites (octahedral coordinated). The ionic mobility consequently becomes very high. The behavior is known as superionic conduction, it is observed in a variety of materials with the fluorite structure [24].

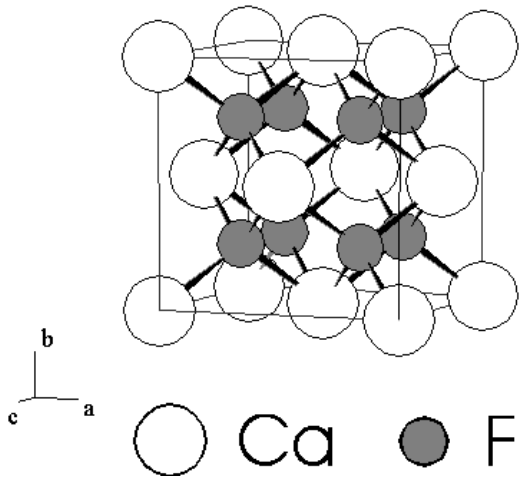

Fig. 1. Unit cell representation of CaF_2 structure.

Single crystal CaF_2 used in the optical devices can be of natural origin - fluorite, under which name is often referred to in literature [25], and synthetic single crystal CaF_2 which is usually obtained by the growth from the melt. CaF_2 requires the use of special growth conditions to obtain quality crystals because of its specific chemical and physical properties: relatively high melting point (over 1300 °C), high chemical aggressiveness of fluorine at these temperatures, relatively small chemical stability at high temperatures and very strong ability to react with traces of water vapor. Therefore, the growth of a single crystal CaF_2 may take place either in vacuum or in an inert gas atmosphere (argon or helium) at purity of at least 99.99% in order to prevent the presence of traces of moisture or oxygen.

It may be noted that the Bridgman method is one of the most popular methods of crystal growth because it is very easy to perform in a vacuum and in an inert atmosphere [26, 27]. The method consists in the fact that the rate of the entire batch of CaF_2 in the crucible, which is of cylindrical shape with a conical bottom, and then is lowered into the crucible

colder part of the furnace, so that the crystallization process begins at the bottom of the crucible at the top of the cone. Reviewing the literature it can be noted that the crucible can be made from spectroscopically pure graphite [20, 21, 25, 28, 29] or platinum [30].

The aim of our work was to produce CaF_2 single crystal of good optical quality. The structural and optical properties obtained crystals were characterized using Raman, IR and luminescence spectroscopy.

2. Experimental procedure

The BCG365 device was used to obtain single crystals of CaF_2 by Bridgman method. Initial samples of single crystals were mostly transparent, but some were cracked. Therefore, we had to make some changes in conditions of growth and construction of crucible. Experiments have been performed with CaF_2 in the form of a powder. The CaF_2 powder was compacted and sintered in the form of tablets. Crucible could easily be filled with such obtained tablets. Powder CaF_2 (Rare Earth Products Limited) purity of 99.99% was used in the experiment. It was compacted under a pressure of 3500 kg cm^{-2}, and the sintering of the obtained tablets was carried out at 900 °C under an inert atmosphere of argon. We tried out combinations of various growth rates and generator powers with the aim to define the optimal growth conditions. Power generator was initially P_{gen} = 3.8 kW, and was later increased to P_{gen} = 3.94 kW. The crystal growth rates were 6 mm h^{-1}, 12 mm h^{-1}, 24 mm h^{-1}, and 48 mm h^{-1}.

The observations relating to the dislocation were recorded by observing an etched surface of CaF_2 crystal, using a Metaval of Carl Zeiss Java metallographic microscope with magnification of 270x. A selected CaF_2 single crystal was cut into several tiles with the diamond saw. The plates were polished, first with the silicon carbide, then the paraffin oil, and finally with a diamond paste. The obtained finely polished sample, which were later used for the characterization of Raman, IR and luminescence spectroscopy. The crystal plane of cleavage of calcium fluoride crystal is <111>. Thin panels for testing dislocations we obtained by splitting of individual pieces of crystal. Conc. H_2SO_4 is used as an etching solution, gave a sample that was etched for 15 min.

The Raman scattering measurements of CaF_2 crystal was performed in the backscattering geometry at room temperature in the air using a Jobin-Yvon T64000 triple spectrometer, equipped with a confocal microscope (100x) and a nitrogen-cooled charge coupled device detector (CCD). The spectra have been excited by a 514.5 nm line of Coherent Innova 99 Ar^+ - ion laser with an output power of less than 20 mW to avoid local heating due to laser irradiation. Spectra were recorded in the range from 100 to 800 cm^{-1}.

The room temperature far- infrared reflectivity measurements was carried out with a BOMEM DA-8 FIR spectrometer. A DTGS pyroelectric detector was used to cover the wave number range from 50 to 600 cm^{-1}.

Photoluminescence (PL) studies reported in this work were performed at room temperature using Optical Parametric Oscillator (Vibrant OPO) tuned at 350 nm as excitation source. Time resolved streak images of the emission spectrum excited by OPO system are collected by using a spectrograph (SpectraPro 2300i) and recorded with a Hamamatsu streak camera (model C4334). All streak camera operations are controlled by the HPD-TA (High Performance Digital Temporal Analyzer) software.

3. Results and discussions

CaF_2 single crystals are obtained by the vertical Bridgman method in vacuum. The best results were obtained with a crystal growth rate of 6.8 mm h^{-1}. The obtained single crystal of CaF_2 was 90 mm in length and 20 mm in diameter (Fig. 2).

Fig. 2. Photographs of Bridgman-grown CaF_2 single crystal.

The general conclusion is that in all samples relatively high dislocation density was observed (ranging from 60000 to 140000) as a consequence of greater internal stresses, which have emerged in the process of cooling. From the Fig. 3, the dislocations of CaF_2 can be observed. Etch pits have the shape of a three-sided pyramid. Number of dislocations in CaF_2 crystals which were made by the method of Bridgman was $5x10^4$ - $2x10^5$ per cm^2.

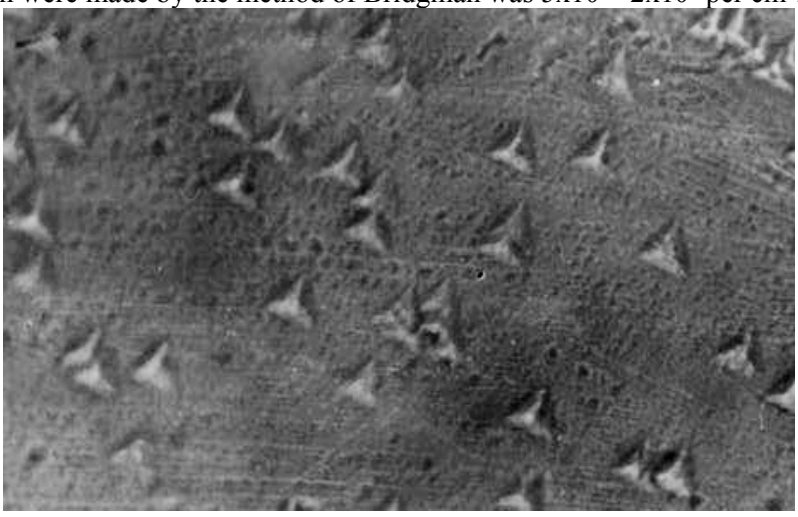

Fig. 3. The microscopic image of the surface CaF_2 crystal plate in the direction <111>. Magnification of 270x.

In order to eliminate stresses in the crystal, we did a crystal annealing. The process of annealing was carried out on the plate and bulk crystal CaF_2 in the inert atmosphere of argon. The temperature of annealing of the plate was 1000 °C for 3 h, and the temperature of annealing of the bulk crystal was 1000 °C and 1080 °C for 1 - 3 h. It was noticed that after annealing, plate CaF_2 had very little stress. Annealed bulk single crystal CaF_2 had less stress than non- annealed. Upon the completion of annealing it has been observed that the crystal on the surface has a thin milky-white layer, so it is assumed that oxygen is diffused very shallow in the crystal forming CaO.

As for group theory analysis, three atoms in cubic O^5_h (Fm3m) primitive cell of the CaF_2 crystal give nine fundamental vibrations, described by the following O_h-irreducible representations (at k = 0): $\Gamma = 2T_{1u}$ (IR) + T_{2g} (Raman). According to several comprehensive work (e.g. [31-36]), their distribution among optical and acoustical are: the triply degenerate T_{2g} optical phonon is Raman active and IR inactive; one of the T_{1u} representations (triply

degenerate as well) corresponds to the zero frequency acoustic mode, while the other T_{1u} mode is actually split into a double degenerate transverse optical mode and a nondegenerate longitudinal optical mode, all the above are IR active. The room-temperature first order T_{2g} one-band Raman scattering spectrum of CaF_2 crystal is shown in Fig. 4. In this single allowed Raman optical mode with frequency ω_{SRS} = 319.7 cm^{-1} Ca^{2+} cation remains stationary and the neighboring substitutional fluoride F^{-1} ions vibrate against each other [36-39].

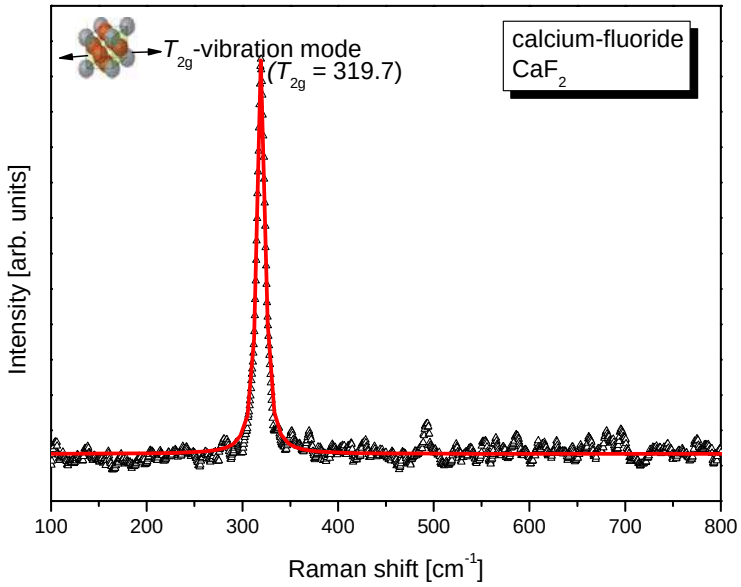

Fig. 4. Raman spectrum of CaF_2 single crystals, recorded at room temperature.

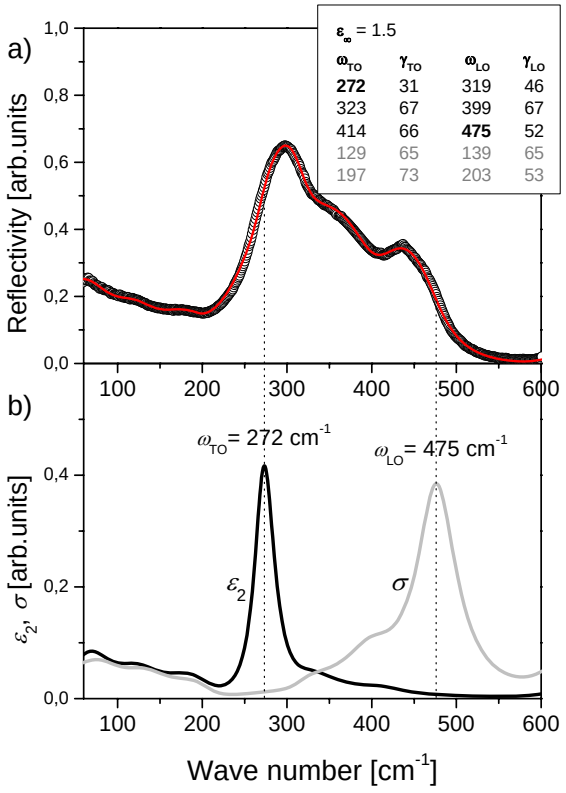

Fig. 5. IR spectrum of CaF_2 single crystals, recorded at room temperature.

The far-infrared reflectivity spectrum of the CaF_2 substrate is shown in Fig. 5. As a result of the best fit we obtained the ω_{TO} = 272 cm^{-1} and ω_{LO} = 475 cm^{-1}, little higher than in Ref. [40] (TO/LO = 257/463). In pure CaF_2, only two infrared active modes are allowed by the crystal symmetry (split TO-LO mode), but we see that the main reflectivity band of CaF_2 exhibits a feature centered about 360 cm^{-1} as a result of a two-phonon combination. This feature has been observed in all stoichiometric fluorite-structured crystals [41]. There are two additional weak modes with relatively high dampings in the range of low energies. We suppose that mode about 130 cm^{-1} could be caused by crystal impurities and about 200 cm^{-1} is a TO-mode from the X point <100>. Kramers-Kröning analysis of far-IR reflectance data gives ω_{TO} = 272 cm^{-1} and ω_{LO} = 475 cm^{-1}, in the accordance with fitting procedure (Fig. 5).

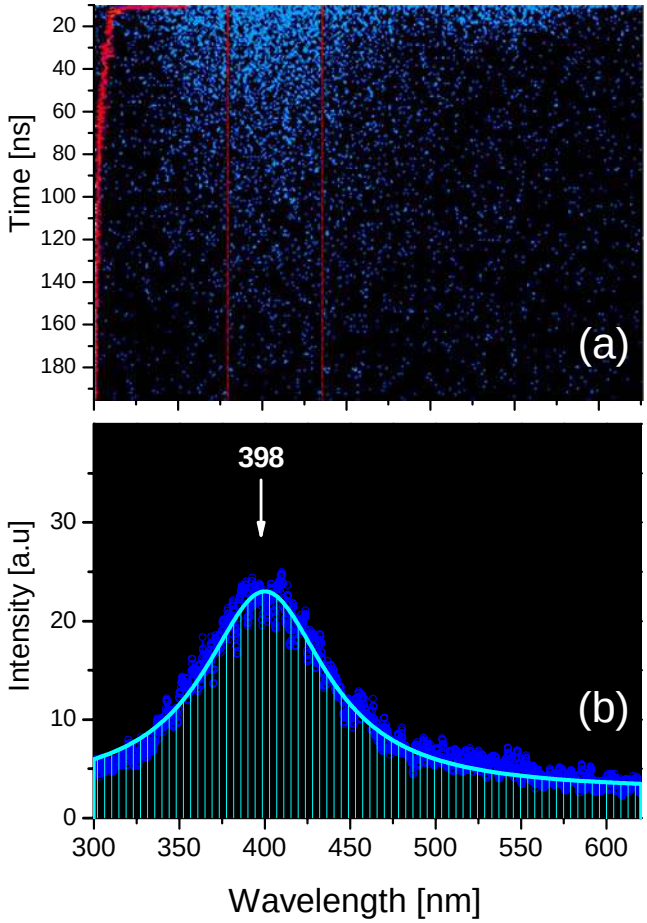

Fig. 6. Photoluminescence response of CaF_2 single crystal sample excited by 320 nm: (a) A streak camera "two-dimensional" image of the time dependent photoluminescence, (b) Fluorescence spectrum of CaF_2 crystal.

We have measured the photoluminescence response of the CaF_2 crystal sample for various excitation wavelengths and different angles of excitation beam. The streak image of the fluorescence emission spectrum of CaF_2 is presented in Fig. 6a. The photoluminescence response was very small, see Fig. 6a where typical optical response of sample is presented. Although the streak images were acquired in photon counting mode using very large number of expositions (20000), very small number of photons were counted. The vertical axis in Fig. 6a corresponds to the fluorescence development in time domain of 200 ns. The beginning of the vertical axis is cut off in order to avoid undesirable part of the spectra (excitation at 320 nm and second harmonic of Nd:YAG laser at 532 nm). Enlarged integrated profile of the

fluorescence of CaF_2 is presented in Fig. 6b. Our pure sample of CaF_2 crystal shows a broad band in 300-500 nm range. A fluorescence spectrum is obtained by averaging all events in time range from 12 ns to 190 ns after excitation. Maximum of fluorescence is on 398 nm. As pointed out in [40] this band might be induced due to the formation of color centers. These centers perhaps could be created by oxygen defects within the host of CaF_2. However, the occurrence of defects in crystal is very rare compared to the nanostructures described in [42], so the luminescence of our sample is very weak compared to the luminescence of structure described in [42]. To obtain good luminescence response, the samples of CaF_2 are doped with Ag, Eu, Tb, Cu or Dy [42, 43]. However, CaF_2 crystal is usually used in applications where high optical transmission is needed and photoluminescence is not desirable characteristics [44].

The fluorescence line profile (fluorescence decay) from image Fig. 6a is selected using the integration process in region from 340 nm to 460 nm. That profile is fitted using High Performance Digital Temporal Analyzer (HPD-TA) software, provided by Hamamatsu. The fluorescence decay is integrated in the range from 375 nm to 425 nm. Estimated lifetime of fluorescence, $\tau = 33$ ns ($\chi 2 = 1.07$), is obtained by fitting of integrated temporal profile.

The properties of the crystal, such as density of dislocations, cystallinity, and impurities concentrations, determine the optical quality.

4. Conclusions

CaF_2 single crystals in diameter of 20 mm are obtained by the vertical Bridgman method in vacuum. The crystal growth rate was 6.0 mm h^{-1}. In order to eliminate stresses in the crystal, a crystal annealing is carried out on the plate and bulk CaF_2. Number of dislocations is of the order of 5×10^4 - 2×10^5 per cm^2. The Raman T_{2g} optical mode at 319.7 cm^{-1} was observed. Kramers-Kröning analyses of the far-IR reflectance data for fluorite structure, as well as the fitting procedure, gave the same values for IR modes: $\omega_{TO} = 272$ cm^{-1} and $\omega_{LO} = 475$ cm^{-1}. Based on our work and observations during the experiment, it could be concluded that the obtained CaF_2 single crystal is of good optical quality, which was the goal of our work.

Acknowledgments

This research was financially supported by the Ministry of Education, Science and Technological Development of the Republic of Serbia through Projects No. III 45003 and TR34011.

5. References

1. D. P. Sanders, Advances in patterning materials for 193 nm immersion lithography, Chem. Rev. 110 (2010) 321-360.
2. Y. Mizumoto, T. Aoyama, Y. Kakinuma, Procedia Engineering 19 (2011) 264-269.
3. H. Ohmori, W. Lin, Y. Yamagata, S. Moriyasu, Development of Large Ultraprecision Aspheric Optics ELID Grinder for Larger X-Ray Mirrors, International Progress on Advanced Optics and Sensors, Edited by H. Ohmori and H. M. Shimizu, Universal Academy Press, Inc., Tokyo, Japan, 2003, 91-98.
4. V. Liberman, T. M. Bloomstein, M. Rothschild, J. H. C. Sedlacek, R. S. Uttaro, A. K. Bates, C. Van Peski, K. Orvek, J. Vac. Sci. Technol. B 17 (1999) 3273.
5. S. E. Swanson, American Mineralogist 62 (1977) 966-978.
6. K. Th. Wilke, J. Bohm, Crystal Growth, Harri Deutsch Press, Thun, Frankfurt/Main, 1988 (ISBN 3-87144-971-7).

7. T. Mizugaki, K. Kimura, S. Takano, US Patent 6, 123, 764 (2000).
8. T. Ohba, T. Ichizaki, US Patent 6, 270, 570 (2001).
9. G. Müller, J. Cryst. Growth 237-239 (2002) 1628-1637.
10. A. Horowitz, S. Biderman, G. B. Amer, U. Laor, M. Weiss, A. Stern, J. Cryst. Growth 85 (1987) 215-222.
11. J. T. Mouchovski, V. T. Penev, R. B. Kuneva, Cryst. Res. Technol. 31 (1996) 727-737.
12. K. A. Pandelisev, US Patent 5,993,540 (1999).
13. S. E. Gianoulakis, US Patent 6,350,310 (2002).
14. R. S. Retherford, R. Sabia, V. P. Sokira, Appl. Surf. Sci. 183 (2001) 264-269.
15. J. M. Ko, S. Tozawa, A. Yoshikawa, K. Inaba, T. Shishido, T.Oba, Y. Oyama, T. Kuwabara, T. Fukuda, J. Cryst. Growth 222 (2001) 243-248.
16. A. R. West, Solid State Chemistry and Its Applications, John Wiley&Sons, 2007.
17. P. P. Fedorov, V. V. Osiko, Bulk Crystal Growth of Electronic, Optical and Optoelectronic Materials, Edited by P. Capper, John Wiley&Sons, 2005.
18. 18. L. Su, Y. Dong, W. Yang, T. Sun, Q. Wang, J. Xu, G. Zhao, Mater. Res. Bull. 40 (2005) 619-628.
19. 19. H. Yanagi, T. Nawata, Y. Inui, Y. Hatanaka, E. Nishijima, T. Fukuda, Proc. SPIE 5377, Optical Microlithography XVII, 1886 (May 28, 2004); doi:10.1117/12.556614.
20. N. Senguttuvan, M. Aoshima, K. Sumiya, H. Ishibashi, J. Crys. Growth 280 (2005) 462-466.
21. J. Xu, M. Shi, B. Lu, X. Li, A. Wu, J. Crys. Growth 292 (2006) 391-394.
22. S. Hull, Rep. Prog. Phys. 67 (2004) 1233-1314.
23. C. Kittel, Introduction to Solid State Physics, New York, Wiley, 4th ed. 1971.
24. B. M. Voronin, S. V. Volkov, J. Phys. Chem. Solids 62 (2001) 1349-1358.
25. I. V. Stepanov, P. P. Feofilov, (1957). Artificial fluorite. In Rost kristalov (Vol. I, pp. 229), Moscow, Russia: Akademia Nauk SSSR. (in Russian).
26. D. Luković, P. M. Nikolić, S. Vujatović, S. Savić, D. Urošević, Sci. Sinter. 39 (2007) 161-167.
27. P. M. Nikolić, S. S. Vujatović, T. Ivetić, M. V. Nikolić, O. Cvetković, O. S. Aleksić, V. Blagojević, G. Brankovic, N. Nikolić, Sci. Sinter. 42 (2010) 45-50.
28. G. V. Molev, V. E. Bozhevolnov, V. I. Korobkov, V. V.Karelin, J. Crys. Growth 19 (1973) 117-121.
29. K. Recker, R. Leckebusch, J. Crys. Growth 9 (1971) 274-280.
30. H. Guggenheim, J. Appl. Phys. 34 (1963) 2482-2485.
31. R. K. Chang, B. Lacina, P. S. Pershan, Phys. Rev. Lett. 17 (1966) 755-758.
32. J. R. Ferraro, H. Horan, A. Quattrochi, J. Chem. Phys. 55 (1971) 664-666.
33. D. G. Mead, G. R. Wilkinson, J. Phys. C 10 (1977) 1063-1072.
34. D. J. Oostra, H. W. den Hartog, Phys. Rev. B 29 (1984) 2423-2432.
35. P. C. Ricci, A. Casu, G. de Giudici, P. Scardi, A. Anedda, Chem. Phys. Let. 444 (2007) 145-148.
36. A. A. Kaminskii, S. N. Bagayev, H. J. Eichler, H. Rhee, K. Ueda, K. Takaichi, K. Oka, H. Shibata, Y. Hatanaka, Y. Matsumoto, Laser Phys. Lett. 3 (2006) 385-391.
37. J. Tu, S. A. FitzGerald, J. A. Campbell, A. J. Sievers, J. Non-Cryst. Solids 203 (1996) 153-158.
38. L. Su, J. Xu, W. Yang, X. Jiang, Y. Dong, Chinese Optics Letters 3 (2005) 219-221.
39. J. P. Russell, Proceedings of the Physical Society 85 (1965) 194-196.
40. S. Ganesan, E. Burstein, Journal de Physique France 26 (1965) 645-648.

41. Kaiser, W. G. Spitzer, R. H. Kaiser, L. E. Howarth, Phys. Rev. 127 (1962) 1950-1954.
42. V. S. Singh, C. P. Joshi, S. V. Moharil, P. L. Muthalc, S. M. Dhopte, Luminescence 30 (2015) 1101-1105.
43. N. Salah, N. D. Alharbi, S. S. Habib, S. P. Lochab, J. Nanomaterials (2015) 136402, http://dx.doi.org/10.1155/2015/136402.
44. Fairfield Crystal Technology, http://www.fairfieldcrystal.com.

Садржај: *Мора се напоменути да је главни циљ овог истраживања био да се добију монокристали калцијум флуорида - CaF_2, а након тога су кристали испитивани различитим спектроскопским методама карактеризације. За раст монокристала је коришћена Брицманова метода. Под оптималним условима раста, добијени су кристали пречника до 20 mm са оријентацијом <111>. Број дислокација у кристалима CaF_2 је био 5×10^4 - 2×10^5 по cm^2. Изабрани кристал је сечен на неколико плочица дијамантском тестером. Плочице су полиране, прво силицијум карбидом, затим парафинским уљем, и на карју дијамнтском пастом. Добијени кристал је испитиван методам Раман и ИЦ спектроскопијом. Кристална структура је потврђена рендгенско структурном анализом. У складу са теоријом група примећен је један Раман и два инфрацрвена оптичка мода. Ниска фотолуминисценција сведочи о томе да је концентрација дефеката кисеоника у CaF_2 мала. Сва обављена истраживања показују да добијени монокристал CaF_2 има добар оптички квалитет, што је и био циљ овог рада.*

Кључне речи: *CaF_2, Раман спектроскопија, инфрацрвена спектроскопија, фотолуминисценција*

Science of Sintering, **49** (2017) 277-284

doi: https://doi.org/10.2298/SOS1703277L

UDK 543.42, 621.926.087

Yttrium Orthoferrite Powder Obtained by the Mechanochemical Synthesis

Zorica Ž. Lazarević[1,*)], Čedomir Jovalekić[2], Martina Gilić[1], Valentin Ivanovski[3], Ana Umićević[3], Dalibor Sekulić[4], Nebojša Ž. Romčević[1]

[1]Institute of Physics, University of Belgrade, Pregrevica 118, Zemun, Belgrade, Serbia

[2]The Institute for Multidisciplinary Research, University of Belgrade, Belgrade, Serbia

[3]Institute of Nuclear Sciences Vinča, University of Belgrade, Belgrade, Serbia

[4]Faculty of Technical Sciences, University of Novi Sad, Novi Sad, Serbia

Abstract:

Yttrium orthoferrite ($YFeO_3$) powder was prepared by a mechanochemical synthesis from a mixture of Y_2O_3 and α–Fe_2O_3 powders in a planetary ball mill for 2.5 h. The obtained $YFeO_3$ powder sample was characterized by X–ray diffraction (XRD), Raman and infrared spectroscopy. The average crystallite size calculated by the Scherrer equation was 12 nm. The Mössbauer spectroscopy at room temperature confirms the superparamagnetic character of $YFeO_3$ orthoferrite sample.

Keywords: *$YFeO_3$; Raman spectroscopy; IR spectroscopy; Mössbauer spectroscopy.*

1. Introduction

In the past few years, a renewed interest has grown in the study of orthorhombically distorted perovskites. An important example of this trend is the family of orthoferrites, with a general formula $R\mathrm{FeO_3}$, where R is the trivalent rare-earth metal ion or yttrium [1]. Orthoferrites have been extensively studied for their physical properties and potential applications [2-4]. These materials are of considerable interest on account of their novel magnetic, optical and magneto–optical properties [5]. Also, Y and rare–earth orthoferrites exhibit interesting physical and chemical properties because of their ionic and electronic defects [6, 7]. However, systematic spectroscopic investigations of orthoferites have not been done jet. Reviewing the literature, one can find the analysis of Raman spectra rare–earth orthoferrites [8] and $\mathrm{YFeO_3}$ [15], but far and mid IR reflectivity measurements are not available.

The family of orthorhombically distorted perovskites have the same *Pnma* space group and 4 formula units per unit cell [8-11]. The basic building units of orthoferrites are $\mathrm{FeO_6}$ octahedral that are corner–connected along the *b* axis. Four corner–connected oxygen atoms, O1, and additional charge balancing yttrium cations, which occupy interstitial positions between octahedral, are in ***4c*** Wyckoff–site with C_s^{xz} symmetry (Fig. 1). The eight

*) **Corresponding author:** lzorica@yahoo.com

oxygen atoms (O2) found in the ac plane occupy Wyckoff positions ***8d*** and possess site symmetry *C1*. According to the recent inelastic neutron scattering measurements the lattice constants of $YFeO_3$ single crystal, are a = 5.282Å, b = 7.605 Å, and c = 5.596 Å [12]. Below 640 K, $YFeO_3$ is a noncollinear antiferromagnet [12, 13]. The direct interaction between nearest neighbour Fe magnetic moments in yttrium and rare–earth orthoferrite crystals is negligible. The spins are coupled through the oxygen atoms by the super exchange mechanism. This interaction is predominantly antiferromagnetic with an anti-symmetric component (Dzyaloshinsky–Moriya anti–symmetric exchange [14]) which causes a slight canting of the moments of adjacent iron atoms and a resultant weak ferromagnetic moment as well.

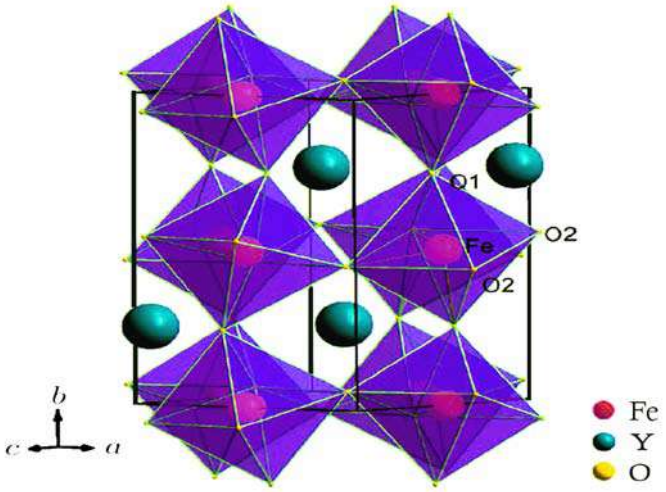

Fig. 1. Structure of $YFeO_3$.

The usual method for synthesizing such compounds, viz. by sintering stoichiometric mixtures of the rare-earth oxide (R_2O_3) and Fe_2O_3 is unsuitable in this case because it leads to the formation of garnets as well as orthoferrites at low temperatures. Most of mentioned approaches for synthesis of single phase perovskite $YFeO_3$ require the calcination process at high temperature around 1173 K, which results in energy and time consumption usually associated to multistage synthesis [15].

Rare–earth orthoferrites are often prepared from high temperature solid-state reactions of the corresponding pure oxides [16]. However, this process suffers from problems such as excessive crystal growth, irregular atomic stoichiometric ratio, and formation of undesirable phases. Polycrystalline rare–earth orthoferrites ($RFeO_3$) and iron garnets ($R_3Fe_5O_{12}$) are usually prepared by sintering mixtures of rare earth oxide (R_2O_3) and Fe_2O_3 at elevated temperatures (> 1300 °C). This method, however, often involves the formation of impurity phases such as garnets (in the orthoferrites) and magnetite. Multiple firings are usually necessary to obtain materials which are single phase with respect to XRD measurements. On the other hand, Racu and co-authors [17] present a new, fast and high yield synthesis method for obtaining microcrystalline $YFeO_3$ orthoferrite, based on hydrothermal technique. The advantage of the method consists in the direct crystallization of the material without the necessity of the calcination. Other synthesis routes have also been proposed including the precipitation method, thermal decomposition process, solvothermal treatment, sonochemical approach, combustion route, alkoxide method and solid state reaction [18-24].

Mechanical activation is a very effective method for obtaining a highly dispersed system as mechanical action stress fields form in solids during the milling procedure [25]. During milling, heat is released, new surfaces and different crystal lattice defects are formed and a solid-state reaction is initiated. The accumulated deformation energy is the key of

understanding the route of irreversible changes of the crystal structure and consequently microstructure, causing changes of material properties [25]. In many cases, the mechanical activation is superior to the conventional solid-state reaction for the ceramic powder preparation for several reasons. It uses low–cost and widely available oxides as starting materials and skips the calcinations step at an intermediate temperature, conducting to simplified process [26].

In this work, we were investigated the nanocrystalline $YFeO_3$ powder obtained by the mechanochemical synthesis in a planetary ball mill. The mechanochemical reaction leading to formation of the $YFeO_3$ phase was followed by XRD, Raman and IR spectroscopy. The Mössbauer spectroscopy at room temperature confirms the superparamagnetic character of $YFeO_3$ orthoferrite sample.

2. Experimental procedures

The starting material were: yttrium (III)–oxide (Y_2O_3, Alfa Aesar 99.9 % purity) and hematite (α–Fe_2O_3, Merck 99 % purity). Mechanochemical synthesis was performed in air atmosphere in planetary ball mill (Fritsch Pulverisette 5).

Characterization of the sample obtained after 2.5 h milling time was carried out by several methods.

• XRD analysis was performed on X-ray diffractometer (Rigaku Corporation, Japan) at room temperature. CuKα radiation (λ = 0.15418 nm) with a step size of 0.01° in the range of 2θ = 10-80° was used. The peaks were identified using the Powder Diffraction File (PDF) database created by International Centre for Diffraction Data (ICDD).

• The micro-Raman spectra were taken in the backscattering configuration and analyzed by Jobin Yvon T64000 spectrometer, equipped with nitrogen cooled charged coupled device detector. As an excitation source the 532 nm line of Ti was used: Sapphire laser, with laser power 20 mW. The measurements were performed in the spectrum range 100 – 800 cm^{-1}.

• The infrared (IR) measurements were carried out with a BOMMEM DA–8 FIR spectrometer. A DTGS pyroelectric detector was used to cover the wave number range 50 – 700 cm^{-1}.

• The measurements of the Mössbauer effect in $YFeO_3$ nanocrystalline powder were performed in a transmission geometry using a ^{57}Co(Rh) source at the room temperature (RT). The spectra have been examined by WinNormos–Site or WinNormos–Dist/Xls software packages [27]. The former is based on the least squares method whereas the latter combines distribution of Lorentz lines and subspectra based on the histogram and the least squares method, respectively. The Wissel spectrometer was calibrated by the spectra of natural iron foil. Sample thickness correction was carried out by a transmission integral. Isomer shift values are in reference to a metallic alpha iron (δ = 0).

3. Results and discussions

Fig. 2 presents the XRD pattern of: the starting mixture after 2.5 h of milling. Obtained diffractogram is compared with the data from the Powder Diffraction Files: PDF#39–1489 for yttrium orthoferrite, PDF#33–0664 for hematite and PDF#41–1105 for yttrium (III) oxide. After 2.5 h of milling the orthorhombic distorted perovskite structure with space group of *Pnma* become dominant. Only a few percents of Y_2O_3 and Fe_2O_3 indicate that the reaction is practically completely finished.

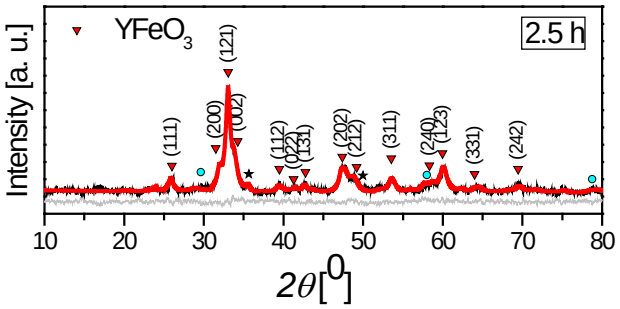

Fig. 2. XRD pattern of $YFeO_3$ orthoferrite obtained from the mixture of Y_2O_3 and α–Fe_2O_3 powders after 2.5 h milling time (symbols in red ∇ – $YFeO_3$; blue • – Fe_2O_3; black ∗ – Y_2O_3 are assigned to identified phases).

The crystallite size (S) of $YFeO_3$ powder mechanochemically treated for 2.5 h was calculated by means of Scherrer equation [28-30] using XRD data for the most prominent (121) Bragg reflection as:

$$S = 0.9\,\lambda / (\beta \cos\,\theta) \quad (1)$$

where λ – X–ray wavelength, β – full width at half–maximum, θ – Bragg angle. Estimated average crystallite size is 12 nm.

The group theory [31-33] predicts 60 vibration modes at the centre of Brilouin zone: $\Gamma = 7A_g + 8A_u + 5B_{1g} + 10B_{1u} + 7B_{2g} + 8B_{2u} + 5B_{3g} + 10B_{3u}$. Therefore, for unpolarised spectra of a polycrystalline sample, we would expect at most 24 Raman bands ($7A_g + 5B_{1g} + 7B_{2g} + 5B_{3g}$) and 25 infrared–active ones ($9B_{1u} + 7B_{2u} + 9B_{3u}$), $8(8A_u)$ are silent, and $3(B_{1u} + B_{2u} + B_{3u})$ are acoustic modes.

Unpolarised Raman spectra presented in Fig. 3 are excited by laser line λ= 532 nm and recorded in backscattering geometry at room temperature. As Fe atoms are in centre of symmetry they do not participate in Raman active modes. The corresponding modes in different orthorhombically distorted perovskites with symmetry *Pnma* are not different too much. So we could assign modes in our Raman spectra of nanosized $YFeO_3$ in accordance with literature data [8, 34, 35]. We observed all 7 A_g modes at 146, 177.5, 289, 335, 405, 494 and 525 cm^{-1}. Two strong B_{2g} modes are at 221 and 608 cm^{-1} and one B_{1g} at 434 cm^{-1}. The origin of a strong wide feature at 655 cm^{-1} arises from two-phonon process and probably due to crystal disorder. In the Raman spectra of single crystals this band is hardly visible [8, 35], but in the spectra of polycrystalline samples is much exaggerated. Mandal at al. [36] deconvoluted this band (at 648 cm^{-1} in $YFe_{0.6}Mn_{0.4}O_3$) and found that at this energy there are two (second order) phonons with different symmetries – B_{2g} and B_{3g}.

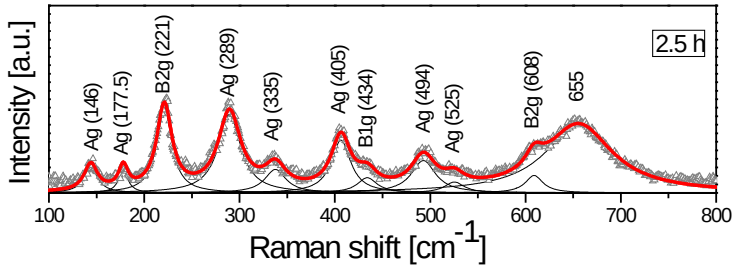

Fig. 3. Raman spectrum of $YFeO_3$ orthoferrite obtained from the mixture of Y_2O_3 and α–Fe_2O_3 powders after 2.5 h milling time at room temperature.

Infrared reflectivity spectrum of the practically pure $YFeO_3$ phase after 2.5 h of milling is presented in Fig. 4. A number of modes that can be related to an $YFeO_3$ phase are visible. As a result of the best fit we obtained 10 modes with parameters listed in Fig. 4.

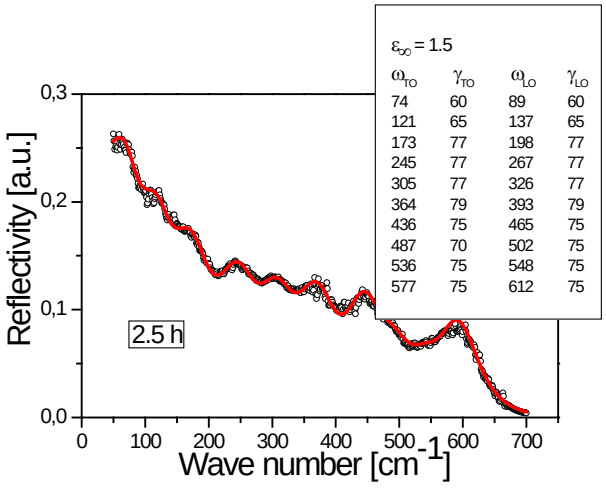

Fig. 4. IR spectrum of $YFeO_3$ orthoferrite obtained from the mixture of Y_2O_3 and α–Fe_2O_3 powders after 2.5 h milling time at room temperature.

To the best of our knowledge, about the reflectivity measurements of $YFeO_3$ in the far and mid infrared range in literature and only two references have reported the transmittance of $YFeO_3$, but in the range of wave numbers higher than 400 cm^{-1}. This assertion can be seen in the works that show investigation nanocrystals of $YFeO_3$ obtained by sol-gel auto-combustion process [37] and sintered samples (as a part of investigation of $YFe_{1-y}Mn_yO_3$) [38]. Comparing theoretical [31, 33, 39] and experimental data for IR modes from available literature, together with results obtained by fitting procedure in this work, we can conclude that IR modes of various orthoferrites are very close, even modes of orthoferrite and orthomanganite, as has already been shown for Raman modes. IR modes generally can be assigned to three different types of motion (came up from splitting of modes in ideal perovskite structure): 1)Y (or rare–earth) – external modes at the lowest frequencies, 2) Fe-O bending modes in the intermediate range from 270 cm^{-1} to 500 cm^{-1}, and 3) oxygen stretching modes at higher frequencies. Considering that our nanosized samples are obtained by ball milling (mechanochemical reaction) it is possible that the presence of numerous defects, like disturbed octahedrons, can result in broadening of modes, or even arising of new modes. We suppose that merged modes centered at about 570 cm^{-1} correspond to stretching vibration(s). The strongest mode at 436 cm^{-1} is a little lower than reported [37, 38]. All other lower energy modes can be compared only with modes of some other compounds with the same *Pnma* structure, or with theoretically obtained values for rare–earth orthoferrites [32] and lanthanum orthomanganite [33, 39]. It can be concluded that the first fitted mode at ω_{TO} = 74 cm^{-1} (ω_{LO} = 89 cm^{-1}) has B_{1u} symmetry. Rather broad mode 121(137) cm^{-1} can be a combination of two close modes B_{1u} and B_{3u}. Modes at 173(198) cm^{-1} and 245(267) cm^{-1} have symmetry B_{1u} and B_{2u}, respectively. Those are so called external modes, mixed vibrations of Y and octahedra FeO_6. The higher frequency modes do not involve motions of Y atoms, but only vibrations of O–Fe–O bond in octahedra. The second group of phonons with frequencies lying between 270 and 500 cm^{-1} is expected to originate from splitting of the bending mode of the ideal perovskite structure. These are modes B_{3u} at 305(326) cm^{-1}, B_{1u} at 364(393) cm^{-1}, B_{1u} at 436(465) cm^{-1} and B_{3u} at 487(502) cm^{-1} (Fig. 4). In the third group are stretching modes B_{3u} at 536(548) cm^{-1} and strong B_{2u} at 577(612) cm^{-1}. Even though if we were not able to assign all IR modes, at least two most prominent modes (B_{1u} at 436(465) cm^{-1} and B_{2u} at 577(612) cm^{-1}) confirm that after 2.5 h of milling orthoferrite *Pnma* structure is obtained.

The Mössbauer spectrum (Fig. 5) obtained for 2.5 h milled sample is resolved by five sextets and three doublets. The sextet with the hyperfine interaction parameters which

correspond to hematite is clearly identified. Its relative amount is 6.0(3) %. The remaining four sextets are recognized to represent response from the yttrium orthoferrite. The relative amount of well crystallized large particles is 16(2) %. The other three sextets that follow the reduction of particles´ volume are in accordance with the findings of Modi et al., i.e. hyperfine field magnitude and isomer shift values decrease with decreasing particle size or increasing milling time [40]. Two superparamagnetic doublets show that further milling produced additional more than 10% small sized particles. Pinkas et al. reported the measured isomer shift value of 0.34 mm s^{-1} and quadrupole splitting of 0.79 mm s^{-1} for the amorphous $YFeO_3$ at 300 K [41]. These results are in agreement with the parameters of doublet obtained in our measurement. The doublet with the largest quadrupole splitting value of 2.32(1) mm s^{-1} provokes the most doubts in interpretation. The $YFeO_3$ with hexagonal structure is a metastable phase. There is only one non-equivalent Fe site in hexagonal $YFeO_3$ whereas the observation of two Fe sites in this phase was related to the small crystallites of the Fe–rich compound [42, 43]. The reported hyperfine parameters for these two Fe sites at room temperature are 2.13(2) and 1.18(2) mm s^{-1} for the quadrupole splitting and the isomer shift of 0.29(2) and 0.30(2) mm s^{-1}, respectively. The ratio of relative area is 4:3 [44]. The relative amount of the doublet is probably under detection limit of XRD as an aggravating circumstance. Taking into account that our parameters do not entirely match the cited values, while partially agree with the ones of Modi et al. [40], this doublet is attributed to the smallest $YFeO_3$ particles. The creation of oxygen vacancies during milling might have reduced some of the Fe^{3+} ions to Fe^{2+} ions [40]. The distinctive isomer shift high value was not identified in our spectra. Thus, we conclude that the yttrium orthoferrite represents 94 % of the sample obtained after 2.5 h milling time. After normalization with respect to the yttrium orthoferrite amount, the following distribution of particle size is obtained: 17 % large, 38 % medium sized and 45 % small particles.

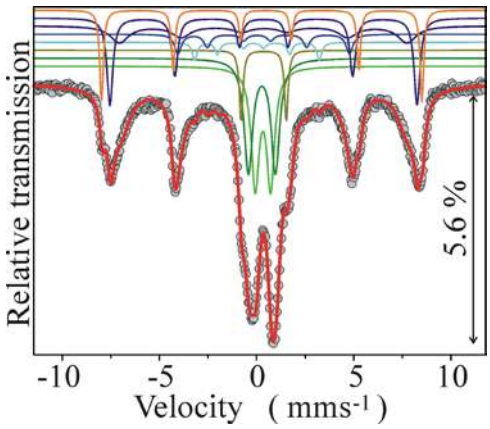

Fig. 5. Mössbauer spectrum at T = 294 K of $YFeO_3$ orthoferrite obtained from the mixture of Y_2O_3 and α–Fe_2O_3 powders after 2.5 h milling time. The experimental data are presented by solid circles and the fit is given by the red solid line. Vertical arrow denotes relative position of the lowermost peak with respect to the basal line. The fitted lines of subspectra are plotted above the main spectrum fits.

4. Conclusions

Nanosized yttrium orthoferrite ($YFeO_3$) powder was synthesized by mechanochemical treatment of Y_2O_3 and α–Fe_2O_3 mixture in planetary ball mill for 2.5 h. XRD shows that yttrium orthoferrite structure is dominant in the form of fine crystallites with average size 12 nm. The eleven Raman active modes are observed in first-order Raman

spectra at the room temperature. An IR reflectivity spectrum is fitted by 10 modes. Mössbauer measurement analysis shows that the dominant part of the yttrium orthoferrite phase are small and medium sized nanoparticles. After 2.5 h of milling the mixture contains 6 % of unreacted hematite.

Acknowledgments

This research was financially supported by the Ministry of Education, Science and Technological Development of the Republic of Serbia through Projects No. III 45003 III 45015, III 45018 and research project under the agreement of scientific collaboration between Polish Academy of Science and Institute of Physics Belgrade.

5. References

1. N. Singh, J. Y. Rhee, J. Korean Phys. Society, 53 (2008) 806-811.
2. Y. S. Didosyan, H. Hauser, H. Wolfmayer, J. Nicolics, P. Fulmek, Sens. Actuators A, 106 (2003) 168-171.
3. Y. S. Didosyan, H. Hauser, W. Toriser, Int. J. Appl. Electrom., 13 (2001) 277-283.
4. P. Ripka, G. Vértesy, J. Magn. Magn. Mater., 215-2016 (2000) 795-799.
5. A. R. Akbashev, A. S. Semisalova, N. S. Perov, A. R. Kaul, Appl. Phys. Lett., 99 (2011) 122502.
6. E. Traversa, P. Nunziante, L. Sangaletti, B. Allieri, L. E. Depero, H. Aono, Y. Sadaoka, J. Am. Ceram. Soc., 83 (2000) 1087-1092.
7. M. Cherry, M. S. Islam, C. R. A. Catlow, J. Solid State Chem., 118 (1995) 125-132.
8. S. Venugopalan, M. Dutta, A. K. Ramdas, J. P. Remeika, Phys. Rev. B, 31 (1985) 1490-1497.
9. M. Derras, N. Hamdad, Results in Physics, 3 (2013) 61-69.
10. P. Coppons, M. Eibschutz, Acta Crystallogr., 19 (1965) 524-531.
11. M. Marezio, J. P. Remeika, P. D. Derrier, Acta Crystallogr. B, 26 (1970) 2008-2022.
12. S. E. Hahn, A. A. Podlesnyak, G. Ehlers, and G. E. Granroth, R. S. Fishman, A. I. Kolesnikov, E. Pomjakushina, K. Conder, Phys Rev B, 89 (2014) 014420.
13. R. Nirat, V. W. Umesh, Phys.Rev. B, 77 (2008) 134112-134121.
14. I. Dzyaloshinsky, J. Phys. Chem. Solids, 4 (1958) 241-255.
15. P. Ayyub, M. S. Multani, A. Gurjar, Mater. Lett., 2 (1983) 122-126.
16. A. Sztaniszlav, E. Sterk, L. Fetter, M. Farkas-Jahnke, J. Magn. Magn. Mater., 41 (1984) 75-78.
17. A.V. Racu, D. H. Ursu, O. V. Kuliukova, C. Logofatu, A. Leca, M. Miclau, Mater. Lett., 140 (2015) 107-110.
18. S. Nakayama, J. Mater. Sci., 36 (2001) 5643-5648.
19. D. S. Todorovsky, R. V. Todorovska, St. Groudeva-Zotova,Mater. Lett., 55 (2002) 41-45.
20. M. Inoue, T. Nishikawa, T. Nakamura, T. Inui, J. Am. Ceram. Soc., 80 (1997) 2157-2160.
21. M. Sivakumar, A. Gedanken, W. Zhong, Y. H. Jiang, Y. W. Du, I. Brukental, D. Bhattacharya, Y. Yeshurun, I. Nowik, J. Mater. Chem., 14 (2004) 764-769.
22. Q. Ming, M. D. Nersesyan, A. Wagner, J. Ritchie, J. T. Richardon, D. Luss, A. J. Jacobson, Y. L. Yang, Solid State Ionics, 122 (1999) 113-121.
23. Y. Matsuura, S. Matsushima, M. Sakamoto, Y. Sadaoka, J. Mater. Chem., 3 (1993) 767-769.
24. J. G. McCarty, H. Wise, Catal. Today, 8 (1990) 231-248.

25. M. M. Vijatović, J. D. Bobić, B. D. Stojanović, Sci. Sinter., 40 (2008) 155-165.
26. Z. Ž. Lazarević, B. D. Stojanović, M. J. Romčević, N. Ž. Romčević, Sci. Sinter., 41 (2009) 19-26.
27. R. A. Brand, WinNormos Mössbauer fitting program. Universität Duisburg (2008).
28. V. I. Popkov, O. V. Almjasheva, V. N. Nevedomskiy, V. V. Sokolov , V. V. Gusarov, Nanosyst.: Phys., Chem., Math., 6 (2015) 866-874.
29. A. Patterson,Phys. Rev., 56 (1939) 978-982.
30. Z. Ž. Lazarević, Č. Jovalekić, D. Sekulić, M. Slankamenac, M. Romčević, A. Milutinović, N. Ž. Romčević, Sci. Sinter., 44 (2012) 331-339.
31. M. A. Islam, J. M. Rondinelli, J. E. Spanier, J. Phys.: Condens. Matter., 25 (2013) 175902.
32. H. C. Gupta, M. K. Singh, L. M. Tiwari, J. Raman Spectrosc., 33 (2002) 67-70.
33. I. S. Smirnova, Physica B, 262 (1999) 247-261.
34. M. N. Iliev, M. V. Abrashev, H.-G. Lee, V. N. Popov, Y. Y. Sun, C. Thomsen, R. L. Meng, C. W. Chu, Phys. Rev. B, 57 (1998) 2872-2877.
35. N. D. Todorov, M. V. Abrashev, V. G. Ivanov, G. G. Tsutsumanova, V. Marinova, Y.-Q. Wang, M. N. Iliev, Phys. Rev. B, 83 (2011) 224303.
36. P. Mandal, Venkata Srinu Bhadram, Y. Sundarayya, Chandrabhas Narayana A. Sundaresan, C. N. R. Rao, Phys. Rev. Letters, 107 (2011) 137202.
37. W. Zhang, C. Fang, Wenhui Yin, Y. Zeng, Mat. Chem. Phys., 137 (2013) 877-883.
38. X. Cao, C. S. Kim, H. I. Yoo, J. Am. Ceram. Soc., 84 (6) (2001) 1265-1272.
39. A. Paolone, P. Roy, A. Pimenov, A. Loidl, O. K. Mel'nikov, A. Ya. Shapiro, Phys. Rev. B, 61 (2000) 11255-11258.
40. K. Modi, S. N. Dolia, P. U. Sharma, Indian Journal of Physics, 89 (5) (2015) 425-436.
41. J. Pinkas, V. Reichlova, A. Serafmidisova, Z. Moravec, R. Zboril, D. Jancik, P. Bezdicka, J. Phys. Chem. C, 143 114 (32) (2010) 13557-13564.
42. E. Murad, John Cashion, Mössbauer Spectroscopy of Environmental Materials and their Industrial Utilization, Springer US, Springer Science+Business Media New York, 2004.
43. P. Jiang, J. Li, A. W. Sleight, M. A. Subramanian, Inorg. Chem., 50 (13) (2011) 5858-5860.
44. L. J. Downie, R. J. Goff, W. Kockelmann, S. D. Forder, J. E. Parker, F. D. Morrison, P. Lightfoot, J. Solid State Chem., 190 (2012) 52-60.

Садржај: *Итријум ортоферит ($YFeO_3$) је добијен из смеше прахова Y_2O_3 и α–Fe_2O_3 механохемијском синтезом након 2.5 часа млевења у планетарном млину. Добијени прах $YFeO_3$ је био карактерисан методом рендгенске дифракције, Раман и инфрацрвеном спектроскопијом. Просечна величина кристалита израчуната Шереровом једначином је била 12 nm. Мосбауер спектроскопија на собној температури потврђује суперпарамагнетни карактер узорка $YFeO_3$.*
Кључне речи: *$YFeO_3$; Раман спектроскопија; инфрацрвена спектроскопија; Мосбауер спектроскопија.*

Spectroscopy study of $Bi_{12}GeO_{20}$ single crystals

Z. Ž. LAZAREVIĆ[a,*], S. KOSTIĆ[a], V. RADOJEVIĆ[b], M. J. ROMČEVIĆ[a], B. HADŽIĆ[a], J. TRAJIĆ[a], N. Ž. ROMČEVIĆ[a]
[a]*Institute of Physics, University of Belgrade, P.O. Box 68, Belgrade, Serbia*
[b]*Faculty of Technology and Metallurgy, University of Belgrade, Belgrade, Serbia*

In this work single crystals of bismuth germanium oxide ($Bi_{12}GeO_{20}$) have been grown by the Czochralski method. Growth conditions were studied. The critical diameter and the critical rate of rotation were calculated. Suitable polishing and etching solutions were determined. The structure of the $Bi_{12}GeO_{20}$ has been investigated by X-ray diffraction, Raman and FTIR spectroscopy. The obtained results are discussed and compared with published data. On the basis of the measurements by Raman spectroscopy, we observed 15 modes.

(Received October 4, 2012; accepted February 20, 2013)

Keywords: $Bi_{12}GeO_{20}$, Czochralski method, XRD, Raman spectroscopy, FTIR

1. Introduction

Sillenit crystals $Bi_{12}MO_{20}$ (M = Ge, Si, Ti) have a number of properties important for practical applications, such as piezoelectric sensors, filters and delay lines of electromagnetic signals, electro-optical and magneto-optical field strength meters, space–time modulators, etc. It is known [1] that these devices require crystals with a low dislocation density and high optical homogeneity. Owing to the great diversity of physical effects in sillenite-type crystals and the possibility of employing them in electronic and optoelectronic devices for various technological applications, a wide variety of techniques have been used to grow both bulk single crystals and epitaxial layers (films) of sillenites. Most research effort has been concentrated on $Bi_{12}GeO_{20}$ (BGO), $Bi_{12}SiO_{20}$ (BSO), and $Bi_{12}TiO_{20}$(BTO) crystals. The approaches most frequently used to prepare BGO, BSO, and BTO crystals are melt growth (Czochralski(CZ)), Bridgman, Stepanov, and edge-defined film-fedgrowth (EFG) processes) and hydrothermal crystallization. Films of these compounds can be produced by liquid phase epitaxy (LPE), physical sputtering, chemical vapor transport, and solution growth [2].

Most BGO single crystals for acoustic and optical applications are grown by CZ pulling. Using this technique, BGO single crystals 50–70 mm in diameter and up to 400 mm in length have been grown [2].

Bismuth germanium oxide ($Bi_{12}GeO_{20}$) is usually abbreviated as BGO in common usage. The $Bi_{12}GeO_{20}$ crystal structure is described by the cubic space group $I23$. The unit cell of $Bi_{12}GeO_{20}$ contains two formula units, the Ge atoms residing in the centre and in the vertices of the cube. Each one of the Ge atoms is tetrahedral, coordinated by oxygen atoms. The framework of the $Bi_{12}GeO_{20}$ structure is formed by the [BiO_5E] polyhedra (E= $6s^2$ is the non-shared electron pair of Bi) which form dimmers by means of a common edge [3]. The $Bi_{12}GeO_{20}$ has considerable applications due to its photoconduction, photochromism, photorefractive and other properties [4–7].

In this paper we have studied the growth of a $Bi_{12}GeO_{20}$ single crystal and characterized it by XRD, Raman and FTIR spectroscopy. In this paper, we have studied a $Bi_{12}GeO_{20}$ single crystal, which produced growth by the Czochralski technique. The $Bi_{12}GeO_{20}$ single crystal was characterized using different methods of characterizations.

2. Experimental procedures

The $Bi_{12}GeO_{20}$ single crystals were grown by the Czochralski technique using an MSR 2 crystal puller controlled by a Eurotherm. The temperature fluctuations were typically lower than 0.2 ºC. The crystal diameter was set and automatically kept constant by an additional weighing assembly that monitored the crucible weight continuously. The absolute value of the deviation from the given diameter was below 0.1 mm. The melt was contained in a platinum crucible (ϕ 40 mm, 40 mm depth), which was placed in an alumina vessel on zircon-oxide wool. The whole system forms a kind of protection against excessive radiative heat loss. To reduce thermal gradients in the crystal and the melt, a cylindrical silica glass after heater was installed around the system with the crucible [8]. The crystals were grown in an air atmosphere. The BGO seed was oriented in the <111> direction.

The charge was a stoichiometric mixture of Bi_2O_3 (99.9999 wt. %) and GeO_2 (99.9999 wt. %). The starting materials were mixed together in the stoichiometric ratio (6:1). Various pull rates were examined and the best results were obtained using pull rates in the range 2.8-3 mm h^{-1}. The rate of crystal rotation was calculated to be 20 rpm. The crucible was not rotated during the growth. After

the growth run, the crystal bole was cooled at a rate of about 50 ºC h^{-1} down to room temperature.

Attempts were made to find the optimal solution for the chemical polishing and etching of $Bi_{12}GeO_{20}$ single crystals. The combination for the etching solution were: HF + HNO_3 in the ratio 2:1, HCl + H_2O in the ratio 1:2, and HCl + H_2O in the ratio 1:5. For the chemical polishing of the bismuth germanium oxide crystals a solution of HCl + HNO_3 + H_2O we tried the ratio 1:1:5.

The observations relating to the dislocation were recorded by observing an etched surface of $Bi_{12}GeO_{20}$ crystal, using a Metaval of Carl Zeiss Java metallographic microscope with magnification of 240x.

The X-ray diffraction (XRD) data for $Bi_{12}GeO_{20}$ was determined using a CuKα radiation and a monochromator (Model Philips PW 1710 diffractometer) under the following experimental conditions: 40 kV and 20 mA, $20^o < 2\theta < 90^o$, $2\theta = 0{,}02^o$ for 0.5 s.

Raman spectroscopy measurement was performed at room temperature in the spectral range from 100 to 1000 cm^{-1}, in back scattering geometry, using a Jobin Yvon T64000 spectrometer, equipped with nitrogen cooled charge-coupled device detector. As an excitation source we used the 514 nm line of an Ar-ion laser. The measurements were performed at 20 mW.

The Infrared (IR) spectrum of the powder was obtained with a Fourier transform infrared (FTIR) transmission-KBr disk spectroscopy (Hartmann & Braun, MB-series). The scanning range of FTIR was between 2000 and 400 cm^{-1}.

3. Results and discussion

Part of a polished slice of a $Bi_{12}GeO_{20}$ single crystal with etched pits of dislocations is shown in Fig. 1. To examination of the dislocations in crystal was used Metaval of Carl Zeiss Java metallographic microscope with magnification from 240x. The absence of a core was confirmed by viewing polished crystal slices in both normal and polarized light. The observations related to the dislocation were recorded by observing an etched surface of $Bi_{12}GeO_{20}$ crystal, using a metallographic microscope. Grain boundaries can be seen in the image well. The whole area looks like as a wave. From the wavy surface as the sticking black triangles. Also, in Fig. 1 can be observed the appearance of regular pyramid, approximate orientation <111> with distinctive peaks.

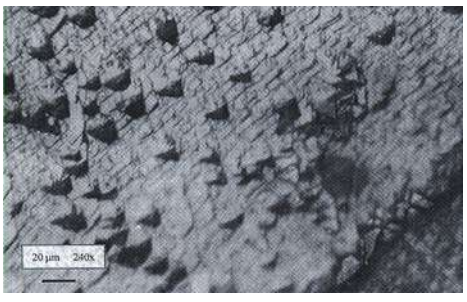

Fig. 1. A view of an etched plate of $Bi_{12}GeO_{20}$ crystal with triangles of dislocations. Magnification 240x.

Fig. 2 presents the XRD pattern of $Bi_{12}GeO_{20}$. The diffractometer was used in the 2θ range from 3º to 95º. XRD indicates that all peaks belong to the $Bi_{12}GeO_{20}$ phase, which is in good agreement with the JCPDS Card No. 34-0096. The unit cell of $Bi_{12}GeO_{20}$ was calculated by the least square method using all 24 reflections, including more $K\alpha_2$ for 5 reflections. The XRD spectrum of BGO shows a typically crystal structure with the strongest peak centered at $2\theta = 27.8^o$, as shown in Fig. 1.

Many of the reflections correspond to $Bi_{12}GeO_{20}$ crystals with the parameter of cubic *I*-centered cell a = 10.1462 Å, and x = 12. Our calculated results for the lattice parameter are in good agreement with published data. It should also be mentioned that a value of x = 12 for crystals $Bi_xGeO_{1.5x+2}$ where the diameters are 10 to 12 mm for a crucible diameter of about 40 mm, have been reported in the literature [9]. This is in accordance with the dimensions of the crystals obtained in this work.

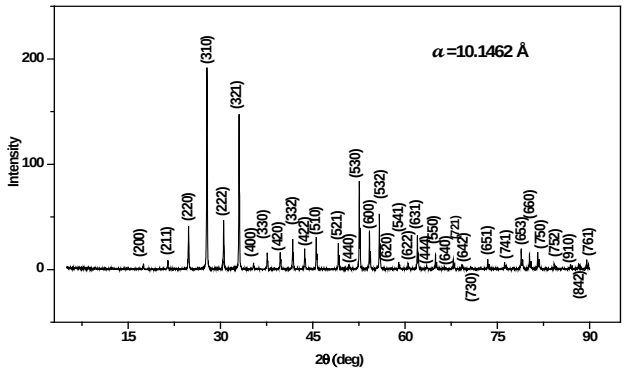

Fig. 2. X-ray diffraction pattern of a $Bi_{12}GeO_{20}$ single crystal.

The Raman spectra of $Bi_{12}GeO_{20}$ single crystals formed by the Czochralski technique, in the spectral range from 50 to 900 cm^{-1} at room temperature is shown in Fig. 3. Raman spectra are often analysed with the help of a Lorentzian curve. Our interest is quantitative analysis with a partial discussion of trend, and we assume that all lines are of the Lorentzian type (Eq. (1)). Solid lines in Fig. 3, were obtained by adding 15 different profiles:

$$I(\omega) = I_0 + \frac{2A}{\pi} \cdot \frac{W}{4(\omega - \omega_c)^2 + W^2} \tag{1}$$

Here I – is the line intensity, I_0 – the height of the baseline, ω_c – the position of the maximum, W – the half-width of the peak and A – a parameter that depends on W. For BGO, group-theoretical analysis gives:

$$\Gamma = 8A + 8E + 25F$$

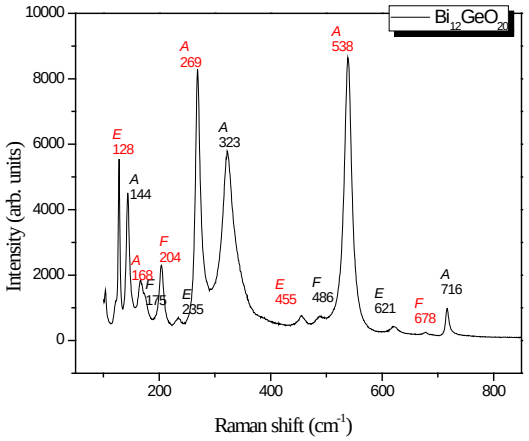

Fig. 3. Raman spectra of $Bi_{12}GeO_{20}$ single crystals at room temperature.

The triply degenerated oscillations ($F \equiv TO+LO$, TO, LO) are manifested in the Raman and IR spectra, and the nondegenerated (A) and doubly degenerated (E) oscillations are manifested in the Raman spectra. Because all these oscillations are manifested in the Raman spectra, these spectra give the most complete information on the internal crystal oscillations. This spectrum contains 14 Raman modes of different relative intensities, indicated as strong, medium and weak. The spectrum of $Bi_{12}GeO_{20}$ exhibits intense modes at about 121, 128, 144, 168, 175, 204, 235, 269, 323, 455, 486, 538, 621, 678 and 716 cm^{-1} (Fig. 3). In the low-frequency region, the Raman spectra of sillenites, together with the spectra of other complex oxide compounds of bismuth, are similar to the Raman spectra of the α-Bi_2O_3. Among numerous intense lines in the spectra of $Bi_{12}GeO_{20}$ narrow lines are observed which coincide with an accuracy of several cm^{-1} with the lines at 121 and 128 cm^{-1} in the Raman spectra of sillenites. The oscillations in the region ω < 150 cm^{-1} in the Raman spectrum of α-Bi_2O_3 are related to the external oscillations of the Bi atom. The oscillations of O lie in the region ω > 150 cm^{-1}. The internal modes should be sought in the range from 200 to 600 cm^{-1}. This fact confirms once more that the main contribution to the vibration spectrum of sillenites in the region ω < 650 cm^{-1} is given by excitations of the bismuth–oxygen sublattice.

At the same time, for a number of oscillations, especially in the high-frequency region (ω > 650 cm^{-1}), an opposite situation takes place. The frequencies of these oscillations depend substantially on the mass of the atom M. The main contribution to these oscillations of the crystal lattice is given by oscillations of the tetrahedral [MO_4]. In accordance with the structural data, the tetrahedron [MO_4] is surrounded by twelve heavy atoms of bismuth, and its oscillations do not cause notable displacements. Indeed, the calculation of the normal oscillation frequencies for the complex molecule $M[O_4(Bi)_3]_4$ (M = Ge, Si, Ti) shows that the values of these frequencies are in good agreement with the experimentally measured ones and are close to the values of the corresponding frequencies of the group $[MO_4]^{4-}$.

Registered Raman modes on Fig. 3 are shown: 5A, 4E and 5F (1TO, 1LO and 3(TO+LO)). The intensity modes at about 168, 171, 269, 323, 5381 and 716 cm^{-1} belong to the symmetry type A. These modes are characterized by the type of vibration, which shows ``breathing`` of Bi and O atoms [10]. Also, these vibrations are combinations of bending and stretching modes in Bi_3O_4 - Bi-O stretching, O-Bi-O bending, O-Ge bending, and symmetric Ge-O stretching. The modes at about 128, 235, 455 and 621 cm^{-1} belong to the symmetry type E and show Bi and O vibrations elongating the cluster along either <100> or <001>, <100> or <010>, respectively. These modes can be present combinations of bending and stretching modes in Bi_3O_4, Bi-O stretching, O-Bi-O bending, and O-Ge bending. Also, the modes at about 121, 175, 204, 486 and 678 cm^{-1} belong to the symmetry type F, while the symmetry type (TO) have modes at about 175 cm^{-1}. They describe the vibrations in the GeO_4 (MO_4) unit: rocking of GeO_4, asymmetric stretching mode in GeO_4. The modes at about 121, 486 and 678 cm^{-1} can be present by symmetry type (TO+LO). The mode at about 323 cm^{-1} can be described as rotation of the GeO_4 unit. The mode at 204 cm^{-1} has symmetry type LO. It should be noted that the frequency of the asymmetric stretching mode of the MO_4 tetrahedral is lower than that of the symmetric one. This is due to the strong influence of the Bi-O framework on the vibration behaviour of the MO_4 tetrahedral in sillenites. It is characteristic of the MO_4 structure. This is in agreement with literature data. The subject of our future study of the $Bi_{12}GeO_{20}$ single crystal will still be with the help of Raman spectroscopy.

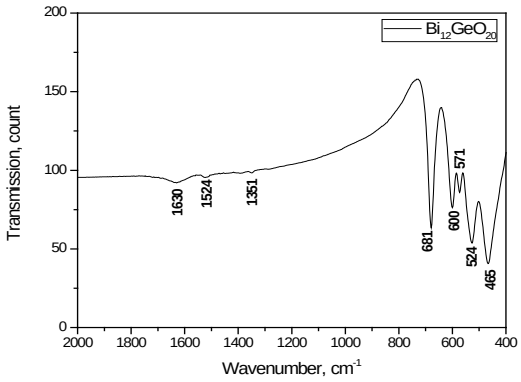

Fig. 4. FTIR transmittance spectra of $Bi_{12}GeO_{20}$ single crystals at room temperature.

Fig. 4 has the IR spectra of samples of $Bi_{12}GeO_{20}$. The IR absorption spectra of $Bi_{12}GeO_{20}$ could be associated directly with the spectra of Bi_2O_3. We expect to have a good agreement with the Raman and IR spectra of the crystalline BGO. Also, the infrared spectrum is in good agreement with the data reported in the literature. The major line BGO was identified in our $Bi_{12}GeO_{20}$ single crystal. Five IR active modes are observed in the range from 400 to 900 cm^{-1} (Fig. 4).

All modes are *TO* symmetry. The FTIR spectrum shows well-defined peaks located at 681, 600, 571, 524 and 465 cm^{-1}. The peak located at 741 cm^{-1} is due to the stretching vibration mode of Bi–O–Ge bonds. In the present case, in the Bi–O–Ge bonds, when the vibrations of the Bi–O and Ge–O are in phase, the absorption is located at 740 cm^{-1} and 712 cm^{-1}. The shift observed in the bands` location can be associated with the difference between the atomic masses of germanium and bismuth atoms. There are small peaks at 1351, 1524 and 1630 cm^{-1}. These belong to the stretching mode of OH- groups as the $Bi_{12}GeO_{20}$ single crystals were grown in an air atmosphere. The positions of the OH- group at this point are in accordance with those found in the literature [11].

The peak at 600 cm^{-1} is related to the cationic vibrations in the network or Bi-O vibration. The peak located at 571 cm^{-1} is associated with the bending vibration mode of the distorted tetrahedron formed by the $(GeO_4)^{4-}$groups. The band located at 524 cm^{-1} is assigned to the deformation vibration of isolated $(GeO_4)^{4-}$ groups. The band located at 465 cm^{-1} is related to Ge-O bond rocking and interaction by the $[BiO_6]$ polyhedron.

The $Bi_{12}GeO_{20}$ single crystal prepared by the Czochralski technique was pale yellow (Fig. 5). The crystal has no central core.

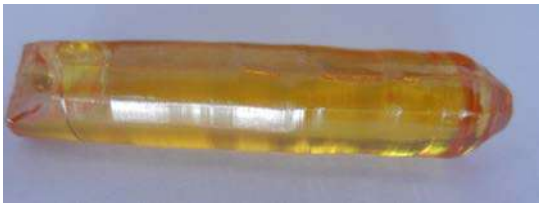

Fig. 5. Photographic image of the studied obtained crystal of $Bi_{12}GeO_{20}$.

4. Conclusions

In conclusion, the Czochralski technique has been used successfully to produce a $Bi_{12}GeO_{20}$ single crystal. The obtained crystal was studied by X-ray diffraction, Raman and FTIR spectroscopy. The single crystal structure $Bi_{12}GeO_{20}$ was confirmed by XRD. The Raman and FTIR spectroscopy results suggest that way synthesis leads to the formation of BGO, as seen by X-ray diffraction analysis. We observed 15 *Raman* and 5 *IR* modes. It can be concluded, that the obtained single crystal of BGO is pale yellow in colour and there is no central core.

Acknowledgements

This research was supported financially by the Ministry of Education, Science and Technological Development of the Republic of Serbia through Project No. III45003.

References

[1] V. N. Shlegel, D. S. Pantsurkin, Crystallogr. Rep. **56**, 339 (2011).
[2] V. M. Skorikov, Yu. F. Kargin, A. V. Egorysheva, V. V. Volkov, M. Gospodinov, Inorg. Mater. **41**, S24 (2005).
[3] S. F. Radaev, V.I. Simonov, Y. F. Kargin, Eur. J. Solid State Inorg. Chem. **29**, 383 (1992).
[4] D. Bloom, S. W. S. McKeever, J. Appl. Phys. **77**, 6511 (1995).
[5] S. L. Sochava, K. Buse, E. Krätzig, Phys. Rev. B **51**, 51 (1995).
[6] P. S. Yu, L. B. Su, H. L. Tang, X. Guo, H. Y. Zhao, Q. H. Yang, J. Xu, Sci. China Tech. Sci. **54**, 1287 (2011).
[7] V. N. Shlegel, D. S. Pantsurkin, Crystallography Reports **54**, 1261 (2009).
[8] A A. Golubovic, S. Nikolic, R. Gajic, S. Djuric, A. Valcic, J. Serb. Chem. Soc., **64**, 553 (1999).
[9] T. I. Milenov, P. M. Rafailov, R. Petrova, Y. F. Kargin, M. M.Gospodinov, Mater. Sci. Eng. B **138**, 35 (2007).
[10] W. Wojdowski, Crystals Phys. Status Solidi B **130**, 121 (1985).
[11] P. Beneventi, R. Cappalletti, L. Kovács, Á. Péter, A. M. Lanfredi Manotti, F. Ugozzoli, J. Phys. Condens. Matter. **6**, 6329 (1994).

*Corresponding author: lzorica@yahoo.com

Plasmon – ionized impurity – phonon interaction in PbTe doped with Ni

J. TRAJIĆ*, N. ROMČEVIĆ, M. ROMČEVIĆ, Z. LAZAREVIĆ, T. A. KUZNETSOVA[a], D. R. KHOKHLOV[a]
Institute of Physics, P.O. Box 68, University of Belgrade, 11080 Belgrade, Serbia
[a]Department of Physics, Moscow State University, 119899 Moscow, Russia

Vibrational properties of PbTe single crystals doped with Ni are determined using far – infrared spectroscopy in wide temperature range. Far – infrared reflection spectra were analyzed using a fitting procedure based on the modified plasmon – ionised impurity – phonon interaction model. Together with the strong coupling we obtained three local modes of Ni at about 130, 165 and 190 cm^{-1}, which correspond to the impurity atoms in different valence states. The positions of these modes depend on the impurity center charge, while their intensities depend on the temperature and Ni concentration.

(Received March 22, 2013; accepted July 11, 2013)

Keywords: Semiconductors, Crystal growth, Phonons, Plasmon – phonon interaction

1. Introduction

The coupling of elementary excitations in solids [1 – 3] and free – carrier absorption by phonon – ionised impurity – plasmon processes [4, 5] has been investigated by many authors. These processes are important for polar semiconductors with high static (lattice) dielectric constant and high carrier concentration. Free – carrier absorption consists then in individual – carrier excitations (individual – carrier scattering), as well as in collective carrier excitations (plasmon generation).

Photon – plasmon processes were studied, as a rule, in more general framework of photon – plasma – imperfection (deformation) interactions, where also individual – carrier excitations were taken into account [6 – 9]. Both nondegenerate and degenerate plasmas were considered. Usually, a theory is formulated starting from the knowledge of dielectric function for free carriers in perfect crystals. Phenomenological approach to this problem is formulated by several authors [9 – 11]. Our approach [10, 11] is based on creating specific dielectric function, which has to explain registered process, while comparisons with parameters obtained by classical approach [1, 2] yield the physical explanation of the processes that are taking place in the doped semiconductors.

The doping of $A^{IV}B^{VI}$ semiconductor compounds with transition metal impurities has significant scientific and practical interest due to the new materials preparing possibilities. Lead telluride (PbTe) belongs to the $A^{IV}B^{VI}$ IR – sensitive narrow – gap semiconductor group, which acquire new properties as a consequence of doping [12 – 14]. Electrical properties in such manner obtained materials strongly depend on the type and concentration of the added impurity. For instance, when PbTe is doped with chromium, free carrier concentration *n* increases to $1.3 \cdot 10^{19}$ cm^{-3}, and after that slowly decreases to $1.2 \cdot 10^{19}$ cm^{-3} with the further increase of the Cr concentration, up to the chromium solubility limit [14]. This means that Cr in small concentration enter the PbTe lattice as donor impurity in the 3+ state. Further, when concentration increases, we have both 3+ and 2+ (as neutral) states, and finally in highly doped semiconductor we have impurities in all three – valence states: 3+, 2+ and 1+ (as acceptor). The mentioned behaviour of transition elements causes strong correlation between an impurity center and the lattice. A change of the electronic state of the impurity center provokes a change of the frequency of the local mode [4].

In this paper, we present further studies of far – infrared reflection spectra of Ni doped PbTe single crystal samples. Ni doped PbTe crystals were already subject of our research. Considering our new experimental and theoretical work, we analyzed these spectra using a fitting procedure based on the modified plasmon – phonon interaction model. Also, we obtained three local modes of Ni, which correspond to the impurity atoms in different valence states.

2. Samples and experiment

Single crystals of PbTe(Ni) were grown by the Bridgman method in evacuated sealed 12 – 15 mm quartz tubes with a cone shaped lower end by moving in the temperature gradient of 15 – 20 K/cm. The impurity concentrations in the starting mixture were $3.3 \cdot 10^{20}$ and 4.6×10^{20} at./cm^3. The Ni concentration in the crystals used here were 1×10^{19} and 2×10^{19} at./cm^3 respectively, determined by chemical analysis. Solibility limit and segregation effect for Ni doped PbTe were discussed in more details in Ref. [15]. The structural characteristics were obtained by the XRD powder technique. All the samples were examined under the same conditions; using a Philips PW 1729 X –ray generator, a Philips 1710 difractometer and the original APD software. The

radiation source was an X–ray LLF tube with copper radiation and graphite monocromator. The radiations were $\lambda_{CuK\alpha 1}$ = 0.154178 and 0.154438 nm. The anode tube load was 40 kV and 30 mA. Slits of 1.0 and 0.1 mm were fixed. For product identification, the MPDS program and JCPDS (ASTM) (Joint Committed on Powder Diffraction Standards) cards files were used. The unit cell was calculated by the least square methods. All the registered reflections corresponded to PbTe crystals and gave the parameter of the cubic unit cell of a = 0.6455(3), which are in good agreement with values citied in literature [16]. The dislocation densities were $(5 – 7)\cdot 10^{-4}$ cm^{-2}, registered by selective etching [17].

The Hall effect and conductivity measurements showed that the both crystals exhibit n – type conductivity with room – temperature electron concentration of $6\cdot 10^{16}$ cm^{-3} (in sample with Ni concentration of $1\cdot 10^{19}$ at./cm^3) and $4\cdot 10^{16}$ cm^{-3} (sample with $2\cdot 10^{19}$ at./cm^3). The far – infrared measurements were carried out with a BOMEM DA - 8 FIR spectrometer. A DTGS pyroelectric detector was used to cover the wave number rang from 40 to 400 cm^{-1}.

3. Reflectivity analysis and fitting procedure

The theoretical model of the bulk dielectric function has been discussed by several authors [11, 18]. For a description of the PbTe optical properties simple model for dielectric function were used [19]:

$$\varepsilon = 1 + \chi_{valenceelectrons} + \chi_{polarphonon} + \chi_{freecarriers} \quad (1)$$

Interaction of electromagnetic radiation with plasmons in nonperfect lattices may become comparable or even higher than single – particle scattering [4]. This is especially the case for semiconductors with high – static dielectric constant. Because of that, the FIR spectra might be interpreted with the help of a frequency dependent dielectric function with no less than two classical oscillators ($l \geq 2$) corresponding to the TO modes superimposed by a Drude part taking into account the free carrier contribution [2, 3]:

$$\varepsilon(\omega) = \varepsilon_\infty + \sum_{k=1}^{l} \frac{\varepsilon_\infty\left(\omega_{LOk}^2 - \omega_{TOk}^2\right)}{\omega_{TOk}^2 - \omega^2 - i\gamma_{TOk}\omega} - \frac{\varepsilon_\infty \omega_P^2}{\omega(\omega + i\gamma_P)} \quad (2)$$

where ε_∞ is the bound charge contribution and it is considered as a constant, ω_{LOk} and ω_{TOk} are the longitudinal and transverse optical – phonon frequencies, ω_P is the plasma frequency, and γ_{TOk} and γ_P are the phonon and plasma damping.

In the doped PbTe – based systems the pure LO – modes ($\omega_{LO,PbTe}$) of the lattice are strongly influenced by the plasmon mode (ω_P) of free carriers. As a result a combined plasmon – LO phonon modes (ω_j, j = 1, 2) were observed [1], whereupon in the experimental spectra only coupled mode positions were observable. Therefore, the determination of LO mode is connected with the elimination of free carrier influence [9, 10, 20]. Impurity local modes have the same behaviour. This means that impurity local mode, characterized by its characteristic frequency ω_0, can interact with free carriers [21]. In this case there is no separation on TO and LO mode, and as a result, coupled frequency could appear [4, 21]. Considering this fact, in the analysis of reflectivity spectra of Ni doped PbTe we have decided to use dielectric function that takes into account the existence of free carriers – phonon interaction in advance [9]:

$$\varepsilon(\omega) = \varepsilon_\infty \frac{\prod_{j=1}^{2}\left(\omega^2 + i\gamma_{lj}\omega - \omega_{lj}^2\right)\cdot\prod_{k=1}^{n}\left(\omega^2 + i\gamma_{Lk}\omega - \omega_{Lk}^2\right)}{\omega^{n+1}(\omega + i\gamma_P)\left(\omega^2 + i\gamma_t\omega - \omega_t^2\right)\prod_{k=1}^{n}\left(\omega^2 + i\gamma_{0k}\omega - \omega_{0k}^2\right)}\prod_{m=1}^{s}\frac{\omega^2 + i\gamma_{LOm} - \omega_{LOm}^2}{\omega^2 + i\gamma_{TOm} - \omega_{TOm}^2} \quad (3)$$

In our case n is number of local phonons. The first term in Eq. 3 represents the coupling of one plasmon and n + 1 phonons, and second term represents the uncoupled modes of the crystal (s), while $l = n + s + 1$. The first term in Eq. 3 consist of two parts. The ω_{lj} (j = 1, 2), ω_t and γ_P represents plasma and PbTe LO phonon mode interaction (ω_{lj} and ω_t are frequencies and γ_P is damping).The second part of this term represents interaction between plasma and nickel local phonons, where the ω_{0k} (k = 1, n) is local phonon characteristic frequencies and ω_{Lk} is coupled frequency; γ_{0k} and γ_{Lk} are the damping. The second term represents uncoupled crystal modes, where the ω_{LOm} and ω_{TOm} are the longitudinal and transverse uncoupled modes frequencies, while γ_{LOm} and γ_{TOm} are damping.

The parameters adjustment was carried out automatically, by means of the least – square fitting of theoretical (R) and experimental (R_e) reflection coefficients at q arbitrarily taken points:

$$\sigma = \sqrt{\frac{1}{q}\sum_{j=1}^{q}\left(R_{ej} - R_j\right)^2}, \quad (4)$$

where:

$$R = \left|\frac{\sqrt{\varepsilon} - 1}{\sqrt{\varepsilon} + 1}\right|^2 \quad (5)$$

and ε is given by Eq. 3. The value of σ was minimized until it became comparable with the usual experimental error (less than 2%). The cross – sections of multi – dimensional $\sigma(\omega_j, \gamma_j)$ surface were calculated, multiplying each parameter alternately by a varying factor $(1 \pm \delta)$ while all the others were fixed on a determined level. Such sections gave evidence of the precision of the analyses. Practically, for all samples the determination errors of the eigenfrequencies and damping coefficients were in the range of 3 – 6 % and 10 – 15 %, respectively.

4. Results and discussion

The far – infrared reflection spectra of PbTe(Ni) with Ni concentration of 1×10^{19} (a) and 2×10^{19} at./cm^3 (b) single crystals in the temperature range from 80 to 300 K, and spectral range from 40 – 400 cm^{-1} are shown in Fig. 1.

The experimental data are marked by circles. The solid line was obtained using the dielectric function from Eq. 3, where $n = 1$ (Fig. 1.a) and $n = 3$ (Fig. 1.b). This means that in the sample with 1×10^{19} at./cm^3, besides PbTe TO/LO pair exists one Ni local phonon which also interacts with free carriers, while in sample with $2\cdot10^{19}$ at./cm^3 where Ni existed in the three valence states, there are three Ni local phonons participating in the interaction. Mode at about 73 cm^{-1} ($s = 1$ in Eq. 3), denoted with x in Fig. 1.a, is well known PbTe Brillouin zone edge mode [20].

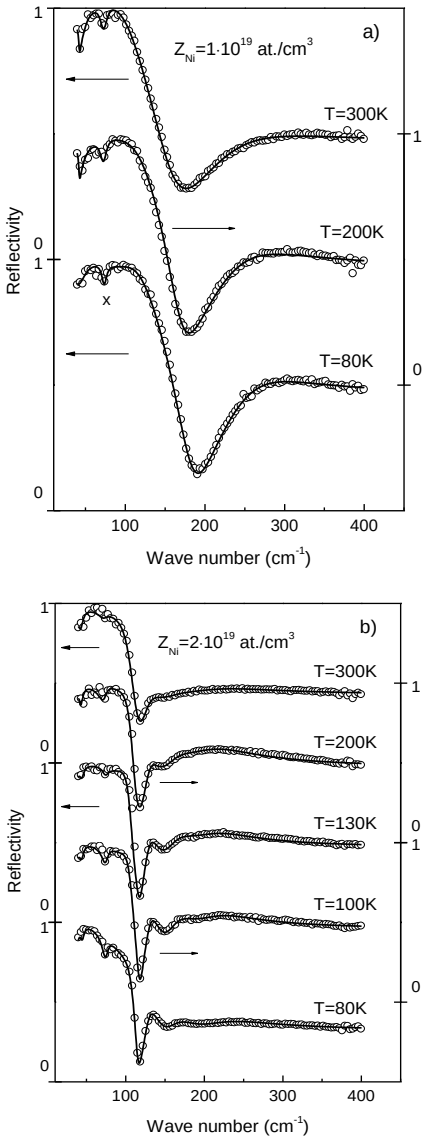

Fig. 1. Far – infrared reflection spectra of PbTe(Ni) single crystals: $Z_{Ni} = 1\cdot10^{19}$ at./cm^3 (a) and $2\cdot10^{19}$ at./cm^3 (b) in the temperature range from 80 to 300 K. Experimental spectra are presented by circles. Solid line is calculated spectra obtained by the fitting procedure based on the model for plasmon – phonon coupling (Eq. 3): (a) n = 1, s = 1and (b) n = 3, s = 1.

Theoretical spectra fit experimental results very well. In Figs. 2 and 3 characteristic spectra for plasmon – phonon interaction are presented. Obtained results describe the relationship between the results obtained on the basis of Eq. 3 and of the traditional approach presented with Eq. 2. Interactions that correspond to different Ni concentrations are represented in figures. Thus, in Fig. 2, interaction of one plasmon with PbTe TO/LO pair and one Ni local phonon is presented, and in Fig. 3 is presented interaction of plasmon – PbTe TO/LO pair and three Ni local phonons. The solid line, in all figures, represents coupled frequencies, and as it was given in [9] the positions of the coupled mode were defined as the solutions of Eq. 2 ($\mathrm{Re}\{\varepsilon\} = 0$). Dashed lines, obtained experimentally as the best fit, correspond to TO phonon positions, Ni local phonon characteristic frequencies (ω_{0k}, $k = 1, 3$) and well – known value for PbTe LO phonon [24]. Positions of coupled frequencies, obtained as the best fit using the appropriate Eq. 3, are presented as symbols: the solid circles (●) refer to Ni local frequencies and stars (∗) to PbTe TO phonon and squares (□) to PbTe LO phonons. The obtained results can be explained in the following way: Ni in PbTe substitutes the Pb, and Ni is a substitution impurity ion. The impurity mode can arise simply due to the difference between masses and force constants of the impurity ion and the ion of the host material [21], or their appearance can be caused by more complex mechanism of electron – phonon interaction [7, 8, 22]. Taking into account the change of mass and force constants between an impurity and its surrounding, we have demonstrated that this is the case of the Ni impurity local modes. That is, if the semiconductor is doped with a substitution impurity [21] (in this case Ni), when substitution of the heavier mass (Pb) is made by a lighter impurity, one gets two modes: a local mode situated above the optical band and a gap mode situated above the acoustic band but below the optical band of the host lattice. Ni impurity modes are situated above the PbTe host optical band (Figs. 2 and 3), so they are local modes.

Taking into account both the FIR and Hall measurements, we assume that in the case of very low concentration, Ni enters in PbTe lattice as a donor impurity in Ni^{3+} state. With further increase of Ni concentration, free carrier concentration stays the same, like in the case of Cr impurities [23]. So, we can conclude that Ni enters as a Ni^{3+} (as a donor) and as a Ni^{2+} (as a neutral) [24]. Further Ni concentration increasing causes the appearance of another local phonon, which corresponds to Ni^{1+} (acceptor state). The mentioned electronic behaviour of Ni dopant causes strong change in correlation between an impurity center and a lattice. A change of the electronic state of an impurity center leads to a change of a force constant between an impurity atom and a lattice, which leads to the changing of the local mode frequency. According to our results, and results for PbTe doped with III group of elements [25, 26], we concluded that mode at about 190 cm^{-1} (which is seen for both samples) corresponds to Ni^{3+}; mode at about 130 cm^{-1} corresponds to Ni^{2+} (narrow line) and mode at about 165cm^{-1} to Ni^{1+}. Registered mode frequencies are between the characteristic Ga and In frequencies [25 – 27], but they do not satisfy the isotopic effect, which is consequence of the interaction between an impurity center and a lattice.

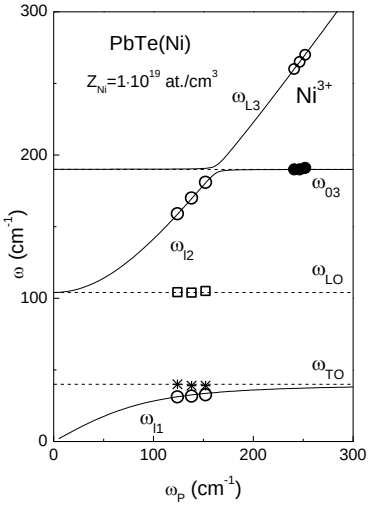

Fig. 2. The eigenfrequencies of the plasmon – phonon modes for single crystal PbTe(Ni) with $Z_{Ni} = 1 \cdot 10^{19}$ at./cm^3: the solid lines are calculated spectra [Re{ε} = 0; ε is given by Eq. 2, l = 3]; ● – ω_{03}; ○ - ω_{l1}, ω_{l2} and ω_{L3} (Eq3); ∗ – experimentally determined values for ω_{TOPbTe}; □ – ω_{LOPbTe}. Dashed lines are visual aid.

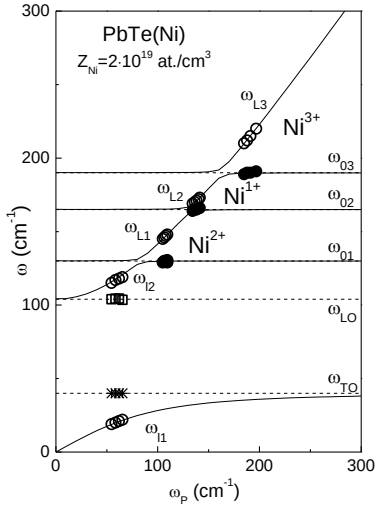

Fig. 3. The eigenfrequencies of the plasmon – phonon modes for single crystal PbTe(Ni) with $Z_{Ni} = 2 \cdot 10^{19}$ at./cm^3: the solid lines are calculated spectra [Re{ε}=0; ε is given by Eq. 2, l = 5]; ● – ω_{01}, ω_{02}, ω_{03}; ○ – ω_{l1}, ω_{l2}, ω_{L1}, ω_{L2} and ω_{L3} (Eq. 3); ∗ - experimentally determined values for ω_{TOPbTe} and □ - ω_{LOPbTe}. Dashed lines are visual aid.

We presumed that PbTe phonons interact with plasma only, e.g. this interaction is not influenced by impurity centers directly. Therefore, we can determine the value of the LO phonon and the plasma frequency, as described in Ref. 10. Since the calculated value for the LO phonon coincides with the values from the literature, we conclude that this approach was justified. If we followed the described procedure for the local phonons of Ni also, e.g. if we join positions of the coupled phonons with, by this manner, calculated plasma, we would obtain large difference for values of coupled frequencies calculated from Eq. 2 and Eq. 3. That is the reason why we positioned coupled frequencies on the theoretical curves, and then we read the value of the plasma frequency. We observe linear shift of the plasma frequency values when the ionisation state of the impurity center increases. Hereby, the interaction between ionised center and the free carriers becomes stronger. One of the mechanisms that can describe this situation is related with changes of the density of the free carriers in the vicinity of the ionised center [3]. Besides, it is possible that near ionised centre different plasma modes are formed. In former case, the Coulomb interaction of different plasma modes forms in the limits of one energy band the single collective excitation, which is displayed in our spectra with an eigenfrequency equal to

$$\omega_P = \left[\sum_{j=1}^{m} \omega_{jP}^2 \right]^{1/2} \tag{6}$$

Assume that in this case free carriers are in a some way tied to close neighbourhood around the charged impurity center. Also, we shall assume that here we have a two – component plasma around each impurity center, where one component is determined from PbTe coupling. Calculated values of the second component of the corresponding impurities centers, at T = 300K, are given in Table 1.

Table 1. Calculated values for the two – component plasma based on Eq. 6.

PbTe(Ni)	ω_{1P} [cm^{-1}]	**Ni^{1+}** - ω_{2P} [cm^{-1}]	**Ni^{2+}** - ω_{2P} [cm^{-1}]	**Ni^{3+}** - ω_{2P} [cm^{-1}]
1×10^{19} at./cm^3	152	—	—	187
2×10^{19} at./cm^3	65	126	88	186

Obtained results should be understood only qualitatively. Namely, noticed plasmon – ionised impurity – phonon interaction can be described in several manners [see for example Refs. 4, 7, 8, 19, 21]. However, in all cases the increase in the amount of interaction must be

observed, while the ionisation state of the impurity center increases, as well as its local character.

5. Conclusion

As a method to investigate phonon properties of Ni doped PbTe single crystals we used far – infrared spectroscopy. We obtained three local modes of Ni at about 130, 165 and 190 cm^{-1}, which corresponded to the impurity atoms in different valence states. The positions of these modes depend on impurity centre charge, and their intensities depend on temperature and Ni concentration. We also revealed that in this system plasmon – ionised impurity – phonon coupling existed.

Acknowledgements

This work was supported by the Serbian Ministry of Education, Science and Technological Development (Project III45003).

References

[1] S. Takaoka, T. Hamaguchi, S. Shimomura, K. Murase, Solid State Commun. **54**, 99 (1985).
[2] V. Gopal, Infrared phys. **18**, 121 (1978).
[3] M. Cardona, G. Gunterodt (Eds.), Light Scattering in Solids, Top. Appl. Phys., **8**, Springer, Berlin, 1975.
[4] J. Mycelski, A. Mycelski, Phys. Rev. B. **18**, 1859 (1978).
[5] A. Ron, N. Tzoar, Phys. Rev. **131**, 12 (1963).
[6] E–Ni Foo, N. Tzoar, Phys. Rev. **187**, 1000 (1969).
[7] D. E. McCumber, Phys. Rev. **154**, 790 (1967).
[8] D. E. McCumber, Rev. Mod. Phys. **38**, 494 (1966).
[9] A. A. Kuharskii, Solid State Commun. **8**, 1275 (1970).
[10] J. Trajić, N. Romčević, M. Romčević, V. N. Nikiforov Materials Research Bulletin **42**, 2192 (2007).
[11] M. A. Kinch, D. D. Buss, Solid State Commun. **11**, 319 (1972).
[12] B. A. Volkov, O. M. Ruchaiskii, Pis'ma Zh. Eksp. Teor. Fiz. 62**,** 205 (1995) [JETP Lett. 62**,** 217 (1995)].
[13] D. R. Khokhlov, B. A. Volkov, in Proc. of the 23rd Inter. Conf. On the Phys. Of Semiconductors, July 21–26, Berlin, Vol. **4** ed., M. Schefler Singapore: World Scientific, 1996 p. 2941.
[14] J. Trajić, M. Romčević, N. Romčević, A. Golubović, S. Đurić, V. N. Nikiforov, Journal of Alloys and Compounds **365**, 89 (2004).
[15] V. P. Zlomanov, T. A. Kuznetsova, S. G. Dorofeev, V. D. Volodin, O. I. Tananaeva, Crystallogr. Rep. **47**, (Suppl. 1) 128 (2002).
[16] JCPDS card number 38 – 1435.
[17] O. N. Krylyuk, A. M. Gas'kov, V. P. Zlomanov, Vestn. Mosk. Univ., Ser. 2: Khim., **6**, 571 (1986).
[18] E. Burstein, A. Pinczuk, R. F. Wallis, in: D. L. Carter, R. T. Bate (Eds.), The Physics of Semimetals and Narrow–Gap Semiconductors, Pergamon, New York, 1971, p. 251.
[19] H. Burkhard, G. Bauer, A. Lopez–Otero, Phys. Rev. B. **18**, 2935 (1978).
[20] N. Romčević, A. Golubović, M. Romčević, J. Trajić, S. Nikolić, S. Đurić, V. N. Nikiforov, J. Alloys and Compounds **402**, 36 (2005).
[21] A. A. Maradudin, in F. Seitz, D. Turnball (Eds.), Solid State Physics, vol. **19**, New York, Academic, 1966.
[22] N. Romčević, J. Trajić, A. T. Kuznetsova, M. Romčević, B. Hadžić, D. R. Khokhlov, Journal of Alloys and Compounds, **442**, 324 (2007).
[23] B. A. Akimov, P. B. Verteleckii, V. P. Zlomanov, L. I. Ryabova, O. I. Tananaeva, N. A. Shirokova, Phys. Techn. of Semiconductors **23**, 244 (1989).
[24] B. A. Volkov, L. I. Ryabova, D. R. Khoklov, Physics – Uspekhi **45**, 819 (2002).
[25] N. Romčević, M. Romčević, D. R. Khokhlov, A. I. Belogorokhov, I. I. Ivanchik, W. Konig, Infrared Physisc and Technology **40**, 453 (1999).
[26] M. Romčević, N. Romčević, D. R. Khokhlov, I. I. Ivanchik, J. Phys.: Condens. Matter **12**, 8737 (2000).
[27] N. Romčević, Z. V. Popović, D. R. Khokhlov, J. Phys.: Condens. Matter **4**, 4323 (1992).

*Corresponding author: jelena@ipb.ac.rs

Ferroelectrics, 448:1–11, 2013

ISSN: 0015-0193 print / 1563-5112 online
DOI: 10.1080/00150193.2013.822257

Taylor & Francis
Taylor & Francis Group

Study of $NiFe_2O_4$ and $ZnFe_2O_4$ Spinel Ferrites Prepared by Soft Mechanochemical Synthesis

Z. Ž. LAZAREVIĆ,[1,*] Č. JOVALEKIĆ,[2] A. MILUTINOVIĆ,[1] D. SEKULIĆ,[3] M. SLANKAMENAC,[3] M. ROMČEVIĆ,[1] AND N. Ž. ROMČEVIĆ[1]

[1]Institute of Physics, University of Belgrade, Pregrevica 118 Zemun, Belgrade, Serbia
[2]The Institute for Multidisciplinary Research, University of Belgrade, Belgrade, Serbia
[3]Faculty of Technical Sciences, University of Novi Sad, Novi Sad, Serbia

Two types of ferrites, $NiFe_2O_4$ and $ZnFe_2O_4$ were prepared by soft mechanochemical synthesis. XRD and Raman spectroscopy were used to characterize the ferrite samples. On the basis of magnetic measurements was confirmed that the degree of inversion changes after sintering. The conduction activation energy, ΔE was determined by fitting the DC conductivity data with the Arrhenius relation. The effect of temperature on impedance parameters was studied using an impedance analyzer in a wide frequency range (100 Hz - 10 MHz). It was observed that the impedance spectra of $NiFe_2O_4$ and $ZnFe_2O_4$ ferrites include both grain and grain boundary effects.

Keywords Ferrites; XRD; Raman spectroscopy; magnetic measurements; impedance spectroscopy

I. Introduction

The spinel ferrites have attracted considerable attention owing to their technological importance in the application areas, such as microwave devices-microwave absorbers and waveguides in the GHz region, high speed digital tape and disk recording, repulsive suspension for use in levitated systems, ferrofluids, catalysis, and magnetic refrigeration systems [1].

It is well know that properties of ferrite materials strongly depend on the preparation conditions. Consequently, different preparation methods for ferrite are described in the literature [2–4]. By choosing the method that reduces particle size, magnetic properties (such as coercive field, Curie temperature, saturation magnetization and absorption coefficients) may change significantly in comparison with the bulk material.

Ferrites with the spinel ferrite structure contain all the material as MFe_2O_4 (normal spinel $M[Fe_2]O_4$, where M as Zn, Cd, and Ca and inverse spinel $Fe[MFe]O_4$ where M as Ni, Co, Fe, Mn, Cu). Spinel ferrite crystal structure possesses the space group, *Fd3m*, structure and consists of 56 atoms; 32 are oxygen anions assuming a close packed cubic

Received September 14, 2012; in final form March 3, 2013.
*Corresponding author: Tel.: +381 11 37 13 035; Fax: +381 11 3160 531. E-mail: lzorica@yahoo.com

GFER #822257, VOL 00, ISS 00

Study of $NiFe_2O_4$ and $ZnFe_2O_4$ Spinel Ferrites Prepared by Soft Mechanochemical Synthesis

Z. Ž. LAZAREVIĆ, Č. JOVALEKIĆ, A. MILUTINOVIĆ, D. SEKULIĆ, M. SLANKAMENAC, M. ROMČ EVIĆ AND N. Ž.ROMČ EVIĆ

QUERY SHEET

This page lists questions we have about your paper. The numbers displayed at left can be found in the text of the paper for reference. In addition, please review your paper as a whole for correctness.

There are no Editor Queries for this paper.

TABLE OF CONTENTS LISTING

The table of contents for the journal will list your paper exactly as it appears below:

Study of $NiFe_2O_4$ and $ZnFe_2O_4$ Spinel Ferrites Prepared by Soft Mechanochemical Synthesis
Z. Ž. Lazarević, Č. Jovalekić, A. Milutinović, D. Sekulić, M. Slankamenac, M. Romč Ević and N. Ž.Romč Ević

Ferroelectrics, 00:1–11, 2013

ISSN: 0015-0193 print / 1563-5112 online
DOI: 10.1080/00150193.2013.822257

Taylor & Francis
Taylor & Francis Group

Study of $NiFe_2O_4$ and $ZnFe_2O_4$ Spinel Ferrites Prepared by Soft Mechanochemical Synthesis

Z. Ž. LAZAREVIĆ,[1,*] Č. JOVALEKIĆ,[2] A. MILUTINOVIĆ,[1] D. SEKULIĆ,[3] M. SLANKAMENAC,[3] M. ROMČEVIĆ,[1] AND N. Ž. ROMČEVIĆ[1]

[1]Institute of Physics, University of Belgrade, Pregrevica 118 Zemun, Belgrade, Serbia
[2]The Institute for Multidisciplinary Research, University of Belgrade, Belgrade, Serbia
[3]Faculty of Technical Sciences, University of Novi Sad, Novi Sad, Serbia

Two types of ferrites, $NiFe_2O_4$ and $ZnFe_2O_4$ were prepared by soft mechanochemical synthesis. XRD and Raman spectroscopy were used to characterize the ferrite samples. On the basis of magnetic measurements was confirmed that the degree of inversion changes after sintering. The conduction activation energy, ΔE was determined by fitting the DC conductivity data with the Arrhenius relation. The effect of temperature on impedance parameters was studied using an impedance analyzer in a wide frequency range (100 Hz - 10 MHz). It was observed that the impedance spectra of $NiFe_2O_4$ and $ZnFe_2O_4$ ferrites include both grain and grain boundary effects.

Keywords ferrites; XRD; Raman spectroscopy; magnetic measurements; impedance spectroscopy

I. Introduction

The spinel ferrites have attracted considerable attention owing to their technological importance in the application areas, such as microwave devices-microwave absorbers and waveguides in the GHz region, high speed digital tape and disk recording, repulsive suspension for use in levitated systems, ferrofluids, catalysis, and magnetic refrigeration systems [1].

It is well know that properties of ferrite materials strongly depend on the preparation conditions. Consequently, different preparation methods for ferrite are described in the literature [2–4]. By choosing the method that reduces particle size, magnetic properties (such as coercive field, Curie temperature, saturation magnetization and absorption coefficients) may change significantly in comparison with the bulk material.

Ferrites with the spinel ferrite structure contain all the material as $M Fe_2O_4$ (normal spinel $M[Fe_2]O_4$, where M as Zn, Cd, and Ca and inverse spinel $Fe[MFe]O_4$ where M as Ni, Co, Fe, Mn, Cu). Spinel ferrite crystal structure possesses the space group, *Fd3m*, structure and consists of 56 atoms; 32 are oxygen anions assuming a close packed cubic

Received September 14, 2012; in final form March 3, 2013.
*Corresponding author: Tel.: +381 11 37 13 035; Fax: +381 11 3160 531. E-mail: lzorica@yahoo.com

structure of lattice parameter $a_0/2$, where a_0 is the length of a ferrite unit structure, and the remainder are metal cations residing on 8 of the 64 available tetrahedral (A) sites and 16 of the 32 available octahedral [B] sites. Depending on cation distribution, a spinel can be *normal*, *inverse*, or *partially inverse*. Both, normal ($ZnFe_2O_4$) and inverse ($NiFe_2O_4$) ferrites are the most important ferrite binary oxides with the spinel structure, and are usually as a ferrimagnet with the strong dependence of magnetic properties on the state of chemical order and the cation site occupancy in the materials [5, 6]. The structural formulas are generally written as $(M^{2+}{}_{1-\lambda}Fe^{3+}{}_{\lambda})[M^{2+}{}_{\lambda}Fe^{3+}{}_{2-\lambda}]O_4$, where round and square brackets denote sites of tetrahedral (A) and octahedral [B] coordination, respectively, and where λ represents the degree of inversion defined as the fraction of the (A) sites occupied by Fe^{3+}. The presentations of the unit cells of the $NiFe_2O_4$ and $ZnFe_2O_4$ spinel structure show in Fig. 1.

Many techniques were applied for the synthesis of *M*-type ferrites, e.g. co-precipitation, low-temperature combustion-synthesis, sol-gel, mechanical alloying, mechanical activation and solid-state synthesis. The mechanochemical synthesis can deliver the designed phases and structures in a single-step with high-energy milling conducted in an enclosed activation chamber at room temperature [7]. Usually, the compete formation of spinel ferrites was obtained only after milling followed by sintering, i.e. by employing two processing steps. It has been shown that the combined mechanochemical-thermal treatment yields a well-ordered spinel phase in ferrites at lower annealing temperatures and shorter durations than those required in conventional ceramic methods [8]. Of course, in such case the morphology of crystallite, agglomerate and particle is changed significantly.

A mechanochemical method, especially so-called a soft mechanochemical method has a great potential for the synthesis of inorganic precursors because of its versatility and simple operational requirements [9]. Soft mechanochemical reactions usually utilize surface hydroxyl groups, adsorbed, hydrated or contained in a hydroxide. Mechanochemical reactions then occur more beneficially as a consequence of polarization of surface hydroxyl groups. Charge transfer across the boundary of dissimilar solid species is, then, promoted, enabling formation of hetero bridging bonds between two different metallic species abridged by an oxygen atom in between. Bridging bonds in turn increase homogeneity of the reacting mixture and favour to keep the stoichiometry, being decisive for phase purity. This is reflected primarily in the simplicity of the procedure and equipment used [7]. In many cases, when it comes to classical synthesis reaction sintering process, requires high temperatures, which can present an additional problem in industrial production. Mechanochemical derived precursors exhibit significantly higher reactivity and thus lower the calcination and sintering temperature.

In this article, we investigated sintered samples of $NiFe_2O_4$ and $ZnFe_2O_4$ ferrites prepared by soft mechanochemical treatment, via high-energy milling of binary hydroxide precursors. In both cases, soft mechanochemical reaction leading to formation of the spinel phase was followed by X-ray diffraction and Raman spectroscopy. The magnetic measurements at room temperature are done in magnetic fields up to about $\pm 80\ kA\ m^{-1}$. The electric property of the synthesized ferrites has been analyzed by impedance spectroscopy.

2. Experimental Procedure

For mixtures of crystalline powders, denoted by case (1) and (2), the starting material were: (1) nickel(II)-hydroxide ($Ni(OH)_2$, Merck 95% purity) and $Fe(OH)_3$ and (2) zinc(II)-hydroxide ($Zn(OH)_2$, Merck 95% purity) and $Fe(OH)_3$ in equimolar ratio. The $Fe(OH)_3$

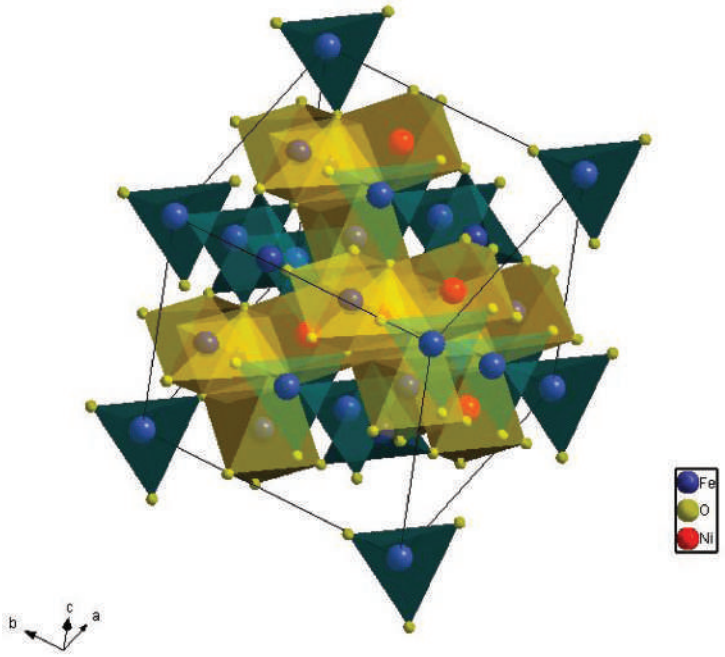

(a)

4C/Art

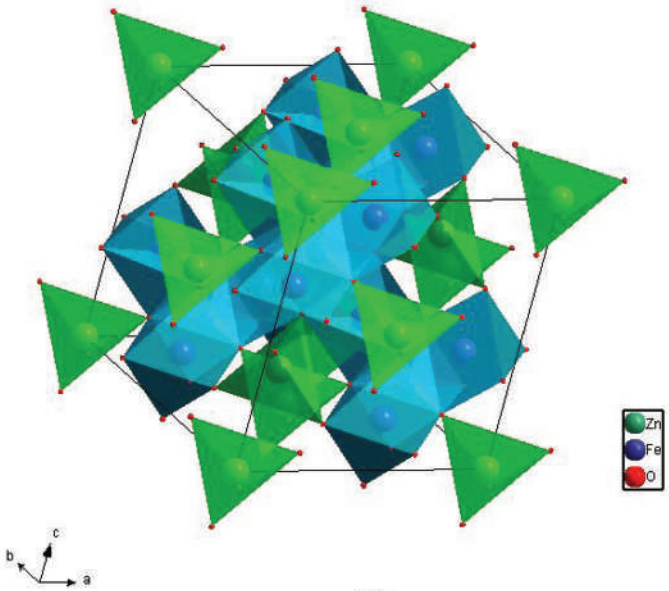

(b)

Figure 1. Schematic presentation of the unit cell of the spinel structure of (a) $NiFe_2O_4$ and (b) $ZnFe_2O_4$ ferrites (Color figure available online).

powder was made by adding equimolar amounts of NaOH solution (25% mass), made from 99% purity NaOH (Merck) to the $FeCl_3$ solution (25% mass), made from 99% purity $FeCl_3 \times 6H_2O$ (Merck) [10]. Soft mechanochemical synthesis was performed in an air atmosphere in a planetary ball mill (Fritsch Pulverisette 5) for 25 h (case 1) and 18 h (case 2). A hardened-steel vial of 500 cm^3 volume, filled with 40 hardened steel balls with a diameter of 13.4 mm, was used as the milling medium. The mass of the powder was 20 g and the balls-to-powder mass ratio was 20:1. The powder mixture was pressed into a pellet using a cold isostatic press (8 mm in diameter and ∼3 mm thick). The powder mixture was sintered at 1100 °C for 2 h (Lenton-UK oven) without pre-calcinations step. Heating rate was 10 °C min^{-1}, with nature cooling in air atmosphere.

The formation of phase and crystal structure of sintered powders of $NiFe_2O_4$ and $ZnFe_2O_4$ were examined via the X-ray (XRD). Model Philips PW 1050 diffractometer equipped with a PW 1730 generator (40 kV × 20 mA) was used with Ni filtered CoKα radiation of 1.78897 Å at the room temperature. Measurements were done in 2θ range of 10–80° with scanning step width of 0.05° and 10 s scanning time per step.

Raman measurements of the powder mixtures and sintered samples were performed using a Jobin-Ivon T64000 monocromator. An optical microscope with 100x objective was used to focus the 514 nm radiation from a Coherent Innova 99 Ar^+ laser on the sample. The same microscope was used to collect the backscattered radiation. The scattering light dispersed was detected by a charge-coupled device (CCD) detection system. Room temperature Raman spectra are in the spectral range from 100 to 800 cm^{-1}.

The magnetization measurements were done at room temperature using VSM (vibrating sample magnetometer) 200 cryogenic magnetometer in magnetic field from 0 A m^{-1} to $\pm$ 6.4 × 10^6 A m^{-1}.

The electrical DC resistivity/conductivity in the temperature range 298–423 K was measured on a SourceMeter Keithley 2410. Impedance measurements were carried out in the frequency range 100 Hz to 10 MHz on a HP-4194A impedance/gain-phase analyzer using a HP-16048C test fixture at the temperature of 298–423 K.

3. Results and Discussion

Figure 2 shows the X-ray diffraction patterns of $NiFe_2O_4$ and $ZnFe_2O_4$ samples sintered at 1100°C for 2h. All detected peaks in both case clearly pointed to the formation of the spinel phase of $NiFe_2O_4$ (JCPDS card 89–7412) and $ZnFe_2O_4$ (JCPDS card 89–7412). The peaks are well indexed to the crystal plane of spinel ferrites (*k h l*) (111), (220), (311), (222), (400), (422), (511) and (440). The average grains size, measured from the FWHM of (311) peak using Scherrer formula [11–13] were about 91 nm for $NiFe_2O_4$ and 48 nm for $ZnFe_2O_4$.

Raman spectroscopy is a nondestructive material characterization technique and is sensitive to structural disorder. It provides an important tool to probe the structural properties of mechanochemically synthesized materials. There are five first order Raman active modes ($A_{1g} + E_g + 3F_{2g}$) in the normal spinel structure, and all these modes were observed at ambient conditions, as shown in Fig. 3. The A_{1g} mode is due to symmetric stretching of oxygen atoms along Fe-O (or *M*-O) tetrahedral bonds, E_g and $F_{2g}(3)$ are due to symmetric and asymmetric bending of oxygen with respect to Fe (*M*), respectively and $F_{2g}(2)$ is due to asymmetric stretching of Fe (*M*) - O bond, $F_{2g}(1)$ is due to translational movement of the whole tetrahedron. Raman spectrum of sintered $ZnFe_2O_4$ ferrite exhibits a normal spinel structure with symmetric peaks. In the case of the $NiFe_2O_4$ all five Raman peaks seem asymmetric (or dissociated). Deconvolution of the spectrum demonstrates that each peak

4C/Art

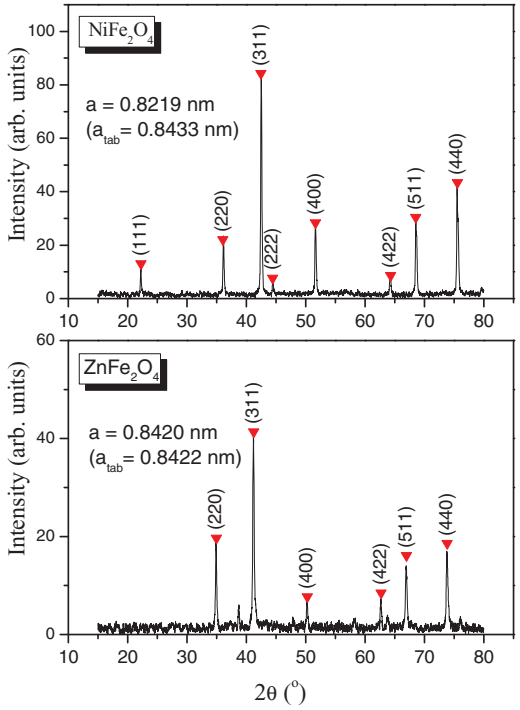

Figure 2. X-ray diffraction patterns of the $NiFe_2O_4$ and $ZnFe_2O_4$ ferrites (Color figure available online).

4C/Art

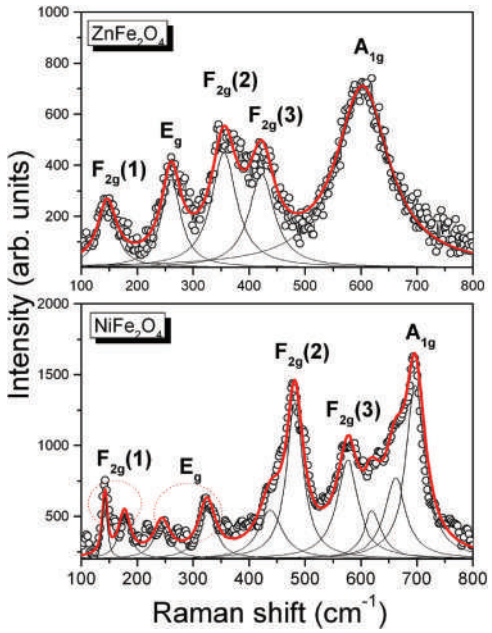

Figure 3. Raman spectra of the $NiFe_2O_4$ and $ZnFe_2O_4$ ferrites (Color figure available online).

4C/Art

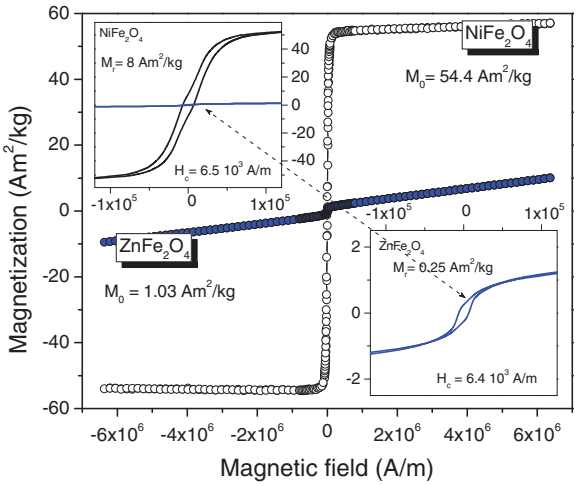

Figure 4. The magnetic hysteresis curves of the $NiFe_2O_4$ and $ZnFe_2O_4$ ferrites. The insets show low magnetization behavior (Color figure available online).

can be represented as a doublet, which is a characteristic of the inverse spinel structure [14, 15].

The magnetization curves of the nickel and zinc ferrites measured at room temperature are shown in Fig. 4. We have characterized the magnetic behavior of mechano-synthesized $NiFe_2O_4$ and $ZnFe_2O_4$ focusing on the study of the size-dependent magnetization. These measurements have revealed that the magnetic behavior of soft mechanochemical synthesized $NiFe_2O_4$ is different from that of the $NiFe_2O_4$ powder prepared using the conventional ceramic method. As can be seen (Fig. 4), the magnetization of the mechanochemical synthesized sample does not saturate even at the maximum field attainable ($H_{ext} = 6.4 \times 10^6$ A m^{-1}). This is in contrast to the magnetic behavior of the bulk $NiFe_2O_4$, whose magnetization reaches a saturation value easily. An absence of saturation can be attributed to the effect of spin canting. Even in sintered mechano-synthesized nickel ferrite, the surface/volume ratio is rather great and the dangling bonds (uncompensated electrons) at the surface of the particles can contribute to magnetization.

The measurement of the coercivity warrants the determination of the magnetization response with better accuracy and resolution particularly at small applied fields. Hence, a separate set of hysteresis curves was showed for each sample with an applied field of -1.2×10^5 A m^{-1} to 1.2×10^5 A m^{-1} at room temperature (the *inset M–H* curves in Fig. 4). The hysteresis curve at low applied fields shows the values of the coercive field, $H_c \approx 6.4 \times 10^3$ A m^{-1} and the remanent magnetization, $M_r \approx 8$ A m^2 kg^{-1} and $M_r \approx 0.25$ A m^2 kg^{-1} for sample of $NiFe_2O_4$ and $ZnFe_2O_4$, respectively. The extrapolated magnetization M_0 measured on the $NiFe_2O_4$ spinel ferrite obtained by a soft mechanochemical synthesis is higher than that for spinel ferrites produced by other methods [16].

The magnetic properties of the $NiFe_2O_4$ with an inverse spinel structure can be explained in terms of the cations distribution and magnetization originates from Fe^{3+} ions at both tetrahedral and octahedral sites and Ni^{2+} ions in octahedral sites. Hysteresis loops in Fig. 4 are typical for soft magnetic materials and the "S" shape of the curves together with the negligible coercivity ($H_c \approx 6.5 \times 10^3$ A m^{-1}) indicate the presence of small magnetic

particles exhibiting superparamagnetic behaviors. In superparamagnetic materials, responsiveness to an applied magnetic field without retaining any magnetism after removal of the magnetic field is observed. This behavior is an important property for magnetic targeting carriers. In fact, the difference between ferromagnetism and superparamagnetism fabricates in the particle size. Literature data imply that when the diameter of particles is less than 50 nm, the particles show the character of superparamagnetism.

Figure 4 shows the tiny magnetic hysteresis loop for $ZnFe_2O_4$ sample. The curve is "S" shape with low coercivity (6.4×10^3 A m^{-1}) and extremely small remanence magnetization. This sample shows superparamagnetic behavior superposed to paramagnetic behavior. In fact, the magnetic behavior of zinc ferrite is very sensitive to the crystallinity and particle and grain size [17]. Greater particle size (and smaller tension inside the particle) implies a structure that is closer to normal spinel structure: this means that Fe is only in the octahedral positions, with very low exchange interaction. The bulk zinc ferrite is paramagnetic at ambient temperature.

The increase in electrical conductivity σ_{DC} with temperature is due to the increase in the thermally activated drift mobility of charge carriers according to the hopping conduction mechanism. The activation energy for the thermally activated hopping process was obtained by fitting the DC conductivity data with the Arrhenius relation [18]

$$\sigma_{DC}(T) = \sigma_0 \exp\left(-\frac{\Delta E}{kT}\right),$$

where σ_0 is the pre-exponential factor with the dimensions of $(\Omega\text{cm})^{-1}\text{K}$, ΔE is the activation energy for DC conductivity, T is the absolute temperature and k is the Boltzmann's constant. The slope of the $\log(\sigma_{DC})$ versus $(1/T)$ straight line is a measure of activation energy of the $NiFe_2O_4$ and $ZnFe_2O_4$ ferrites. By using Arrhenius equation, the determined values of the conduction activation energy ΔE are 0.452 eV and 0.395 eV for $NiFe_2O_4$ and $ZnFe_2O_4$, respectively. If we analyze the obtained values for the conduction activation energy, one can see that $NiFe_2O_4$ has a higher value compared to $ZnFe_2O_4$ sample. This showed that more energy is required for electron exchange between Fe^{2+} and Fe^{3+} ions for the $NiFe_2O_4$. As shown in Fig. 5, $NiFe_2O_4$ has a lower DC conductivity than $ZnFe_2O_4$. It is in good accordance with the fact that the higher activation energy is associated with

4C/Art

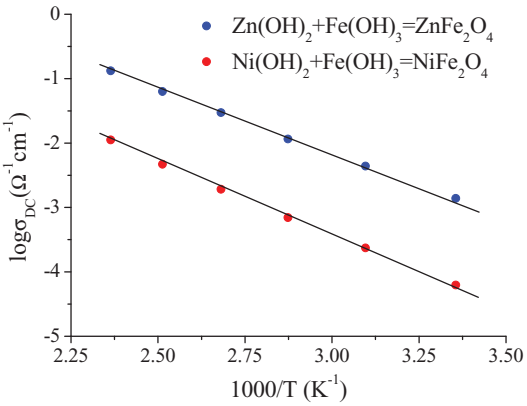

Figure 5. Temperature dependence of DC electrical conductivity on $NiFe_2O_4$ and $ZnFe_2O_4$ ferrites at different temperatures (Color figure available online).

the lower electrical conductivity. Also, there is no remarkable change in the slope in the measured temperature range for both samples.

Complex impedance spectroscopy [19] is a powerful technique in solid states because of its ability to understand the electrical conduction mechanism of the synthesized materials. In the present analysis, the impedance spectroscopy has been used as a well-developed tool to separate out the grain/bulk and grain boundary contribution to the total conductivity of $NiFe_2O_4$ and $ZnFe_2O_4$ ferrite. Depending on the electrical properties of the samples, the AC response can be modeled with two semi-circles in the impedance plane, the first in a low frequency domain represents the resistance of grain boundary. The second one obtained in a high frequency domain corresponds to the resistance of grain or bulk properties [20].

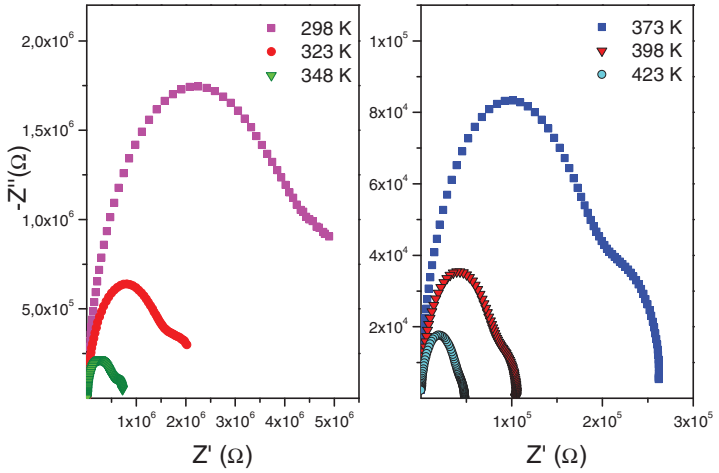

(a)

4C/Art

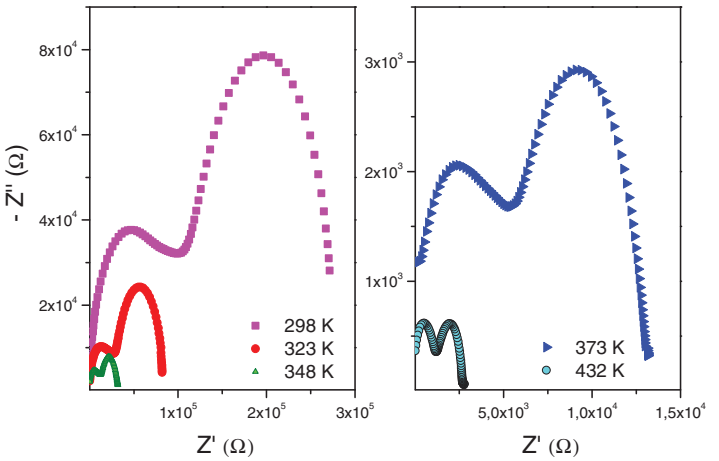

(b)

Figure 6. *Cole-Cole* plots for the sample of the (a) $NiFe_2O_4$ and (b) $ZnFe_2O_4$ ferrites at different temperatures (Color figure available online).

Figure 6 shows the complex impedance plane plots of sintered $NiFe_2O_4$ and $ZnFe_2O_4$ ferrites as a function of frequency at different temperatures. Generally, two semicircles are observed in the *Cole-Cole* plots of both samples between the frequency range 100 Hz–10 MHz. A larger one at low frequency represents the resistance of the grain boundary and a smaller one obtained at the higher frequency side corresponds to the resistance of grain of bulk properties. It is noticeable that the impedance spectra of $NiFe_2O_4$ and $ZnFe_2O_4$ ferrites include both grain and grain boundary effects. This appearance of two semicircles indicates a phenomenon which is typically related to the presence of a distribution of relaxation time.

As one can see in impedance spectra of both ferrites, the diameters of the semicircles exhibit decreasing trends with the increase in temperature. It indicates that the conductivity increases with increase in temperature supporting the typical negative temperature coefficient of resistance behavior of $NiFe_2O_4$ and $ZnFe_2O_4$ usually shown by semiconductors. On impedance spectra is observed that $NiFe_2O_4$ has a higher impedance value of $ZnFe_2O_4$ at all temperatures, so it is in good accordance with the fact that the conductivity of $NiFe_2O_4$ is lower than conductivity of $ZnFe_2O_4$. The impedance value of both samples is decreased by two orders of magnitude, which is due to thermal activation mechanism. The rise of temperature brings with an enhanced conductivity, and hence, decreasing the impedance values.

In order to correlate the electrical properties of the $NiFe_2O_4$ and $ZnFe_2O_4$ sample with the microstructure of the material, an equivalent circuit model consisting of two serially connected parallel *R-CPE* elements, shown in Fig. 7, has been used to interpret the impedance spectra. Here R_g and R_{gb} represent the grain and grain boundary resistance and CPE_g and CPE_{gb} are the constant phase elements for grain interiors and grain boundaries, respectively. The resistance of the circuit represents a conductive path and a given resistor in a circuit account for the bulk conductivity of the sample. The constant phase element *CPE* is used to accommodate the non-ideal behavior of the capacitance which may have its origin in the presence of more than one relaxation process with similar relaxation times. The impedance of a *CPE* can be described as [21]

$$Z_{CPE} = A^{-1}(j\omega)^{-n},$$

where ω is the angular frequency, A and n ($0 \leq n \leq 1$) are fitted parameters. When $n = 1$, then the *CPE* describes an ideal capacitor with $C = A$, while when $n = 0$ the *CPE* describes an ideal resistor with $R = 1/A$. The capacitances are generally associated with space charge polarization regions. The *CPE* elements in the equivalent circuit model have been used to describe non ideal Debye-like behavior [22, 23] and enable taking into account phenomena occurring in the interface regions, associated with inhomogeneity and diffusion processes [24, 25].

Analysis and simulation of impedance spectra was performed using EIS Spectrum Analyzer software [26]. The different electrical parameters calculated from the complex

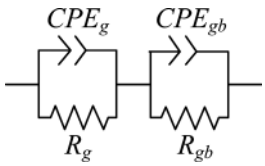

Figure 7. Proposed equivalent circuit model for analysis of the impedance spectroscopy data.

impedance plots at selected temperatures. In these types of ferrites, the value of the grain boundary resistance is generally larger than the resistance of the grain, $R_{gb} \geq R_g$. Additionally, the semicircle representing the grain boundaries lays on the lower frequency side since the relaxation time of the grain boundaries is much larger than that of the grains. Also, it is observed that the both resistances decrease with increasing temperature. It indicates that the conductivity of $NiFe_2O_4$ and $ZnFe_2O_4$ ferrites increases with increase in temperature. The higher values of resistance of both grain and grain boundary for $NiFe_2O_4$ mean this ferrite has a lower conductivity than $ZnFe_2O_4$. This decrease in the resistance of grains and grain boundaries has been suggested to be due to the thermal activation of the localized charges. Two types of thermal activations, i.e., carrier density in the case of band conduction and carrier mobility in case of hopping, are responsible for the reduction in the resistive properties with temperature [27]. For all the temperatures the capacitance of the grain boundary is larger than that of the grain for both types of ferrite samples, which can be explained on the basis that capacitance is inversely proportional to the thickness of the media.

4. Conclusions

The ferrites have been prepared by soft mechanochemical synthesis starting from the mixture of the powders. Single phase nanosized powders of $NiFe_2O_4$ and $ZnFe_2O_4$ ferrites were synthesized for 25 h and 18 h by ball milling and sintered at 1100 °C for 2 h. X-ray diffraction of the prepared samples show single phase cubic spinel structure. In the Raman spectra, all first-order Raman active modes are observed in the forms characteristic for $NiFe_2O_4$ inverse and $ZnFe_2O_4$ normal spinel structures. Both of the ferrites were superparamagnetic at room temperature. $ZnFe_2O_4$ ferrite was very poor magnetic.The conduction activation energy, ΔE is 0.452 eV and 0.395 eV for $NiFe_2O_4$ and $ZnFe_2O_4$ ferrites, respectively. The analysis of the complex impedance data shows that the capacitive and reactive properties of the sintered ferrites are mainly attributed due to the processes which are associated with the grain and grain boundary. The grain and grain boundary resistances of sintered samples exhibit decreasing trends with an increase in temperature.

Acknowledgments

This research was financially supported by the Ministry of Education, Science and Technological Development of the Republic of Serbia through Projects No. III 45003.

References

1. Z. H. Zhou, J. M. Xue, J. Wang, H. S. O. Chan, T. Yu, and Z. X. Shen, $NiFe_2O_4$ nanoparticles formed in situ in silica matrix by mechanical activation. *J. Appl. Phys.* **91**, 6015 (2002).
2. Y. Cheng, Y. Zheng, Y. Wang, F. Bao, and Y. Qin, Synthesis and magnetic properties of nickel ferrite nano-octahedra. *J. Solid State Chem.* **178**, 2394 (2005).
3. A. Ahlawat, V. G. Sathe, V. R. Reddy, and A. Gupta, Mossbauer, Raman and X-ray diffraction studies of superparamagnetic $NiFe_2O_4$ nanoparticles prepared by sol-gel auto-combustion method. *J. Magn. Magn. Mater.* **323**, 2049 (2011).
4. S. Bid, and S. K. Pradhan, Preparation of zinc ferrite by high-energy ball-milling and microstructure characterization by Rietveld's analysis. *Mat. Che. Phys.* **82**, 207 (2003).
5. A. B. Nawale, N. S. Kanhe, K. R. Patil, S. V. Bhoraskar, V. L. Mathe, and A. K. Das, Magnetic properties of thermal plasma synthesized nanocrystalline nickel ferrite ($NiFe_2O_4$). *J. Alloys Compd.* **509**, 4404 (2011).

6. Z. Wang, D. Schiferl, Y. Zhao, H. St, and C. O'Neill, High pressure Raman spectroscopy of spinel-type ferrite $ZnFe_2O_4$. *J. Phys. Chem. Solids* **64**, 2517 (2003).
7. E. Avvakumov, M. Senna, and N. Kosova, Soft mechanochemical synthesis: a basis for new chemical technologies. Kluwer Academic Publishers, Boston, 2001.
8. V. Šepelák, I. Bergmann, A. Feldhoff, P. Heitjans, F. Krumeich, D. Menzel, F. J. Litterst, S. J. Campbell, and K. D. Becker, Nanocrystalline nickel ferrite, $NiFe_2O_4$: mechanosynthesis, nonequilibrium cation distribution, canted spin arrangement, and magnetic behavior. *J. Phys. Chem. C* **111**, 5026 (2007).
9. M. Senna, Incipient chemical interaction between fine particles under mechanical stress—a feasibility of producing advanced materials via mechanochemical routes. *Solid State Ionics* **63–65**, 3 (1993).
10. Z. Ž. Lazarević, Č. Jovalekić, A. Recnik, V. N. Ivanovski, M. Mitrić, M. J. Romčević, N. Paunović, B. Đ. Cekić, and N. Ž. Romčević, *J. Alloys Compd.* **509**, 9977 (2011).
11. J. I. Langford, and A. J. C. Wilson, Scherrer after sixty years: a survey and some new results in the determination of crystallite size. *J. Appl. Cryst.* **11**, 102 (1978).
12. K. Nejati, and R. Zabihi, Preparation and magnetic properties of nano size nickel ferrite particles using hydrothermal method. *Chem Cent J.* **6**, 23 (2012).
13. B. Sachin, and B. Sambaji, Synthesis, Characterization and hydrophilic properties of nanocrystalline ZnFe2O4 oxide. *Res.J.Recent Sci.* **1**, 202 (2012).
14. A. Ahlawat, and V. G. Sathe, Raman study of $NiFe_2O_4$ nanoparticles, bulk and films: effect of laser power. *J. Raman Spectrosc.* **42**, 1087 (2011).
15. M. H. Sousa, F. A. Tourinho, and J. C. Rubim, Use of Raman micro-spectroscopy in the characterization of $M^{II}Fe_2O_4$ (M = Fe, Zn) electric double layer ferrofluids. *J. Raman Spectrosc.* **31**, 185 (2000).
16. A. Alarifi, N. M. Deraz, and S. Shaban, Structural, morphological and magnetic properties of $NiFe_2O_4$ nano-particles. *J. Alloys Compd.* **486**, 501 (2009).
17. E. C. Mendonça, C. B. R. Jesus, W. S. D. Folly, C. T. Meneses, J. G. S. Duque, and A. A. Coelho, Temperature dependence of coercive field of $ZnFe_2O_4$ nanoparticles. *J. Appl. Phys.* **111**, 053917 (2012).
18. S. M. Savic, M. V. Nikolic, O. S. Aleksic, M. P. Slankamenac, M. B. Zivanov, and P. M. Nikolic, Intrinsic resistivity of sintered nickel manganite vs. powder activation time and density. *Sci. Sinter.* **40**, 27 (2008).
19. E. Barsoukov, and J. R. Macdonald, Impedance spectroscopy: theory, experiment and applications, 2nd Ed., John Wiley&Sons, New York, (2005).
20. W. Chen, W. Zhu, O. K. Tan, and X. F. Chen, Frequency and temperature dependent impedance spectroscopy of cobalt ferrite composite thick film. *J. Appl. Phys.* **108**, 034101 (2010).
21. J. R. Macdonald, *Impedance spectroscopy: emphasizing solid materials and analysis*, John Wiley&Sons, New York, (1987).
22. E. J. Abram, D. C. Sinclair, and A. R. West, A strategy for analysis and modelling of impedance spectroscopy data of electroceramics: doped lanthanum gallate. *J. Electroceramics* **10**, 165 (2003).
23. J. R. Macdonald, and R. L. Hurt, Some simple equivalent circuits for ionic conductors. *J. Electroanal Chem.* **200**, 69 (1986).
24. F. D. Morrison, D. J. Jung, and J. F. Scott, Constant-phase-element (CPE) modeling of ferroelectric random-access memory lead zirconate-titanate (PZT) capacitors. *J. Appl. Phys.* **101**, 094112 (2007).
25. B. Y. Chang, and S. M. Park, Electrochemical impedance spectroscopy. *Annu. Rev. Anal. Chem.* **3**, 207 (2010).
26. A. S. Bondarenko, and G. Ragoasha, EIS spectrum analyser (a freeware program for analysis and simulation of impedance spectra), http://www.abc.chemistry.bsu.by/vi/analyser/.
27. M. Younas, M. Nadeem, M. Atif, and R. Grossinger, Metal-semiconductor transition in $NiFe_2O_4$ nanoparticles due to reverse cationic distribution by impedance spectroscopy. *J. Appl. Phys.* **109**, 093704 (2011).

Spectroscopy investigation of nanostructured zinc ferrite obtained by mechanochemical synthesis

Z. Ž. LAZAREVIĆ[a,*], Č. JOVALEKIĆ[b], A. MILUTINOVIĆ[a], D. SEKULIĆ[c], M. ROMČEVIĆ[a], M. SLANKAMENAC[c], N. ROMČEVIĆ[a]
[a]*Institute of Physics, University of Belgrade, P.O. Box 68, Belgrade, Serbia*
[b]*The Institute for Multidisciplinary Research, University of Belgrade, Serbia*
[c]*Faculty of Technical Sciences, University of Novi Sad, Novi Sad, Serbia*

$ZnFe_2O_4$ has been obtained by soft mechanochemical synthesis in a planetary ball mill. $Zn(OH)_2$ and α-Fe_2O_3 are used as initial compounds. This mixture was activated mechanically for 18 h, uniaxially pressed and sintered at 1100°C/2h. The phase composition and cation distribution of the as-prepared and the sintered samples were analysed by XRD, Raman and IR spectroscopy and magnetic measurements. Morphology was examined by SEM. For investigation of the relaxation mechanism in the sintered $ZnFe_2O_4$ we used the complex impedance measurement, which suggested that the resistance of grain boundary and the resistance of bulk (grain) coexist in the temperature range 298-423 K and give adequate frequency-dependent responses.

(Received March 5, 2013; accepted September 18, 2013)

Keywords: $ZnFe_2O_4$, Raman spectroscopy, Magnetic properties

1. Introduction

The spinel ferrites are very important materials because of their excellent magnetic and electrical properties [1]. These materials have been used in many applications including electronics, magnetic storage, ferrofluid technology, as carriers for magnetically guided drug delivery, and as contrast agents in magnetically resonance imaging [2]. The chemical formula of the spinel ferrite can be written as MFe_2O_4, where *M* (*M* = Mn, Ni, Zn) is a divalent metal cation. The M^{2+} and Fe^{3+} cations can be distributed into two crystal sites of spinel structure: tetrahedral (A) and octahedral [B] sites. A whole range of distribution of cations is possible in ferrites, whose crystal chemical formula can be generally represented by $(M^{2+}_{1-\lambda}Fe^{3+}_{\lambda})[M^{2+}_{\lambda}Fe^{3+}_{2-\lambda}]O_4^{2+}$, where parentheses and square brackets denote cation sites of tetrahedral and octahedral coordination, respectively [3]. λ represents the so-called degree of inversion defined as the fraction of the (A) sites occupied by Fe^{3+} cations. The cation arrangement can vary between two extreme cases. One is the normal spinel ($\lambda = 0$), where all the divalent *M* cations occupy (A) sites and all the trivalent Fe cations occupy [B] sites. The other one is the inverse spinel ($\lambda = 1$), where all the divalent ions occupy [B] sites and trivalent cations are equally distributed between (A) and [B] sites. Spinels with the cation distribution intermediate between normal and inverse (i.e., partially inverse spinels; $0 < \lambda < 1$) are also very frequent.

Many methods, such as traditional ceramic synthesis [4], hydrothermal synthesis [5], sol-gel techniques [6], co-precipitation [7], mechanical milling [8, 9] etc., have been used to fabricate the ferrites starting from various precursors. Mechanochemical processing is a novel and low- cost effective method of producing a wide range of nanopowders. It involves the use of a high energy ball mill to initiate chemical reactions and structural changes. It was shown that mechanochemical processing is a very promising technique that can be applied to the synthesis and processing of various high-tech materials. Soft mechanochemical synthesis method developed by Senna [10] posseses some advantageous because highly reactive compounds containing oxygen-hydrogen groups are used as a precursors. In fabricating of ferrites used method and sintering temperature dramatically affect the crystal sizes and cation distribution.

Zinc ferrite is not only interesting in basic researches in magnetism, but also has great potential in technological application. Previously, we have prepared $MnFe_2O_4$ and $NiFe_2O_4$ ferrites [11, 12]. The objective of present work is primarily to prepare of $ZnFe_2O_4$ ferrite by soft mechanochemical synthesis and to study this ferrite using different methods of characterization.

2. Experimental procedures

For The following crystalline powders were used as starting materials: zinc(II)-hydroxide ($Zn(OH)_2$, Merck 95% purity) and hematite (α-Fe_2O_3, Merck 99% purity). Soft mechanochemical synthesis was performed in air atmosphere in planetary ball mill (Fritsch Pulverisette 5) for 18 h. The powder mixture was pressed into pallet using a cold isostatic press (8 mm in diameter and ~3 mm thick and sintered at 1100 °C for 2 h (Lenton-UK oven) without pre-calcinations step. Heating rate was 10 °C min^{-1}, with

nature cooling in air atmosphere. Characterization of the obtained samples was carried out by several methods.

The formation of phase and crystal structure of the $ZnFe_2O_4$ was verified via the X-ray diffraction measurements (XRD). Model Philips PW 1050 diffractometer equipped with a PW 1730 generator (40 kV x 20 mA) was used with Ni filtered CoKα radiation of 1.78897 Å at the room temperature. Measurements were done in 2θ range of 15-80° with scanning step width of 0.05° and 10 s scanning time per step.

Raman measurements of mixture powder and sintered sample were performed using Jobin-Ivon T64000 monochromator. An optical microscope with 100x objective was used to focus the 514 nm radiation from a Coherent Innova 99 Ar^+ laser on the sample. The same microscope was used to collect the backscattered radiation. The scattering light dispersed was detected by a charge-coupled device (CCD) detection system. Room temperature Raman spectra are in spectral range from 100 to 800 cm^{-1}.

The infrared (IR) measurements were carried out with a BOMMEM DA-8 FIR spectrometer. A DTGS pyroelectric detector was used to cover the wave number range from 50-700 cm^{-1}.

The microstructure of sintered sample was examined using scanning electron microscope (SEM, Model Sirion 200 SITP, operated at 10 kV).

The magnetization measurements were done at room temperature using VSM 200 cryogenic magnetometer in magnetic field from 0 kOe to ± 80 kOe.

Impedance measurements were carried out in the frequency range 100 Hz to 10 MHz on a HP-4194A impedance/gain-phase analyzer using a HP-16048C test fixture at the temperature of 298-423 K.

2. Results and discussion

Fig. 1 show the X-ray diffraction patterns of $ZnFe_2O_4$ powder obtained from stoichiometric mixture of powders $Zn(OH)_2$ and α-Fe_2O_3 in a ball mill for 18 h and after sintered at 1100 °C for 2 h. Both, the powder and sintered $ZnFe_2O_4$ are single-phase ferrites with spinel structure. To get more information, the crystallite sizes of powder and sintered sample were calculated from X-ray peak broadening using the Scherrer formula [13]:

$$L = K\,\lambda_{Co} / (\beta \cos \theta_{hkl}) \qquad (1)$$

where L is the crystallite size, λ_{Co} is the wavelength of X-ray radiation (1.78897 Å for Co-K_α), θ_{hkl} is the Bragg angle and β is the full width at half maximum (FWHM) of the diffraction peak (reflection from (*hkl*) crystal plane) reduced for instrumental broadening. K is a Scherrer constant. The estimated average particle size is 13 nm for powder and 100 nm for the sample sintered at the temperature of 1100 °C for 2 h.

The obtained XRD patterns show clear peaks whose positions and relative intensities correspond to the bulk $ZnFe_2O_4$ (JCPDS card 89-7412) and are well indexed as cubic spinel phase with the *fcc* structure [14]. The diffractograms show different reflection planes indexed as (*hkl*): (111), (220), (311), (222), (400), (422), (511) and (440). Based on the measured positions of diffraction peaks it can be calculated lattice constant by well-known relation:

$$a = \lambda_{Co}\,(h^2 + k^2 + l^2)^{1/2}/(2\sin\theta_{hkl}) \qquad (2)$$

Calculated lattice constant for sintered sample is a = 0.8419 nm, slightly (0.035%) less than in the bulk (JCPDS card 89-7412, a = 0.8422 nm). Lattice constant of powder sample is 0.8402 nm, 0.24% less than crystal lattice constant, what indicates presence of nano effects.

Raman spectra of samples obtained from mixture of $Zn(OH)_2$ and α-Fe_2O_3 powders for 18 h milling time and after sintered are analyzed by deconvolution (Fig. 2). Crystal $ZnFe_2O_4$ has normal spinel structure. The group theory predicts 5 Raman active modes in spinel structure: $A_{1g} + E_g + 3F_{2g}$. All five Raman peaks in sintered $ZnFe_2O_4$ are clearly visible and have symmetric form, what is a characteristic of normal spinel structure. Raman spectra of $ZnFe_2O_4$ nanocrystalline samples, obtained by mechanochemical method at low temperature have visible doublets and it could be concluded that spinel structure of these samples is mostly inversed.

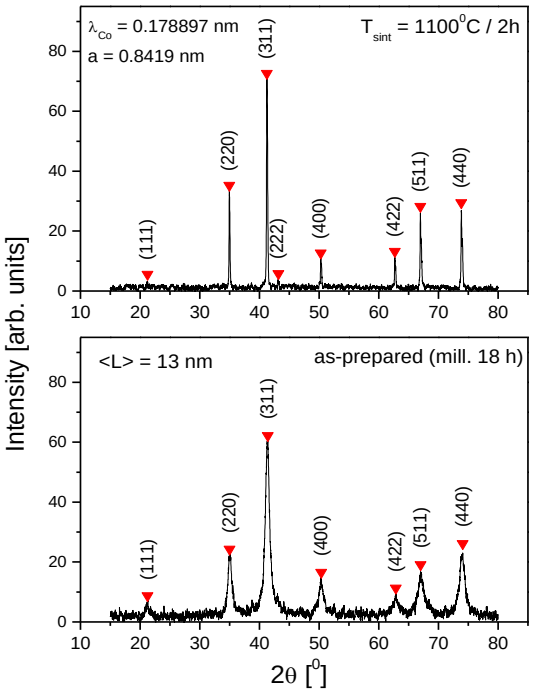

Fig. 1. X-ray diffraction patterns of the $ZnFe_2O_4$ obtained for 18 h milling time and after sintered at 1100 °C for 2 h.

In the cubic ferrites, the strongest modes above 600 cm^{-1} correspond to symmetric stretching of oxygen in tetrahedral AO_4 groups, so the modes about 630 cm^{-1} can be reasonably considered as A_g symmetry. E_g (~ 250 cm^{-1}) is due to symmetric bending of oxygen with respect to cation in tetrahedral surrounding. $F_{2g}(2)$ (~ 350 cm^{-1}) and

$F_{2g}(3)$ (~ 450 cm^{-1}) correspond to the vibrations of octahedral group: $F_{2g}(2)$ is due to asymmetric stretching and $F_{2g}(3)$ is caused by asymmetric bending of oxygen. $F_{2g}(1)$ (~ 160 cm^{-1}) is due to translational movement of the whole tetrahedron. Double modes in the as-prepared 18 h milled sample imply that ordered sublattice of Zn ions in tetrahedral sites exist together with sublattice of Fe-ions.

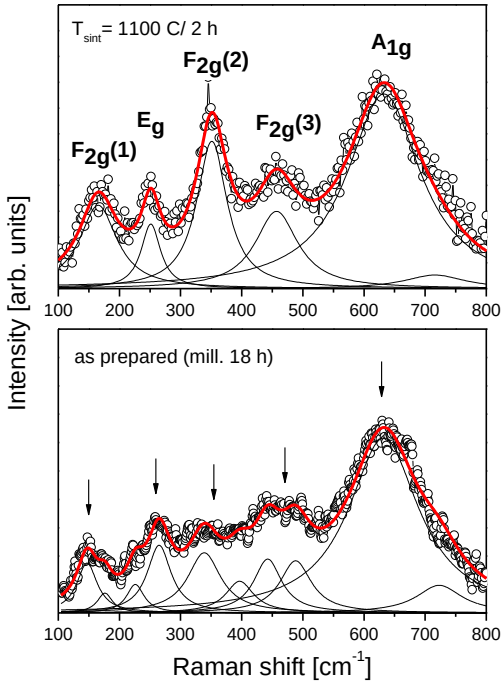

Fig. 2. Raman spectra at room temperature of the $ZnFe_2O_4$ obtained for 18 h milling time and after sintered at 1100 ℃ for 2 h.

For further characterization of the synthesized $ZnFe_2O_4$ ferrite, IR spectra were recorded in the range of 50-700 cm^{-1} (Fig. 3), where all the group theory predicted spinel modes (4 F_{1u}) are expected to be [15]. The most exaggerated features in spectra, $F_{1u}(3)$ and $F_{1u}(4)$, correspond to the stretching of cation-oxygen bond in in octahedral and tetrahedral sites, respectively. It is known that the higher band at ~700 cm^{-1} corresponds to the intrinsic vibrations of tetrahedral site and the lower band at ~400 cm^{-1} is attributed to the vibrations of octahedral site. The different values of the energy position for these modes are due to different values of metal ion - O^{2-} distances for octahedral and tetrahedral sites. In reflectivity spectra of $ZnFe_2O_4$ TO-LO splitting of the most intensive $F_{1u}(4)$ IR mode is visible. Fitted values of TO and LO modes in the sintered sample agree well with values in bulk. Values of the corresponding modes in the as-prepared powder sample are expectedly modified due to superposition of bulk and surface effects.

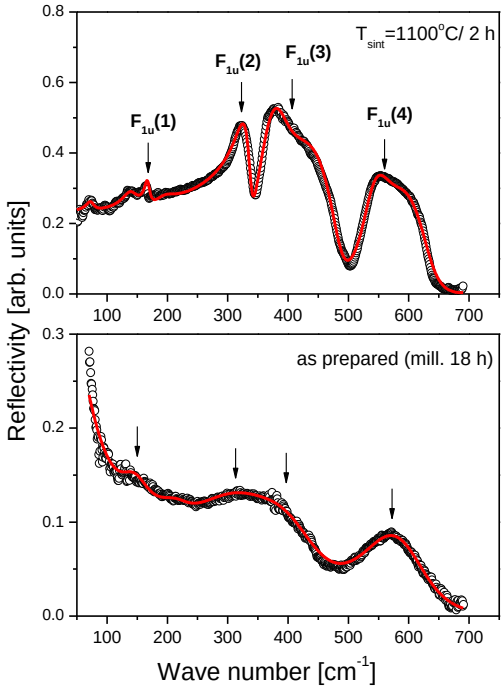

Fig. 3. IR spectra at room temperature of the $ZnFe_2O_4$ obtained for 18 h milling time and after sintered at 1100 ℃ for 2 h.

Fig. 4 shows the SEM micrograph for the sample obtained from the mixture of $Zn(OH)_2$ and α-Fe_2O_3 powders by the soft mechanochemical synthesis for 18 h milling time, than sintered at 1100 °C for 2 h. The sintered zinc ferrite consists of polygonal grains, with relatively homogeneous grain distribution, with an average grain size varying from 0.2-1 μm. It is well known that the microstructure of materials strong influences on the magnetic and electrical properties, so it will be done detailed research in the future.

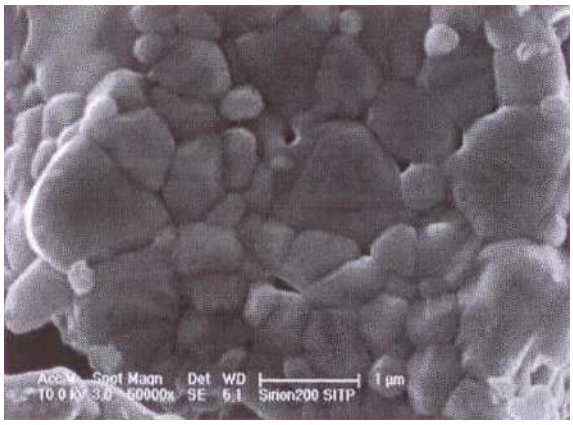

Fig. 4. SEM micrograph image of the $ZnFe_2O_4$ sintered at 1100 ℃ for 2h.

The magnetization curves of the zinc ferrite measured at room temperature are shown in Fig. 5. Sintered sample

exhibits a paramagnetic behavior, what is expected in the case of bulk, or crystalline material with crystalline size of 100 nm order. Such material is practically without internal tensions and in the case of sintered $ZnFe_2O_4$ a normal spinel structure with fully populated antiferromagnetic tetrahedral [B] sites is established. ([B] - [B] superexchange interaction is weak and bulk $ZnFe_2O_4$ became antiferromagnetic at about 10 K.) On the other hand, in the as-prepared sample with nano-sized crystallites can be recognized a superparamagnetic behavior [16, 17]. The estimated value of saturation magnetization is M_{sat} = 51.13 emu/g what is a result of the inversion of cations. The largest superexchange interaction in spinel ferrites, in the case of $ZnFe_2O_4$ established between Fe^{3+} ions in (A) and [B] sites, generates such high value of magnetisation. Nano-powder of $ZnFe_2O_4$ in the as-prepared sample is predominantly of mono-domen crystallites what is confirmed by a small remanence magnetization, M_{rem} = 5 emu/g. Open hysteresis loop, with coercive field, H_{coerc} = 100 Oe (in combination with high magnetization), shows that ferrimagnetic transition temperature is well above the room temperature. The fact that magnetization does not achieve a saturation in the magnetic fields up to ± 80 kOe implies a surface spin disorder. Ordering of these spins in a magnetic field contributes in the magnetic moment of the mono-domen $ZnFe_2O_4$ crystallites, also.

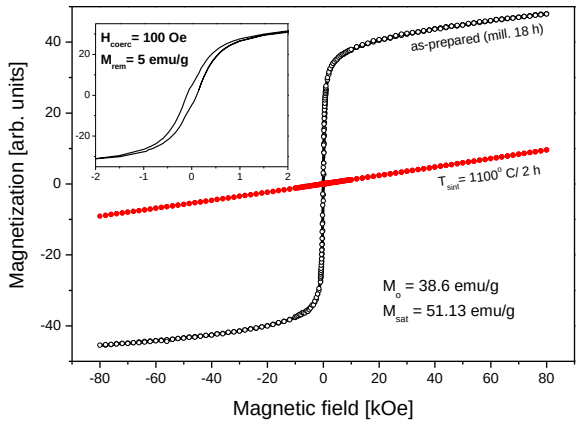

Fig. 5. Magnetic measurements of the $ZnFe_2O_4$ obtained for 18 h milling time and after sintered at 1100 ℃ for 2 h.

In the present investigation, the impedance spectroscopy [18] is used as well-developed tool to study the electrical properties of ferrites. By using this method, the AC response can be modeled with two semi-circles in the impedance plane; the first in a low frequency domain represents the impedance of grain boundary. The second one obtained in a high frequency domain corresponds to the impedance of grain or bulk properties [19]. *Cole-Cole* plots of impedance data for sintered $ZnFe_2O_4$ ferrite as a function of frequency at different temperatures are presented in Fig. 6. As one can see, the impedance spectrum shows presence of two semi-circles for measured frequency range 100 Hz -10 MHz. It suggests that there are two effects pertaining to the microstructural inhomogeneity: grain and grain boundary. The diameters of these semi-circles exhibit decreasing trends with the increase in temperature. This indicates that the conductivity increases with increase in temperature supporting the negative temperature coefficient of resistance behavior of the $ZnFe_2O_4$ usually shown by semiconductors. Additionally, the impedance value of investigated zinc ferrite decreases by two orders of magnitude, which is due to thermal activation mechanism [20]. The rise of temperature brings to an enhanced conductivity, and hence, decreasing the impedance values.

Successful modeling of the impedance response is achieved using an equivalent circuit consisting of two serially connected parallel *R-CPE* elements taking into account grain and grain boundary effects, see *inset* in Fig. 6. Here R_g and R_{gb} correspond to the grain and grain boundary resistance and CPE_g and CPE_{gb} are the constant phase elements for grain interiors and grain boundaries, respectively. The constant phase element (*CPE*) is used to accommodate the nonideal Debye-like behavior of the capacitance which is given by relation $C = Q^{1/n}R^{(1-n)/n}$, where the value of parameter n is 1 for a pure capacitor [21]. The electrical parameters of proposed circuit were calculated for every temperature measurement by analyzing the impedance data using EIS Spectrum Analyzer software [22] and are given in the Table 1. It is observed that resistance and capacitance have higher values for the grain boundary than for the grain. The fact that the capacitance of grain boundary (C_{gb}) is larger than capacitance of grain (C_g) can be explained on the basis that capacitance is inversely proportional to the thickness of the media. As temperature increases, both the grain resistance (R_g) and grain boundary resistance (R_{gb}) are found to decrease, which is indicated by a shift in the radius of the semicircular arcs towards left side of the real (Z') axis. This provides convincing evidence that the electrical properties of sintered $ZnFe_2O_4$ ferrite are dependent on microstructure as well as temperature. Since the relaxation time of grain ($\tau_g = R_gC_g$) and grain boundary ($\tau_{gb} = R_{gb}C_{gb}$) are different, the impedance spectroscopy allows separation of those. For temperature range from 298 K to 423 K, the calculated values of τ_g of the $ZnFe_2O_4$ sample fall in the range of 7.78 μs to 0.068 μs, respectively. Besides, the calculated values for τ_{gb} are from 8.31 ms to 0.312 ms in the same temperature range. In addition, grain boundary relaxation times are about three orders of magnitude larger than those of the grain-interior. This means that in the grain boundary structure the time spent in the relaxation process is longer. Also, it is observed that the decrease of both resistances with increasing temperature results in the decrease of relaxation time. This variation of relaxation times with temperature is a clear proof that the relaxation process is temperature dependent [23-25].

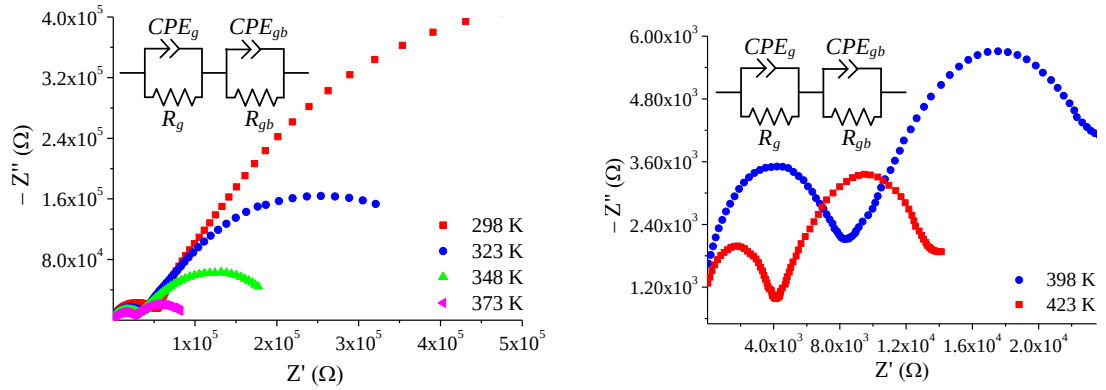

Fig. 6. Cole-Cole plots for the sample of the $ZnFe_2O_4$ ferrite at different temperatures. Inset: proposed equivalent circuit model for analysis of the impedance spectroscopy data.

Table 1. Impedance parameters calculated from the complex impedance plots at different temperatures.

T [K]	R_g [Ω]	C_g [F]	n_g	R_{gb} [Ω]	C_{gb} [F]	n_{gb}
298	5.44E+04	1.43E-10	0.83979	1.17E+06	7.11E-09	0.80709
323	3.98E+04	2.35E-10	0.82919	4.51E+05	9.53E-09	0.79713
348	3.42E+04	3.00E-10	0.81115	1.77E+05	1.36E-08	0.78479
373	2.45E+04	1.66E-10	0.85086	6.53E+04	2.87E-08	0.72616
398	7.80E+03	7.81E-11	0.89961	1.89E+04	4.58E-08	0.69429
423	3.87E+03	1.76E-11	0.98706	1.08E+04	2.89E-08	0.74088

4. Conclusions

In this paper, we obtained $ZnFe_2O_4$ ferrite by soft mechanochemical synthesis starting from the mixture of $Zn(OH)_2$ and α-Fe_2O_3 powders and sintered at 1100 °C/2h. It has been shown that mechanochemical treatment of mixture with starting materials leads to forming the phase of $ZnFe_2O_4$ after 18 h of milling. In the Raman and IR spectra are observed all of the group theory predicted first-order active modes characteristic for spinel structure. Raman modes of sintered $ZnFe_2O_4$ are in the form characteristic for normal spinel structure, and in the case of powder, Raman spectra show a presence of cation inversion. A high magnetization of a milled sample confirms cation inversion, also. Sintered sample has a normal spinel structure and, as a consequence, paramagnetic behavior at 300 K. The sintered $ZnFe_2O_4$ consists of the polygonal grains. The analysis of the complex impedance data shows that the capacitive and reactive properties of the sintered $ZnFe_2O_4$ ferrite are mainly attributed due to the processes which are associated with the grain and grain boundary. Also, it is seen that the radius of curvature of *Cole-Cole* plots is decreased with increasing temperature, suggesting a mechanism of temperature-dependent on relaxation.

Acknowledgements

This research was financially supported by the Ministry of Education, Science and Tehnological Development of the Republic of Serbia through Projects No. III45003 and III43008.

References

[1] M. J. Nasr Isfahani, M. Myndyk, V. Šepelák, J. Amighian, J. Alloy Compd. **470**, 434 (2009).
[2] V. Šepelák, P. Heitjans, K. D. Becker, J. Therm. Anal. Calorim. **90**, 93 (2007).
[3] S. H. Pradhan, S. Bid, M. Gateshki, V. Petkov, Mater. Chem. Phys. **93**, 224 (2005).
[4] C. N. Chinnasamy, A. Narayanasamy, N. Ponpandian, K. Chattopadhyay, H Guérault, J-M. Greneche, J. Phys.- Condens. Mat. **12**, 7795 (2000).

[5] S. H. Yu, T. Fujino, M. Yoshimura, J. Magn. Magn. Mater. **256**, 420 (2003).
[6] S. Khorrami, F. Gharib, G. Mahmoudzadeh, S. Sadat Sepehr, S. Sadat Madani, N. Naderfar, S. Manie, Int. J. Nano. Dim. **1**, 221 (2011).
[7] M. Maletin, Ž. Cvejić, S. Rakić, L. M. Nikolić, V. V. Srdić, Mater. Sci. Forum **518**, 91 (2006).
[8] S. Mornet, S. Vasseur, F. Grasset, P. Veverka, G. Goglio, A. Demourgues, J. Portier, E. Pollert, E. Dugust, Prog. Solid State Chem. **34**, 237 (2006).
[9] T. F. Marinca, I. Chicinaş, O. Isnard, V. Pop, Optoelectron. Adv. Mater. – Rapid Comm. **5**, 39 (2011).
[10] M. Senna, in Powder Technology Handbook, 3rd Edition, Eds. H. Masuda, K. Higashitani, H. Yoshida, CRC Press, Boca Raton, 2006.
[11] Z. Ž. Lazarević, Č. Jovalekić, A. Rečnik, V. N. Ivanovski, M. Mitrić, M. J. Romčević, N. Paunović, B. Đ. Cekić, N. Ž. Romčević, J. Alloys Compd. **509**, 9977 (2011).
[12] Z. Ž. Lazarević, Č. Jovalekić, A. Milutinović, M. J. Romčević, N. Ž. Romčević, Acta. Phys. Pol. A **121**, 682 (2012).
[13] Scherrer and Warren equations (B. E. Warren, X-ray Diffraction, Addison Wesley: Reading MA, (1969).
[14] Y. Li, R. Yi, A. Yan, L. Deng, K. Zhou, X. Liu, Solid State Sci. **11**, 1319 (2009).
[15] R. D. Waldron, Phys. Rev. **99**, 1727 (1955).
[16] C. N. Chinnasamy, A. Narayanasamy, N. Ponpandian1, K. Chattopadhyay, H. Guérault, J-M. Greneche, Scripta Mater. **44**, 1407 (2001).
[17] C. Yao, Q. Zeng, G. F. Goya, T. Torres, J. Liu, H. Wu, M. Ge, Y. Zeng, Y. Wang, J. Z. Jiang, J. Phys. Chem. C **111**, 12274 (2007).
[18] N. Bonanos, B. C. H. Steele, E. P. Butler, in Impedance Spectroscopy: Theory, Experiment, and Applications, 2nd Edition, Eds. E. Barsoukov, J. R. Macdonald, John Wiley&Sons, 2005, pp. 205-343.
[19] W. Chen, W. Zhu, O. K. Tan, X. F. Chen, J. App. Phys. **108**, 0341011 (2010).
[20] Z. Lazarević, A. Milutinović, M. Romčević, N. Romčević, Č. Jovalekić, D. Sekulić, M. Slankamenac, ISAF ECAPD PFM 2012, Aveiro, Portugal, the USBs electronic conference Proceedings, No 07 (2012).
[21] M. Younas, M. Nadeem, M. Atif, R. Grossinger, J. App. Phys. **109**, 093704 (2011).
[22] A. S. Bondarenko, G. A. Ragoisha, EIS Spectrum Analyser (a freeware program for analysis and simulation of impedance spectra), see http://www.abc.chemistry.bsu.by/vi/analyser/.
[23] S. Dutta, R. N. P. Choudhary, P. K. Sinha, Ceram. Int. **33,** 13 (2007).
[24] Z. Ž. Lazarević, Č. Jovalekić, D. L. Sekulić, M. P Slankamenac, M. Romčević, A. Milutinović, N. Ž. Romčević, Sci. Sinter. **44**, 331 (2012).
[25] K. Verma, S. Sharma, Phys. Status Solidi B **249**, 209 (2012).

*Corresponding author: lzorica@yahoo.com

Spectroscopy investigation of nanostructured nickel-zinc ferrite obtained by mechanochemical synthesis

Z. Ž. LAZAREVIĆ[a,*], Č. JOVALEKIĆ[b], A. MILUTINOVIĆ[a], N. DANEU[c], M. ROMČEVIĆ[a], Đ. JOVANOVIĆ[a], N. ROMČEVIĆ[a]
[a]*Institute of Physics, University of Belgrade, P.O. Box 68, Belgrade, Serbia*
[b]*The Institute for Multidisciplinary Research, University of Belgrade, Serbia*
[c]*Department for Nanostructured Materials, Jožef Stefan Institute, Ljubljana, Slovenia*

Nickel-zinc ferrite, $Ni_{0.5}Zn_{0.5}Fe_2O_4$ was prepared by a soft mechanochemical route from mixtures of $Ni(OH)_2$, $Zn(OH)_2$ and $Fe(OH)_3$ powders in a planetary ball mill. The mechanochemical treatment provoked reaction leading to the formation of the $Ni_{0.5}Zn_{0.5}Fe_2O_4$ spinel phase what was monitored by XRD, TEM, SEM, IR and Raman spectroscopy. The spinel phase was first observed after 5h of milling and its formation was completed after 10 h. The synthesized $Ni_{0.5}Zn_{0.5}Fe_2O_4$ has a nanocrystalline structure with a crystallite size of about 16 nm. Four active modes are seen in the far-infrared reflectivity spectra. The Raman spectrum suggests an existence of mixed spinel structure in the obtained nano-powder samples.

(Received March 21, 2014; accepted January 21, 2015)

Keywords: $Ni_{0.5}Zn_{0.5}Fe_2O_4$, Soft mechanochemical synthesis, XRD, TEM, Raman spectroscopy, IR spectroscopy

1. Introduction

Spinel ferrites have attracted intense interest in fundamental science, especially for addressing the basic relationship between magnetic properties and their crystal chemistry and structure [1-3]. The spinel structure is shown in Fig. 1. Ferrites have been extensively investigated in recent years for their useful electrical and magnetic properties and applications in information storage systems, magnetic bulk cores, magnetic fluids, microwave absorbers and high frequency devices [4, 5]. Among the spinel ferrites, Ni-Zn ferrite is a magnetic material that is much used by the modern electronics industry due to its high electrical resistivity, high values of magnetic permeability, low dielectric loss, together with high mechanical strength, good chemical stability, and low coercivity [6].

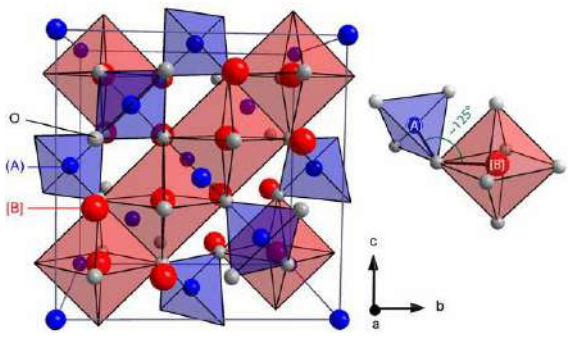

Fig. 1. The cubic unit cell of spinel oxides consists of 56 ions: 32 anions (O^{2-}) and 24 cations. In ternary spinel ferrites, MFe_2O_4, M and Fe cations are distributed over the sites of tetrahedral (A) and octahedral [B] coordination.

It is well known that nickel ferrite has an inverse spinel structure with Ni^{2+} ions at octahedral [B] sites and Fe^{3+} ions equally distributed at tetrahedral (A) and octahedral [B] sites. Whereas, zinc ferrite has a normal spinel structure with Zn^{2+} ions at A-sites and Fe^{3+} ions at B-sites. Therefore, when Ni^{2+} is substituted with Zn^{2+} in $Ni_{1-x}Zn_xFe_2O_4$, the cation distribution can be represented as $(Zn^{2+}{}_xFe^{3+}{}_{1-x})[Ni^{2+}{}_{1-x}Fe^{3+}{}_{1+x}]O^{2-}{}_4$ [7].

Since the particle size is reduced to a nanometer level, $NiFe_2O_4$ and $ZnFe_2O_4$ show a change of magnetic ordering [8, 9] and a magnetic moment that is attributed to the cation redistribution in the form of a mixed spinel structure with variation of 'x' depending on the thermal history [10]. Indeed, nanostructured materials exhibit unusual physical and chemical properties, significantly different from those of the bulk materials due to their extremely small size or large specific surface area [11]. The spinel ferrite powders are usually prepared through conventional solid-state reaction [12, 13], sol-gel technique [14, 15], hydrothermal synthesis [16], co-precipitation [8, 17] and mechanochemical process [18]. Mechanochemical synthesis is the general name given to the process of milling of powders which is accompanied by chemical reactions. It was first developed for the preparation of intermetallic compounds and nano-crystalline alloys. Novel approach to mechanochemical synthesis, based on reactions of solid acids, based hydrated compounds, crystal hydrates, basic and acidic salts, has been called soft mechanochemical synthesis [19]. The dissolved substances in the solid state substantially change their nature. It can influence on the comparison and properties of the final product. Peculiarities of soft mechanochemical reactions consist in the high reactivity of surface functional groups, notably, OH groups [19-21].

The major advantages of soft mechanochemical synthesis lie in the formation of reaction products at a room or a low temperature and the refinement of produced powders to a nanometer size range. This is reflected primarily in the simplicity of the procedure and equipment used. In many cases, when it comes to classical synthesis reaction sintering process, requires high temperatures, which can present an additional problem in industrial production. Mechanochemical derived precursors exhibit significantly higher reactivity and thus lower the sintering temperature.

Previously, we have used this method synthesis to prepare Mn-, Ni- and $ZnFe_2O_4$ ferrites [22]. The objective of present work is primarily to prepare the $Ni_{0.5}Zn_{0.5}Fe_2O_4$ ferrite by soft mechanochemical synthesis and to study this ferrite using different methods of characterization.

2. Experimental procedures

For mixtures of crystalline powders, the starting material were: nickel(II)-hydroxide ($Ni(OH)_2$, Merck 95% purity), zinc(II)-hydroxide ($Zn(OH)_2$, Merck 95% purity) and iron-hydroxide ($Fe(OH)_3$) in equimolar ratio. Soft mechanochemical synthesis was performed in air atmosphere in planetary ball mill (Fritsch Pulverisette 5) for 10 h. Characterization of the obtained samples was carried out by several methods.

The formation of phase of the $Ni_{0.5}Zn_{0.5}Fe_2O_4$ was verified via the X-ray diffraction measurements (XRD). Model Philips PW 1050 diffractometer equipped with a PW 1730 generator (40 kV x 20 mA) was used with Ni filtered CoKα radiation of 1.78897 Å at the room temperature. Measurements were done in 2θ range of 15-80° with scanning step width of 0.05° and 10 s scanning time per step.

Raman measurement of the obtained powder was performed using Jobin-Ivon spectrometer. An optical microscope with 100x objective was used to focus the 514 nm radiation from a Coherent Innova 99 Ar^+ laser on the sample. The backscattered light was collected by a charge-coupled device (CCD) detection system. Room temperature Raman spectra are in spectral range from 100 to 800 cm^{-1}.

The reflectivity measurements were carried out with a BOMMEM DA-8 spectrometer. A DTGS pyroelectric detector was used to cover the wave number range from 50-700 cm^{-1}.

TEM studies were performed using a 200 kV TEM (JEM-2100 UHR, Jeol Inc., Tokyo, Japan) equipped with an ultra-high resolution objective lens pole piece having a point-to-point resolution of 0.19 nm, being sufficient to resolve the lattice images of nanoparticles. Due to relatively small size of the nanoparticles selected area electron diffraction patterns (EDP) over the multiple nanocrystals was recorded to obtain the characteristic diffraction rings with structure-specific *d*-values.

The morphology of powder sample of soft Ni-Zn ferrite was synthesized by planetary mill and the size of crystallite was examined by Scanning Electron Microscopy SEM (JEOL JSM-5200).

3. Results and discussion

The X-ray diffraction pattern of ferrite sample having general formula $Ni_{(1-x)}Zn_{(x)}Fe_2O_4$ where x = 0.5 are shown in Fig. 2. The diffractogram of the mixtures of starting $Ni(OH)_2/Zn(OH)_2/Fe(OH)_3$ hydroxide powders, Fig. 2, suggests that hydroxides are amorphous (0 h of milling). After 10 h of milling, there are no traces of starting materials, ie any other intermediate reaction product. The pattern was indexed using PCPDFWIN data (PDF #52-0278) for Ni-Zn ferrite. There are no extra peaks indicating purity of the sample synthesized. The positions of the Bragg lines were used to obtain the interplanar spacing, Table 1. The result is in agreement with the reports in the literature [12]. The average crystallite size (L) obtained from the most intense line (3 1 1) was (16 nm) as estimated by Scherrer equation as follows [23]:

$$L = K\,\lambda_{Co} / (\beta \cos \theta_{hkl})$$

where L is the crystallite size, λ_{Co} is the wavelength of X-ray radiation (1.78897 Å for Co-K_α), θ_{hkl} is the Bragg angle and β is the full width at half maximum (FWHM) of the diffraction peak (reflection from (*hkl*) crystal plane) reduced for instrumental broadening. K is a Scherrer constant.

The obtained XRD patterns show clear peaks whose positions and relative intensities correspond to the bulk $Ni_{0.5}Zn_{0.5}Fe_2O_4$ and are well indexed as cubic spinel phase with the *fcc* structure [16]. The diffractograms show different reflection planes indexed as (*hkl*): (111), (220), (311), (222), (400), (422), (511) and (440). Based on the measured positions of diffraction peaks it can be calculated lattice constant by well-known relation for cubic crystals:

$$a = \lambda_{Co}\,(h^2 + k^2 + l^2)^{1/2}/(2\sin\theta_{hkl})$$

Calculated lattice constant for obtained nanopowder $Ni_{0.5}Zn_{0.5}Fe_2O_4$ is 8.3734 Å (in PCPDFWIN data is given a = 8.382 Å for bulk).

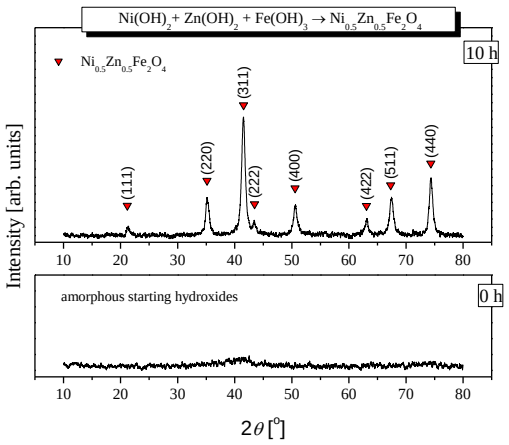

Fig. 2. X-ray diffraction patterns of the mixture of amorphous starting $Ni(OH)_2/Zn(OH)_2/Fe(OH)_3$ hydroxide powders and the $Ni_{0.5}Zn_{0.5}Fe_2O_4$ obtained for 10 h of milling time.

Table 1. Calculated d-values from XRD data and from EDP.

hkl	d_{XRD} **(nm)**	**ring no.**	d_{EDP} **(nm)**
(111)	0.4834	1	0.4841
(220)	0.2960	2	0.2959
(311)	0.2546	3	0.2531
(400)	0.2093	4	0.2093
(422)	0.1709	5	0.1707
(511)	0.1611	6	0.1619
(440)	0.1481	7	0.1482

The structure of normal spinel (like bulk $ZnFe_2O_4$) is face-centered space group Fd3m [O_h^7], with $8M^{II}Fe_2^{III}O_4$ units per full unit cell containing 56 atoms, and the smallest Bravais cell consists of 2 formula units with 14 atoms [24]. The irreducible representation at the zone center modes could be described as follows by factor group analysis [25]:

$$\Gamma = A_{1g}(R) + E_g(R) + F_{1g} + 3F_{2g}(R) + 2A_{2u} + 2E_u + 4F_{1u}(IR) + 2F_{2u}$$

where *R* and *IR* denote Raman and infrared activity of the modes, respectively. There are predicted five symmetry-allowed, first-order Raman active modes ($A_{1g} + E_g + 3F_{2g}$) and four IR active modes. It is common to use this representation for inverse or partially inverse spinels for the sake of simplicity.

In the present study of $Ni_{0.5}Zn_{0.5}Fe_2O_4$ more than 5 Raman modes are visible in Fig. 3. Compared with Ref-s. [25-28], these peaks are characteristics for Ni-Zn ferrite. More than five peaks in Raman spectra are the consequence of the inversion of cations, as well as the existence of three types of cations. The analysis of the deconvoluted spectrum shows that above 600 cm^{-1} are 3 modes with A_{1g} symmetry, originated from symmetric stretching of oxygen tetrahedrons with different cations inside. At the lowest wave number, about 636 cm^{-1}, is a contribution of the most massive Zn^{2+}-ions in tetrahedral surrounding, followed by Ni^{2+} at about 687 cm^{-1} and Fe^{3+} at 720 cm^{-1}. Similar situation is with other Raman modes, also. E_g modes (two of them are separated) are due to symmetric bending of oxygen with respect to cations in tetrahedral surrounding. $F_{2g}(2)$ and $F_{2g}(3)$ correspond to the vibrations of octahedral group. $F_{2g}(1)$ are due to translational movement of the whole tetrahedrons.

Small intensity of Fe-O_4 component of A_{1g} mode and high intensity of Ni-O_4 component suggest that there is a small amount of Fe^{3+} ions, but high amount of Ni^{2+} in tetrahedral sites, what implies that cations are redistributed.

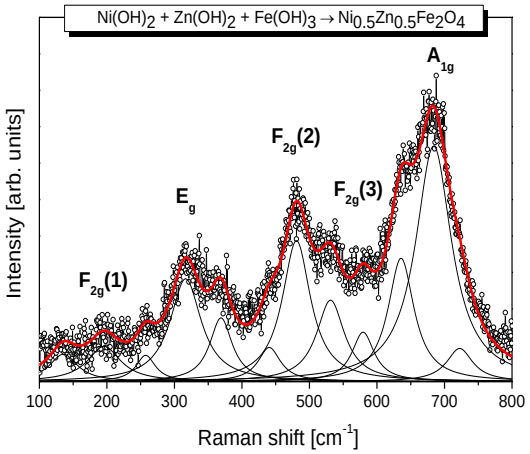

Fig. 3. Raman spectra at room temperature of the $Ni_{0.5}Zn_{0.5}Fe_2O_4$ obtained for 10 h milling time.

Far infrared reflectivity spectra of the synthesized $Ni_{0.5}Zn_{0.5}Fe_2O_4$ ferrite were recorded at room temperature, Fig. 4. Expectedly weak intensity of the reflectivity spectrum of nanopowder and broadness of the recorded IR modes don't allow separation of the different cations contributions in the observed bands. The highest energy band $F_{1u}(4)$ at ~ 580 cm^{-1} corresponds to the vibrations of cation-oxygen bonds in tetrahedral sites and the lower band $F_{1u}(3)$ at ~ 360 cm^{-1} is attributed to the vibrations of the cation-oxygen bond in octahedral site.

FIR spectrum, presented at Fig. 4 is fitted by plasmon - phonon interaction model of dielectric function [29, 30]:

$$\varepsilon = \varepsilon_\infty \left(\prod_i^n \frac{\omega_{LO_i}^2 - \omega^2 - j\omega\gamma_{LO_i}}{\omega_{TO_i}^2 - \omega^2 - j\omega\gamma_{TO_i}} - \frac{\omega_p^2}{\omega^2 + j\omega\gamma_p} \right),$$

where $\omega_p = \sqrt{\dfrac{ne^2}{4\pi\varepsilon_0\varepsilon_\infty m^*}}$ [rad s^{-1}].

The first term in equation is the lattice vibration contribution, whereas the second term is the Drude term for the free-carrier contribution to the dielectric constant. $\omega_{LO(TO)}$ are longitudinal (transverse) frequencies and $\gamma_{LO(TO)}$ their dampings, ω_p is plasma frequency, γ_p plasma damping, *n* free charier concentration, m^* their effective mass, ε_0 is dielectric constant of vacuum ($8.854\cdot10^{-12}$ F m^{-1}) *and* ε_∞ is the high frequency dielectric constant. Spectrum is fitted with one plasmon and 5 phonons. Besides 4 zone centre modes, it was necessary to introduce one mode more to describe a discrete feature in the low energy of FIR spectrum (probably activated by disorder). Fitting parameters are listed in Fig. 4. On the basis of obtained value of the plasma frequency, it is possible, knowing the effective mass, to estimate the concentration of free carriers, as $n = (4\pi\omega_p{}^2\varepsilon_0\varepsilon_\infty m^*)/e^2$. To our knowledge, the effective mass for various types of charge carriers is estimated only for $SiMg_2O_4$, $SiZn_2O_4$ and $SiCd_2O_4$ in Ref. [31]. An approximate value from the

mentioned study $m^* = 0.4 \cdot m_0$ was used in the calculation of carrier concentration and obtain $n = 5.4 \cdot 10^{18}$ cm^{-3}.

The concentration calculated from FIR measurement correspond to free band carriers that could be excited at a given temperature. Due to relatively wide energy gap in $Ni_xZn_{1-x}Fe_2O_4$ (1.9 - 2.26 eV) [32, 33], amount of these carriers is relatively small at ambient temperature.

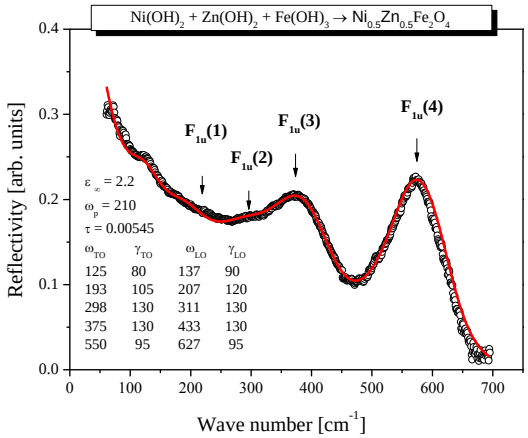

Fig. 4. IR spectrum of the $Ni_{0.5}Zn_{0.5}Fe_2O_4$ recorded at room temperature is presented by open circles; The fit of spectrum is presented by red line. Fitting parameters are given in the inset.

The mechanochemical synthesis of $Ni_{0.5}Zn_{0.5}Fe_2O_4$ is feasible and complete after 10 h milling time. This is considerably less time compared with the time (346.5 ks or 96 h) for which the spinel $Ni_{0.5}Zn_{0.5}Fe_2O_4$ obtained in the work by Todaka and co-authors [34]. It can be seen that the nanoparticles are about 30 nm in diameter. Fig. 5 shows the TEM micrograph for the sample obtained from the mixture of $Ni(OH)_2$, $Zn(OH)_2$ and $Fe(OH)_3$ powders by the soft mechanochemical synthesis for 10 h milling time. TEM analysis on our sample revealed that ferrite sample is composed of nanosized particles with size around 20 nm, what is in accordance with obtained XRD-value (16 nm). Jovalekić and co-authors [18] were synthesized nanocrystalline $Ni_{0.5}Zn_{0.5}Fe_2O_4$ in a high energy planetary mill starting from the NiO, ZnO and Fe_2O_3 oxide powders. The obtained nickel-zinc ferrite has many inhomogeneities and a distorted spinel structure.

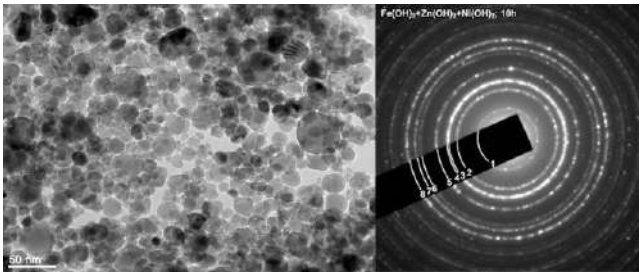

Fig. 5. TEM micrograph image and electron diffraction patterns (Debye-Sherrer rings) of the $Ni_{0.5}Zn_{0.5}Fe_2O_4$ ferrite sample obtained by milling for 10h from the mixture of $Ni(OH)_2$, $Zn(OH)_2$ and $Fe(OH)_3$ hydroxide powders.

TEM analysis revealed that ferrite sample is composed of roundish nanosized particles with size around 20 nm, what is in accordance with obtained XRD-value (16 nm). In the Fig. 5 electron diffraction pattern (EDP) is given. The calculated d-values for one sample are shown in Table 1 together with values obtained from XRD-analysis.

SEM micrograph (Fig. 6) shows powder sample of $Ni_{0.5}Zn_{0.5}Fe_2O_4$ ferrite that was synthesized by planetary mill synthesis procedure. The nanoscale crystallite tend to agglomerate because of the dipolar feild of each crystallite [35]. Agglomerated crystallites form grains with sizes substantially greater than 20 nm.

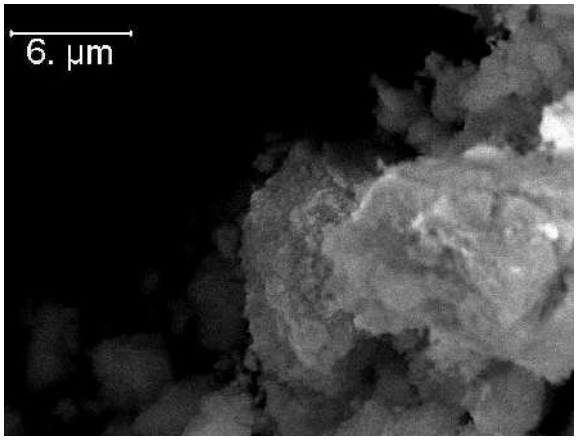

Fig. 6. SEM image of the $Ni_{0.5}Zn_{0.5}Fe_2O_4$ ferrite sample obtained by milling for 10h from the mixture of $Ni(OH)_2$, $Zn(OH)_2$ and $Fe(OH)_3$ hydroxide powders.

4. Conclusions

In this paper, we obtained $Ni_{0.5}Zn_{0.5}Fe_2O_4$ ferrite by soft mechanochemical synthesis starting from the mixture of appropriate amounts of hydroxide powders. It has been shown that mechanochemical treatment of mixture with starting materials leads to forming the pure phase of $Ni_{0.5}Zn_{0.5}Fe_2O_4$ after 10 h of milling. In the Raman and IR spectra are observed all of the group theory predicted first-order active modes characteristic for spinel structure.

Acknowledgements

This research was financially supported by the Ministry of Education, Science and Tehnological Development of the Republic of Serbia through Projects No. III 45003 and 45015.

References

[1] M. A. Gabal, Reda M. El-Shishtawy, Y. M. Al Angari, J. Magn. Magn. Mater. **324**, 2258 (2012).
[2] D. S. Mathew, R. S. Juang, Chem. Eng. J. **129**, 51

(2007).
[3] K. M. Batoo, Nanoscale Res. Lett. **6**, 499 (2011).
[4] M. Atif, M. Nadeem, R. Grössinger, R. Sato Turtelli, J. Alloy Compd. **509**, 5720 (2011).
[5] J. L. Dorman, D. Fiorani (Eds.), Magnetic Properties of Fine Particles, Amesterdam, North-Holland, 1992.
[6] E. S. Murdock, R. F. Simmons, R. Davidson, IEEE Trans. Magn. **28**, 3078 (1992).
[7] J. Smit, H. P. J. Wijn, Ferrites-Physical Properties of Ferrimagnetic Oxides in Relation to Their Technical Applications, N. V. Philip's Gloeilampenfabrieken, Eindhoven/Holland, 1959 (Chap. VIII), pp. 136-176.
[8] D. G. Chen, X. G. Tang, J. B. Wu, W. Zhang, Q. X. Liu, Y. P. Jiang, J. Magn. Magn. Mater. **323**, 1717 (2011).
[9] G. F. Goya, H. R. Rechenberg, J. Magn. Magn. Mater. **203**, 141 (1999).
[10] M. Ajmal, A. Maqsood, Mater. Sci. Eng. B **139**, 164 (2007).
[11] H. Yang, X. C. Zhang, W. Q. Ao, G. Z. Qiu, Mater. Res. Bull. **39**, 833 (2004).
[12] Abdul Samee Fawzi, A. D. Sheikh, V. L. Mathe, J. Alloy Compd. **502**, 231 (2010).
[13] Dong-Lin Zhao, Qiang Lv, Zeng-Min Shen, J. Alloy Compd. **480**, 634 (2009).
[14] Hong-Wen Wang, Shong-Chung Kung, J. Magn. Magn. Mater. **270**, 230 (2004).
[15] Jeevan Job Thomas, A. B. Shinde, P. S. R. Krishna, Nandakumar Kalarikkal, J. Alloy Compd. **546**, 77 (2013).
[16] R. M. Freire, T. S. Ribeiro, I. F. Vasconcelos, J. C. Denardin, E. B. Barros, Giuseppe Mele, L. Carbone, S. E. Mazzetto, P. B. A. Fechine, J. Nanopart. Res. **15**, 1616 (2013).
[17] T. J. Shinde, A. B. Gadkari, P. N. Vasambekar, J. Magn. Magn. Mater. **333**, 152 (2013).
[18] Č. Jovalekić, A. S. Nikolić, M. Gruden-Pavlović, M. Pavlović, J. Serb. Chem. Soc. **77**, 497 (2012).
[19] E. Avvakumov, M. Senna, N. Kosova, Soft Mechanochemical Synthesis: A Basis For New Chemical Technologies, Kluwer Academic Publishers, Boston, 2001.
[20] M. Senna, Solid State Ionics **63-65**, 3 (1993).
[21] V. V. Boldyrev, Solid State Ionics **63-65**, 537 (1993).
[22] Z. Ž. Lazarević, Č. Jovalekić, A. Milutinović, D. Sekulić, M. Romčević, M. Slankamenac, N. Ž. Romčević, Optoelectron. Adv. Mater. **7**, 720 (2013).
[23] Scherrer and Warren equations (B. E. Warren, X-ray Diffraction, Addison Wesley: Reading MA, (1969).
[24] W. B. White, B. A. Deangelis, Spectrochim. Acta A **23**, 985 (1957).
[25] Z. W. Wang, D. Schiferl, Y. S. Zhao, H. St. C. O'Neilr, J. Phys. Chem. Solids **64**, 2517 (2003).
[26] T. Yu, Z. X. Shen, Y. Shi, J. Ding, J. Phys. Condens. Matter. **14**, L613 (2002).
[27] Z. H. Zhou, J. M. Xue, J. Wang, H. S. O. Chan, T. Yu, Z. X. Shen, J. Appl. Phys. **91,** 6015 (2002).
[28] Z. H. Zhou, J. M. Xue, H. S. O. Chan, J. Wang, Mater. Chem. Phys. **75**, 181 (2002).
[29] A. Barker, Phys. Rev. **136,** A1290 (1964).
[30] D. Berreman, F. Unterwald, Phys. Rev. **174**, 791 (1968).
[31] D. Allali, A. Bouhemadou, E. Muhammad Abud Al Safi, S. Bin-Omran, M. Chegaar, R. Khenata, A. H. Reshak, Physica B **443**, 24 (2014).
[32] P. H. Borse, J. S. Jang, S. J. Hong. J. S. Lee, J. H. Jung, T. E. Hong, C. W. Ahn, E. D. Jeong, K. S. Hong, J. H. Yoo, H. G. Kim, J. Korean Phys. Soc. **55**, 1472 (2009).
[33] M. Meinert, G. Reiss, J. Phys. Condens. Matter. **26**, 115503 (2014).
[34] Y. Todaka, M. Nakamura, S. Hattori, K. Tsuchiya, M. Umemoto, Mater. Tran. **44**, 277 (2003).
[35] E. Manova, B. Kunev, D. Paneva, I. Mitov, L. Petrov, C. Estournes, C. D. Orleans, J.-L. Rehspringer, M. Kurmoo, Chem. Mater. **16**, 5689 (2004).

*Corresponding author: lzorica@yahoo.com

Optical properties of $Cd_{1-x}Mn_xS$ nanoparticles: off-resonance Raman spectroscopy

M. PETROVIĆ, M. ROMČEVIĆ, R. KOSTIĆ, N. ROMČEVIĆ, W. D. DOBROWOLSKI[a], M. GILIĆ, B. HADŽIĆ, J. TRAJIĆ, D. STOJANOVIĆ, Z. LAZAREVIĆ
Institute of Physics, Pregrevica 118, Belgrade, 11080 Serbia
[a]Institute of Physics PAS, Lotnikow 32/46, Warsaw, 02-668 Poland

$Cd_{1-x}Mn_xS$ nanoparticles (x=0.05-0.4) with average particle size of about 2.2nm were synthesized using the colloidal chemistry method and characterized by Raman scattering measurements. The dominant Raman line of $Cd_{1-x}Mn_xS$ nanoparticles was at about 300cm^{-1} showing asymmetric broadening for ω<300cm^{-1}. Significant change in the line intensity for different Mn content x and excitation wavelength λ was noticed.

(Received February 4, 2015; accepted April 5, 2016)

Keywords: Nanostructured materials, Semiconductors, Optical properties, Raman spectroscopy

1. Introduction

$Cd_{1-x}Mn_xS$ nanoparticles (NPs) with size quantum confinement belong to the diluted magnetic semiconductor quantum dot class of materials that has been widely studied in the last few years. The study of diluted magnetic semiconductors, such as $Cd_{1-x}Mn_xS$ quantum dots, is strongly motivated due to the localization of magnetic ions in the same places as the free-like electron and hole carriers occurring in these nanomaterials [1,2]. This interesting phenomenon causes unique properties in diluted magnetic semiconductors dots that can be explored in different technological applications, such as wavelength tunable laser [3], solar cells [4,5], spintronic devices [6], etc. $Cd_{1-x}Mn_xS$ is a typical example of diluted magnetic semiconductor. Mn^{2+} ions can be incorporated in $A^{II}B^{VI}$ semiconductor host in large proportions without substantially altering the crystallographic quality of the material. Finally, Mn^{2+} ion is electrically neutral in an $A^{II}B^{VI}$ host, thus avoiding the formation of any acceptor or donor impurities in the crystal.

Vibrational spectroscopy (Raman spectroscopy) is a powerful, non-destructive technique sensitive to local environment, ideal for *in site* probing during growth and device fabrication and operation [7]. Similar as for the bulk materials, Raman spectroscopy provides information about optical vibrational modes of semiconductor nanoparticles [8-10].

In this paper, we present a continuation of our effort to understand the properties of powders consisting of nanosized diluted magnetic semiconductors preparated using colloidal chemistry method. The influence of the composition and the excitation wavelength on the Raman active vibrations were studied in detail.

2. Synthesis and characterization

Colloidal dispersions consisting of $Cd_{1-x}Mn_xS$ NPs were prepared by mixing a solution containing $Cd(NO_3)_2$ and $MnSO_4$ with a solution containing Na_2S in the presence of surface active agent hexametaphosphate $(NaPO_3)_6$. The concentration of cations ($[Cd^{2+}] + [Mn^{2+}]$) was constant (2×10^{-3}M), while S^{2-} ions were used in excess (2.4×10^{-3}M). The concentration of $(NaPO_3)_6$ was 2×10^{-2}M. Light and air were excluded during the preparation of this colloid. After precipitation of colloidal particles, the solvent was removed by vacuum evaporation at room temperature. The obtained yellow powders could be redisolved in water to give a colloid with the same structured absorption spectrum as the solution before evaporation. The content of Mn^{2+} ions was up to x=0.3 and was checked out by X-ray dispersive fluorescence analysis technique. This technique gives results with uncertainty of 10%.

The X-ray diffraction analysis of $Cd_{1-x}Mn_xS$ NPs showed hexagonal wurtzite crystal structure. UV-Vis absorption spectra were recorded on Perkin-Elmer Lambda 5 instrument. A blue shift of the absorption onset of the $Cd_{1-x}Mn_xS$ nanoparticles compared to the bulk $Cd_{1-x}Mn_xS$ was about 0.3eV. The radius of the particles was calculated using an effective mass approximation model [11]. The calculated value for the particle size of $Cd_{1-x}Mn_xS$ nanoparticles was found to be 2.2nm. The results of experimental and theoretical studies of the Raman active vibrations in nanosized CdS crystals we reported in Ref. [12].

3. Results and discussion

The unpolarized Raman spectra were excited by 488, 496.5, 501.7 and 514.5nm lines of an argon laser in the

back-scattering geometry. The Jobin Yvon U-1000 monochromator, with a conventional photo counting system was used. Measurements were performed in spectral region from 150 to 450cm^{-1} at room temperature. The main feature in measured Raman spectra was mode at ≈300cm^{-1}. Raman mode at ≈300cm^{-1} is slightly asymmetric and broadened toward lower frequencies and can be well identified as LO type phonon mode confined in a spherical nanocrystal.

All $Cd_{1-x}Mn_xS$ NPs samples showed significant changes in experimental Raman line shape, mainly in intensity, as a function of excitation energy. For each Mn content (x), the intensity of the line decreases with the increase of the excitation wavelength λ, where the rate of the decrease depends on the Mn content (x). As an example, the Raman spectra of $Cd_{0.9}Mn_{0.1}S$ sample for various excitation wavelengths (λ= 488, 496.5, 501.7 and 514.5nm) are presented in Fig.1. The ratio of Raman intensities (I_{488}/I_{514}) of mode at about 300cm^{-1} for various contents of Mn^{2+} is given in Fig. 2. This picture summarizes the change in the intensity for all contents (x=0; 0.05; 0.1; 0.15; 0.3) and applied excitations. From Fig. 2 it is clear that the ratio of Raman intensities changes nonlineary as a function of Mn^{2+} content and has a maximum at x=0.1. The observed effect can be explained by the fact that the band gap energy of $Cd_{1-x}Mn_xS$ NPs is a function of particle size and content of Mn^{2+}.

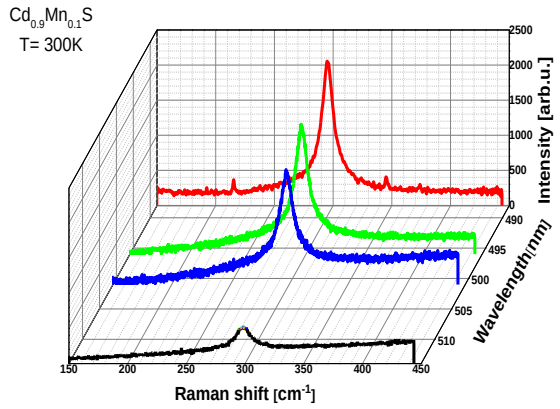

Fig. 1. Raman spectra of the $Cd_{0.9}Mn_{0.1}S$ nanoparticles at different laser excitations (488, 496.5, 501.7 and 514.5nm).

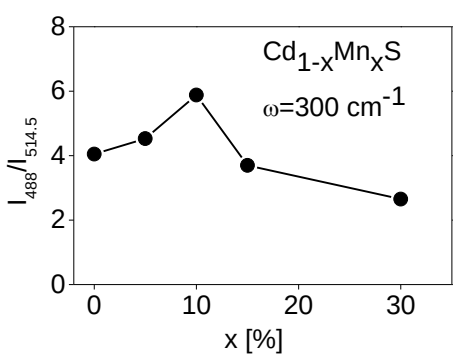

Fig. 2. Ratio of Raman intensities (I_{488}/I_{514}) as a function of Mn^{2+} content.

Decrease of semiconductor nanocrystals size leads to an increase in band gap energy. For a fixed size of $Cd_{1-x}Mn_xS$ nanoparticles the band gap energy is a function of Mn^{2+} content and has a minimum around x=0.1 [13]. Because of that, among the $Cd_{1-x}Mn_xS$ NPs with different Mn^{2+} content, the nanocrystals with x=0.1 are the closest to the resonant regime, and potentially have the strongest intensity of Raman line. The experimental data confirmed that the strongest intensity of Raman line is for the x=0.1 sample for all applied excitation energies.

The $Cd_{1-x}Mn_xS$ NPs were not theoretically treated at this moment, because it is complicate to distinguish the influence of size and Mn^{2+} content on the phonon properties. In the Mn^{2+} doped bulk CdS samples new impurity modes appear between TO-LO frequencies of CdS [14,15]. The TO-LO modes originating from the impurities are not well resolved for the samples with low Mn^{2+} content.

4. Conclusion

We investigated Raman spectra of $Cd_{1-x}Mn_xS$ nanoparticles synthesized using colloidal chemistry method and small enough to show effects due to the phonon confinement. In the Raman spectra an asymmetric line was observed at about 300cm^{-1}. Registered nonlinear change in intensity for different Mn^{2+} content x and excitation energies is connected to nonlinear changes of energy gap.

Acknowledgements

This work was supported under the Agreement of Scientific Collaboration between Polish Academy of Science and Serbian Academy of Sciences and Arts. The work in Serbia was supported by Serbian Ministry of Education, Science and Technological Development (Project 45003) and in Poland by National Science Center granted under decision No. DEC-2011/01/B/ST5/06602.

References

[1] P. I. Archer, S. A. Santangelo, D. R. Gamelin, Nano. Lett. **7**, 1037 (2007).
[2] R. Beaulac, P. I. Archer, S. T. Ochsenbein, D. R. Gamelin, Adv. Funct. Mater. **18**, 3873 (2008).
[3] D. J. Norris, A. L. Efros, S. C. Erwin, Science. **319**, 1776 (2008).
[4] I. Gur, N. A. Fromer, M. L. Geier, A. P. Alivisatos, Science. **310**, 462 (2005).
[5] S. C. Erwin, L. Zu, M. L. Haftel, A. L. Efros, T. A. Kennedy, D. J. Norris, Nature. **436**, 91 (2005).
[6] H. J. Yu, X. Liu, K. E. Kweon, J. Joo, J. Park, K. T. Ko, D. W. Lee, S. Shen, K. Tivakornsasithorn, J. S. Son, J.-H. Park, Y.-W. Kim, G. S. Hwang, M. Dobrowolska, J. K. Furdyna, T. Hyeon, Nature Materials. **9**, 47 (2010).

[7] P. Moriarty, Rep. Prog. Phys. **64**, 297 (2001).
[8] M. P. Chamberlain, C. Trallero-Giner, M. Cardona, Phys. Rev. B **51**, 1680 (1995).
[9] E. Roca, C. Trallero-Giner, M. Cardona, Phys. Rev. B **49**, 13074 (1994).
[10] A. G. Rolo, M. I. Vasilevskiy, M. J. M. Gomes, O. V. Vikhrova, Yu. P. Rakovich, M. V. Artemyev, Proc. Mater. Res. Soc. Symp. **571**, 217 (2000).
[11] L. E. Brus, J. Chem. Phys. **80**, 4403 (1984).
[12] R. Kostic, N. Romcevic, Phys. Stat. Sol. (c) **1**(11), 977 (2004).
[13] L. Levy, D. Ingert, N. Feltin, M. P. Pileni, J. Cryst. Growth **184/185**, 377 (1988).
[14] E.-K. Suh, A. K. Arora, A. K. Ramdas, S. Rodriguez, Phys. Rev. B **45**, 3360 (1992).
[15] S. Venugopalan, A. Petrou, R. R. Galaska, A. K. Ramdas, S. Rodriguez, Phys. Rev. B **25**, 2681 (1982).

*Corresponding author: milicap@ipb.ac.rs

Growth, characterization and optical quality of calcium fluoride single crystals grown by the Bridgman method

HANA IBRAHIM ELSWIE[a], SLOBODANKA KOSTIĆ[b], VESNA RADOJEVIĆ[a], NEBOJŠA Ž. ROMČEVIĆ[b], BRANKA HADŽIĆ[b], JELENA TRAJIĆ[b], ZORICA Ž. LAZAREVIĆ[b,*]
[a]*Faculty of Technology and Metallurgy, University of Belgrade, Belgrade, Serbia*
[b]*Institute of Physics, University of Belgrade, P.O. Box 68, Belgrade, Serbia*

Calcium fluoride - CaF_2 single crystals were grown using the Bridgman technique. By optimizing growth conditions, <111>-oriented CaF_2, crystals up to 20 mm in diameter were grown. Number of dislocations in CaF_2 crystals which were made by the method of Bridgman was 5×10^4 - 2×10^5 per cm^2. In this paper we used XRD, Raman spectroscopy and the measurement of transmission in the mid IR-range to investigated structural and optical properties of obtained CaF_2 single crystals.

(Received November 2, 2015; accepted August 3, 2016)

Keywords: CaF_2, Optical materials, Crystal growth, XRD, Raman spectroscopy

1. Introduction

A calcium fluoride (here after abbreviated as CaF_2) single crystal has excellent transmission characteristics down to the vacuum ultraviolet region, and it is utilized as a lens material in the wafer-stepper of semiconductor lithography technology together with synthetic quartz. CaF_2 single crystals of more than 10 in diameter are required for the lens materials. Such large CaF_2 single crystals are grown by the Czochralski method [1, 2] or the vertical Bridgman method [3, 4]. Extremely high material performances are required for the lens material in the wafer-stepper to achieve high resolution of lithography. Among them, the reduction of birefringence caused by the residual stress is one of the technical problems. In the Czochralski method, residual stress is induced in the crystal by thermal stress, where as, in the vertical Bridgman method, residual stress is induced not only by thermal stress but also due to mechanical stress caused by the contact of the crystal and crucible. Generally as-grown single crystals with larger diameter have larger residual stress, which results in larger birefringence in as-grown crystals. Therefore, annealing after single-crystal growth is in dispensable process, when CaF_2 single crystals are used for the lens material in the wafer-stepper. Such annealing reduces the residual stress and suppresses the birefringence at a low level, but a very long annealing period is required to reduce the birefringence to the target value. Numerical simulations of residual stress and birefringence play an important role for searching effective annealing conditions.

CaF_2 is an ionic crystal with the fluorite structure. The lattice is a face centered cubic (*fcc*) structure with three sublattices. The unit cell of the material is most easily described as a simple cubic lattice formed by the F^- ions where a Ca^{2+} ion is contained in every second cube. The remaining empty cubes (called interstitial or hollow sites) are important for defect formation and diffusion, but also for the accommodation of unwanted impurities like rare earth ions and dopants. The lattice constant is a = 5.4626 Å [5] (Fig. 1).

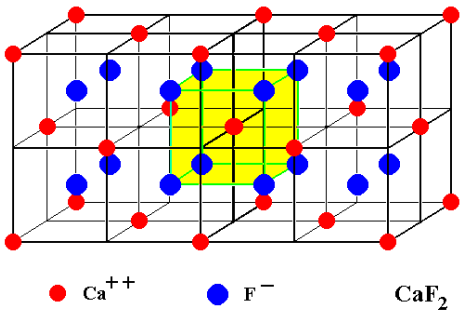

Fig. 1. Unit cell representation of CaF_2 structure

Single crystal CaF_2 used in the optical device can be of natural origin - fluorite, under which name is often referred to in literature [6] and synthetic single crystal CaF_2 which is usually obtained growth from the melt. By its chemical and physical properties of the single crystal CaF_2 is very different from other materials that have been developed techniques to obtain single crystals. The relatively high melting point (over 1300 °C), high chemical aggressiveness of fluorine at these temperatures, relatively small chemical compounds CaF_2 stability at high temperatures and very strong ability to react CaF_2 with traces of water vapor, require the use of special growth conditions to obtain quality crystals. Therefore, the growth of a single crystal CaF_2 may take place either in vacuum or in an inert gas atmosphere (argon or helium) at purity of at

least 99.99% in order to prevent the presence of traces of moisture or oxygen.

The aim of the present work was to obtain single crystal CaF_2 optical quality. The structural and optical properties obtained crystal was characterized using XRD, Raman and FTIR spectroscopic characterization.

2. Experimental procedures

The Bridgman method of crystal growth is relatively simple and allows operation in a vacuum, and also in an inert atmosphere. In this method, the crucible uses a cylindrical shape with a conical bottom. The procedure consisted of the following: the crucible cylindrical shape with melted batch CaF_2 down from the upper hot chamber of the furnace in the cooler lower chamber of the same furnace. The bottom of the crucible was in the shape of a cone and that in the formation of germs and begins the process of crystallization. The crucible was from spectroscopically pure graphite [2-8]. One of the main drawback of this method is that in the course of growth can be seen the process of crystal growth, so that if it comes to the appearance of polycrystalline, this can be concluded only after the completion of the process of growth and cooling crystals.

To obtain single crystals of CaF_2 by the Bridgman method in a vacuum has been used device BCG 356. Initial samples of single crystals were mostly clear and transparent, but some were cracked. Because of the small temperature gradient there were a sudden crystallization process and the appearance of dendrites in the lower part of the crucible, and therefore made changes to the structure of the crucible. With this change we have achieved that cone of the lower part of the crucible is in the form of a tube. Therefore we have achieved that by the sudden crystallization takes an extended part of the crucible, thus avoiding the occurrence of dendrites. The crystals that were obtained on the crucible constructed in this way were of better quality. However, when grinding the upper surface of the crystal, because the dirt that clung to that, there have been cracks crystal along a plane of cleavage.

Experiments have been performed with CaF_2 in the form of a powder. Since this device works in a vacuum, there was a danger that the air contained in the powder CaF_2, when you turn on the vacuum pump, disperses the powder throughout the apparatus. Therefore, the CaF_2 powder was compaction and sintered in the form of pills. With such obtained pills could easily and quickly be filled crucible. Power generator was initially P_{gen} = 3.8 kW, and was later increased to P_{gen} = 3.94 kW. The crystal growth rates were 6 mm h^{-1}, 12 mm h^{-1}, 24 mm h^{-1} and 48 mm h^{-1}.

The observations relating to the dislocation were recorded by observing an etched surface of CaF_2 crystal, using a Metaval of Carl Zeiss Java metallographic microscope with magnification of 270x. To test the dislocations were used CaF_2 samples that are obtained by cleaving the crystals CaF_2 per plane splitting <111>. The samples were etched with concentrated sulfuric acid from 10 to 30 min. It has been shown that the best results are obtained on the sample crystal is etched for 15 min.

The crystal structure of CaF_2 single crystal was approved using the X-ray diffractometer (XRD, Model Philips PW 1050 diffractometer equipped with a PW 1730 generator, 40 kV x 20 mA, and using CuKα radiation of 1.540598 Å at the room temperature. Measurements were done in 2θ range of 10-90° with scanning step width of 0.05° and 10 s scanning time per step.

The Raman scattering measurements of CaF_2 crystal was performed in the backscattering geometry at room temperature in the air using a Jobin-Yvon T64000 triple spectrometer, equipped with a confocal microscope (100x) and a nitrogen-cooled charge coupled device detector (CCD). The spectra have been excited by a 514.5 nm line of Coherent Innova 99 Ar^+ - ion laser with an output power of less than 20 mW to avoid local heating due to laser irradiation. Spectra were recorded in the range from 100 - 800 cm^{-1}.

The transmission a spectrum of CaF_2 sample (powdered and pressed in the disc with KBr) was obtained by transmission Fourier transforms infrared (FTIR) Hartmann&Braun spectrometer, MB-series. The FTIR spectrum was recorded between 4000 and 400 cm^{-1} with a resolution of 4 cm^{-1}.

3. Results and discussion

CaF_2 single crystals are obtained by the vertical Bridgman method in vacuum. Experiments were carried out with the crystal growth rate of 6-48 mm h^{-1}. The best result was obtained with a crystal growth rate of 6 mm h^{-1}. If the growth rate of the single crystal CaF_2 larger, experiments showed that these crystals contain more stress and that in this case it is more likely to obtain polycrystals. Stresses in single crystals we have tried to eliminate annealing of crystals. The process of annealing was carried out on the plate and bulk crystal CaF_2. The temperature of annealing of the plate was at 1000 °C for 3 h, and the temperature of annealing of the bulk crystal was at 1000 °C and 1080 °C for 1 - 3 h. Annealing is carried out under an inert atmosphere of argon. It was noticed that after annealing, plate CaF_2 did not have enough stress. Annealing bulk single crystal CaF_2 had less stress than non-annealing. The obtained single crysta of CaF_2 was 20 mm in diameter and 90 mm in length. A polished plate of CaF_2 with a diameter of 20 mm is displayed in Fig. 2.

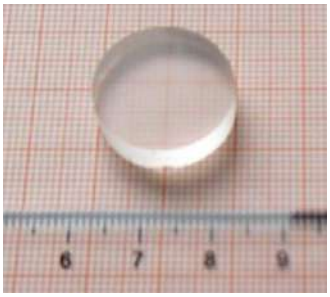

Fig. 2. Photographs of Bridgman-grown CaF_2 single crystals

The general conclusion is that in all samples was observed relatively high dislocation density (ranging from 60000 to 140000) as a consequence of greater internal stresses, which have emerged in the process of cooling. From the Fig. 3 it can be observed dislocations on CaF_2 single crystal. Etch pits have the shape of a three-sided pyramid. Number of dislocations in CaF_2 crystals which were made by the method of Bridgman was $5 \cdot 10^4$ - $2 \cdot 10^5$ per cm^2 (Fig. 3).

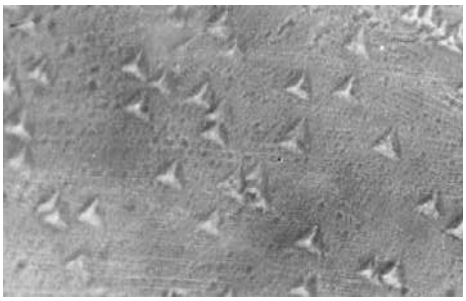

Fig. 3. The microscopic image of the surface CaF_2 crystal plate in the direction <111>. Magnification of 270x

The sample of CaF_2 single crystal was of cubic structure with the *Fm*3*m* space group [9]. XRD pattern (Fig. 4) was indexed by using JCPDS database (card no. 87-0971). The XRD pattern was found to match exactly with those reported in the literature [10, 11]. The displayed peaks correspond to (*h k l*) values of (1 1 1), (2 2 0), (3 1 1), (4 0 0), (3 3 1) and (4 2 2). Using the (*h k l*) values of different peaks, the lattice constant (*a*) of the sample was calculated. Their lattice parameter was calculated from the equation of plane spacing for cubic crystal system and Bragg's law for diffraction [12]. The lattice parameter was 5.452±0.011 Å, calculated from the obtained XRD diagram, which was in good agreement with the literature [5, 13].

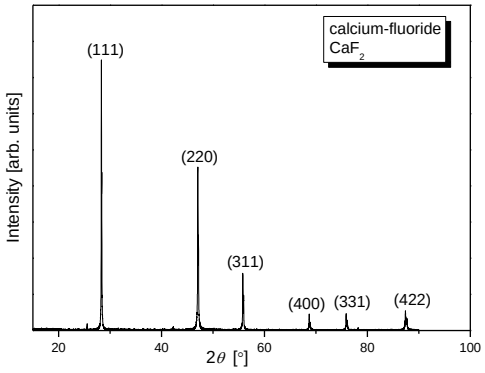

Fig. 4. X-ray diffraction pattern of the CaF_2 powdered sample

Three atoms in cubic O^5_h (*Fm*3*m*) primitive cell of the CaF_2 crystal are given nine fundamental vibrations, described by the following O_h-irreducible representations (at $k = 0$): $\Gamma = 2T_{1u} + T_{2g}$. According to several comprehensive work (see, e.g. [14-19]), their distribution among optical and acoustical are: the triply degenerate T_{2g} optical phonon is Raman active and IR inactive; one of the T_{1u} representations (triply degenerate as well) corresponds to the zero frequency acoustic mode, while the other T_{1u} species is actually split into a double degenerate transverse optical mode and a nondegenerate longitudinal optical mode, all the above are IR active. The room-temperature first order T_{2g} one-band spontaneous Raman scattering spectra of CaF_2 crystal is shown in Fig. 5. In this single allowed SRS-promoting optical mode with frequency ω_{SRS} = 319.7 cm^{-1} Ca^{2+} cation remains stationary and the neighboring substitutional fluoride F^{-1} ions vibrate against each other [19-21].

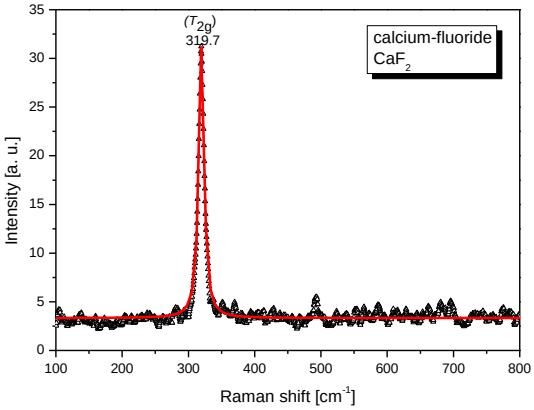

Fig. 5. Raman spectra of the CaF_2 single crystal at room temperature

FTIR transmission was measured in order to check the purity of the obtained CaF_2. As shown in Fig. 6, the sharp peaks of the absorption at 2854 cm^{-1} and 2936 cm^{-1} are assigned to the symmetric and antisymmetric stretching vibration of $-CH_2$ groups [22]. Also, the spectra shows two broad IR absorption peaks at ~3432 cm^{-1} and 1628 cm^{-1} are assigned to the symmetrically stretching vibration and antisymmetric stretching vibration of hydroxyl groups -OH, implying the presence of H_2O molecules [23, 24]. The peak at 671 cm^{-1} in the FTIR spectra was assigned to the Ca-F stretching vibration of CaF_2 [25]. The band at ~2357 cm^{-1} is due to KBr pellets used for recording FTIR spectrum [26].

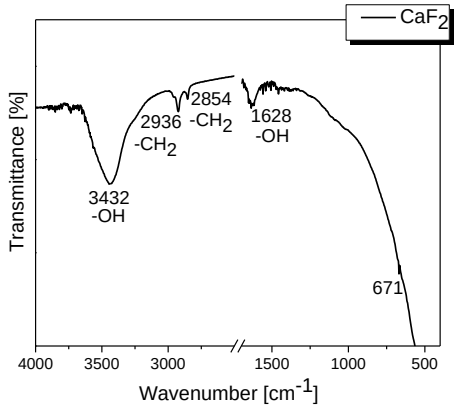

Fig. 6. FTIR spectra of CaF_2

The properties of the crystal, such as density of dislocations, cystallinity, and impurities concentrations, determine the optical quality.

4. Conclusions

CaF_2 single crystals in diameter of 20 mm are obtained by the vertical Bridgman method in vacuum. The crystal growth rate was 6.0 mm h^{-1}. Number of dislocations is of the order of 5×10^4 - 2×10^5 per cm^2. The crystal structure was confirmed by XRD. The Raman T_{2g} optical mode at 319.7 cm^{-1} was observed. The FTIR transmission spectra indicate that there are some amounts of -CH2, -OH or water molecules and organic groups adhering to the surfaces. Based on our work and observations during the experiment, it could be concluded that the obtained transparent single crystal CaF_2 of good optical quality, which was the goal of our work.

Acknowledgements

This research was financially supported by the Ministry of Education, Science and Technological Development of the Republic of Serbia through Projects No. III45003 and TR34011.

References

[1] L. Su, Y. Dong, W. Yang, T. Sun, Q. Wang, J. Xu, G. Zhao, Mater. Res. Bull. **40**, 619 (2005).
[2] H. Yanagi, T. Nawata, Y. Inui, Y. Hatanaka, E. Nishijima, T. Fukuda, Proc. SPIE 5377, Optical Microlithography XVII, 1886 (May 28, 2004); doi:10.1117/12.556614.
[3] N. Senguttuvan, M. Aoshima, K. Sumiya, H. Ishibashi, J. Crys. Growth **280**, 462 (2005).
[4] J. Xu, M. Shi, B. Lu, X. Li, A. Wu, J. Crys. Growth **292**, 391 (2006).
[5] G. Scholz, I. Dörfel, D. Heidemann, M. Feist, R. Stösser, J. Solid State Chem. **179**, 1119 (2006).
[6] I. V. Stepanov, P. P. Feofilov, Artificial fluorite. In Rost kristalov (Vol. I), Moscow, Russia: Akademia Nauk SSSR. (in Russian), 1957, p. 229.
[7] G. V. Molev, V. E. Bozherolnog, J. Cryst. Growth **19**, 117 (1973).
[8] K. Recker, R. Leckebusch, J. Cryst. Growth **9**, 274 (1971).
[9] L. Gerward, J. S. Olsen, S. Steenstrup, M. Malinowski, S. Åsbrink, A. Waskowska, J. Appl. Crystallogr. **25**, 578 (1992).
[10] B.-C. Hong, K. Kawano, J. Alloys Compd. **408-412**, 838 (2006).
[11] N. D. Alharbi, J. Nanomaterials **2015**, Article ID 136957, 8 pages, http://dx.doi.org/10.1155/2015/136957.
[12] S. Biswas, S. Kar, S. Chaudhuri, J. Cryst. Growth **299**, 94 (2007).
[13] L. G. DeShazer, S. C. Rand, B. A. Wechsler, in: M. J. Weber (ed.) Handbook of Laser Science and Technology, **V**, Optical Materials: Part 3(CRC Press, Boca Raton, FL), 1988, pp.281.
[14] R. K. Chang, B. Lacina, P. S. Pershan, Phys. Rev. Lett. **17**, 755 (1966).
[15] J. R. Ferraro, H. Horan, A. Quattrochi, J. Chem. Phys. **55**, 664 (1971).
[16] D. G. Mead, G. R. Wilkison, J. Phys. C **10**, 1063 (1977).
[17] D. J. Oostra, H. W. den Hartog, Phys. Rev. B **29**, 2423 (1984).
[18] P. C. Ricci, A. Casu, G. de Giudici, P. Scardi, A. Anedda, Chem. Phys. Let. **444**, 145 (2007).
[19] A. A. Kaminskii, S. N. Bagayev, H. J. Eichler, H. Rhee, K. Ueda, K. Takaichi, K. Oka, H. Shibata, Y. Hatanaka, Y. Matsumoto, Laser Phys. Lett. **8**, 385 (2006).
[20] L. Su, J. Xu, W. Yang, X. Jiang, Y. Dong, Chinese Optics Letters **3**, 219 (2005).
[21] J. P. Russell, Proceedings of the Physical Society **85**, 194 (1965).
[22] J. Song, G. Zhi, Y. Zhang, B. Mei, Nano-Micro Lett. **3**, 73 (2011).
[23] L. Zhou, D. Chen, W. Luo, Y. Wang, Y. Yu, F. Liu, Mater. Lett. **61**, 3988 (2007).
[24] G. A. Kumar, C. W. Chen, J. Ballato, R. E. Riman, Chem. Mater. **19**, 1523 (2007).
[25] K. Tahvildari, M. Esmaeili Pour, Sh. Ghammamy, H. Nabipour, Int. J. Nano Dim. **2**, 269 (2012).
[26] C. Pandurangappa, B. N. Lakshminarasappa, B. M. Nagabhushana, J. Alloys Compd. **489**, 592 (2010).

*Corresponding author: lzorica@yahoo.com

Raman spectroscopy study of anodic film on $Ag_{43}Cu_{37}Zn_{20}$ alloy

S. P. DIMITRIJEVIĆ[a], Z. Ž. LAZAREVIĆ[b, *], M. RAJČIĆ-VUJASINOVIĆ[c], S. B. DIMITRIJEVIĆ[d], M. PETROVIĆ[b], M. GILIĆ[b], B. M. JOKIĆ[e]

[a]*Innovation Center Faculty of Technology and Metallurgy, University of Belgrade, Belgrade, Serbia*
[b]*Institute of Physics, University of Belgrade, P.O. Box 68, Belgrade, Serbia*
[c]*Technical Faculty in Bor, University of Belgrade, Bor, Serbia*
[d]*Mining and Metallurgy Institute Bor, Bor, Serbia*
[e]*Faculty of Technology and Metallurgy, University of Belgrade, Belgrade, Serbia*

The objective of this study was characterization of anodic film obtained when $Ag_{43}Cu_{37}Zn_{20}$ alloy was treated electrochemically in 3.5% wt. NaCl under potentiostatic conditions. At the potential of +0.25 V a complex multilayer film is formed. XRD shows that it consists of CuCl and zinc hydroxichlorides with a small amount of Cu_2O, probably formed in the film pores. The anodic film is a mixture of Cu_2O, CuCl, $Zn_5(OH)_8 \cdot H_2O$ and β-Zn(OH)Cl. Phases of the alloy, Ag and Cu rich, show different anodic behavior. It was assumed that all phonon lines in the obtained Raman spectra were of the Lorentzian type, which is one of the common type of lines for this kind of analysis. Phases of Ag, CuCl, β-Zn(OH)Cl, Cu_2O and $Zn_5(OH)_8(Cl)_2 \cdot H_2O$ were all registered by XRD.

(Received July 8, 2015; accepted September 29, 2016)

Keywords: $Ag_{43}Cu_{37}Zn_{20}$ alloy, Anodic film, Brazing materials, Raman spectroscopy

1. Introduction

Silver based brazing filler alloy are used for joining most ferrous and nonferrous metals, except Al and Mg. This classification includes a range of silver based filler metal compositions which may have various additions such as Cu, Zn, Cd, Sn, Mg, Ni and Li.

Generally speaking, the addition of Zn lowers the melting temperature of the Ag-Cu binary alloys and helps wet Fe, Co and Ni. Cd is also effective in lowering the brazing temperature of these alloys and assists in wetting a variety of base metals. Especially, Cd and Zn are vaporized during brazing.

The joining technique of copper alloy to steel has been widely applied in nuclear, aerospace and industry fields [1-3]. The conventional fusion welding of these materials usually leads to the irregularity interface and welding deficiency between copper alloy and steel [4, 5].

Silver based brazing filler alloys are commercially available as both wrought and cast products, including wire and cable, sheet, strip, plate, rod, bar, tubing, forgings, extrusions, castings and powder metallurgy shapes. Certain mill products, chiefly wire, cable and most tubular products, are used by customers without further metal working. On the other hand, most flat rolled products, rod, bar, mechanical wire, forgings and castings go through multiple metal working, machining, finishing and/or assembly operations before emerging as finished products.

Electrochemical properties in chloride solutions of the alloys that belong to the Ag-Zn-Cu system are investigated recently [6, 7]. These alloys do not show an anodic passive film region on polarization curves, although they have anodic film on the surface. The aim of the present work was to structural and spectroscopic study of electrochemically treated Ag-Cu-Zn alloy in 3.5% wt. NaCl.

2. Experimental procedures

The silver (99.99%), copper (99.99%) and zinc (99.995%) for electrode preparation were produced by recycling process. More details of the process and analytics can be found elsewhere [8-10]. The alloy for the electrode was prepared by ingot metallurgy method in two phases. The second, repeated, process was required due to high zinc losses for small charges. The obtained ingot was machined into cylinders with 7.14 mm diameter. It was subjected to homogenization annealing at 600 °C (T=0.92 Tmelt.) for 24 h in nitrogen atmosphere and slowly cooled for the next 8 h to the room temperature in the same protective atmosphere. Finally, the specimen was mounted in polytetrafluoroethylene mould. Chemical composition (wt.%) of the alloy used in the present study was 43.5% Ag, 37.7% Cu, 18.8% Zn, and trace amounts (in total less than 20 wt. ppm) of Pb, Sn, Ni, Fe and Cd, according chemical analysis performed by inductively coupled plasma atomic emission spectroscopy. This composition fulfills requirements of BS1845:1984 Ag5 standard [11].

All chemicals were of analytical grade produced by Merck (Germany). All solutions were prepared with ultra-

pure water of resistivity not less than 18 MΩ·cm. Test solution, 3.5 wt. % NaCl, was prepared by dissolving 35.000 g of NaCl in 1000 ml glass flask to the total mass of solution of 1000.00 g. pH value was adjusted to pH = 6.70 ± 0.15 by dropwise addition of 0.1 M NaOH solution.

X-ray Powder Diffraction (XRPD) patterns of investigated sample were obtained on a Philips PW-1050 diffractometer, operated at 40 kV and 30 mA, using Ni-filtered $CuK_{\alpha 1,2}$ radiation. The Bragg-Brentano focusing geometry was used with a fixed 1° divergence and 0.1° receiving slits. The patterns were taken in 10-100° 2θ range with step of 0.05° and exposure time of 6 s per step. For X-ray structural phase analysis, software EVA 9.0 Release 2003, Bruker AXS GmbH, Karlsruhe, Germany, was used.

The micro-Raman spectra were taken in the backscattering configuration and analyzed using a JobinYvon T64000 spectrometer, equipped with a nitrogen cooled charge-coupled-device detector. As an excitation source we used the 532 nm line of a Ti:sapphire laser. The measurements were performed at 20 mW laser power.

The alloy surface and corrosion products were studied using the scanning electron microscope (SEM model: JOEL JSM-6610LV operated at 20 kV) and field emission scanning electron microscopy (FEG-SEM model: TESCAN MIRA3 operated at 20 kV). Chemical composition of the alloy surface and products on surface were determined using energy dispersive X-ray spectroscopy (EDS). EDS detector was Oxford Instruments model X-Max SDD.

3. Results and discussion

Fig. 1 shows the results of X-ray diffraction (XRD) of the specimen after the potentiostatic test. The peaks of phases, ($Ag_{1-x-y}Cu_yZn_x$) solid solution and Cu_3Zn (α-brass) are present, as well as before the potentiostatic test.

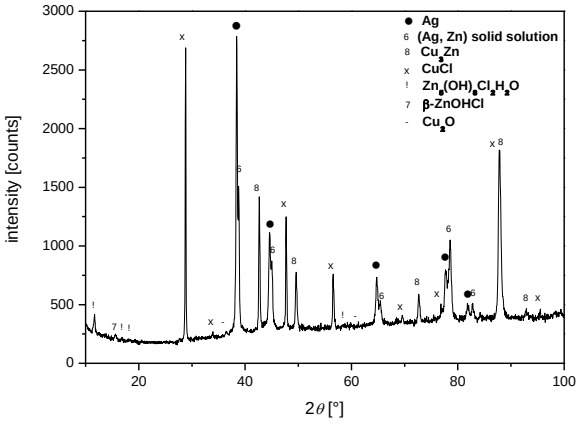

Fig. 1. RD pattern of the $Ag_{43}Cu_{37}Zn_{20}$ electrode after anodic potentiostatic polarization treatment at +0.25 V for 5 min in 3.5% wt. NaCl solution at 25 °C.

X-ray structural phase analysis was applied for identification the new phases formed after potentiostatic test using the EVA 9.0 computing program. It can be noticed that beside the peaks that belong to ($Ag_{1-x-y}Cu_yZn_x$) solid solution phase, the peaks that correspond to pure Ag phase also have appeared. They have been formed by reduction of Zn and Cu content in solid solution during the potentiostatic polarization at +250 mV. The peaks of ($Ag_{1-x-y}Cu_yZn_x$) solid solution phase are positioned at somewhat larger 2theta (2θ) values than the peaks of pure Ag phase. This difference increases with an increase of 2θ angles, meaning that the lattice parameter of Ag-rich phase is smaller than the lattice parameter of pure Ag phase, which can be explained by larger ionic radius of Ag than ionic radii of Zn and Cu. Noticeable increase of relative ratio of ($Ag_{1-x-y}Cu_yZn_x$) solid solution and pure Ag phases with the increase of 2θ angle implies that electrode surface is covered by pure Ag in thin layer beneath which is ($Ag_{1-x-y}Cu_yZn_x$) solid solution phase.

Fig. 2 shows the Raman spectra of the $Ag_{43}Cu_{37}Zn_{20}$ alloy recorded after anodic potentiostatic polarization treatment at +0.25 V for 5 min in 3.5% wt. NaCl solution at room temperature. The main Raman peaks are indicated in the spectrum. The presence of silver (Ag), cuprous chloride (CuCl), zinc hydroxychloride (β-Zn(OH)Cl), cuprous oxide (Cu_2O) and simonkolleite ($Zn_5(OH)_8(Cl)_2 \cdot H_2O$) is registered.

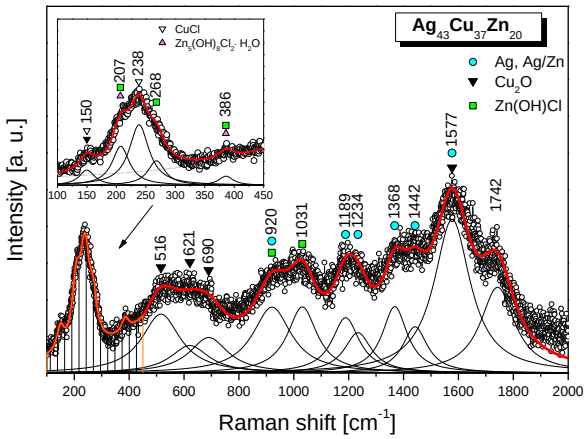

Fig. 2. Raman spectra of the $Ag_{43}Cu_{37}Zn_{20}$ alloy at room temperature.

Very strong silver peaks (cyan circles) indicate the formation of Ag areas, segregate from the Cu-Zn alloy. Observed Ag peaks at 920, 1189, 1234, 1368, 1442 and 1577 cm^{-1} are in general agreement with the previously published results [12].

Cuprous chloride has the cubic zinc blende structure with two atoms in the primitive cell so that there is only one triply degenerate fundamental optic mode, which is both Raman and infrared active. The first-order phonons of CuCl visible in Raman spectra (open triangles) are *TO*-phonon at 150 cm^{-1} and *LO*-phonon at 238 cm^{-1} [13, 14]. β-Zn(OH)Cl (green squares) are illustrated in Fig. 2. Three main peaks are observed at 207 and 268 cm^{-1}, assigned to a Zn-Cl bond, and 386 cm^{-1}, attributed to a Zn-O vibration

characteristic of this structure. Zinc hydroxychloride is also characterized by two main OH fundamental stretching bands at 920 and 1031 cm^{-1} [15, 16].

Cu_2O crystallizes in a cubic lattice with two molecules per unit cell and space group Pn3m. Since it exhibits inversion symmetry, its electronic and vibrational states are of definite parity. In the Raman spectra of treated alloy are seen several Cu_2O modes (black triangles). A weak mode at about 150 cm^{-1} can be a combination of *TO*-mode of CuCl and mode of Cu_2O. At 515, 621 and 690 cm^{-1} are modes of Cu_2O [17-19]. The Raman peaks at 207 and 386 cm^{-1} indexed by pink triangle, which agree very well with what are found in the [12], were assigned to $Zn_5(OH)_8(Cl)_2 \cdot H_2O$ (simonkolleite). A peak at 207 cm^{-1} was attributed to the Zn-Cl bond and that at 386 cm^{-1} to Zn-O which had a vibration characteristic of a simonkolleite structure. The presence of Ag, CuCl, β-Zn(OH)Cl, Cu_2O and $Zn_5(OH)_8(Cl)_2 \cdot H_2O$ is in agreement with the XRD results.

Fig. 3 shows a typical SEM image of surface film formed under potentiostatic condition over the Cu_3Zn phase. Two characteristics formations are observed, dark and bright features. At the level of surface of 100-200 pm^2 relatively homogeneously distributed crystals on the film surface are evident. Among the numerous crystals of irregular shape, those with tetrahedral structure are particularly recognized. CuCl has this structure although octahedral Cu_2O and hexagonal ZnO could have similar appearance. Dark parts of the image are micropores in the film structure. Position of the *fcc* structured crystals suggests chemical origin of the deposition. It is a characteristic of CuCl surface films on pure copper and brass. Fig. 3 indicates rapid crystal nucleation.

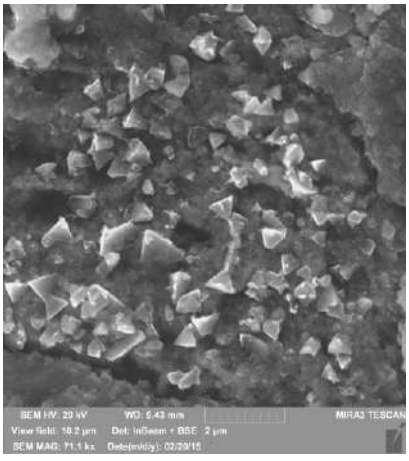

Fig. 3. FE SEM micrograph of the $Ag_{43}Cu_{37}Zn_{20}$ *alloy sample after potentiostatic polarization at +250 mV and for 300 s, part of surface film over* Cu_3Zn *phase*

These crevices are deep and could directly connect electrode surface and electrolyte. Crystals of CuCl smaller than 1 μm in different phases of formation and sizes in the range of magnitude order, from a few tens up to few hundreds of nm. Rounded grains are probably redeposited copper and black basic matrix is mixture of copper and zinc compounds revealed by XRD and Raman. This indicates that darker surfaces of anodic film originated from Cu_3Zn phase. It is possible that insoluble compounds of Cu and Zn originated form Ag solid solution as well, but since lower concentrations of soluble Cu (copper chloride complexes like $CuCl_2^-$ and $CuCl_3^{2-}$) it is unlikely that activity of these ions in the outer Helmholz plane exceeds the solubility equilibrium for the reaction: $CuCl_2^- \leftrightarrow CuCl_{(film)} + Cl^-$ [20]. Similar is for Zn soluble chloride complexes $ZnCl_4^{2-}$ and $Zn(OH)_2Cl_2^{2-}$ in relation with Zn(OH)Cl [21].

Very different surface is observed in the areas of over the silver solid solution (Fig. 4). These parts are formed over Ag-rich phase. Nanosized white grains are the main part of structure with some micro sized irregular shaped agglomerated particles. Basic structure (without agglomerates) is probably result of dealloying (mainly dezincation but also decopperization) of the Ag-rich phase as suggested from XRD analysis. SEM micrograph (Fig. 4) indicates that the structure is even more porous than the previous one shown in Fig. 3.

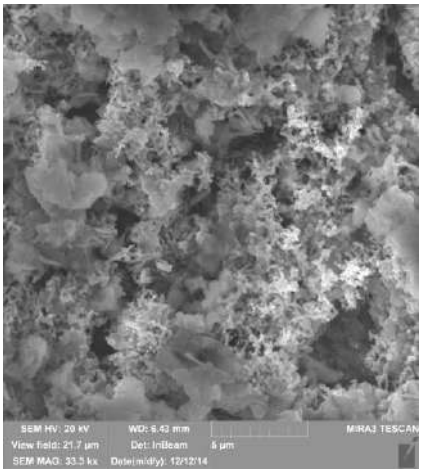

Fig. 4. FE SEM micrograph of the $Ag_{43}Cu_{37}Zn_{20}$ *alloy sample after potentiostatic polarization at +250 mV for 300 s, part of surface film over (Ag, Zn) solid solution.*

The compositions of areas shown in Fig. 3 and Fig 4, were determined by means of EDS. Absence of silver is characteristics of area in Fig. 3 and low concentration of Cu and Zn of area in Fig. 4. Lower concentration of Zn indicates dealloying of silver solid solution.

Table 1. EDS analysis in Fig. 3 and Fig 4.

Element/	O		Cl		Cu		Zn		Ag	
Area	At. %	Wt. %	At. %	Wt. %	At. %	Wt. %	At. %	Wt. %	At. %	Wt. %
Fig. 3	16.86	5.55	25.45	18.57	47.27	61.82	10.38	13.97	0.04	0.09
Fig. 4	21.51	4.70	9.11	4.41	15.98	13.87	2.82	2.52	50.58	74.50

4. Conclusions

The anodic film formed on alloy in 3.5% NaCl solution under potentiostatic conditions is a mixture of Cu_2O, CuCl, $Zn_5(OH)_8 \cdot H_2O$ and β-Zn(OH)Cl. Phases of the alloy, Ag and Cu rich, show different anodic behavior. For analysis of the Raman spectra it was assumed that all phonon lines were of the Lorentzian type, which is one of the common type of lines for this kind of analysis. That analysis combined with the XRD proved that phases of Ag, CuCl, β-Zn(OH)Cl, Cu_2O and $Zn_5(OH)_8(Cl)_2 \cdot H_2O$ form the anodic product on the electrode surface. Porosity of film at surface is confirmed by SEM images.

Acknowledgements

This research was financially supported by the Ministry of Education, Science and Technological Development of the Republic of Serbia through Projects No. III45003 and TR34033.

References

[1] A. F. Rowcliffe, S. J. Zinkle, J. F. Stubbins, D. J. Edwards, D. J. Alexander, J. Nucl. Mater. **258-263**, 183 (1998).
[2] K. Ioki, F. Elioa, V. Barabash, V. Chuyanov, V. Rozov, X. Wang, J. Chen, L. Wang, P. Lorenzetto, A. Peacock, M. Enoeda, H. Nishi, B. G. Hong, Y. H. Jeong, A. Gervash, I. Mazul, T. Tanaka, M. Ulrickson, Fusion Eng. Des. **82**, 1774 (2007).
[3] G. Le Marois, C. Dellis, J. M. Gentzbittel, F. Moret, J. Nucl. Mater. **233-237**, 927 (1996).
[4] H. Wang, K. Wang, R. Zheng, K. S. Prasad, S. P. Ringer, Mater. Charact. **59,** 542 (2008).
[5] I. Magnabosco, P. Ferro, F. Bonollo, L. Arnberg, Mater. Sci. Eng. A **424**, 163 (2006).
[6] A. Ntasi, Y. Al Jabbari, W. D. Mueller, G. Eliades, S. Zinelis, Angle Orthod. **84**, 508 (2014).
[7] S. P. Dimitrijević, M. Rajčić-Vujasinović, Ž. Kamberović, S. B. Dimitrijević, V. Grekulović, B. Trumić, A. Ivanović, Materials Transactions **56**, 2088 (2015).
[8] S. P. Dimitrijević, Z. Anđić, Ž. Kamberović, S. B. Dimitrijević, N. S. Vuković, Bulg. Chem. Commun. **46**, 814 (2014).
[9] A. Ivanović, S. Dimitrijević, S. Dimitrijević, B. Trumić, V. Marjanović, J. Petrović, N. Vuković, Optoelectron. Adv. Mat. **6,** 465 (2012).
[10] Z. Stanojević-Šimšić, S. Dragulović, S. Dimitrijević, V. Trujić, V. Conić, A. Ivanović, V. Gardić, Optoelectron. Adv. Mat. **6,** 1197 (2012).
[11] A. C. Davies, The science and practice of welding, **2**, The practice of welding, Cambridge University Press, Cambridge, United Kingdom (1993).
[12] H. Liang, Z. Li, W. Wang, Y. Wu, H. Xu, Adv. Mater. **21**, 4614 (2009).
[13] K. Fukushi, M. Nippus, R. Claus, Phys. Stat. Sol. (b) **86**, 257 (1978).
[14] S. Iwasa, E. Burstein, J. Physique **26**, 614 (1965).
[15] M. C. Bernard, A. Hugot-Le Goff, D. Massinon, N. Phillips, Corros. Sci. **35**, 1339 (1993).
[16] H. D. Lutz, M. Schmidt, B. Weckler, J. Raman Spectrosc. **24**, 797 (1993).
[17] A. L. Ma, S. L. Jiang, Y. G. Zheng, W. Ke, Corros. Sci. **91,** 245 (2015).
[18] A. Compaan, H. Z. Cummins, Phys. Rev. Lett. **31**, 41 (1973).
[19] R. J. Eliot, Phys. Rev. **124**, 340 (1961).
[20] D. Tromans, R. Sun, J. Electrochem. Soc. **138**, 3235 (1991).
[21] T. Kosec, I. Milošev, B. Pihlar, Appl. Sur. Sci. **253**, 8863 (2007).

*Corresponding author: lzorica@yahoo.com

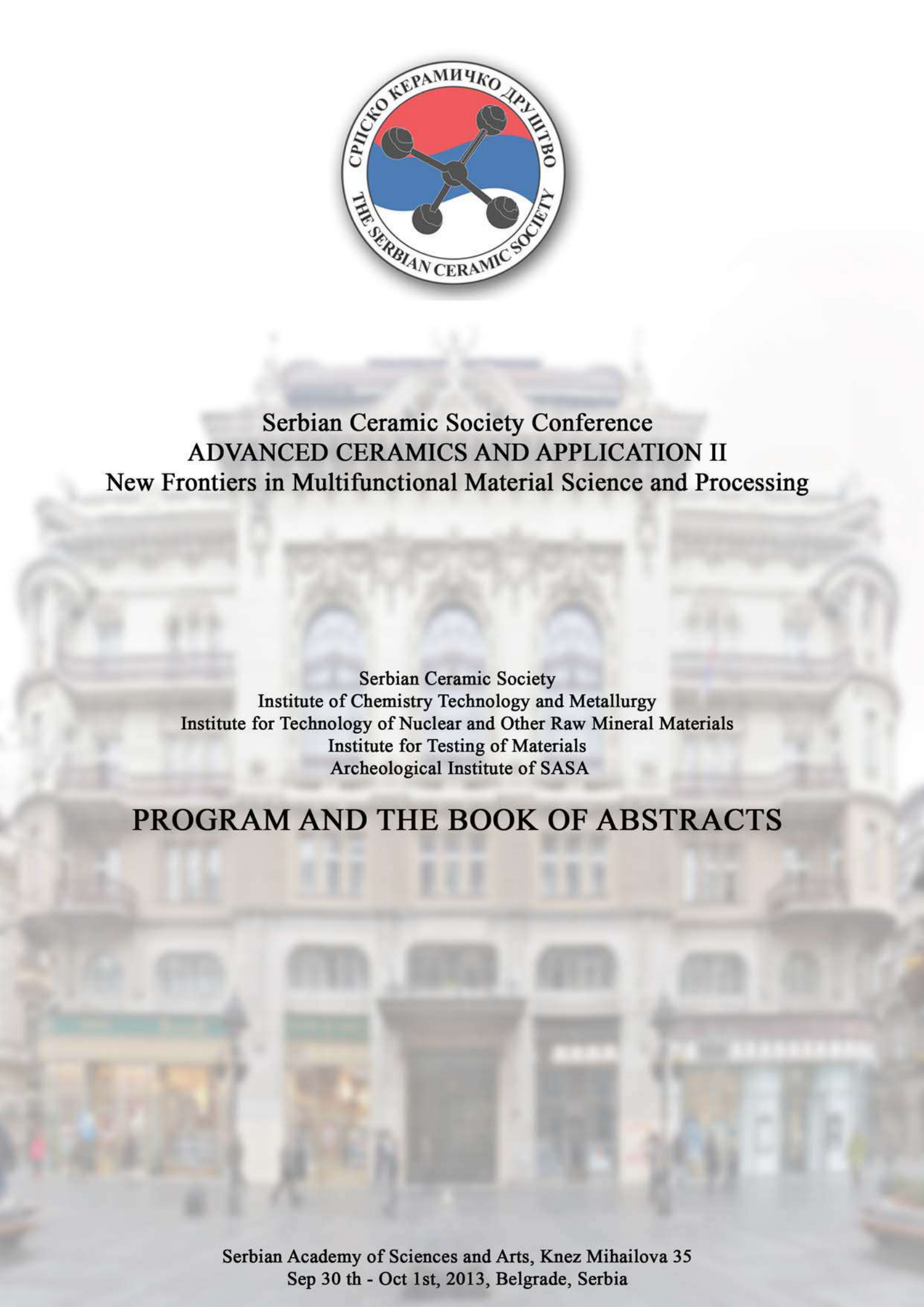

Serbian Ceramic Society Conference
ADVANCED CERAMICS AND APPLICATION II
New Frontiers in Multifunctional Material Science and Processing

Serbian Ceramic Society
Institute of Chemistry Technology and Metallurgy
Institute for Technology of Nuclear and Other Raw Mineral Materials
Institute for Testing of Materials
Archeological Institute of SASA

PROGRAM AND THE BOOK OF ABSTRACTS

Serbian Academy of Sciences and Arts, Knez Mihailova 35
Sep 30 th - Oct 1st, 2013, Belgrade, Serbia

INV2

New approach and comparative studies of structura; and electrical properties of nano spinel ferrites prepared by soft mechanochemical synthesis

Z. Ž. Lazarević[1], D. Sekulić[2], Č. Jovalekić[3],
M. Romčević[1], A. Milutinović[1], N. Ž. Romčević[1]

[1]Institute of Physics, University of Belgrade, Pregrevica 118, Zemun, Belgrade, Serbia
[2]Faculty of Technical Sciences, University of Novi Sad, Novi Sad, Serbia
[3]The Institute for Multidisciplinary Research, University of Belgrade, Belgrade, Serbia

Ferrites are very attractive materials for technological applications due to their combined properties as magnetic conductors (ferrimagnetic) and electric insulators. Spinel ferrites, by virtue of their structure, can accommodate a verity of cations at different sites enabling a wide variation in electrical and magnetic properties. Spinel ferrites MFe$_2$O$_4$ (M=Mn, Ni, Zn) were obtained by soft mechanochemical synthesis in a planetary ball mill. The appropriate mixture of oxides and hydroxides were used as initial compounds. This mixture was mechanically activated, uniaxial pressed and sintered at 1100°C/2h. The phase composition of the sintered samples was analyzed by XRD, Raman and IR spectroscopy. Morphologies were examined by SEM. In this study, DC-resistivity was measured as a function of temperature from 298-473 K and activation energy of sintered samples was determined. The AC-conductivity measurements in the same temperature range were carried out in the frequency range 100Hz-1MHz. The electrical conductivities show an increase with increasing temperature indicating the semiconducting behavior of the studied ferrites. The conduction phenomenon of the investigated samples has been explained on the basis of hopping model. Analysis of the complex impedance spectra has been used to study the effect of grain and grain boundary on the electrical properties of ferrites.

Serbian Ceramic Society Conference
ADVANCED CERAMICS AND APPLICATION IV
New Frontiers in Multifunctional Material Science and Processing

Serbian Ceramic Society
Institute for Testing of Materials
Institute of Chemistry Technology and Metallurgy
Institute for Technology of Nuclear and Other Raw Mineral Materials
School of Electrical Engineering and Computer Science of Applied Studies

PROGRAM AND THE BOOK OF ABSTRACTS

Serbian Academy of Sciences and Arts, Knez Mihailova 35
Serbia, Belgrade, 21-23. September 2015

INV1

Electrical and Dielectric Characterization of $Zn_xNi_{1-x}Fe_2O_4$ Ferrite Ceramics Prepared by Sintering of Nanopowders

Dalibor L. Sekulić[1], Z. Ž. Lazarević[2], Č. Jovalekić[3], N. Ž. Romčević[2]
[1]*Faculty of Technical Sciences, University of Novi Sad, Novi Sad, Serbia*
[2]*Institute of Physics, University of Belgrade, Belgrade, Serbia*
[3]*The Institute for Multidisciplinary Research, University of Belgrade, Serbia*

Nanostructured $Zn_xNi_{1-x}Fe_2O_4$ (x= 0.0, 0.5 and 1) ferrite ceramics were successfully prepared by a conventional sintering of nanosized powders (10–25 nm), synthesized by soft mechanochemical treatment of high–purity Ni(II), Zn(II) and Fe(III) hydroxides as precursors. Electrical properties, such as DC resistivity as a function of temperature and AC conductivity as a function of frequency and temperature, were examined. The variation of DC resistivity with temperature well obeys the Arrhenius law, indicating semiconductor–like behavior of the prepared ferrites. The drift mobility was estimated from the DC resistivity data and found to increase with increasing temperature from ambient to 200°C. The experimental results reveal that AC electrical conductivity of all three samples increases with increasing frequency of the applied field from 100 Hz to 10 MHz. Analysis of the AC conductivity data by means of Jonscher's universal power law shows that correlated barrier hopping mechanism is the most probable mechanism of electrical conduction for $Zn_xNi_{1-x}Fe_2O_4$ ferrites. As part of a systematic study, dielectric constant and dielectric loss ($\tan\delta$) are also studied as a function of frequency and temperature. The dielectric behavior of ferrite ceramics can be explained by using the mechanism of polarization process, which is correlated to hopping of charge between Fe^{2+} and Fe^{3+} ions at octahedral sites of the spinel lattice.

INV2

Study of Nanodimensional Spinel $Ni_{0.5}Zn_{0.5}Fe_2O_4$ Ferrite Prepared by Mechanochemical Synthesis

Zorica Lazarević
Institute of Physics, University of Belgrade, Pregrevica 118, Zemun, Belgrade, Serbia

The nanodimensional $Ni_{0.5}Zn_{0.5}Fe_2O_4$ ferrites were prepared from mixture of $NiO/ZnO/\alpha\text{-}Fe_2O_3$ and $Ni(OH)_2/Zn(OH)_2/Fe(OH)_3$ powders by (soft) mechanochemical synthesis after 5 and 10 h of milling time. The XRD of the sample obtained after 10 h milling time shows single phase cubic spinel structure. TEM analysis revealed that all samples are composed of more or less agglomerated nanosize particles. The average size of nano crystallites is ~20 nm. The degree of the cation inversion of NZF is estimated for spinel fraction in all samples by Rietveld analysis. In the Raman and IR spectra are observed all of first-order active modes. In the spectra of the single phase "hydroxide" samples it is visible that the energy position and intensity of modes is dependent on the composition and cation distribution. It was shown that the modes in Raman spectra of nickel-zinc ferrite that originate from vibrating of different cations could be clearly distinguished. From the ratio of intensities

of the A_{1g} -type Raman modes, it is possible to estimate the inversion of cations. The Mössbauer spectra were fitted by several subspectra and according to known subspectral areas of both iron sites the degree of inversion was calculated, also. The cation inversion is δ = 0.36(3) for ferrite sample obtained from the mixture of appropriate hydroxide for 10 h milling.

INV3

EPMA, BIB-SEM and FIB-SEM Investigations on Gas Shales from the Dniepr Donets Basin (Ukraine): Evolution of Micro- and Nanoscale Porosity during Thermal Maturation

David Misch[1], F. Mendez-Martin[2], J. Klaver[3], D. Gross[1], G. Hawranek[2], J. Schmatz[3], R.F. Sachsenhofer[1]

[1]Chair of Petroleum Geology, Montanuniversitaet Leoben, Leoben, Austria
[2]Chair of Physical Metallurgy and Metallic Materials, Montanuniversitaet Leoben, Austria
[3]Structural Geology, Tectonics and Geomechanics, Energy and Mineral Resources Group (EMR), RWTH Aachen University, Lochnerstrasse 4-20, 52056 Aachen, Germany

Porosity and permeability are essential parameters for reservoir rocks. As these parameters are directly related to the rock fabric, high resolution techniques are increasingly used to determine reservoir quality of shale gas plays. Techniques developed for conventional reservoir rocks, characterized by large (>10 μm) pores, cannot fully be applied to study gas shales.

The Dniepr Donets Basin (DDB) is a Devonian rift-structure located within the East European Craton. It is filled with Devonian syn-rift sediments and a thick Carboniferous to Mesozoic post-rift succession. The basin hosts more than 200 conventional oil and gas fields. Apart from that, recent investigations focus on the potential for unconventional hydrocarbon production (shale gas). Because of their high average content of total organic carbon (5-6 %), Upper Visean Rudov Beds are one of the main target horizons for shale gas exploration within the DDB. The organic rich black shales can be subdivided into different facies zones according to their mineralogical composition. Those facies zones, predefined by x-ray diffraction measurements on core samples, have been visualized in detail using SEM imaging of fresh broken surfaces, allowing a rapid assessment of mineral distribution and rock fabric. Changing permeability and fraccability, which are essential for reservoir characterization, are directly related to microscale changes in rock texture and mineralogical composition. In case of Rudov Beds, a basin-centered, brittle siliceous facies is most likely referred to a high contribution from deep water radiolaria and is separated from a transitional clayey and a marginal carbonate rich facies. In contrast, a higher abundance of coaly layers as well as inertinite macerals, derived from syn-depositional wildfires, reflects increased terrestrial influence in the marginal areas of the basin.

Another major issue in terms of reservoir quality is represented by type and distribution of organic matter (OM) within the inorganic mineral matrix. Combined SEM imaging, EDX and WDX element mapping on polished sections help visualizing the complex distribution of organic particles within the fine-grained matrix as well as interactions of OM and inorganic phases like clay minerals. Light element mapping of finely dispersed OM, as

Serbian Ceramic Society Conference
ADVANCED CERAMICS AND APPLICATION VI
New Frontiers in Multifunctional Material Science and Processing

Serbian Ceramic Society
Institute of Technical Sciences of SASA
Institute for Testing of Materials
Institute of Chemistry Technology and Metallurgy
Institute for Technology of Nuclear and Other Raw Mineral Materials

PROGRAM AND THE BOOK OF ABSTRACTS

Serbian Academy of Sciences and Arts, Knez Mihailova 35
Serbia, Belgrade, 18-20. September 2017.

present in the world for several decades already. Nevertheless, in Serbia the discipline is just at the beginning of development. In this paper I'll try to explain the importance of the ethnoarchaeological research at local level and in wider, regional frames.

INV-REHA2
Fluorine doping of cathode materials for rechargeable batteries

Dragana Jugović

Institute of Technical Sciences of SASA, Belgrade, Serbia

In the continuing search for alternative cathode materials for rechargeable batteries with improved electrochemical performances, there is a need for a versatile approach that will address concerns regarding low reversible capacity, poor capacity retention, low operating voltage and structural instability. So far, a lot of investigation was focused on cation doping. On the other hand, there is much less investigation on anion doping of cathode materials. Taking olivine-type $LiFePO_4$ and layered Na_xCoO_2 as example materials for lithium- and sodium- ion batteries, respectively, the influence of fluorine doping on both the structure and the electrochemical performances was examined. The crystal structure refinement revealed that fluorine incorporation preserves the parent structure. Furthermore, small oxygen replacement by fluorine ions changes electronic structure and consequently modifies electrical properties.

INV-REHA3
Spectroscopy study of $LiFePO_4$ catode materials for Li-ion battery prepared in the thermo-acoustic reactor

Zorica Ž. Lazarević[1], Janez Križan[2], Gregor Križan[2], Valentin N. Ivanovski[3], Miodrag Mitrić[3], Martina Gilić[1], Nebojša Ž. Romčević[1]

[1]*Institute of Physics, University of Belgrade, Pregrevica 118, Zemun, Belgrade, Serbia*
[2]*Maistrova ulica 19A, 2250 Ptuj, Slovenija*
[3]*Institute of Nuclear Sciences Vinča, University of Belgrade, Belgrade, Serbia*

$LiFePO_4$ is a potential cathode candidate for the next generation of secondary lithium batteries. The iron based olivine type cathodes (mainly lithium iron phosphate, $LiFePO_4$) are regarded as possible alternatives to cathodes based on rare metal composites. Industry uses mostly methods in solids and less hydrothermal synthesis. The pilot reactor was built according to the principles of the thermos-acustic burner. It consists of a burner on the basis of the Helmholtz resonator. The sample synthesized in incomplete combustion and resonance mode of reactor and calcined at 700°C. The obtained samples were characterized by X-ray diffraction, Raman and Mössbauer spectroscopy. The aim of this work is to show that is possible to achieve a desired crystal phase with only a proper mode of operation. The seemingly rapid transformation of amorphous into pure phase material was attributed to two mechanisms; increasing the number of particles due to the reduction in size and a larger number of collisions between particles due to the strong turbulent flow associated with explosive combustion.

RAMAN SPECROSCOPY STUDY OF ANODIC FILM ON $Ag_{43}Cu_{37}Zn_{20}$ ALLOY

Zorica Lazarević[1], Stevan Dimitrijević[2], Miodrag Mitrić[3], Silvana Dimitrijević[4], Milica Petrović[1], Martina Gilić[1], Nebojša Romčević[1]

[1]Mining and Metal Institute of Physics, University of Belgrade, Belgrade, Serbia, lzorica@yahoo.com
[2]Innovation Center Faculty of Technology and Metallurgy, University of Belgrade, Karnegijeva 4, 11000 Belgrade, Serbia, stevad@gmail.com
[3]Vinča Institute of Nuclear Science, University of Belgrade, Belgrade, Serbia, mmitric@vinca.rs
[4]Mining and Metallurgy Institute Bor, Zeleni bulevar 35, 19210 Bor, Serbia, silvana.dimitrijevic@irmbor.co.rs

ABSTRACT

The aim of the present work is characterization of electrochemically treated Ag_{43}-Cu_{37}-Zn_{20} alloy in near neutral chloride solutions by the X-ray diffraction and Raman spectroscopy. At potential of +0.25 V, a complex multilayer film is formed. XRD shows that it consists of CuCl and zinc hydroxichlorides with small amount of Cu_2O, probably formed in the film pores. It can be concluded that the Raman spectroscopy is observed almost all the modes that are registered with the XRD analysis.

***Keywords**: alloy, XRD, Raman spectroscopy*

1 INTRODUCTION

Silver based brazing filler alloys have been widely used in various industries including high-tech like: electronics, automotive, aerospace and similar. They are suited filler materials for joining ferrous and non-ferrous metals, and alloys, except aluminum and magnesium. Inclusion of cadmium in brazing fillers gives the following advantages: reduces the brazing temperature, lowers cost and improve mechanical properties of alloys. Owing to the inherent toxicity of cadmium, legislation all over the world restricting the use of cadmium in brazing alloys, especially for application in the food industry and medicine. Cadmium-free silver brazing alloys that can replace Ag based brazing alloys containing cadmium, are the ternary AgCuZn or multi-component alloys based on them or Ag-Cu system with the addition of Ga, Sn, In and Ni [1]. The investigated alloy has the composition of BS1845:1984 Ag5 commercial alloy, i.e. Ag_{43}-Cu_{37}-Zn_{20}. Electrochemical behavior of ternary brazing alloys of the Ag-Cu-Zn system has not been extensive investigated. Some interest existed in the eighties, but the investigations had a limited scope. The main aspects of the studies were a type of corrosion at brazed joints, open circuit potential in chloride solutions (brazing alloys and binary silver alloys) and electrochemical galvanic action between the coexisting phases as responsible for corrosion of filler metal and interface [2].

The aim of present work has been characterized by the X-ray diffraction and Raman spectroscopy electrochemically formed $Ag_{43}Cu_{37}Zn_{20}$ alloy after treatment in near neutral chloride solutions (in 3.5 wt.% NaCl).

2 EXPERIMENTAL

High purity metals (99.99%) for electrode preparation were produced by the recycling process. More details of the process and analytics can be found elsewhere [3]. The alloy for

the electrode was prepared by two consecutive steps of ingot casting in a graphite mould. The second, repeated, process was performed in the aim to correct composition caused by high zinc loses for small charges. The obtained ingot was lathe machining into cylinder with 7.14 mm diameter. It was subjected to homogenization annealing at 873 K ($T \approx 0.9\ T$(m)) for 24 h in nitrogen atmosphere and slowly cooled to the room temperature in the same protective atmosphere. Finally, the specimen was mounted in polytetrafluoroethylene (PTFE) mould. Chemical composition (wt.%) of the alloy used in the present study was 43.5% Ag, 37.7% Cu, 18.8% Zn, and trace elements (Sn, Pb, Fe, Ni) as analyzed by the inductively coupled plasma atomic emission spectroscopy. Chemical composition fulfills the requirements for BS1845:1984 Ag5 standard.

The all chemicals were of analytical grade produced by Merck (Germany). All solutions were prepared with ultra-pure water of resistivity not less than 18 MΩ cm^{-1}. Test solution, 3.5 wt. % NaCl, was prepared by dissolving 35 g of NaCl in 1000 ml glass flask to the total mass of solution of 1000 g. pH value was adjusted to pH=6.70.

The X-ray Powder Diffraction (XRPD) patterns of investigated sample were obtained on the Philips PW-1050 diffractometer, operated at 40 kV and 30 mA, using Ni-filtered Cu $K_{\alpha 1,2}$ radiation. The Bragg–Brentano focusing geometry was used with a fixed 1° divergence and 0.1° receiving slits. The patterns were taken in 10-100° 2θ ranges with a step of 0.05° and exposure time of 6 s per step. For the X-ray structural phase analysis, software EVA 9.0 Release 2003, Bruker AXS GmbH, Karlsruhe, Germany, was used.

The micro-Raman spectra were taken in the backscattering configuration and analyzed using a JobinYvon T64000 spectrometer, equipped with a nitrogen cooled charge-coupled-device detector. As an excitation source we used the 532 nm line of a Ti:sapphire laser. The measurements were performed at 20mW laser power.

RESULTS AND DISCUSSION

Figure 1 shows the results of X-ray diffraction (XRD) of the specimen after the potentiostatic test. The peaks of both phases, ($Ag_{1-x-y}Cu_yZn_x$) solid solution and Cu_3Zn (α-brass) are present, as well as before the potentiostatic test. X-ray structural phase analysis was applied for identification the new phases formed after potentiostatic test using the EVA 9.0 computing program. It can be noticed that beside the peaks that belong to ($Ag_{1-x-y}Cu_yZn_x$) solid solution phase, the peaks that correspond to pure Ag phase also have appeared. They have been formed by reduction of Zn and Cu content in solid solution during the potentiostatic polarization at +250 mV. The peaks of ($Ag_{1-x-y}Cu_yZn_x$) solid solution phase are positioned at somewhat larger 2theta (2θ) values than the peaks of pure Ag phase. This difference increases with an increase of 2θ angles, meaning that the lattice parameter of Ag-rich phase is smaller than the lattice parameter of pure Ag phase, which can be explained by larger ionic radius of Ag than ionic radii of Zn and Cu. Noticeable increase of relative ratio of ($Ag_{1-x-y}Zn_xCu_y$) solid solution and pure Ag phases with the increase of 2θ angle implies that electrode surface is covered by pure Ag in thin layer beneath which is ($Ag_{1-x-y}Cu_yZn_x$) solid solution phase.

Figure 2 shows the Raman spectra of the $Ag_{43}Cu_{37}Zn_{20}$ alloy recorded after anodic potentiostatic polarization treatment at +0.25 V for 5 min in 3.5% wt. NaCl solution at room temperature. The main Raman peaks are indicated in the spectrum. The presence of silver (Ag), cuprous chloride (CuCl), zinc hydroxychloride (β-Zn(OH)Cl), cuprous oxide (Cu_2O) and simonkolleite ($Zn_5(OH)_8(Cl)_2 \cdot H_2O$) is registered.

Very strong silver peaks (cyan circles) indicate the formation of Ag areas, segregate from the Cu-Zn alloy. Observed Ag peaks at 920, 1189, 1234, 1368, 1442 and 1577 cm^{-1} are in general agreement with the previously published results [4].

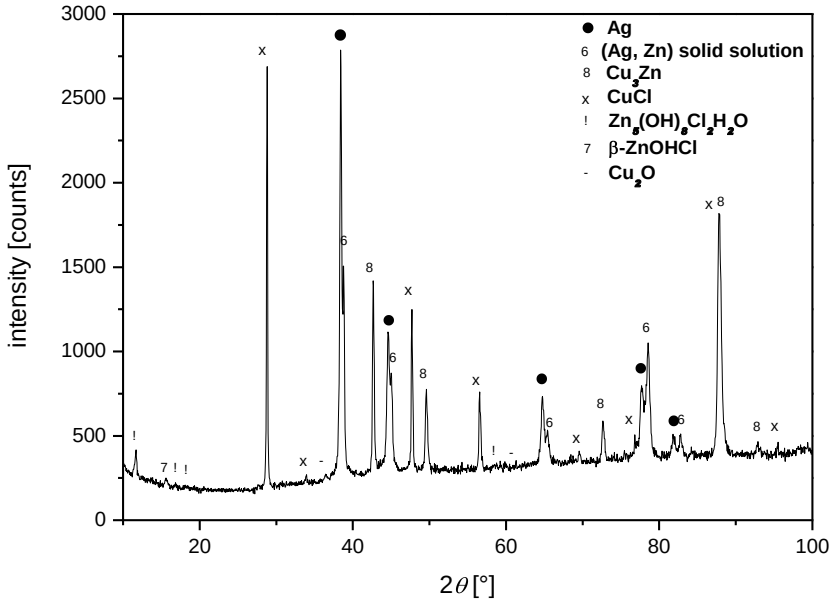

Figure 1 *XRD pattern of the $Ag_{43}Cu_{37}Zn_{20}$ electrode after anodic potentiostatic polarization treatment at +0.25 V vs SCE for for 5 min in unbuffered 3.5% wt. NaCl solution at 25 °C*

Cuprous chloride has the cubic zincblende structure with two atoms in the primitive cell so that there is only one triply degenerate fundamental optic mode, which is both the Raman and infrared active. The first-order phonons of CuCl visible in the Raman spectra (open triangles) are *TO*-phonon at 150 cm^{-1} and *LO*-phonon at 238 cm^{-1} [5, 6]. β-Zn(OH)Cl (green squares) are illustrated in Figure 2. Three main peaks are observed at 207 and 268 cm^{-1}, assigned to a Zn-Cl bond, and 386 cm^{-1}, attributed to a Zn-O vibration characteristic of this structure. Zinc hydroxychloride is also characterized by two main OH fundamental stretching bands at 920 and 1031 cm^{-1} [7, 8].

Cu_2O crystallizes in a cubic lattice with two molecules per unit cell and space group Pn3m. Since it exhibits inversion symmetry, its electronic and vibrational states are of definite parity. In the Raman spectra of treated alloy are seen several Cu_2O modes (black triangles). A weak mode at about 150 cm^{-1} can be a combination of *TO*-mode of CuCl and mode of Cu_2O. At 515, 621 and 690 cm^{-1} are modes of Cu_2O [9-11]. The Raman peaks at 207 and 386 cm^{-1} indexed by pink triangle, which agree very well with what are found in the [7], were assigned to $Zn_5(OH)_8(Cl)_2 \cdot H_2O$ (simonkolleite). A peak at 207 cm^{-1} was attributed to the Zn-Cl bond and that at 386 cm^{-1} to Zn-O which had a vibration characteristic of a simonkolleite structure.

The presence of Ag, CuCl, β-Zn(OH)Cl, Cu_2O and $Zn_5(OH)_8(Cl)_2 \cdot H_2O$ is in agreement with the XRD results.

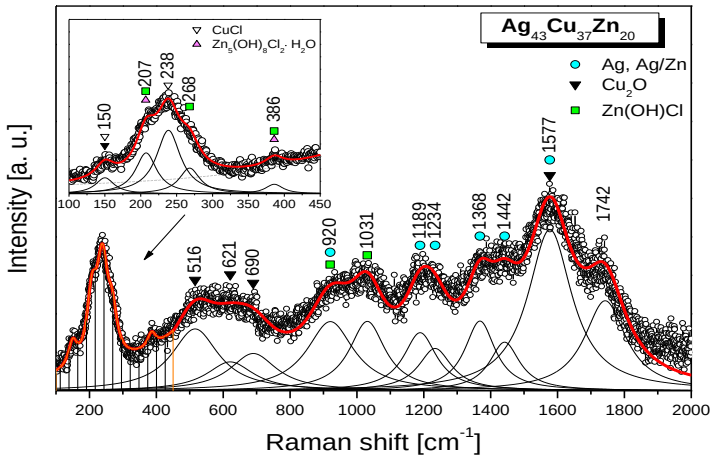

Figure 2 *Raman spectra of the $Ag_{43}Cu_{37}Zn_{20}$ alloy at room temperature*

CONCLUSION

The anodic film is a mixture of Cu_2O, CuCl, $Zn_5(OH)_8 \cdot H_2O$ and β-Zn(OH)Cl. Phases of the alloy, Ag and Cu rich, show different behavior under anodic polarization. For analysis of the Raman spectra we assumed that all phonon lines were of the Lorentzian type, which is one of the common type of lines for this kind of analysis. It has already mentioned, phases of Ag, CuCl, β-Zn(OH)Cl, Cu_2O and $Zn_5(OH)_8(Cl)_2 \cdot H_2O$ were all registered by the XRD.

ACKNOWLEDGEMENTS

This research was financially supported by the Ministry of Education, Science and Technological Development of the Republic of Serbia through the Projects No. III45003 and TR3403.

REFERENCES

[1] L. Zhongmin, X. Songbai, H. Xianpeng, G. Liyong., Mat. Eng., 39 (2010) 397̃400.
[2] T. Takemoto, I. Okamoto., J. Weld., 63 (1984) 300̃307.
[3] S. P. Dimitrijević, Z. Anđić, Ž. Kamberović, S. B. Dimitrijević, N. S. Vuković., Bulg. Chem. Commun., 46 (2014) 814̃824.
[4] H. Liang, Z. Li, W.Wang, Y. Wu, H. Xu., Adv. Mater., 21 (2009) 4614̃4618.
[5] K. Fukushi, M. Nippus, R. Claus., Phys. Stat. Sol. (b)., 86 (1978) 257̃262.
[6] S. Iwasa, E. Burstein., J. Physique., 26 (1965) 614.
[7] M. C. Bernard, A. Hugot-Le Goff, D. Massinon, N. Phillips., Corros. Sci., 35 (1993) 1339̃1349.
[8] H. D. Lutz, M. Schmidt, B. Weckler., J. Raman Spectrosc., 24 (1993) 797̃804.
[9] A. L. Ma, S. L. Jiang, Y. G. Zheng, W. Ke., Corros. Sci., 91 (2015) 245̃261.
[10] A. Compaan, H. Z. Cummins., Phys. Rev. Lett., 31 (1973) 414̃4.
[11] R. J. Eliot., Phys. Rev., 124 (1961) 340̃345.

ATLANTIS PRESS

William E. Lee
Rainer Gadow
Vojislav Mitic
Nina Obradovic *Editors*

Proceedings of the III Advanced Ceramics and Applications Conference



Optical Properties of Plastically Deformed Copper: Ellipsometry and Raman Study

M. Gilić, M. Petrović, B. Hadžić, Z.Ž. Lazarević, M. Romčević, J. Trajić and N.Ž. Romčević

Abstract In this paper, we used Raman spectroscopy and spectroscopic ellipsometry to investigate optical properties of plastically deformed copper. Chemically pure copper prepared in a sample of square cross section (10×10 mm^2) and about 50 mm long was extremely plastically deformed with the repeated application of Equal Channel Angular Pressing. Information about microstructure with ultrafine grains is obtained by atomic force microscopy. The structure of the sample surface —the copper oxide and surface roughness over-layer—was registered by spectroscopic ellipsometry. By Raman spectroscopy, two types of lines are registered: narrow, with the width ~7 cm^{-1}; and wide, ~40 cm^{-1}, which implies that nano-sized crystal structures related to three-dimensional amorphous boundary spaces exist in the specimen.

Keywords Copper · Amorphization · Plastic deformation · Spectroscopic ellipsometry · Raman spectroscopy

1 Introduction

In last two decades, a great interest has been expressed in research regarding a severe plastic deformation technique called Equal Channel Angular Pressing (ECAP). Vast number of papers has been published in wake of pioneering work of Valiev et al. [1] and Segal [2]. The reason for this interest lies in the fact that metals and alloys that endured ECAP exhibit a very small grain size and, as a consequence, their tensile strength is remarkably improved. All relevant work about this severe plastic deformation technique is summarized in the [3]. In the studies of [4] and [5], a model is developed that describes how, in severely deformed materials, grain subdivision

M. Gilić (✉) · M. Petrović · B. Hadžić · Z.Ž. Lazarević · M. Romčević · J. Trajić · N.Ž. Romčević
Institute of Physics, University of Belgrade, Belgrade, Serbia
e-mail: martina@ipb.ac.rs

W.E. Lee et al. (eds.), *Proceedings of the III Advanced Ceramics and Applications Conference*, DOI 10.2991/978-94-6239-157-4_12

occurs by the formation of cell blocks separated by sets of dislocations. Within these cells, there are regions relatively free of dislocations, which are bounded with low-angle boundaries. Cell blocks become narrower and narrower with increasing the degree of deformation, which leads to transformation of cell boundaries into high-angle boundaries. This fact, often observed in plastically deformed metals and alloys, seems to explain the formation of very small grains [6, 7].

On the other hand, copper is used in a vast variety of products in both domestic and industrial domains as a thermal and electrical conductor, as well as a constituent of various metal alloys [8]. Among metals, only silver has higher electrical conductivity, but copper is much cheaper and more abundant. Due to this property, copper has been used widely as an electrode in electrochemical studies [9]. Since it is both ductile and malleable copper is easy to treat. The ease with which it can be drawn into wire makes it useful for electrical work, in addition to its excellent electrical properties. Copper can be machined, although it is usually necessary to use an alloy for complicated parts, to get really good mixed characteristics. Good thermal conduction makes it useful for heat sinks and in heat exchangers. Copper has good corrosion resistance, nevertheless not as good as gold. It has excellent brazing and soldering properties and can also be welded, and the best results are obtained with gas metal arc welding [10].

The colour of copper samples is usually reddish to brownish due to the existence of thin layers on their surface (mostly oxide), which are formed gradually when gases (especially oxygen) react with them in the air. Still, the colour of the clean surface is much brighter (pink or bright brown). Copper has its characteristic colour because of its unique band structure. Copper, caesium, and gold are the only three elemental metals with a natural colour other than grey or silver [11]. The usual grey colour of metals depends on their "electron sea", which is capable of absorbing and re-emitting photons over a wide range of frequencies.

In this paper, we present the results of AFM, spectroscopic ellipsometry, and Raman spectroscopy measurements of plastically deformed copper.

2 Experimental

2.1 Samples Preparation

A chemically pure copper sample (99.99), prepared as a specimen of square cross section (10×10 mm^2) and about 50 mm long, was extremely plastically deformed with the repeated application of Equal Channel Angular Pressing (ECAP). ECAP, which is known as one of the discontinuous processes of severe plastic deformation, was applied as an effective technique for producing bulk nano-scaled structures.

The experiments were performed in our experimental hydraulic press (VEB WEMA 250 MP), equipped with a tool for Equal Channel Angular Pressing (ECAP). The tool consists of two intersecting channels of the same cross

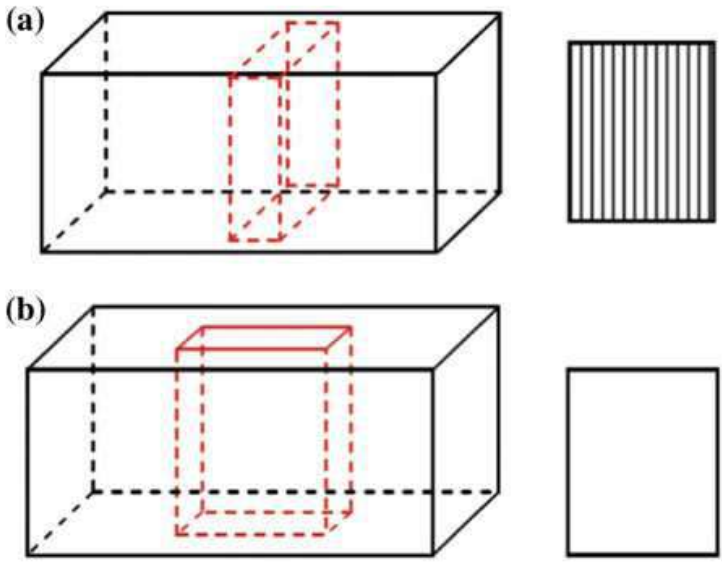

Fig. 1 Obtaining samples: **a** Cu 1.1P; **b** Cu 1.2V

section (10 × 10 mm^2) that meet at the angle 2Φ = 90°. The geometry of the tool provides that the material is deformed by simple shear at ideal, frictionless conditions. The cross section of the specimen remains almost equal before and after each step of the process; thus, it is possible to subject one specimen to ECAP several times in order to reach high degrees of plastic deformation. In our case, the sample of chemically pure copper was subjected eight times to the ECAP process at room temperature (20 °C). This processing, performed at low homologous temperatures, led to a subdivision of the initially coarse-grained microstructure into a hierarchical system of cell blocks and dislocation cells. With increasing strain of the material, the size of both of these constituents decreased.

Two samples were prepared for microstructure investigation: Cu 1.1P—cross-sectional surface and Cu 1.2V—longitudinal section surface, Fig. 1.

2.2 *Devices and Measurements*

The surface morphology of thin films was investigated by atomic force microscopy (AFM). AFM imaging was done using the NTEGRA Prima system from NT–MDT. Typical tip curvature radius was 8–10 nm. All AFM measurements were performed at room temperature and under ambient conditions.

The ellipsometric measurements were performed using a variable angle spectroscopic ellipsometer (VASE) SOPRA GES5-IR in the rotating polarizer configuration. The data were collected over the range 1.5–4.2 eV with the step of 0.05 eV for three different angles of incidence 65°, 70°, and 75°. The 70° angle was chosen for its maximum sensitivity of the ellipsometric data.

The fitting of the model to the experimental data was done using the Levenberg–Marquardt algorithm, to minimize the value of the following merit function [12, 13]:

$$\chi^2 = \frac{1}{2N-P-1}\sum_{i=1}^{N}\frac{\left(<\tan(\psi)>_{\exp} - <\tan(\psi)>_{\text{cal}}\right)^2}{\sigma_{1,i}^2} + \frac{\left(<\cos(\Delta)>_{\exp} - <\cos(\Delta)>_{\text{cal}}\right)^2}{\sigma_{2,i}^2} \quad (1)$$

where N is the total number of data points; P is the number of fitted parameters; $<\tan(\psi)>_{\exp}$, $<\tan(\psi)>_{\text{cal}}$ and $<\cos(\Delta)>_{\exp}$, $<\cos(\Delta)>_{\text{cal}}$ represent the experimental and calculated values of ellipsometric quantities, $\tan(\psi)$ and $\cos(\Delta)$; and σ_i is the error of each measured quantity. All calculations were made using Winelli_II, Version 2.0.0.0.

The micro-Raman spectra were taken in the backscattering configuration and analyzed by Jobin Yvon T64000 spectrometer, equipped with nitrogen-cooled charge-coupled device detector. As an excitation source, we used the 514.5-nm line of an Ar-ion laser. The measurements were performed at different laser power.

3 Results and Discussion

3.1 Atomic Force Microscopy

The surfaces of the samples have been investigated using atomic force microscopy (AFM). Figure 2a shows a typical picture of a started Cu sample. Figure 2b, c shows typical topological morphology in two directions (longitudinal and transverse). On the transverse surface, more contour particles can be seen, which probably correspond to the nano-sized crystalline phases. Contrary to this, on the longitudinal surface, there are essentially less phases, which could be compared to the phases formed on the transverse surface.

3.2 Spectroscopic Ellipsometry

Spectroscopic ellipsometry (SE) is a surface-sensitive, non-destructive optical technique used to characterize surface changes, optical constants of bulk or layered materials, over-layer thicknesses, multi-layer structures, and surface or interface roughness [13]. Ellipsometry measures $\tan(\psi)$ and $\cos(\Delta)$ spectra which are, respectively, the amplitude and projected phases of the complex ratio:

$$\rho = r_p/r_s = \tan(\psi)e^{i\Delta} \quad (2)$$

where r_p and r_s are the complex reflectance coefficients of light, polarized parallel (p), and perpendicular (s) to the plane of incidence, respectively. Ellipsometric

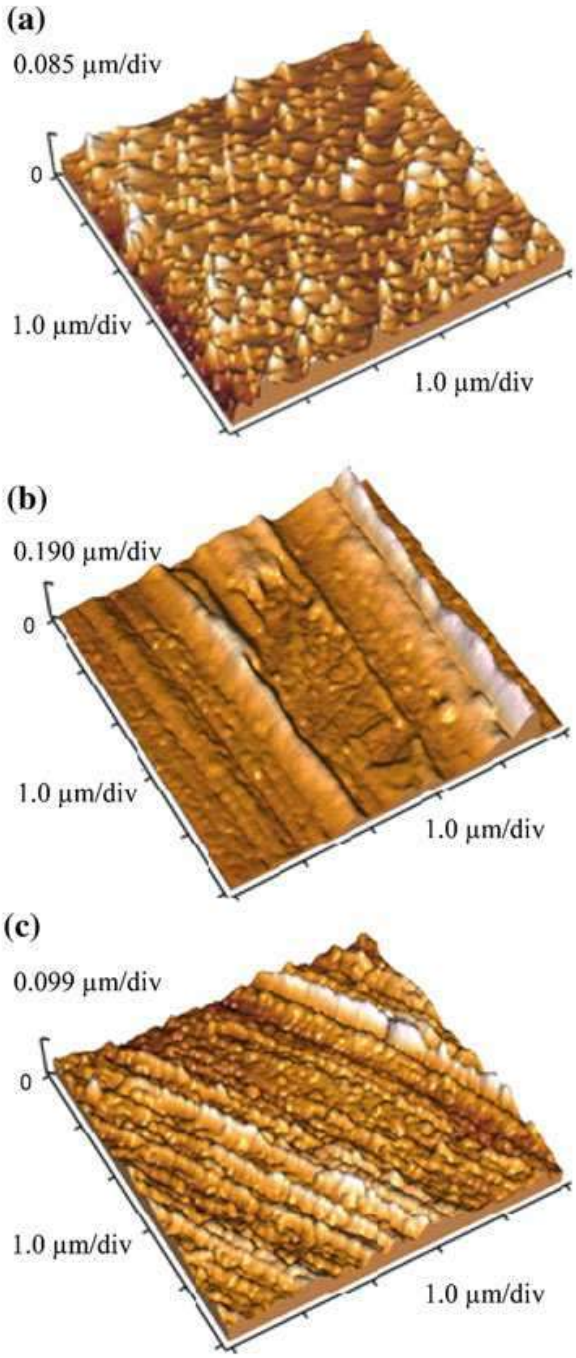

Fig. 2 AFM image of surface of the **a** pure Cu; **b** Cu 1.2V; **c** Cu 1.1P sample

quantities ψ and Δ are sensitive to changes of different parameters such as surface conditions, over-layer structure, and dielectric function of the material and others.

When it is exposed to oxygen, copper oxidizes naturally to copper (I) oxide (Cu_2O). The influence of the surface roughness also has to be taken into account. Figure 3 presents both real and imaginary parts of pseudodielectric function for the bulk copper and samples Cu 1.1P and Cu 1.2V. Therefore, the ellipsometric spectra (tan(ψ), cos(Δ)) of the two samples Cu 1.1P and Cu 1.2V were fitted using a two-film model: Cu as a substrate, an over-layer of Cu_2O, and a surface roughness layer, Fig. 4c. The surface roughness over-layer is composed of the bulk copper

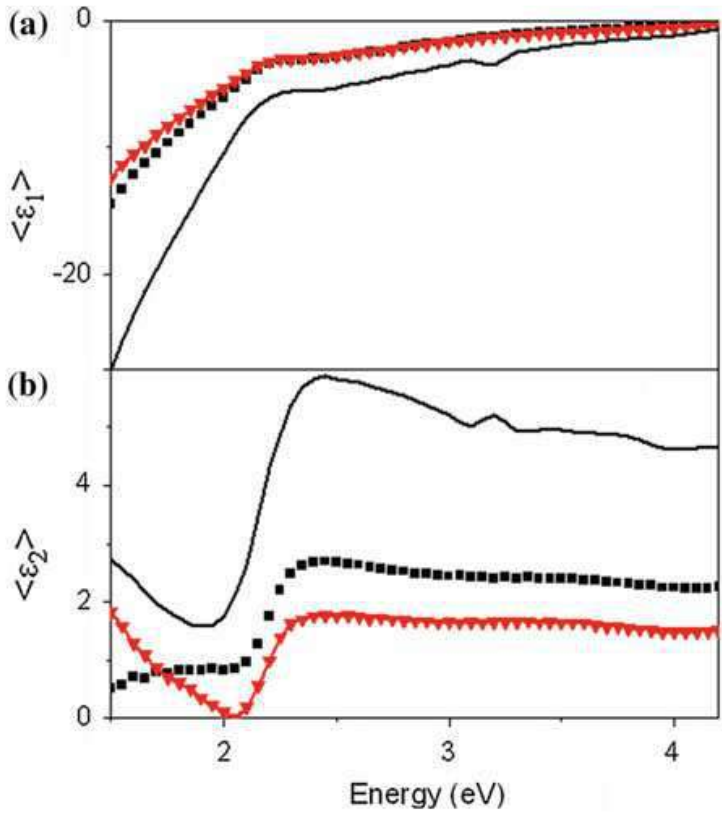

Fig. 3 **a** Real and **b** imaginary part of pseudodielectric function for Cu1.1P (*squares*), Cu1.2V (*triangles*), and bulk copper (*solid line*)

oxide and an ambient. Using Bruggeman effective medium approximation [6], we calculated the volume fraction of the constituents.

Figure 4a presents the experimental and the best fitting data of the sample Cu 1.1P. The thickness of the Cu_2O is ~1.5 nm, and the roughness over-layer, with 80 % of Cu_2O and 20 % of void, is ~25.6 nm. For the energies above 2 eV, this fit is better than for the energies around and below this value. This may indicate that the dielectric function of the sample substrate is different from the one of the bulk copper taken from Palik [14] and that these changes are due to plastic deformation.

The best fit to the model of the sample Cu 1.2V is presented in Fig. 4b. The thickness of the copper oxide is ~1.7 nm, and the roughness over-layer, with 81 % of the oxide and 19 % of the void, is ~35 nm. Comparing these two fits, one can see that, in the case of the Cu 1.1P sample, the model with Cu_2O and surface roughness is better suited than in the case of the Cu 1.2V sample.

3.3 *Raman Spectroscopy*

Pure copper in principle crystallized in the face-centred cubic type structure (O_h space group symmetry), so the first-order Raman modes are not active. However, plastic deformation of the sample and the penetration of oxygen into the sample (and creating CuO) cause the appearance of Raman active modes. Factor group analysis for CuO yields [15]:

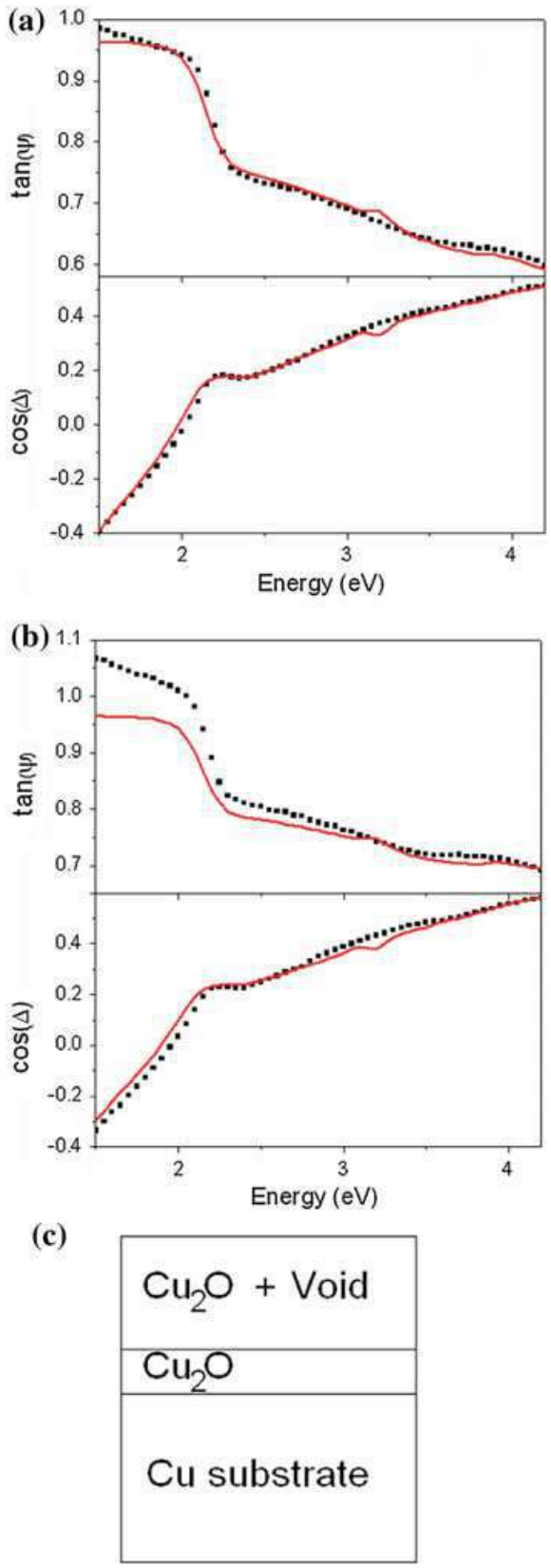

Fig. 4 **a** Experimental data (*dots*) and fitted data (*solid line*) of the sample Cu 1.1P; **b** experimental data (*dots*) and fitted data (*solid line*) of the sample Cu 1.2V; **c** sketched model

$$\mathrm{Cu}(C_i): \Gamma = 3A_u + 3B_u \tag{3}$$

$$\mathrm{O}(C2): \Gamma = A_g + 2B_g + A_u + 2B_u \tag{4}$$

$$\Gamma CuO = A_g + 2B_g + 4A_u + 5B_u \tag{5}$$

Of these modes, $1A_u(T_y)$ and $2\mathrm{B_u}(T_x, T_z)$ are acoustical modes, so that the total of vibrational modes ($\mathbf{q} = 0$) and their activity is:

$$\Gamma_{CuO}^{vib} = A_g(R) + 2B_g(R) + 3A_u(IC) + 3B_u(IC) \tag{6}$$

Thus, three Raman (A_g, B_g) and six infrared (A_u, B_u) active modes are to be expected in the spectra of CuO.

The Raman spectra of Cu 1.2V and Cu 1.1P are presented in Figs. 5 and 6. In addition to a very narrow line (with a width of $\sim$2 cm^{-1}), two types of lines are clearly visible in the spectra: narrow (~7 cm^{-1}) and wide (~40 cm^{-1}) lines. To demonstrate the nature of these very narrow lines in the range up to 120 cm^{-1}, the spectrum of nitrogen is given on the insert of Fig. 5. It is obvious that the positions of these narrow lines from the insert match corresponding lines registered in the spectrum on Figs. 5 and 6. So it can be concluded that they are the parasite lines. The narrow lines are well defined, so we used the deconvolution method in analysis of the wide lines. Raman scattering spectra are often analyzed with the help of a Lorentzian function or by the convolution of a Lorentzian and Gaussian curves [16]. As the quality of the spectra in Figs. 5 and 6 is such that it allows only a qualitative analysis with a partial discussion of the trend, we assumed that all lines are of the Lorentzian type. A typical line shape obtained in this way is also shown in Figs. 5 and 6. Dashed lines correspond to the Rayleigh scattering and

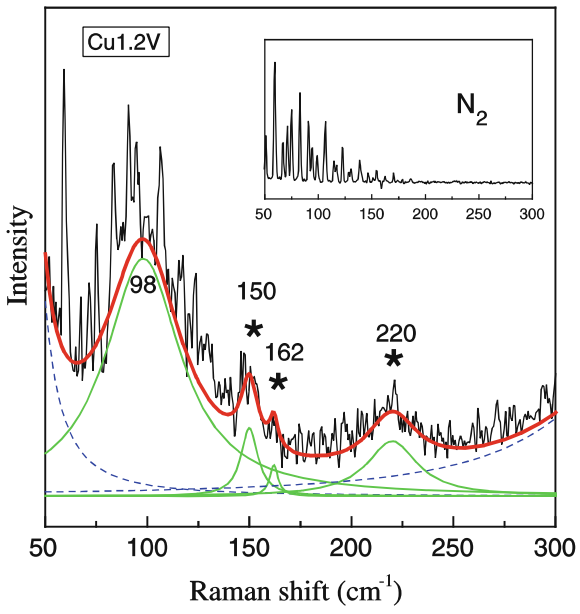

Fig. 5 Raman spectra of Cu 1.2V sample. *Inset* Raman spectra of N_2

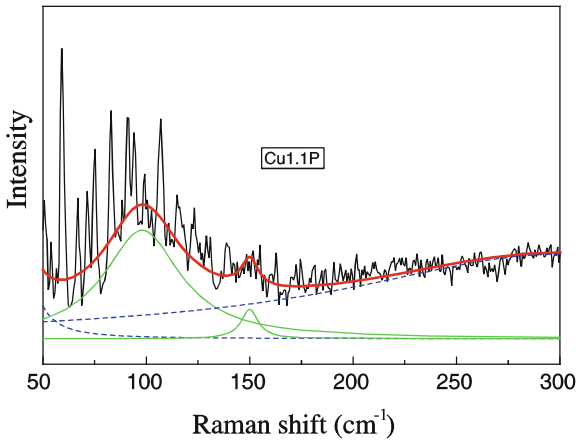

Fig. 6 Raman spectra of Cu 1.1P sample

luminescence [17]. Well-resolved peaks appear at about 98, 150, 162, and 220 cm^{-1} for the sample Cu 1.2V (Fig. 5) and at 98 and 150 cm^{-1} are observed for the sample Cu 1.1P (Fig. 6). Differences in the spectra originated from the different deformation.

Narrow lines, which are marked by stars in Fig. 5, originated from the crystal structures Cu and CuO. The appearance of CuO modes, as we have already said, is a consequence of the oxygen penetration in the sample. The registered lines originate from Cu–Cu and Cu–O [15]. The wide line is a consequence of the amorphous state. Namely, the wide line at 98 cm^{-1} originated from CuO that became amorphous. In this range, the CuO phonon state density is large [15], and therefore, the line is no longer narrow.

The mode at 220 cm^{-1} is probably a consequence of the multi-phonon process. The absence of those structures in the Cu 1.1P Raman spectra points to the influence of material treatments on the structure of Cu and CuO. The existence of two types of lines indicates that nano-sized crystal structures of both Cu and CuO related to three-dimensional amorphous boundary spaces exist in the specimen, which indicates that the plastic deformation of the sample did not lead to total amorphization of the specimen.

4 Conclusion

In our research, we investigated optical properties of two samples of plastically deformed copper: Cu 1.1P—cross-sectional surface and Cu 1.2V—longitudinal surface. The two-film model was used to calculate the thickness of spontaneously formed copper oxide and surface roughness (ellipsometric measurements). In Raman spectra, two types of lines are registered: narrow (with width of ~7 cm^{-1}) and wide (~40 cm^{-1}). Narrow lines originate from crystal phases of Cu and CuO. Wide line at 98 cm^{-1} originates from CuO that became amorphous. The existence of two types of lines indicates that nano-sized crystal structures of both Cu and CuO

are surrounded in all three dimensions with amorphous phases, which implies that the plastic deformation of the sample did not lead to total amorphization of the specimen.

Acknowledgment This work was supported under the Programme of Scientific and Technological Cooperation between the Republic of Slovenia and the Republic of Serbia. Work in Serbia is supported by the Serbian Ministry of Education and Science (Project 45003). This paper is part of the Slovenian MNT ERA-NET Project No. 3211-07-000023:Nano Structured Metal Ceramic Composites.

References

1. R. Valiev, A. Korznikov, R. Mulykov, Structure and properties of ultrafine-grained materials produced by severe plastic deformation. Mater. Sci. Eng. A **168**, 141–148 (1993)
2. V. Segal, Materials processing by simple shear. Mater. Sci. Eng. A **197**, 157–164 (1995)
3. R. Valiev, T. Langdon, Principles of equal-channel angular pressing as a processing tool for grain refinement. Prog. Mater. Sci. **51**, 881–981 (2006)
4. Q. Liu, N. Hansen, Macroscopic and microscopic subdivision of a cold-rolled single crystal of cubic orientation. Proc. R. Soc. **A454**, 2555–2591 (1998)
5. B. Bay, N. Hansen, D. Huges, D. Kuhlmann-Wilsdorf, Overview no. 96 evolution of f.c.c. deformation structures in polyslip, Acta Merallurgica Materialia, **40**, 205–219 (1992)
6. Y. Iwahashi, Z. Horita, M. Nemoto, T. Langdon, The process of grain refinement in equal-channel angular pressing. Acta Mater. **46**, 3317–3331 (1998)
7. C. Xu, M. Furukawa, Z. Horita, T. Langdon, Developing a model for grain refinement in equal-channel angular pressing. Mater. Sci. Forum **503–504**, 19–24 (2006)
8. N. Habbache, N. Alane, S. Djerad, L. Tifouti, Leaching of copper oxide with different acid solutions. Chem. Eng. J. **152**, 503–508 (2009)
9. G. Karim-Nezhad, R. Jafarloo, P. Seyed Dorraji, Copper (hydr)oxide modified copper electrode for electrocatalytic oxidation of hydrazine in alkaline media, Electrohimica Acta **54**, 5721–5726 (2009)
10. W.F. Smith, J. Hashemi, *Foundations of Materials Science and Engineering*, 4th edn. (McGraw-Hill, Boston, 2006)
11. C. William, C. Robert, *Chambers's Information for the People.L*, 5th edn. (W. & R. Chambers, Edinburgh, 1884)
12. M. Losurdo, Relationships among surface processing at the nanometer scale, nanostructure and optical properties of thin oxide films. Thin Solid Films **455–456**, 301–312 (2004)
13. R.M.A. Azzam, N.M. Bashara, *Ellipsometry and Polarized Light* (North-Holland, Amsterdam, 1977)
14. E.D. Palik, *Handbook of Optical Constants of Solids* (Academic Press, Waltham, 1985)
15. G. Kliche, Z.V. Popovic, Far-infrared spectroscopic investigations on CuO. Phys. Rev. B **42**, 10060–10066 (1990)
16. Z.Ž. Lazarević, S. Kostić, M.J. Romčević, J. Trajić, B. Hadžić, D. Stojanović, N.Ž. Romčević, Study of Bi12SiO20 single crystals obtained by Czochralski method. Optoelectron. Adv. Mater.—Rapid Commun. **5**, 150–152 (2011)
17. B.N. Henry, in *Raman Spectroscopy: Sixty Years On*, vol. 10, ed. by J.R. During (Elsevier, Amsterdam, 2008)

Optical Properties and Electron–Phonon Interactions of $CdTe_{1-X}Se_x$(In) Single Crystal

M. Petrović, J. Trajić, M. Gilić, M. Romčević, B. Hadžić, Z. Lazarević and D. Stojanović

Abstract The far-infrared reflectivity spectra of $CdTe_{0.97}Se_{0.03}$ and $CdTe_{0.97}Se_{0.03}$(In) single crystals were measured at different temperatures. The analysis of the far-infrared spectra was carried out by a fitting procedure based on the dielectric function which includes spacious distribution of free carrier as well as their influence on the plasmon–phonon interaction. We found that the long wavelength optical phonon modes of $CdTe_{1-x}Se_x$ mixed crystals exhibit a two-mode behavior. The local In mode at about 160 cm^{-1} is observed. In both samples, a surface layer with a low concentration of free carriers is formed.

Keywords Semiconductors · Electron–phonon interactions · Light absorption and reflection

1 Introduction

The optical, structural, and electrical properties of II–VI compound semiconductors with band gap energies ranging from 0 to 4 eV are appealing for ultrasensitive multiplexing/multicolor applications in a variety of emerging areas of biotechnology, nanoscale optoelectronics, and nanophotonics. By varying the composition and controlling the lattice constants in ternary or quaternary alloys, we can achieve greater flexibility of tuning emission and absorption wavelengths for high-efficiency solid-state light emission sources.

These compounds crystallize in zinc-bland and wurtzite structure. These structures are the two combinations of the tetrahedral sp^3 bonded lattice sites with the outermost cations d-states influencing the bonding. These states lie in or close to the energy regime of the usual valence states which affect the band structure and optical

M. Petrović (✉) · J. Trajić · M. Gilić · M. Romčević · B. Hadžić · Z. Lazarević · D. Stojanović
Institute of Physics, University of Belgrade, Belgrade, Serbia
e-mail: milicap@ipb.ac.rs

W.E. Lee et al. (eds.), *Proceedings of the III Advanced Ceramics and Applications Conference*, DOI 10.2991/978-94-6239-157-4_13

properties. Intermediate values of energy gaps, lattice parameters, and other properties can be obtained by forming ternary and quaternary compounds. Ternary compounds have been extensively studied by vibration spectroscopy with a emphasize on nanometer-size-related effects [1–5].

The subject of this paper is $CdTe_{1-x}Se_x$ mixed crystal doped with In. In this work, the reflectivity spectra of the $CdTe_{0.97}Se_{0.03}$ and $CdTe_{0.97}Se_{0.03}$(In) at different temperatures have been present. These spectra were analyzed using the dielectric function which includes plasmon–phonon interaction [6]. As the result of the best fit, the TO and LO local mode frequencies were determined. The model of phonon mode behavior for these mixed crystals based on Genzel's model [7] was used.

2 Experimental

Single crystals of $CdTe_{1-x}Se_x$ were grown by the Bridgman method at the Institute of Physics, Polish Academy of Sciences, Warsaw.

Far-infrared reflection spectra were measured at 80 and 300 K in the spectral range from 80 to 650 cm^{-1}, carried out with a BOMEM spectrometer.

3 Results and Discussion

The far-infrared reflection spectra of $CdTe_{0.97}Se_{0.03}$ single crystal sample are shown in Fig. 1. The experimental data are represented by circles. In the spectra, two dominant structures at about 140 and 170 cm^{-1} are clearly visible. As we will show later, the feature at about 140 cm^{-1} corresponds to the longitudinal–transverse (LO–TO) splitting of the CdTe-like mode. The feature at about 170 cm^{-1} is related to the CdSe-like mode.

The theoretical model for the bulk dielectric function has been discussed by several authors [8, 9]. We note briefly that the low-frequency dielectric properties of CdTe and CdSe have been described with not less than two classical oscillators ($l \geq 2$) corresponding to the TO modes, superimposed by a Drude part that takes into account the free carrier contribution [10]:

$$\varepsilon_S(\omega) = \varepsilon_\infty + \sum_{k=1}^{l} \frac{\varepsilon_\infty\left(\omega_{LOk}^2 - \omega_{TOk}^2\right)}{\omega_{TOk}^2 - \omega^2 - i\gamma_{TOk}\omega} - \frac{\varepsilon_\infty \omega_P^2}{\omega(\omega + i\gamma_P)} \tag{1}$$

where ε_∞ is the bound charge contribution and is considered as a constant, ω_{LOk} and ω_{TOk} are the longitudinal and transverse optical phonon frequencies, and ω_P is the plasma frequency, while γ_{LOk} and γ_{TOk} indicate the damping of uncoupled

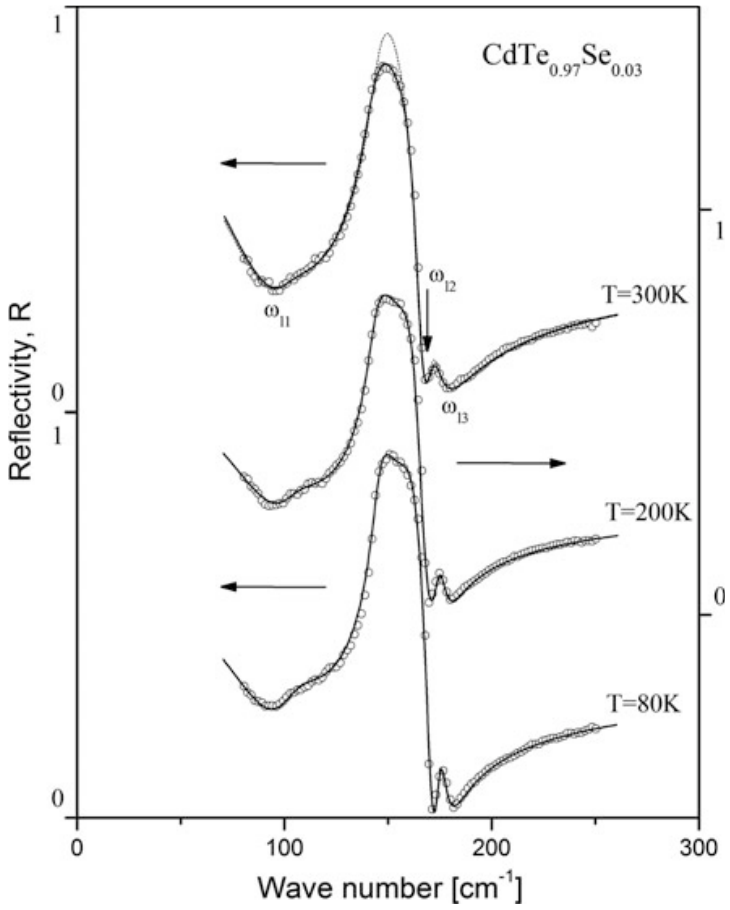

Fig. 1 Far-infrared reflection spectra of $CdTe_{0.97}Se_{0.03}$ at different temperatures. The experimental spectra are presented by *circle*. The *solid* and *dashed lines* are calculated spectra obtained by fitting procedure based on the model given by Eqs. (1) and (2)

modes of the host crystal and the γ_P value describes the plasmon mode damping coefficient. As a result, a combined plasmon–LO phonon modes (ω_{lj}) were observed. In the experimental spectra, only coupled mode positions are observable. Therefore, the LO mode could be determined only if the influence of the free carrier contraction will be eliminated [11]. In the analysis of reflectivity spectra of $CdTe_{1-x}Se_{x,}$ we have decided to use dielectric function which takes into account the existence of plasmon–LO phonon interaction in advance [11]:

$$\varepsilon(\omega) = \varepsilon_\infty \frac{\prod_{j=1}^{m+n}\left(\omega^2 + i\gamma_{lj}\omega - \omega_{lj}^2\right)}{\omega^m \prod_{i=1}^{m}(\omega + i\gamma_{Pi}) \prod_{i=1}^{n}(\omega^2 + i\gamma_{ti}\omega - \omega_{ti}^2)} \times \prod_{k=1}^{s} \frac{\omega^2 + i\gamma_{LOk}\omega - \omega_{LOk}^2}{\omega^2 + i\gamma_{TOk}\omega - \omega_{TOk}^2} \times \frac{\omega^2 + i\gamma_L\omega - \omega_L^2}{\omega^2 + i\gamma_{0k}\omega - \omega_0^2} \tag{2}$$

The first term in Eq. 2 represents coupling m plasmons and n phonons, while the second term represents uncoupled modes of the crystal (s), while $l = n + s$. The ω_{lj} and γ_{lj} parameters of the first numerator are eigenfrequencies and damping coefficients of the longitudinal plasmon–n phonon waves. The parameters of the first denominator correspond to the similar characteristics of the transverse (TO) vibrations.

The second term represents uncoupled crystal mode, where the ω_{LOk} and ω_{TOk} are the longitudinal and transverse frequencies, while γ_{LOk} and γ_{TOk} are damping of uncoupled modes. In the case of plasmon–LO phonon coupling, $m = 1$ and $n = 1$. The third term in Eq. 2 represented indium local phonon, where ω_0 is local phonon characteristic frequencies and ω_L is connected to the intensity of local mode oscillator ($s(\omega_0) \sim (\omega_L^2\text{-}\omega_0^2)$).

We have decided to use dielectric function which takes into account the existence of plasmon–two different LO phonon interaction in the analysis of the reflectivity spectra $CdTe_{1-x}Se_x$ which corresponds to $l = 2$ in dielectric function given by Eq. 1. As we already observed, the coupled mode positions are defined as the solutions of the real part of Eq. 1 ($\mathrm{Re}\{\varepsilon_s = 0\}$). In this case, there are three coupled modes, which can be calculated by solving the equations:

$$\omega^6 - A\omega^4 - B\omega^2 - C = 0 \tag{3}$$

where:

$$A = \omega_{LO1}^2 + \omega_{LO2}^2 + \omega_P^2 \tag{4}$$

$$B = \omega_{LO1}^2 \cdot \omega_{LO2}^2 + \omega_P^2(\omega_{TO1}^2 + \omega_{TO2}^2) \tag{5}$$

$$C = \omega_{TO1}^2 \cdot \omega_{TO2}^2 \cdot \omega_P^2 \tag{6}$$

On the other hand, if we use the dielectric function defined by Eq. 2, the values of initial ω_{LO1} and ω_{LO2} (which are two different phonons) and ω_P modes can be determined by:

$$\omega_P = \frac{\omega_{l1}\omega_{l2}\omega_{l3}}{\omega_{t1}\omega_{t2}} \tag{7}$$

$$\omega_{LO1,2} = \frac{1}{2}(\omega_{l1}^2 + \omega_{l2}^2 + \omega_{l3}^2 - \omega_P^2) \pm \sqrt{\left(\frac{1}{4}\left(\omega_{l1}^2 + \omega_{l2}^2 + \omega_{l3}^2 - \omega_P^2\right)^2 - \omega_{l1}^2\omega_{l2}^2 - \omega_{l2}^2\omega_{l3}^2 - \omega_{l1}^2\omega_{l3}^2 + \omega_P^2\left(\omega_{t1}^2 + \omega_{t2}^2\right)\right)} \tag{8}$$

Dashed lines in Fig. 1 (T = 300 K) obtained by a fitting procedure based on the model given by Eq. 2 for the case $m = 1$, $n = 2$ and $s = 1$. The first term in Eq. 2 (where $n = 2$) represents the structures at about 140 and 170 cm^{-1} and can be identified as some of the lattice vibrations modes of $CdTe_{1-x}Se_x$. A difference between theoretical spectra and experimental data for wave numbers from 140–160 cm^{-1} to 170–175 cm^{-1} was noted. This imperfection was improved by using the modified dielectric function (2). In $CdTe_{1-x}Se_x$ mixed crystal [12], a surface layer with a low concentration of free carriers could be formed. This means that first term in Eq. 2 must be used twice, for each layer (each plasma frequencies)

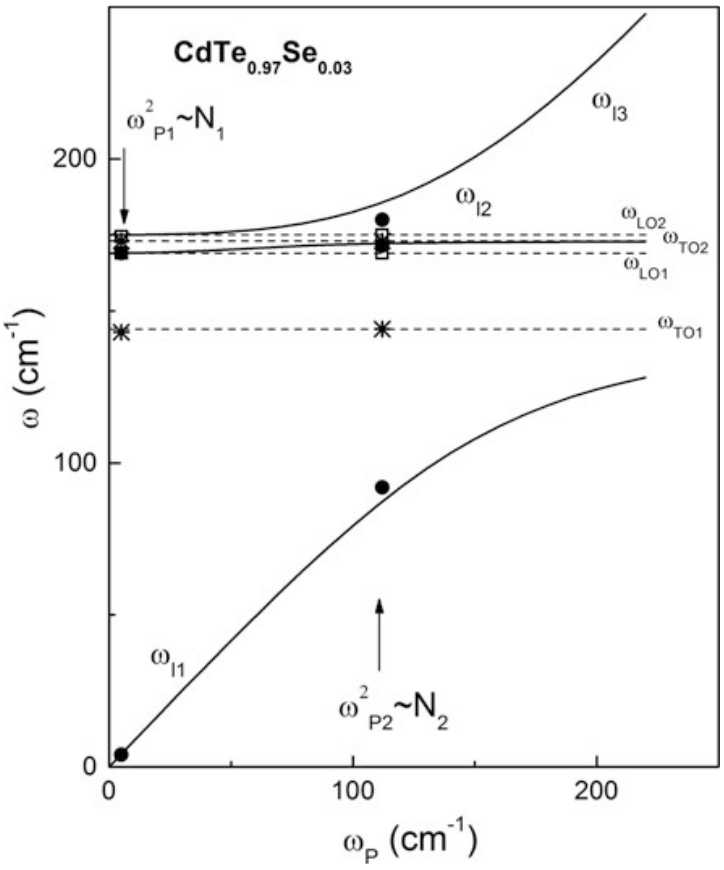

Fig. 2 The eigenfrequencies of the plasmon–phonon modes for single crystal $CdTe_{0.97}Se_{0.03}$. The *solid lines* calculated spectra [Re $\{\varepsilon_s\} = 0$; ε is given by Eq. (1)]; ●—ω_{l1}, ω_{l2} and ω_{l3}; □—ω_{LO1} and ω_{LO2}; ⁎—ω_{TO1} and ω_{TO2}

separately. The excellent agreement between the experimental data and theoretical spectra (solid line) is obtained.

As a result of the best fit, we obtained the frequencies of plasmon–phonon coupled modes (ω_{l1}, ω_{l2}, and ω_{l3}) and TO optical phonons (Eq. 2). Values for ω_{LO1}, ω_{LO2}, and ω_P are calculated from Eqs. 3–8. The characteristic parameters obtained by described procedure are shown in Fig. 2, where the solid lines are obtained using Eq. 3, the solid circles (●) refer to eigenfrequencies spectra ω_{lj} (j = 1, 2 and 3), values corresponding ω_{TO1} and ω_{TO2} are given by stars (⁎), and the open squares (□) represent the calculated values for ω_{LO1} and ω_{LO2} (Eq. 8). The agreement of the plasmon–LO phonon mode frequencies obtained theoretically with the experimentally ones is very good. The plasma frequency (Eq. 7)) of surface layer (ω_{P1}, where $\omega_{P1} \sim N_1^{1/2}$) is lower than the plasma frequencies inside the sample (ω_{P2}, $\omega_{P2} \sim N_2^{1/2}$), what is expected for this type of material.

To study the phonon mode behavior for the ternary compounds $CdTe_{1-x}Se_x$, we used the model based on Genzel's model [7]. This model gave good results in previous studies [13–15] for describing the phonon behavior in the ternary mixed crystals. In our calculations, the basic assumptions of REI model (random element isodisplacement model) [16] were applied. Namely, in the $AB_{1-x}C_x$ type of mixed crystals, the crystal lattice of a mixed system comprises two sublattices: one of them filled by A atoms only and second filed by B and C atoms, randomly distributed. The local electric field (E_{loc}) was taken into account, and a connection between the

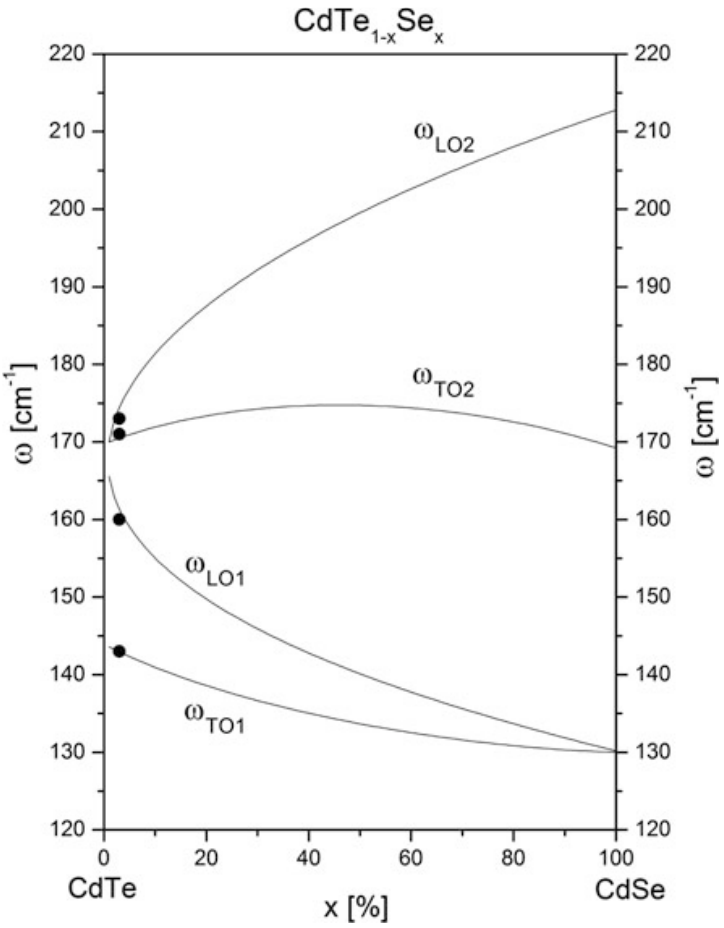

Fig. 3 Concentration dependence of the frequency of the optical mode $CdTe_{1-x}Se_x$ single crystals

microscopic and macroscopic parameters was made using the Born–Huang procedure, where the dependence of the force constant between first neighbors on concentration (x) was neglected, but the second-neighbor force constant was involved. The curves shown in Fig. 3 were obtained using this model. The experimental values for the TO and LO modes are marked by full circles. The results shown in Fig. 3 suggest that the phonons in $CdTe_{1-x}Se_x$ exhibit the two-mode behavior, according to Genzel's notation [7], i.e., each TO–LO mode pair for the end members degenerates to an impurity mode. The agreement between the experimental and theoretical results is very good, with regard to the approximations on which these models are based.

The far-infrared reflection spectra of the $CdTe_{0.97}Se_{0.03}$(In) single crystal sample are shown in Fig. 4. The experimental data are represented by circles. The solid line is obtained using the same procedure we described for Fig. 1. We used dielectrical function given by Eq. 2, where $m = 1$, $n = 2$, and $s = 1$ with one local mode. Surface layer with the lowest free carrier concentration than the rest part of the sample is considered. The excellent agreement between the experimental data and theoretical spectra (full line) is obtained.

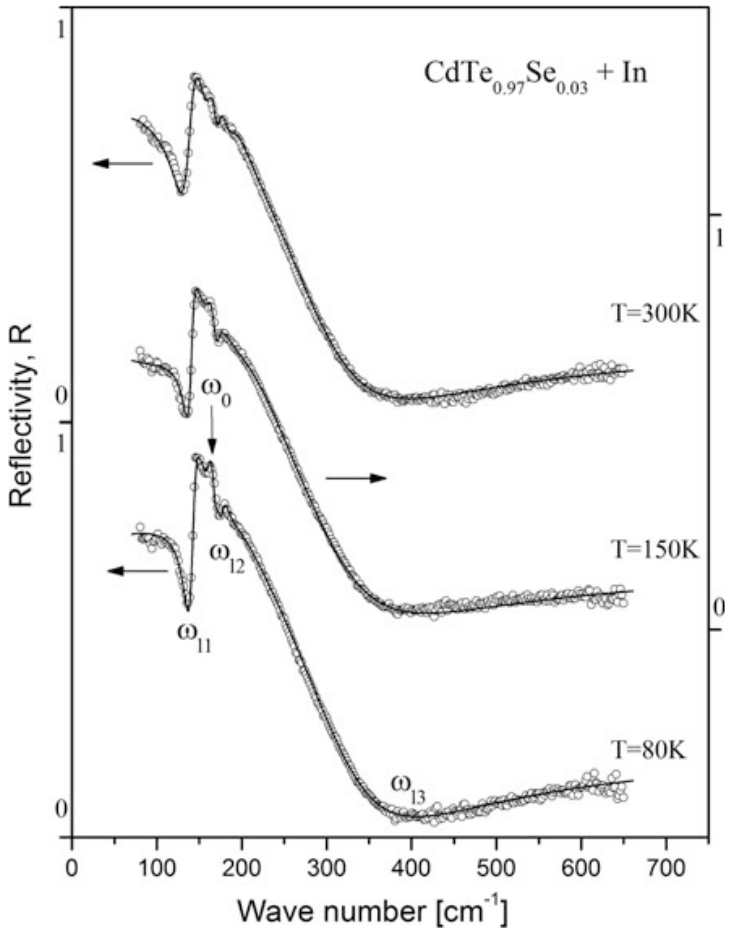

Fig. 4 Far-infared reflection spectra of $CdTe_{0.97}Se_{0.03}$(In) single crystals at temperature 80, 150, and 300 K. The experimental spectra are presented by *circles*. The *solid lines* are calculated spectra obtained by fitting procedure based on the model given by Eq. (2)

Doping $CdTe_{0.97}Se_{0.03}$ with In causes two consequences:

1. Local phonon mode appearance: Indium in $CdTe_{1-x}Se_x$ system is substitution impurity mode. The impurity mode can arise due to the difference between masses and force constants of the impurity ion and the ion of the host material [17], or their appearance can be caused by more complex mechanism of electron–phonon interaction [18]. In our case, $CdTe_{1-x}Se_x$ substitutes Cd. Difference between masses of Cd and In ions is very small; consequently, local mode is situated very close to CdTe LO phonon mode. In Fig. 4, it is visible as independent mode ($\omega_{0)}$ at about 160 cm^{-1}.
2. Free carrier concentration at all mixed crystal, including surface layer increase, what is seen in Fig. 4 as a global minimum shift to higher wave numbers. Figure 5 is obtained using the same procedure we used for Fig. 2. The plasma frequency (Eq. 7) of surface layer (ω_{P1}') is lower than the plasma frequencies inside the sample (ω_{P2}'); hence, the plasma frequency (free carrier concentration) increased at doped sample.

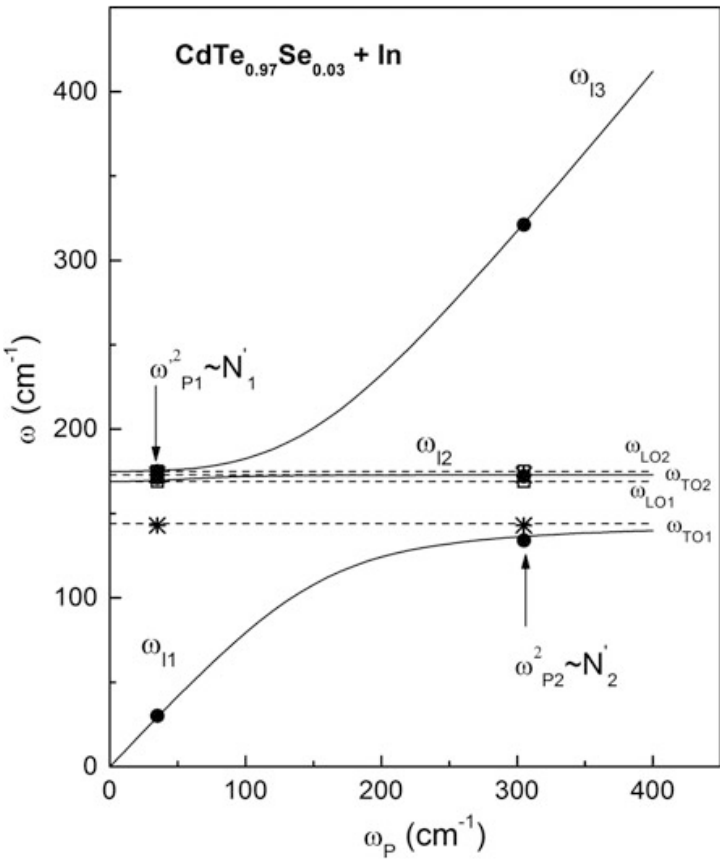

Fig. 5 The eigenfrequencies of the plasmon–phonon modes for single crystal $CdTe_{0.97}Se_{0.03}$(In). The *solid lines* are calculated spectra [$Re\{\varepsilon_s\} = 0$; ε is given by Eq. (1)]; ●—ω_{l1}, ω_{l2}, and ω_{l3}; □—ω_{LO1} and ω_{LO2}; ⁎—ω_{TO1} and ω_{TO2}

4 Conclusions

In this paper, we used far-infrared reflectivity measurements to obtain phonon properties of the ternary $CdTe_{0.97}Se_{0.03}$ and $CdTe_{0.97}Se_{0.03}$(In) single crystals. We found that the long wavelength optical phonon modes of mixed crystals exhibit a two-mode behavior. In doped sample, the local In mode at about 160 cm^{-1} is observed. In both samples, a surface layer with a low concentration of free carriers is formed.

Acknowledgment This work was supported under the Agreement of Scientific Collaboration between Polish Academy of Science and Serbian Academy of Sciences and Arts. The work in Serbia was supported by Serbian Ministry of Education, Science and Technological Development (Project 45003) and in Poland by National Science Center granted under decision No. DEC-2011/01/B/ST5/06602.

References

1. A. Tu, P.D. Persans, Raman scattering as a probe of composition in II-VI ternary semiconductor-glass composites. Appl. Phys. Lett. **58**, 1506–1508 (1991)
2. A. Mlayah, A.M. Brugman, R. Carles, J.B. Renucci, M.Y. Valakh, A.V. Pogorelov, Surface phonons and alloying effects in (CdS)x (CdSe)1 − x nanospheres. Sol. St. Commun. **90**, 567–570 (1994)

3. A. Roy, A.K. Sood, Surface and confined optical phonons in CdSxSe1 − x nanoparticles in a glass matrix. Phys. Rev. B **53**, 12127–12129 (1996)
4. A. Ingale, K.C. Rustagi, Raman spectra of semiconductor nanoparticles: disorder-activated phonons, Phys. Rev. B, **58**, 7197–1201 (1998)
5. Yu.M. Azhniuk, A.G. Milekhin, A.V. Gomonnai, V.V. Lopushansky, V.O. Yukhymchuk, S. Shulze, E.I. Zenkevich, D.R.T. Zahn, Resonant Raman studies of compositional and size dispersion of $CdS_{1-x}Se_x$ nanocrystals in a glass matrix. J. Phys. Condens. Matter **16**, 9069–9073 (2004)
6. A.A. Kukharskii, Plasmon-phonon coupling in GaAs. Solid State Commun. **13**, 1761–1764 (1973)
7. L. Genzel, T.P. Martin, C.H. Perry, Model for long-wavelenght optical-phonon modes of mixed crystals. Phys. Status Solidi B **62**, 83–86 (1974)
8. E. Burstein, A. Pinczuk, R.F. Wallis, in D.L. Carter, R.T. Bate (Eds.), The Physics of Semimetals and Narrow-Gap Semicon, (Pergamon, New York, 1971), 251–267
9. M.A. Kinch, D.D. Buss, Far I.R. determination of the transverse optic lattice mode in PbTe at low temperature. Solid State Commun. **8**, 1275–1279 (1970)
10. V. Gopal, Analysis of the infrared plasma reflectivity spectra of semiconductors. Infrared Phys. **18**, 121–127 (1978)
11. A.A. Kukharskii, Solid State Commun. **11**, 319–324 (1972)
12. D. Jovanovic, D. Milivojevic, M. Romcevic, B. Babic-Stojic, N. Romcevic, Optical and magnetic properties of Hg1-xMnxSe alloys. Mater. Sci. Forum **494**, 277–281 (2005)
13. N. Romcevic, M. Romcevic, A. Golubovic, A. Le Vai Khoi, D. Mycielski, D. Jovanovic, S. Stojanovic, S. Djuric Nikolic, Far-infrared and Raman spectroscopy of Cd1-xMnxTe1-ySey: phonon properties. J. Alloy Compd. **397**, 52–57 (2005)
14. N. Romcevic, M. Romcevic, V. Le Khoi, A. Mycielski, V.A. Kulbachinskii, P.D. Maryanchuk, I.A. Churilov, Plasmon-two phonon interaction in $PbTe_{0.95}S_{0.05}$ alloy. Phys. Stat. Sol. (c) **1**, 977–1002 (2004)
15. S. Perkowitz, R.H. Shoskley, G.L. Person, Far-infrared study of free carriers and the plasmon-phonon interaction in CdTe. Phys. Rev. B **9**, 545–549 (1974)
16. M. Cardona, G. Gunterodt (Eds.), *Light Scattering in Solids IV*, vol. 54 (Springer, Berlin, 1984), 63–128
17. A. A. Maradudin, in F. Seitz, D. Turnball (Eds.), *Theoretical and Experimental Aspects of the Effects of Point Defects and Disorder on the Vibrations of Crystals***—1 Solid, State. Physics*. vol. 19 (Academic, New York, 1966)
18. N. Romcevic, J. Trajic, A.T. Kuznetsova, M. Romcevic, B. Hadzic, D.R. Khokhlov, Far-infrared study of impurity local modes in Ni- doped PbTe. J. Alloys Compd. **442**, 324–329 (2007)

ATLANTIS PRESS

Bill Lee
Rainer Gadow
Vojislav Mitic
Editors

Proceedings of the IV Advanced Ceramics and Applications Conference

Structural, Electrical Conduction and Dielectric Studies of Mechano-synthesized Manganese Nanoferrite

Dalibor L. Sekulić, Zorica Ž. Lazarević and Nebojša Z. Romčević

Abstract In this paper, we have investigated the structural, electrical and dielectric properties of nanostructured manganese ferrite of 49 nm grain size, synthesized by mechanochemical technique. The structural studies have been made by using the X-ray diffraction, TEM and Raman spectroscopy, which confirmed the formation of spinel phase and nanostructure of prepared $MnFe_2O_4$. The electrical measurements were made in the frequency range 10^2–10^6 Hz at different temperatures between 25 and 175 °C. The temperature dependence of DC conductivity satisfies the Arrhenius relation, which indicates the semiconducting nature of sintered sample. The drift mobility was estimated from the DC conductivity measurement and it has been found that the temperature dependent. Analysis of the experimental AC electrical conductivity data shows that correlated barrier hopping mechanism is the most probable mechanism of conduction for prepared manganese ferrite. The dielectric permittivity and loss tangent of $MnFe_2O_4$ decrease with increase in frequency, while these parameters increase with increasing temperature. Such dielectric behavior is explained by using the mechanism of polarization process, which is correlated to hopping of charge between Fe^{2+} and Fe^{3+} ions as well as between Mn^{2+} and Mn^{3+} ions at octahedral sites.

Keywords Manganese ferrite · Nanostructured ceramics · Electrical conductivity · Dielectric properties

D.L. Sekulić (✉)
Faculty of Technical Sciences, University of Novi Sad, Novi Sad, Serbia
e-mail: dalsek@uns.ac.rs

Z.Ž. Lazarević · N.Z. Romčević
Institute of Physics, University of Belgrade, Belgrade, Serbia

B. Lee et al. (eds.), *Proceedings of the IV Advanced Ceramics and Applications Conference*, DOI 10.2991/978-94-6239-213-7_13

1 Introduction

Ferrite materials as semiconductors have always attracted lots of attention due to their unique set of physical properties which may be used for wide range of the technological applications. An important property of these materials is their higher electrical resistance, compared with that of other magnetic materials, which greatly reduces eddy current losses at high frequencies [1]. In recent decades, it has been demonstrated that spinel ferrites exhibit improved electrical and dielectric properties in the nanocrystalline form compared with those of the micrometre sized grains [2, 3]. In general, the spinel ferrites can be represented by formula DM_2O_4, where D and M are divalent and trivalent cations, respectively. The cation distribution between the tetrahedral (A) and octahedral [B] has the form $(D_{1-x}M_x)[D_xM_{1-x}]O_4$, where x is the so-called degree of inversion defined as the fraction of tetrahedral (A) sites occupied by trivalent cations D [4].

Among the spinel ferrites, manganese ferrites are the subject of extensive investigation because of their broad applications in several technological fields, including microwave devices, computer memory chips, transformer cores, rod antennas, magnetic drug delivery, and many other branches of electronic and telecommunication engineering [5]. These materials belong to a group of soft ferrites characterized by high resistivity and low dielectric loss. Mn-ferrite, represented by general formula $MnFe_2O_4$, has a face-centred cubic structure with two types of lattice sites: a tetrahedral site (A) formed by four oxygen anions and an octahedral lattice site [B] formed by six oxygen anions. Earlier studies have shown that $MnFe_2O_4$ is a partial inverse spinel ferrite, where in the bulk form it was about 20 % inverse, but a higher inversion up to 60 % was reported in nanosized manganese ferrite [6].

It is well established that the electrical and dielectric properties of ferrites, as well as structural and magnetic, are strongly dependent on the preparation conditions, sintering temperature and time, chemical composition, particle size and doping of additives [3, 7]. These physical properties are of great importance for ferrites, not only from the application point of view, but also from the fundamental point of view. Hereof, the investigation of such properties at different temperatures and frequencies may provide valuable information for the preparation of high quality ferrite materials for various applications in electronics. The study of dielectric properties and electrical conductivity provides useful knowledge about the behavior of localized electron charge carriers leading to greater understanding of the mechanism of the dielectric polarization in the investigated ferrites [8].

Attempts towards improving the technological performance of ferrites have led to the development of various techniques for the synthesis of homogeneous and reproducible ferrites. In recent years, manganese ferrite has been successfully synthesized by using a several methods, such as co-precipitation [5, 6], sol-gel [5, 9], citrate [5, 10], solid-state reaction [11, 12] and other techniques that have been proposed. Most of these methods have achieved particles of the required sizes and shapes, but they are difficult to employ on a large scale because of their expensive

and complicated procedures, high reaction temperatures, long reaction times, toxic reagents and by-products, and their potential harm to the environment. In order to get good quality and low-cost Mn-ferrite with desired physical properties for electronic applications, a recently reported novel approach to mechanochemical method, so-called soft mechanochemical synthesis [13], has been used to prepare this ferrite material. The peculiarity of soft mechanochemical reactions consists in the high reactivity of surface functional groups, notably, OH groups. Unlike the other methods mentioned above, this technique is effective method of producing a wide range of nanopowders, environmentally friendly, does not require expensive starting materials or extremely high temperature.

In view of the technological importance of manganese ferrites, the present studies were undertaken to understand the structural, electrical and dielectric properties of nanostructured manganese ferrite prepared using soft mechanochemical synthesis. In order to provide valuable information for the potential application of synthesized $MnFe_2O_4$, we have carried out a detailed study about electrical conductivity and dielectric permittivity over a wide range of frequencies as a function of temperature.

2 Experimental Details

2.1 Sample Preparation and Structure Characterization

Spinel manganese ferrite was prepared by soft mechanochemical method. Starting compounds used for synthesizing of Mn-ferrite nanopowder were manganese(II)-hydroxide ($Mn(OH)_2$, Merck 95 % purity) and hematite (α-Fe_2O_3, Merck 99 % purity) in equimolar ratio. The starting hydroxides were amorphous, while hematite was crystalline. Mechanochemical synthesis was performed in air atmosphere in planetary ball mill (Fritsch Pulverisette 5) for 25 h. The synthesis procedure was reported in detail in our earlier publication [14]. The obtained $MnFe_2O_4$ ferrite powder was pressed into circular disc shaped pellet using a cold isostatic press. The pressed pellet with a dimension of 1 mm thick and 7 mm diameter was sintered at 1100 °C for 2 h (Lenton-UK oven) without pre-calcinations step. Heating rate was 10 °C/min with nature cooling in air atmosphere.

The formation of phase and crystal structure of mechano-synthesized manganese ferrite was approved using the X-ray diffractometer (XRD, Model Philips PW 1050 diffractometer). TEM study was performed using a 200 kV transmission electron microscope (Model JEOL JEM-2100 UHR) equipped with an ultra-high resolution objective lens pole piece having a point-to-point resolution of 0.19 nm, being sufficient to resolve the lattice images of nanoparticles. Raman measurement of sintered sample was performed using Jobin-Ivon T64000 monochromator. The room temperature Raman spectra are in spectral range from 100 to 800 cm^{-1}.

2.2 Electrical Measurements

For electrical measurements $MnFe_2O_4$ pellet was polished and coated with high purity silver paste on adjacent faces as electrodes, thus forming parallel plate capacitor geometry with ferrite material as the dielectric medium. In such a way prepared sample can be considered as electrical equivalent to a capacitance C_p in parallel with a resistance R_p, as shown in Fig. 1. These parameters were measured directly in the frequency range 10^2–10^6 Hz at different temperatures between 25 and 175 °C using an Impedance Analyzer HP-4194A. The temperature was regulated with an accuracy of ±0.5 °C using a Beckman CTC 250 temperature controller. In this measurement setup, a personal computer with in-house built software implemented by LabVIEW was used for acquisition of measured data.

As dielectric permittivity is complex in nature $\varepsilon(\omega) = \varepsilon'(\omega) + j\varepsilon''(\omega)$, the real part of dielectric permittivity was determined using the following relation:

$$\varepsilon'(\omega) = \frac{C_p d}{\varepsilon_0 A}, \tag{1}$$

where d is the thickness of the sample, A the cross sectional area at surface of the ferrite pellet and ε_0 represents the permittivity of free space equal to 8.85×10^{-12} F/m. The imaginary part of dielectric permittivity was calculated using the following equation:

$$\varepsilon''(\omega) = \frac{d}{\omega \varepsilon_0 R_p A}. \tag{2}$$

The loss factor or dissipation factor (tan δ) in sintered Mn-ferrite as dielectric material is given by the relation:

$$\tan\delta = \frac{\varepsilon''(\omega)}{\varepsilon'(\omega)}. \tag{3}$$

From the real part of the dielectric permittivity and the loss factor, the AC conductivity of $MnFe_2O_4$ sample was evaluated using the relation:

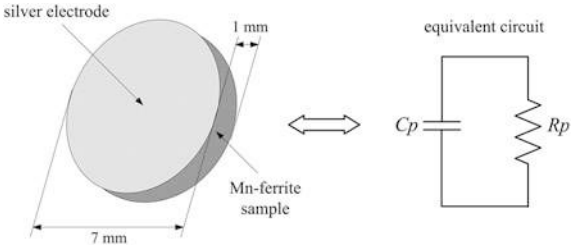

Fig. 1 Schematic representation of prepared manganese ferrite and its equivalent electric circuit

$$\sigma_{AC}(\omega) = \omega\varepsilon_0\varepsilon' \tan\delta. \tag{4}$$

The temperature dependent DC conductivity of the prepared manganese ferrite was measured by simple two probe method within temperature range 25–175 °C. A Source Meter Keithley 2410 was used for the said purpose. The DC conductivity was calculated by using the following formula:

$$\sigma_{DC} = \frac{d}{RA}, \tag{5}$$

where R is the measured resistance, A is area of cross section of the sample and d is the thickness of the sample.

From temperature dependent DC conductivity, the drift mobility of the charge carriers in the present sample is determined by the following well-known equation [15]

$$\mu_{\mathrm{d}} = \frac{\sigma_{\mathrm{DC}}}{ne}, \tag{6}$$

where e is the charge of electron and n is the concentration of charge carrier that can be calculated from the equation [3]:

$$n = \frac{\mathrm{N_A}\rho_{\mathrm{s}}B_{\mathrm{Fe}}}{M}. \tag{7}$$

Here, $\mathrm{N_A}$ is the Avogadro's number, ρ_{s} the measured bulk density of sintered sample, B_{Fe} the number of iron atoms in the chemical formula of the ferrite and M is the molar mass of the sample.

3 Results and Data Analysis

3.1 Structural Analysis

Figure 2 shows the X-ray diffraction spectra of $MnFe_2O_4$ powder and appropriate ferrite sample after sintering at 1100 °C/2 h. All peaks detected at about the 2θ = 22°, 36°, 42°, 44°, 51°, 64°, 68° and 75° clearly pointed to the formation of the new phase of $MnFe_2O_4$ (JCPDS card 74-2403). The peaks are well indexed to the crystal plane of spinel ferrite (k h l) (111), (220), (311), (222), (400), (422), (511) and (440), respectively. This confirms that the mechanochemical synthesis of Mn-ferrite is feasible and complete after 25 h milling time of the mixture of the $Mn(OH)_2$/α-Fe_2O_3 and sintered at 1100 °C/2 h. The size crystallite has been estimated from the broadening of the XRD peaks using the Scherrer's equation [3, 8]:

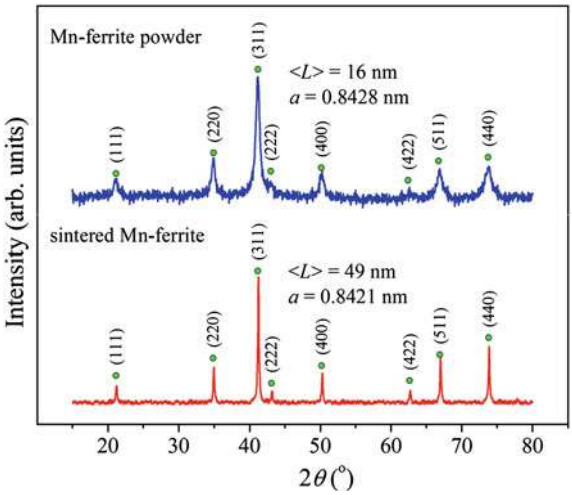

Fig. 2 X-ray diffraction patterns of the manganese ferrite powder and sintered sample at 1100 °C/2 h

$$L = \frac{0.9\lambda_{C_o}}{(w - w_1)\cos\theta}, \tag{8}$$

where $\lambda_{C_o} = 1.78897$ Å is wavelength of used X-ray source, θ is the angle of diffraction, w and w_1 are the half intensity width of the relevant diffraction peak and the instrumental broadening, respectively. The mean size was found to be 16 and 49 nm for powder and sintered manganese ferrite sample, respectively. Based on the measured positions of diffraction peaks, the lattice constant a of the sample was determined by using well-known relation [16]:

$$a = \frac{\lambda}{2\sin\theta} \times \sqrt{h^2 + k^2 + l^2}. \tag{9}$$

The obtained lattice constants are 8.428 Å and 8.421 Å for powder and sintered Mn-ferrite sample, respectively.

The shape, size and morphology of mechano-synthesized Mn-ferrite particles are characterized by direct observation via transmission electron microscope (TEM). The representative TEM images with corresponding EDP of the powder sample obtained after appropriate milling time is depicted in Fig. 3. Bright-field TEM reveals the nanoscale nature of the manganese ferrite particles, mostly in the size ranges between 10 and 50 nm. The shape of the majority of the nanoparticles appears spherical. The crystallites in this system are rounded and tend to agglomerate into larger clusters with diameters of several hundreds of nanometers. Measurements of the diffraction rings confirmed that they correspond to the crystal planes of spinel structure.

Figure 4 shows Raman spectra for the $MnFe_2O_4$ ferrite prepared by the soft mechanochemical synthesis. To simplify, peaks are assigned as for normal spinel

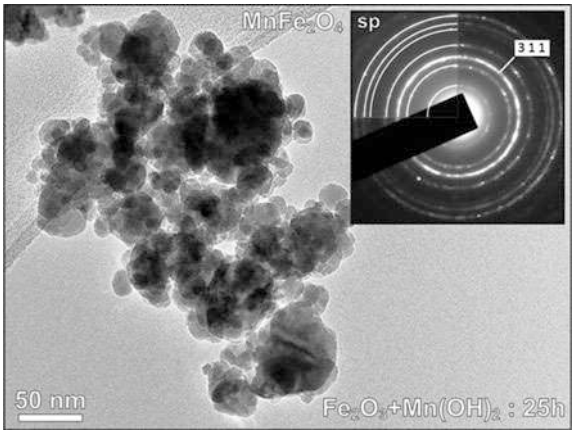

Fig. 3 Transmission electron microscopy image of mechano-synthesized manganese ferrite nanoparticles

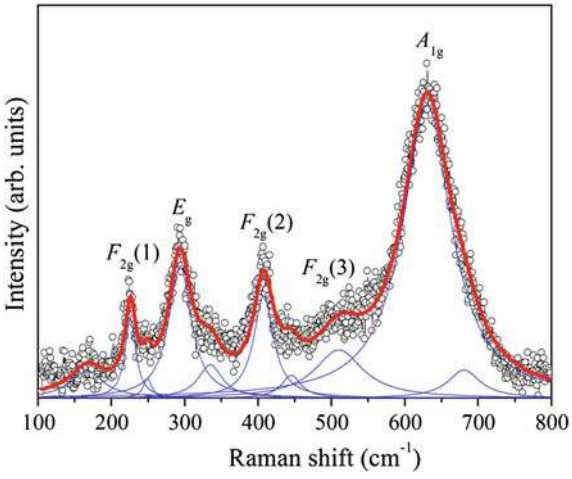

Fig. 4 Raman spectra for the manganese ferrite sintered at 1100 °C/2 h

structure. But, all five Raman peaks are asymmetric with shoulder on the low energy side. Each peak can be presented like a doublet, what is a characteristic of the inverse spinel structure. At a microscopic level the structure of Mn-ferrite can be considered as a mixture of two sublattices with Fe^{3+} and Mn^{2+}. It is supposed that Fe^{3+} and Mn^{2+} are ordered over the [B]-sites. In nanocrystalline samples asymmetry is partly due to confinement and size-distribution of nanoparticles. The A_{1g} mode is due to symmetric stretching of oxygen atoms along Fe–O (and M–O) bonds in the tetrahedral coordination. E_g is due to symmetric bending of oxygen with respect to the metal ion and $F_{2g}(3)$ is caused by asymmetric bending of oxygen. The $F_{2g}(2)$ is due to asymmetric stretching of Fe (Mn) and O. The $F_{2g}(2)$ and $F_{2g}(3)$ correspond to the vibrations of octahedral group. $F_{2g}(1)$ is due to translational movement of the tetrahedron, metal ion at tetrahedral site together with

four oxygen atoms. There is a negligible displacement of metal atoms in modes A_{1g}, E_g and $F_{2g}(3)$ [17].

The density of ferrite materials also plays an important role in the variation of electrical and dielectric properties. Less amount of pores leads to a lower diffusion resistance of electrons and holes through the ferrite. As a result, higher density (lower porosity) causes an increase in the value of electrical conductivity and dielectric constant [16, 18]. The sintered bulk density was determined by measuring the mass m and the dimensions of sample and using equation

$$\rho_s = \frac{m}{\pi r^2 h}, \tag{10}$$

where r is the radius of the sample and h is the width of the sample. The obtained value of sintered density is of the order of 4.46 g/cm^3 for prepared Mn-ferrite. On the other hand, the X-ray density of the sample was calculated using the relation

$$\rho_x = \frac{8M}{a^3 \mathrm{N_A}}, \tag{11}$$

where a is crystal lattice parameter obtained in the XRD analysis, M is the molecular weight of the sample, $\mathrm{N_A}$ is the Avogadro's number. As there are 8 molecules in the unit cell, so 8 is included in the formula. It was obtained that the value of ρ_x is of the order of 5.14 g/cm^3 for sintered manganese ferrite. The X-ray density is higher than that of the sintered density and this difference is primarily due to the porosity of the Mn-ferrite [3]. Taking into account these two density values, it was found that the porosity of $MnFe_2O_4$ under study is about 13.2 % by using the expression $P = (1 - \rho_s/\rho_x) \times 100$. The formation of pores is usually affected by many factors such as the pressing procedure, the sintering time and the sintering temperature.

3.2 DC Electrical Conductivity and Drift Mobility

From the application point of view, the DC electrical conductivity is one of the most important parameters of ferrite materials. The low value of conductivity is necessary for most electronic applications that require negligible eddy currents, which degrade the ferrite performance. The results of DC conductivity measurements of nanostructured manganese ferrite under study are depicted in Fig. 5. It can be seen that the DC conductivity increases with the increase of temperature in accordance with the literature, since spinel ferrites possess the typical semiconducting behavior [19]. The low DC conductivity of 3.91×10^{-6} $(\Omega\mathrm{cm})^{-1}$ is obtained at room temperature, which may be contributed to nanosized ferrite particles. Ferrite materials with smaller particles consist of more number of grain boundaries which act as barriers to the flow of electrons [20]. It is also evident that

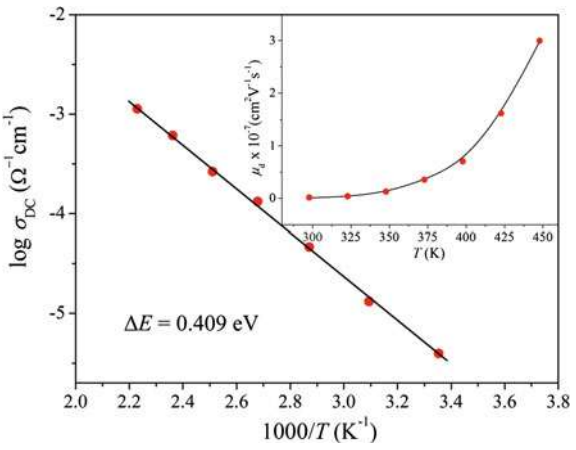

Fig. 5 Variation of DC electrical resistivity with temperature for manganese nanoferrite. *Inset* shows temperature dependence of drift mobility of the charge carriers

there is a linear increase in measured DC conductivity of present ferrite for almost three orders of magnitude with temperature varying from 25 to 175 °C. This behavior could be related to the increase in the drift mobility of the thermally activated charge carriers according to the hopping conduction mechanism and not to thermally creation of the charge carriers [21]. It is widely known that the charge carriers in ferrites are considered as localized at the ions or vacant sites and conduction occurs via a hopping process. The hopping probability depends upon the activation energy which is associated with the electrical energy barrier. Activation energy for the thermally activated hopping process was determined from the slope of the linear plots of DC electrical conductivity using Arrhenius equation [22]:

$$\sigma_{DC}(T) = \sigma_0 \exp\left(-\frac{\Delta E}{k_B T}\right). \tag{12}$$

Here σ_0 is the pre-exponential factor with the dimensions of $(\Omega\text{cm})^{-1}$, ΔE is the activation energy in (eV), k_B is the Boltzmann's constant and T is absolute temperature. The calculated value of the activation energy of 0.409 eV clearly suggests that the conduction mechanism in synthesized Mn-ferrite is due to small polaron hopping according to Klinger [23].

Using the experimental data for DC electrical conductivity of present manganese ferrite at each temperature, the drift mobility of the charge carriers was determined according to the relations (6) and (7). The temperature dependence of drift mobility is depicted in the inset of Fig. 5. It can be seen that the drift mobility shows a same behavior as well as DC conductivity; it strongly dependent on the temperature and increases exponentially with increasing temperature. Moreover, values of the estimated drift mobility are very low (about 1×10^{-9} to 3×10^{-7} cm^2 (V s)$^{-1}$) compared to those expected in the case of normal semiconductors (about 1–100 cm^2(V s)$^{-1}$). Such low values are not new as far as manganese ferrite, since low values of the drift mobility were reported earlier [24]. This is clear evidence

that the band conduction mechanism is omitted in the studied temperature range and the hopping conduction mechanism is responsible for the conduction process. Due to the lattice vibrations, the localized charge carriers start hopping from one site to another as the temperature increases [25].

3.3 AC Conductivity and Conduction Mechanism

In order to obtain a clear understanding of the conduction mechanism, the AC electrical conductivity of sintered $MnFe_2O_4$ ferrite was studied as a function of frequency at different temperatures between 25 and 175 °C. The conductivity is calculated from the experimental data using Eq. (4). Frequency variation of AC conductivity of the sample at selected measuring temperatures is presented in Fig. 6. It is noticed that electrical conductivity shows an increasing trend as the frequency increases, which is a general behavior of ferrites. At room temperature, the AC conductivity at 100 Hz is of the order of 4.2×10^{-6} $(\Omega cm)^{-1}$, which is very close to DC conductivity values, and then it increases to 5.3×10^{-5} $(\Omega cm)^{-1}$ at 1 MHz as given in Table 1. However, it is clear that the Mn-ferrite sample exhibits two types of AC conductivity behavior at two different regions, low-frequency and high-frequency region, which are valid for all temperatures. Characteristic transitional frequency between these two regions is around 1 kHz at 25 °C and reaches to 10 kHz at 175 °C. From Fig. 6 it is evident that this transitional frequency shifts to higher values as temperature rises. Such frequency dependence of conductivity may be attributed to the structural parameters in the ferrites like grain boundaries and grains [19, 26]. The grain boundaries are the region of mismatch between the energy states of adjacent grains and hence act as a barrier to the flow of electrons. In the low-frequency region values of AC conductivity are nearly the same, which is due to that grain boundaries are much more active than grain at low frequencies, so the hopping probability of charge carriers is less [3, 27].

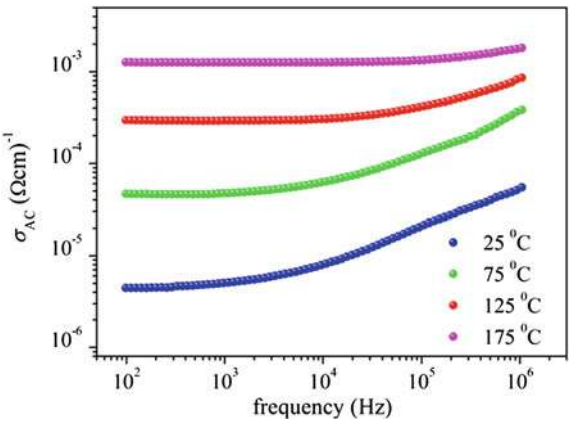

Fig. 6 Frequency dependence of AC electrical conductivity for manganese nanoferrite at selected temperatures

Table 1 The values of AC conductivity, dielectric permittivity and dielectric loss tangent for sintered manganese ferrite at selected frequencies and temperatures

Temperature (°C)	Frequency (Hz)	σ_{AC} (Ω^{-1} cm^{-1})	ε'	ε''	tan δ
	10^2	4.28×10^{-6}	1163	789	0.678
25	10^4	7.85×10^{-6}	392	14	0.036
	10^6	5.31×10^{-5}	331	1	0.003
	10^2	4.58×10^{-5}	1751	8138	4.647
75	10^4	6.14×10^{-5}	415	106	0.255
	10^6	3.77×10^{-4}	335	6	0.017
	10^2	2.89×10^{-4}	4918	52,301	10.634
125	10^4	3.01×10^{-4}	524	553	1.055
	10^6	8.43×10^{-4}	348	14	0.040

In the high-frequency region, the ferrite grains became more active and increase in AC conductivity obeys universal Jonscher's power law behavior [28]:

$$\sigma_{AC}(\omega, T) = A(T)\omega^{s(T)}. \tag{13}$$

where ω is angular frequency of AC field, A and s ($0 \leq s \leq 1$) are the temperature dependent parameters; A has the unit of electrical conductivity whereas s is dimensionless. The experimental data yields a value of Jonscher's coefficient s, whose nature of the temperature dependence determines the conduction mechanism of the ferrite material [29]. Qualitatively, small polaron mechanism is usually associated with increase in s with increasing temperature, while correlated barrier hopping model shows a decrease in s with increasing temperature. In overlap large polaron mechanism of AC conduction, value of parameter s first decreases reaching a minimum value and then starts increasing again [30].

The parameter s was calculated from the slope of $\log(\sigma_{AC})$ versus $\log(\omega)$ at each temperature. For the examined Mn-ferrite sample, values of Jonscher's coefficient decrease from 0.397 to 0.196 with increasing temperature from 25 to 175 °C as given in Fig. 7. A linearly decreasing trend of this parameter s with temperature suggests that correlated barrier hopping model [31] is suitable for explaining AC conduction mechanism in sintered manganese ferrite. The same mechanism for AC conduction was proposed in the case of nanocrystalline $MnFe_2O_4$ synthesized by co-precipitation method [8]. According to this model, the charge carrier hops between the sites over the potential barrier separating them and temperature dependent parameter s is given with the following equation [32]:

$$s(T) = 1 - \frac{6k_BT}{W_m}. \tag{14}$$

In this relation, W_m is the effective barrier height, k_B is Boltzmann's constant and T is absolute temperature. The value of barrier height was calculated from the slope

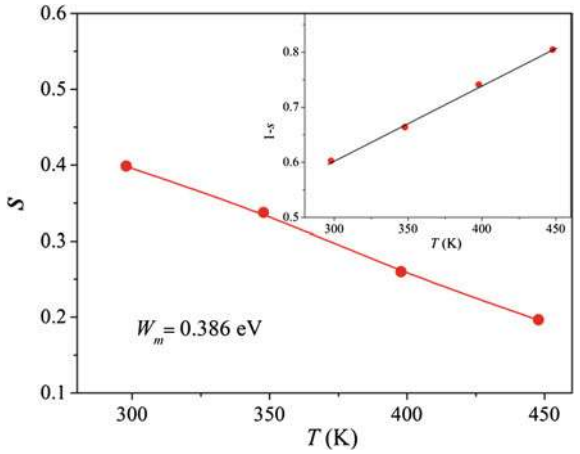

Fig. 7 Variation of Jonscher's coefficient s with temperature

of $1-s$ versus temperature in the range from 25 to 175 °C and it was found to be equal to 0.386 eV, see inset of Fig. 7.

3.4 Dielectric Properties

The effect of applied electric field frequency on the real part of dielectric permittivity (ε') at selected temperatures is represented in Fig. 8. It is clear from the analysis of the graph that ε' decreases continuously with increasing frequency, exhibiting a normal dielectric behavior [3, 33]. In fact the real part of dielectric permittivity of sintered manganese ferrite reduces from 1163 to 331 when frequency increases from 10^2 to 10^6 Hz at room temperature, see Table 1. It is also

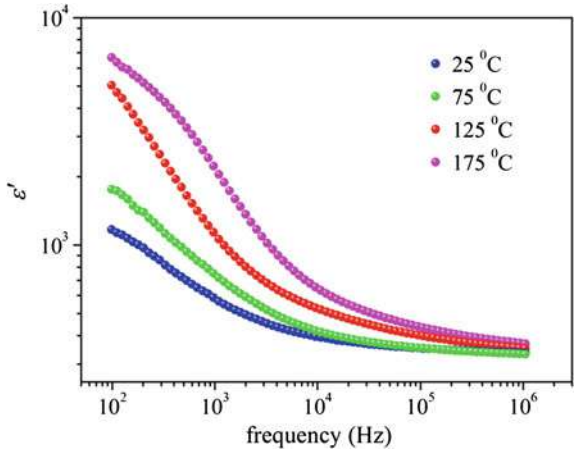

Fig. 8 Frequency dependence of real part of dielectric permittivity (ε') for manganese nanoferrite at selected temperatures

can be seen that the dielectric dispersion is rapid at lower frequencies, up to 10^4 Hz, while it remains almost independent of applied field at high frequency side. Such behavior, observed in a number of ferrite materials, is mainly due to the Maxwell–Wagner type of interfacial polarization [34] which is a result of inhomogeneous nature of the dielectric structure in the sample. Based on this, space charges carriers, located at the grain boundary in polycrystalline materials, act as dipoles under an alternating electric field and contribute to polarization [35]. At frequencies higher than 10^4 Hz, a relatively independent value of ε' with frequency is attributed to the electronic and ionic polarizations that are frequency independent.

According to Rabinkin and Novikova [36], it is observed that the mechanism of dielectric polarization is similar to the mechanism of electrical conduction in ferrites. It is well known that the exchange of electrons between Fe^{2+} and Fe^{3+} ions and the exchange of holes between Mn^{3+} and Mn^{2+} ions in the octahedral sites of manganese ferrites result in local displacement of charge carriers in the direction of applied field, which is responsible for polarization [8, 9, 35]. The decrease in the polarization with increasing frequency is due to the fact that frequency of charge carrier exchange is not able to follow the alternating field [16]. Consequently, the dielectric permittivity remains approximately the same. Even at the frequency of 10^6 Hz, the synthesized Mn-ferrite has the appreciable value of dielectric permittivity of 331 at room temperature, which makes it useful for the high-frequency applications.

Further, Fig. 8 indicates an increase in the real part of dielectric permittivity with increasing temperature which is the normal dielectric behavior of magnetic semiconductor ferrites [3]. It is obvious that the variation of ε' with temperature at lower frequencies is much more pronounced than at higher frequencies. The rapid increase in dielectric permittivity with temperature at low frequencies can be explained on the basis of the fact that interfacial and dipolar polarizations are strongly temperature dependent [6]. The accumulation of charges at the grain boundary increases with the increasing temperature, causing an increase in the interfacial polarization. As a result, the net dielectric polarization increases, leading to a significant changes in ε' with temperature. The relatively insignificant variation of dielectric permittivity with temperature observed at higher frequencies can be attributed to electronic and ionic polarizations, which are main contributors and independent of both temperature and frequency [11].

The frequency dependence of imaginary part of the dielectric permittivity (ε'') at selected temperatures is shown in Fig. 9. By observation of graph it can be noticed that ε'' decreases more slowly in compared to ε' with increasing frequency, because ε'' is proportional to the $1/\omega$ while ε' is proportional to the $1/\omega^2$ [37]. Further, the behavior of ε'' with temperature for sintered sample is qualitatively analogous with the variation of ε' with temperature, but with higher values at higher temperatures, see Table 1.

The loss of electrical energy into the ferrite materials is usually characterized by the value of dielectric loss tangent (tan δ), which is defined as the ratio of the imaginary part of the dielectric permittivity to the real part, see Eq. (3). Figure 10 demonstrates the frequency variation of tan δ of nanostructured $MnFe_2O_4$ ferrite

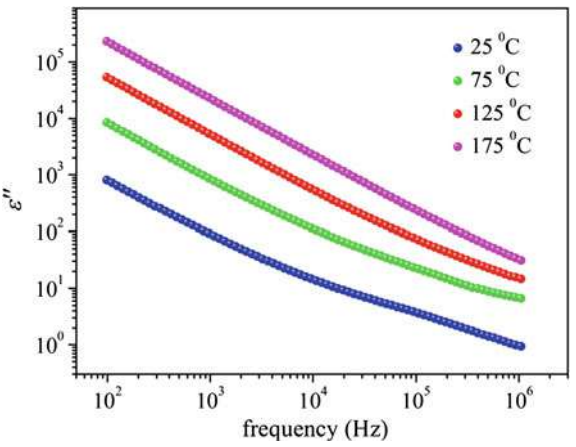

Fig. 9 Frequency dependence of imaginary part of dielectric permittivity (ε″) for manganese nanoferrite at selected temperatures

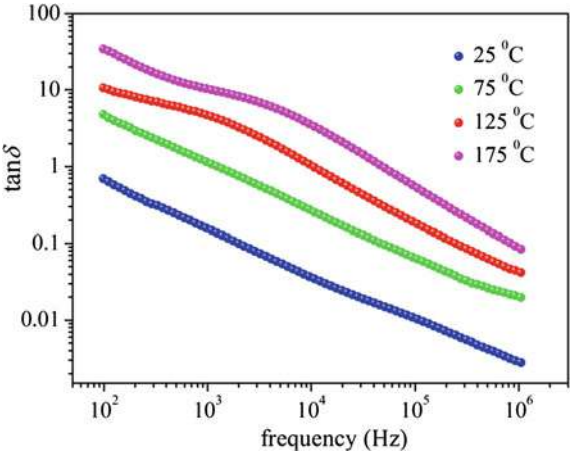

Fig. 10 Frequency dependence of dielectric loss tangent (tan δ) for manganese nanoferrite at selected temperatures

under investigation at some selected temperatures. In general, it can be inferred that the dielectric loss decreases with increasing frequency, thereby showing a qualitatively similar behavior with frequency as well as ε''. The tan δ shows normal dielectric behavior at temperatures up to 75 °C. Beyond that temperature in frequency response of the dielectric loss tangent is observed an anomalous behavior, where are apparently present small Debye peaks. These peaks appear when the frequency of the external AC field is approximately equal to the hopping frequency of the charge carriers and the phenomenon is termed as ferromagnetic resonance [30]. In the case of Mn-ferrite similar behavior of tan δ was observed by Batoo et al. [11]. As the temperature increases, the shifting of these Debye peaks towards higher frequency region is often attributed to the increase in the rate of hopping of charge carriers. Also, Fig. 10 shows that temperature dependence of dielectric loss exhibits increasing trend, which is a result of the increasing electrical conductivity of the

ferrite sample with temperature [38]. This was expected due to the increase in thermally activated drift mobility of electric charge carriers according to the hopping conduction mechanism [39]. In the present study, the values of sample's dielectric loss tangent, in the range of 6×10^{-1} to 3×10^{-3} at room temperature as given in Table 1, makes the synthesized manganese ferrite technologically important. Such low value of tan δ can be attributed to more homogeneous ferrite processed by soft mechanochemical technique.

4 Conclusions

In summary, the effects of temperature and frequency on the electrical and dielectric properties of nanostructured manganese ferrite successfully prepared by the soft mechanochemical method were studied in detail. The DC electrical conductivity measurement indicated the typical semiconductor like nature of sample. In addition, the temperature dependence of DC conductivity well obeys the Arrhenius law and the activation energy is calculated from the slope of conductivity plots. Temperature variation of drift mobility shows the same behavior as the DC conductivity; it increases with increasing temperature. The AC electrical conductivity of present Mn-ferrite remains almost constant at low-frequency region, up to 1 kHz at 25 °C, and becomes sensitive at the high-frequency side. The variation of Jonscher's coefficient with temperature in the power law frequency dependent AC conductivity indicates that correlated barrier hopping model is suitable for explaining conduction mechanism. The variation of real and imaginary part of dielectric permittivity with frequency of an applied electric field shows the usual dielectric dispersion, which was explained in the light of Maxwell–Wagner theory of interfacial polarization in accordance with Koop's phenomenological theory. At temperatures above 75 °C, the present anomalous frequency dependence of dielectric loss tangent can be attributed to the resonance effect. In view of the studied electrical and dielectric properties, the mechano-synthesized $MnFe_2O_4$ nanoferrite with low value of the conductivity and appreciable value of the dielectric permittivity is promising candidate for various electronic devices applications.

Acknowledgments This research was financially supported by the Ministry of Education, Science and Technological Development of the Republic of Serbia through Projects No. III43008 and III45003.

References

1. A. Goldman, *Modern ferrite technology*, 2nd edn. (Springer, New York, 2006)
2. N. Sivakumar, Influence of structural ordering on electrical conductivity of nanostructured manganese zinc ferrite. Mater. Chem. Phys. **138**, 102–107 (2013)

3. D.L. Sekulic, Z.Z. Lazarevic, M.V. Sataric, C.D. Jovalekic, N.Z. Romcevic, Temperature-dependent complex impedance, electrical conductivity and dielectric studies of $M\mathrm{Fe_2O_4}$ (M = Mn, Ni, Zn) ferrites prepared by sintering of mechanochemical synthesized nanopowders. J. Mater. Sci.: Mater. Electron. **26**, 1291–1303 (2015)
4. K.M. Batoo, S. Kumar, C.G. Lee, Alimuddin, Study of ac impedance spectroscopy of Al doped $\mathrm{MnFe_{2-2x}Al_{2x}O_4}$. J. Alloy. Compd. **480**, 596–602 (2009)
5. M.A. Ahmed, N. Okasha, S.I. El-Dek, Preparation and characterization of nanometric Mn ferrite via different methods. Nanotechnology **19**, 065603 (2008)
6. E.V. Gopalan, K.A. Malini, S. Saravanan, D.S. Kumar, Y. Yoshida, M.R. Anantharaman, Evidence for polaron conduction in nanostructured manganese ferrite. J. Phys. D Appl. Phys. **41**, 185005 (2008)
7. K.M. Batoo, M.S. Abd El-sadek, Electrical and magnetic transport properties of Ni–Cu–Mg ferrite nanoparticles prepared by sol–gel method. J. Alloy Compd. **566**, 112–119 (2013)
8. M.J. Akhtar, M. Younas, Structural and transport properties of nanocrystalline $\mathrm{MnFe_2O_4}$ synthesized by co-precipitation method. Solid State Sci. **14**, 1536–1542 (2012)
9. P.P. Hankare, R.P. Patil, U.B. Sankpal, S.D. Jadhav, I.S. Mulla, K.M. Jadhav, B.K. Chougule, Magnetic and dielectric properties of nanophase manganese-substituted lithium ferrite. J. Magn. Magn. Mater. **321**, 3270–3273 (2009)
10. N.S. Gajbhiye, G. Balaji, Synthesis, reactivity, and cations inversion studies of nanocrystalline $\mathrm{MnFe_2O_4}$ particles. Thermochim. Acta **385**, 143–151 (2002)
11. K.M. Batoo, S. Kumar, C.G. Lee, Alimuddin, Study of dielectric and ac impedance properties of Ti doped Mn ferrites. Curr. Appl. Phys. **9**, 1397–1406 (2009)
12. K.M. Batoo, Study of dielectric and impedance properties of Mn ferrites. Phys. B **406**, 382–387 (2011)
13. Z.Z. Lazarevic, C. Jovalekic, A. Milutinovic, D. Sekulic, V.N. Ivanovski, A. Recnik, B. Cekic, N.Z. Romcevic, Nanodimensional spinel $\mathrm{NiFe_2O_4}$ and $\mathrm{ZnFe_2O_4}$ ferrites prepared by soft mechanochemical synthesis. J. Appl. Phys. **113**, 187221 (2013)
14. Z.Z. Lazarevic, C. Jovalekic, A. Recnik, V.N. Ivanovski, M. Mitric, M.J. Romcevic, N. Paunovic, B.Đ. Cekic, N.Z. Romcevic, Study of manganese ferrite powders prepared by a soft mechanochemical route. J. Alloy. Compd. **509**, 9977–9985 (2011)
15. U. Ghazanfar, S.A. Siddiqi, G. Abbas, Study of room temperature dc resistivity in comparison with activation energy and drift mobility of NiZn ferrites. Mater. Sci. Eng., B **118**, 132–134 (2005)
16. Z.Z. Lazarević, C. Jovalekic, D.L. Sekulic, A. Milutinovic, S. Balos, M. Slankamenac, N.Z. Romcevic, Structural, electrical and dielectric properties of spinel nickel ferrite prepared by soft mechanochemical synthesis. Mater. Res. Bull. **48**, 4368–4378 (2013)
17. A. Ahlawat, V.G. Sathe, Raman study of $\mathrm{NiFe_2O_4}$ nanoparticles, bulk and films: effect of laser power. J. Raman Spectrosc. **42**, 1087–1094 (2011)
18. B. Liu, L. Zhang, K. Zhou, Z. Li, H. Wang, Electrical conductivity and molten salt corrosion behavior of spinel nickel ferrite. Solid State Sci. **13**, 1483–1487 (2011)
19. D.L. Sekulic, Z.Z. Lazarevic, C.D. Jovalekic, A.N. Milutinovic, N.Z. Romcevic, Impedance spectroscopy of nanocrystalline $\mathrm{MgFe_2O_4}$ and $\mathrm{MnFe_2O_4}$ ferrite ceramics: effect of grain boundaries on the electrical properties. Sci. Sinter. **48**, 17–28 (2016)
20. M. Gupta, B.S. Randhawa, Mössbauer, magnetic and electric studies on mixed Rb–Zn ferrites prepared by solution combustion method. Mater. Chem. Phys. **130**, 513–518 (2011)
21. J. Chand, M. Singh, Electric and dielectric properties of $\mathrm{MgGd_{0.1}Fe_{1.9}O_4}$ ferrite. J. Alloy. Compd. **486**, 376–379 (2009)
22. Z.Z. Lazarevic, C. Jovalekic, D. Sekulic, M. Slankamenac, M. Romcevic, A. Milutinovic, N.Z. Romcevic, Characterization of nanostructured spinel $\mathrm{NiFe_2O_4}$ obtained by soft mechanochemical synthesis. Sci. Sinter. **44**, 331–339 (2012)
23. M.I. Klinger, Two-phase polaron model of conduction in magnetite-like solids. J. Phys. C: Solid State Phys. **8**, 3595–3607 (1975)
24. E.M.M. Ibrahim, The effect of sintering time and temperature on the electrical properties of MnZn ferrites. Appl. Phys. A **89**, 203–208 (2007)

25. S.A. Mazen, A.M. El Taher, The conduction mechanism of Cu–Ge ferrite. Solid State Commun. **150**, 1719–1724 (2010)
26. T. Javed, A. Maqsood, A.A. Malik, Structural, electrical and dielectric properties of Co–Mn spinel nanoferrites prepared by co-precipitation technique. J. Supercond. Nov. Magn. **24**, 2137–2144 (2011)
27. K. Verma, A. Kumar, D. Varshney, Effect of Zn and Mg doping on structural, dielectric and magnetic properties of tetragonal $CuFe_2O_4$. Curr. Appl. Phys. **13**, 467–473 (2013)
28. A.K. Jonscher, The 'universal' dielectric response. Nature **267**, 673–679 (1977)
29. M. Younas, M. Nadeem, M. Atif, R. Grossinger, Metal-semiconductor transition in $NiFe_2O_4$ nanoparticles due to reverse cationic distribution by impedance spectroscopy. J. Appl. Phys. **109**, 093704 (2011)
30. M.A. Rahman, A.K.M.A. Hossain, Electrical transport properties of Mn–Ni–Zn ferrite using complex impedance spectroscopy. Phys. Scr. **89**, 025803 (2014)
31. S.R. Elliott, AC conduction in amorphous chalcogenide and pnictide semiconductors. Adv. Phys. **36**, 135–217 (1987)
32. E. Senturk, Y. Koseoglu, T. Sasmaz, F. Alan, M. Tan, RC circuit and conductivity properties of $Mn_{0.6}Co_{0.4}Fe_2O_4$ nanocomposite synthesized by hydrothermal method. J. Alloy. Compd. **578**, 90–95 (2013)
33. M.M. Haque, M. Huq, M.A. Hakim, Densification, magnetic and dielectric behaviour of Cu-substituted Mg–Zn ferrites. Mater. Chem. Phys. **112**, 580–586 (2008)
34. K.W. Wagner, Zur Theorie der unvollkommenen Dielektrika. Ann. Phys. (Leipzig) **40**, 817–855 (1913)
35. N. Sivakumar, A. Narayanasamy, B. Jeyadevan, R.J. Joseyphus, C. Venkateswaran, Dielectric relaxation behaviour of nanostructured Mn–Zn ferrite. J. Phys. D Appl. Phys. **41**, 245001 (2008)
36. I.T. Rabinkin, Z.I. Novikova, *Ferrites* (Doklady Akademii Nauk SSSR, Minsk, USSR, 1960)
37. I. Ali, M.U. Islam, M.N. Ashiq, H.M. Khan, M.A. Iqbal, M. Najam-Ul-Haq, Effect of Eu–Ni substitution on electrical and dielectric properties of Co–Sr–Y-type hexagonal ferrite. Mater. Res. Bull **49**, 338–344 (2014)
38. Z.Z. Lazarevic, C. Jovalekic, A. Milutinovic, D. Sekulic, M. Romcevic, M. Slankamenac, N. Romcevic, Spectroscopy investigation of nanostructured zinc ferrite obtained by mechanochemical synthesis. Optoelectron. Adv. Mater. Rapid Comm. **7**, 720–725 (2013)
39. A.M. Abdeen, Dielectric behaviour in Ni–Zn ferrites. J. Magn. Magn. Mater. **192**, 121–129 (1999)

Study of Nanodimensional Spinel $Ni_{0.5}Zn_{0.5}Fe_2O_4$ Ferrite Prepared by Mechanochemical Synthesis

Zorica Ž. Lazarević, Martina Gilić, Milica Petrović, Nebojša Romčević, Čedomir Jovalekić, Dalibor L. Sekulić and Valentin N. Ivanovski

Abstract The nanodimensional $Ni_{0.5}Zn_{0.5}Fe_2O_4$ ferrites were prepared from mixture of NiO/ZnO/α-Fe_2O_3 and $Ni(OH)_2$/$Zn(OH)_2$/$Fe(OH)_3$ powders by (soft) mechanochemical synthesis after 5 and 10 h of milling time. The XRD of the sample obtained after 10 h milling time shows single phase cubic spinel structure. TEM analysis revealed that all samples are composed of more or less agglomerated nanosize particles. The average size of nano crystallites is ~20 nm. The degree of the cation inversion of NZF is estimated for spinel fraction in all samples by Rietveld analysis. In the Raman spectra are observed all of first-order active modes. In the spectra of the single phase "hydroxide" samples it is visible that the energy position and intensity of modes is dependent on the composition and cation distribution. It was shown that the modes in Raman spectra of nickel-zinc ferrite that originate from vibrating of different cations could be clearly distinguished. From the ratio of intensities of the A_{1g}-type Raman modes, it is possible to estimate the inversion of cations. The Mössbauer spectra were fitted by several subspectra and according to known subspectral areas of both iron sites the degree of inversion was calculated, also. The cation inversion is $\lambda = 0.36(3)$ for ferrite sample obtained from the mixture of appropriate hydroxide for 10 h milling.

Keywords Magnetic materials · $Ni_{0.5}Zn_{0.5}Fe_2O_4$ · X-ray diffraction · Mössbauer spectroscopy

Z.Ž. Lazarević (✉) · M. Gilić · M. Petrović · N. Romčević
Institute of Physics, University of Belgrade, Belgrade, Serbia
e-mail: lzorica@yahoo.com

Č. Jovalekić
The Institute for Multidisciplinary Research, University of Belgrade, Belgrade, Serbia
e-mail: jovalek@imsi.rs

D.L. Sekulić
Faculty of Technical Sciences, University of Novi Sad, Novi Sad, Serbia
e-mail: dalsek@yahoo.com

V.N. Ivanovski
Institute of Nuclear Sciences Vinča, University of Belgrade, Belgrade, Serbia
e-mail: valiva@vinca.rs

B. Lee et al. (eds.), *Proceedings of the IV Advanced Ceramics and Applications Conference*, DOI 10.2991/978-94-6239-213-7_15

1 Introduction

Interest in nanosized spinel ferrites has greatly increased in the past few years due to their importance in understanding the fundamentals of nanomagnetism [1] and their wide range of applications such as high-density data storage, ferrofluid technology, sensor technology, spintronics, magnetocaloric refrigeration, heterogeneous catalysis, magnetically guided drug delivery, and magnetic resonance imaging [1–5]. It is widely appreciated that the cation distribution in spinel ferrites, upon which many physical and chemical properties depend, is a complex function of processing parameters and depends on the preparation method of the material [6–9].

The ideal crystal structure of cubic spinel ferrites (Fig. 1) $M^{2+}Fe_2{}^{3+}O_4{}^{2-}$ (M = Mg, Mn, Fe, Co, Ni, Zn) has a face centered cubic unit cell of 32 oxygen anions with cations in 24 of possible 96 interstitial sites: 8 tetrahedral (A-sites) (1/8 of the total tetrahedral sites number) and 16 octahedral [B-sites] (1/2 of total number) [10, 11].

The structural formula of NZF is usually written as $(Zn^{2+}_{1-\lambda}Fe^{3+}_{\lambda})$ $[Ni^{2+}_{\lambda}\ Fe^{3+}_{2-\lambda}]$ $\{O^{2-}\}_4$, where round and square brackets denote sides of tetrahedral (A) and octahedral [B] coordination respectively, and λ represents the degree of inversion [defined as the fraction of (A) sites occupied by Fe^{3+} cations]. Considering the absence of Zn^{2+} cations in the ferrite, the amount of iron in both atomic sites would be equal and their contribution to the magnetic dipole moment would be canceled, and the formation of the material magnetic dipole moment would be responsibility for Ni^{2+} cations. Doping the ferrite with Zn^{2+} cations, there is a migration of Fe^{3+} cations from tetrahedral sites to octahedral sites, unbalancing initial equality of Fe^{3+} cations. Therefore there is an abrupt increase in magnitude of the magnetic dipole moment, because Fe^{3+} and Zn^{2+} cations are contributing to the dipole moment of the material. Thus, it is possible to produce a large number of intrinsically magnetic ferrite by appropriate substitution of metallic ions. Figure 2 presents a representation of a portion of nickel-zinc ferrite with $Ni_{0.5}Zn_{0.5}Fe_2O_4$ stoichiometry and structure type inverse spinel, with octahedral sites FeO_6 or NiO_6 in blue and tetrahedral sites FeO_4 or ZnO_4 in red.

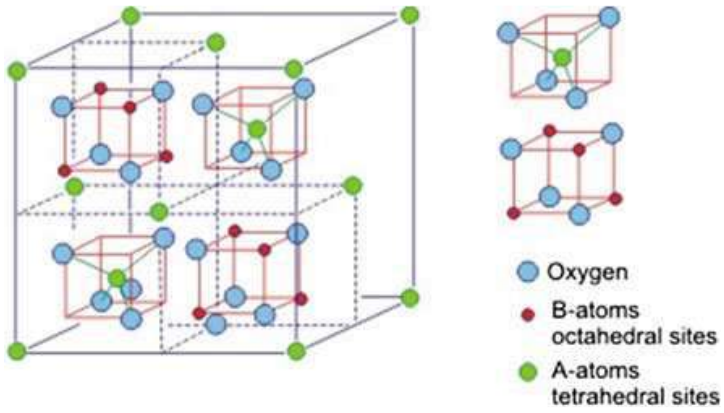

Fig. 1 Spinel structure with tetrahedral (**a**) and octahedral (**b**) sites

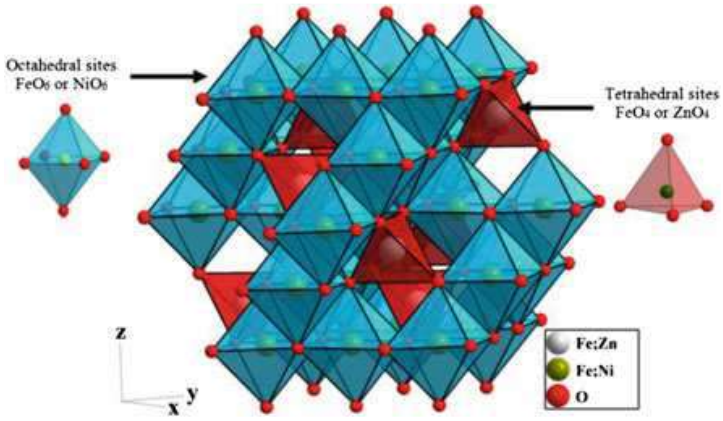

Fig. 2 Oxide nickel-zinc ferrite representation, with stoichiometry $Ni_{0.5}Zn_{0.5}Fe_2O_4$ with structure type inverse spinel. Octahedral sites FeO_6 or NiO_6 are presented in *blue* and tetrahedral sites FeO_4 or ZnO_4 are presented in *red*

Ferrites are classified according to cations degree of inversion λ (positioning between normal ($\lambda = 0$) and inverse ($\lambda = 1$) extreme patterns). The space group symmetry of normal cubic spinels is *Fd3m* [12]. The most of cubic ferrites at the nanosized scale have partially inverse (or "mixed") structure.

The zinc concentration and distribution among A and B sites in a NZF has a crucial influence on the material's microstructure, dielectric and magnetic properties [13]. It was referred that nano crystalline NZF was prepared by different method of synthesis [14]. To the best of our knowledge it is not referred on soft mechanochemical method of the NZF nano powder synthesis.

The aim of this work was the synthesis of nanosized nickel-zinc ferrite by ball milling of two different starting powder mixtures: (1) oxide mixture and (2) hydroxide mixture under the same conditions. The efficiencies of mechanochemical activating in these two cases, are compared. The "conventional mechanochemical route" hereinafter will mean a mechanochemical activating of oxide mixture. According to Avvakumov et al. [15], the phrase "soft mechanochemical route" will be used for the reaction of hydroxides. Progress of the reaction and characterization of NZF nano powder samples are investigated by XRD, TEM, EDS, Raman and Mössbauer spectroscopy.

2 Experimental

Starting materials for the conventional and soft mechanochemical synthesis of $Ni_{0.5}Zn_{0.5}Fe_2O_4$ samples were: Merck oxides NiO, ZnO and Fe_2O_3 with 99 % purity and Merck zinc and nickel hydroxides with 95 % purity. Ferric-hydroxide was made in laboratory. NaOH solution (25 % mass), made from 99 % purity NaOH (Merck) was added to the $FeCl_3$ solution (25 % mass), made from 99 % purity $FeCl_3 \times 6H_2O$ (Merck) [16]. Obtained hydrated ferric-hydroxide ($Fe(OH)_3 \times nH_2O$) in the form of dark brown precipitate was filtrated, washed with large amounts of water and dried in a vacuum desiccator. Before milling, the

$Fe(OH)_3 \times nH_2O$ powder was heated at 105 °C for 24 h. The material prepared in this way had 99.5 % $Fe(OH)_3$. It was confirmed by potentiometric redox titration.

Mechanochemical synthesis was performed in air atmosphere in planetary ball mill Fritsch Pulverisette 5 (Fig. 3). Balls-to-powder mass ratio was 20:1. The angular velocity of the supporting disc and vial was 32 and 40 rad s^{-1}, respectively. The powders obtained after milling were pressed into disc shaped samples with thickness of 2.0 mm and diameter 8.0 mm.

For XRD analysis the X-ray diffractometer, Model Philips PW 1050, equipped with a PW 1730 generator (40 kV × 20 mA) was used. X-ray source was Ni filtered Co*K*α radiation of 1.78897 Å. Measurements were done at room temperature in 2θ range of 10°–80° with scanning step width of 0.05° and 10 s scanning time per step.

Transmission electron microscopy (Fig. 4) studies were performed using a JEOL JEM-2100F Microscope (Jeol Inc., Tokyo, Japan) with maximum acceleration voltage of 200 kV equipped with an ultra-high resolution objective lens pole piece having a point-to-point resolution of 0.19 nm, being sufficient to resolve the lattice images of nanoparticles. Electron diffraction patterns (EDP) of nano crystals were recorded to obtain the diffraction rings with specific structure d-values and in that way verify the crystal structure.

Electron energy dispersive X-ray spectroscopy (EDS) (Fig. 5), as part of transmission electron microscopy, was used to examine the chemical composition of selected crystallites.

The Raman scattering measurements of NZF nano powder samples were performed in the backscattering geometry at room temperature in the air using a Jobin-Yvon T64000 triple spectrometer, equipped with a confocal microscope (100×) and a nitrogen-cooled charge coupled device detector (CCD) (Fig. 6). The spectra have been excited by a 514.5 nm line of Coherent Innova 99 Ar^+—ion laser

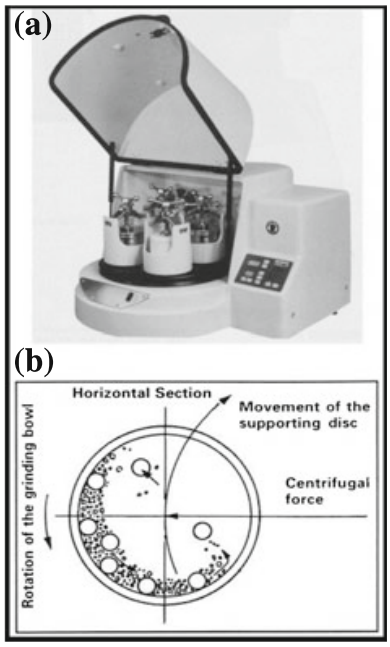

Fig. 3 **a** A planetary ball mill (Fritsch Pulverisette 5). **b** Working principle of planetary ball mill. Schematic view of motion of the ball and powder mixture

Fig. 4 Transmission electron microscopy (TEM)

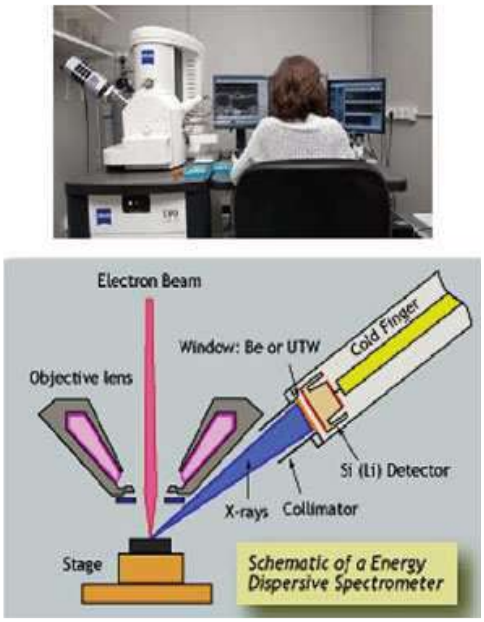

Fig. 5 Electron energy dispersive X-ray spectroscopy (EDS) was used to examine the chemical composition of the product

with an output power of less than 20 mW to avoid local heating due to laser irradiation. Spectra were recorded in the range from 100 to 800 cm^{-1}.

The Mössbauer spectra were collected at the room temperature in the transmission mode with a constant acceleration, using a $^{57}Co/Rh$ source. The calibrations of spectra were done by laser. The isomer shift (IS) values were in agreement with values for a standard α-Fe foil at 300 K. Least squares fits were calculated using the SITE option of the WinNormos software. Line width corrections were carried out by the transmission integral. The DIST/ISO option of the program, based on the histogram method, was used to perform distributions of Mössbauer's lines [17].

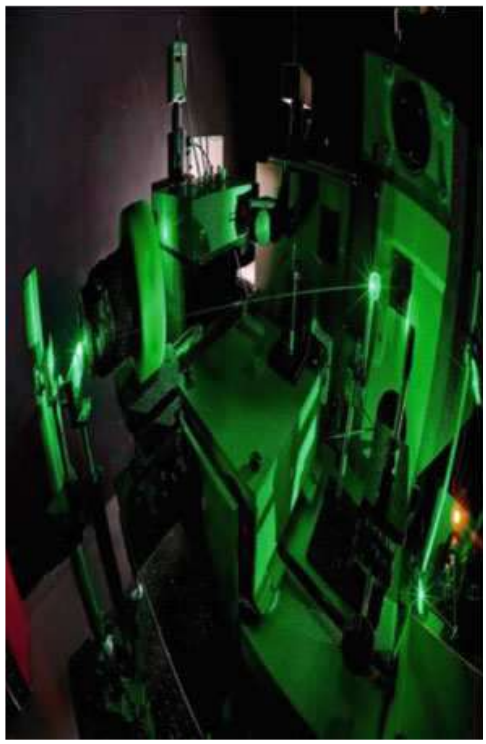

Fig. 6 Raman spectrometer—Jobin Yvon T64000

3 Results and Discussion

Figures 7 and 8 show the X-ray diffractograms of partially, or completely, reacted powders after 5 and 10 h of mechanochemical treatment. In the oxide mixture after 5 h of milling the reaction begins and the spinel peaks become observable in the corresponding diffractogram, Fig. 7.

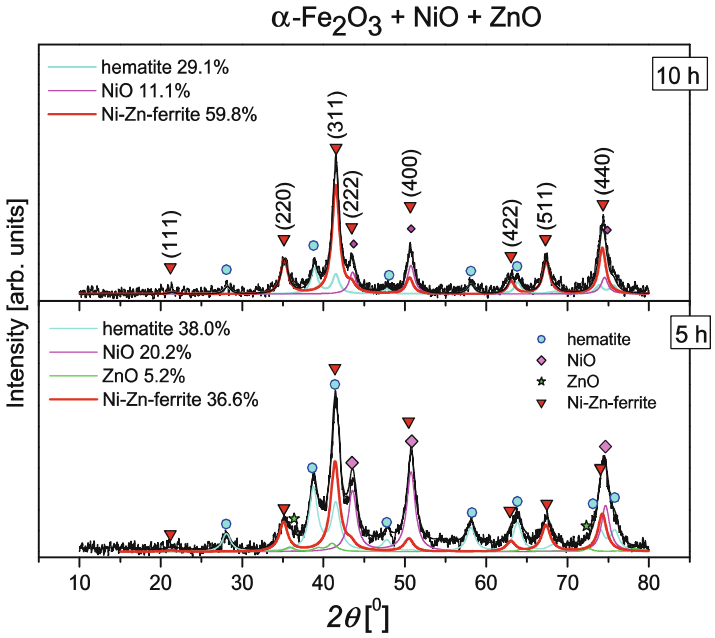

Fig. 7 XRD spectra of the mixture of starting NiO, ZnO and α-Fe_2O_3 powders after milling for 5 and 10 h

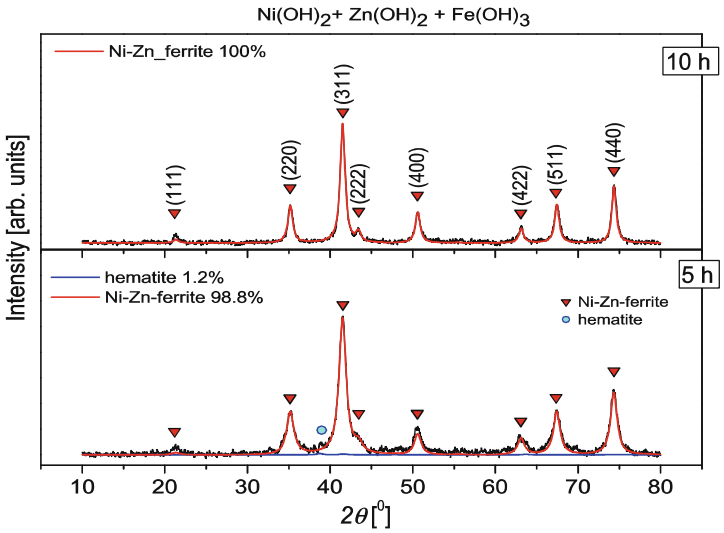

Fig. 8 XRD spectra of the mixture of starting $Ni(OH)_2$, $Zn(OH)_2$ and $Fe(OH)_3$ powders after milling for 5 and 10 h

Considering that the starting oxide materials have crystallites with average sizes ~50 nm ZnO to ~90 nm α-Fe_2O_3, there is still a lot of unreacted starting oxides after 5 h, but in the form of smaller nano crystallites. The Rietveld analysis suggests that there are 36.6 % of spinel NZF phase, 38.0 % of hematite, 20.2 % nickel oxide and 5.2 % of zinc oxide with crystallites smaller than 13 nm. After 10 h of milling, Fig. 7, in the diffractogram dominate spinel peaks (about 60 % of NZF phase), but diffraction peaks of hematite and nickel oxide are still present. A conventional mechanochemical reaction between anhydrous starting oxides was used in [10, 11], also. A precise comparison is not possible because milling conditions were not the same (a speed of the vials and ball-to-powder mass ratio), but it was shown that a milling time longer than 10 h is needed for the obtaining a single phase NZF, as evidenced by our experiment, as well.

NZF can be obtained directly from oxide mixture at about 500 °C. The reaction becomes possible after a certain activation time, as milling reduces the particle size, thoroughly mixes the components, and increases the number of chemically active defect sites [18]. Obviously, due to a great size and hardness of the oxide crystallites, for the formation of pure phase of NZ-ferrite (under the used milling conditions) a more time is required.

The starting hydroxides are amorphous and very reactive which facilitates the chemical reaction [15] and after 5 h of milling the reaction was almost complete, Fig. 8. Rietveld analysis shows that there is 98.8 % NZF in the form of small nano crystallites (about 14 nm) and only 1.2 % of hematite. After 10 h of milling, Fig. 8, there are no traces of starting materials, i.e. any other intermediate reaction product.

In the case of starting hydroxide mixture the synthesis occurred in two stages. The first of the two stages was followed by the evolution of water vapour. For instance, the ferric-hydroxide $Fe(OH)_3$ can be easily transformed in hematite during milling through thermal decomposition [16].

All hydroxides undergo the similar reaction at about 300–350 °C [15]. The second step in the synthesis of NZF is a direct synthesis of the obtained amorphous NiO, ZnO and α-Fe_2O_3 oxides. The extremely small dimensions of the obtained

oxide crystallites (amorphous) provide a better adhesion between particles (what is a prerequisite for a faster reaction at lower temperature). A occurrence of substantial amount of water that is formed during soft mechanochemical reactions between hydroxides, in comparison with a much smaller amount of physically adsorbed water that can liberated from pores of oxide crystallites, contributes to better energy transfer from milling media to reacting materials and to acceleration of the formation rate. All stated above are well known advantages of the soft mechanochemical synthesis what is discussed in detail in [15, 19, 20].

In Figs. 7 and 8, for 10 h of milling, the positions of NZF diffractions are indicated. Positions of the peaks and their intensities correspond to the reference PCPDFWIN data (PDF #52-0278) for $Ni_{0.5}Zn_{0.5}Fe_2O_4$-spinel ferrite Bragg reflections. The lattice constant depends not only to chemical composition, but to the crystallite size and cation distribution, also. The lattice constants of obtained NZF (a), average crystallite sizes (<*L*>) in various samples and the distribution of cations over tetrahedral and octahedral sites, which gives the best fit to observed diffractograms, are estimated by Rietveld refinement. In the samples originated from oxide mixture a and <*L*> are calculated for the NZF participation in the mixture. It should be noted that peaks profile in diffractograms of samples obtained by milling of hydroxides for 10 h are fitted by Pseudo-Voight2 function and for other samples the Lorentz profile was more convenient.

The XRD—analysis of the powder samples obtained after 5 and 10 h milling of starting mixtures shows that the soft mechanochemical activation (i.e. milling of amorphous hydroxides) gives practically pure NZF phase after 5 h. During further milling process the crystallites continue to growth and their cation distribution changes. In the case of the oxide mixture the formation of NZF phase is much slower.

TEM analysis, Fig. 9, revealed that all samples are composed of nanosized particles (around 20 nm). The size of the particles in the samples prepared form

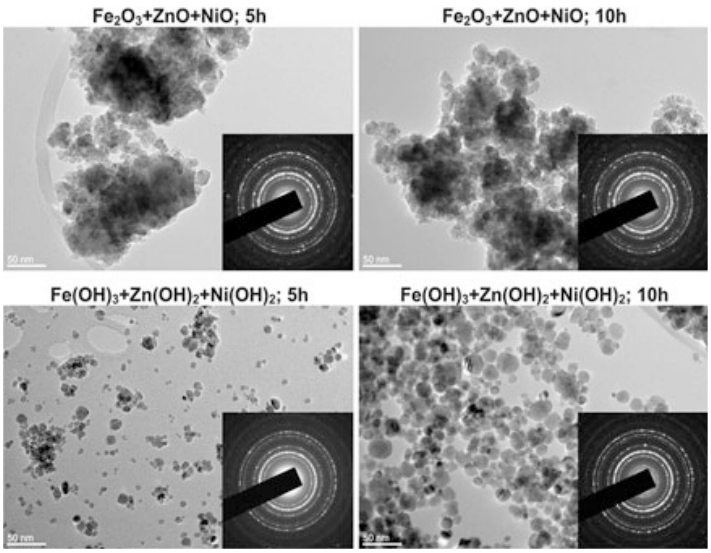

Fig. 9 TEM images with corresponding electron diffraction patterns (EDP *insets* in the *lower right corners*) of the samples obtained from the mixtures of NiO, ZnO and α-Fe_2O_3 oxide and the mixture of $Ni(OH)_2$, $Zn(OH)_2$ and $Fe(OH)_3$ hydroxide powders for 5 and 10 h of milling time

oxides is similar after 5 and 10 h, whereas in the samples prepared from hydroxides, the size of the particles is larger in the 10 h sample.

The particles in the oxide samples (5 and 10 h) have irregular shape and are highly agglomerated, while the particles in the hydroxide samples (5 and 10 h) are roundish and less agglomerated.

Electron energy dispersive X-ray spectra (EDS) were measured in each sample on several nanosized particles. Obtained spectra illustrate a progress of the reaction in milling powders. In Fig. 10a is a TEM image of a sample obtained after 5 h milling of crystalline oxides with inserted EDS of two selected grains. It is obvious that in this sample a number of large particles of the precursor oxides is present. In Fig. 10b is presented a TEM image of single phase sample obtained after 10 h milling of starting hydroxides with EDS of one chosen grain.

The similar chemical composition ratios are achieved in all tested grains of this sample. Large remnant precursor particles were much rarer in the "oxide" sample after 10 h milling, whereas precursor particles were not observed in the samples prepared from hydroxides.

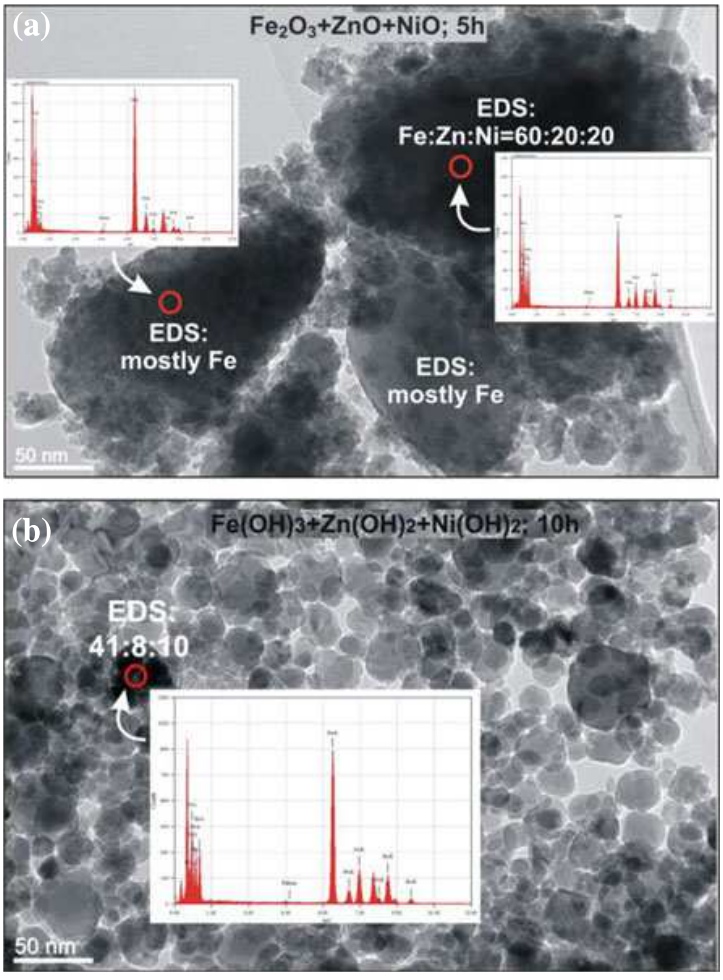

Fig. 10 TEM images with corresponding EDS of selected grains in the case of **a** a sample obtained after 5 h milling of starting oxides and **b** a single-phase sample obtained after 10 h milling of starting hydroxides

Mechanochemically produced nano powder samples of nickel-zinc ferrite have mixed spinel structure and belongs to *P*4322 tetragonal space group [21]. However, it is usual, for the sake of simplicity, to assign Raman and IR modes as in normal cubic spinel, as the symmetry group is *Fd*3*m*. The factor group analysis predicts 5 Raman active mode: $A_{1g} + E_g + 3F_{2g}$ and 4 IR active modes $4F_{1u}$ from the center of Brillouin zone in the normal spinel.

The Raman spectra recorded on the samples obtained during mechanochemical activation of oxide and hydroxide starting mixtures are presented in Fig. 11. The characteristic features of spinel ferrite are recognizable in Raman spectrum already after 5 h of milling oxide mixture, although XRD and TEM suggest that it must be present a lot of unreacted starting oxides in the samples. The strong modes of hematite (indicated by arrows in Fig. 11a) are superposed to spinel modes. Hematite modes are still clearly visible in the oxide sample obtained after 10 h of milling. In the spectrum of the sample made from hydroxides after 5 h of milling a narrow hematite peak testifies that the amount of hematite is very small. After 10 h there is no traces of any other phase in NZF hydroxide sample.

It is obvious that all samples have more than 5 Raman active modes predicted by group theory in the normal spinel structure. Deconvolution of measured spectra allows one to conclude that all complex bands in the spectra are made of individual

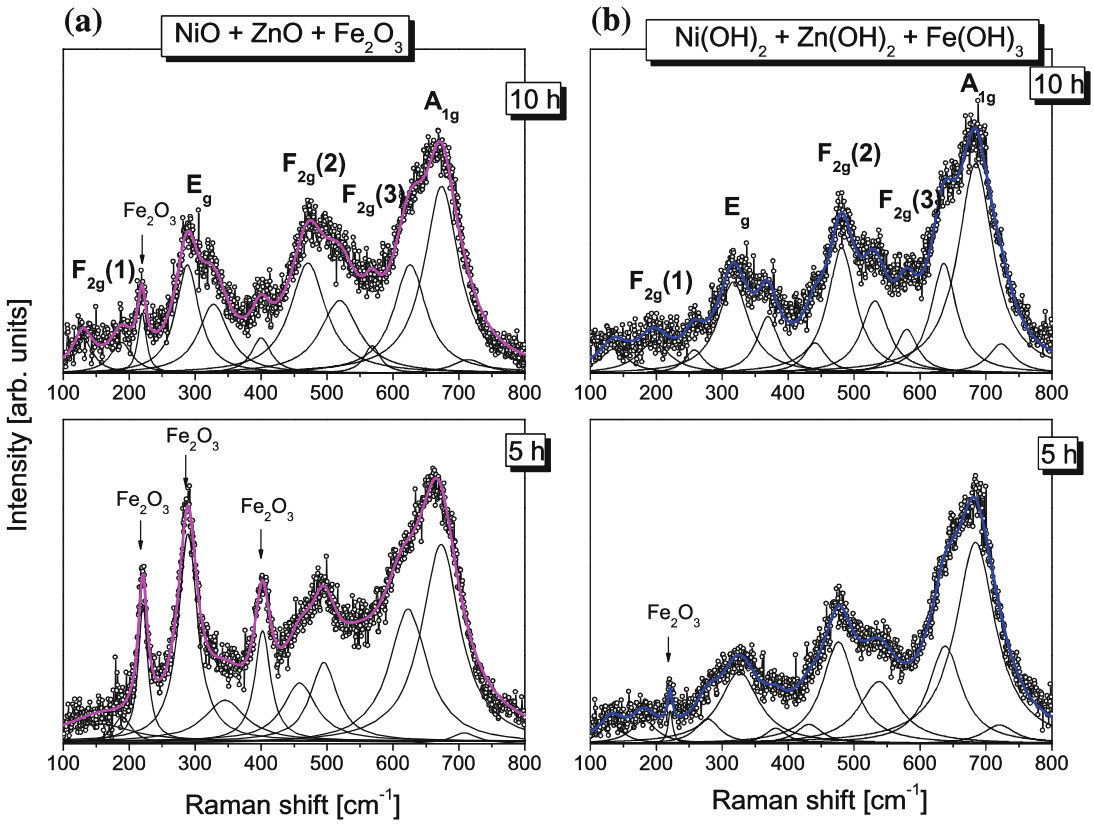

Fig. 11 Raman spectra of the samples obtained from the mixtures of starting **a** NiO, ZnO and α-Fe_2O_3 oxide powders and **b** $Ni(OH)_2$, $Zn(OH)_2$ and $Fe(OH)_3$ hydroxide powders after mechanochemical treatment for 5 and 10 h. *Arrows* indicate peaks of unreacted hematite

peaks with the intensities that vary from spectrum to spectrum. In order to determine the origin of the peaks, we have compared the Raman spectra of previously investigated $NiFe_2O_4$ and Zn Fe_2O_4 [22–24], with the spectrum of single phase NZF. On the example of single phase sample of $Ni_{0.5}Zn_{0.5}Fe_2O_4$ obtained by milling of hydroxides for 10 h it is visible that modes originated from vibrating of different cations (in Ni-ferrite, or Zn-ferrite) are reproduced in Raman spectra of mixed NZF.

The high frequency first order mode A_{1g} is due to symmetric stretching of oxygen atoms along Zn–O, Fe–O and Ni–O bonds in the tetrahedral coordination [25]. The mode at 637 cm^{-1} is related with stretching along Zn–O bonds in tetrahedrons [26, 27]. The mode at 670 cm^{-1} is related with Fe–O bonds stretching [28], at 689 cm^{-1} with Ni–O bonds [16, 29] and a small mode at 721 cm^{-1} corresponds to A_{1g} mode of maghemite, i.e. to oscillations of Fe–O in uncompleted tetrahedrons (with oxygen vacancies) [30]. In principle, modes $F_{2g}(2)$ and $F_{2g}(3)$ correspond to the vibrations of the octahedral group, but it seems that components of these modes can hardly be resolved in the Raman spectra of NZF. At about 370 cm^{-1} is the Zn-component of $F_{2g}(2)$ mode, at 480 cm^{-1} is Ni—$F_{2g}(2)$ and between them Zn—component of $F_{2g}(3)$ mode. These modes are not very strong and the possible fitting error can be too high because of rather high level of noise. For that reason we tried to analyse the most exaggerate A_{1g} mode and to estimate the inversion parameter from the ratio of the intensities of A_{1g} components. The integrated intensity of certain component of A_{1g} mode is proportional approximately to the contribution of the corresponding cations in A-sites.

The Mössbauer spectra show distributions of hyperfine fields. In order to investigate valence and coordination number (CN) of iron cations in the spinel, distributions are partitioned on disjunct subspectra based on Lorentzian lines. The Mössbauer spectrum of the sample obtained from the mixture of NiO/ZnO/α-Fe_2O_3 powders milled for 5 h, is divided into seven subspectra (see Fig. 12a).

The initial hematite is present, however fits with the characteristic sextet (IS = 0.37 mm s^{-1}; Δ = −0.197 mm s^{-1}; B_{hf} = 51.75 T) are somewhat ambiguous. We resorted to the use of distribution of hyperfine fields. This yields a Gaussian—like distribution with centroid at 51.03 T and with the standard deviation of 0.68 T. The average isomer shift (IS) has value of 0.383(5) mm s^{-1}. The quadrupole shift has value of −0.180(2) mm s^{-1}. The parameters of distribution suggest that a superposition of resonant signal occurs from hematite and ^{57}Fe at the octahedral site of the larger crystalline spinel ferrite. In order to simplify the calculation of the relative amount of phases in the sample from the areas of subspectra, we estimate that the factors of recoilless fraction are equal for all iron sites. The distribution covers 16.7(1.4) % of the total fitted area.

Generally, the bond length of Fe^{3+}–O^{2-} at the tetrahedral site is smaller than the similar length at the octahedral site, allowing larger overlapping of orbitals and respectively more covalent bond at the tetrahedral site. The consequence is smaller value for the isomer shift. That explains why the sextet A1 is associated with the tetrahedral site, and B1 and B2 with the octahedral site. The large value of the quadrupole shift (2ε) at the combined interaction, sextet A1, and large line width (Γ)

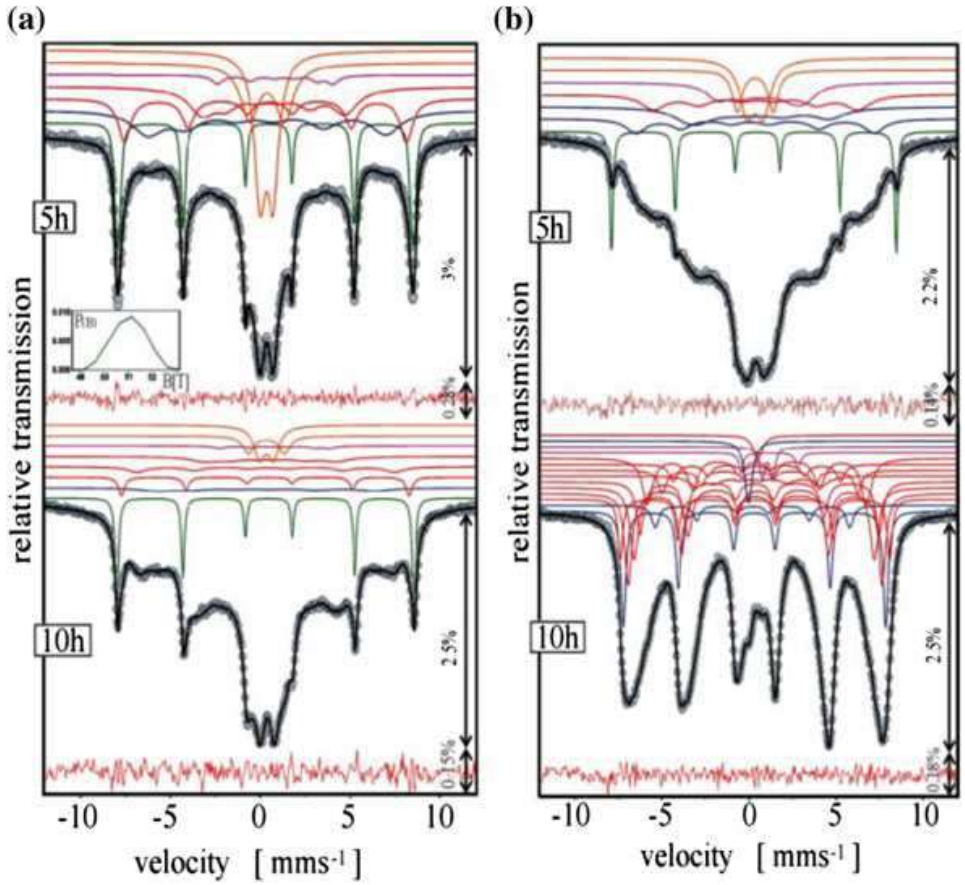

Fig. 12 Mössbauer spectra at room temperature after 5 and 10 h milling time of the mixture **a** NiO/ZnO/α-Fe_2O_3 and **b** $Ni(OH)_2/Zn(OH)_2/Fe(OH)_3$. *Inset* shows a distribution of hyperfine field in the "oxide" sample obtained after 5 h of milling. The experimental values of relative transmission are shown by the *grey circles*. The *fitted lines* of subspectra are plotted above the main spectra fits

show that this sextet occurs in response to overall changes in the [B]-sublattice. Overall changes include all combinations of iron, zinc, and nickel ions and holes intra [B]-sites that interact via the four oxygen anions, lowering the cube point symmetry (T_d) at the place of interaction and reducing the magnitude of hyperfine interaction (B_{hf}). By comparing the data from our previous work on the nickel ferrite nanopowder spinel, we conclude that sextet B1 belongs to the octahedral site [16]. The negative signs of the quadrupole shifts of these sextets are only consequences of the orientation of direction of B_{hf} relative to the principle axis of the electric field gradient tensor. The sextet B2 is assigned to the octahedral site as well. The low value of magnetic strength might be explained by the presence of a diamagnetic Zn^{2+} ($3d^{10}$) at the both sites, lowering the strong antiferromagnetic coupling. The volume size should also be taken into account. There is a sextet which has 1.07(4) mm s^{-1} isomer shift (*IS*) and B_{hf} = 20.0(3) T. It is assigned to Fe^{2+} with CN = 6. Its existence might be explained by the magnetite structure where [Fe^{3+}] is replaced by another cation or a hole, breaking down the Verwey's electron exchange. The relative amount of this sextet is 2.5(0.7) %, as seen

previously [16, 31]. The doublet SPD1 indicates superparamagnetism, occurring in the limitation on $KV \ll k_BT$, where V is the volume of particle and K is the magnetic anisotropy constant [32]. The value of IS = 0.384(9) mm s^{-1} should not be interpreted as the value of the bulk spinel ferrite, since the nanoparticle values (for IS) are always somewhat bigger. Hence, we consider that this value is the average of both sites [33]. The high value of the quadrupole splitting is due to chemical disorder. The large amount of the relative area, 19.8(1.0) %, belongs to the second doublet, SPD2. Its Mössbaer's parameters, IS = 0.358(2) mm s^{-1} and Δ = 0.72(1) mm s^{-1} are identical to the parameters of the natural ferrihydrite obtained by Coey and Readman [34]. Likewise, they are similar to parameters of the synthetic iron oxide gels [35]. The line width of SPD2 is much larger than width of lines at the cited samples. Hence, SPD2 is assigned to another superparamagnetic doublet.

The relative amount of the hematite in the same mixture, but now milled for 10 h, is 8(1) %. The sextet from Fe^{2+} has 3(1) % of total fitted area. The superparamagnetic phase of spinel totals 23(3) %. All three sextets represent the response from the octahedral sites and have the combined value of 42(3) % of the total fitted area. According to known subspectral areas of both iron sites and using the formula A(A)/A[B] = f(A)/f[B] × $\lambda(2 - \lambda)$ we can estimate λ, the degree of inversion [36]. By taking the ratio of recoil-less fractions to be 0.94, as is estimated for the magnetite at ambient temperature [37] and calculating the degree of inversion only from representation of large particles, we obtain λ = 0.76(11). The error is estimated from the weighted error of summed areas.

The Mössbauer spectrum of the sample obtained from the mixture of $Ni(OH)_2$/$Zn(OH)_2$/$Fe(OH)_3$ powders milled for 5 h consists of seven subspectra (Fig. 12b). It reveals spinel structure of the sample, excluding the formed hematite in amounts of 3(1) % of the total fitted area.

The Mössbauer spectrum of the sample obtained from the mixture of $Ni(OH)_2$/$Zn(OH)_2$/$Fe(OH)_3$ powders after 10 h of milling is fitted by 10 sextets, two superparamagnetic doublets and two singlets (Fig. 12b). Two sextets with the smallest isomer shift are referred to tetrahedral A-site with different occupation numbers and the other sextets are referred to B-site surrounded with different number of magnetic ions or disturbed in other way. Two doublets (SPD), with high isomer shift, could be connected with Fe^{3+} ions in very small superparamagnetic nano particles. There are also two superparamagnetic singlets (SPS), which could be assigned to the tetrahedral (SPSA) and to the octahedral (SPSB) site. All subspectra correspond to the pure spinel ferrite phase. We find that the degree of inversion estimated for the single phase nickel-zinc ferrite sample obtained during 10 h milling of starting hydroxides is λ = 0.36(3). The presented analysis of the Mössbauer spectra of all NZ-ferrite samples is in good agreement with conclusions of previous measurements (XRD, EDP, EDS and Raman spectroscopy).

4 Conclusions

This study shows that under the laboratory conditions it is simple to prepare the good quality nanosized $Ni_{0.5}Zn_{0.5}Fe_2O_4$ ferrite powders by (soft) mechanochemical synthesis. It was examined evolution of the synthesis of nano $Ni_{0.5}Zn_{0.5}Fe_2O_4$ starting from two mixtures of powders milled in different duration time. The starting materials were: case (1) mixture of NiO/ZnO/α-Fe_2O_3 oxide and case (2) mixture of $Ni(OH)_2$/$Zn(OH)_2$/$Fe(OH)_3$ hydroxide powders. The samples obtained after 5 and 10 h of milling time are compared and investigated using various characterization methods. The X-ray diffractogram of the sample obtained after 10 h milling time in case (2) shows single phase cubic spinel structure. TEM analysis revealed that all samples are composed of more or less agglomerated nanosize particles. The average size of nano crystallites is ~20 nm. Crystallites are smaller after 5 h of milling and grow with milling time. This result is in agreement with the results of XRD analysis. The degree of the cation inversion of NZF is estimated for spinel fraction in all samples by Rietveld analysis. In the Raman spectra are observed all of first-order Raman active modes. In the spectra of the single phase "hydroxide" samples it is visible that the energy position and intensity of modes is dependent on the composition and cation distribution. It was shown that the modes in Raman spectra of nickel-zinc-ferrite that originate from vibrating of different cations (Ni-ferrite-like, Zn-ferrite-like, or magnetite-like) could be clearly distinguished. From the ratio of intensities of the A_{1g}-type Raman modes, it is possible to estimate the inversion of cations. The Mössbauer spectra of samples were fitted by several subspectra and according to known subspectral areas of both iron sites the degree of inversion was calculated, also. In the case of single phase sample obtained from the mixture of appropriate hydroxide powders for 10 h milling the cation inversion is $\lambda = 0.36(3)$.

Acknowledgment This research was financially supported by the Ministry of Education, Science and Technological Development of the Republic of Serbia through Project No. III45003.

References

1. C. Zhou, T.C. Schulthess, D.P. Landau, Monte Carlo simulations of $NiFe_2O_4$ nanoparticles. J. Appl. Phys. **99**, 08H906 (2006)
2. Z.L. Wang, Y. Liu, Z. Zhang, *Handbook of nanophase and nanostructured materials*, vol. 3 (Kluwer Academic/Plenum Publishers, New York, 2002)
3. M. Sugimoto, The past, present, and future of ferrites. J. Am. Ceram. Soc. **82**, 269–280 (1999)
4. M.A. Willard, L.K. Kurihara, E.E. Carpenter, S. Calvin, V.G. Harris, Chemically prepared magnetic nanoparticles. Int. Mater. Rev. **49**, 125–170 (2004)
5. U. Lüders, A. Barthélémy, M. Bibes, K. Bouzehouane, S. Fusil, E. Jacquet, J.-P. Contour, J.-F. Bobo, J. Fntcuberta, A. Fert, $NiFe_2O_4$: a versatile spinel material brings new opportunities for spintronics. Adv. Mater. **18**, 1733–1736 (2006)

6. V. Šepelák, A. Feldhoff, P. Heitjans, F. Krumeich, D. Menzel, F.J. Litterst, I. Bergmann, K.D. Becker, Nonequilibrium cation distribution, canted spin arrangement, and enhanced magnetization in nanosized $MgFe_2O_4$ prepared by a one-step mechanochemical route. Chem. Mater. **18**, 3057–3067 (2006)
7. V. Šepelák, I. Bergmann, A. Feldhoff, P. Heitjans, F. Krumeich, D. Menzel, F.J. Litterst, S.J. Campbell, K.D. Becker, Nanocrystalline nickel ferrite, $NiFe_2O_4$: mechanosynthesis, nonequilibrium cation distribution, canted spin arrangement, and magnetic behaviour. J. Phys. Chem. C **111**, 5026–5033 (2007)
8. V. Šepelák, K.D. Becker, Mechanochemistry: from mechanical degradation to novel materials properties. J. Korean Ceram. Soc. **49**, 19–28 (2012). doi:10.4191/kceRrse.2v0i1e2.w49.1.019
9. Z.Ž. Lazarević, Č. Jovalekić, A. Recnik, V.N. Ivanovski, M. Mitrić, M.J. Romčević, N. Paunović, B.Đ. Cekić, N.Ž. Romčević, Study of manganese ferrite powders prepared by a soft mechanochemical route. J. Alloy. Compd. **509**, 9977–9985 (2011)
10. M. Mohapatra, S. Anand, Int. J. Eng. Sci. Technol. **2**, 127–146 (2010). www.ijest-ng.com
11. A.R. Tanna, H.H. Joshi, Computer aided X-ray diffraction intensity analysis for spinels: hands-on computing experience. World Acad. Sci. Eng. Technol. **7**, 70–77 (2013)
12. W.H. Bragg, The structure of the spinel group of crystals. Phil. Mag. **30**, 305–315 (1915)
13. Q. Liu, L. Lv, J.P. Zhou, X.M. Chen, X.B. Bian, P. Liu, Influence of nickel-zinc ratio on microstructure, magnetic and dielectric properties of $Ni_{(1-x)}Zn_xFe_2O_4$ ferrites. J. Ceram. Process. Res. **13**, 110–116 (2012)
14. Z.Ž. Lazarević, A.N. Milutinović, Č.D. Jovalekić, V.N. Ivanovski, N. Daneu, I. Mađarević, N.Ž. Romčević, Spectroscopy investigation of nanostructured nickel-zinc ferrite obtained by mechanochemical synthesis. Mater. Res. Bull. **63**, 239–247 (2015)
15. E. Avvakumov, M. Senna, N. Kosova, *Soft mechanochemical synthesis: a basis for new chemical technologies* (Kluwer Academic Publishers, Boston, 2001)
16. Z.Ž. Lazarević, Č. Jovalekić, A. Rečnik, V.N. Ivanovski, A. Milutinović, M. Romčević, M.B. Pavlović, B. Cekić, N.Ž. Romčević, Preparation and characterization of spinel nickel ferrite obtained by the soft mechanochemically assisted synthesis. Mater. Res. Bull. **48**, 404–415 (2013)
17. R.A. Brand, *WinNormos Mössbauer fitting program* (Universität Duisburg-Essen, Germany, 2008)
18. L. Takacs, Self-sustaining reactions induced by ball milling. Prog. Mat. Sci. **47**, 355–414 (2002)
19. P. Baláž, M. Achimovičová, M. Baláž, P. Billik, Z. Cherkezova-Zheleva, J. Manuel Criado, F. Delogu, E. Dutková, E. Gaffet, F. José Gotor, R. Kumar, I. Mitov, T. Rojac, M. Senna, A. Streletskii, K. Wieczorek-Ciurowa, Chem. Soc. Rev. **42**, 7571–7637 (2013)
20. V.V. Boldyrev, Mechanochemistry and mechanical activation of solids. Russ. Chem. Rev. **75**, 177–189 (2006)
21. V.G. Ivanov, M.V. Abrashev, M.N. Iliev, M.M. Gospodinov, J. Meen, M.I. Aroyo, Short-range B-site ordering in the inverse spinel ferrite $NiFe_2O_4$. Phys. Rev. B **82**, 024104 (2010)
22. Z.Ž. Lazarević, Č. Jovalekić, A. Milutinović, D. Sekulić, V.N. Ivanovski, A. Rečnik, B. Cekić, N.Ž. Romčević, Nanodimensional spinel $NiFe_2O_4$ and $ZnFe_2O_4$ ferrites prepared by soft mechanochemical synthesis. J. Appl. Phys. **113**, 187221 (2013)
23. Z.Ž. Lazarević, Č. Jovalekić, A. Milutinović, D. Sekulić, M. Romčević, M. Slankamenac, N. Romčević, Spectroscopy investigation of nanostructured zinc ferrite obtained by mechanochemical synthesis. Optoelectron. Adv. Mat. **7**, 720–725 (2013)
24. Z.Ž. Lazarević, Č. Jovalekić, A. Milutinović, D. Sekulić, M. Slankamenac, M. Romčević, N.Ž. Romčević, Study of $NiFe_2O_4$ and $ZnFe_2O_4$ spinel ferrites prepared by soft mechanochemical synthesis. Ferroelectrics **448**, 1–11 (2013)
25. Z.W. Wang, P. Lazor, S.K. Saxena, G. Artioli, High-pressure Raman spectroscopic study of spinel ($ZnCr_2O_4$). J. Solid State Chem. **165**, 165–170 (2002)

26. M. Maletin, E.G. Moshopoulou, A.G. Kontos, E. Devlin, A. Delimitis, V.T. Zaspalis, L. Nalbandian, V.V. Srdić, Synthesis and structural characterization of In-doped $ZnFe_2O_4$ nanoparticles. J. Eur. Ceram. Soc. **27**, 4391–4394 (2007)
27. A. Milutinović, Z.Ž. Lazarević, Č. Jovalekić, I. Kuryliszyn-Kudelska, M. Romčević, S. Kostic, N.Ž. Romčević, The cation inversion and magnetization in nanopowder zinc ferrite obtained by soft mechanochemical processing. Mat. Res. Bull. **48**, 4759–4768 (2013)
28. O.N. Shebanova, P. Lazor, Raman study of magnetite (Fe_3O_4): laser-induced thermal effects and oxidation. J. Raman Spectrosc. **34**, 845–852 (2003)
29. A. Ahlawat, V.G. Sathe, Raman study of $NiFe_2O_4$ nanoparticles, bulk and films: effect of laser power. J. Raman Spectrosc. **42**, 1087–1094 (2011)
30. Ž. Cvejić, S. Rakić, A. Kremenović, B. Antić, Č. Jovalekić, P. Colomban, Nanosize ferrites obtained by ball milling: crystal structure, cation distribution, size-strain analysis and Raman investigations. Solid State Sci. **8**, 908–915 (2006)
31. M. Menzel, V. Šepelák, K.D. Becker, Mechanochemical reduction of nickel ferrite. Solid State Ionics **141–142**, 663–669 (2001)
32. S. Morup, Magnetic hyperfine splitting in Mössbauer spectra of microcrystals. J. Magn. Magn. Mater. **37**, 39–50 (1983)
33. N.N. Greenwood, T.C. Gibb, *Mössbauer spectroscopy* (Chapman and Hall Ltd, London, 1971)
34. J.M.D. Coey, P.W. Readman, Characterisation and magnetic properties of natural ferric gel. Earth Planet. Sci. Lett. **21**, 45–51 (1973)
35. E. Murad, U. Schwertmann, The Mössbauer spectrum of ferrihydrite and its relations to those of other iron oxides. Am. Mineral. **65**, 1044–1049 (1980)
36. V. Šepelák, D. Baabe, K.D. Becker, Mechanically induced cation redistribution and spin canting in nickel ferrite. J. Mater. Synth. Process. **8**, 333–337 (2000)
37. G.A. Sawatzky, F. Van der Woude, A.H. Morrish, Mössbauer study of several ferrimagnetic spinels. Phys. Rev. **187**, 747–757 (1969)

Structural Properties of Cu-Se-$CuSe_2$ Thin Films

M. Gilić, M. Petrović, B. Hadžić, M. Romčević, J. Trajić, N. Romčević and Z. Lazarević

Abstract This paper describes the structural and optical properties of Cu-Se-$CuSe_2$ thin films. The surface morphology of thin films was investigated by atomic force microscopy (AFM) and scanning electron microscopy (SEM). Formation of thin films is concluded to proceed unevenly, in the form of islands which later grew into agglomerates. The structural characterization of Cu-Se-$CuSe_2$ thin film was investigated using X-ray diffraction pattern (XRD). The presence of two-phase system is observed. One is the solid solution of Cu in Se and the other is low-pressure modification of $CuSe_2$. The Raman spectroscopy was used to identify and quantify the individual phases present in the films. Red shift and asymmetry of Raman mode characteristic for $CuSe_2$ enable us to estimate nanocrystal dimension. In the analysis of the far-infrared reflection spectra, numerical model for calculating the reflectivity coefficient of layered system, which includes film with nanocrystallite inclusions (modeled by Maxwell–Garnet approximation) and substrate, has been applied. UV–VIS spectroscopy and photoluminescence spectroscopy are employed to estimate direct and indirect band gap of $CuSe_2$.

M. Gilić (✉) · M. Petrović · B. Hadžić · M. Romčević · J. Trajić · N. Romčević · Z. Lazarević
Institute of Physics, University of Belgrade, Belgrade, Serbia
e-mail: martina@ipb.ac.rs

M. Petrović
e-mail: milicap@ipb.ac.rs

B. Hadžić
e-mail: branka@ipb.ac.rs

M. Romčević
e-mail: romcevic@ipb.ac.rs

J. Trajić
e-mail: jelena.trajic@ipb.ac.rs

N. Romčević
e-mail: romcevi@ipb.ac.rs

Z. Lazarević
e-mail: zorica.lazarevic@ipb.ac.rs

B. Lee et al. (eds.), *Proceedings of the IV Advanced Ceramics and Applications Conference*, DOI 10.2991/978-94-6239-213-7_18

Keywords Thin films · Optical properties · Spectroscopy · Maxwell–Garnett mixing model

1 Introduction

Nanostructures—either thin films, nanorods, nanotubes or quantum dots—have received growing interest as a result of their fascinating properties and applications that are superior to their bulk counter parts. Materials of nanoscopic dimensions have received rapid advance and widespread interest in the last decade [1–6]. As for copper selenides, they are metal chalcogenide semiconductors that exist in many phases and crystallographic forms: different stoichiometric such as CuSe (mineral klockmannite), Cu_2Se, $CuSe_2$ (mineral marcasite), Cu_3Se_2 (mineral umangite), Cu_5Se_4 (mineral athabaskite), Cu_7Se_4 as well as in non-stoichiometric form as $Cu_{2-x}Se$ (mineral berzelianite) and can be constructed into several crystallographic forms (monoclinic, cubic, tetragonal, orthorhombic, hexagonal, etc.). The phase diagram of copper–selenium system [7] shows us that the thermal stability of these compounds is highly dependent on the stoichiometric form.

Cu-Se thin films are *p*-type semitransparent highly conducting semiconductors [8, 9] that found numerous applications in devices such as thin film solar cells, photodetectors, superionic materials, optical filters [10, 11]. Moreover, $CuSe_2$ is superconductor at low temperatures with a transition temperature $T_C \sim 2.4$ K [12]. $CuSe_2$ is reported to be weak ferromagnetic below 31 K [13, 14] implying the possible coexistence of ferromagnetism and superconductivity in this compound.

The optical and electrical properties of copper selenide films depend on the used fabrication method due to compositional complexity of this compound, and possible phase transitions. Numerous methods have been reported for the deposition of these films of different crystalline modifications and varying stoichiometry. These methods can be primarily categorized in two processes. One is solution-based process: chemical bath deposition [9, 15], solution growth [8], hydrothermal method [16], etc. Another one is vacuum based process: vacuum evaporation techniques [17–20].

This paper reports optical and structural characterization of Cu-Se-$CuSe_2$ thin films of three different thicknesses. These films are obtained by rather simple and low-cost vacuum evaporation technique, using Mo boat onto glass substrate at room temperature. Characterization was performed using XRD, SEM, Raman, far-infrared reflection, UV–VIS and photoluminescence measurements. The structure of the obtained films is discussed on the basis of XRD data along with SEM measurements. The above properties have been reviewed with respect to the results of the Raman and far-infrared spectroscopy. Optical properties i.e. band gap determination was done with help of UV–VIS and photoluminescence measurements.

2 Samples Preparation

Thin films were obtained by evaporating commercially high purity CuSe powder (99.99 %) bought at Aldrich. The powder was deposited onto a highly pre-cleaned glass substrates with use of Mo boat. The procedure was done in a high—vacuum environment with typical background pressures of 3 mPa. The deposition rate, 10 nm/s, was monitored by quartz crystal thickness monitor—FTM4, Edwards. The final thicknesses of the films were found to be 56 nm (film1), 79 nm (film2) and 172 nm (film3).

3 Results and Discussion

3.1 Scanning Electron Microscopy

Scanning electron microscopy (SEM) images were obtained for Cu-Se-$CuSe_2$ thin films deposited on glass substrate in order to study the surface morphology and agglomeration of the samples. SEM imaging was done using scanning electron microscope equipped with a high brightness Schottky Field Emission gun (FEGSEM, TESCAN) operating at 4 kV. The samples were coated with gold/palladium to make them conductive.

Top view and tilted micrographs of thin films are presented in Fig. 1. From top view micrographs we may observe that the surface of our samples is relatively uneven and rather rough, with presence of cracks and voids. Formation of thin films is concluded to proceed unevenly, in the form of islands which later grew into agglomerates. Agglomerated clusters of few hundreds nanometers in diameter are distributed non-uniformly along the surface. In order to obtain the film thicknesses, the samples are tilted at 30°. The estimated thicknesses are: $\sim$56 nm for film1, $\sim$78 nm for film2 and $\sim$171 nm for film3. The thickness values estimated by SEM analysis match the ones obtained during the preparation of thin films.

3.2 XRD

The structural characterization of thin film was investigated by using X-ray diffraction pattern. X-ray diffraction measurements were performed on a Philips 1050 X-ray powder diffractometer using a Ni-filtered CuK_α radiation and Bragg-Brentano focusing geometry. The patterns were taken in the 10–80° 2θ range with step of 0.05° and exposure time of 6 s per step.

X-ray diffraction patterns of our samples are presented in Fig. 2. There is wide diffraction structure in region 20–40° characteristic for nanocrystal materials. Good defined peaks are signs of crystal structure formation.

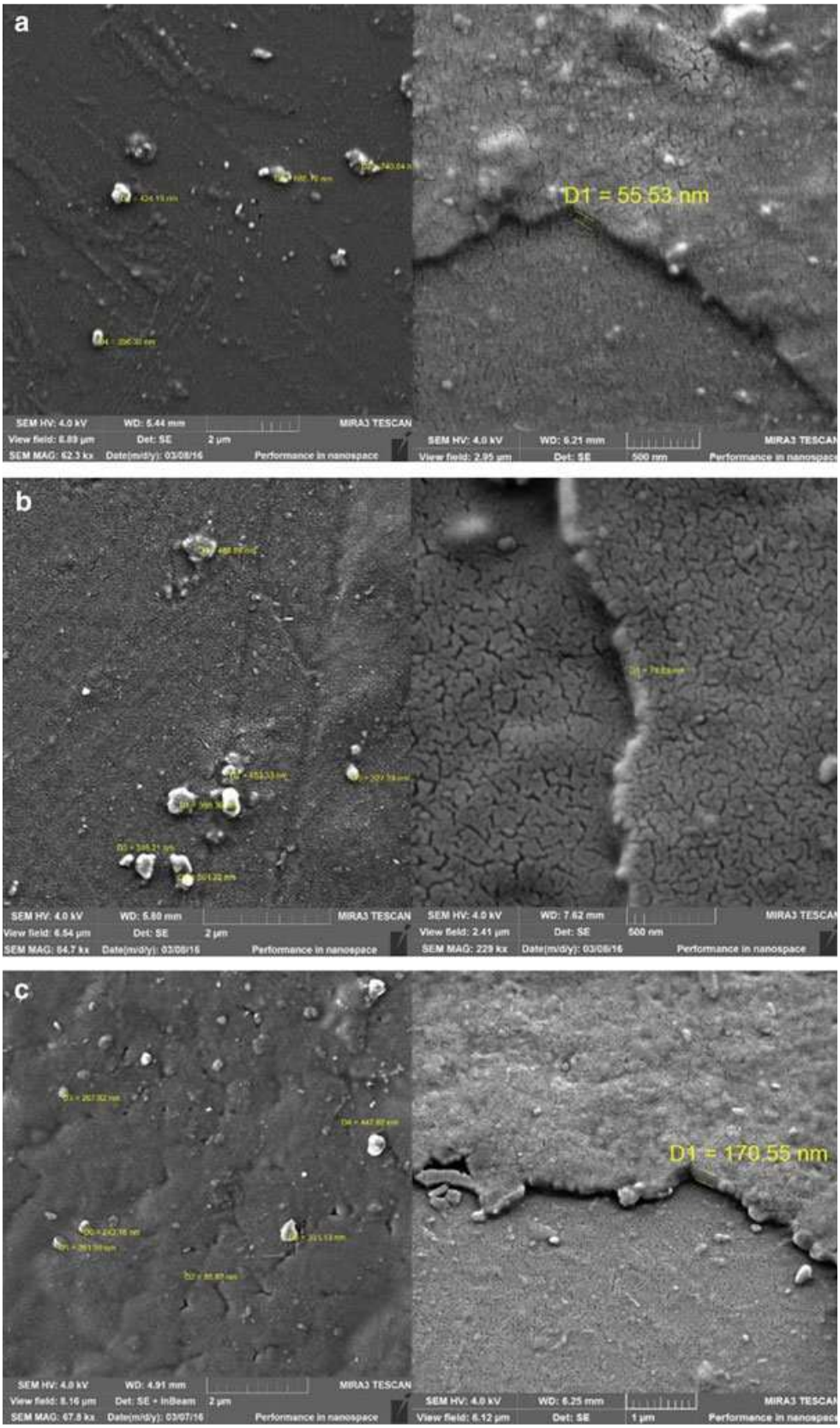

Fig. 1 Top view and tilted micrographs of **a** film1, **b** film2, **c** film3 at room temperature using SEM

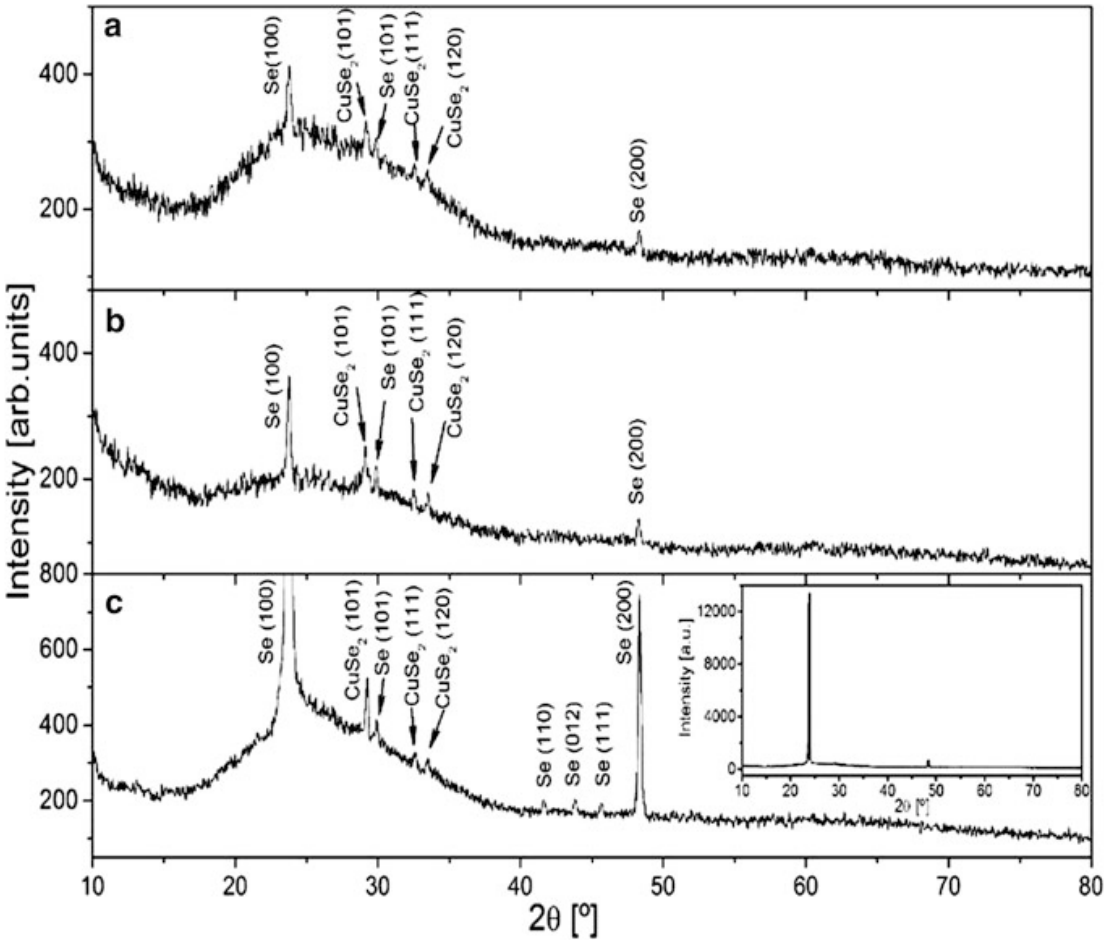

Fig. 2 XRD spectra of **a** film1 **b** film2 and **c** film3; inset: full intensity spectrum of film3

Reflections are clearly seen at Bragg angles (2θ) of about 24°, 29°, 30°, 32.6°, 33.4°, 42°*, 44°*, 46°* and 48.5°. Reflections at angles with asterisk are noticed only for the sample film3. The inset in Fig. 2c presents the full intensity spectrum of film3. The intensities of peaks that rise up with film thickness are signs of the crystal growth. The structural phase analysis was performed on the obtained diffractograms by using EVA 9.0 computing program. It has been observed that the two-phase samples are obtained. Two crystal structures were identified. More prominent one is hexagonal selenium and less prominent is orthorhombic marcasite structure of $CuSe_2$.

The dominant phase is solid solution of Cu in Se. Namely, according to phase diagrams in works of Chakrabarti and Laughlin [21] and Heyding [7], selenium and copper make solid solution even at 67 % of Se. Selenium, the solvent, has hexagonal structure [22] which is by no means the only stable phase of Se under normal conditions of temperature and pressure, with $Z = 3$ atoms per unit cell.

Selenium atoms are arranged in helical chains which are oriented along the *c*-axis of the hexagonal elementary cell (Fig. 3a). One chain is always surrounded by six chains in corners of a hexagon to yield the 3D structure (Fig. 3b). The bonding of atoms within a given chain is covalent where as the bonding between neighboring chains is by weaker Van der Waals forces. Reflections at 24° (100), 30° (101), 42°* (110), 44°*(012), 46°*(111) and 48.5° (200) are attributed to this phase.

The second one is low-pressure modification of $CuSe_2$, with Bragg reflections at 29° (101), 32.6° (111) and 33.4° (120) [PDF-2 74-0280]. This modification of $CuSe_2$ has the orthorhombic marcasite structure with $Z = 2$ formula units per unit cell [23], Fig. 4. In this structure each Cu atom is surrounded by six Se atoms in a distorted octahedral arrangement, in plane by 4Se with Cu-Se distance 2.62 Å and out of plane by two more Se neighbors with Cu-Se distance 2.60 Å. These octahedra are corner-sharing in the (*ab*) plane and edge-sharing along *c* axis. Each Se atom is in a distorted tetrahedral configuration, surrounded by three Cu neighbors and one *Se* neighbor (*Se-Se* distance 2.29 Å).

Small intensity of Bragg reflections characteristic for $CuSe_2$ indicates small amount of $CuSe_2$, probably in a form of crystallites of very small dimension. The absence of great number of peaks characteristic for the diffractograms of these phases indicates there is no random distribution of crystallites, but the preferentially oriented structures—which indeed was expected for thin films.

3.3 *Raman Spectroscopy*

The micro-Raman spectra were taken in the backscattering configuration and analyzed by Jobin–Yvon T64000 spectrometer, equipped with nitrogen cooled charged-coupled-device detector. As an excitation source we used the 532 nm line

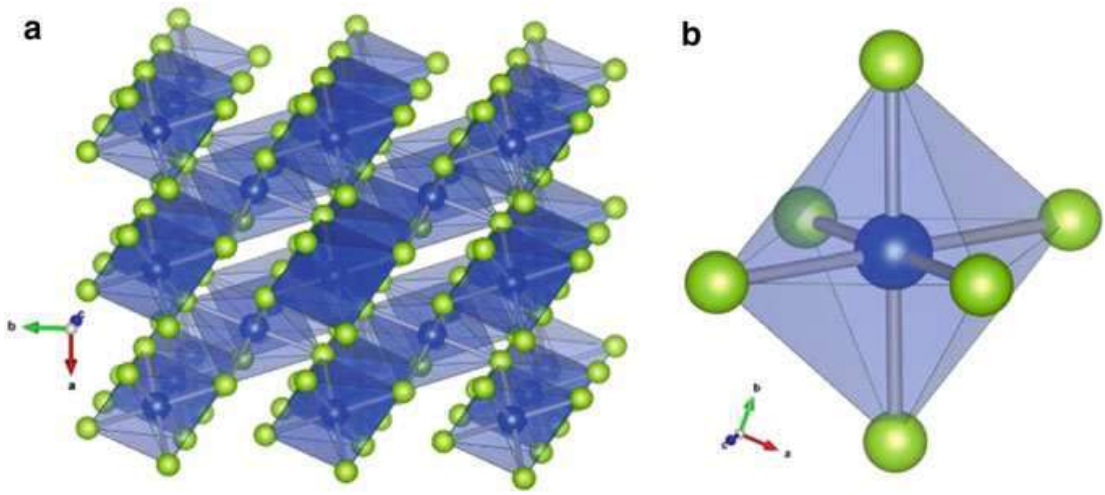

Fig. 3 Crystal structure of hexagonal Se; **a** atoms oriented along *c*-axis; **b** one chain surrounded by six nearest-neighbor helices

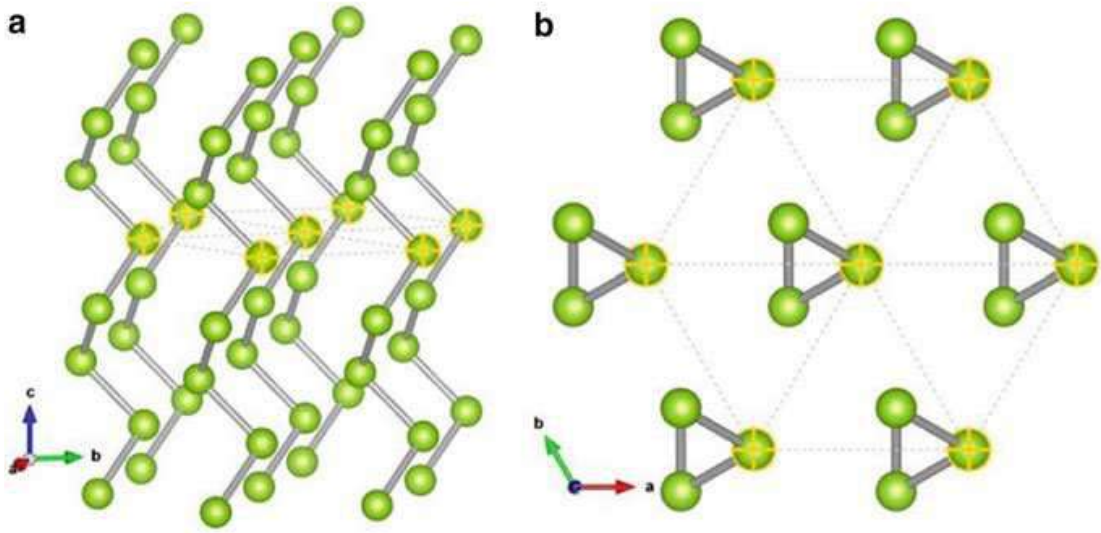

Fig. 4 Crystal structure of orthorhombic $CuSe_2$; *blue spheres*—copper ions, *green spheres*—selenium ions; **a** 2 × 2 × 2 unit cells—coordination polihedra around Cu^{2+} ions; **b** one separated coordination polyhedron around Cu^{2+} ion

of Ti: Sapphire laser, with laser power 20 mW. The measurements were performed in the spectrum range 100–400 cm^{-1}.

The Raman spectra of Cu-Se-$CuSe_2$ thin films of different thickness are shown in Fig. 5. Experimental Raman scattering spectra (presented as open dots) are analyzed by the deconvolution to Lorentzian curves. The dominant structure is in region 230–240 cm^{-1}. Ten modes can be reconstructed.

Eight modes (thick green lines on Fig. 5a) are recognized as fundamental and second order modes of hexagonal selenium and listed in Table 1. Factor-group analysis predicts three fundamental Raman active modes. The dominant structure is mainly formed of two fundamental selenium modes of close energy that are assigned as E^2 ($\sim$232 cm^{-1}) and A_1 ($\sim$236 cm^{-1}) modes of hexagonal Se structure. Mode at $\sim$143 cm^{-1} is identified as E^1 mode. Low intense mode at $\sim$105 cm^{-1} is identified as A_2 mode. This fundamental mode is IR active and Raman forbidden. This mode was already registered in hexagonal Se Raman spectra [24]. Wide structures of small intensity at $\sim$185, $\sim$208, $\sim$287 and $\sim$354 cm^{-1} are assigned as second order modes and listed in Table 1, as in [24].

Two modes of low intensity, denoted with blue lines in Fig. 5, are in spectral region close to dominant selenium fundamental modes. These two lines i.e. Raman active modes are associated to $CuSe_2$. The more intense one is at $\sim$255, $\sim$252 and $\sim$251 cm^{-1} for samples film1, film2 and film3 respectively. In Raman spectra of marcasite type $CuSe_2$ one expects dominant scattering structure centered at $\sim$260 cm^{-1} mostly from A_g^1 stretching mode activity. A_g^1 phonon branch goes down in all directions in Brillouin zone (BZ). In the case of very small particles i.e. nanoparticles, effects of confinement is to push A_g^1 mode to lower frequencies. In nanocrystals optical modes are confined, bulk selection rules are ruined, high surface to volume ratio increases the role of surface properties, but there is

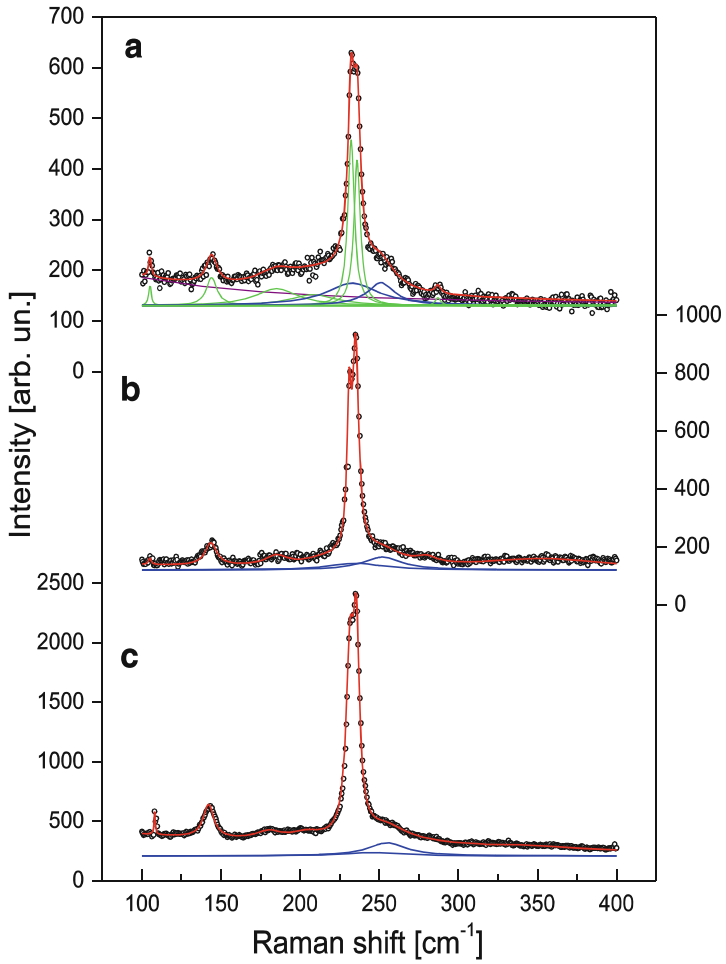

Fig. 5 Raman spectra of Cu-Se-$CuSe_2$ thin films of different thicknesses: **a** film1; **b** film2; **c** film3

Table 1 Position of registered Raman (infrared) active modes (cm^{-1}) of hexagonal Se

Film1	Film2	Film3	[24]	Assignment
Fundamental modes				
105 (105)	105 (105)	108 (105)	102	A_2 (IR)
144 (152)	143.5 (–)	142.6 (–)	143	E^1 (Raman, IR)
232 (230)	232 (230)	232 (230)	233	E^2 (Raman, IR)
236	236	236	237	A_1 (Raman)
Second order modes				
185	185	183	183	–
208 (200)	208 (200)	206 (205)	206	$2A_2$ (IR)
287 (272)	280 (280)	273 (270)	273	$2E^1$ (Raman, IR)
345 (350)	345 (358)	345 (358)	345	–

fundamental track of bulk properties. As A_g^1 dispersion relation decreases in all directions in BZ, we expect the frequencies of confined mode to be below 260 cm^{-1}. Analysis of the Raman spectra presented in Fig. 5 concerns to the spectral region below 260 cm^{-1} (ω_{Ag}^1).

A continuum model of the optical phonon confinement in nanocrystal is used. Parameters were transferred from the bulk phonon dispersion curves. It is limited to nanoparticles of regular shape. Although this is not the case in real nano-crystallites, we present results of calculation for ideal spherical $CuSe_2$ nanocrystals. One small spherical $CuSe_2$ crystal, isotropic and homogeneous inside, is considered. This consideration of confined optical vibrations in nanocrystals is based on macroscopic equation for the relative displacement of the positive and negative ions [25, 26]. This equation is solved in spherical coordinates. The spherically symmetric solutions of equation must belong to the irreducible representations of the three-dimensional rotation-inversion group $O(3)$ labeled as D_l^g (even) and D_l^u (odd upon inversion). Raman transition operator for allowed scattering belongs to D_0^g and D_2^g [27]. Frequencies of the spherical ($l = 0$) and spheroidal quadrupolar modes ($l = 2$) can be calculated and generally observed by resonant Raman scattering.

If we assume, as in [28, 29], that at the surface of the sphere all components of displacement are almost zero, the electrostatic potential and the normal component of the electric displacement are continuous. Then one can obtain frequencies of the Raman active modes ($l = 0$ and $l = 2$, $n = 1, 2, 3, \ldots$), l and n being the spherical quantum numbers. The most important contribution to one-phonon Raman scattering corresponds to $l = 0$. This mode is excited for parallel polarizations of the incident and scattered light. The corresponding frequencies are:

$$\omega_n^2 = \omega_o^2 - \beta\left(\frac{\mu_n}{r}\right)^2 \tag{1}$$

ω_0 is the optical bulk frequency i.e. $\omega_0 = 260\ \mathrm{cm}^{-1}$ in $CuSe_2$, r is the radius of the sphere, μ_n is the nth node of the Bessel spherical function j_1 ($\mu_1 < \mu_2 < \mu_3 < \ldots$). Frequency shift (difference between ω_n and ω_0) for fixed r depends on $\beta \cdot \beta_1 = 1.5\ 10^3$ m/s for bulk $CuSe_2$. ω_n increases as the radius of the dot (r) increases, and in the limit: $r \to \infty$ frequencies ω_n converge to ω_0. Figure 6 presents the optical vibration modes frequencies dependence ($l = 0$, $n = 1, 2, 3$) on the radius of $CuSe_2$ nanocrystals. The smaller the radius the lower is the frequency of confined mode. As for intensity, this model predicts the most intensive peak in Raman spectra to be the mode ω_n ($n = 1$).

Exact positions of modes at $\sim$251, $\sim$252 and $\sim$255 cm^{-1} (Table 2 and Fig. 5), for three samples: film1, film2 and film3 respectively, are marked with stars in Fig. 6. These modes are tentatively assigned as $l = 0$, $n = 1$. It is evident that experimental values determine nanocrystals dimension. Modes at frequencies $\sim$233, $\sim$235 and $\sim$246 cm^{-1} (Table 2 and Fig. 5), for samples film1, film2 and film3 respectively, fall on the calculated curves. These modes are tentatively assigned as $l = 0$, $n = 2$. Nanocrystals dimension established by $l = 0$, $n = 1$ modes is definitely confirmed. Despite the situation that in reality there is nanocrystal size distribution, nanocrystal shape irregularity, inhomogeneity inside, Raman spectroscopy enable detection of average particle size as: $r \sim 3.3$ nm (film1), $r \sim 3.4$ nm (film2) and $r \sim 4.3$ nm (film3).

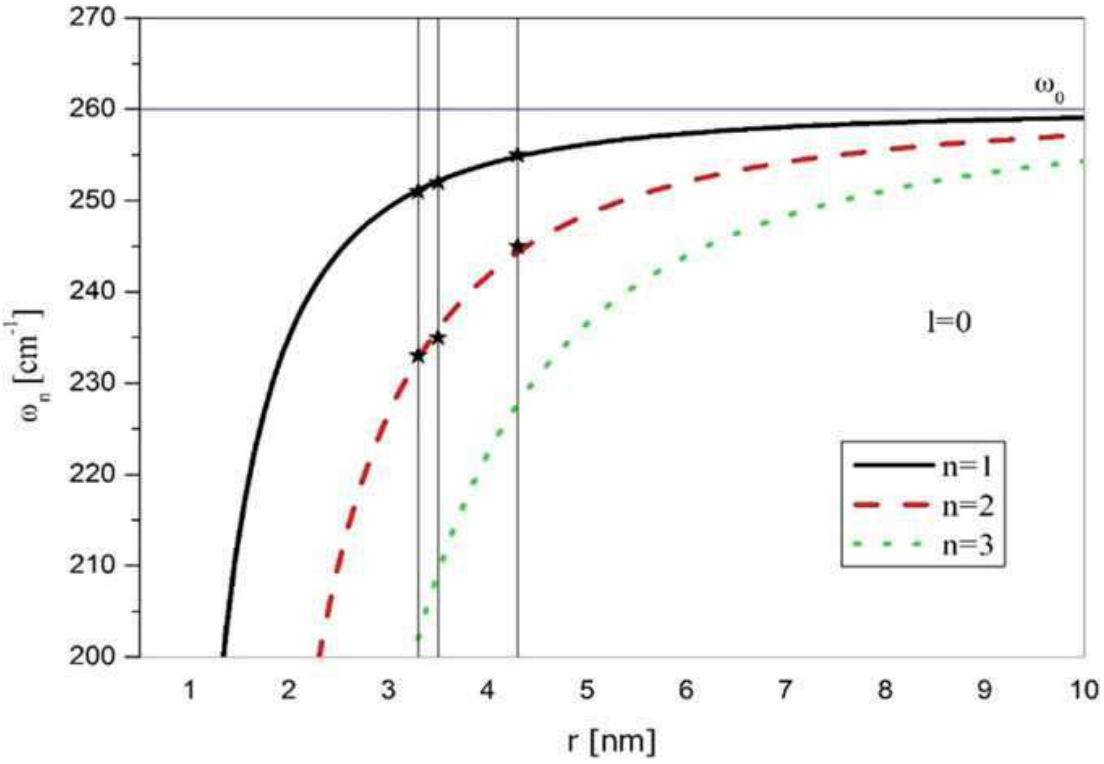

Fig. 6 The radial dependence of $l = 0$ optical modes for $CuSe_2$ spherical nanocrystals

Table 2 Position of registered Raman (IR) active modes (cm^{-1}) of marcasite $CuSe_2$

$l = 0$	Film1	Film2	Film3	[30, 31]	Assignment
$n = 1$	251 (251)	252 (252)	255 (255)	260	A_g^1
$n = 2$	233	235	243		

The mode originating from $CuSe_2$ is broadened and shifted toward lower frequencies in comparison to the bulk system [30, 31]. Shift toward lower frequencies is characteristic for modes of decreasing phonon dispersion relation in bulk. The results of Raman spectroscopy are in good agreement with XRD results. The presence of two crystal phases in synthesized film, the hexagonal Se and orthorhombic $CuSe_2$, is confirmed once again. Small amount of $CuSe_2$ evidenced by XRD is confirmed by low intensity of $CuSe_2$ modes.

3.4 *Far-Infrared Spectroscopy*

The far-infrared measurements were carried out with a BOMEM DA-8 FIR spectrometer. A DTGS pyroelectric detector was used to cover the wave number range from 90 to 600 cm^{-1}.

The penetration depth of the infrared electromagnetic waves into a nontransparent crystal is approximately 3 μm. Thickness of our films is from 56 to 172 nm, so reflectivity spectra contain information about films together with information about substrate. Three-layer structure is schematically presented in Fig. 7, where medium 1 is air with dielectric function ε_1 ($\varepsilon_1 = 1$), medium 2 is thin Se-$CuSe_2$ mixture layer with corresponding dielectric function ε_2 and medium 3 is glass substrate with dielectric function ε_3. In this case:

$$R_A = \frac{A_r}{A_i} = \frac{\mathbf{r}_{12}\mathrm{e}^{-i\alpha} + \mathbf{r}_{23}\mathrm{e}^{i\alpha}}{\mathrm{e}^{-i\alpha} + \mathbf{r}_{13}\mathbf{r}_{23}\mathrm{e}^{i\alpha}} \tag{2}$$

where A_i and A_r are amplitudes of incident and reflection beams, $r_{ij} = (n_i - n_j)/(n_i + n_j) = (\sqrt{\varepsilon_i} - \sqrt{\varepsilon_j})/(\sqrt{\varepsilon_i} + \sqrt{\varepsilon_j})$ are Fresnel coefficients, n_i is complex refractive index of corresponding medium, ε_i complex dielectric constant and $\alpha = 2\pi\omega d(\varepsilon_2)^{1/2}$ is the complex phase change related to the absorption in the medium 2 with the thickness d. The corresponding reflectance (R) is:

$$R = |R_A| \tag{3}$$

The dielectric function of homogeneous medium is:

$$\varepsilon(\omega) = \varepsilon_\infty \prod_{k=1}^{k=N} \frac{\omega_{LOk}^2 - \omega^2 + i\gamma_{LOk}\omega}{\omega_{TOk}^2 - \omega^2 + i\gamma_{TOk}\omega} \tag{4}$$

where ω_{TO} and ω_{LO} are the transversal and longitudinal optical vibrations, and γ_{TO} and γ_{LO} are damping parameters.

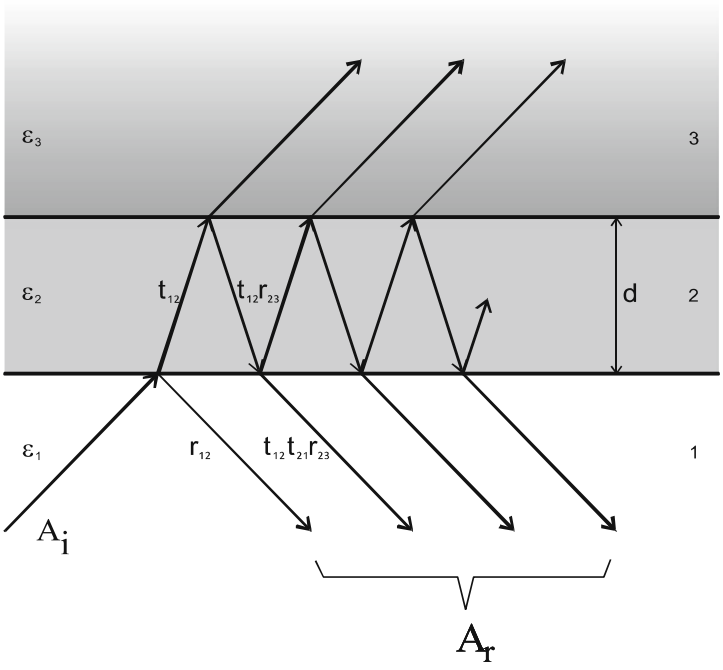

Fig. 7 Schematic presentation of a three-layer structure

The Se-$CuSe_2$ thin films we threat as a mixture of uniformly distributed spherical inclusions of $CuSe_2$ in homogeneous Se. Namely, when visible light interacts with semiconducting nanoparticles (characteristic size L, dielectric function ε'') which are distributed in a medium with the dielectric constant ε', the heterogeneous composite can be treated as a homogeneous medium, and so-called effective medium theory applies.

There are many mixing models for the effective dielectric permittivity of such a mixture [32]. XRD and Raman measurements imply that the structure of our films can be treated as Se film with separated nanocrystals of $CuSe_2$ inside. We decided to use Maxwell–Garnet model for present case, as we did in our previous works [3, 33–36]. For the spherical inclusions case, the prediction of the effective permittivity of mixture ε_{eff} according to the Maxwell–Garnet mixing rule reads [37, 38]:

$$\varepsilon_2 = \varepsilon_{eff} = \varepsilon' + 3f\varepsilon' \frac{\varepsilon'' - \varepsilon'}{\varepsilon'' + 2\varepsilon' - f(\varepsilon' - \varepsilon'')} \tag{5}$$

Here, spheres of permittivity ε'' are located randomly in homogeneous environment of permittivity ε'. Spheres of permittivity ε'' occupy a volume fraction f. ε' and ε'' are also in form of Eq. (4).

The far-infrared reflection spectra of Se-$CuSe_2$ thin films mixture on glass are presented in Fig. 8. Film thickness increases from the bottom to the top of the Figure. Experimental data are presented by circles, while the solid lines are calculated spectra obtained by a fitting procedure based on the previously presented model.

The far-infrared reflectivity spectrum of the glass substrate is shown in Fig. 8 (bottom). The calculated spectrum, presented by solid line, was obtained using the dielectric function given by Eq. (4). As a result of the best fit we obtained two modes (N = 2). Frequencies of these two modes are $\omega_{TO1} = 438\ \text{cm}^{-1}$, $\omega_{LO1} = 439\ \text{cm}^{-1}$ and $\omega_{TO2} = 471\ \text{cm}^{-1}$, $\omega_{LO2} = 523\ \text{cm}^{-1}$. Frequency values of these modes have remained the same during the fitting procedure for all thin film samples. As the thickness of the film increases, these substrate reflectivity structures become weaker. As concerns fitting procedure, this weakening is the consequence of increasing the film thickness d.

As we know, there are three infra-red active modes: A_2, E^1 and E^2. We assumed permittivity of Se ε' in form given by Eq. (4) at positions $\omega_{A2} \sim 105\ \text{cm}^{-1}$, $\omega_{E1} \sim 152\ \text{cm}^{-1}$ and $\omega_{E2} \sim 230\ \text{cm}^{-1}$ (N = 3). To achieve coinciding with the experimental spectra, we modeled, permittivity of $CuSe_2$ ε'' in form given by Eq. (4) (N = 1) at positions 250–255 cm^{-1}. Volume fraction f is of the order of few percentages. Effective permittivity of film is $\varepsilon_2 = \varepsilon_{\text{eff}}$ given by Eq. (5). Additional parameter is the thickness d of the film. Reflectance of the whole structure was calculated by using Eqs. (2) and (3). The best fitting parameters are listed in Tables 1 and 2.

FIR reflectivity measurements are in accordance with the XRD and Raman spectroscopy results. Synthesized films are thin and $CuSe_2$ particles are small. There is certain roughness of the sample surface, and that is why the most phonon

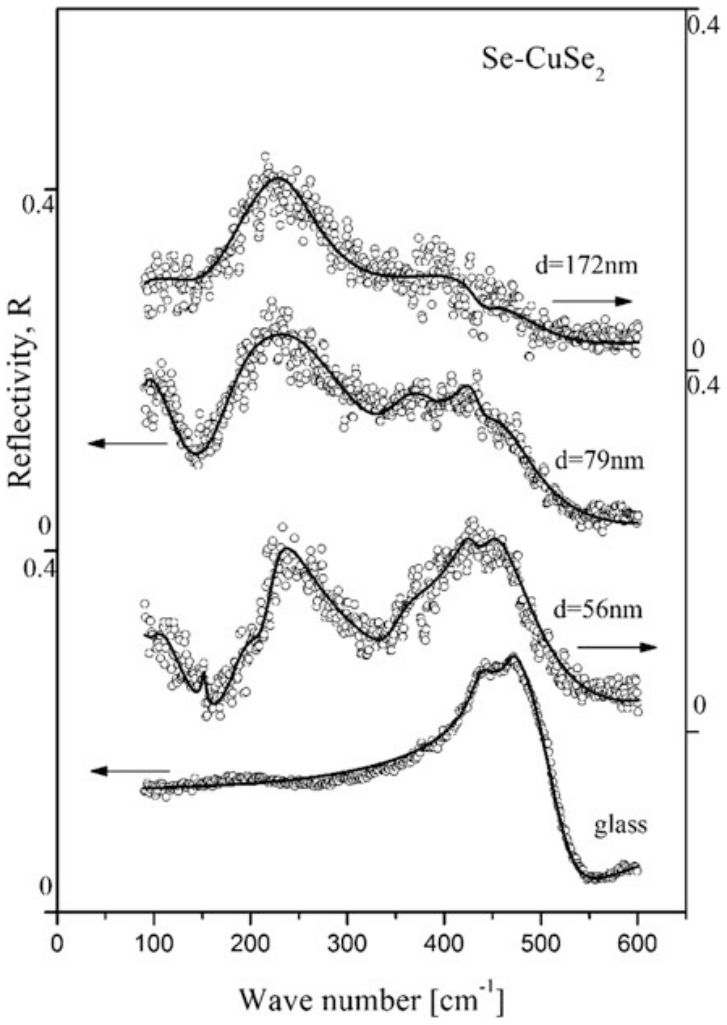

Fig. 8 Far-infrared reflectivity spectra of Se-$CuSe_2$ thin films mixture on glass substrate. Reflectivity spectra from the *bottom* to the *top*: glass substrate; film1; film2; film3

structures in FIR reflectivity spectra are wide and of low intensity. In the central region, 200–300 cm^{-1}, the modes overlap each the other. As a result there is wide and complex structure in this spectral region. Low reflectivity level and high noise compared to it, results in the shape of experimental spectra presented in Fig. 8. Phonon characteristics are practically transferred from Raman measurements. After careful and demanding fitting procedure we achieved that calculated FIR reflectivity spectra reproduce experimental results completely. FIR results, in this case, are used as kind of control and confirmation of samples structure established by XRD and Raman spectroscopy.

3.5 UV–VIS Spectroscopy

The UV–VIS diffusion reflectance and transmittance spectra were recorded in the wavelength range of 300–1000 nm on a Shimadzu UV-2600 spectrophotometer

equipped with an integrated sphere. The diffuse reflectance and transmittance spectra were measured relative to a reference sample of $BaSO_4$.

In this study we used Tauc plot for the determination of optical band gap from diffuse reflectance measurements. The determination of band gap in semiconductors is significant for obtaining the basic solid state physics. The relation expression proposed by Tauc, Davis and Mott [39–41] is following:

$$\alpha h\nu = A(h\nu - E_g)^{1/n} \tag{6}$$

where h is a Planck's constant, A is the transition probability constant depending on the effective mass of the charge carriers in the material, E_g is the band gap, $h\nu$ is the photon energy and α is absorption coefficient which is defined as the relative rate of decrease in light intensity along its propagation path, i.e. a property of a material that defines the amount of light absorbed by it. The value of n denotes the nature of the transition. In case of direct transitions n equals 1/2 and 3/2 for allowed and forbidden transitions, respectively. As for indirect transitions, n equals 2 and 3 for allowed and forbidden transitions, respectively. Since $CuSe_2$ exhibits both direct and indirect allowed transitions, $n = 1/2$ and $n = 2$.

Then, the acquired diffuse reflectance spectra are converted to Kubelka–Munk function [42]:

$$\alpha = \frac{(1-R)^2}{2R} \tag{7}$$

So using this function, a plot of $(\alpha h\nu)^{1/n}$ against $h\nu$ is obtained. The energy band gap is determined by extrapolating the linear portion of $(\alpha h\nu)^{1/n}$ versus $h\nu$ to the energy axis at $(\alpha h\nu)^{1/n} = 0$. The intercept of these plots on the energy axis gives the energy band gap. Such plots are given in Fig. 9. Direct transitions (left part of Fig. 9) reveal band gap for both selenium and $CuSe_2$, while indirect transitions (right part of Fig. 9) reveal band gap for $CuSe_2$ only.

The experimentally determined values of energy gaps for $CuSe_2$ show slight decrease with film thickness and their values range from 2.75 to 2.72 eV for direct transitions, and from 1.75 to 1.71 eV in the case of indirect transitions. As for selenium, estimated band gaps follow the same trend with film thickness and range between 2.33 and 2.36 eV. The estimated band gap positions of each sample are given in Table 3. The difference in film thicknesses causes the small difference in band gaps in second decimal place and they follow the well-established trend—the smaller the thickness, the wider is the band gap. Also, their values are quite wider than the ones that can be found in literature.

References report a large range of energy band gap values for Cu-Se. For direct transitions that values usually go between 2 and 3 eV. Bari et al. [43] obtained the value of 2.51 eV for the sample thickness of 150 nm, and with the increase of film thickness they reported the decrease of band gap width. Grozdanov [44], Garcia et al. [15] and Sakr et al. [45] obtained the value of 2.33, 2.13–2.38 and 2.74 eV respectively. The latter is very similar to the results obtained in this paper. Rajesh

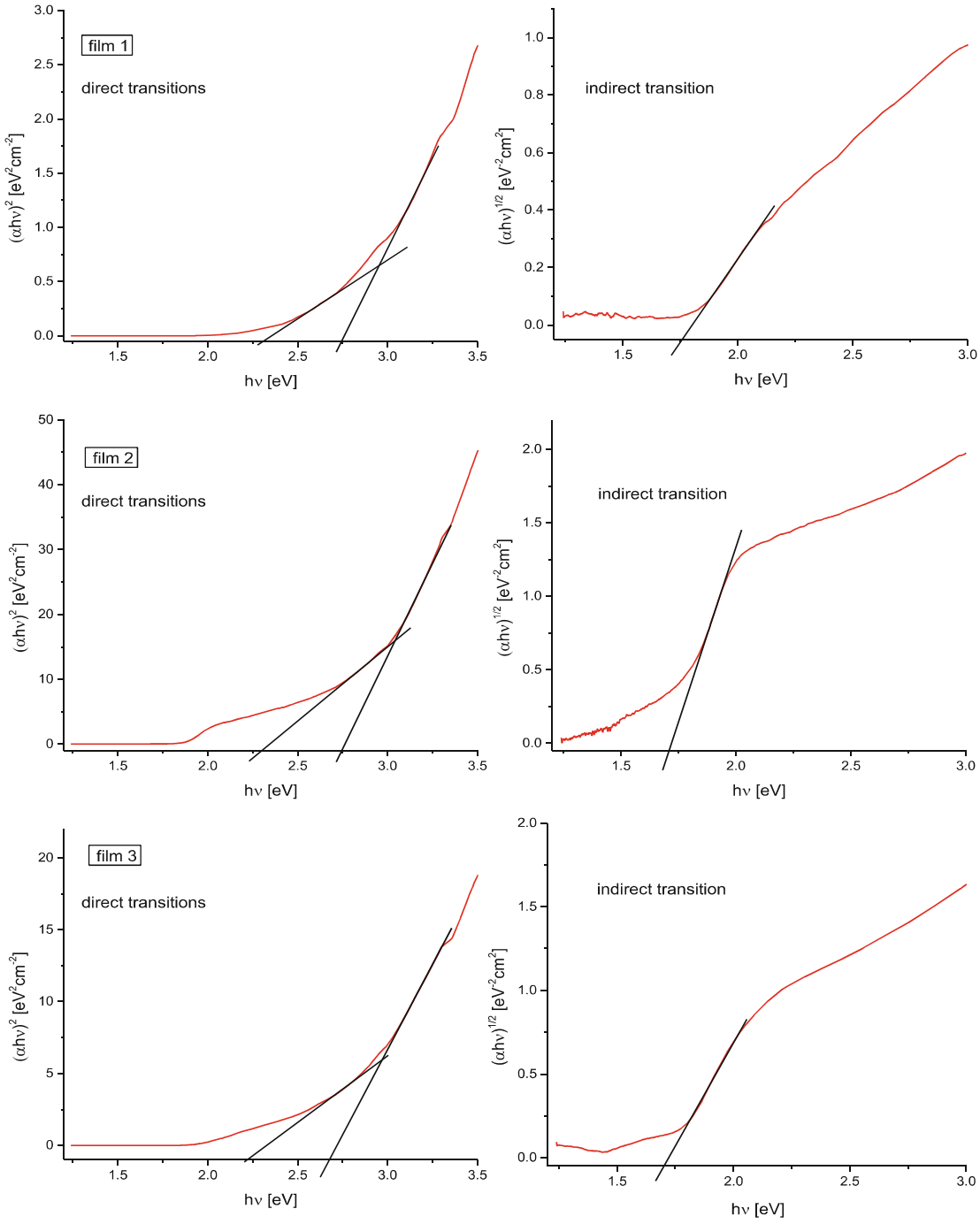

Fig. 9 Dependence of the $(\alpha h\nu)^2$ of the photon energy (hν)—*left side*, and dependence of the $(\alpha h\nu)^{1/2}$ of the photon energy (hν)—*right side*

Table 3 The estimated band gap energies of complex thin films

	Film1	Film2	Film3
$CuSe_2$ direct transition (eV)	2.75	2.74	2.72
$CuSe_2$ indirect transition (eV)	1.75	1.72	1.71
Se direct transition (eV)	2.36	2.34	2.33

et al. [46] got a diversity of band gaps ranging from 1.95 (the thickest film) to 3.70 eV (the thinnest film). As for indirect transitions, they received less attention. In [15] the obtained values are 1.22–1.34 eV, whereas in [47] the value is about 1.4 eV. The values we obtained, ∼1.7 eV, are wider than reported in literature. In our opinion, the larger indirect band gap values are due to quantum confinement effect [48, 49] where by the electrons are localized in individual crystallites.

As for selenium, the direct band gap is reported to be about 2 eV for the bulk [50, 51] and 2.20–2.06 for the thin films of thickness 130–290 nm [52]. Our films are thinner than the ones mentioned in the literature and it is not surprising that we obtained wider band gap values, about 2.3 eV.

3.6 Photoluminescence Spectroscopy

Photoluminescence measurements were obtained by Jobin–Yvon U1000 spectrometer, equipped with RCA-C31034A photomultiplier with housing cooled by Peltier element, amplifiers and counters. As an excitation source, the 488 nm laser line of Argon laser was used.

Photoluminescence spectra can be used for investigation the possible outcomes of photo-induced electrons and holes in a semiconductor, since photoluminescence emission results from the recombination of free charge carriers. A semiconductor is characterized with the electronic band structure and its main features—the valence band or the highest occupied molecular orbital (HOMO) and the conduction band or the lowest unoccupied molecular orbital (LUMO). The difference between the valence band and the conduction band in the means of energy is called band gap (*Eg*). We talk about two types of photoluminescence phenomenon according to its attributes and formation mechanism: the band-to-band photoluminescence and the excitonic photoluminescence [53]. The band-to-band PL spectrum regards the separation situation of photo-generated charge carriers. The excitonic PL spectrum, however, cannot directly reflect the separation situation of photo-induced carriers. If discrete energy levels are present in the band gap, these may dominate the optical spectrum. PL measurements then yield information about the energetic positions of the electronic states in the gap. Such localized states can originate from various types of imperfections like vacancies, interstitial atoms, atoms at surfaces and grain boundaries. However, it is often difficult to determine the exact position and origin of these states.

Photoluminescence spectra of Cu-Se-$CuSe_2$ thin films on various temperatures are presented in Fig. 11. At room temperature (Fig. 10) in all spectra, the band in red area at about 1.63 eV is clearly seen. According to the UV–VIS results (see previous chapter), we can attribute this mode to band-to-band transition for indirect transition in $CuSe_2$. In green area, a broad band is observed at 2.32 eV which originates from direct transitions in selenium (also see prev. chapter).

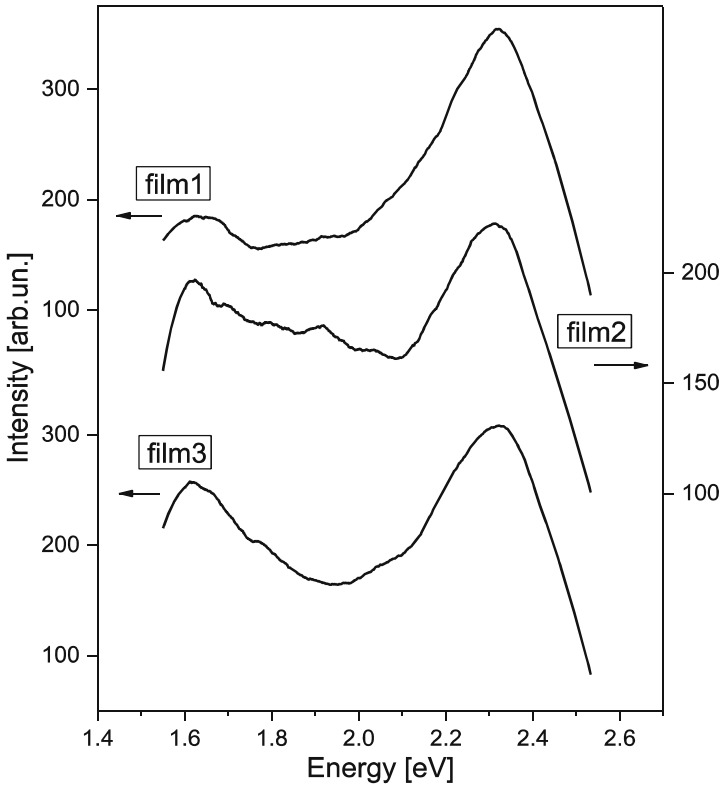

Fig. 10 Photoluminescence spectra of Cu-Se-$CuSe_2$ thin films at room temperature

At lower temperatures (Fig. 11a–c) there are several peaks in green, yellow and cyan areas of the spectra, which in our opinion belong to dislocation luminescence or defect luminescence. The mode at $\sim$1.8 eV is clearly seen. According to literature data [51] this band is attributed to selenium defect mode-negative U-center. This mode is expected to appear at 0.5 eV from the band edges. In all spectra, the uprise of peak intensity with lowering temperature is observed.

Temperature dependence of a PL emission bands is shown in Fig. 12. We observe blue shift with increasing temperature for all bands. Shrinking of the band gap with lowering temperature is observed.

A model is proposed by Shen et al. [54] to explain those discrepancies. It involves surface electron accumulation as a result of severe band bending in nanorods. However, the same trend is observed in thin film samples (including ours), whose curvature-less surface does not support a spatial charge separation such as in 1D nanostructures. Wei et al. [55] gave more exact explanation of this phenomenon in their work. They began the analysis by making difference between E_{PL} and E_g:

$$E_{PL}(n,T) = E_g(n,T) + E_{Fn}(n,T) - E_{Fp}(n,T) \tag{8}$$

where E_{Fn} and E_{Fp} are the electron and hole quasi-Fermi levels measured from bottom of conduction band and top of valence band, respectively. So the

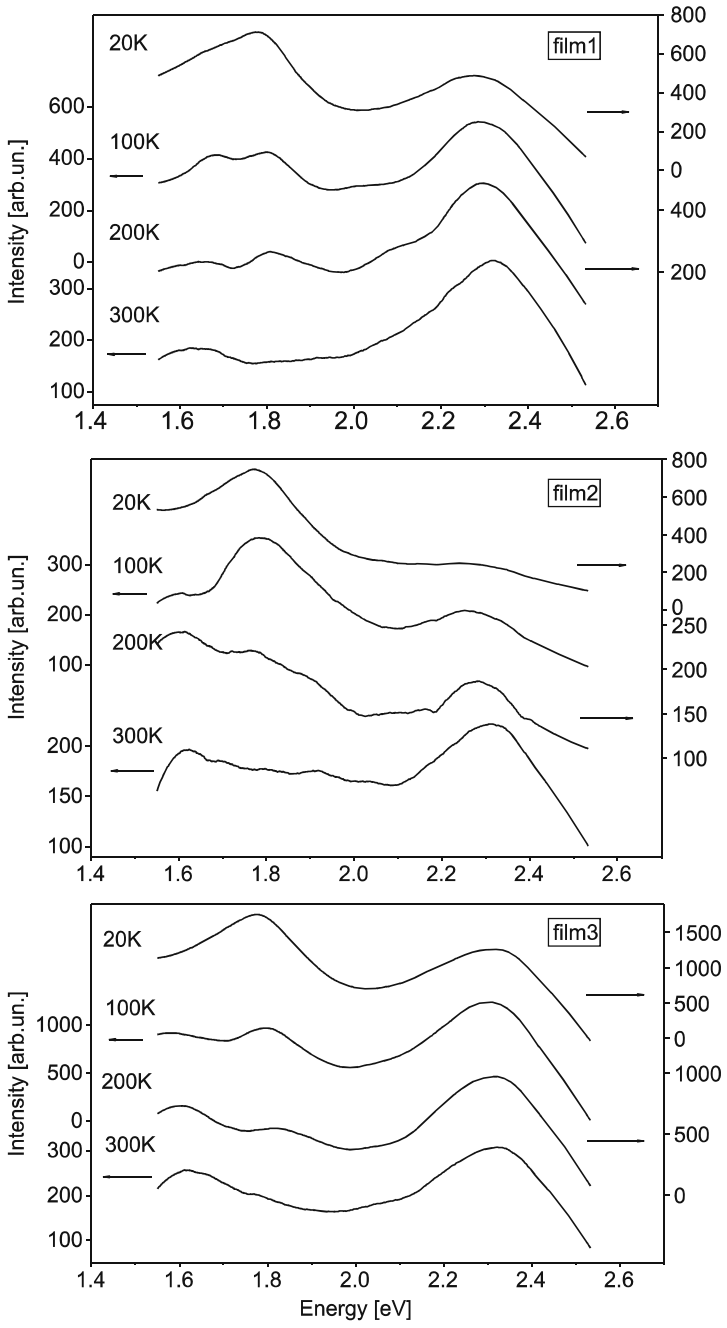

Fig. 11 Photoluminescence spectra of Cu-Se-$CuSe_2$ thin films at various temperatures: **a** film1, **b** film2, **c** film3

temperature dependence of the band gap shift is the competition between the lattice dilation dE_g/dT on one hand, and the sum $(dE_{Fn}/dT - dE_{Fp}/dT)$ on the other. The former results in conventional red shift of the band gap with increasing temperature, and the latter gets a blue shift. The resulting shift depends on the magnitude of these two contributions. Usually when the electron density n is high, the thermal response in the material is governed by electronic rather than photonic interactions, the sum $(dE_{Fn}/dT - dE_{Fp}/dT)$ becomes dominant thus the blue shift of E_{PL} is observed, as in our case.

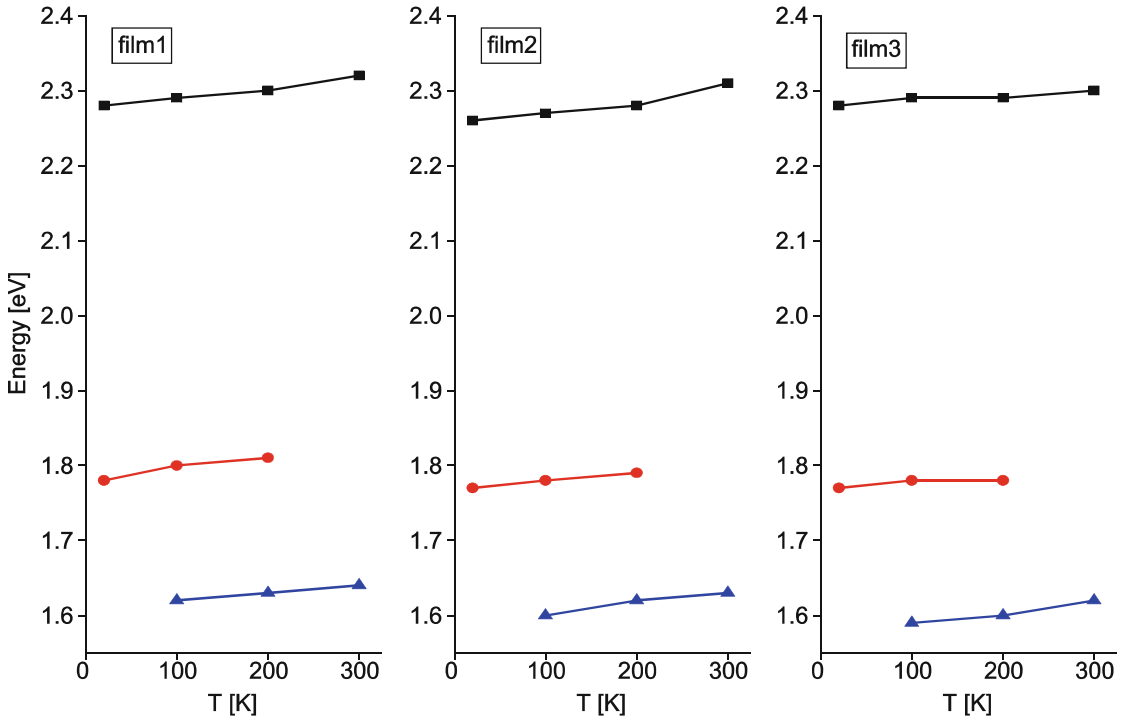

Fig. 12 Temperature dependence of photoluminescence emission bands

4 Conclusions

The optical and structural parameters have been studied for Cu-Se-$CuSe_2$ thin films. The surface morphology of thin films was investigated by AFM and SEM. X-ray diffraction results indicate that thin films have two phases, the solid solution of Cu in Se and the low-pressure modification of $CuSe_2$.

Raman active modes of hexagonal Se are clearly seen and assigned. We tentatively assign modes at 251–255 and 233–243 cm^{-1} as $l = 0$, $n = 1$ and $n = 2$ confined $CuSe_2$ A_g^1 mode. Although assumed model concerns to an ideal spherical nanocrystal, it works well in real samples where there is nanocrystal size distribution, shape irregularity, inside inhomogeneity. Raman spectroscopy enables detection of average particle size as: $r \sim 3.3$ nm (film1), $r \sim 3.4$ nm (film2) and $r \sim 4.3$ nm (film3). Infrared active modes of hexagonal Se that dominate in the reflectivity spectra are identified. Presence of $CuSe_2$ nanocrystals in predominantly Se film was modeled by effective medium theory. Calculated FIR reflectivity spectra reproduce completely experimental ones. FIR reflectivity results confirm the sample structure established by XRD and Raman spectroscopy.

UV–VIS reflectance measurements revealed values for both direct and indirect band gap in $CuSe_2$: ~2.7 and 1.7 eV respectively, and direct band gap in Se at ~2.3 eV for. The existence of indirect band gap in $CuSe_2$ on this value, somehow wider then in literature, is confirmed by photoluminescence measurements. A band

at ~1.8 eV, registered by PL measurements at low temperatures, is attributed to defect level of selenium-negative U-center. In this paper we proved that simple and low-cost technique as vacuum evaporation is capable of producing a high-quality thin films.

Acknowledgments This work was supported by Serbian Ministry of Education, Science and Technological Development under Project III45003.

References

1. M. Gilic, J. Trajic, N. Romcevic, M. Romcevic, D. Timotijevic, G. Stanisic, I. Yahia, Optical properties of CdS thin films. Opt. Mat. **35**, 1112–1117 (2013)
2. N. Romcevic, M. Petrovic-Damjanovic, M. Romcevic, M. Gilic, L. Klopotowski, W. Dobrowolski, J. Kossut, I. Jankovic, M. Comor, Magnetic field influence on optical properties of $Cd_{1-x}Mn_xS$ (x = 0; 0.3) quantum dots: Photoluminescence study. J. Alloy. Comp. **553**, 75–78 (2013)
3. M. Gilic, N. Romcevic, M. Romcevic, D. Stojanovic, R. Kostic, J. Trajic, W. Dobrowolski, G. Karczewski, R. Galazka, Optical properties of CdTe/ZnTe self-assembled quantum dots: Raman and Photoluminescence spectroscopy. J. Alloy. Comp. **579**, 330–335 (2013)
4. M. Rabasovic, D. Sevic, J. Krizan, M. Rabasovic, S. Savic-Sevic, M. Mitric, M. Petrovic, M. Gilic, N. Romcevic, Structural properties and luminescence kinetics of white nanophosphor YAG:Dy. Opt. Mat. **50**, 250–255 (2015)
5. B. Hadzic, N. Romcevic, M. Romcevic, I. Kuryliszin-Kudelska, W. Dobrowolski, M. Gilic, M. Petrovic Damjanovic, J. Trajic, U. Narkiewicz, D. Sibera, Raman study of surface optical phonons in ZnO(Co) nanoparticles prepared by calcination method. J. Optoelectron. Adv. Mat. **16**, 508–512 (2014)
6. M. Petrović, N. Romčević, M. Romčević, G. Stanišić, D. Vasiljević-Radović, J. Trajić, Z. Lazarević, S. Kostić, Spectroscopy characterization of MnSe nanoclasters randomly distributed in HgMnTe single crystal. J. Crystal Growth **338**, 75–79 (2012)
7. R.D. Heyding, The copper/selenium system. Can. J. Chem. **44**, 1233–1236 (1966)
8. S. Gosavi, N. Deshpande, Y. Gudage, R. Sharma, Physical, optical and electrical properties of copper selenide (CuSe) thin films deposited by solution growth technique at room temperature. J. Alloy. Comp. **448**, 334–338 (2008)
9. P. Hankare, A. Khomane, P. Chate, K. Rathad, K. Garadkar, Preparation of copper selenide thin films by simple chemical route at low temperature and their characterization. J. Alloy. Comp. **469**, 478–482 (2009)
10. V.J. Fulari, V.P. Malekar, S.A. Gangawane, Measurement of properties of copper telluride thin films using holography. Prog. Electromagn. Res. C **12**, 53–64 (2010)
11. H.M. Pathan, C.D. Lokhande, D.P. Amalnerkar, T. Seth, Modified chemical deposition and physicochemical properties of copper (I) selenide thin films. Appl. Surf. Sci. **211**, 48–56 (2003)
12. Y. Takana, N. Uchiyama, S. Ogawa, N. Mori, Y. Kimishima, S. Arisawa, A. Ishii, T. Hatano, K. Togano, Superconducting properties of $CuS_{2-x}Se_x$ under high pressure. Phys. C **341**, 739–740 (2000)
13. G. Krill, P. Panissod, M.F. Lapierre, F. Gautier, C. Robert, M.N. Eddine, Magnetic properties and phase transitions of the metallic CuX_2 dichalcogenides (X = S, Se, Te) with pyrite structure. J. Phys. C **9**, 1521–1533 (1976)
14. M. Kontani, T. Tutui, T. Moriwaka, T. Mizukoshi, Specific heat and NMR studies on the pyrite-type superconductors CuS_2 and $CuSe_2$. Phys. B **284**, 675–676 (2000)

15. V. Garcia, P. Nair, M. Nair, Copper selenide thin films by chemical bath deposition. J. Cryst. Growth **203**, 113–124 (1999)
16. A. Sobhani, M. Salavati-Niasari, A new simple route for the preparation of nanosized copper selenides under different conditions. Ceram. Inter. **40**, 8173–8182 (2014)
17. P. Peranantham, Y. Jeyachandran, C. Viswanathan, N. Praveena, P. Chitra, D. Mangalaraj, S. K. Narayandass, The effect of annealing on vacuum-evaporated copper selenide and indium telluride thin films. Mater. Charact. **58**, 756–764 (2007)
18. H. Okimura, T. Matsumae, Electrical properties of $Cu_{2-x}Se$ thin films and their application for solar cells. Thin Solid Films **71**, 53–59 (1980)
19. G.G. Rusu, M. Rusu, M. Girtan, Optical characterization of vacuum evaporated CdZnTe thin films deposited by a multilayer method. Vacuum **81**, 1476–1482 (2007)
20. A.M. Hermman, L. Fabick, Research on polycrystalline thin-film photovoltaic devices. J. Crys. Growth **61**, 658–664 (1983)
21. D.J. Chakrabarti, D.E. Laughlin, The Cu-Se (Copper-Selenium) System. Bull. Alloy Phase Diagrams **2**, 305–315 (1981)
22. P. Cherin, P. Unger, The crystal structure of trigonal selenium locality: synthetic. Inorg. Chem. **6**, 1589–1591 (1967)
23. G. Gattow, Z. Arong, Allg. Chem. **340** (1965) (Calculated from ICSD using POWD-12++, 1997)
24. G. Lucovsky, A. Mooradian, W. Taylor, G.B. Wright, R.C. Keezer, Identification of the fundamental vibrational modes of trigonal, α-monoclinic and amorphous selenium. Solid State Commun. **5**, 113–117 (1967)
25. M.P. Chamberlain, C. Trallero-Giner, M. Cardona, Theory of one-phonon Raman scattering in semiconductor microcrystallites. Phys. Rev. B **51**, 1680–1693 (1995)
26. R. Roca, C. Trallero-Giner, M. Cardona, Polar optical vibrational modes in quantum dots. Phys. Rev. B **49**, 13704–13711 (1994)
27. E. Duval, Far-infrared and Raman vibrational transitions of a solid sphere: selection rules. Phys. Rev. B **46**, 5795–5797 (1992)
28. C. Trallero-Giner, A. Debernardi, M. Cardona, E. Menendez-Proupin, A.I. Ekimov, Optical vibrons in CdSe dots and dispersion relation of the bulk material. Phys. Rev. B **57**, 4664–4669 (1998)
29. J. Trajic, R. Kostic, N. Romčević, M. Romčević, M. Mitric, V. Lazovic, P. Balaz, D. Stojanovic, Raman spectroscopy of ZnS quantum dots. J. Alloy. Comp. **637**, 401–406 (2015)
30. C. Sourisseau, R. Cavagnat, M. Fouassier, The vibrational properties and valence force fields of FeS_2, RuS_2 Pyrites and FeS_2 Marcasite. J. Phys. Chem. Solids, **52**, 537–544 (1991)
31. X. Wu, M. Kanzaki, S. Qin, G. Steinle-Neumann, L. Dubrovinsky, Structural study of FeP_2 at high pressure. High Press. Res. **29**, 235–244 (2009)
32. K. Karkkainen, A. Saviola, K. Nikoskinen, in *IEEE Transaction on Geosciences and Remote Sensors*, vol. 39, pp. 1013–1018 (2001)
33. M. Gilic, M. Petrovic, R. Kostic, D. Stojanovic, T. Barudzija, M. Mitric, N. Romcevic, U. Ralevic, J. Trajic, M. Romcevic, I. Yahia, Structural and optical properties of $CuSe_2$ nanoparticles formed in thin solid Cu-Se film. Infrared Phys. Technol. **76**, 276–284 (2015)
34. J. Trajic, M. Gilic, N. Romcevic, M. Romcevic, G. Stanisic, Z. Lazarevic, D. Joksimovic, I. Yahia, Far-infrared investigations of the surface modes in CdS thin films. Phys. Scr. **T162**, 014031–014034 (2014)
35. J. Trajić, N. Romčević, M. Gilić, M. Petrović Damjanović, M. Romčević, V.N. Nikiforov, Optical properties of PbTe0.95S0.05 single crystal at different temperatures: far-infrared study. J. Optoelectron. Adv. Mat. **6**, 543–546 (2012)
36. R. Kostić, M. Petrović-Damjanović, N. Romčević, M. Romčević, D. Stojanović, M. Čomor, Far-infrared spectroscopy of $Cd_{1-x}Mn_xS$ quantum dots. J. Alloy. Comp. **521**, 134–140 (2012)
37. J.C.M. Garnett, Colours in metal glasses and in metallic films. Trans. R. Soc. CCIII, 385–420 (1904)

38. A. Saviola, I. Lindell, in *PIER 6 Progress in Electromagnetic Research*. Dielectric properties of heterogeneous materials (Amsterdam, Elsevier), pp. 101–51
39. J. Tauc, R. Grigorovici, A. Vancu, Optical properties and electronic structure of amorphous Germanium. Phys. Status Solidi **15**, 627 (1966)
40. J. Tauc, F. Abeles, in *Optical Properties of Solids* (North Holland, 1972)
41. E. Davis, N. Mott, Conduction in non-crystalline systems V. Conductivity, optical absorption and photoconductivity in amorphous semiconductors. Phil. Mag. **22**, 903–922 (1970)
42. P. Kubelka, F. Munk, Ein Beitrag zur Optik der Farbanstriche. Z. Tech. Phys. **12**, 593–601 (1931)
43. R. Bari, V. Ganesan, S. Potadar, L. Patil, Structural, optical and electrical properties of chemically deposited copper selenide films. Bull. Mater. Sci. **32**, 37–42 (2009)
44. I. Grozdanov, Electroconductive copper selenide films on transparent polyester sheets. Synth. Metals. **63**, 213 (1994)
45. G. Sakr, I. Yahia, M. Fadel, S. Fouad, N. Romcevic, Optical spectroscopy, optical conductivity, dielectric properties and new methods for determining the gap states of CuSe thin films. J. Alloy. Comp. **507**, 557–562 (2010)
46. D. Rajesh, R. Chandrakanth, C. Sunandana, Annealing effects on the properties of copper selenide thin films for thermoelectric applications. J. Appl. Phys. **4**, 65–69 (2013)
47. V.M. Bhuse, P.P. Hankare, K.M. Garadkar, A.S. Khomane, A simple, convenient, low temperature route to grow polycrystalline copper selenide thin films. Mater. Chem. Phys. **80**, 82–87 (2003)
48. G. Hodes, A. Albu-Yayor, F. Decker, P. Motisuke, High thin-film yield achieved at small substrate separation in chemical bath deposition of semiconductor thin films. Phys. Rev. B **36**, 4215–4219 (1987)
49. V. García, M. Nair, P. Nair, R. Zingaro, Chemical deposition of bismuth selenide thin films using N,N-dimethylselenourea. Semicond. Sci. Technol. **12**, 645–649 (1997)
50. S. Kasap, J.B. Frey, G. Belev, O. Tousignant, H. Mani, L. Laperriere, A. Reznik, J.A. Rowlands, Amorphous selenium and its alloys from early xeroradiography to high resolution X-ray image detectors and ultrasensitive imaging tubes. Phys. Status Solid **246**, 1794–1801 (2009)
51. M. Benkhedir, Defect levels in amorphous selenium bandgap. Katholieke Universiteit Leuven PhD Thesis (2006)
52. M. Singh, K. Bhahada, Y. Vijay, Optical band gap of $In_{0.1}Bi_{1.9}Te_3$ thin films. Indian J. Pure Appl. Phys. **43**, 129–135 (2005)
53. F.B. Li, H.Z. Li, Photocatalytic properties of gold/gold ion-modified titanium dioxide for wastewater treatment. Appl. Catal. A **228**, 15–23 (2002)
54. C.H. Shen, H.Y. Chen, H.-W. Lin, S. Gwo, A.A. Klochikhin, V.Y. Davydov, Structure and photoluminescence properties of epitaxially oriented GaN nanorods grown on Si (111) by plasma-assisted molecular-beam epitaxy. Appl. Phys. Lett. **88**, 253104–253112 (2006)
55. P. Wei, S. Chattopadhyay, F. Lin, C. Hsu, S. Jou, J. Chen, P. Huang, H. Hsu, H. Shih, K. Chen, L. Chen, Origin of the anomalous temperature evolution of Photoluminescence peak energy in degenerate InN nanocolumns. Opt. Express. **17**, 1160–11697 (2009)

2017 IEEE 30th INTERNATIONAL CONFERENCE ON MICROELECTRONICS

PROCEEDINGS

Niš, Serbia
October 9th-11th, 2017

organized by
IEEE Serbia and Montenegro Section - ED/SSC Chapter

in cooperation with
Serbian Academy of Science and Arts - Branch in Niš
Faculty of Electronic Engineering, University of Niš

under the co-sponsorship of
IEEE Electron Devices Society

under the auspices of
Serbian Ministry of Education, Science and Technological Development
Academy of Engineering Sciences of Serbia
Society for ETRAN

IEEE Catalog No. CFP17432-USB
ISBN 978-1-5386-2562-0

Characterization of Yttrium Orthoferrite ($YFeO_3$) Nanoparticles as Humidity Sensor Materials at Room Temperature

D.L. Sekulic, Z. Lazarevic, C. Jovalekic and N. Romcevic

Abstract - In the recent years more and more attention has been directed to the study of potential application of ferrite nanoparticles as the humidity sensing materials. In this paper, we reports the humidity sensing characteristics of yttrium orthoferrite ($YFeO_3$) nanoparticles synthesized by a mechanochemical route from mixture of Y_2O_3 and α–Fe_2O_3 powders in a planetary ball mill. Structural analysis of ultrafine $YFeO_3$ nanoparticles with an average size of about 12.4 nm was performed by means of SEM and X–ray diffraction measurements. The electrical measurements were made in the frequency range 100 Hz to 5 MHz. The dependence of impedance response on the relative humidity has been also examined. The relative humidity was generated is in the range from 15% RH to 85% RH at room temperature. Under these conditions, the linear response in the entire relative humidity range was observed at relatively low measurement frequency i.e. at 5 kHz. Good repeatability and stability was also observed.

I. Introduction

Nanostructured ferrite materials as semiconductors have always attracted lots of attention due to their unique set of physical properties which may be used for wide range of the technological applications. In recent years ferrite nanoparticles are being increasingly recognized as a prerequisite for obtaining high humidity sensitivity for the fabrication of humidity sensors [1]. Humidity sensors based on ferrite nanomaterials have certain advantages compared to other types of humidity sensors, such as the chemical and thermal high stability, low cost, simple construction and small size [2]. Basically, these sensors can detect humidity on the principle of measuring a change in the electrical properties (resistivity, permittivity or general impedance) by water vapor adsorption and by their penetration through the open pores throughout the material, resulting significant changes in their electrical characteristics [3]. For this purpose, ferrite nanoparticles are very suitable materials because of their high specific surface area and high resistivity which can significantly decrease when the surrounding humidity increases [4].

Dalibor L. Sekulic is with the Faculty of Technical Sciences, University of Novi Sad, Trg Dositeja Obradovica 6, 21000 Novi Sad, Serbia, E–mail: dalsek@uns.ac.rs

Z. Lazarevic, and N. Romcevic are with the Institute of Physics, University of Belgrade, Pregrevica 118, 11000 Belgrade, Serbia, E–mails: lzorica@ipb.ac.rs, and romcevi@ipb.ac.rs

C. Jovalekic is with the Institute for Multidisciplinary Research, University of Belgrade, Kneza Viseslava 1, 11030 Belgrade, Serbia, E–mail: jovalek@imsi.rs

As one of four types of the ferrite crystal structure, orthoferrites have been extensively studied from fundamental and technical points of view due to their specific combination of electric, magnetic and optic properties allowing the design of multifunctional devices. In general, the orthoferrites represented by chemical formula $RFeO_3$ (where R is normally a rare earth ion) crystallize in an orthorhombic distorted perovskite structure with the *Pnma* space group [5]. Yttrium orthoferrite ($YFeO_3$), as a typical member of orthoferrite family, has been extensively studied because of interesting physical and chemical properties which result from their ionic and electronic defects [6]. However, the synthesis of single phase $YFeO_3$ has been reported to be a difficult task due to the preferred formation of secondary phases like $Y_3Fe_5O_{12}$ and Fe_3O_4 [7], probably arising from its thermodynamic instability. Attempts towards improving the technological performance of yttrium orthoferrite have led to the development of various techniques for their synthesis such as sol–gel, coprecipitation, low temperature hydrothermal technique, simple solution method and others.

With the aim to provide valuable information both from the viewpoint of fundamental scientific interest and its potential application to various nanodevices, we have carried out a study about electrical properties of mechano-chemical synthesized $YFeO_3$ nanoparticles over a wide range of frequencies at room temperature. The dependence of impedance response of yttrium orthoferrite nanoparticles on the relative humidity has been examined. The results show that these ultrafine nanoparticles can be proposed as promising material for humidity sensing devices.

II. Experimental details

A. Synthesis

$YFeO_3$ nanoparticles were synthesized by means of mechanochemical processing using mixtures of high–purity precursors: yttrium (II) oxide (Y_2O_3, Alfa Aesar 99.9% purity) and hematite (α–Fe_2O_3, Merck 99% purity) in equimolar ratio. Mechanochemical synthesis was carried out by planetary ball mill (Fritsch Pulverisette 5) in air atmosphere for 2.5 h. The required milling time for obtaining single–phase yttrium orthoferrite nanoparticles was determined experimentally by X–ray diffraction technique. Using a cold isostatic press, synthesized ultrafine

978-1-5386-2562-0/17/$31.00 ©2017 IEEE

$YFeO_3$ powders were pressed into circular disc shaped pellet with a diameter of 10 mm and a thickness of 1.5 mm and as such it was used for further testing.

B. Characterization

The crystalline structure and phase purity evaluation were carried out applying X–ray diffraction (XRD, Model Philips PW 1050 diffractometer) at room temperature. For structural analysis of the prepared samples, XRD data were collected using CoKα radiation (λ = 1.78897 Å) in a wide range of Bragg's angles 2θ ($10° \leq 2\theta \leq 80°$) with a scanning step size of 0.01° in a 10 s per step of counting time. The particle size and morphology of the product was examined by means of scanning electron microscopy (SEM, Model JEOL JSM–6460LV).

The electrical and dielectric properties of synthesized $YFeO_3$ nanoparticles were studied over a wide frequency range of 100 Hz to 5 MHz at room temperature using a computer–controlled Impedance Analyzer HP–4194A with a laboratory set of temperature control equipment. To perform these measurements, the surfaces of pellet were polished properly and electrodes were formed by high purity silver paste deposited on opposite sides of the pellets, which were cured for 48 h, thus forming parallel plate capacitor geometry with ferrite material as the dielectric medium.

For the humidity sensing measurements, $YFeO_3$ orthoferrite pellet as sensor element was placed in a closed test glass chamber between two silver electrodes which are connected to the Impedance Analyzer HP–4194A to measure the change in impedance with respect to relative humidity at 27°C ± 1°C. The compressed air directed into the chamber was firstly dehydrated over silica gel and $CaCl_2$ and then humidity level was varied from 15% to 85% by bubbling air through water and mixing it with dry air. In such measurement system, relative humidity and temperature were monitored by a commercial humidity and temperature probe (Tecpel DTM–321).

III. Results and Discussion

A. Structure analysis

The room temperature X–ray diffraction pattern of the as–synthesized $YFeO_3$ nanoparticles is presented in Fig. 1. The XRD results confirm the formation of orthorhombic distorted perovskite structure with *Pnma* space group (PDF#39–1489). There was no evidence of the presence of secondary phase indicating the high quality and single phase of yttrium orthoferrite nanoparticles prepared by mechanochemical processing in a planetary ball mill after 2.5 hours of milling. The existence of broad peaks in the XRD pattern can be attributed to the ultrafine nature and small crystallite size of the particles [8]. From the full width at half maximum of the most intense line (121) in the

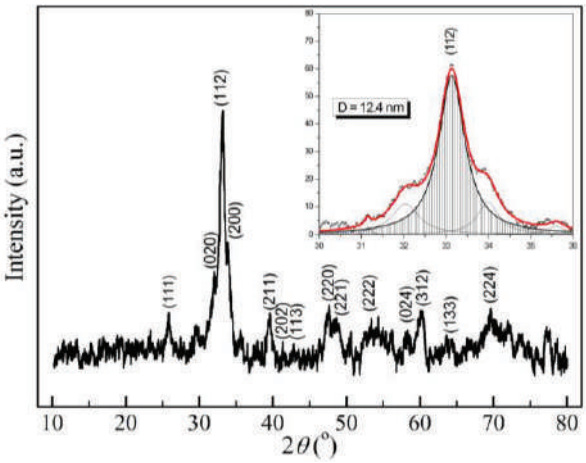

Fig. 1. The room temperature X–ray diffraction pattern of the as–synthesized $YFeO_3$ nanoparticles.

XRD spectra and by using the well–known Scherrer's equation [8], the average crystallite size of prepared $YFeO_3$ nanoparticles was estimated to be 12.4 nm

The room temperature SEM image of prepared $YFeO_3$ nanoparticles is shown in Fig 2. The microstructural analysis shows that the synthesized nanopowder contains the particles (crystallite) with almost regular spherical morphology. It was also found that these nearly spherical nanoparticles have a narrow size distribution between 5 and 30 nm which is in good agreement with results of X–ray structure analyse.

B. Electrical conductivity and dielectric constant

Frequency dependence of AC electrical conductivity σ_{AC} (i.e. conductivity spectrum) for prepared $YFeO_3$ nanoparticles at room temperature is shown in Fig. 3. It is clear from this plot that the electrical conductivity shows an increasing trend as the frequency increases, which is a general behavior of ferrite materials. Namely, the conductivity spectrum of yttrium orthoferrite nanoparticles shows two distinct regimes in the studied frequency range. At low frequency the conductivity is almost independent of the frequency and can be ascribed to DC conductivity,

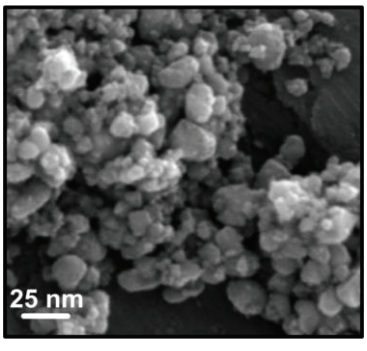

Fig. 2. SEM image of prepared $YFeO_3$ nanoparticles.

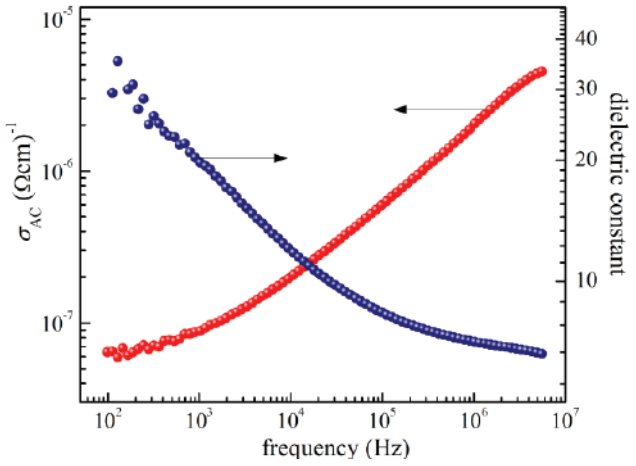

Fig. 3. Frequency dependence of AC electrical conductivity and dielectric constant for $YFeO_3$ nanoparticles at room temperature.

whereas AC conductivity exhibits dispersion in power law fashion at higher frequencies [9]. At room temperature, the AC conductivity at 1 kHz is of the order of 7×10^{-8} Scm^{-1} indicating high resistance which is very desirable property for humidity sensing application [4]. The low value of conductivity can be attributed to nanosize of $YFeO_3$ particles considering that ferrite materials with smaller particles consist of more number of grain boundaries which act as barriers to the flow of electrons [10].

The effect of applied field frequency on the relative dielectric constant of the prepared $YFeO_3$ nanoparticles at room temperature is also represented in Fig 3. As a general trend, the dielectric constant of sample decreases with increase in frequency showing a more significant dispersion in low frequency region. Such behavior can be explained based on the fact that the dielectric constant, in general, is directly related to the dielectric polarization [9]. In as–prepared $YFeO_3$ nanoparticles, there is a finite contribution from surface polarization which gives initial higher values of dielectric constant that fall rapidly with frequency as it cannot follow the applied frequency. At frequencies higher than 500 kHz, very small decrease in the dielectric constant value can be attributed to the atomic and electronic polarizations that are almost independent of frequency [8].

C. Humidity sensing properties

In order to study the humidity sensing performance, the impedance Z of fabricated YFeO3 nanoparticles was measured as a function of relative humidity (RH) at different frequencies and room temperature (27°C). In the RH range between 15% and 85%, the obtained results are depicted in Fig. 4. The linear response in the entire RH range was observed at relatively low measurement frequency. Namely, linear fit $\log Z(\Omega) = 7.746 - 0.033\times\mathrm{RH}$, $R^2 = 0.9983$(R^2 represents the correlation coefficient) to the experimental data at 5 kHz indicates the good quality of fit and high linear response. At this frequency, the impedance changes by two orders of magnitude from 1.74×10^7 Ω to 9.12×10^4 Ω as relative humidity increases from 15% to 85%. This significant decrease in impedance value with RH can be attributed to the adsorption of water molecules onto the surface of YFeO3 nanoparticles [11]. At high measurement frequency (i.e. 50 kHz), the impedance plot becomes flat since the adsorbed water molecules are not polarized due to the rapid change in the direction of the applied electric field at higher frequency.

Humidity hysteresis is one of the most important characteristics which is defined as the maximum difference between the adsorption and desorption curves. The hysteresis curve in Fig. 5 shows the process of adsorption and desorption at room temperature. As can be seen, the sensing curves for the humidification and desiccation processes almost overlap with each other showing very small hysteresis. Humidity hysteresis error was determined using well–known expression $\pm\Delta RH_{max}/(2F_{FS})$ [12], where

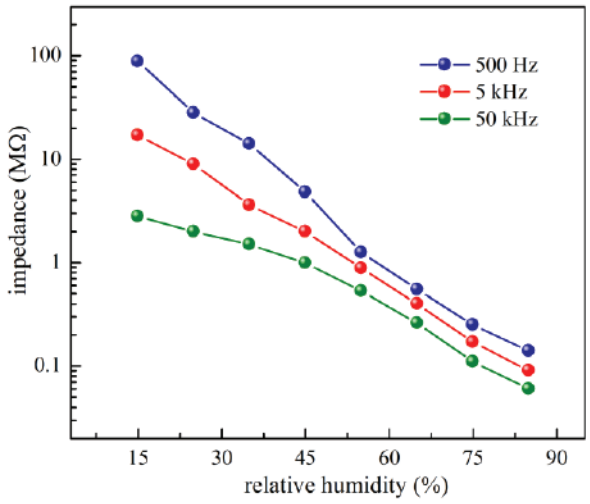

Fig. 4. Relative humidity dependence of impedance of $YFeO_3$ nanoparticles at various frequencies and room temperature.

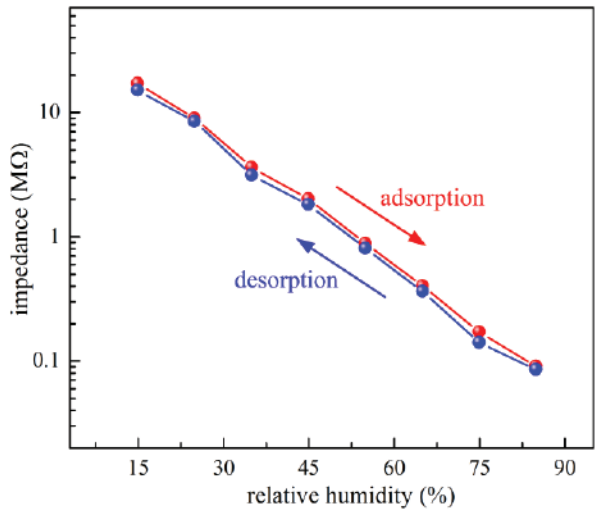

Fig. 5. Humidity hysteresis at 5 kHz nad room temperature.

where ΔRH_{max} is the difference in output for the process of adsorption and desorption and F_{FS} is the full scale output. The hysteresis error was calculated to be 1.9% indicating a good reliability.

The stability is also important parameter of humidity–sensing properties. The prepared YFeO3 nanoparticle pallet was tested repeatedly once in two days under fixed humidity levels (15%, 35%, 55%, and 75% RH) at 5 kHz in a period of 10 days. As shown in Fig. 6, there are slight fluctuations in the impedances with time, which directly confirm the good stability.

IV. Conclusion

In summary, low cost $YFeO_3$ nanoparticles with an average size of about 12 nm were successfully synthesized by a mechanochemical treatment of high–purity initial precursors. The electrical measurement results show that prepared yttrium orthoferrite nanoparticles possess a low conductivity value and usual value of a dielectric constant. With increasing frequency, these parameters show normal behaviour of ferrite materials at room temperature. For the first time the humidity sensing properties of fabricated $YFeO_3$ nanoparticles were also evaluated in the relative humidity range between 15% and 85% at room temperature. These ultrafine nanoparticles exhibit good humidity sensing characteristics such as high linearity and response, hysteresis within 2%, good repeatability, stability and broad range of operation (15–85% RH). Therefore, yttrium orthoferrite nanoparticles are quite promising material for the fabrication of a humidity sensor. Further research is also needed regarding the response and recovery time.

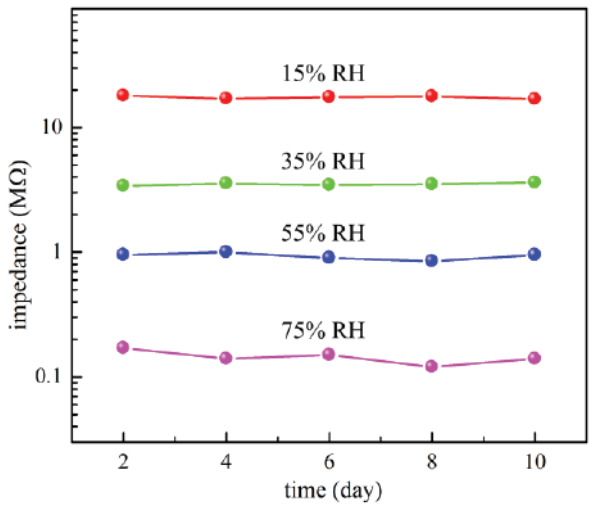

Fig. 6. Stability of response monitored at different humidity conditions for 10 days.

Acknowledgement

This research was financially supported by Ministry of Education, Science and Technological Development of the Republic of Serbia through Projects No. III43008 and III45003.

References

[1] Y. Koseoglu, I. Aldemir, F. Bayansal, S. Kahraman, and H. A. Cetinkara, "Synthesis, characterization and humidity sensing properties of $Mn_{0.2}Ni_{0.8}Fe_2O_4$ nanoparticles", *Materials Chemistry and Physics*, 2013, vol. 139, pp. 789–793.

[2] N. Rezlescu, C. Doroftei, E. Rezlescu, and P. D. Popa, "Structure and humidity sensitive electrical properties of the Sn^{4+} and/or Mo^{6+} substituted Mg ferrite", *Sensors and Actuators B: Chemical*, 2006, vol. 115, pp. 589–595.

[3] I. Petrila, and F. Tudorache, "Influence of partial substitution of Fe^{3+} with W^{3+} on the microstructure, humidity sensitivity, magnetic and electrical properties of barium hexaferrite", *Superlattices and Microstructures*, 2014, vol. 70, pp. 46–53.

[4] N. Bagum, M. A. Gafur, A. H. Bhuiyan, and D. K. Saha, "$MgCl_2$ doped $Cu_xZn_{1-x}Fe_2O_4$ ferrite humidity sensors", *Physica Status Solidi A*, 2010, vol. 207, pp. 986–992.

[5] J. L. Ye, C. C. Wang, W. Ni, and X. H. Sun, "Dielectric properties of $ErFeO_3$ ceramics over a broad temperature range", *Journal of Alloys and Compounds*, 2014, vol. 617, pp. 850–854.

[6] L. Wu, J. C. Yu, L. Zhang, X. Wang, and S. Li, "Selective self-propagating combustion synthesis of hexagonal and orthorhombic nanocrystalline yttrium iron oxide", *Journal of Solid State Chemistry*, 2004, vol. 177, pp. 3666–3674.

[7] A. V. Racu, D. H. Ursu, O. V. Kuliukova, C. Logofatu, A. Leca, and M. Miclau, "Direct low temperature hydrothermal synthesis of $YFeO_3$ microcrystals", *Materials Letters*, 2015, vol. 140, pp. 107–110.

[8] D. L. Sekulic, Z. Z. Lazarevic, M. V. Sataric, C. D. Jovalekic, and N. Z. Romcevic, "Temperature–dependent complex impedance, electrical conductivity and dielectric studies of MFe_2O_4 (M = Mn, Ni, Zn) ferrites prepared by sintering of mechanochemical synthesized nanopowders", *Journal of Materials Science: Materials in Electronics*, 2015, vol. 26, pp. 1291–1303.

[9] Z. Z. Lazarevic, C. Jovalekic, D. L. Sekulic, A. Milutinovic, S. Balos, M. Slankamenac, and N. Z. Romcevic, "Structural, electrical and dielectric properties of spinel nickel ferrite prepared by soft mechanochemical synthesis", *Materials Research Bulletin*, 2013, vol. 48, pp. 4368–4378.

[10] D. L. Sekulic, Z. Z. Lazarevic, C. D. Jovalekic , A. N. Milutinovic, and N. Z. Romcevic, "Impedance spectroscopy of nanocrystalline $MgFe_2O_4$ and $MnFe_2O_4$ ferrite ceramics: effect of grain boundaries on the electrical properties", *Science of Sintering*, 2016, vol. 48, pp. 17–28.

[11] V. R. Khadse, S. Thakur, K. R. Patil, and P. Patil, "Humidity–sensing studies of cerium oxide nanoparticles synthesizedby non-isothermal precipitation", *Sensors and Actuators B: Chemical*, 2014, vol. 203, pp. 229–238.

[12] D. Bauskar, B. B. Kale, and P. Patil, "Synthesis and humidity sensing properties of $ZnSnO_3$ cubic crystallites", *Sensors and Actuators B: Chemical*, 2012, vol. 161, pp. 396–400.

The Serbian Ceramic Society
Vinča Institute of Nuclear Sciences, University of Belgrade
Institute for Multidisciplinary Research, University of Belgrade
Institute of Physics, University of Belgrade

PROGRAM AND THE BOOK OF ABSTRACTS

1st Conference of the Serbian Ceramic Society

March 17-18. 2011.
Belgrade, Serbia
1CSCS-2011

Edited by:
Snežana Bošković
Zorica Branković
Jasmina Grbović Novaković

RHEOLOGICAL PROPERTIES OF AQUEOUS Al_2O_3 SUSPENSIONS

Marijo Lalić, Marijana Majić, Lidija Ćurković, Sara Salopek

Faculty of Mechanical Engineering and Naval Architecture, University of Zagreb, Croatia

The aim of the present work was to investigate rheological behavior of alumina suspensions, considering different amounts of polyvinyl alcohol as a binder. Three different aqueous suspensions were prepared, containing 60, 70 and 80 wt.% of alumina powder.

Spinel was added as a sintering agent and Darvan 821-A as a dispersant, in the amount of 0.08 and 0.4 wt.% of dry powder weight, respectively.

The alumina suspensions flow curves were recorded and fitted satisfactorily to the power law, Herschel-Bulkley and Bingham models.

Obtained results indicate that apparent viscosity of alumina suspensions increases with increasing Al_2O_3 and polyvinyl alcohol amount.

CHARACTERIZATION OF BARIUM BISMUTH TITANATE OBTAINED BY MECHANOCHEMICAL SYNTHESIS

Zorica Ž. Lazarević[1], Jelena D. Bobić[2], Nebojša Ž. Romčević[1], Biljana D. Stojanović[2]

[1]Institute of Physics, University of Belgrade, Belgrade, Serbia
[2]The Institute for Multidisciplinary Research, Belgrade, Serbia

Barium bismuth titanate, $BaBi_4Ti_4O_{15}$ (BBT) was prepared by homogenization and sintering of mixture of stoichiometric quantities of $BaTiO_3$ and $Bi_4Ti_3O_{12}$ obtained via mechanochemical synthesis. The reaction mechanism of $BaBi_4Ti_4O_{15}$ formation and the characteristics of BBT powders and ceramics were studied using XRD, Raman spectroscopy and SEM. The results confirmed that $BaBi_4Ti_4O_{15}$ was formed by tetragonal symmetry. Only 4 Raman modes are clearly observed. Ba^{2+} ions randomly occupy the Bi sites of a pseudo-perovskite layer and may enter in a bismuth oxide layer. $BaBi_4Ti_4O_{15}$ ceramics possess the plate-like structure typical for layered structure materials.

Fifteenth Annual Conference

YUCOMAT 2013

Hunguest Hotel Sun Resort Herceg Novi, Montenegro, September 2–6, 2013
http://www.mrs-serbia.org.rs

PROGRAMME &
THE BOOK OF ABSTRACTS

Organised by
MATERIALS RESEARCH SOCIETY OF SERBIA

under the auspices of
FEDERATION OF EUROPEAN MATERIALS SOCIETIES (FEMS)
MATERIALS RESEARCH SOCIETY (MRS)

P.S.B.24.

GROWTH AND SPECTROSCOPIC CHARACTERIZATION OF $Y_3Al_5O_{12}$ - YAG SINGLE CRYSTALS

Z.Ž. Lazarević, S. Kostić, N.Ž. Romčević
Institute of Physics, University of Belgrade, Zemun, Belgrade, Serbia

During the crystals growth process it is possible, according to the Czochralski`s method, to influence the shape of the liquid/solid interface through the growth parameters, such as both the growth and crystal rotation rate, as well as the temperature gradient. It also has a great effect on the growth mechanism affecting crystals characteristics. During the growth of $Y_3Al_5O_{12}$ - YAG crystals there appear faces on the liquid/solid interface parts parallel to facets (211) and (110). The mechanism of the crystals growth is different as the sections where faces appear and where they do not appear. These sections have various parameters of lattice causing strain in the crystals. Laser rods of high quality could be obtained by cutting crystals of a large diameter out of parts without strain. In our experimental work we found the conditions in which the facets scarcely appeared or are completely avoided. YAG single crystals were grown by the Czochralski technique under an argon atmosphere. The conditions for growing YAG single crystals were calculated by using a combination of Reynolds and Grashof numbers. The critical crystal diameter and the critical rate of rotation were calculated from the hydrodynamics of the melt. Raman and IR spectra of YAG single crystal were recorded in the range 50-1200 cm^{-1} and 40-4000 cm^{-1}, respectively. The obtained results were discussed and compared with published data.

INV2

Electrical and Dielectric Characterization of Nanostructural Ceramic Materials by Complex Impedance Spectroscopy

D. L. Sekulić[1], Z. Ž. Lazarević[2], N. Ž. Romčević[2]

[1]*Faculty of Technical Sciences, University of Novi Sad, Novi Sad, Serbia*
[2]*Institute of Physics, University of Belgrade, Belgrade, Serbia*

A complex impedance spectroscopy is a powerful technique to understand the electrical and dielectric behavior of ceramic materials, especially of ferroelectric materials such as ferrites. The concept microstructure is fundamental to ceramics and the link between microstructure and electrical properties is not always obvious or straightforward. The ability of this useful method to differentiate the transport characteristics of grains and the grain boundaries, two main components that comprise the microstructure, is very important in understanding the overall properties of ceramics. The measurement data can be analyzed in terms of electrical impedance, dielectric permittivity and electric modulus, which represent the same information expressed in various ways. Specifically, our results are discussed for four different nanostructured ferrite materials, MFe$_2$O$_4$ (M = Mn, Ni, Zn, Mg), obtained by soft mechanochemical synthesis. The experimental data equivalents to the real and imaginary parts of complex electrical quantities were measured as a function of the frequency of the applied electric field from 100 Hz to 40 MHz at several temperatures. The importance of choosing the correct and appropriate equivalent electrical circuit to represent the data is presented in the case of nanocrystalline ferrites, with their characteristic temperature-dependent capacitance.

INSTITUTE OF SENSOR AND
ACTUATOR SYSTEMS

10th European Conference on Magnetic Sensors and Actuators

EMSA 2014

Vienna, Austria

July 6-9, 2014

Book of Abstracts

Organized by:

Vienna University of Technology

Faculty of Electrical Engineering and Information Technology

Institute of Sensor and Actuator Systems

Volume Editor: Dr. Ioanna Giouroudi

Contact: Vienna University of Technology
Faculty of Electrical Engineering and Information Technology
Institute of Sensor and Actuator Systems
Department of Industrial Sensor Systems
Gusshausstrasse 27-29/366-ISS, 1040, Vienna, Austria
E-mail: ioanna.giouroudi@tuwien.ac.at
Tel: +43-1-58801-76691
Fax: +43-1-58801-36699

Printed by: Vienna University of Technology
Faculty of Electrical Engineering and Information Technology
Institute of Sensor and Actuator Systems
&
"Resch Druck", Thomas Resch e.U., Rosinagasse 19, A-1150 Vienna

ISBN: 978-3-85465-021-8
EAN: 9783854650218

TP26

Characterization of nanostructured Ni-ferrites as humidity sensor materials at room temperature

Dalibor L. Sekulic[1], Zorica Z. Lazarevic[2], Cedomir D. Jovalekic[3], Milos B. Zivanov[1], Nebojsa Z. Romcevic[2]

[1]Faculty of Technical Sciences, University of Novi Sad, Novi Sad, Serbia
[2]Institute of Physics, University of Belgrade, Belgrade, Serbia
[3]The Institute for Multidisciplinary Research, University of Belgrade, Belgrade, Serbia

In recent years nanostructured materials are being increasingly recognized as a prerequisite for obtaining high humidity sensitivity for the fabrication of humidity sensors [1, 2]. Using magnetic materials such as ferrites in humidity sensor applications require focusing mainly on their electrical properties rather than the magnetic properties [2, 3]. In this paper, humidity sensitivity of nanostructured Ni-ferrites synthesized by soft mechanochemical technique [4] from different mixtures of starting powders has been studied. Spinel structure of ferrite samples, sintered at 1100 °C for 2 h, was confirmed by X-ray diffraction analysis. Scanning electron microscopy was provided information related to the crystallite size and pores, which play an important role in determining the humidity sensitivity. Because sintered Ni-ferrites possess a porous structure, their electrical properties at different humidity conditions were characterized and analyzed. The relative humidity was generated is in the range from 15% RH to 85% RH at room temperature. Under these conditions, the significant variations of electrical resistivity and dielectric permittivity of present Ni-ferrites were observed. Such behavior suggests that these nanostructured ferrite materials can be the favorable choice for both capacitive and resistive humidity sensor applications. The sensitivity factor, response and recovery times were determined.

References

[1] Y. Koseoglu, I. Aldemir, F. Bayansal, S. Kahraman, H. A. Cetinkara, Synthesis, characterization and humidity sensing properties of $Mn_{0.2}Ni_{0.8}Fe_2O_4$ nanoparticles, *Materials Chemistry and Physics* 139 (2013) 789-793.
[2] C. Doroftei, P. D. Popa, F. Iacomi, Study of the influence of nickel ions substitutes in barium stannates used as humidity resistive sensors, *Sensors and Actuators A: Physical* 173 (2012) 24-29.
[3] I. Petrila, F. Tudorache, Humidity sensor applicative material based on copper-zinc-tungsten spinel ferrite, *Materials Letters* 108 (2013) 129-133.
[4] Z. Z. Lazarevic, C. Jovalekic, A. Milutinovic, D. Sekulic, V. N. Ivanovski, A. Recnik, B. Cekic, N. Z. Romcevic, Nanodimensional spinel $NiFe_2O_4$ and $ZnFe_2O_4$ ferrites prepared by soft mechanochemical synthesis, *Journal of Applied Physics* 113 (2013) 187221.

Acknowledgments: This research was financially supported by the Ministry of Education, Science and Technological Development of the Republic of Serbia through Projects No. III43008 and III45003.

Corresponding author: Dalibor L. Sekulic, Faculty of Technical Sciences, University of Novi Sad, Trg Dositeja Obradovića 6, Novi Sad, Serbia, Phone: +381 21 48 52 538; Fax: +381 21 47 50 572; E-mail: dalsek@uns.ac.rs.

ID-72

Study on Electrical and Dielectric Properties of Ni–Zn ferrite Nanoparticles Synthesized by Soft Mechanochemical Technique

Dalibor L. Sekulic[a], Zorica Z. Lazarevic[b], Cedomir D. Jovalekic[c],Milos B. Zivanov[a], Nebojsa Z. Romcevic[b]

[a]Faculty of Technical Sciences, University of Novi Sad, Novi Sad, Serbia

[b]Institute of Physics, University of Belgrade, Belgrade, Serbia

[c]The Institute for Multidisciplinary Research, University of Belgrade, Belgrade, Serbia

E-mail: dalsek@uns.ac.rs

Abstract

The electrical and dielectric properties of nanocrystalline Ni–Zn ferrite powders with average particle size 15 – 24 nm synthesized by a soft mechanochemical method have been studied as a function of frequency and temperature. Staring from mixture of high–purity Ni(II), Zn(II) and Fe(III) hydroxides, $Ni_{0.5}Zn_{0.5}Fe_2O_4$ nanoparticles have been successfully prepared in a planetary ball mill after 5 and 10 hours of milling. X-ray diffraction measurements and TEM study confirm the formation of cubic spinel structure and nano-dimensional nature of the prepared samples, respectively. It was found that the electrical dc resistivity decreases with increase in temperature and well obeys the Arrhenius law, indicating that the samples have semiconductor like behavior. The activation energy and drift mobility were evaluated from the temperature variation of dc resistivity. The experimental results reveal that dielectric constant and dielectric loss tangent decrease, whereas ac electrical conductivity increases with increasing frequency of the applied field. This normal behavior of dielectric properties and ac conductivity for ferrites is attributed to the Maxwell–Wagner type interfacial polarization in general and hopping mechanism of charge carriers between Fe^{2+} and Fe^{3+} ions at octahedral sites of the spinel lattice. Frequency dependent ac conductivity was analyzed by Jonscher's universal power law.

INV1

Electrical and Dielectric Characterization of $Zn_xNi_{1-x}Fe_2O_4$ Ferrite Ceramics Prepared by Sintering of Nanopowders

Dalibor L. Sekulić[1], Z. Ž. Lazarević[2], Č. Jovalekić[3], N. Ž. Romčević[2]
[1]*Faculty of Technical Sciences, University of Novi Sad, Novi Sad, Serbia*
[2]*Institute of Physics, University of Belgrade, Belgrade, Serbia*
[3]*The Institute for Multidisciplinary Research, University of Belgrade, Serbia*

Nanostructured $Zn_xNi_{1-x}Fe_2O_4$ (x= 0.0, 0.5 and 1) ferrite ceramics were successfully prepared by a conventional sintering of nanosized powders (10–25 nm), synthesized by soft mechanochemical treatment of high–purity Ni(II), Zn(II) and Fe(III) hydroxides as precursors. Electrical properties, such as DC resistivity as a function of temperature and AC conductivity as a function of frequency and temperature, were examined. The variation of DC resistivity with temperature well obeys the Arrhenius law, indicating semiconductor–like behavior of the prepared ferrites. The drift mobility was estimated from the DC resistivity data and found to increase with increasing temperature from ambient to 200°C. The experimental results reveal that AC electrical conductivity of all three samples increases with increasing frequency of the applied field from 100 Hz to 10 MHz. Analysis of the AC conductivity data by means of Jonscher's universal power law shows that correlated barrier hopping mechanism is the most probable mechanism of electrical conduction for $Zn_xNi_{1-x}Fe_2O_4$ ferrites. As part of a systematic study, dielectric constant and dielectric loss ($\tan\delta$) are also studied as a function of frequency and temperature. The dielectric behavior of ferrite ceramics can be explained by using the mechanism of polarization process, which is correlated to hopping of charge between Fe^{2+} and Fe^{3+} ions at octahedral sites of the spinel lattice.

INV2

Study of Nanodimensional Spinel $Ni_{0.5}Zn_{0.5}Fe_2O_4$ Ferrite Prepared by Mechanochemical Synthesis

Zorica Lazarević
Institute of Physics, University of Belgrade, Pregrevica 118, Zemun, Belgrade, Serbia

The nanodimensional $Ni_{0.5}Zn_{0.5}Fe_2O_4$ ferrites were prepared from mixture of $NiO/ZnO/\alpha\text{-}Fe_2O_3$ and $Ni(OH)_2/Zn(OH)_2/Fe(OH)_3$ powders by (soft) mechanochemical synthesis after 5 and 10 h of milling time. The XRD of the sample obtained after 10 h milling time shows single phase cubic spinel structure. TEM analysis revealed that all samples are composed of more or less agglomerated nanosize particles. The average size of nano crystallites is ~20 nm. The degree of the cation inversion of NZF is estimated for spinel fraction in all samples by Rietveld analysis. In the Raman and IR spectra are observed all of first-order active modes. In the spectra of the single phase "hydroxide" samples it is visible that the energy position and intensity of modes is dependent on the composition and cation distribution. It was shown that the modes in Raman spectra of nickel-zinc ferrite that originate from vibrating of different cations could be clearly distinguished. From the ratio of intensities

P14

Photocatalytic properties of Al_2O_3/ZnO coatings formed by plasma electrolytic oxidation on aluminum substrate

N. Tadić[1], A. Peleš[2], N. Radić[3], B. Stojadinović[4], B. Grbić[3], R. Vasilić[1], S. Stojadinović[1]
[1] *University of Belgrade, Faculty of Physics, Studentski trg 12-16, 11000 Belgrade, Serbia*
[2] *Institute of Technical Sciences SASA, Knez Mihailova 35/4, 11000 Belgrade, Serbia*
[3] *University of Belgrade, Institute of Chemistry, Technology and Metallurgy, Department of Catalysis and Chemical Engineering, Njegoševa 12, 11000 Belgrade, Serbia*
[4] *University of Belgrade, Institute of Physics, Pregrevica 118, 11080 Belgrade, Serbia*

Mixed Al_2O_3/ZnO coatings obtained by plasma electrolytic oxidation process (PEO) of aluminum in water solution boric acid and borax with addition ZnO nanoparticles. The oxide coatings were characterized by Scanning electron microscopy equipped with energy dispersive x-ray spectroscopy, x-ray diffraction, and Raman spectroscopy. It was found that chemical and phase compositions strongly depend on PEO time. It was shown that photocatalytic activity was improved by longer time of PEO process.

P15

Structural and optical properties of chemically deposited copper selenide thin films

M. Petrovic[1], M. Gilic[1], B. Hadzic[1], M. Romcevic[1], N. Romcevic[1], J. Trajic[1], Z. Lazarevic[1]
[1]*Institute of Physics, University of Belgrade, Pregrevica 118, Belgrade, Serbia*

Copper selenides are interesting metal chalcogenide semiconductor materials. They exist in many phases and structural forms: different stoichiometries such as CuSe (mineral klockmannite), Cu_2Se, Cu_2Se_x, $CuSe_2$ (mineral marcasite), á - Cu_2Se, Cu_3Se_2 (mineral umagnite), Cu_5Se_4 (mineral athabaskite), Cu_7Se_4 etc. as well with non - stoichiometric form such as $Cu_{2-x}Se$ (mineral berzelianite) and can be constructed into several crystallographic forms (monoclinic, cubic, tetragonal, hexagonal, etc.). Copper selenides in different stoichiometries are semiconductors with p - type conductivity, and have been widely used in optical filters, solar cells, photo detectors, supersonic materials…
The paper describes the structural and optical properties of copper selenide thin films. The films of tree different thicknesses (56.75, 79.74 and 172.70 nm) were grown by thermal evaporation on glass substrate, at room temperature and pressure better than 1 mPa. The surface morphology of thin films was investigated by atomic force microscopy (AFM). Formation of Cu - Se thin films is concluded to proceed unevenly, in the form of islands which later grew into agglomerates. The structural characterization of Cu - Se thin film was investigated using X - ray diffraction pattern. The presence of two - phase - system is observed. The first one is low - pressure modification of $CuSe_2$. The second phase is solid solution of Cu in Se. The Raman spectroscopy was used to identify and quantify the individual phases presented in the Cu - Se films. The results of Raman spectroscopy are in good agreement with XRD results, and the presence of two phases in our system, the trigonal Se and orthorhombic $CuSe_2$, is confirmed once again.

INV4

Electrical characterization of $YFeO_3$ nanoferrite and its potential application for humidity sensing

Dalibor L. Sekulić[1], Zorica Ž. Lazarević[2], Čedomir D. Jovalekić[3], Nebojša Ž. Romčević[2]
[1]University of Novi Sad, Faculty of Technical Sciences, Novi Sad, Serbia
[2]University of Belgrade, Institute of Physics, Belgrade, Serbia
[3] University of Belgrade, The Institute for Multidisciplinary Research, Belgrade, Serbia

Yttrium orthoferrite ($YFeO_3$) nanoparticles with an average size of about 12 nm were successfully synthesized by a mechanochemical treatment of high–purity yttrium(II) –oxide (Y_2O_3) and hematite (α–Fe_2O_3) as initial precursors. X–ray diffraction analysis of prepared $YFeO_3$ confirms the formation of the pure orthorhombic crystal structure and their nano–dimensional nature. The nature of variation of AC conductivity spectra with frequency of the applied electric field from 100 Hz to 10 MHz is found to obey Jonscher's universal power law at different temperatures from ambient to 190°C. In addition, detailed analysis of the AC conductivity data has shown that correlated barrier hopping (CBH) mechanism is the most probable mechanism of electrical conduction for $YFeO_3$ nanoparticles. The activation energy for electrical conduction has been calculated from the Arrhenius plot using the results of DC resistivity measurement. Detailed study of complex impedance and related parameters indicate that the synthesized nanoparticles exhibit semiconducting nature (NTCR–type behavior) and non–Debye type of relaxation phenomena. Further, analysis of impedance spectra by means of an equivalent circuit model revealed the presence of a single temperature dependent relaxation. Decrease in resistances and relaxation times with temperature confirms the involvement of thermally activated conduction mechanism in this material. In view of the analyses of dielectric properties, it was noticed the usual dielectric dispersion, which was explained in the light of Maxwell–Wagner theory of interfacial polarization in accordance with Koop's phenomenological theory. As part of a systematic study, the humidity sensing properties of fabricated $YFeO_3$ nanoparticles were also evaluated in the relative humidity range between 15% and 85% at room temperature. The results revealed that sample responds well to the humidity by showing the significant variations in DC electrical resistivity values. High sensitivity, linearity of the sensitivity characteristic and relatively quick response time recommend that this ferrite material can be the favorable choice for the realization of a very good resistive humidity sensor.

(MOS). Furthermore, the properties of these components used as switches will be analysed from the power consumption in stable states; switching times; and influence of parasitics point of view, for the first time. To achieve as realistic simulation results as possible the (SPICE) transistor models used here were obtained from the component producers.

OR3

The nonorthogonality effects on capacitive behaviour of quantum dot

Miloš S. Dražić, Ivana Đurišić, Viktor Z. Cerovski and Radomir Žikić
Institute of Physics, University of Belgrade, Pregrevica 118, Belgrade

It is known that the overlap between atomic orbitals produce nontrivial effects on chemical bonds strength, resonance molecular energies, sensitivity of bond orders and charge densities in hetero-molecules. It is also strongly involved in population analysis problem. In quantum transport through a molecule/quantum dot attached between two electrodes, numerical codes rely on some predefined nonorthogonal basis sets. In steady state transport nonorthogonality has no influence on final results for transmission or current. The situation significantly changes when we have to deal with time dependent transport where charge starts to pile up in central region consisting of a molecule with additional neighboring parts of electrodes, chosen in such a way to provides complete screening of a molecule. The nonorthogonality introduces a problem due to nonunique definition of time dependent partial charges associated with electrodes and central region, which is a consequence of nonorthogonality between complementary subspaces, making the corresponding projectors non-Hermitian. The problem is solved in nonequilibrium Green's functions formalism within linear response theory and the derived current expression clearly indicates that the occurrences of additional contributions on interfaces, compared with orthogonal description, can be associated with the displacement current. In a simple comparative analysis it is demonstrated that there is a frequency range around resonances where capacitive response is only due to nonorthogonality.

OR4

Spectroscopy Characterization of $YFeO_3$ Obtained by the Mechanochemically Synthesis

Zorica Ž. Lazarević[1], Čedomir Jovalekić[2], Dalibor Sekulić[3], Valentin N. Ivanovski[4], Ana Umićević[4], Martina Gilić[1], Nebojša Ž. Romčević[1]
[1]Institute of Physics, University of Belgrade, Pregrevica 118, Zemun, Belgrade, Serbia
[2]The Institute for Multidisciplinary Research, University of Belgrade, Belgrade, Serbia
[3]Faculty of Technical Sciences, University of Novi Sad, Novi Sad, Serbia
[4]Institute of Nuclear Sciences Vinča, University of Belgrade, Belgrade, Serbia

In the past few years, a renewed interest has grown in the study of rare-earth orthorhombic perovskites. An important example of this trend is the family of rare-earth orthoferrites, which a general formula $RFeO_3$, where R is the trivalent rare-earth metal ion. $YFeO_3$ has been prepared by a mechanochemical synthesis in a planetary ball mill. The mechanochemical reaction leading to formation of the $YFeO_3$ phase was followed by X-ray diffraction, Raman and infr-

arad spectroscopy. The ortoferrite phase formation was first observed after 1 h of milling and its formation was completed after 2.5 h. The synthesized $YFeO_3$ ferrite has a nanocrystalline structure with a crystallite size of about 12.4 nm. There are five Raman active modes. ^{57}Fe Mössbauer spectroscopy was performed in order to provide information on Fe compounds in the Y_2O_3 and α-Fe_2O_3 mixture.

OR5

Synthesis and structural characterization of some cathode materials for lithium-ion batteries

Dragana Jugović[1] and Miodrag Mitrić[2]
[1]Institute of Technical Sciences of SASA, Belgrade, Serbia
[2]Vinča Institute of Nuclear Sciences, University of Belgrade, Belgrade, Serbia

Lithium-ion batteries are under intense scrutiny as alternative energy/power sources. Their electrochemistry is based on intercalation/deintercalation reactions of lithium ions within a crystal structure of an electrode material. Therefore, the structure itself determines both the electrode operating voltage and the transport pathways for lithium ions. Some oxide- and polyanion-based materials are synthesized and studied as positive electrodes. Several synthetic routes were investigated. The crystal structure refinement of an X-ray powder diffraction data was based on the Rietveld full profile method. All relevant structural and microstructural crystal parameters that could be significant for electrochemical intercalation/deintercalation processes were determined. Structural analysis revealed different dimensionality of lithium ion motion. It was also shown that the structural and microstructural properties are significantly dependent on the synthesis condition.

OR6

Application of ceramic components in knee arthroplasties

Aleksandar Radunović MD,MMA,Belgrade, Serbia
Popović Zoran MD, PhD, Vožd clinic,Belgrade, Serbia
Aleksandar Jevtić MD, MMA, Belgrade ,Serbia

Total knee arthroplasty is considered as very reliable and efficient procedure with excellent good-therm results. Despite significant improvements in endoprosthesis design and materials for their fabrication, debris induced aseptic loosening of the endoprosthesis is, accompanied by the malpositioning of the components, most frequent cause of the need for revision surgery. Beside this problems, there is growing number of reports of metal allergy as possible causer of procedure failure. For above mentioned, ceramics with its properties attracts attention as a material for endoprosthesis manufacturing. After relatively bad results in the early years of use, followed by improvements in materials and design of endoprosthesis, ceramics look like a promising solution, especially for patients with allergies on metal.

P37

Highly efficient macroporous silica/iron oxide based adsorbent for arsenic removal

Slavko Mijatov[1], Jelena Rusmirović[2], Zlate Veličković[3],
Aleksandra Perić-Grujić[1], Aleksandar Marinković[1]
[1]Faculty of Technology and Metallurgy, University of Belgrade, Belgrade, Serbia
[2]Innovation center, Faculty of Technology and Metallurgy, University of Belgrade, Karnegijeva 4, Belgrade, Serbia
[3] Military Academy, 33 General Pavle Jurišić – Šturm street, Belgrade, Serbia

Synthesis of macroporous silica based adsorbent impregnated with hydrous iron oxide (goethite -GT) applicable for efficient arsenic removal is presented in this work. The synthesis procedure was conducted in two successive steps: first step includes introduction of amino active sites by silica surface modification with (3-aminopropyl)trimethoxysilane, while the second step includes precipitation of GT on the surface of the modified silica (SiO_2/GT). The effectiveness of introduction of amino groups on silica surface, as well as structures of synthesized adsorbent were confirmed by FTIR analysis. The crystal structure of GT was determined by X-ray diffraction (XRD). The results of textural parameters and surface properties (specific surface area and adsorbent porosity), determined by Brunauer–Emmett–Teller analysis, indicate higher surface area and moderate pore diameter for the adsorbent with GT, comparing to amino modified silica. Morphology parameters, such as shape and adsorbent particle size, were examined by scanning electron microscopy (SEM). The SiO_2/GT adsorbent has spherical shape with the mean diameter of 1–2 mm and highly porous surface. High arsenic removal capacity of 35.9 mg g^{-1} at 25 °C and optimal pH values of 6.6-7.4 indicates that this adsorbent is efficient and reusable for arsenic removal from natural water in the batch mode.

P38

The Bridgman method growth, spectroscopic characterization and photoluminescence of calcium fluoride single crystals

Zorica Ž. Lazarević[1], Hana Ibrahim Elswie[2, 3], Vesna Radojević[2],
Slobodanka Kostić[1], Maja Rabasović[1], Dragutin Šević[1], Nebojša Ž. Romčević[1]
[1]Institute of Physics, University of Belgrade, Pregrevica 118, Zemun, Belgrade, Serbia
[2]Faculty of Technology and Metallurgy, University of Belgrade, Belgrade, Serbia
[3]Faculty of Science, Tripoli University, Tripoli, Libya

Calcium fluoride - CaF_2 single crystals were grown using the Bridgman technique. By optimizing growth conditions, <111>-oriented CaF_2, crystals up to 20 mm in diameter were grown. Number of dislocations in CaF_2 crystals was 5×10^4 - 2×10^5 per cm^2. Selected CaF_2 single crystals is cut into several tile diamond saw. The plates were polished, first with the silicon carbide, then the paraffin oil, and finally with a diamond paste. The obtained crystals were studied by X-ray diffraction, Raman spectroscopy, far-IR reflectivity and by the measurement of trans-

mission in the mid IR-range. The crystal structure is confirmed by XRD. One Raman and two IR optical modes predicted by group theory are observed. In the transmission spectra, except modes originated from vibration of -CH_2 groups, hydroxyl groups -OH and KBr, is visible a peak at 671 cm^{-1} assigned to the Ca-F stretching vibrations. A low photoluminescence testifies that the concentration of oxygen defects within the host of CaF_2 is small. All performed investigations show that the obtained CaF_2 single crystal has good optical quality.

P39

Long-term monitoring of photocatalytic coating functional properties inreal environmental conditions

S. Vučetić[1], S. Markov[1], A. Vidaković[1], B. Miljević[1], H. Hiršenberger[2],
S. Pašalić[3] J. Ranogajec[1]
[1]University of Novi Sad, Faculty of Technology, Bul. Cara Lazara 1, 21000 Novi Sad, Serbia
[2] University of Novi Sad, Faculty of Technical Sciences,Novi Sad, Serbia
[3] University of Belgrade,"Vinča" Institute of Nuclear Sciences, Belgrade, Serbia

The work studies functional properties of a photocatalytic coating (TiO_2/Zn-Al) applied on the experimental wall inreal environmental conditions. It is possible to find several methods for photocatalytic activity assessment in laboratory conditions, but the methods for *insitu* measurements of photocatalytic activity can hardly be found in any publication.
Our study was conducted by using modern surface analysis (FTIR spectroscopy, DRIFT mode) and traditional microbiological techniques, in order to understand fungal colonization on the façades covered with a photocatalytic coating (previously developed and proved in laboratory as a good antifungal material). For this purpose, an experimental wall was build and covered with a commercial façade paint and (TiO2/Zn-Al) photocatalytic coating. In order to induce fungal growth, the autochthonous microorganisms (*Aspergillus niger* and *Cladosporium*sp.) were isolated from the vicinity of a wall and applied by spray technique on the experimental wall. The monitoring of the fungal growth and surface analysis was done during the period of 3 years.
The obtained results show good functional properties of the applied photocatalyticTiO2/Zn-Al coating. Furthermore, the results provedthe need for a long term monitoring of the coating functional properties in real environmental conditions in order to obtain measurable and valid values.

INV-BMS1

Characterization of Au-mercaptotriazole crystals using the spectroscopy methods

Silvana B. Dimitrijević[1], Z. Ž. Lazarević[2], S. P. Dimitrijević[3]

[1]Mining and Metallurgy Institute Bor, Zeleni bulevar 35, 19210 Bor, Serbia
[2]Institute of Physics, University of Belgrade, Pregrevica 118, Zemun, Belgrade, Serbia
[3]Innovation Center Faculty of Technology and Metallurgy, University of Belgrade, Belgrade, Serbia

At the Institute of Mining and Metallurgy Bor a completely new electrolyte based on gold complex with mercaptotriazole was synthesized in a wide pH range from acid to alkaline media (pH=2–12). Synthesis of the electrolyte for hard and decorative plating was developed and tested. In this investigation detailed characterization of the complex in liquid and solid state in the whole range of its stability was performed.

It was shown that the new electrolyte can be successfully used in electrolytic baths for hard and decorative plating. Contrary to the previous organics complexes of gold, it retained a sufficient stability in a period of at least three months. Electrochemical characteristics of mercaptotriazole gold complex at pH value of two and nine remained unchanged for a period of one year. In that period any visual changes did not appear. Based on detailed experimental investigations, it was concluded that the quality of decorative gold plating, obtained from a gold complex based on mercaptotrizole, satisfies all requirements of decorative gold plating. The most important advantage of this electrolyte is ecological, as the gold could be regenerated by simply settling with hydrogen peroxide in which the sulfur is precipitated. Infrared (IR) and Raman spectroscopy were used for the characterization of the crystals of gold complexes based on mercaptotrazole obtained from solutions with different pH values (2, 4, 7, and 9). The most important finding of IC/Raman spectroscopy analysis is that the Raman spectroscopy has provided a definitive confirmation of bond established between metal ion and sulfur atom. Also, both techniques indicated that the nitrogen atom in the ring of obtained Au-MT compound, remains protonated at pH = 9, which does not support an assumption formulated from the analysis of UV-spectra, that MT molecules at this pH may interact with the metal ion not only through the sulfur, but also through the nitrogen atom.

P3
Crystal of SR-Feldspar obtained by Rirtveld analysis

Ana S. Radosavljević-Mihajlović[1], Goran V. Janjic[2]

[1]*Institute for Technology of Nuclear and Other Mineral Raw Materials, P.O. Box 390, Franche d'Esperey Street 86, 11000 Belgrade, Serbia.*
[2] *Institute of Chemistry, Technology and Metallurgy, University of Belgrade, Njegoševa 12, P.O. Box 473, 11000 Belgrade, Serbia*

Monoclinic Sr feldspar has been prepared from Sr-LTA zeolite precursor.The crystal structures of Sr-feldspar are solved and refined using X-ray powder diffraction (XRPD) data by Rietveld method. The crystal structure of Sr-feldspar is refined in the space group *I*2/*c* and results indicate ordering distribution of Si and Al (unit cell parameters is a = 8.365, b = 12.944 c=14.229 Å and agreement factors: R_{exp}= 15.3 R_p=19.9, R_{wp}=19.0, R_B=15.0 R_F=4.08). The microsturcural parameters size and strain, are determine with two crystalographic program Breadth and Fullprof.

P4
Characterization of optical polymer composites based on single crystals

Hana Ibrahim Elswie[1, 2], Zorica Ž. Lazarević[3], Vesna Radojević[2]

[1]Faculty of Technology and Metallurgy, University of Belgrade, Belgrade, Serbia
[2]Faculty of Science, Tripoli University, Tripoli, Libya
[3]Institute of Physics, University of Belgrade, Pregrevica 118, Zemun, Belgrade, Serbia

In this work the possibility of synthesis of optical active composites with improved mechanical, thermal properties and functionality was investigated. Composites with a polymer matrix based on single crystals have great potential in the field of optical communication systems where active micro to nano crystals dispersed in an optically transparent matrix. Synthesis and characterization of nano to micro modified polymer composites on the basis of single crystal are performed. CaF_2 single crystals in diameter of 20 mm are obtained by the vertical Bridgman method in vacuum. Composite films PMMA-CaF_2 was obtained with preserved optical properties of single crystals, whereas the thermal and mechanical properties improved. Composite films PMMA-CaF_2 was obtained with preserved optical properties of single crystals, whereas the thermal and mechanical properties improved. For characterization composite films were used the following methods: DSC, Raman spectroscopy, FTIR and nanoindentation test. Results od DSC analysis for composite films PMMA-CaF_2 revealed that the thermal propertis od polymer was improved by embeding inorganic particles. T_g for composit was higher the for pure polymer. FTIR spectrum of composites there are well defined peaks for PMMA and some of the vibration modes of Ca–F bond at 671 cm^{-1}. This means that CaF_2 crystals in the composite have been identified and that no other bounds with PMMA were created during the processing. The Raman spectra of CaF_2 single crystal, PMMA and the composites revelaed all modes found are well matched with literatures. By addition of 1% and 2% CaF_2 crystals can be seen the peaks are the same as in the spectrum of PMMA. The intensity of these peaks in the composite is about 364, 481,

600, 812 and 964 cm^{-1}. It was also noted a sharp peak at 323 cm^{-1} which is characteristic of CaF_2. A weak band near 400 cm^{-1} in possibly be δ(C—O—C) in spectrum of the PMMA and the composites 1% and 2% CaF_2 with PMMA.

P5

Electrical properties of doped $BaTiO_3$ Ceramics

Miloš Đorđević[1], Vesna Paunović[1], Vojislav V.Mitić[1,2], Zoran Prijić[1], Miloš Marjanović[1]

[1]*University of Nis, Faculty of Electronic Engineering, Aleksandra Medvedeva 14, Niš, Serbia*
[2]*Institute of Technical Sciences of SASA, Belgrade, Serbia*

The electrical resistivity (ρ) and PTCR (Positive Temperature Coefficient of Resistivity) effect doped $BaTiO_3$ ceramics with different dopant were investigated in this paper, The content of additive in doped samples were ranged from 0.01 to 1.0 at% Er/Yb. The samples were prepared by a conventional solid state sintering procedure and sintered at 1320° for 4 hours. For samples doped with Er_2O_3 (0.01 at% Er/Yb), SEM analysis shows abnormal grain growth with the average size range between 20 μm - 40 μm. For samples doped with Yb_2O_3 the average size was from 30 μm - 50 μm. With increase of dopants concentration the average grain size decreases, and for samples doped with 1.0 at% Er/Yb, grain size range between 3 μm - 20 μm for samples doped with Er and between 1 μm - 10 μm for samples doped with Yb_2O_3. The specific electrical resistance were measured in temperature range from 25°C to 170°C at different frequencies, ranged from 100Hz to 1MHz. To a temperature of 120°C, resistance has a slight increase with increasing of temperature, but above this temperature the resistance rapidly increasing. The value of the specific electrical resistance decreases with increasing concentration of Er/Yb, reached the minimum at certain dopant content (0.5 at% Er/Yb), then increased rapidly with dopant content in high doping level.

P6

Application of Curcumin in Dye-Sensitized Solar Cells

Stefan Ilic, Vesna Paunović

[1]*University of Nis, Faculty of Electronic Engineering, Aleksandra Medvedeva 14, Niš, Serbia*

Dye-sensitized solar cells are the closest mankind has come to replicating nature's photosynthesis. The type of a dye influence the efficiency of these cells. In this paper we studied curcumin dye as sensitizer in dye-sensitized solar cells and compared him with mostly used cyanidin. The results have shown that curcumin has higher efficiency and higher absorption in the visible part of the spectrum compared to cyanidin. Model dye molecules, curcumin and cyanidin, are deprotonated upon adsorption on the titanium dioxide surface. The energy levels obtained from the calculation indicate a higher probability of electron transition from molecule to titanium dioxide surface in the case of curcumin than in the case of cyanidin. Based on these results, we concluded that curcumin dye has better properties as sensitizer in dye-sensitized solar cells.